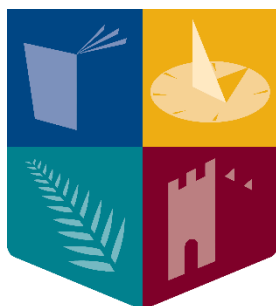# Responsive Synthetic Peptide Conjugates –
From Sensors to Peptidomimetics

Maynooth University
National University of Ireland Maynooth

A thesis submitted to Maynooth University in fulfilment of the requirements for the degree of

Doctor of Philosophy

By

Conor Wynne, B.Sc.

Department of Chemistry

Maynooth University

Maynooth

Co. Kildare, Ireland

January 2024

Research Supervisor: Dr. Robert Elmes

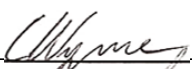**Head of Department: Prof. Denise Rooney**

Table of Contents

Declaration

I declare that the work presented in this thesis was carried out in accordance with the regulations of Maynooth University. The work is original, except where indicated by reference, and has not been submitted before, in whole or in part, to this or any other university for any other degree.

Signed: _____   Date: 26/01/2024

Conor Wynne, B.Sc. (Hons)

Acknowledgements

…Journey before Destination.

My supervisor, Dr Robert Elmes – The man, the myth, the Squaramide. The Elmes group has grown a lot since my joining in 2019, and I don't think it'll stop growing for some time yet. Indeed, the group – and the work we produce – is a reflection of your character, your determination, and your drive towards continuous improvement. However, this wouldn't be a *true* acknowledgment if it didn't include some well-deserved banter. Rob is the kind of supervisor that responds very rapidly to his students' questions. His favourite method of communication is the humble "thumbs up" emoji, adequately conveying his in-depth response to a paragraph-long enquiry. Even in his new faculty-level position, Rob is a researcher at heart. He is intimately invested in his research, and is not afraid to delegate *"quick little side-projects"* that span the course of 15 years…

In all seriousness, Rob, I would like to express my sincere gratitude, for your unwavering support, guidance, and invaluable insights throughout the entire journey of my doctoral research. Your mentorship has been instrumental in shaping the success of my scholarly pursuits and navigating the challenges that arose during my time as your PhD student. This is not the first acknowledgement section that has been dedicated to you, nor will it be the last. I wish you and your family all the best in the years to come, and I'm sure I'll see your name in lights (again) sometime soon. I will be keeping an eye out for that Angewandte Chemie.

I extend my appreciation to the technical staff (past and present) within the chemistry department, namely; Barbara, Karen, Ann, Orla, Sarah, Michelle, Maryanne, Carmel, Elaine, Ollie, Walter, and a special thanks to Noel – *The Fixer of Everything*™ – for your tireless efforts in creating a helpful and friendly research environment. I have purposely excluded a name from the above list, as I believe she deserves her own acknowledgement. Ria – a selfless beacon of kindness that none of us deserved. My last 4 years were merely a blip in your colossal 45-year career with the Chemistry Department… I was lucky to have you around.

Thank you for everything, and I hope retirement treats you well. I'm sure I'll see you around Maynooth walking the dogs, or bump into you in Dunnes. I would like to thank the academic staff for their insightful suggestions and friendly advice. I will also extend my fondest regards to the admin dream-team, Donna & Carol – the twin pillars of administrative prowess, of which the Chemistry Department would crack and splinter without.

To Sinéad, I must've been some dose to deal with these last few months, getting needlessly stressed over everything, but at the same time, stubbornly not wanting to take a break either. Thank you for tolerating my nonsense and being by my side. I deeply appreciate your never-ending encouragement, love, and support. You are the best!

To the people that passed through before me, specifically Drs Amanda, Harlie, and Steely, you remain MU Chemistry icons to this day. Thank you for your friendly advice when I joined the department as a 1st year postgrad. On that note, to Docteur Luke Marchetti. My mentor, my supervisor in leu, and fellow gamer. Most of my postgrad career was shaped by your insightful advice, whether it was how to use a certain piece of equipment, locating specific glassware, or analysing spectra. You were a wealth of knowledge and expertise that I was lucky to have.

The Elmes Group – the lads, the boys, the troublemakers, and my colleagues. I hope this message finds ye well, as ye ruthlessly disregard the rest of the document on your way to find this paragraph. To Gero, we started down this (seemingly never ending) path together 4 years ago, as true patrons of the Roost. We spent many late evenings in the lab working on our chemistry, always offering each other advice and suggestions. As luck would have it, we'll be finishing at the same time. It's been a pleasure lad; I'll be seeing you in the pharma sector. Luke B, even though you're the only *Luke* that remains upstairs now, I guess that nomenclature has stuck with me. Staying in academia is bad for your health, but someone's got to do it, and you'll do it well. I'm sure you'll grace my twitter feed again soon with another high-impact publication. Best of luck in Germany! Faz & Ste, the two lads who injected a new lease of laughter and camaraderie into the group when they joined together. Whether ye like it or not, ye're going to be the senior members of the group soon. Thanks for all the

good chats and banter, cheers boys. Thank you to past-members Ales and Hua, and best of luck to the new(er) additions Xuanyang, Emily, Jordan, and Lea.

To Eoin & Kyle, who also started at the same time as me 4 years ago. I'm going to pretend that I wasn't sickly jealous of ye completing yer Vivas while I was still writing my thesis. Well-earned lads, I'm sure our paths will cross again in the future. LHS members – Keela, Adam, and Darren. Thank you for making the synthesis lab a friendly and welcoming place, even when we RHS folk *forgot* to clean up after ourselves. Again, best of luck to the new LHS postgrads, Giulia, Rachel, Ciara, Oliwer, and Shane. Downstairs postgrads – to Colm & Caitlyn who have gone on to become academics in their own right, thank you for all the good laughs and friendship. Thank you to Andreea, Athira, and Joe for the tearoom craic and lunchtime gossip, and everyone else whom I've forgotten to include. Best of luck with the rest of your research!

To Fabian, Diana & Kelsey – The OG PharmaChem squad. We survived undergrad together, then ye went on to become rather successful adults… I'm finally starting to catch up. I was lucky to fall in with such a caring and determined bunch of people. We leaned on each other for support many a time, but in doing so, gently pushed one another to be better. Cheers for all the late-night drunkenly banter, and the holidays together. We definitely need another night out soon!

I'm nearly finished, I promise. To Julie and Dach who always look after me when I visit. To my cousin Tom, who is like a brother to me, thank you for all the shenanigans and gaming sessions throughout the years. We'll get a few pints in, before you head away to Amsterdam. I've no doubt you'll smash it over there, as you do with everything you put your mind to. Aunty Grace, to whom I (drunkenly) said I would include in my thesis those many years ago in The Bailey on Duke Street… the West remembers. To the incredible nana Rose & granddad Brendan, thank you for your enduring kindness and generosity throughout my entire life, let alone the last 4 years. I wish you all the best, and be seeing you soon.

Last but not least, I owe an immeasurable debt of gratitude to my family – Roseanne, Derek, and Sean. Their unwavering support, understanding, and encouragement sustained me through the highs and lows of this challenging journey. Their belief in my capabilities was the source of my strength, and I am profoundly grateful for the sacrifices they made to see me succeed.

This thesis stands as a testament to the collective efforts and support of these individuals, without whom this document would not have been possible.

Abstract

The importance of luminescent peptide sensors and peptidomimetics lies in their ability to address challenges in detection, imaging, drug development, and various other fields. More specifically, luminescent peptide-conjugates are often biocompatible and can detect analytes at trace-levels. This makes them effective tools for the visualisation of cellular processes and molecular interactions, while aiding in early diagnosis and monitoring disease progression. Indeed, peptidomimetics are designed to mimic the biological activity of peptides while often offering enhanced stability and bioavailability, overcoming some of the many limitations associated with native peptides. This thesis will focus on the use of modified synthetic peptide-conjugates as potential luminescent sensors for the visualisation of Caspase-3, and the design of a completely new peptidomimetic-scaffold based on *Squaratides* – a hybrid mix of squaramides and peptides.

The thesis opens with a literature review (Chapter 1) documenting the therapeutic history of peptides and the inherent functionalities that facilitate their diverse chemistries, all the way up to the luminescent applications of peptide-conjugates for selective sensing/visualisation of specific disease-related enzymes. Chapter 2 details the design, synthesis, and characterisation of a ratiometric fluorescent caspase-3 probe. This novel peptide-conjugate was investigated as a potential probe for the visualisation of caspase-3 via UV-vis/Fluorescence studies, enzyme kinetic(s) experiments, and selectivity studies. The probe was shown to be highly selective towards caspase-3, with kinetic data comparable to others reported in literature, while benefiting from the advantages of ratiometric detection. The design of a potential red-emitting naphthalimide-peptide probe for caspase-3 visualisation is also discussed.

Chapter 3 aims to build on the idea of fluorescent visualisation using traditional organic fluorophores, but instead employs lanthanide luminescence, with their prolonged luminescence lifetimes and tuneable emission colours. This chapter reports the synthesis and characterisation of a family of novel, water-soluble squaramide-based cyclen ligands with varying symmetry and substitution patterns, including one ligand that may have the potential to act as a lanthanide-based caspase-3 probe. The photophysical properties of each squaramide

antenna was investigated, with preliminary metal-centred luminescence emission spectra being obtained for Eu^{3+} and Tb^{3+} complexes.

The final section (Chapter 4) documents the attempted synthesis of a novel class of peptidomimetics featuring a squaramide motif. The aim was to investigate the use of squaramides as potential peptidomimetics, by generating synthetic analogues of a previous pharmaceutical drug – *Cilengitide* – with the hope of improving its overall stability. This chapter outlines a versatile synthetic methodology for the production of N^{β}-Fmoc alkyl-amines (from their respective commercially available amino acids) and their incorporation into cyclic *Squaratide* peptidomimetics.

Abbreviations

AA	Amino Acid
Acm	Acetamidomethyl
ADC	Antibody-Drug Conjugate
ADMET	Absorption, Distribution, Metabolism, Excretion & Toxicity
AIDS	Acquired Immunodeficiency Syndrome
AIE	Aggregation-induced Emission
Alloc	Allyloxycarbonyl
ALPS	Autoimmune Lymphoproliferative Syndrome
AMPs	Antimicrobial Peptides
APT	Attached-proton Test
Arg	Arginine
Asn	Asparagine
Asp	Aspartic Acid
Bn	Benzyl
Boc	*tert*-butyloxycarbonyl
Bpoc	2-(4-biphenyl) isopropoxycarbonyl
BrOAc*O*t*Bu	*tert*-Butyl bromoacetate
CAGR	Compound Annual Growth Rate
Cam	Carbamoylmethyl
CBM	Centre de Biophysique Moléculaire
CHCl$_3$	Chloroform
Cit	Citrulline
CNRS	Centre National de la Recherche Scientifique

COVID-19	Corona Virus Disease 2019
CPPs	Cell-penetrating Peptides
Cys	Cysteine
DBF	Dibenzofulvene
DCC	Dicyclohexylcarbodiimide
DCM	Dichloromethane
DEPT	Distortionless Enhancement by Polarisation Transfer
Dde	1-(4,4-dimethyl-2,6-dioxocyclohex-1-ylidene)-3-ethyl
Ddz	α,α-Dimethyl-3,5-dimethoxybenzyloxycarbonyl
DESq	Diethyl squarate
DIC	Diisopropylcarbodiimide
DIPEA	Diisopropylethylamine
Dmab	Dimethyldioxocyclohexylidene aminobenzyl
DMAP	Dimethylaminopyridine
Dmb	2,4-Dimethoxybenzyl
DMF	Dimethylformamide
DMSO	Dimethyl sulfoxide
DOTA	1,4,7,10-tetraazacyclododecane-1,4,7,10-tetraacetic acid
DTPA	Diethylenetriaminepentaacetic acid
DTT	Dithiothreitol
EDA	Ethylene diamine
EDC	*N*-ethyl-*N'*-(3-dimethylaminopropyl) carbodiimide
EDT	Ethanedithiol
EDTA	Ethylenediaminetetraacetic acid
EEDQ	2-ethoxycarbonyl-2-ethoxy-1,2-dihydroquinoline

Abbreviations

ELISA	Enzyme-linked Immunosorbent Assay
EPL	Expressed Protein Ligation
Esc	Ethanesulfonylethoxycarbonyl
ESI	Electrospray Ionisation
Et	Ethyl
EtOAc	Ethyl acetate
EtOH	Ethanol
Fmoc	Fluorenylmethyloxycarbonyl
FRET	Förster Resonance Energy Transfer
GBM	Glioblastoma multiforme
Gln	Glutamine
Glu	Glutamic Acid
Gly	Glycine
HATU	Hexafluorophosphate Azabenzotriazole Tetramethyl Uronium
HBTU	*O*-(Benzotriazol-1-yl)-tetramethyluronium
HFIP	Hexafluoroisopropanol
Hgn	D-homoglutamine
His	Histidine
HOAt	1-hydroxy-7-azabenzotriazole
HOBt	1-hydroxybenzotriazole
HPLC	High Performance Liquid Chromatography
HRMS	High-Resolution Mass Spectrometry
ICT	Internal-Charge Transfer
INEPT	Insensitive Nuclei Enhanced by Polarisation Transfer
iPr	Isopropyl

ivDde	1-(4,4-Dimethyl-2,6-dioxocyclohex-1-ylidene)-3-methylbutyl
LC-MS	Liquid-Chromatography Mass Spectrometry
LiOH	Lithium hydroxide
Lys	Lysine
Me	Methyl
MeCN	Acetonitrile
MeOH	Methanol
MRI	Magnetic Resonance Imaging
NaOH	Sodium Hydroxide
NCL	Native Chemical Ligation
NMM	*N*-methyl morpholine
NMR	Nuclear magnetic resonance
Nps	2-nitrophenylsulfenyl
NRPS	Non-ribosomal Peptide Synthetase
NSAID	Non-steroidal anti-inflammatory drug
Orn	Ornithine
OS	Overall Survival
PABA	*para*-aminobenzyl alcohol
PABC	para-aminobenzyl carbamate
Pbf	2,2,4,6,7-pentamethyl-dihydrobenzofuran-5-sulfonyl
PEG	Polyethylene Glycol
PEGA	Poly(ethylene glycol)-poly-(*N,N*-dimethylacrylamide)
PET	Photoinduced Electron Transfer
PFS	Progression-free Survival
Phe	Phenylalanine

Abbreviations

PRRT	Peptide-receptor Radionuclide Therapy
Pro	Proline
PS	Polystyrene
PyBOP	1-benzotriazolyloxy-tris-pyrrolidinophosphonium
Ser	Serine
SFTI-1	Sunflower Trypsin Inhibitor-1
SPPS	Solid-Phase Peptide Synthesis
SPS	Solution-Phase Synthesis
TATE	Tyr^3-octreotate
TBAF	Tetrabutylammonium fluoride
***t*Bu**	*tert*-butyl
TEA	Triethyl amine
TEACl	Tetraethylammonium chloride
TES	Triethylsilane
TFA	Trifluoroacetic Acid
THF	Tetrahydrofuran
Thr	Threonine
TIPS	Triisopropylsilane
TLC	Thin-layer chromatography
TPE	Tetraphenylethene
tRNA	Transfer RNA
Trp	Tryptophan
Trt	Trityl
Tyr	Tyrosine
US-FDA	United States Food & Drug Administration

XRT   X-ray Therapy

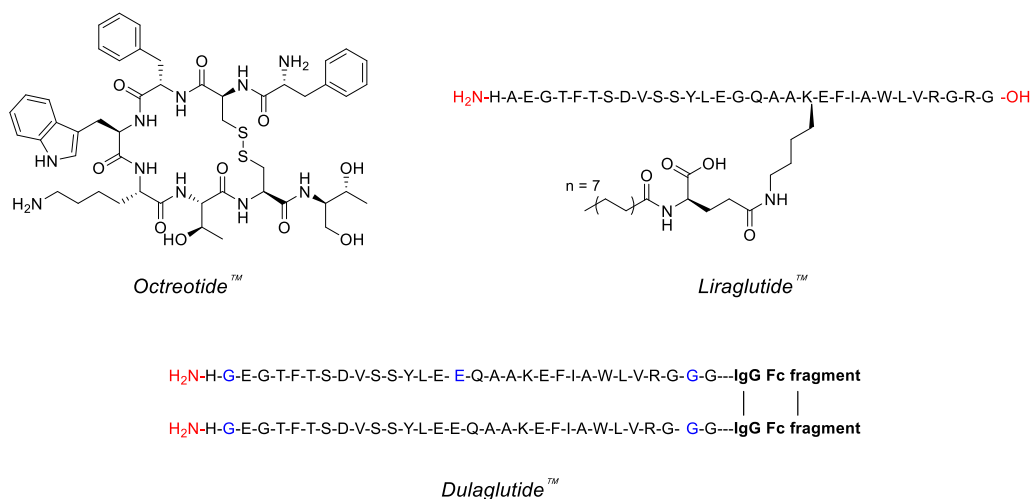**Z**   Benzyloxycarbonyl

Chapter 1

Introduction

1. Introduction

"A feeling sparked in your mind will translate as a peptide being released somewhere" – Dr. Candace Pert

Peptides are physiologically active compounds made up of short chains of amino acid (AA) monomers connected by amide bonds (peptide bonds). The beginning of peptide chemistry has long been attributed to the year 1901, when chemists Emil Fischer, and Ernest Fourneau published the first ever "synthetic peptide" – a dipeptide called glycyl-glycine (Gly-Gly).[1] One of the most significant scientific successes in peptide drug discovery was the development of insulin, a peptide containing 51 amino acids. It was discovered in 1921 by Frederick Banting and further refined by Frederick and Charles Best.[2,3] Peptide chemistry received little attention for the next 30 years, until the medicinal use of peptides really kicked off after World War 2. Following this, oxytocin was synthesized by du Vigneaud in 1953, a major achievement for peptide chemistry and a synthetic milestone.[4] However, these methods required a huge amount of time and synthetic effort for even the most trivial of peptides. It wasn't until Bruce Merrifield revolutionised peptide chemistry in 1963 with Solid-Phase Peptide Synthesis (SPPS).[5] This technology pioneered the way for quick, easy, and efficient preparation of peptides, and was the basis for his 1984 Nobel Prize in Chemistry. SPPS substantially accelerated progress across the chemical and medicinal sciences. Furthermore, peptide's inherent specificity and excellent efficacy have made them attractive building blocks for the design of novel therapeutics.[6]

Peptides are frequently involved in human physiology, acting as hormones,[7] neurotransmitters,[8] growth factors,[9] or ion channel ligands.[10] Moreover, peptides tend to act as intrinsic signalling molecules for many of these physiological functions, opening up the possibility for peptide-therapeutic mediation that closely resembles the natural process.[11] Indeed, utilising peptide-based therapeutics has been commercially proven to help treat many diseases/disorders such as, type 2 diabetes, multiple sclerosis, acromegaly and osteoporosis – with the likes of Eli Lilly® (*Trulicity*™), Novo Nordisk® (*Victoza*™) and Novartis® (*Sandostatin*™) dominating this space (**Figure 1.1**).[12]

H$_2$N-H-A-E-G-T-F-T-S-D-V-S-S-Y-L-E-G-Q-A-A-K-E-F-I-A-W-L-V-R-G-R-G -OH

Octreotide^{TM}

Liraglutide^{TM}

H$_2$N-H-G-E-G-T-F-T-S-D-V-S-S-Y-L-E- E-Q-A-A-K-E-F-I-A-W-L-V-R-G- G-G---**IgG Fc fragment**

H$_2$N-H-G-E-G-T-F-T-S-D-V-S-S-Y-L-E-E-Q-A-A-K-E-F-I-A-W-L-V-R-G- G-G---**IgG Fc fragment**

Dulaglutide^{TM}

Figure 1.1: Chemical structures of commercially significant peptide therapeutics (single-letter abbreviations used for amino acids to ensure clarity).

In recent years, over 60 peptide drugs have been approved by the US-FDA, Europe, and Japan: over 150 are in active clinical development, and an additional 260 have been tested in human clinical trials.[10,13] This translates to a global peptide therapeutics market currently valued at $39.34 Bn (US dollars), with projected growth of 8.8% (CAGR) to $91.25 Bn by 2031 (**Figure 1.2**).[14] Over 21 peptide therapeutics are currently being utilised to treat COVID-19, including 15 synthetic peptides in development against SARS-Cov-2 infection-related respiratory disorders.[15] Peptide therapeutics are also being examined as a COVID-19 treatment option. As a result, significant industry participants reported a rise in revenue during the COVID-19 epidemic.[14] Through the many lockdowns and long working-from-home periods, much of the population experienced more sedentary lifestyles. Coupled with the corresponding bad habits and unhealthy diets, a surge in chronic disease prevalence and incidence may be on the horizon. To this end, the worldwide peptide therapeutics market is likely to be driven by an increase in metabolic disorders forecast for the coming years.[16]
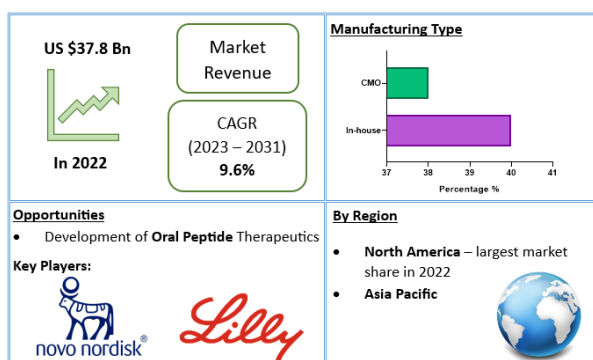
Figure 1.2: Global peptide therapeutics market value and financial forecasts.[14]

Peptides interact with cell-surface receptors and cascade intracellular reactions with high affinity and specificity, similar to large biologics such as proteins and antibodies.[17] However, peptide-therapeutics provoke less of an immune response and typically have reduced production costs.[18,19] Small-molecule drugs also benefit from low production costs and tend to have good oral bioavailability and membrane permeability.[20] On the other hand, the clinical use of small-molecule therapeutics can be restricted due to their low specificity compared to peptide drugs. Peptide-based therapeutics usually have two inherent shortcomings: their ability to penetrate the cell-membrane(s) to reach intracellular targets, and *in vivo* stability – as their amide bonds can be hydrolysed by domestic enzymes.[21] These inherent benefits and drawbacks of peptide therapeutics provide both challenges in peptide drug development, as well as opportunities for peptide design and drug discovery. Peptides remain a distinct family of pharmaceutical compounds that are molecularly positioned somewhere between small molecules and proteins (**Figure 1.3**), while being biochemically and therapeutically distinct from both.[22]
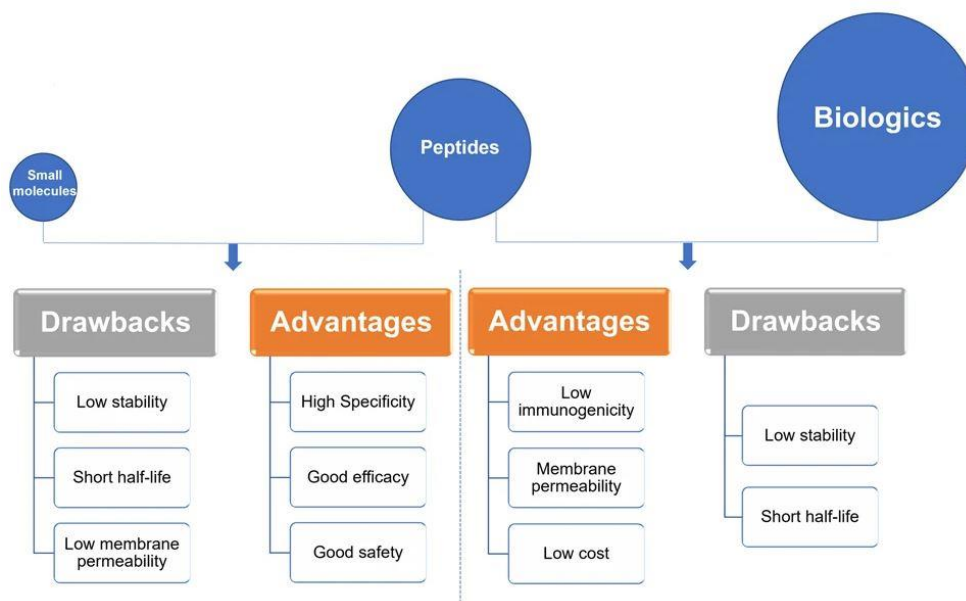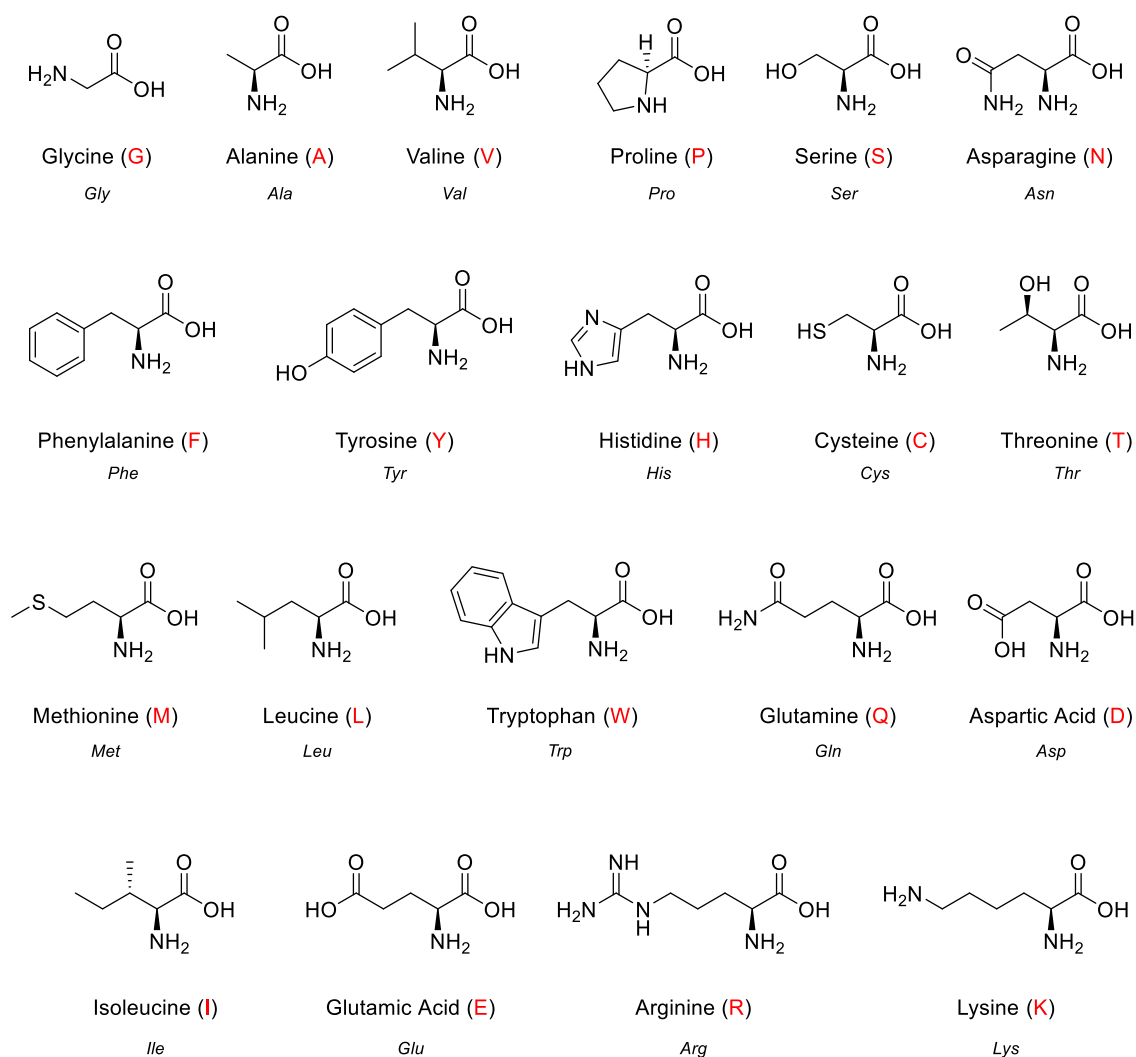

Figure 1.3: Peptides versus small molecules and biologics. Comparison of advantages and drawbacks between peptides and small molecules or biologics.[22]

1.1 Chemical Methods for Peptide Synthesis

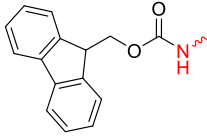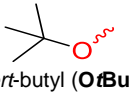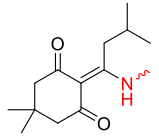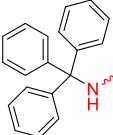*"Continuous improvement is better than delayed perfection" – Mark Twain*

Since Merrifield introduced us to SPPS back in 1963, research in the peptide space has grown remarkably. Although the classical methods of SPPS provided a vital boost for peptide synthesis, it was limited by the dramatic decrease in purity as the number of coupling steps increased.[23] Building on the success of the Boc and Fmoc protecting groups,[24] innovative AA protecting groups and new methodologies were incorporated to produce high quality peptide products with superb yields. One early-stage method was fragment condensation via prior thiol capture, but this technique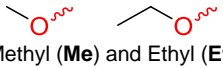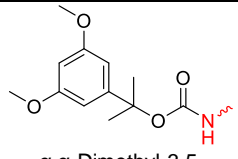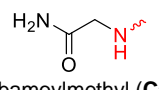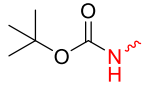 suffered from racemisation and other reaction complications.[25] An improvement on this coupling reaction was achieved by Kent & co-workers by the chemoselective reaction of unprotected peptides, they coined this – Native Chemical Ligation (NCL).[26] Other ligation methods include (but not limited to) Expressed Protein Ligation (EPL),[27] the Staudinger ligation,[28] and "click" or "switch" peptide ligation.[29] This section will focus on key AA protecting groups for peptide synthesis, and the two major synthetic methods for peptide production – SPS and SPPS.

Glycine (G)
Gly

Alanine (A)
Ala

Valine (V)
Val

Proline (P)
Pro

Serine (S)
Ser

Asparagine (N)
Asn

Phenylalanine (F)
Phe

Tyrosine (Y)
Tyr

Histidine (H)
His

Cysteine (C)
Cys

Threonine (T)
Thr

Methionine (M)
Met

Leucine (L)
Leu

Tryptophan (W)
Trp

Glutamine (Q)
Gln

Aspartic Acid (D)
Asp

Isoleucine (I)
Ile

Glutamic Acid (E)
Glu

Arginine (R)
Arg

Lysine (K)
Lys

Figure 1.4: The 20 natural amino acids – names, 3 letter codes and 1 letter codes.

1.1.1 Amino Acid Protecting Groups

Amino acids naturally contain various reactive moieties (**Figure 1.4**) that need to be protected in order to sequester any potential side-reactions that may impact yield and/or purity. The first avant-garde AA protecting group was the benzyloxycarbonyl (Z), fashioned by Bergmann and Zervas.[30] The Z protecting group masks the nucleophilic nature of the alpha-amine and prevents unwanted reactivity. It is an ideal candidate as it can be easily functionalised onto the amino group of interest, it is resistant to a wide variety of reaction conditions, and it can be efficiently removed to allow further manipulation of the liberated amine. In general, the protecting group should confer solubility in common coupling solvents (e.g., DMF, DCM), limit epimerization, and produce byproducts that are convenient to remove.[31]

| Base labile protecting groups		Acid labile protecting groups	
Name	**Removal Conditions**	**Name**	**Removal Conditions**
Fluorenylmethyloxycarbonyl (**Fmoc**)	20% Piperidine in DMF [32]	*tert*-butyl (**OtBu**)	95:2.5:2.5 TFA/H$_2$O/TIPS [33]
1-(4,4-Dimethyl-2,6-dioxocyclohex-1-ylidene)-3-methylbutyl (**ivDde**)	Hydrazinolysis [34]	Trityl (**Trt**)	1% TFA in DCM [35]
Ethanesulfonylethoxycarbonyl (**Esc**)	0.05M TBAF in DMF [36]	2,4-Dimethoxybenzyl (**Dmb**)	1% TFA in DCM [37]
4-(N-[1-(4,4-dimethyl-2,6-dioxocyclohexylidene)-3-methylbutyl]amino)benzyl (**Dmab**)	2% Hydrazine (aq.) in DMF [38]	2-(4-Biphenyl)isopropoxycarbonyl (**Bpoc**)	0.2-0.5% TFA [39]
Methyl (**Me**) and Ethyl (**Et**)	LiOH [40]	α,α-Dimethyl-3,5-dimethoxybenzyloxycarbonyl (**Ddz**)	1-5% TFA in DCM [41]
Carbamoylmethyl (**Cam**)	NaOH in DMF [42]	*tert*-Butyloxycarbonyl (**Boc**)	50:50 TFA/DCM [43]
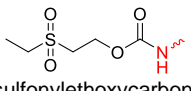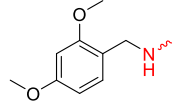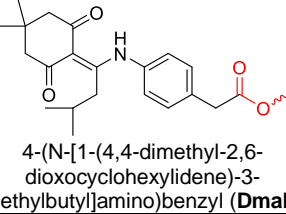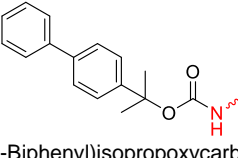
Table 1.1: Examples of Acid/Base labile protecting groups used in peptide synthesis.

The orthogonal approach teaches us that two (or more) distinct protecting groups can be removed under separate conditions, in any order, and in the presence of one another.[44,45] During solution-phase synthesis, examples of amino-protecting groups used are the Z, the Bpoc [2-(4-biphenyl) isopropoxycarbonyl] and the Nps (2-nitrophenylsulfenyl), usually used with *t*Bu-side-chain protection, or the Boc group in combination with Bn side-chain protection.[46] In the case of protecting the carboxylic acid, *tert*-butyl protection may be employed.[47] However, the protection of the *C*-terminal carboxylic acid in SPPS is not required because it is conjugated to the resin itself – acting in lieu of the protecting group. Strategies for protecting the amino group in SPPS include two popular approaches, the Fmoc/*t*Bu and Boc/Bn functionalities. Both strategies contain protecting groups that can be removed under (relatively) mild conditions,

yield by-products that are readily soluble, and are easily removed (**Table 1.1**). Fmoc-protected amines can be released under basic conditions: 20% piperidine in dimethylformamide (DMF).[32] The advantage of using an organic base such as piperidine is that the highly reactive by-product – dibenzofulvene (DBF) – is almost immediately *trapped* to form a stable (soluble) adduct.[48] Boc and *t*Bu-protecting groups can be removed under acidic conditions; 50:50 TFA/DCM and 95:2.5:2.5 TFA/H_2O/TIPS solutions respectively. TIPS is added as a *scavenger* to the TFA cleavage cocktail in order to sequester *t*-butyl trifluoroacetate and *t*-butyl cations that may form.[33] The precise manipulation of protecting-group strategies has been shown to maximize the yield and purity of complex peptide products and has become a cornerstone in peptide synthesis.

1.1.2 Solution-Phase Synthesis (SPS)

Traditional SPS involves the coupling of single AA monomers in solution – now commonly referred to as stepwise synthesis (**Scheme 1.1**). This method of SPS is quick, efficient, and can be exploited for the construction of various peptide products.[23]
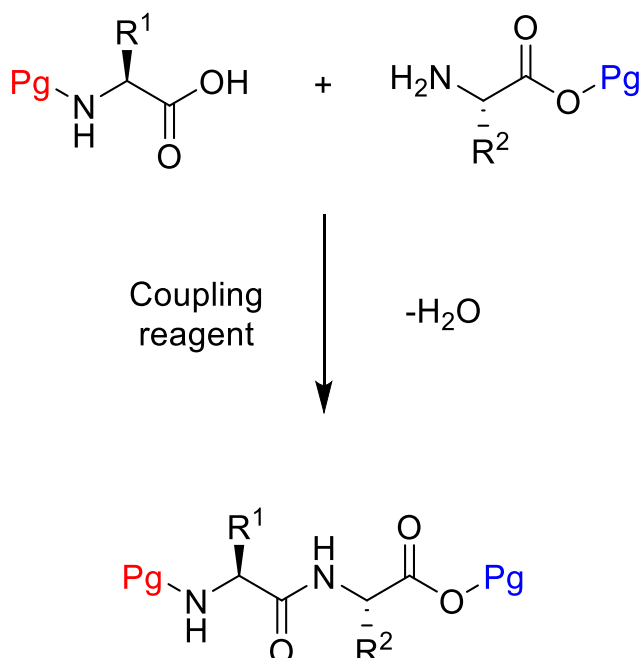
Scheme 1.1: Generic example of a traditional SPS coupling reaction (Pg = protecting group).

1.1.2.1 Native Chemical Ligation (NCL)

To synthesize longer amino acid sequences, this approach utilises a ligation technique to achieve peptide synthesis. Native Chemical Ligation (NCL) involves a reaction between a peptide containing a *C*-terminal thioester and a separate peptide with an *N*-terminal cysteine residue. This transthioesterification reaction results in the formation of an intermediate thioester with the cysteine thiol. The ester-carbonyl intermediate is then subject to nucleophilic attack from the proximal α-amino of the cysteine, resulting in an S → N acyl transfer – spontaneously forming the native amide bond.[49] Many proteins and peptide products have been successfully synthesized using this technique: a serine protease,[50] cytochrome b562,[51] and a trypsin inhibitor,[52] just to name a few classic examples.

1.1.2.2 Expressed Protein Ligation (EPL)

Expressed Protein Ligation (EPL) facilitates the recombinant generation of *C*-terminal thioesters and *N*-terminal cysteine residues for chemical ligation using *in vivo* protein splicing. This ligation mechanism takes advantage of Inteins – sequences of AAs in precursor proteins – that can modify their own innate peptide structure, causing the excision of the intein peptide segment and ligation of the two remaining peptide segments adjacent to the excised section (exteins).[53] Interestingly, the reaction mechanism is very similar to that of NCL if there is a cysteine residue present at the *N*-terminal splice junction side of the intein. Proteins being expressed using this technology will have a *C*-terminal thioester, which allows them to be coupled to almost any compound containing a cysteine group with an available α-amino and thiol moiety.[54]

1.1.2.3 Staudinger Ligation

The "Staudinger reaction" was originally discovered by Nobel laureate Heramann Staudinger,[55] but a considerable alteration to this reaction was developed by Saxon and Bertozzi that they coined the Staudinger Ligation.[56] This reaction is now essentially a covalent coupling reaction that makes use of a modified phosphine-derivative possessing an electrophilic *trap* for the electron-rich nitrogen in the aza-ylide intermediate. The resulting 5-membered ring structure is rapidly hydrolysed in aqueous environments to produce an amide bond functionality between the two previously separate molecules. The ability to incorporate azido-functionality into biomolecules *in vivo* and the bio-orthogonal

nature of the many reagents used in the Staudinger Ligation, the process has been widely celebrated in the field of chemical biology.[57] Although many of these techniques used in SPS can be scaled-up in a simple and relatively inexpensive manor, the long reaction times remain a disadvantage.

1.1.2.4 Polymer-assisted Solution-phase (PASP) synthesis

A hybrid approach for synthesising small to medium length peptides. PASP synthesis streamlines the production of peptides by utilising a polymer support in solution. This method involves anchoring the initial amino acid onto a solid-phase polymer support, followed by stepwise addition of protected amino acids to extend the peptide chain. Coupling reactions are facilitated by activating the carboxyl group of incoming amino acids and reacting them with the amino group of the growing peptide chain. Once the desired sequence is assembled, protective groups are removed, and the peptide is cleaved from the polymer support for purification. This hybrid-phase method allows for easier automation, with high-throughput peptide production.

1.1.3 Solid-Phase Peptide Synthesis (SPPS)

Solid-Phase Peptide Synthesis (SPPS) is used throughout the world at lab-scale and in industry, and is currently the method of choice for the chemical synthesis of peptides. SPPS allows for significant synthetic flexibility when it comes to constructing the peptide sequence and the equipment being used. Automated peptide synthesizers have become increasingly popular among research and industry labs owing to their increased product throughput and (long-term) reduced experimental cost(s).[58] SPPS can also be used to introduce post-translational backbone modifications and non-natural AA moieties, further expanding the method for synthesising peptide products.[59] This section will focus on key considerations and parameters that need to be employed for successful peptide synthesis via SPPS.

1.1.3.1 The Solid Support – Resins & Linkers

It all begins with the Resin. Choosing the appropriate resin and linker combination is crucial, as the entire synthetic strategy going forward is based off this functionality. The resin should provide significant resistance to mechanical shear and be stable in a range of solvents and temperatures. In addition, the resin

must be able to *swell* sufficiently to allow reagents access to the reactive sites. Over the years, there have been many different types of resins developed to facilitate the synthesis of peptide products: polystyrene (PS) resins,[60] PS-functionalised polyethylene glycol (PS-PEG) resins,[61] and crosslinked PEG resins.[62]

Merrifield originally used the PS resin for his SPPS,[63] and is still used today for the chemical synthesis of peptide products. PS resins are extremely useful for synthesising short to medium-sized peptides, with the polymer usually being crosslinked with 1% divinylbenzene (DVB). The swelling properties of PS resins are very good in organic non-polar solvents such as DCM or toluene, but also show similar compatibility in tetrahydrofuran (THF) or DMF.[64] The main disadvantage of this resin is its incompatibility with aqueous environments and in strongly polar solvents. It is also important to consider the peptide sequence to be synthesized, as difficulties may arise with PS resins when involving very hydrophobic AAs, *difficult* peptide sequences and/or peptides that have a propensity to aggregate. In these situations, a more hydrophilic resin may be of benefit.[65]
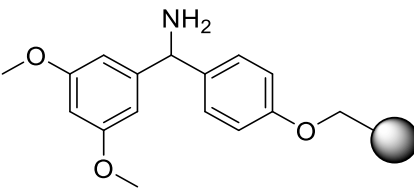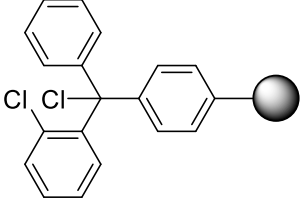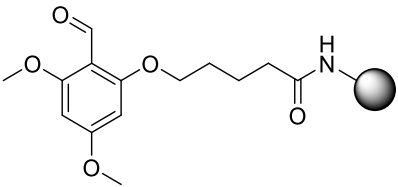
PS-PEG resins perform well in a mixture of polar and non-polar solvents and possess excellent swelling properties. One of the more popular PS-PEG resins is *TentaGel*™ (TG), a co-polymer consisting of a minimal PS matrix cross-linked with PEG. As PEG is an amphiphilic polymer, the functionalised co-polymer displays physicochemical characteristics that are now dominated by the PEG (50-70%) moiety rather than the PS matrix.[66] TG shows great functionality when synthesising longer peptides, when compared to the traditional PS resins.

The last type of resin contains very little PS. Instead, is made up of cross-linked PEG. The main players in this space are the poly(ethylene glycol)-poly-(*N*,*N*-dimethylacrylamide) (PEGA),[62] crosslinked ethoxylate acrylate (CLEAR),[67] and ChemMatrix (CM) resins.[68] All of these demonstrate excellent swelling properties in water which can facilitate the study of peptide-protein interactions. However, the PEGA resin is susceptible to damage when shrunk or dried. Thus, is packaged in its swollen state (in ethanol), due to the nature of the resin beads. Although commercially discontinued, CM resins boast the combined advantages of PS & PEG resins, with increased chemical stability and versatility, making it an interesting choice for synthesising large peptides that contain difficult sequences

or many hydrophobic AAs. Furthermore, because the CM polymer is highly polar, it preserves its exceptional swelling capabilities in numerous polar solvents such as water, methanol and acetonitrile.[69]

Linkers – like the resin they are attached to – are the foundational building blocks of SPPS. They serve two main functions in peptide synthesis: acting as a reversible tether between the peptide sequence and the resin itself, and protection against aggregation during the expansion of the peptide chain.[70] There are many different linkers available for SPPS, however in the interest of relevance, this section will focus on Linkers for Fmoc-based SPPS.

The attachment of the first AA is crucial and must be done efficiently, the linker needs to be stable to further chemical transformations, and the cleavage conditions must be suitable for the final peptide product. The most common release mechanism for linkers is trifluoroacetic acid (TFA) mediated, via *cocktails* containing various concentrations of the acid and other solvents (DCM). A key consideration when choosing an appropriate resin is the final *C*-terminal functionality of the peptide product. Resins like Rink-Amide or Sieber-Amide – as the name suggests – will yield peptide amides,[71,72] and on the other hand, resins like 2-chlorotrityl chloride and Wang will liberate the product as a peptide acid (**Table 1.2**).[73,74]

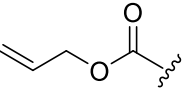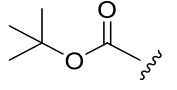| Linker Name	Liberated C-terminal Functionality	Linker Structure	Cleavage Conditions
Rink Amide	Amides		95% TFA [71]
2-chlorotrityl chloride	Carboxylic Acids		30% HFIP in DCM (<0.5% TFA) [73]
Aryl hydrazide	Amide or Esters		Cu(II) cat, pyridine [75]
BAL linker	Aldehydes or Thioesters		95% TFA [76]

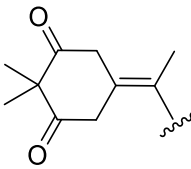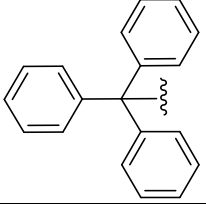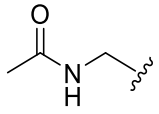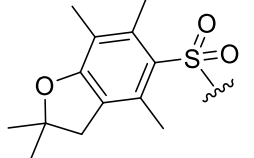**Table 1.2:** Common linkers for Fmoc-based SPPS.

Trityl-based linkers are popular choices for the production of protected peptide products via Fmoc-SPPS. The 2-chlorotrityl chloride linker is attached to the resin (usually PS) via direct synthesis.[77] The steric hinderance of the trityl chloride linker has been shown to prevent diketopiperazine formation, and is favoured when releasing Pro or Gly C-terminal peptides. Attachment of the first AA residue is done via reaction of the Fmoc-protected AA in the presence of a base (e.g. DIPEA). An interesting advantage of this trityl linker is the initial loading reaction does not involve any *activated species*, so it deters any possible epimerisation.[78] It also produces relatively unstable cations that are sufficient for immobilisation of carboxylic acids. The 2-chlorotrityl chloride linker is a fine choice for Fmoc/tBu-based SPPS as it prevents many of the side-reactions that typically occur with benzyl-based linkers.[79] Racemisation does not occur when loading the first AA residue, the sterically hindered trityl cation does not generate alkylation side-reactions with nucleophilic AA side-chains, and cysteine – that is particularly susceptible to epimerisation – does not experience racemisation.[80]

1.1.3.2 Side-chain Protecting Groups

The use of side-chain protecting groups is imperative during SPPS to mask the reactivity of nucleophilic functionalities present on the side chains of many AAs. For Fmoc-SPPS, there have been many side-chain protecting strategies reported in the literature,[81] but one popular method stands out from the crowd. The Fmoc/*t*Bu strategy is constantly exploited for its ability to facilitate the deprotection of various protecting groups under certain chemical conditions, while rendering the other protecting groups untouched (orthogonality).[82] This synthetic flexibility presents the option for more complex manoeuvring during peptide synthesis.

Every AA that possesses a chemically reactive side chain must be appropriately protected during peptide elongation in order to ward off potential by-products and side reactions. These side-chain protecting groups are orthogonal to the α-amino Fmoc-group and can be removed by TFA cocktails of varying concentrations. Different AAs require different protecting groups depending on the nature of their side-chain functionalities: *t*Bu ester(s) for Asp and Glu, *t*Bu ether(s) for Thr, Tyr and/or Ser, the 2,2,4,6,7-pentamethyl-dihydrobenzofuran-5-sulfonyl (Pbf) protecting group for Arg, the trityl (Trt) group for His, Gln, Asn and Cys, and the Boc group for Trp and Lys (**Table 1.3**).

There are other side-chain protecting groups that are stable under both acidic and basic conditions, while retaining their orthogonality to the Fmoc-group and the cleavage conditions. The acetamidomethyl group (Acm) – commonly used for Cys – is selectively removed via thallium trifluoroacetate or iodine solution.[83] Additionally, the 1-(4,4-dimethyl-2,6-dioxocyclohex-1-ylidene)-3-ethyl (Dde) group and the allyloxycarbonyl (Alloc) protecting group – removed via palladium catalyst – are stable in various TFA cocktails and are generally used for the side-chain protection of Lys and Ornithine (Orn).[84]

| TFA Labile		TFA Stable	
Side-chain Protecting Group	**Suggested Amino Acid(s)**	**Side-chain Protecting Group**	**Suggested Amino Acid(s)**
*t*Bu	Asp, Glu – ester(s) Ser, Thr, Tyr – ether(s)	Alloc	Lys
Boc	Lys, Trp	Dde	Lys
Trt	Cys, His, Asn, Gln	Acm	Cys
Pbf	Arg		

Table 1.3: Common side-chain protecting groups used in Fmoc-SPPS.

1.1.3.3 Coupling Reagents

Amide bonds are usually synthesized via the covalent conjugation of amines and carboxylic acids. The covalent bond between these two functional groups does not readily occur at room temperature and pressure, with the essential release of water only taking place at temperatures exceeding 200°C.[85] However, this temperature will likely degrade any substrate or peptide sequence, thus it is paramount that the carboxylic acid is *activated* prior to conjugation. This activation process typically involves converting the -OH group on the carboxylic acid to a better leaving group before reacting with the amine.

One method of activating carboxylic acids for conjugation is the use of "Coupling Reagents", which act as independent entities that generate highly reactive compounds like (mixed) anhydrides, carbonic anhydrides, acid chlorides and/or activated esters. Furthermore, choosing the appropriate coupling reagent is highly important because it needs to be able to facilitate the conjugation of amines with diverse reactivities (e.g. secondary amines, sterically hindered amines, anilines). Coupling reagents have been extensively studied and

documented, with many reviews being published on their application in peptide chemistry,[86,87] highlighting their importance in the synthetic arsenal of the peptide chemist.
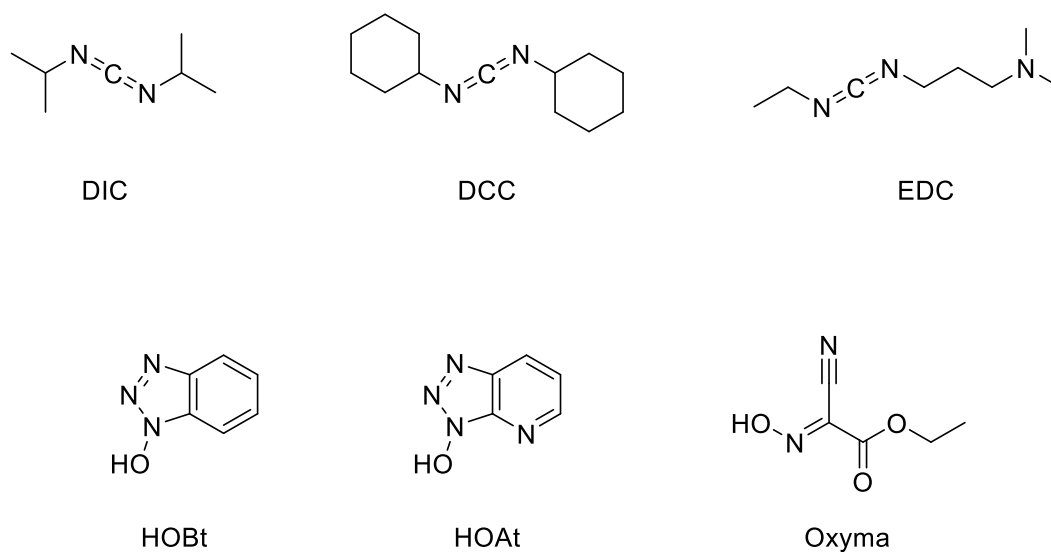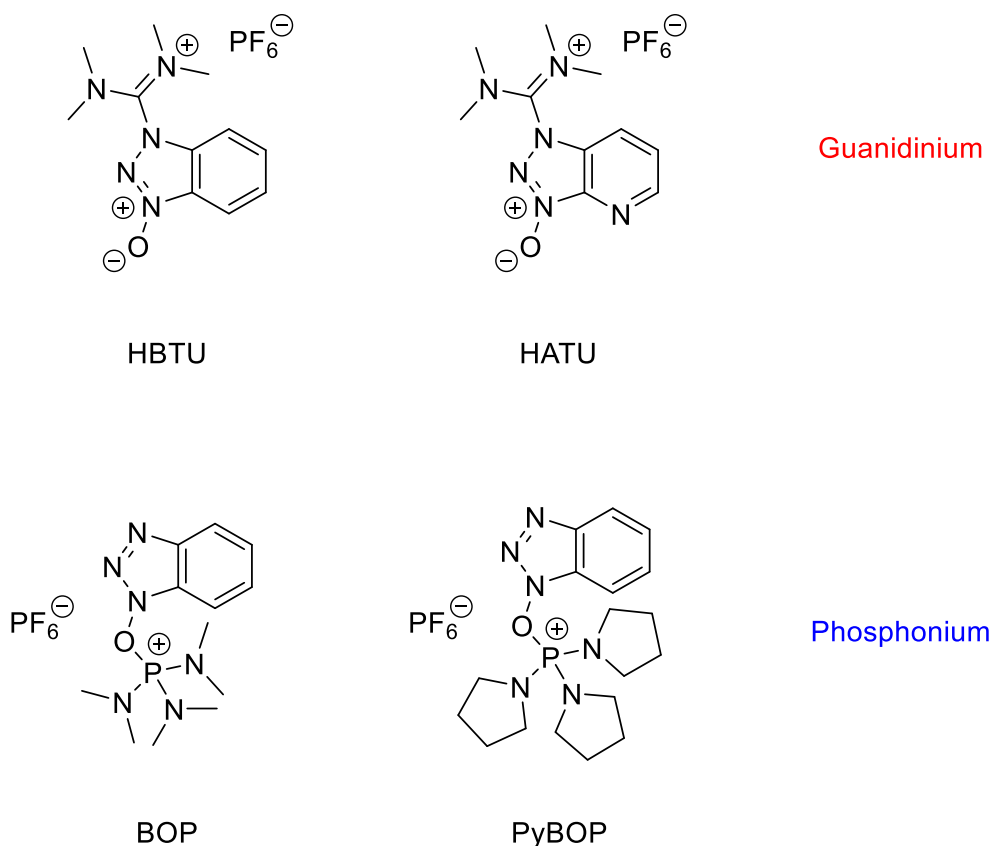

Figure 1.5: Popular Peptide Coupling Reagents used for amide bond formation.

A classic family of coupling reagents are the carbodiimide-based reagents (**Figure 1.5**), including diisopropylcarbodiimide (DIC) and dicyclohexylcarbodiimide (DCC). Both of these compounds contain nitrogen atoms with basic characteristics, which allows for deprotonation of the AA *C*-terminus. This deprotonation initialises the reaction between the acid and the carbodiimide, resulting in the formation in an activated *O*-acylisourea.[88] The urea by-product from the water-soluble EDC can be readily removed via work-up, due to the basicity of the amine functional group. However, DIC is often adopted for use in SPPS as the urea formed is soluble in organic coupling solvents like DCM or DMF. Racemisation suppressing additives are introduced in combination with carbodiimide coupling reagents to minimise unwanted side-reactions like epimerisation or *N*-acylurea formation. 1-hydroxy-7-azabenzotriazole (HOAt) and 1-hydroxybenzotriazole (HOBt) are fantastic for suppressing such side-reactions because they form a less-reactive benzotriazolyl ester after displacement of the *O*-acylisourea.[89] Another carbodiimide coupling reagent that is commonly used is *N*-ethyl-*N'*-(3-dimethylaminopropyl) carbodiimide (EDC), which is extensively employed in solution-phase chemistry. A more recent coupling reagent called *Oxyma* possesses an enhanced ability to suppress racemisation when compared

to HOBt or HOAt, and may be considered as a potential safety replacement for the benzotriazole-based additives due to its lower thermal risk.[90]

After the success of HOBt as an additive for suppressing racemisation, a new family of coupling reagents came to the forefront of SPPS – the phosphonium and uronium salts. The group of Kenner and Co. developed phosphonium salts, more commonly regarded to as the BOP family (**Figure 1.6**).[91] The flagship coupling reagent of this family is 1-benzotriazolyloxy-tris-pyrrolidinophosphonium hexafluorophosphate (PyBOP) and its halide derivatives (Chloro & Bromo) PyCloP and PyBroP, respectively. Popular choices among the guanidinium coupling reagents are *O*-(Benzotriazol-1-yl)-tetramethyluronium hexafluorophosphate (HBTU) and *O*-(7-Azabenzotriazol-1-yl)-tetramethyluronium hexafluorophosphate (HATU).[92] HATU is a very effective coupling reagent for difficult AA sequences and sterically hindered *N*-Terminus'. It is proposed that HATUs increased coupling effectiveness is due to the incoming amine being stabilised through a hydrogen-bonded 7-membered cyclic transition state.[93]

Figure 1.6: Popular phosphonium and guanidinium coupling reagents.

1.1.3.4 Deprotection: Cleavage Cocktails

Once the target peptide sequence is reached, the construct must be released from the resin and the side-chain protecting groups need to be removed. Efficient release of the peptide from the resin and removal of the side-chain protecting groups is crucial for ensuring a high level of yield and purity for the final crude peptide. Reaction conditions, such as choice of cleavage reagent, duration of reaction and scavengers used, are among the most important considerations to facilitate a successful release. The cleavage step has a high risk of producing unwanted side-reactions, thus trapping potential carbocations with effective scavengers has become all but mandatory. The most widely available scavenger is H_2O, however aqueous conditions may not be appropriate and may require organic reagents (**Figure 1.7**) such as: triisopropylsilane (TIPS), triethylsilane (TES), ethanedithiol (EDT), anisole, thioanisole, thiophenol and dithiothreitol (DTT).[33,94]

Triethylsilane   Ethanedithiol   Anisole

Triisopropylsilane   Thiophenol   Thioanisole

Dithiothreitol
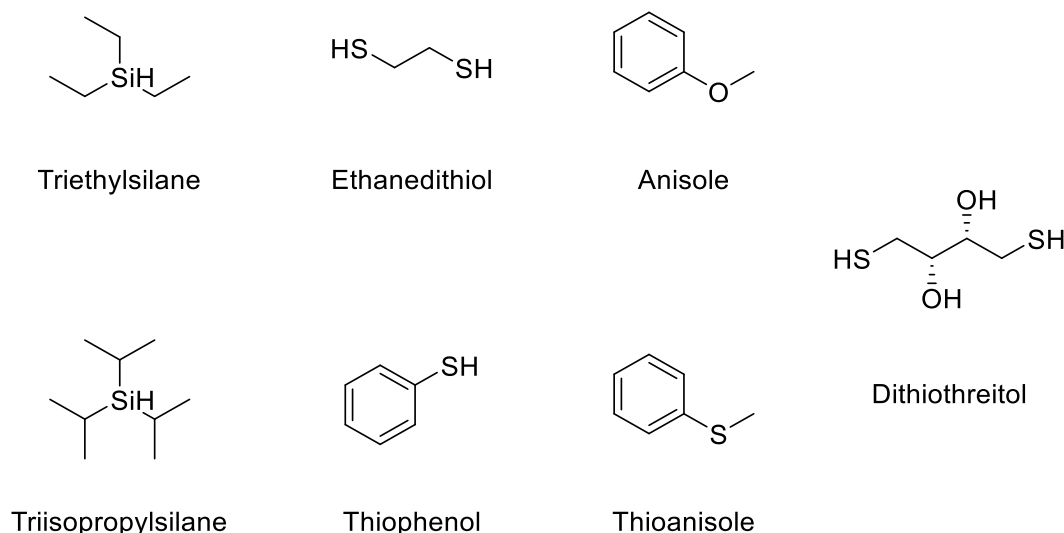
Figure 1.7: Common scavengers used during cleavage/side-chain deprotection.

Carbocations are electron-deficient species, which can be quenched by interacting with other molecules that can donate electrons. Carbocation scavengers typically contain electron-rich groups or functional groups with lone-pairs of electrons, such as nucleophiles or Lewis bases. When a carbocation is formed in a reaction, the scavenger can quickly react with it, forming a more stable species through electron-donation. This stabilises the carbocation and prevents it from participating in undesirable reactions or rearrangements.

Scavengers can also act as nucleophiles that can, for example, influence the deprotection mechanism, moving it toward S_N2. Carbocation scavengers may also stabilise any carbocation intermediates formed during the deprotection step. This stabilisation could alter the kinetics and thermodynamics of the reaction pathway, potentially favouring S_N2-like pathways.

It can be challenging to select an appropriate cleavage cocktail as it depends heavily on the AA residues within the peptide sequence, the side-chain protecting groups present, and the properties of the attached linker.[81] However, cleavage cocktails such as: TFA/H_2O/TIPS (95:2.5:2.5), TFA/H_2O/DTT/TIPS (90:5:3:2) and TFA/Phenol/H_2O/TES (88:5:5:2) have been used extensively in the literature, with typical reaction times of 1 – 4 hours.[95,96] Reaction times longer than this can lead to a significant increase in side-reactions, but shorter times may provoke incomplete deblocking of side-chain protecting groups and cleavage from resin. Cleavage conditions for the 2-chlorotrityl chloride linker usually consist of TFA concentrations <0.5%. However, this is problematic when using the Fmoc/*t*Bu strategy as some of the *t*Bu-protected side chains may be susceptible to cleavage. A solution of 30% hexafluoroisopropanol (HFIP) in DCM will selectively cleave only the trityl linker (~90 minutes), while leaving the *t*Bu-protecting groups completely untouched. This is incredibly useful when further synthetic manipulation is required to produce the final peptide-based product.

1.1.3.5 Future Directions & Challenges

The humble peptide started its journey isolated from livestock glands, and now stands in a league of its own as an established therapeutic niche within the pharmaceutical industry. Peptide therapeutics have continued to grow and develop while working with scientific innovation to expand into new opportunities and molecular targets by exploiting cutting-edge synthetic and purification technologies. Advances in synthetic peptide chemistry and improvements in the synthetic materials and reagents (resins, linkers, coupling reagents etc…), have been crucial in overcoming the challenges associated with peptide manufacturing.

SPPS is currently the preferred option for peptide synthesis (**Scheme 1.2**). However, there remain many intricacies that need to be addressed. The synthesis of longer peptides (>50 AA residues), or peptides with post-translational modifications can be troublesome for peptide chemists, as aggregation and other

phenomena often result in reduced yields and purity. In some cases, the desired peptide may not be achieved at all. Synthetic peptides containing fatty acids or PEG moieties are difficult to automate, and are still constructed manually using traditional solution-phase synthesis. The incorporation of *N*-methylated AA residues can be demanding due to the increased steric hindrance, with more aggressive coupling conditions required for successful conjugation.

This section highlighted the impact SPPS has had on peptide chemistry, providing researchers in academia and the pharmaceutical industry with fantastic tools to produce many different kinds of peptide-based products. The use of SPPS in the creation of peptide therapeutics has been well documented, with advantages in the efficient synthesis of novel peptide variants pertaining improved function and increased resistance to degradation. SPPS can also produce peptide products with high purity and at (relative) low cost compared to protein-based biologics. SPPS involves step-by-step assembly of amino acids on a solid support, which can be automated. The reagents used in SPPS are generally less expensive than those required for producing protein-based biologics. SPPS usually has shorter production cycles compared to protein-based biologics, leading to reduced manufacturing time and associated costs. These advantages are spear-heading an ambitious peptide drug discovery process within the pharmaceutical sector, with ~150 peptide-based compounds in active clinical trials and >500 in pre-clinical development.[59] Although it is likely that the global peptide market will continue to grow substantially in the years to come, there still exists a number of synthetic obstacles that peptide chemists need to surmount, including (but not exhaustive): bicyclic peptides, glycosylated peptides, and peptide-peptoid hybrids. Many of these challenges will be overcome by the academic talent produced by universities around the world, and will inevitably feed into industries that will turn these concepts into life-changing therapies.
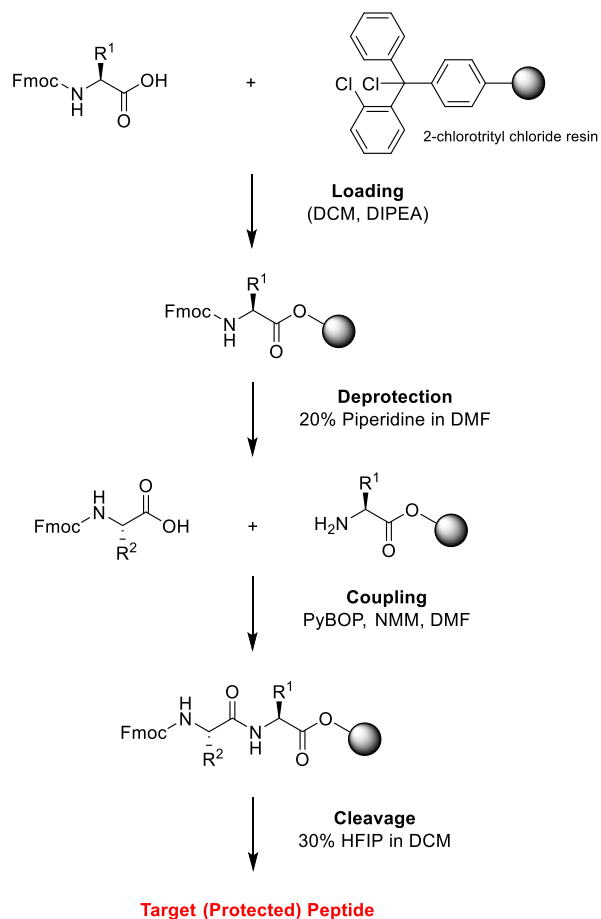
Scheme 1.2: General SPPS steps with Fmoc-chemistry and chlorotrityl resin.

1.2 Chemical Modification of Peptides

"Change does not roll on the wheels of inevitability, but comes through continuous struggle" – Martin Luther King Jr.

The biological activity of peptide therapeutics is closely related to their chemical structure. Sometimes the peptide structure may need to be synthetically modified to achieve an optimal secondary structure for improved biological activity, while retaining stability, selectivity and solubility of the peptide product.[97] Peptide natural products – often isolated from secondary metabolites produced by plants and microorganisms – have gained the appreciation of many research groups and institutions, due to their fascinating biological activity.[98] Most proteins consist of the 20 natural AA residues together with some post-translational modifications (phosphorylation or disulfide bridging), however the peptide-containing secondary metabolites frequently incorporate an assortment of unorthodox AAs.[99,100,101] For this reason, the introduction and/or manipulation of side chain(s) within a peptide sequence presents a dynamic alternative to traditional peptide chemistry, with the possibility of generating many different analogues from one peptide precursor.[102]

1.2.1 Introduction of Peptidomimetic-elements

The classification of peptidomimetics has been cultivated alongside the progress of synthetic peptides in recent years. The classification that will be used throughout this section is based on the modern taxonomy introduced by Grossmann.[103] His categorisation denotes four distinct classes of peptidomimetics – *A*, *B*, *C* and *D* – depending on their resemblance to the natural substrate.[104] Class *A* peptidomimetics closely resemble the parent peptide, utilising very few modified AAs to stabilise the bio-active conformation, with modifications being restricted to the peptide backbone or sidechains. Next is class *B* peptidomimetics, featuring derivatives of class *A* mimetics with small-molecule insertions, uncanonical AAs, and considerable backbone modifications. This class is home to peptoids and foldamers, where the backbones are extensively modified, but the side-chain functionalities are retained in the same order as the parent peptide.[105] Class *C* mimetics are more small-molecule in

stature, containing an non-canonical framework that almost completely replaces the peptide backbone. The orientation of key residues is retained, and the bio-active conformation remains intact. However, the central scaffold bears little resemblance to that of the native peptide. The final category of peptidomimetics – class *D* – are a far-cry from the natural peptide. Class *D* molecules can emulate the mode-of-action of the natural peptide without a remotely similar backbone or side-chain functionalities.
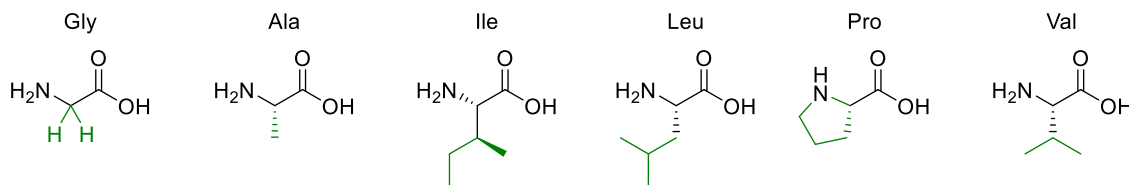
Modification of peptide structures has been a growing area of research in recent years, with side-chain manipulations and backbone modifications being the two popular methods.

Side-chain Modification

One method to achieve side-chain modification of peptides is to replace the canonical AA with its structural analogue during peptide synthesis, this allows the peptide chemist a degree of synthetic flexibility to probe for increased binding affinity and selectivity.[106,107] Non-natural AAs tend to induce protease resistance, such as derivatives of arginine – homoarginine, lysine, citrulline, ornithine, and *N*-isopropylornithine.[108]

Some side chains are more difficult to modify than others, take valine and alanine for example – *aliphatic side-chains* without an obvious functional group present (**Figure 1.8**) – there are relatively few techniques for derivatisation. However, recent breakthroughs in the direct functionalisation of C-H bonds have generated novel technologies for targeted modifications.[109] Of these recent breakthroughs, a notable example by Yu & group demonstrate the Pd-catalysed C-H arylation of *N*-terminal alanine residues.[110] The largest sequence that the group managed to modify using this technique was a tetra-peptide, nonetheless this preliminary study illuminates the (mostly) untapped potential of post-assembly C(sp^3)-H derivatisation as an exciting tool for the modification of aliphatic side-chains.
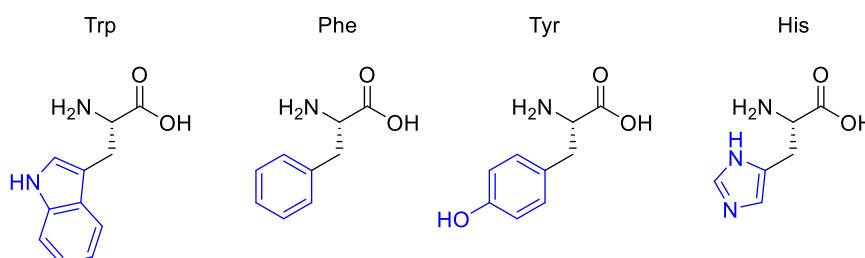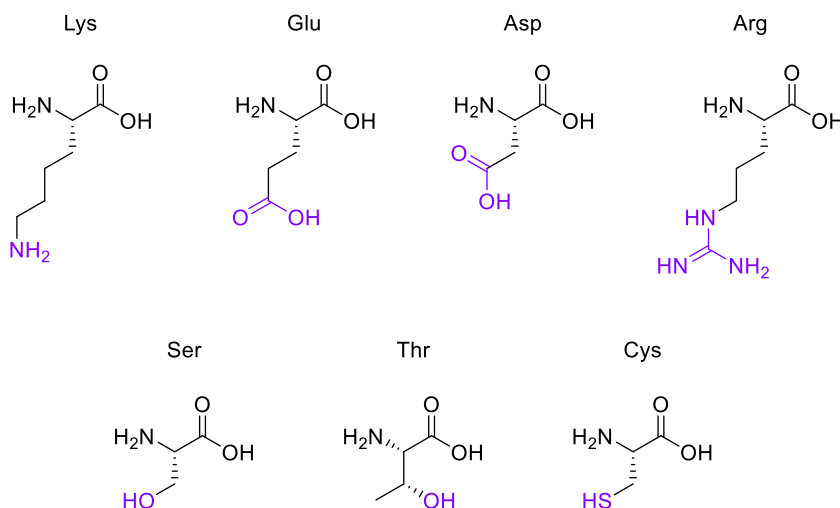
Aliphatic Side-chains

Gly   Ala   Ile   Leu   Pro   Val

Polar, Non-ionisable Side-chains

Gln   Asn   Met

Aromatic Side-chains

Trp   Phe   Tyr   His

Polar, Ionisable Side-chains

Lys   Glu   Asp   Arg
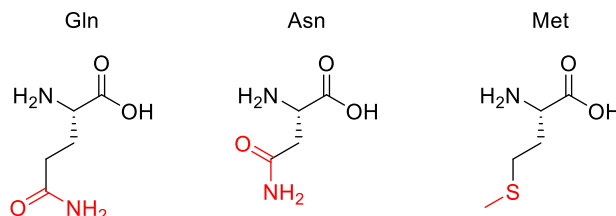
Ser   Thr   Cys

Figure 1.8: The 20 Natural AAs categorised by their side-chain functionality.

Like the aliphatic residues, the *polar non-ionisable side-chains* (primary amides) of glutamine and asparagine remain troublesome targets for derivatisation. Popp and Ball however, employed a molecular recognition strategy which facilitated the selective modification of the Gln and Asn side-chains using dirhodium metallo-peptides.[111] Reactions pursuing the modification

of methionine however, are much more common. Methionine possesses a relatively high oxidation potential, and the reversible oxidation of the thioether is a well-described reaction pathway.[112] Interestingly, it is the only natural AA residue that can be alkylated under acidic conditions.[113]

AA residues with *aromatic side-chains* tend to have a much larger pool of analogues to choose from, such as unnatural heterocycles,[114] and derivatives that include β-methyl groups for added conformational rigidity.[115] Aromatic side-chains can be further categorised into ionisable (tyrosine & histidine), and non-ionisable (phenylalanine & tryptophan). However, tryptophan being an exception in reactivity (pK_a) due to the many specific reaction pathways available to the indole moiety. Barbas introduced us to a powerful new aqueous ene-type reaction that permits click-like Tyr coupling,[116] and has paved the way for the functionalisation of diverse handles, including PEG chains and multi-functional linkers.[117] Albeit an up-and-coming methodology, the progress observed in the C-H derivatisation of aliphatic side-chains is expected to promote the development of novel modification tools for His and Phe.

Unsurprisingly, the AA residues with *polar ionisable side-chains* have been well-studied, with cysteine taking the top spot as the most documented residue within bioconjugation literature.[118] There are many properties of cysteine that make it a convenient target for side-chain modification, like its inherently low pK_a (~8.3) and the considerable nucleophilicity of the thiol group. Although the cysteine-maleimide conjugation has been a popular method of thiol modification,[119,120] the use of transition metals has gained recent recognition with the likes of Buchwald and Pentelute describing a Pd(II)-mediated arylation of Cys under mild conditions.[121] The theory described in this section serves to highlight the potential of side-chain modifications to introduce new functionalities or substituents into a given peptide natural product.

Backbone Modification

The ADMET properties of peptides are intrinsically restricted, with many peptide therapeutics suffering from minimal absorption, poor distribution from the plasma, predominant renal excretion, a metabolic life-time that is critically limited by proteolytic cleavage, and therefore, may have toxicological implications.[106] Consequently, a key motive for *backbone modification* is to enhance the

proteolytic stability of the peptide. Replacing the amide bond with bioisosteres can lead to the development of novel peptidomimetics possessing enhanced biological properties while retaining the intended therapeutic effects. Currently, various classes of amide bioisosteres have been identified, such as imidazole, indole, tetrazole, retro-inverted and reverse amide – just to name a very brief few.[122]

Backbone modification(s) often include other techniques like, insertion of methyl-AA,[123] incorporation of *β*-AAs,[124] peptoids,[125] and substituting *L*-AAs for *D*-AAs (**Figure 1.9**).[126]
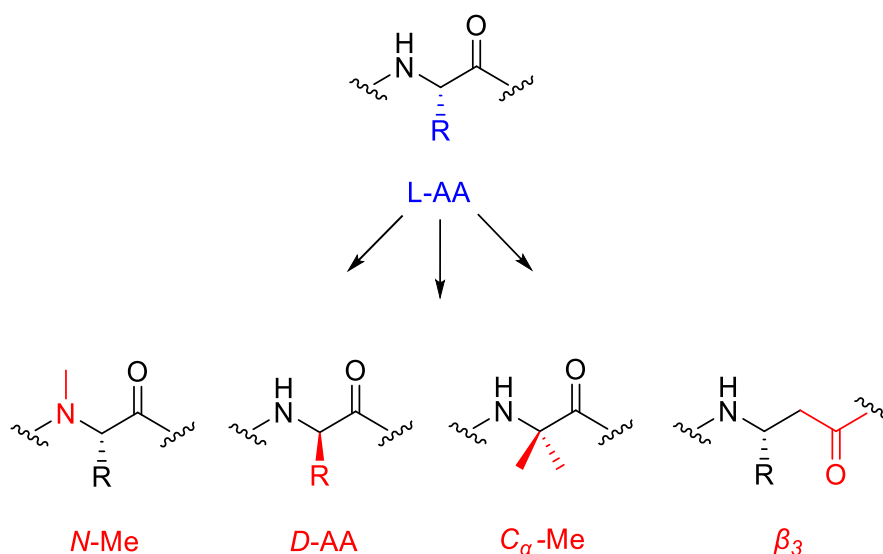
Figure 1.9: Chemical structures of popular peptide backbone modifications.

The introduction of these structurally diverse AAs into the peptide sequence – even more so at the site of proteolysis – can be an effective method for increasing the plasma half-life of peptide therapeutics. An interesting example is Selepressin – an analogue of Vasopressin, containing the backbone modification [Phe[(2)], Ile[(3)], Hgn[(4)], Orn(iPr)[(8)]] – which was being developed by Ferring Pharmaceuticals for the treatment of vasodilatory hypotension in septic shock.[127] Selepressin seen early clinical success, displaying comparable selectivity coupled with an enhanced plasma half-life. However, the phase 2b/3 clinical trial was terminated in February 2018 for futility, as the administration of selepressin, compared with placebo, did not result in any statistically significant improvement.[128] Perhaps further research is required to decide if selepressin will play a potential role in other patient-related conditions due to septic shock.

Significant work regarding backbone modifications was pioneered by Seebach et. al. who introduced side chains into small peptides via enolate chemistry.[129] One of the groups most impressive applications of this technique is the site-selective alkylation of cyclosporin A,[130] where they demonstrate that the deprotonation of amide N-H bonds 'shields' adjacent AAs from deprotonation and prevents epimerisation. This process allowed the compound to undergo nucleophilic substitution with electrophiles to produce the modified cyclosporins in satisfactory yields (~90%) with a diastereomeric selectivity ratio of 5:1 (*Re/Si, D/L*).

As peptide chemists, the use of transition metals has allowed us access to previously unheard-of bioconjugate transformations, this is particularly true in the ever-expanding area of peptide backbone modification.[131,132] A recent example was inspired by known non-ribosomal peptide synthetase (NRPS) pathways, where researchers describe an iron-catalysed oxidative derivatisation.[133] This approach was utilised to generate 21 non-natural AAs from 4 canonical residues while preserving the innate chirality. While this particular use of transition metals is scarce, the opportunities they present for peptide backbone modification, and protein structure/function will surely inspire innovation for novel peptide conjugates. The next section will discuss a few of the main techniques used for the medicinal chemistry optimisation of peptides.

1.2.2 Macrocyclisation

Cyclisation is an essential strategy for the medicinal chemistry optimisation of peptide leads during drug discovery.[134,135] Cyclisation is an excellent method for improving the proteolytic stability of a target peptide. This allows medicinal chemists to take advantage of the high selectivity, increased potency, and low toxicity that are intrinsic to peptides, to progress them as potential biotherapeutic agents. An early example on the use of homodetic-cyclisation during drug design was a cyclic analogue of somatostatin (Veber-Hirschmann peptide).[136] This newly cyclised peptide constrained the sequence into a bioactive conformation while also improving its proteolytic stability, resulting in a peptide-product with increased duration of action and oral bioavailability (**Figure 1.10**). From this

discovery, structural studies on other natural peptides were conducted to probe the use of cyclisation to explore novel bioactive conformations.[137]
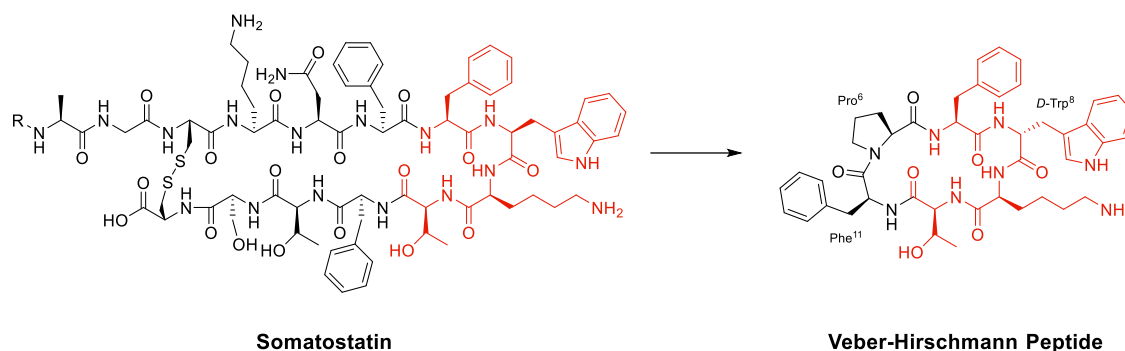
Figure 1.10: Structural comparison between Somatostatin and Veber-Hirschmann analogue.

As can be the case for many novel design scaffolds created by synthetic chemists, Nature did it first. Or at least provided the necessary inspiration to facilitate the discovery. The advantages imparted by cyclisation have been exploited by Nature with the many cyclic peptides found in fungi, bacteria, plants, and animals.[138] One study by Craik et. al. documented the effects of peptide-cyclisation on the activity of sunflower trypsin inhibitor-1 (SFTI-1). This cyclic peptide is comprised of one cross-linking disulfide bond and is the smallest, most potent known inhibitor of trypsin.[139] The group observed that cyclisation was essential to its enzymatic stability and inhibitory activity (**Figure 1.11**).[140] Many natural peptides like SFTI-1 possess exceptional chemical, thermal, and proteolytic stability, which can be (at least partially) attributed to their cyclic backbones. This section will examine the growing interest in macrocyclic peptides, and the various methods for synthesising cyclic peptides.
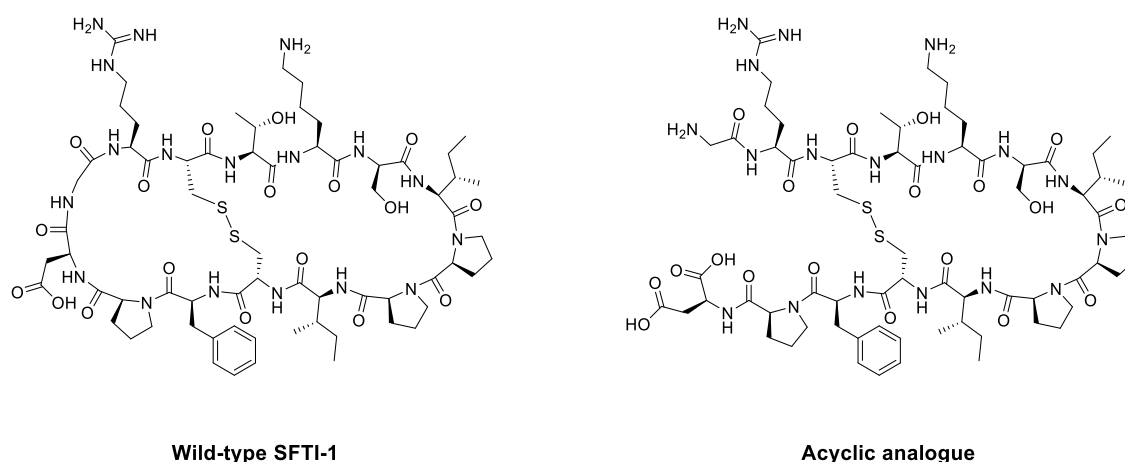
Figure 1.11: Structural comparison between natural SFTI-1 and its acyclic analogue.

27

1.2.1.1 Synthetic Considerations for Cyclisation

In general, there are 4 main routes to facilitate peptide cyclisation: Head-to-tail (*N*-terminus to *C*-terminus), head-to-side chain, side chain-to-tail, and side chain-to-side chain cyclisation (**Figure 1.12**). During the synthesis of cyclic peptides, the final ring-closing reaction can often be a lactonisation (cyclic carboxylic ester),[141] lactamisation (cyclic amide),[86] or produce disulfide-bridge.[142] Peptide cyclisations are generally carried out at high-dilution (< mM conc.) to promote intramolecular interactions and minimise troublesome intermolecular processes like polymerisation.

Macrocyclisation using SPPS has been employed as an effective means to generate cyclic peptides.[143] While the linear peptide is bound to the solid support (Resin), it experiences a sort of pseudo-dilution phenomenon – where the functional groups bound to the resin are less likely to encounter one another in comparison to the *free* molecules within the solution (more apparent in low-substitution resins). This environment promotes the favourable intramolecular interactions necessary for peptide cyclisation. To achieve *on-resin* cyclisation, the linear peptide is usually bound to the solid support via the side chain of one of the AAs in the sequence (e.g. Asp or Glu). At least 3 independent and orthogonal protecting groups (resin included) are required for this strategy. The linear peptide needs to be constructed, *N-* & *C*-termini to be deprotected, cyclised from head-to-tail, and then finally cleaved from the resin.[144] A noteworthy feature of on-resin cyclisation is that basic washing and filtering is usually sufficient to achieve (relative) purity, circumventing intermediate purification steps and solubility issues.
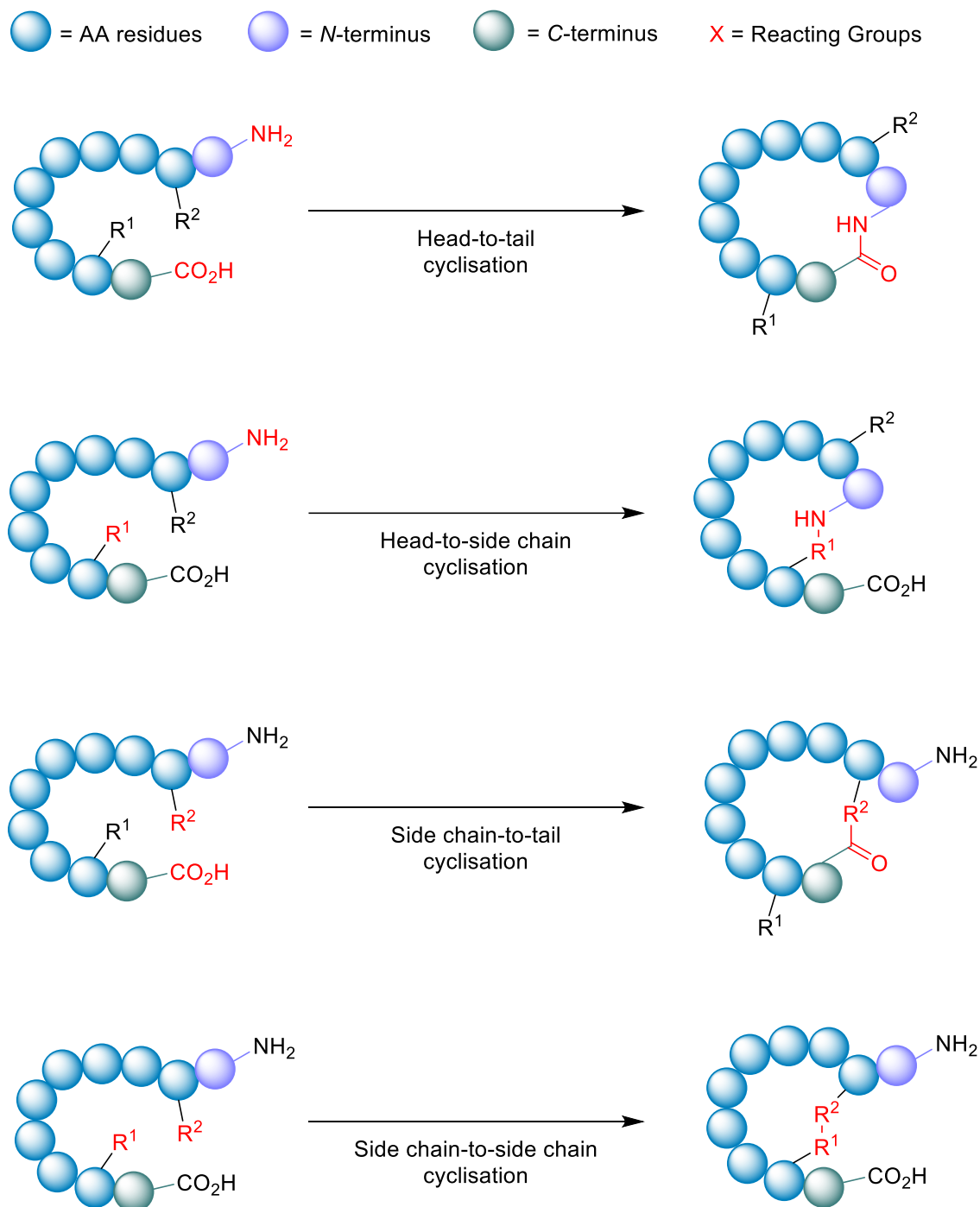
Figure 1.12: Schematic illustration of cyclisation strategies.

One of the most important factors that influence the success of peptide cyclisation is ring size. The cyclisation of large peptides can often be reported as problematic, however peptides containing >7 AA residues usually cyclise without too much difficulty. This is not the case for smaller peptide structures. During the head-to-tail cyclisation of peptides with <7 AA residues, *C*-terminal epimerisation and cyclodimerisation are common pitfalls.[145]

The activation free-energy ($\Delta G^{\ddagger}$) of cyclisation is governed by an enthalpy term ($\Delta H^{\ddagger}$) and an entropy term ($\Delta S^{\ddagger}$): $\Delta G^{\ddagger} = \Delta H^{\ddagger} - T(\Delta S^{\ddagger})$. Using the head-to-tail cyclisation approach as an example, the activation entropy ($\Delta S^{\ddagger}$) of the intramolecular interaction is based on the probability that the *N-* & *C*-termini approach each other at an angle (~107⁰)[146] to facilitate conjugation. This probability is reduced as the AA chain gets longer. One might assume that this should be of benefit to the smaller linear peptides (<7 AAs), however the loss in entropy is almost completely eclipsed by the enthalpic term. The activation enthalpy ($\Delta H^{\ddagger}$) represents the stress on the molecule during the transition state (‡). This value can be very high for peptides containing sub 7 AA residues, as there is significant ring-strain generated by the preferred conformation of the amide bonds within – as all *trans*.[147] One early study highlighted these challenges while synthesising numerous naturally occurring cyclic tetra- and penta-peptides using a head-to-tail style ring-closure. However, results were sparce with most cyclisation reactions proving unsuccessful.[148] They noted that the ring disconnection (site of cyclisation) had to be chosen very carefully, suggesting that product yields could be improved if the site of bond formation was not sterically hindered by the likes of *N*-alkylation or *β*-branched AAs. The authors also documented improved macrocyclisation rates between two AA residues of opposite stereochemical configuration (*D/L*), and when linear peptides had a sufficient level of *pre-organisation* due to certain *turn-inducing* motifs. This study demonstrates the many difficulties that can arise from an apparently straightforward retrosynthetic analysis of cyclic peptides.

1.2.1.2 Conformational Elements for Cyclisation

Macrocyclisation is a fickle process that heavily relies on the ability of the linear peptide to adopt a conformationally pre-organised form that brings the two reactive groups within close proximity to one another before ring-closure. The need for adequate spatial proximity has been well-documented since 1963,[149] resulting in less by-products from intermolecular reactions. Achieving this spatial proximity is one of the main challenges associated with macrocyclisation, because of linear peptides' preference for adopting elongated conformations to reduce strain.[150] This spontaneous process usually puts the reactive groups quite a distance away from each other. There are two main strategies used to counteract this problem: the first focuses on the *internal conformational elements*,

which exploit covalent modifications of the peptide backbone to promote cyclisation. The second strategy utilises molecular scaffolds and template-mediated techniques to facilitate macrocyclisation.

Internal Conformational Elements

As mentioned above, peptide cyclisation is more successful when the linear peptide can accommodate the angular criteria for both reactive groups being in the transition state with the least amount of strain. Smith and Daidone studied this idea and demonstrated that the cyclisation rate of longer polypeptide chains is influenced by the formation of intra-peptide hydrogen bonds. This generates ephemeral *β*-sheet like structures that serve to lower the free-energy of macrocyclisation.[151] The inverse is also true, slower cyclisation kinetics are observed with the absence of these hydrogen bonds in smaller peptides. Peptides with few AA residues lack the structural flexibility to accommodate these intra-peptide formations, thus highlighting their inherent rigidity and reluctance towards cyclisation.

In order to optimise the macrocyclisation of peptides, chemists have yet again sought inspiration from nature to help them overcome their synthetic woes. The secondary structure of proteins – notably, the *reverse turn* – has inspired the introduction of a *cis*-amide bond in the middle of the peptide sequence.[152] This modification is analogous to a *β*-turn and provides an elegant way of obtaining sufficient spatial proximity between the reactive groups. Proline has the highest natural occurrence within these reverse turns, with the *cis*-amide bonds of proline (**Figure 1.13**) being displayed in the crystal structures of many proteins. One classical study took advantage of this fact in the cyclisation of the tri-peptide cyclotri-*L*-prolyl.[153] In a similar fashion, linear precursors containing a di-proline unit with alternating stereochemistry (*L*-Pro-*D*-Pro or vice versa) are solid candidates for macrocyclisation due to their impressive *β*-hairpin inducing features. Robinson & group exploited this to generate cyclic peptides that accurately mimicked canonical conformations of hypervariable loops observed in the crystal structures of antibody fragments.[154]

Xaa-Pro (tertiary amide)

Trans-amide   *Cis*-amide
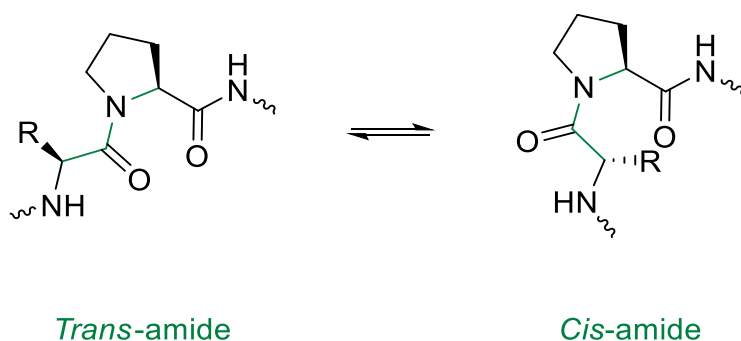
Figure 1.13: *Cis* & *Trans* proline isomerisation around the Xaa-Pro amide bond.

N-methyl AAs have a comparable stereochemical influence on the backbone of peptides to that of the Pro residue. They can also be used to introduce *cis*-amide bonds into the peptide backbone and are well-equipped to generate *β*-turns.[155] Turn-inducing effects are not exclusive to the Pro residue. Indeed the incorporation of other *D*-AAs in to *L*-homopeptides can apply similar contortions, and have been used to improve the yields of several peptide macrocyclisations.[156,157]

External Conformational Elements

External elements for promoting peptide cyclisation operate by *pseudo-isolating* the linear peptide from the bulk solution. This unique micro-environment serves to reduce the chances of polymerisation or cyclo-oligomerisation.[158] Metal ions offer a non-covalent ancillary-based strategy for peptide macrocyclisation.[159] The inspiration for this strategy comes from the well-documented capability of cyclic peptides to act as ionophores – binding metal cations in solution and *in vivo*.[160,161] Beck and co. were one of the first groups to demonstrate linear peptide pre-organisation via metal ions for the use of macrocyclisation.[162] They constructed a cyclic tetra-peptide through a metal-cation-assisted dimerisation of 2 dipeptide methyl esters under basic conditions (**Scheme 1.3**). An interesting caveat for this double head-to-tail lactamisation is that both dipeptides must orientate themselves in a *trans* fashion around the metal centre before nucleophilic attack can occur. This macrocyclisation strategy can facilitate ring sizes of 12- to 18-membered cycles, can incorporate *α* and *β* AAs, and does not require protecting groups, coupling reagents, or high-dilution conditions. The

cyclic peptide product can then be purified via isolation of the coordinated dianion, and the metal ion can be liberated by acid methanolysis.
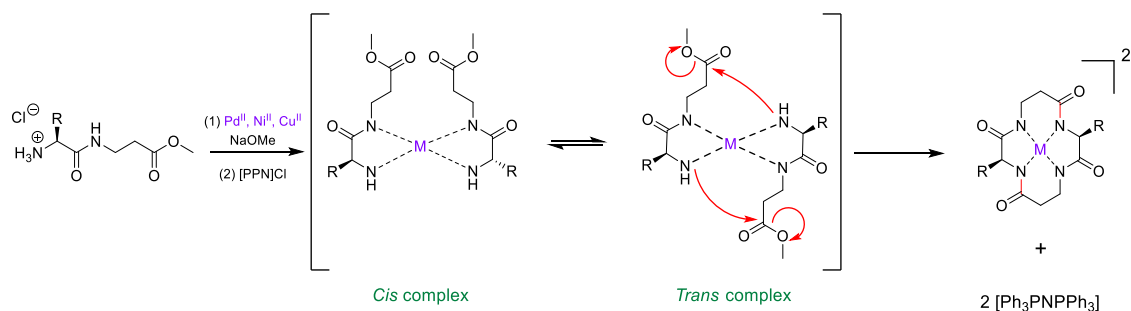
Scheme 1.3: Transition metal-assisted cyclo-dimerisation of dipeptide esters.

An analogous strategy – one that remains underdeveloped and largely unexplored – is the *anion templation* strategy. Although published reports on this strategy remain scant,[163,164] its use suggests that not only cations, but anions can be used for the pre-organisation of linear peptides to promote macrocyclisation. Speranza and Tomišić demonstrate this by using the Cl⁻ anion as a templating agent for the synthesis of cyclic peptides (**Figure 1.14**).[165] They prepared 3 novel cyclic homo-lysines and 6 other cyclic peptides using the head-to-tail lactamisation strategy. Experimental yields of cyclic peptide products – that were Cl⁻ anion templated – were found to be significantly higher than those obtained via the cation approach. Indeed, in some instances, only the anion-mediated synthesis yielded the target cyclic peptides. To further support their theory that the Cl⁻ anion played a major role in the macrocyclisation reaction, they studied the corresponding ring-closure reaction kinetics. Macrocyclisation experiments were conducted using increasing concentrations of TEACl (2-100 eq.), with higher concentrations of TEACl inducing faster cyclisation rates and increased yields. This was evidenced by TLC and quantitative ^{1}H NMR analysis.
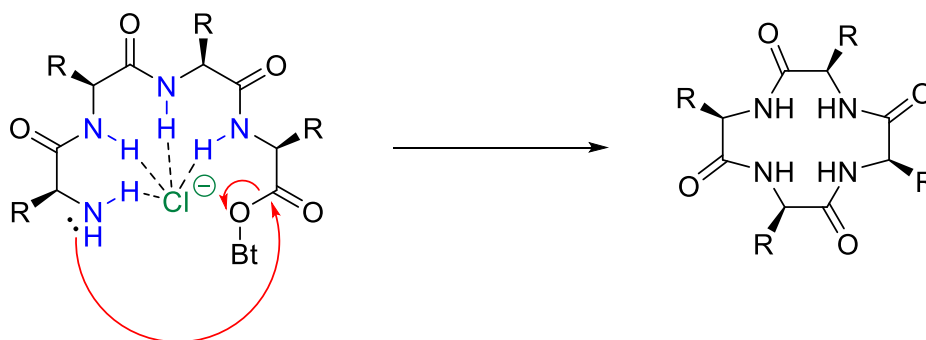
Figure 1.14: Suggested mechanism for the Chloride-mediated macrocyclisation.

It is understood that anion-recognition by cyclic peptides has been well-documented,[166] and many examples exist of their use as templating-agents for the synthesis of organic and inorganic scaffolds,[147,167] however – at the time of writing this thesis – no other example(s) of chloride-templated synthesis of cyclic peptides have been reported. This novel strategy for pre-organisation of linear peptides may promote further research into this vastly under-appreciated method of macrocyclisation.

Peptidomimetic alterations of natural peptides can produce bio-active analogues. Furthermore, macrocyclisation of linear peptides is often used as an effective strategy to provide increased conformational rigidity and more bio-stable products.

1.2.3 Substitution of *L*-amino Acids with *D*-amino Acids

Specific nomenclature has been used to denote the absolute configurations of the 4 substituents around sp^3 carbon atoms. The same notation is used for simple sugars and AAs – the *L*- and *D*-system of absolute configuration(s), suggested by Emil Fischer.[168] He denoted chiral molecules with a configuration related to that of *L*-glyceraldehyde – *L*, while stereoisomers related to *D*-glyceraldehyde were described as *D*. It is also worth mentioning that not all *L*-AAs rotate plane-polarised light to the left, they can also rotate it to the right; and the same holds true for *D*-AAs. Fischer's notation, *L*- and *D*- only refer to the absolute configuration of the substituents about the carbon atom.

D-AAs, the enantiomers of the canonical *L*-AAs, came under investigation in the mid-20th century, prompted by Krebs' discovery of *D*-AA oxidase.[169] However, the use of *D*-AAs to improve proteolytic stability was not employed until much later. Zisman and Seia showed us that the incorporation of *D*-AAs into polypeptide antigens could enhance their proteolytic stability.[170] Building on this work, Tugyi et. al. studied the antigenic properties and proteolytic stability of certain MUC2 peptides partially substituted by *D*-AAs. Their goal was to generate peptides that were resistant to enzymatic degradation while possessing similar, if not increased, binding kinetics compared to the original *L*-homopeptides.[171] The results generated from this study suggested that the activity of the peptides was sustained even in the presence of 2 *D*-AA residues at its *N*-terminal flanking

domain, and up to 3 at its *C*-terminal flanking domain. This novel *D-/L*-heteropeptide also displayed enhanced proteolytic resistance in lysosomal media and diluted human serum. These observations seem to demonstrate the benefits of appropriate *D*-AA modification(s) to produce synthetic antigens with comparable recognition properties and resistance to proteolytic degradation.

A recent study explored the effect(s) of heterogenous-backbone modification for enhancing proteolytic protection. They employed the four most common motifs for this kind of modification: *D*-AA residues, *N*-Me residues, C_α-Me residues, and β^3 residues. From this, the group synthesized a family of compounds – 32 analogues of a control peptide – with residues replaced by the above mentioned motifs.[172] These heterogenous-backbone motifs have already been studied in isolation,[123,173] but what makes this report exciting is that it has ventured to compare and contrast their ability to protect the substrate from proteolytic attack. Interestingly, the team discovered that the level of protection was as follows: *D*-AA > C_α-Me > β^3 > *N*-Me. D-AAs and C_α-Me residues induced proteolytic stability by moving the overall structure away from a conformation that was easily recognised by the enzyme. This imparted a large degree of proteolytic protection, with wide-ranging and synergistic effects when substitutions were combined in a single sequence. *N*-Me AAs were observed to influence proteolytic stability through the disruption of particular enzyme-substrate points of contact, with limited effect to local folding – resulting in short-range effects of humble magnitude, that were only additive when used in tandem. The protection offered via β^3 AAs was rather intricate – imparting only middling levels of stability, yet far-reaching. The authors describe the effects of combined β^3 replacement as partially-synergistic, but noted that the quantity of β^3 AAs did not directly correlate to enzymatic resistance.

Caution is advised when appropriating these findings in a more general sense, as the results generated by the group come from one single serine protease (Chymotrypsin). Nonetheless, the study presents solid hypotheses that will aid the future development of novel peptides/proteins containing enhanced proteolytic stability with minimal unnatural backbone content. *D*-AA residues possess folding characteristics that differ greatly from their *L*-AA counterparts, this makes them rather effective turn-inducers. Building on the results highlighted

in this study – demonstrating the ample proteolytic stability imparted by *D*-AAs – they may well be ideal candidates for bio-compatible backbone modifications.

1.3 Peptide Conjugates

"The whole is greater than the sum of its parts." - Aristotle

The original design of molecular conjugates can be attributed to the German physician/scientist Paul Ehrlich when he introduced us to the iconic phrase *'Magic Bullet'*. This magic bullet is described as a cytotoxic payload that would only become *armed* when selectively delivered to the site of interest by a targeting motif.[174] It wasn't until 1958 when the first few examples were reported,[175,176] and only in 1983 did the first clinical trial of such a conjugate begin.[177] Fast forward another 20 years until the first FDA-approved conjugate (gemtuzumab ozogamicin) – operating under the trade name *Mylotarg*™ – consisting of an antibody bound to calicheamicin for the treatment of acute myeloid leukaemia.[178]

The conjugation of molecular species to peptides is an elegant strategy to tackle substandard aqueous solubility, premature metabolic degradation, and may also be used to promote cellular uptake. Certain peptide sequences can provide targeted-delivery of small molecules to boost local drug concentration. This in turn, helps to reduce the adverse effects pertaining to systemic exposure and from accumulation in healthy tissues.[179] Drug-conjugates that possess peptide carriers can bind to cell-surface receptors with high affinity – similar to that of antibodies – and recognise a whole host of endogenous targets. Clinically, the most famous of these biological receptors are the integrins, tyrosine kinases, and G-protein-coupled receptors. Peptide conjugates have a much smaller molecular size compared to antibodies, and may provide a more efficient delivery to obscure biological targets with decreased immunogenicity.

The pharmacokinetic profile of peptide-drug conjugates is unique, with a shortened circulation time and metabolic half-life in comparison to antibodies. This inherent property gives peptide-based drug conjugates an edge when it comes to the delivery of cytotoxic agents where prolonged exposure is undesirable. However, a significant drawback is encountered when dealing with solid tumours. Treatment of this nature usually requires long-lasting pharmacokinetics, often displayed by antibodies. Nowadays, as peptide chemistry has matured and improved, techniques such as pegylation, lipidation and other modern advancements has made up the difference, making them much

more comparable to antibodies in this respect. The peptide-drug conjugate strategy has the potential to simplify commercial synthesis, streamline compliance with regulatory agencies and consequent criteria during manufacturing, and is a powerful means to achieve preferable disease outcomes that can be conveniently administered at a reasonable price.[180]

1.3.1 Linker & Conjugation Chemistry

The linker is an essential component of the peptide-drug conjugate strategy, and serves to covalently unite the peptide and the small-molecule moiety. The linker supports both the peptide sequence and the payload (drug) by upholding their structural integrity during administration, until such a time when the conjugate has reached its desired destination. To reduce the likelihood of unwanted side-effects, it is desirable for a peptide-drug conjugate to have a linker that only releases the payload after the *target* (cancer cells etc…) has taken up the conjugate intracellularly. However, upon systemic administration – most linkers within peptide conjugates start to break down quickly after being exposed to the blood plasma. The remnants of the *intact-conjugate(s)* are eventually taken up by the target cells, but this vastly diminished concentration can often prove inadequate.[181]

The linker within peptide-drug conjugates (usually) makes two covalent chemical bonds – one between the peptide/substrate and the linker, and another between the payload and the linker. The bond between the payload and the linker should be cleaved to release the free (unmodified) payload at the target site, and the bond between the peptide and the linker should not interfere with the peptide's affinity for its receptor. Many linker functional groups exist in the literature.[182] However, it is generally accepted that they can be arranged into 4 main families: acid-cleavable (carbonate & hydrazone), enzyme-cleavable (carbamate, amide & ester), non-cleavable (oxime, triazole & thioether), and reducible disulfide (**Figure 1.15**). This (rather broad) categorisation was established by monitoring how these functional groups reacted after cellular uptake or in the presence of *in vivo* stress. Because of this, linker chemistry can often dictate whether or not the overall conjugate will be successful in enhancing efficacy. This section will provide a brief summary of the main linker strategies used in the design and

synthesis of peptide-drug conjugates, with a focus on enzyme-cleavable linker chemistries.
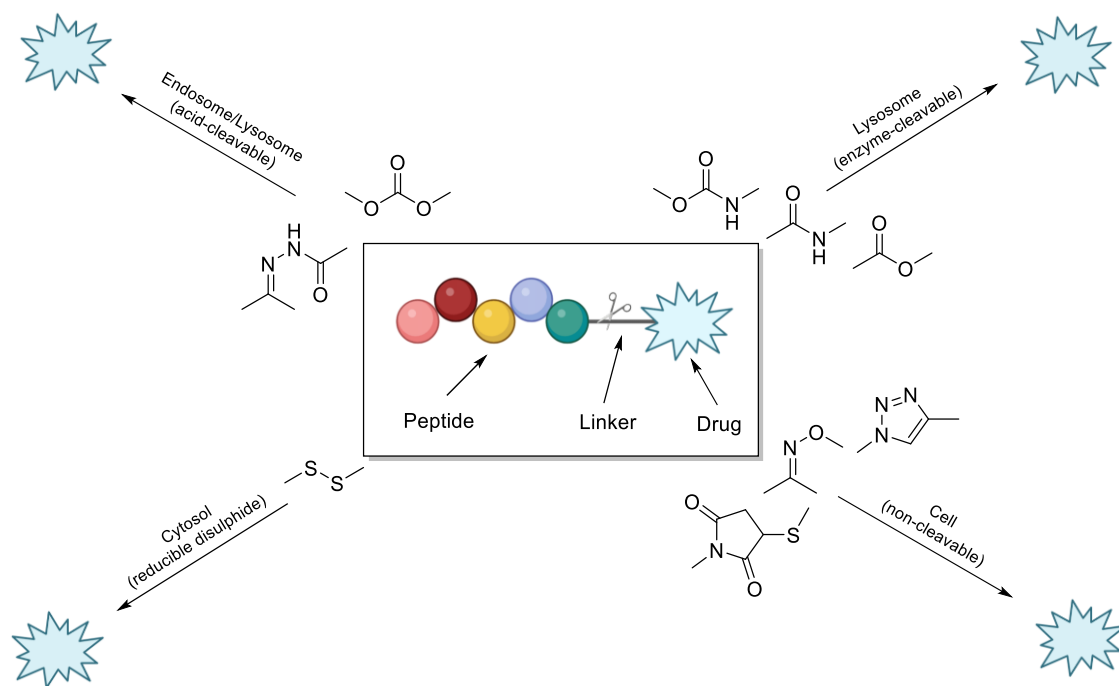
Figure 1.15: Cartoon schematic of a peptide-drug conjugate, and the associated linker chemistries.

Linker chemistries that involve enzyme-cleavable amide or ester bonds have become attractive, as they can be manipulated for site-specific cleavage in lysosomes or tumour microenvironments. Cancer cells' intracellular compartments – such as lysosomes and endosomes – have high levels of esterases and amidases, which can be utilised for site-specific release through upregulated expression of these enzymes. More complex AA-sequences recognised by enzymes like caspase-3 or cathepsin B have been employed as linkers.[183,184] It is important to note that these enzyme-cleavable linker chemistries are not foolproof, as many accidental-cleavage opportunities can arise prior to reaching the intended target. Appropriate control of the linker chemistry is essential for ensuring the overall stability of the conjugate until it reaches the target site.

1.3.1.1 Ester & Amide

Ester and amide functional groups are commonly used in linker chemistry to covalently bind different molecular entities – such as drugs or targeting moieties – in a conjugate. Ester linkers, which are cleaved by esterases, are often used to achieve a controlled release of the drug/payload. Amide linkers, on the

other hand, are generally more stable and resistant to hydrolysis. This makes them suitable for constructing conjugates with enhanced stability, or for creating prodrugs that require metabolic activation. The choice of linker and functional group can have a significant impact on the pharmacokinetics and efficacy of the conjugate.

One study employed an ester bond to couple paclitaxel to a peptide called *angiopep-2*. In this peptide-drug conjugate, the paclitaxel molecules are coupled to the side chain(s) of two Lys residues and the *N*-terminal amine of angiopep-2, to form the complete therapeutic (**Figure 1.16**).[185] This conjugate (ANG-1005) is currently being used for treating patients that display solid tumour or brain metastasis. It works by overcoming the main drawback of (unmodified) paclitaxel, which suffers from poor blood-brain barrier permeability due to the presence of multi-drug resistance efflux pumps in brain tumour cells. The ester bond of the peptide-drug conjugate is selectively cleaved by esterases within the lysosomes, delivering paclitaxel to the brain tumour cells.
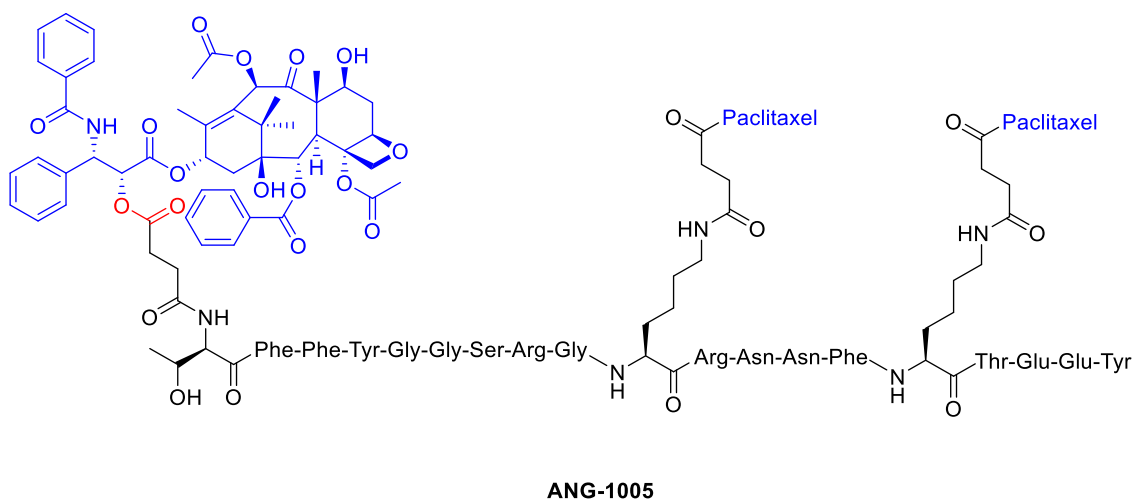
ANG-1005

Figure 1.16: Chemical structure of paclitaxel conjugate ANG-1005 (ester bond highlighted in red).

A radionuclide coupled to the peptide *octreotide* – called ^{177}Lu DOTA-TATE (*Lutathera®*) – was approved by the FDA in 2018 for treatment against neuroendocrine tumours (targeting somatostatin receptors).[186] [177]Lu DOTA-TATE is administered during peptide-receptor radionuclide therapy (PRRT) – a type of internal radiotherapy, also known as radioligand therapy – and was the first peptide-drug conjugate to be approved by the FDA for treating prostate cancer.[187] This conjugate consists of the radionuclide ^{177}Lu chelated to 1,4,7,10-

tetraazacyclododecane-1,4,7,10-tetraacetic acid (DOTA), and DOTA is coupled to Tyr³-octreotate (TATE) by an amide bond (**Figure 1.17**).[188]
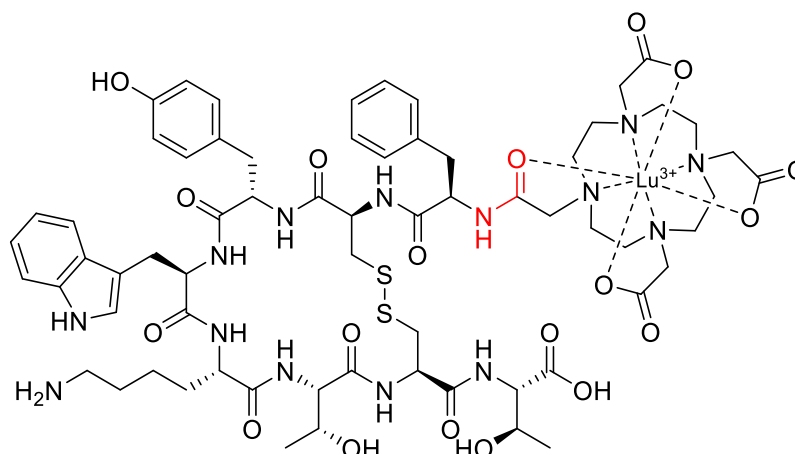
Figure 1.17: Structure of ^{177}Lu DOTA-TATE with amide bond highlighted in red.

To maximise effectiveness, ester and amide linkers need to be carefully manipulated so that they remain inert until within the tumour tissue/cancer cells. Although research in this area has rapidly expanded in recent years, more data is needed to understand what specific manipulations of amide/ester linkers can be employed to enhance chemical stability and efficacy.

1.3.1.2 Carbamate

Peptide-drug conjugates can also utilise the carbamate functional group to fortify their structure. The carbamate linker can be cleaved by particular enzymes present within intracellular endosomes or lysosomes.[182,189] One study (again) focused on synthesising peptide-paclitaxel conjugates using carbonate or carbamate linker chemistries, with the peptide getting selectively cleaved by the prostate-specific antigen (**Figure 1.18**). Evaluation of these peptide-drug conjugates demonstrated that compounds possessing the carbamate linker were more stable than their carbonate analogues.[190] Furthermore, these carbamate conjugates had the desired stability for specific release of the payload in the presence of prostate antigens, thus proving fatal to the prostate cancer cells.
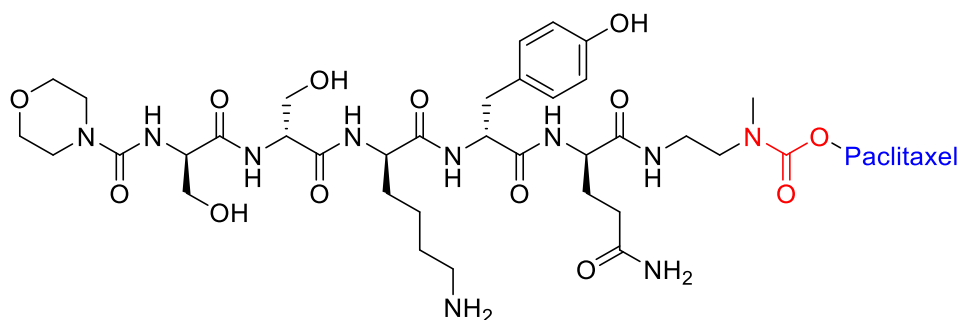
Figure 1.18: Example of peptide-paclitaxel conjugate with carbamate bond highlighted in red.[190]

This study agrees with other reports that suggest that the *in vivo* linker stabilities can be ranked as follows: amide > carbamate > ester > carbonate.[191] However, further studies are required to demonstrate which linker strategy will lead to better efficacy for tumour reduction.

1.3.1.3 Dipeptide & Tripeptide

A different approach demonstrates the use of specific Di- and Tri-peptide sequences for the controlled release of drugs from peptide-drug conjugates. The group of Liang and Co. synthesized compound A (**Figure 1.19**), containing the linker Di-peptide – *Val-Cit* – for targeted cleavage via carboxypeptidase (cathepsin B). In this study, the group seeks to compare the antitumor efficacy of peptide-doxorubicin conjugates by varying covalent linkers strategies.[192] Di-peptide A is covalently bound to Doxorubicin by a *para*-aminobenzyl carbamate (PABC) spacer which experiences a spontaneous electron-cascade via a 1,6-elimination upon enzymatic degradation of the *C*-terminal (amide) Cit-residue. The authors acknowledge that the linker chemistry takes inspiration from a currently FDA-approved Antibody-Drug Conjugate (ADC) called brentuximab vedotin (*Adcetris®*). The Val-Cit sequence is cleaved by cathepsin B – which exists in abundance within the lysosomes of tumour cells – leading to site-specific payload release. The results of this investigation concluded that compound A displayed enhanced cytotoxicity towards tumour cells, increased cellular uptake, and superior *in vivo* efficacy (mice) when compared to other peptide-drug conjugates with different linker functionalities.
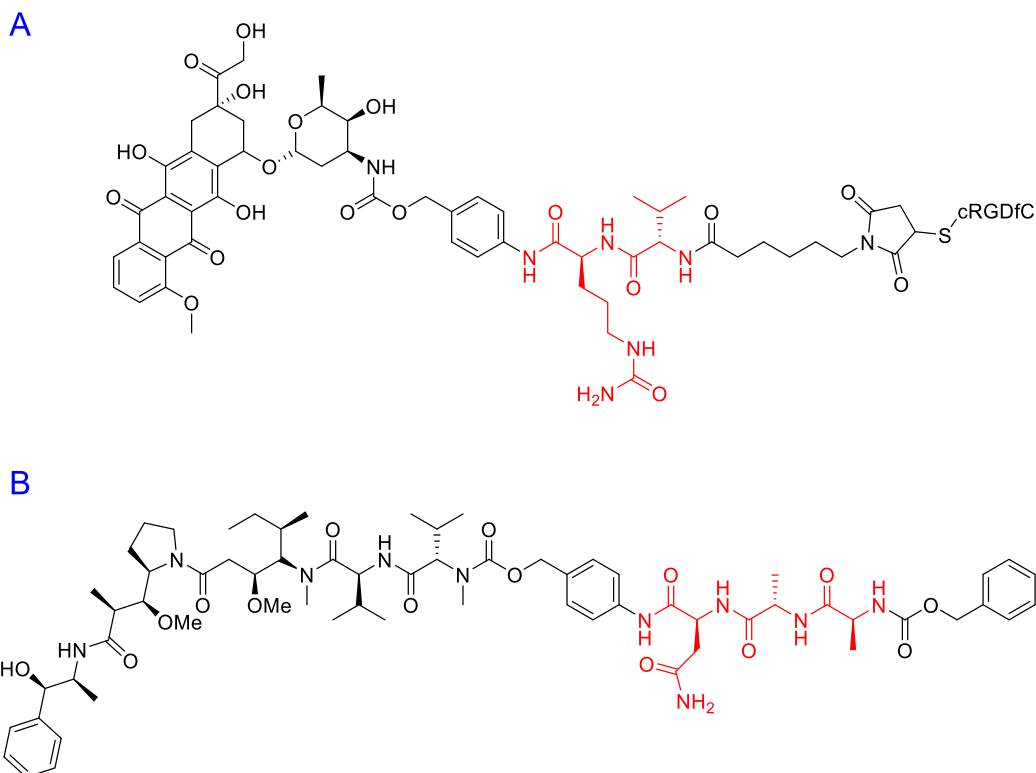
Figure 1.19: Peptide-drug conjugates with Di- and Tri-peptide linkers highlighted in red.

The Tri-peptide sequence has also been used for the site-specific release of payloads within tumour micro-environments. Ala-Ala-Asn is a cleavable sequence that undergoes degradation via the enzyme Legumain.[193] The asparaginyl endopeptidase – Legumain – is reported to be upregulated in tumour cells and specifically cleaves at the *C*-terminus of asparagine.[194] One group was determined to capitalise on this catalytic property for prodrug activation – with potential application(s) in cancer therapy. To this end, Bajjuri and colleagues synthesized distinct prodrugs containing the cytotoxic payload(s) monomethylauristatin E (MMAE) or didesmethylauristatin E (DDAE) conjugated to the Tri-peptide (B) via an amide or carbamate bond (**Figure 1.19**).[193] The absence of a targeting peptide within their synthetic design is noted, however these novel prodrugs display considerable synthetic flexibility and could potentially be functionalised with a specific peptide sequence to enhance their site-specificity. Among the Bajjuri-prodrugs that were synthesized, compound B was found to yield the best results, demonstrating 57% inhibition (4T1 breast cancer) in mice when compared to subjects treated with buffer alone. Interestingly, Tri-peptide prodrug B managed to overcome one of the main drawbacks of MMAE-based therapeutics, displaying no cytotoxicity, in contrast to the high mortality rate observed in mice that were treated with MMAE alone.

The selection of both the linker and functional group holds significant importance in peptide-drug conjugates, as it profoundly impacts the intended pharmacokinetic and pharmacodynamic characteristics of the conjugate. Notably, factors such as linker length, composition, and flexibility play a pivotal role in governing the conjugate's stability, the pace of drug liberation, and its elimination rate from the system. Moreover, the functional group present on the linker exerts an influence on enzymatic breakdown and cellular absorption of the conjugate, thereby ultimately shaping its effectiveness and safety profile.

1.3.2 Fluorescent Peptide Probes

The fields of chemical diagnostics and imaging are constantly being developed and updated, with fluorescence imaging becoming an essential technique for observing changes in biomarkers within living systems.[195,196] The compounds that generate fluorescent-imaging data are called – Fluorogenic Probes. These latent fluorophores can modulate their signal in response to environmental fluctuations, analyte interactions, or chemical modifications.[197] Fluorogenic probes are synthesized by chemically engineering the *parent probe* so that its fluorescence profile is sufficiently distinct from the *released fluorophore* – this activation is usually triggered by a specific event. In the interest of conciseness, this specific introductory section will focus solely on *Enzyme-activated* fluorogenic probes. For more information regarding fluorescent spectroscopic properties and fluorophore chemistry, see the following papers discussed elsewhere.[198,199]

Enzyme-activated fluorogenic probes that take advantage of enzymatic degradation to modulate fluorescence output, can equip researchers with an impressive toolkit for monitoring biological events *in cellulo* and *in vivo*. Initially, many enzyme-activated probes were constructed around xanthene dye motifs, for the detection of esterases,[200] galactosidases,[201] lipases,[202] and phosphatases.[203] Building on from this work, primitive live-cell imaging was possible via cell-permeable probes,[204] paving the way for more advanced fluorometric applications, including Enzyme-linked Immunosorbent Assays (ELISAs),[205] diagnostic tests,[206] and viability assays.[207] Advancements in the design of fluorogenic probes are constantly stimulating the progress of

complementary methodologies and their practical applications in the field of chemistry.

The two main strategies employed for fluorogenic probe design and application are; the latent properties of the fluorophore itself, and the method utilised to hide its fluorescence. Some crucial properties of the parent fluorophore may include; excitation and emission wavelength(s), resistance to photobleaching, quantum yield, and effects of pH on fluorescence output. Recently, researchers have begun to focus their attention on generating fluorogenic probes that do not overlap with auto-fluorescence produced by endogenous species, and result in minimal phototoxicity. Probes that fluoresce in the near-infrared and far-red region have an emission wavelength far above (nm) the auto-fluorescence window.[208,209] It is also worth noting that optimising the spectroscopic properties and brightness (product of quantum yield and extinction coefficient) is quickly becoming an essential part of the design strategy for the synthesis of fluorogenic probes.

The inherent properties of a fluorogenic probe are indeed important, however, the strategy used to mask its fluorescence will likely impact its enzymatic target and determine its effectiveness. An efficient fluorescence masking-strategy would see the probe generate a response selectively for the target enzyme, be chemically inert until within sufficient proximity, and terminate absorption and fluorescence output at the initial excitation wavelength (upon activation).

Fluorescence quenching techniques based on Photoinduced Electron Transfer (PET) and Förster resonance energy transfer (FRET), and to a lesser extent – Ratiometric Imaging, have been very popular in recent years.[210] To further enhance these quenching techniques, self-immolative linkers have been employed to enhance probe stability and performance.[211] Corso and Gennari described self-immolative linkers as *"covalent constructs designed to degrade spontaneously in response to a specific stimuli"*.[212] The two most prevalent self-immolative linker motifs in literature (in regards to enzymatic probes) are, elimination (electron cascade) and acyl-transfer (**Figure 1.20**). In this particular context, the linker is being used to modify the fluorescence profile as a means for detecting the presence of a hydrolytic enzyme. It is worth highlighting that self-immolative linkers have demonstrated their utility in both peptide/small molecule

and macromolecular drug delivery and sensor systems. I believe that with additional refinement, these systems may have the potential to evolve into commercially feasible solutions.
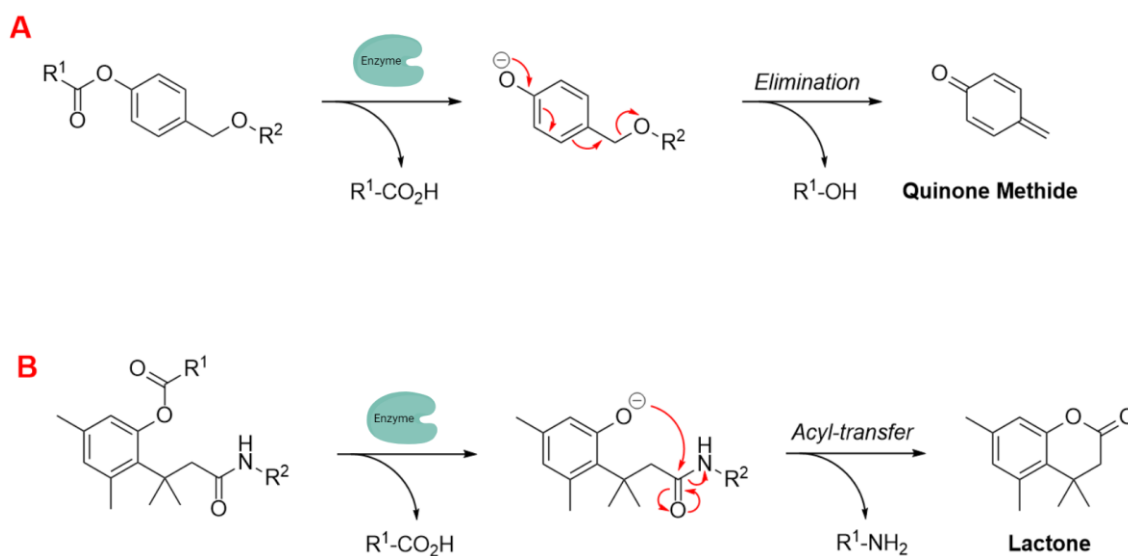
Figure 1.20: Examples of Self-immolative Linker Strategies – Mechanism(s) of Activation, (**A**) Elimination and (**B**) Acyl-transfer.

In the next few sections, we will focus our attention on peptide-based fluorescent probes and build on some of the ideas we discussed above.

1.3.2.1 Intrinsic Peptide-based Fluorescence

It is widely acknowledged that amino acids play a pivotal role as vital nutrients in biological organisms. Consequently, functional materials crafted from naturally occurring amino acids exhibit commendable biocompatibility and environmental friendliness. The aromatic amino acids, including tryptophan, tyrosine, and phenylalanine, possess inherent fluorescence properties (**Table 1.4**), rendering them suitable candidates for developing peptide-based fluorescence probes.[213] To date, numerous such probes – utilising these aromatic residues – have been documented in the literature.[214,215]

One popular use of these aromatic residues is in the study of self-assembling peptides – employing the endogenous fluorescence as a marker. The fluorescence data may be used to probe the conditions necessary for the covalent synthesis of the peptide itself,[215] or to investigate the compound's effect on the micro-environment – by creating self-assembling peptides with fluorescence output that can be altered under different conditions.[216] In the context of peptide conformational changes, the accumulation and internal clustering of amino acids

within peptides can induce structural modifications, and may potentially influence the fluorescent characteristics of the peptides.
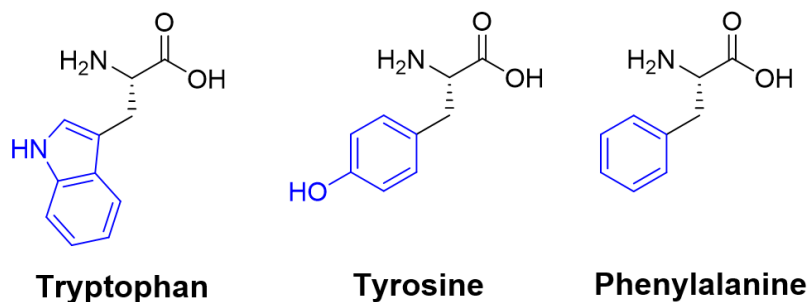
	Tryptophan	Tyrosine	Phenylalanine
$\lambda_{ex}/\lambda_{em}$ (nm)	220/360	225/304	220/285
Absorptivity (ε) (L mol^{-1} cm^{-1})	5600	1400	200
Lifetime (τ) (ns)	3.1	3.6	6.4
Quantum yield (Φ_F)	0.2	0.14	0.04

Table 1.4: Fluorescent properties of 3 natural aromatic AAs.[217,218]

An interesting facet regarding the Trp residue is that the native peptide-bond can act as a weak intermolecular quencher for the fluorescent indole moiety, which is further enhanced (quenching ability) in cyclic peptides.[219] In the case of Tyr fluorescent peptides, the tyrosine kinase protein plays a significant role in influencing peptide fluorescence, as it can induce phosphorylation of Tyr residues within peptides, resulting in the suppression of intrinsic fluorescence.[220] Fluorescent peptides containing the Phe AA can be used for monitoring the *in vitro* interactions with circulating-tumour DNA.[221] This interaction can cause the fluorescence output of the Phe residue(s) to become quenched, and may provide a novel method for DNA detection.

1.3.2.2 Peptide Fluorescence via Coupled Fluorophores

As we have discussed above, the Trp, Tyr and Phe residues are inherently fluorescent, thus, making them potential candidates for naturally occurring fluorophores. However, some of their optical properties can be problematic, such as their low (high energy) excitation and emission wavelengths, poor brightness and photostability – making them substandard for many biological assays. The most popular fluorophore among the natural aromatic AAs – tryptophan, absorbs and emits in the UV region and its fluorescence quantum yield is roughly 20% (**Table 1.4**). Researchers have tried to improve the fluorescent properties of

tryptophan, with initial attempts involving aza-tryptophans as potential isosteric analogues in proteins,[222] and cyano-tryptophans – which possess quantum yields approaching 50%.[223]

Despite significant advancements in the development of probes utilising canonical aromatic AAs to generate fluorescence data, the covalent combination of fluorescent moieties offers an alternative and effective approach for producing peptide structures with tuneable and enhanced optical properties. The synthesis of fluorescent peptides typically involves coupling the fluorophore to a reactive site within the peptide (side chains, *N*-/*C*-termini or incorporated spacer), with initial coupling experiments targeting carboxylic acids, amines and thiols[224] – and more recently phenols[225] and imidazoles.[226] However, the covalent coupling of a fluorophore to a peptide can potentially disrupt and alter the properties of the peptide. Consequently, selecting an appropriate fluorophore is of utmost importance, as different fluorophores exhibit distinct chemical characteristics.

Many organic fluorophores available today possess a wide range of physico-chemical properties, which can impact biologically-active peptides (when coupled together). Antimicrobial peptides (AMPs) are compounds generated by various organisms, including fungi, protozoa, bacteria, plants, and animals as a natural defence mechanism against common human pathogens.[227] Functionalising these peptides with fluorophores has become a useful way for researchers to investigate their mechanism of action and design imaging probes for the swift detection of microorganisms at sites of infection.[228] AMPs have been modified to contain various synthetic handles (carboxylic acid, sulfonyl chloride, alkyne etc…) to facilitate facile coupling with fluorophores without hindering their main identification characteristics.[229,230] A study by the Vendrell group sought to uncover the optimal fluorophore to label AMPs.[231] They found that certain larger fluorophores – like Nile Blue and Rhodamine B – and smaller fluorophores – Naphthalimide and Dansyl – had little effect on their antifungal activity (**Figure 1.21**).
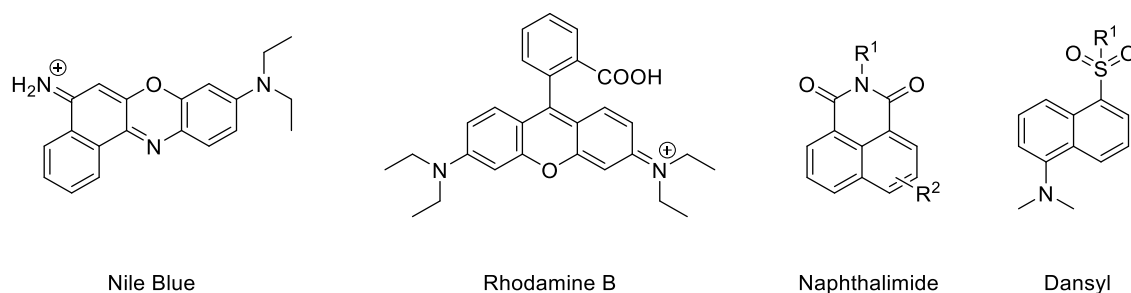
Figure 1.21: Example fluorophores suitable for coupling to AMPs (counter ions omitted for clarity).

Cell-penetrating peptides (CPPs) serve as efficient delivery carriers, and the investigation of their uptake and transportation mechanisms often involves the use of conjugates labelled with fluorophores.[232] Fluorophores tend to be (relatively) planar lipophilic molecules, with a rigid and bulky structure containing a (sometimes extensive) aromatic conjugated double-bond system. Many characteristics of CPPs (cellular uptake, membrane affinity, intracellular transport, and cytotoxicity) can be affected by the inherent properties of the fluorophore.[233] However, Birch demonstrated that CPPs coupled to fluorophores possess enhanced membrane association and display a more defined intracellular localisation pattern.[234] When choosing a fluorophore for conjugation with biologically active peptides found in organisms, it is essential to consider its potential toxicity and any adverse side-effects, as well as the fluorescence intensity it exhibits during its application.

1.3.2.3 Application(s) of Fluorescent Peptide Probes

Peptides serve as exceptional scaffolds for biological investigations, given their ability to facilitate the precise monitoring of specific molecular interactions across a wide spectrum of biomolecules. The conjugation of a peptide to a fluorophore through covalent (bond formation) or other mechanisms not only preserves the inherent benefits of the peptide but also enhances the stability and longevity of the overall probe. In recent years, there has been a growing focus among researchers regarding fluorescent peptide probes, as they can be harnessed for the detection of tumour cells, metal ions, and various other substances. Consequently, the advancement of fluorescent peptide probes holds significant potential for expanding its application within the medical field.

Monitoring protein–protein and protein–DNA interactions

Many biological processes hinge on the interplay between proteins and their binding partners. Within this framework, fluorescent peptide probes have been constructed to gain deeper insights into protein-based interactions at the molecular level. For example, Sainlos engineered a phthalimide-based fluorescent peptide probe to explore the dynamic protein–protein interactions within the PDZ domain – one of the most prevalent protein-interaction domains in eukaryotes.[235] On a similar note, novel fluorogenic peptides have been employed as conformational reporters for Calmodulin – a major calcium signal-transduction protein. Yoshinori and coworkers first identified the calmodulin-binding peptides via *in vitro* selection using tRNA carrying a modified AA,[236] which was later improved (by the same group) with the addition of a 4-*N,N*-dimethylamino-1,8-naphthalimide. This naphthalimide moiety possessed a similar emission wavelength (530 nm), however, it displayed a significantly improved fluorescence output (100-fold increase upon binding to calmodulin).[237]

Monitoring peptide–membrane interactions

Fluorescent peptide probes can also be tailored for investigating peptide-membrane interactions, which play a critical role in peptide-based therapeutics and transfection agents. Cationic peptides – like AMPs – show promise in this regard, owing to their ability to bind to membranes. Analogues of melittin – a major component of bee venom – containing a fluorescent modification on one (or more) of its 26 AAs, has been synthesized by Postupalenko to investigate its orientation within lipid-rich membranes.[238] The group discovered that melittin aligns itself parallel to the surface of cell membranes. Analogous methods have been employed to investigate the membrane binding interactions of neuro-peptides, which act as messengers between neurons.[239]

Real-time Cell Optical Imaging

Optical microscopy has enabled researchers to observe the migration of biomolecules inside the cell with precise accuracy and high resolution. Fluorescent peptide probes are exceptionally well-suited for optical imaging, as they possess the ability to target specific proteins within cells and may incorporate optical reporters that can be readily detected through fluorescence microscopy. To aid the detection of pulmonary infections, Trp-BODIPY fluorescent probes

were synthesized to visualise *Aspergillus fumigatus* in human lung tissue.[228] This modified residue serves as an ideal reporter due to its ability to maintain the molecular recognition properties of the native tryptophan while also offering a fluorescent output upon specific binding to fungal cells (**Figure 1.22**). Additional fluorescent probes – containing antimicrobial peptides – have facilitated the real-time, *in situ* detection of bacteria in excised human lungs through optical endomicroscopy.[240]
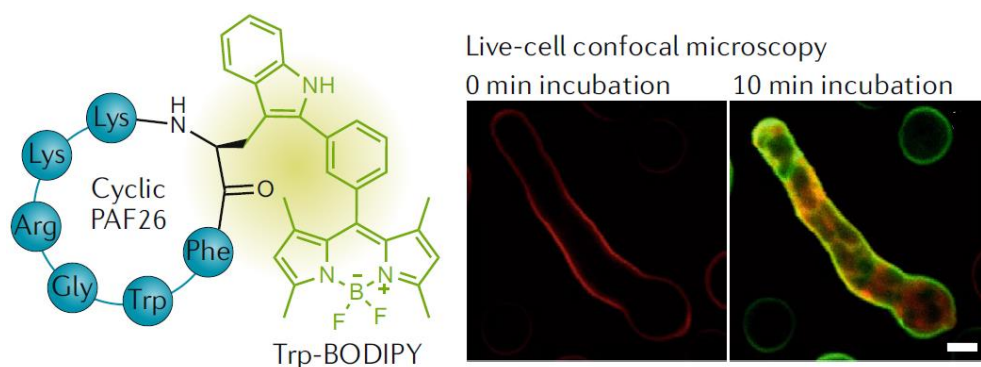
Figure 1.22: Chemical structure of the Trp-BODIPY-labelled cyclic peptide and live-cell confocal imaging of *Aspergillus fumigatus* over time.[228]

Optical imaging studies can also be conducted to obtain substance-related read-outs from cells. For example, fluorescent peptide probes containing coumarin-modified AA residues have been designed to report the endogenous phosphatase activity of protein tyrosine phosphatases in live cells.[241] The wash-free imaging capabilities of fluorescent peptide probes makes them valuable tools for applications where samples need to be analysed quickly with minimal processing steps, as seen in metabolic engineering and clinical diagnostics.

1.3.3 Lanthanide-based Peptide Probes

Luminescent lanthanide Ln^{3+} complexes – particularly those of Eu^{3+} and Tb^{3+} – have garnered significant attention in recent years owing to their unique photophysical properties and potential applications in fluoroimmunology, NIR-spectroscopy, and lighting devices.[242,243] This class of compounds exhibits narrow emission bands, long luminescence lifetimes, and resistance to photobleaching, making them promising candidates for use in biological imaging, sensing, and opto-electronic devices.[244] The prolonged luminescence lifetimes of emissive Ln^{3+} complexes facilitates the use of time-gated detection techniques

(**Figure 1.23A**) to remove the inherent autofluorescence present biological fluorophores, thus enhancing the signal-to-noise ratio of the luminescence output.[245] Additionally, their ability to tune emission colours, and their high quantum yields make them an attractive alternative to traditional organic fluorophores.
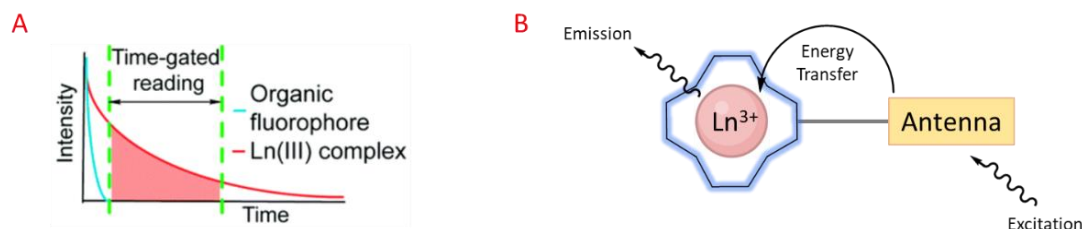
Figure 1.23: Prolonged luminescence lifetime of the Ln^{3+} complex, in contrast to traditional organic fluorophores (A). [246] Cartoon schematic of antenna excitation (B).

Multiple factors must be taken into account when designing a luminescent lanthanide complex. First and foremost, it's important to note that directly exciting Ln^{3+} ions is highly inefficient, primarily due to the Laporte forbidden character of f-f transitions. Ln^{3+} ions in aqueous environments usually do not luminesce due to the efficient non-radiative decay process provided by the surrounding H_2O molecules. Nevertheless, the luminescent characteristics of lanthanides can be enhanced by chelating the ions with appropriately designed ligands that exhibit strong light-absorbing properties – *antennae*.[247] Ln^{3+} ions can therefore be shielded from the solvent environment, and the electronic energy in the form of light absorption from the ligands can be transferred to the metal ion. A cartoon schematic describing the photophysical pathway for Ln^{3+} luminescence is outlined in **Figure 1.23B**. This process involves an energy transfer from the excited state of an (appropriately) absorbing antenna to the Ln^{3+} excited state, which results in metal-centred luminescence.[248] The choice of the sensitising group can be especially valuable when creating responsive lanthanide probes, as alterations to the antenna can influence its absorption or energy transfer properties.

The next thing to consider is, Ln^{3+} ions generally maintain coordination numbers between 8 – 10 in aqueous environments,[249] so the synthesized ligand must be able to facilitate enough hard donors to complete this coordination sphere. There exists many kinetically stable Ln^{3+} complexes containing heptadentate or octadentate ligands, featuring; the carboxylic acid functionalised

cyclen, EDTA, DTPA, and 9N3 macrocycles.[250,251] If the Ln^{3+} coordination sphere is not complete, H_2O molecules will coordinate to the remaining site(s). In this case, there may be a luminescence quenching event due to vibrational energy transfer to O–H oscillators.[252] This quenching effect of coordinated H_2O molecules can be used for the design of responsive Ln^{3+} complexes, where upon displacement of the coordinated water can lead to an increase in luminescence intensity.[242]

1.3.3.1 Coupling Lanthanide Complexes to Peptides and Proteins

The integration of lanthanide complexes into peptides and proteins represents a vibrant area of ongoing research, and will be discussed throughout this section. Tagging peptides and proteins with Ln^{3+} ions most often involves the coupling of a stable Ln^{3+} complex to the AA residues.[253] Similar approaches using traditional fluorophores are widely employed in the development of various biological assays for studying ligand binding and enzyme activity. Lanthanide-based peptide probes have been predominantly utilised for monitoring phosphatase and kinase activity.[254]

An early example of a lanthanide-based peptide probe employed a simple DTPA ligand coupled to dipeptides Ser-Trp and phospho-Ser-Trp – utilising the Trp residue as an antenna. Tremblay and coworkers discovered that Tb^{3+} luminescence was enhanced by the non-phosphorylated (Ser-Trp) ligand, in contrast to the phosphorylated ligand.[255] This phenomenon was ascribed to a transition from a monomeric state to a dimeric state, which occurs in the phosphorylated and non-phosphorylated peptides, respectively. This change in luminescence output was employed to track the enzymatic dephosphorylation of the phosphorylated peptide using alkaline phosphatase. Tremblay developed this idea further by using a non-canonical quinolone antenna, and inserting an isoleucine residue between this new antenna and the phosphor-Tyr AA. This novel peptide-probe facilitated Eu^{3+} and Tb^{3+} luminescence upon phosphorylation (**Figure 1.24A**), and was applied to observe the conversion between non-phosphorylated and phosphorylated peptides using tyrosine kinase or tyrosine phosphatase.[256]
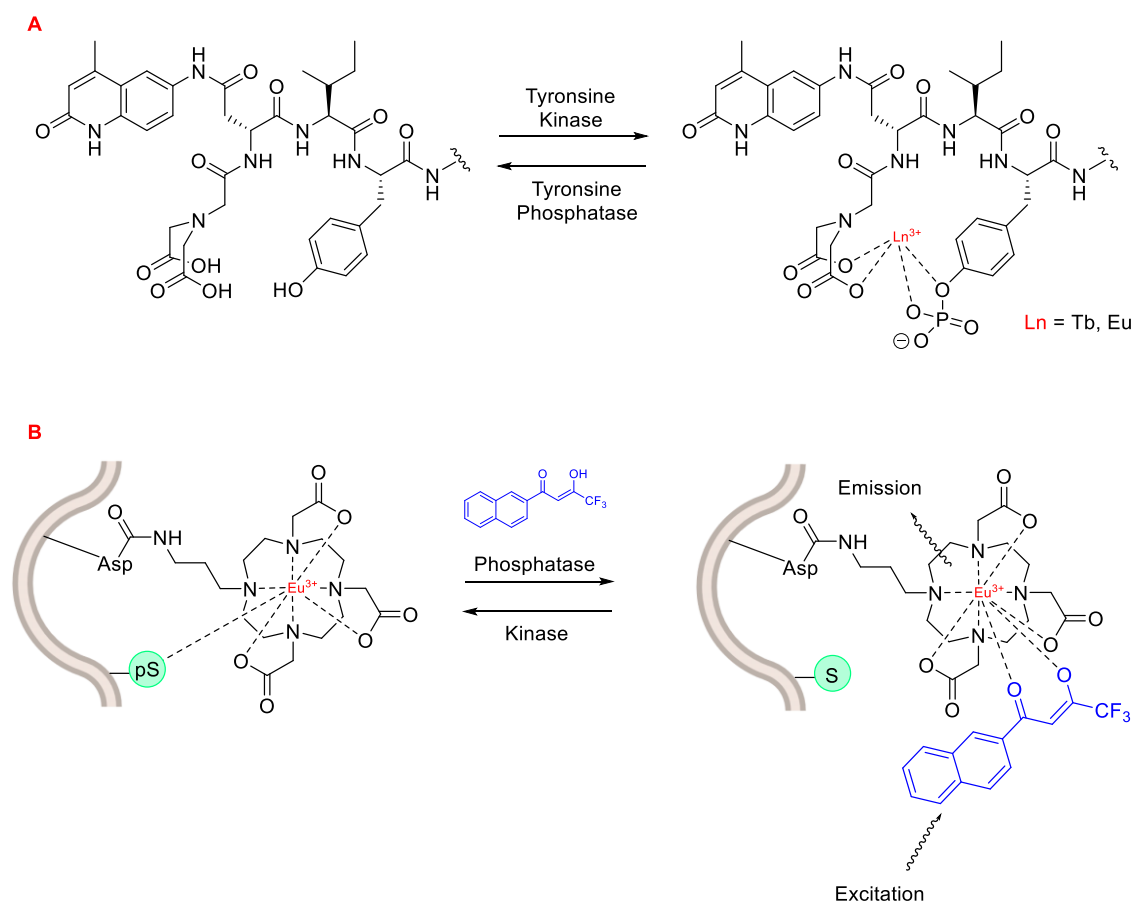
Figure 1.24: Lanthanide-based peptide probes to monitor enzyme activity. (A) Observing tyrosine phosphatase and kinase activity using a 5-residue peptide. (B) Asp-functionalised Eu³⁺ complex within peptide sequence coordinates to phospho-Ser residue.

A lanthanide-based peptide probe containing a DO3A-propylamino ligand was coupled to an aspartic acid residue (resin bound), using typical Fmoc SPPS.[257] Interaction from a nearby phospho-Ser residue induced competitive displacement of the *β*-diketonate antenna from the Eu³⁺ coordination sphere, causing a subsequent decrease in Eu³⁺ luminescence output (**Figure 1.24B**). This "On – Off" change in luminescence was utilised to monitor PKCα-catalysed phosphorylation of the peptide, with the aim of generating Michaelis-Menten kinetic data for the enzyme. On the other hand, the dephosphorylation pathway could be monitored by observing the enhancement in Eu³⁺ luminescence intensity upon preferential coordination to the *β*-diketonate.

Labelling peptides enables the real-time monitoring of enzyme reactions and allows us to use low reagent concentrations. The practice of labelling peptides with conventional organic fluorophores is widespread in many biological assays, and is readily being expanded to harness the numerous benefits offered by luminescent lanthanide complexes. It is essential to exercise caution when

choosing the coupling site and size of the lanthanide complex – to minimise any disruption to the enzymatic reaction. However, considering the extensive use of fluorescently labelled peptides, this is unlikely to pose a significant obstacle to the adoption of this technology. Anticipated progress in the development of lanthanide-based enzyme assays is on the horizon, offering potential attractive alternatives to current commercial assay formats, which may aid in the drug discovery process.

1.4 Aims

The field of peptide-based therapeutics and imaging agents has witnessed remarkable growth and innovation in recent years. The overall aim of the Introduction (above) was to highlight the importance of these versatile biomolecules in advancing precision medicine and enhancing our understanding of complex biological processes. Peptides, with their unique structural diversity, biocompatibility, and tuneable nature, serve as promising candidates for drug development, targeted therapies, and non-invasive imaging modalities.

The work carried out in this thesis will delve into the multifaceted applications of peptide-based probes and their non-natural analogues, highlighting their pivotal role in addressing unmet medical needs, from cancer therapy to neurodegenerative disorders. Emphasis is placed on the design principles that enable precise targeting of specific molecular pathways, minimising off-target effects and enhancing therapeutic efficacy. Furthermore, we explore the synergistic integration of peptides into the realm of molecular imaging, where they serve as indispensable tools for visualising biological events at the molecular and cellular levels.

The first objective is to design a Caspase-3 responsive peptide probe (Chapter 2). Our design strategy will contain 3 distinct motifs that make up the peptide probe – the DEVD sequence (a recognised substrate for the Caspase-3 enzyme), a *p*-aminobenzyl alcohol (PABA) linker, and a Naphthalimide fluorophore. We hypothesise that our probe Ac-DEVD-PABC-Naph (PABC = *p*-aminobenzyl carbamate) would provide a ratiometric fluorescence response for Caspase-3. With this probe in hand, response kinetics toward different concentrations of Caspase-3, probe-activity in the presence of Caspase-3 inhibitors, and the selectivity of the probe for Caspase-3 over other endogenous species will be examined.

The second objective is to develop a versatile methodology for the synthesis of novel, water-soluble DOTA analogues, comprised of a squaramide moiety that may act as an antenna for lanthanide luminescence (Chapter 3). The luminescent properties of various Ln^{3+} ions will be investigated for each individual analogue. We then hope to expand this idea further with the generation of a

lanthanide-based Caspase-3 probe. This Ln^{3+}-peptide probe will build on our success with organic fluorophores – as demonstrated in Chapter 2 – while harnessing the numerous benefits offered by luminescent lanthanide complexes.

The final objective is to try design and synthesize a completely new peptidomimetic scaffold based on Squaratides – a hybrid mix of squaramides and peptides (Chapter 4). In this chapter, we want to utilise the Squaramide moiety as an AA analogue within the cRGD peptide - *Cilengitide®.* We envisage the squaramide motif acting as a bio-isosteric replacement for C=O bonds, and may improve peptide half-lives through increased stability to enzymatic degradation, while retaining bioactivity.

Chapter 2

Utilising a 1,8-naphthalimide Probe

for the Ratiometric Fluorescent

Visualisation of Caspase-3

2. Utilising a 1,8-Naphthalimide Probe for the Ratiometric Fluorescent Visualisation of Caspase-3

2.1 Introduction

"I am almost inclined to coin a word and call the appearance fluorescence, from fluor-spar, as the analogous term opalescence is derived from the name of a mineral." – George Stokes (Sligo lad!)

Apoptosis was first coined by Kerr *et al.* while trying to detail a different form of cell death.[258] Since then, it has become clear that this morphologically-distinct mode of programmed cell death occurs during normal development of multicellular organisms to maintain healthy cell populations.[259] The regulation of apoptosis plays a vital role in various diseases such as cancer,[260] Acquired Immunodeficiency Syndrome (AIDS),[261] Autoimmune Lymphoproliferative Syndrome (ALPS),[262] and neurodegenerative diseases like Parkinson's and Alzheimer's.[263,264] Therefore, the monitoring of apoptosis within multicellular organisms is paramount to improve our understanding of these apoptosis-related diseases.[265]

Caspase(s) 1-14 are a family of cysteine proteases that are important mediators of the apoptotic pathway.[266] The name "Caspase" was originally derived from a cysteine-dependant aspartate-specific protease, as reported by Alnemri *et al.* where cleavage of its substrate is regulated by a Cysteine side-chain (-SH) present on the enzyme, with an inherent (and strict) selectivity for severance on the *C*-terminal aspartic acid residue.[267] Caspase-3 is widely regarded as the most proficient of the family, with a profoundly low K_M (Michaelis constant) and high k_{cat} (turnover number) for its substrates that preferentially cleaves any peptide moiety or proteins containing the sequence – DEVD.[268] Thus, caspase-3 represents a useful biomarker to help gain an insight into the analysis of apoptosis.

Several strategies have been employed to monitor caspase-3 activity in recent years.[269,270,271] In particular, activity-based fluorescence probes have seen success where the use of latent fluorophore-conjugates coupled to the *C*-

terminus of a DEVD peptide substrate can release a fluorescent reporter upon caspase-3 mediated cleavage.[272,273,274] For example, Shi and coworkers have recently reported a DEVD probe conjugated to a hydrophobic Tetraphenylethene (TPE) fluorophore, with Aggregation-induced Emission (AIE) characteristics (**Figure 2.1A**).[183] This probe was virtually non-fluorescent in aqueous media, but experiences a dramatic surge in fluorescence intensity in response to caspase-3. Another popular strategy relies on the use of a dye/quencher pair motif which – when activated by caspase-3 – results in a "switch-on" of the dye fluorescence.[275,276] Shaulov-Rotem and group have used this approach in their recent report on a quenched fluorescent activity-based probe (qABP).[266] A blackberry quencher was incorporated to negate any fluorescent activity, and only emitting a fluorescent signal after covalent modification via caspase-3. Both of these strategies rely on the changes in fluorescence emission wavelength after enzymatic cleavage for analysis of activity. However, the accurate evaluation of caspase-3 activity *in cellulo* remains problematic, with many of the reported fluorogenic probes being affected by cellular localisation and microenvironments.
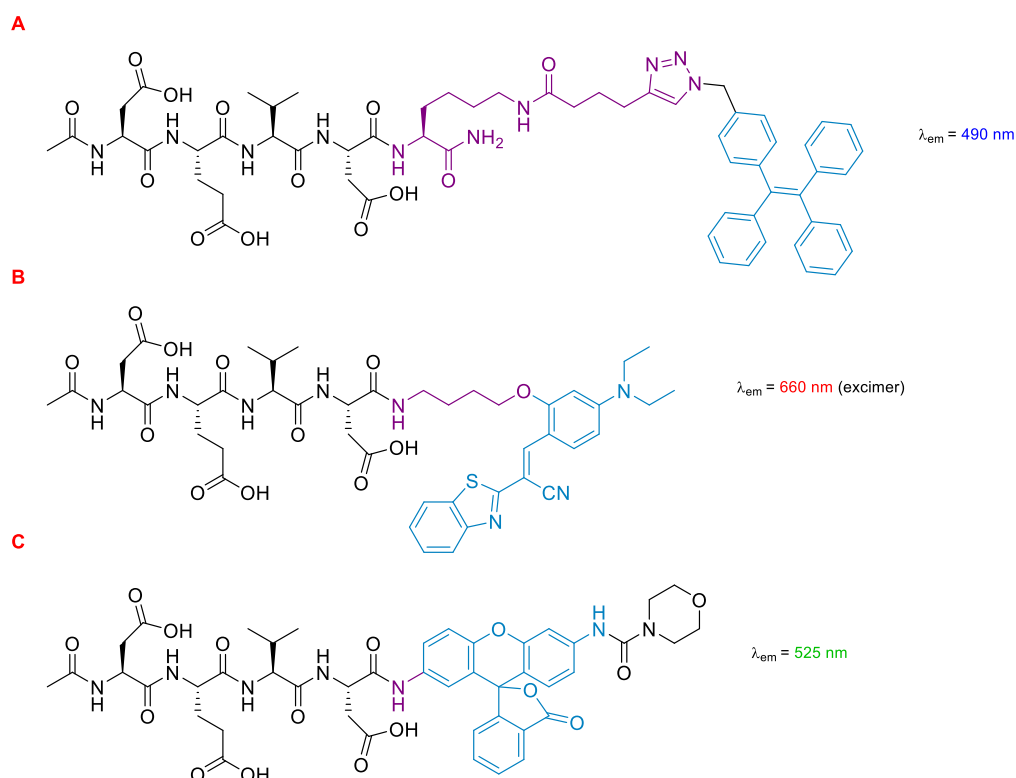
Figure 2.1: Examples of Caspase-3 fluorescent probes (purple denotes the linker, and blue the fluorophore), and their corresponding emission wavelength. (A) Ac-DEVDK-TPE, (B) Ac-DEVD-NH-CV, and (C) Ac-DEVD-MC-R110.

Ratiometric probes may provide an optimal solution to this problem owing to their advantages in quantitative detection.[277] The intensity of fluorescent light is heavily influenced by the quantity of fluorophore in the optical path. The amount of fluorophore in the optical path is determined by the actual concentration of the fluorophore within the cell (which is determined by marker uptake or expression) and the diameter of the specimen. Consequently, it is challenging to directly deduce the concentration of a particular species under investigation solely by observing one single fluorescence intensity.[278] For instance, one cannot definitively state, "An intensity (a.u) of 100 corresponds to 100 nM of free calcium in a cell." To address this challenge and enable accurate measurements of absolute species concentration(s), ratiometric imaging techniques have been developed. Ratiometric methods share a common approach in which the intensity of emitted light is measured twice, and a ratio of these intensities is calculated. In such methods, the fluorophore is typically excited with light of one wavelength, and the emitted light is measured at two different wavelengths. Indeed, this class of probes possess two distinct emission peaks that carry a self-calibration effect, which may adequately reduce many of the interferences mentioned above.[279]

In addition to the aforementioned benefits, the calculation of a ratio provides an additional advantage. During live-cell imaging using fluorophores, minor fluctuations in fluorescence intensity at the respective wavelengths are often encountered. However, in ratio-imaging, it is common to observe an increase in intensity at one wavelength paired with a decrease in intensity at the other wavelength (regardless of whether the probe is excited or detected with two wavelengths). When the ratio of both acquired images is subsequently calculated, the difference between the baseline and signal-amplitude is accentuated, compared to the mere intensity change of the fluorophore. This enhances the sensitivity of detecting changes in the signal.[280]

1,8-naphthalimides have been exploited to great effect in this regard where their tuneable photo-physics and synthetic versatility make them excellent candidates to elicit a ratiometric response.[281,282] The naphthalimide offers two methods for detecting an analyte: through the conventional fluorescence "switch-on" response and, equally, by adjusting the Internal-Charge Transfer (ICT) excited state to produce a ratiometric fluorescence response. First documented by Middleton and colleagues in 1986,[283] the 1,8-naphthalimide core exhibits a

brightness similar to coumarins,[284] along with remarkable resistance to photobleaching and a considerable Stokes shift. The photophysical properties of the naphthalimide fluorophore and its inherent characteristics are strongly impacted by the electronic nature of its substituents. For instance, the -NO$_2$ functional group – when installed at the 4-position on the 1,8-naphthalimide core – triggers a broad absorption band with a λ_{max} ~360 nm but exhibits minimal fluorescence. This is (primarily) due to the highly electronegative oxygen atoms that hinder the conjugation of the donor nitrogen to the rest of the fluorophore, thereby effectively obstructing its ICT. In contrast, the -NH$_2$ derivative in the same position is "unrestricted" and elicits a "push-pull" ICT excited-state, leading to broad absorption and emission bands at approximately 450 and 550 nm, respectively (**Figure 2.2**). Furthermore, the amino-nitrogen enhances the ICT-nature of the fluorophore, causing the emission to red-shift towards longer wavelengths compared to less electron-donating substituents like esters and carbamates. Collectively, these properties impart numerous attributes suitable for biological applications, including assay design and the development of fluorogenic dyes for confocal microscopy. Notably, the capacity to fine-tune the ICT excited-state offers significant opportunities for exploitation.
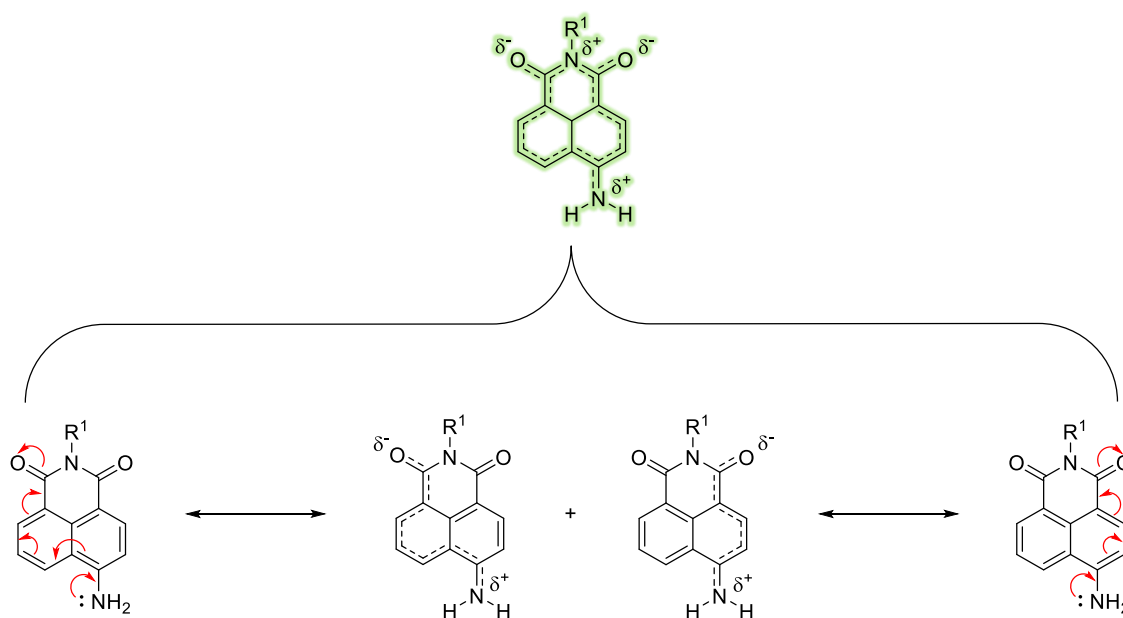
Figure 2.2: Illustration of the ICT within the 4-amino-1,8-naphthalimide fluorophore caused by an electronic "push–pull" system.

Indeed, the ICT excited-state can be modulated effectively by functionalisation at the 4-position, and we (The Elmes group) have recently

reported a 2-nitroimidazole-1,8-naphthalimide conjugate capable of detecting reductive stress in HeLa cells using a similar strategy. In this case, a clear blue to green ratiometric fluorescence response was observed upon reaction with anaerobic oxidoreductases and the impact of reductive stress could be easily monitored using confocal microscopy and flow cytometry.[285] With these considerations in mind, we expected that a similar design strategy could be employed to effectively image caspase-3 activity and provide critical insight into the apoptotic pathway in living biological systems (**Scheme 2.1**).
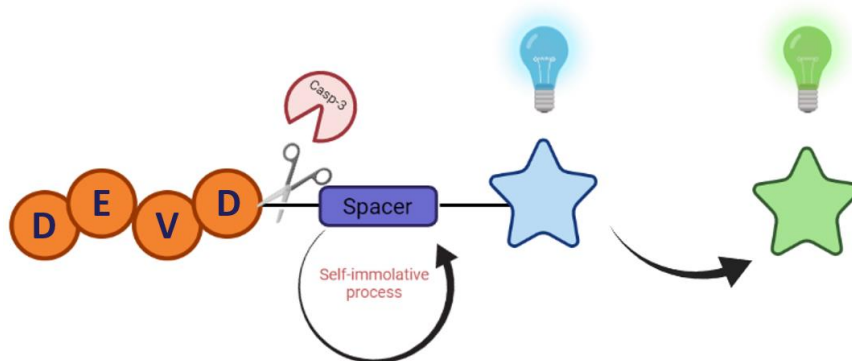
Scheme 2.1: Cartoon schematic of ratiometric probe for the detection of caspase-3.

2.2 Chapter Objective

The objective of this chapter is to synthesize a peptide probe Ac-DEVD-PABC-Naph (**Figure 2.3**) that displays a sensitive, selective and ratiometric fluorescence response for caspase-3. A ratiometric fluorescent probe – that has two distinct emission peaks – possesses a self-calibration effect, which may adequately reduce many of the interferences that hinder traditional caspase probes. Ratiometric probes for the fluorescent visualisation of caspase-3 are rare, and are often complex molecules that require additional components – like cell-penetrating peptides – to achieve effectiveness.[286]

Ac-DEVD-PABC-Naph

Figure 2.3: Structure of Fluorescent Caspase-3 probe (purple denotes the linker, and blue the fluorophore).

The essence of this strategy involves a cell-permeable 1,8-naphthalimide[210] (Naph) fluorophore covalently linked to an Ac-DEVD peptide sequence via a *p*-aminobenzyl alcohol (PABA) linker. We hope that this design will minimise any steric interactions between the cleavable bond and the bulky naphthalimide, while retaining the fast 1,6-elimination afforded by the PABA linker. Reaction with caspase-3 should give rise to a fragmentation of the parent molecule and release of the well-known amino-1,8-naphthalimide fluorophore (**Scheme 2.2**). It is expected that this elimination would lead to significant ICT modulation giving rise to the desired ratiometric response. Herein, we report the synthesis of Ac-DEVD-PABC-Naph and a detailed spectroscopic evaluation in response to caspase-3.

Scheme 2.2: Schematic of Peptide Probe (Ac-DEVD-PABC-Naph) and its release mechanism for the ratiometric sensing of Caspase-3.

2.3 Synthesis and Characterisation of Ac-DEVD-PABC-Naph

The synthetic route to Ac-DEVD-PABC-Naph (**2.6**) is a multi-step pathway involving several peptide-based intermediates before obtaining the deprotected final compound. The first step in the synthetic pathway was to assemble the protected (-O*t*Bu) DEVD sequence. This was completed using 2-Chlorotrityl Chloride resin, with sequential coupling via Fmoc/*t*Bu SPPS (**Scheme 2.3**).
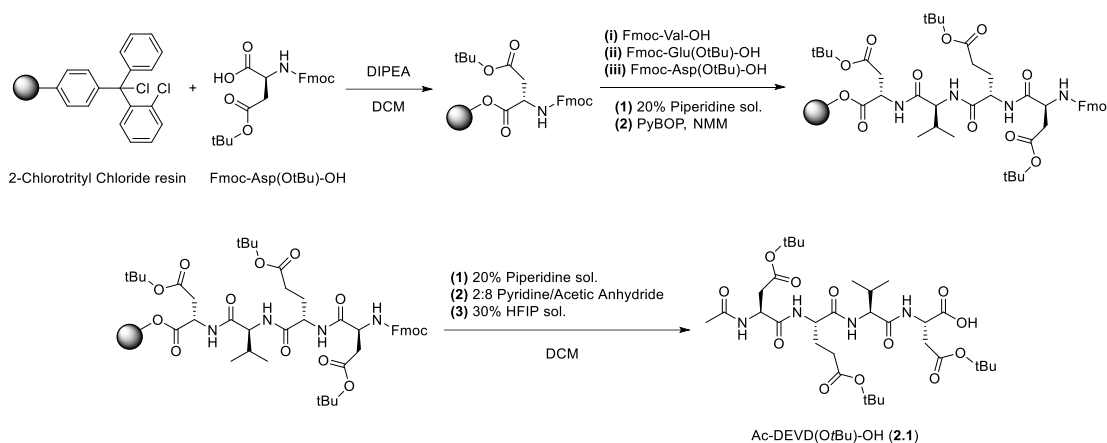
Scheme 2.3: SPPS synthetic pathway for **Ac-DEVD(O*t*Bu)-OH (2.1)**.

After the first AA (Fmoc-Asp(O*t*Bu)-OH) was installed on the resin, it was then washed with a solution of DCM/MeOH/DIPEA to endcap any remaining reactive trityl groups. Estimation of the first residue attachment was achieved spectroscopically. The Fmoc group was then removed by a 20% piperidine in DMF solution, with coupling of subsequent amino acids as follows (**Scheme 2.4**); Fmoc-protected amino acids in the presence of PyBOP and *N*-methyl morpholine (NMM).
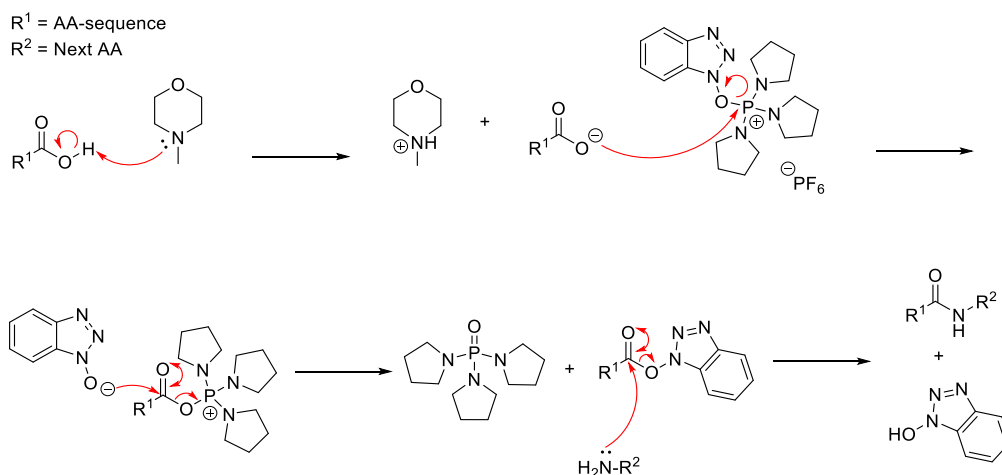
Scheme 2.4: Proposed mechanism of PyBOP/NMM mediated coupling of sequential AAs.

LC-MS characterisation confirmed the successful synthesis of Fmoc-DEVD(O*t*Bu)-OH, with one sharp UV (254nm) peak eluting at a retention time of 42 minutes (**Figure 2.4**). Underneath this peak, ionisation (albeit poor) for the target peptide [M+H]$^+$ = 867.8 gmol^{-1} was observed (see Figure S2.2), and a typical ionisation pattern consisting of the -*t*Bu groups being removed (under ESI) – 1-*t*Bu (811.8 gmol-1), 2-*t*Bu (755.6 gmol^{-1}) and 3-*t*Bu (699.4 gmol^{-1}).
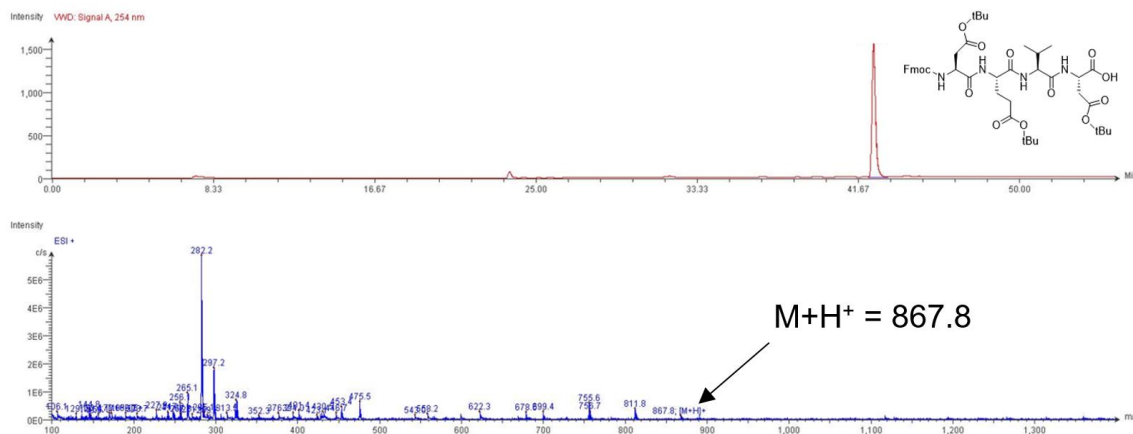
Figure 2.4: LC-MS data for **Fmoc-DEVD(O*t*Bu)-OH**. (Top) HPLC trace generated by a deuterium lamp at 254 nm. *Note:* For detailed information regarding LC-MS instrumentation and interpretation of data, see *Experimental* section(s) *6.1* and *6.5*.

Upon coupling the last AA, the *N*-terminal Aspartic Acid was *capped* via a solution of pyridine/acetic anhydride. The formation of the acetylated amine (amide) was evident from the ^{1}H NMR spectrum (**Figure 2.5**) with the characteristic -CH$_3$ protons appearing as a sharp singlet at 1.83 ppm, integrating for 3H. Other characteristic peptide peaks were also displayed, such as; the four amide N-Hs (one for each residue) appearing as doublets (coupling to nearby -CHs confirmed via COSY, Figure S2.7) furthest downfield from 7.79 – 8.21 ppm each integrating for 1H, and the backbone -CHs being observed as multiplets upfield from 4.15 – 4.58 ppm also integrating for 1H each. In a classic display of intensity, the *t*Bu-CH$_3$ protons appeared quite obviously as singlets around ~1.37 ppm integrating for a total of 27H. The valine side-chain was observed as a multiplet (-CH) at 1.93 ppm integrating for 1H, coupled to a set of doublets (2 x -CH$_3$) at 0.81 ppm which integrated for a total of 6H. It is important to note that one of the amide-NHs (8.09 ppm) and one of the -CHs (4.47 ppm) appeared as broad and somewhat diminished peaks, this might be due to intramolecular hydrogen bonding. However, this issue was corrected later on in the synthesis with the appearance of a much more resolved doublet and multiplet for the -NH

and -CH, respectively. Ninhydrin Test was used to confirm that the *N*-Terminus was completely acetylated (no primary amine present). Finally, the peptide was separated from the resin to undergo further reactions.
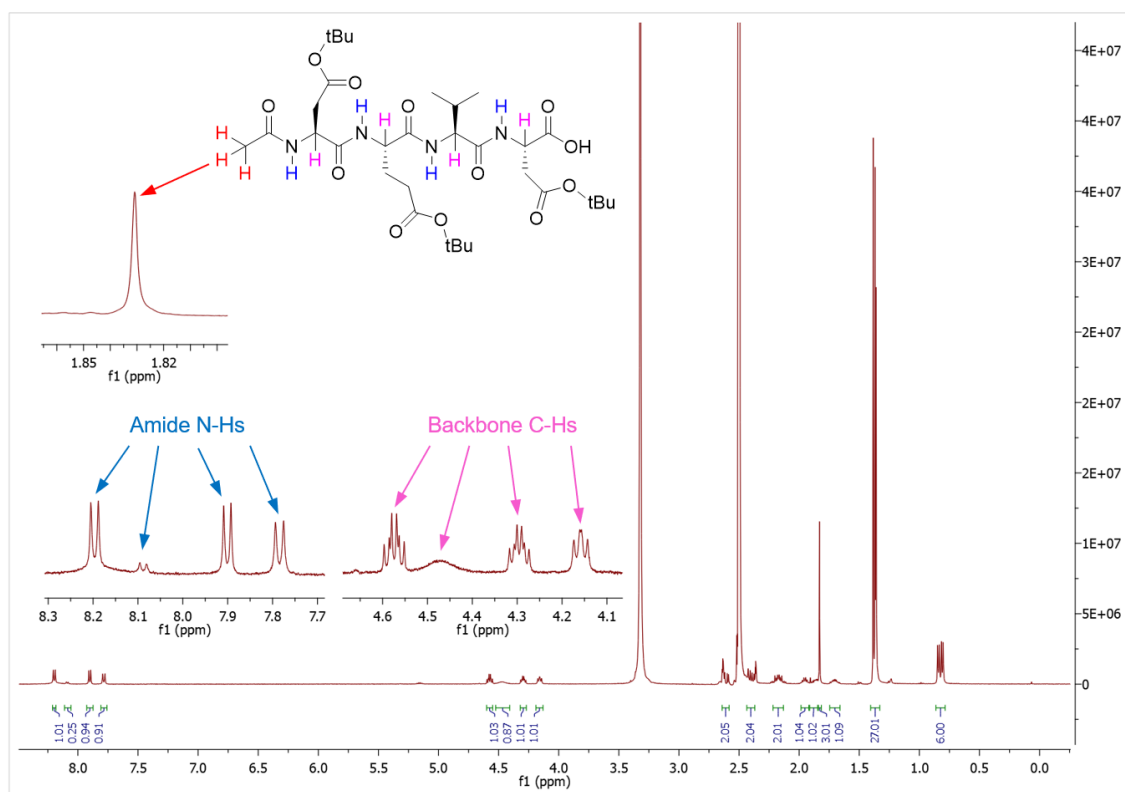
Figure 2.5: ^{1}H NMR spectrum of peptide intermediate **2.1** in DMSO-d_6 (peak annotations removed for clarity, see Figure S2.3).

The next step was to couple **2.1** to the PABA linker. Initially, this synthesis was attempted with EDC.HCl and DMAP as coupling reagents. However, the poor yields of 25–31% after numerous attempts prompted us to explore different coupling conditions. A coupling reagent first reported by Belleau in 1968 called 2-ethoxycarbonyl-2-ethoxy-1,2-dihydroquinoline (EEDQ) proved to be effective,[287] with a greatly enhanced yield of 78% and ease of purification (**Scheme 2.5**).
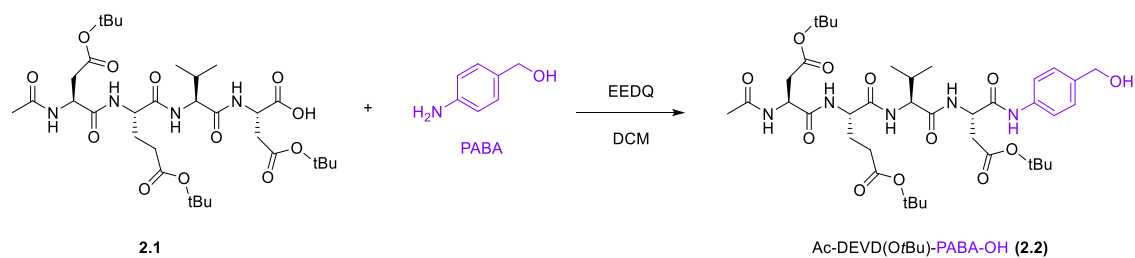
Scheme 2.5: Coupling of PABA to **2.1**, to produce **Ac-DEVD(O*t*Bu)-PABA-OH (2.2)**.

68

One might argue that there are two possible reaction-sites on the unprotected PABA molecule, one might be correct. On one hand, the aromatic -NH$_2$ could nucleophilically attack the activated-ester (provided by EEDQ), but this amine is not likely to be an effective nucleophile since delocalisation reduces electron density around the amino nitrogen (resonance). Conversely, the -OH is nucleophilic in nature and the nearby alkyl group may act as a sigma donor to increase this nucleophilicity. This highlights the possibility of generating two distinct products, one with amide formation, and the other with an ester. This scenario is not ideal, as the whole design principle relies on the self-immolation of the PABA moiety – which can only occur from successful amide-bond formation. Fortunately, after many experimental observations, there appears to be a thermodynamic preference for the amide-product,[288] with no evidence of the ester-product being formed (**Scheme 2.6**).
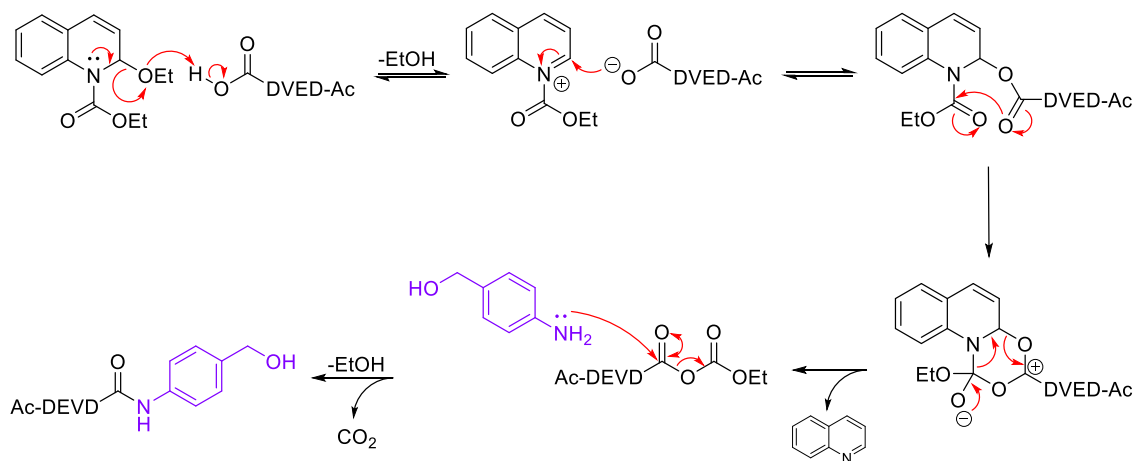
Scheme 2.6: EEDQ coupling mechanism, as proposed by *Valeur* and *Bradley*.[289] Adapted for use with peptide-linker intermediate **2.2**.

The successful amide-bond product between the *C*-terminal aspartic acid and the -NH$_2$ of PABA is observed by the many characteristic peaks present within the ^{1}H NMR spectrum, and further corroborated by one single UV-peak with a retention time (t_R) of 28 minutes on the corresponding HPLC trace (**Figure 2.6**). The aromatic amide bond between PABA and Asp shows up as a singlet (expectedly) far downfield at 9.85 ppm integrating for 1H. Other characteristic peaks such as the *roofing* ortho- and meta-CHs on the benzene ring, appeared as a pair of doublets from 7.22 – 7.55 ppm (respectively), with both sets of peaks integrating for 2H each. The benzyl-CH$_2$ peak showed up as a singlet at 4.42 ppm integrating for 2H. The benzyl-OH peak also appeared nearby at 5.11 ppm, as a

broad singlet which integrates for 1H. Although these benzyl-peaks appeared as singlets, there is ^{1}H-^{1}H coupling evidence from the COSY spectrum (Figure S2.7). LC-MS, ^{13}C NMR, and HSQC confirmed the successful formation of **2.2**. Full characterisation data can be found in the relevant *Experimental* section, and supporting spectra can be viewed in the *Appendix*.
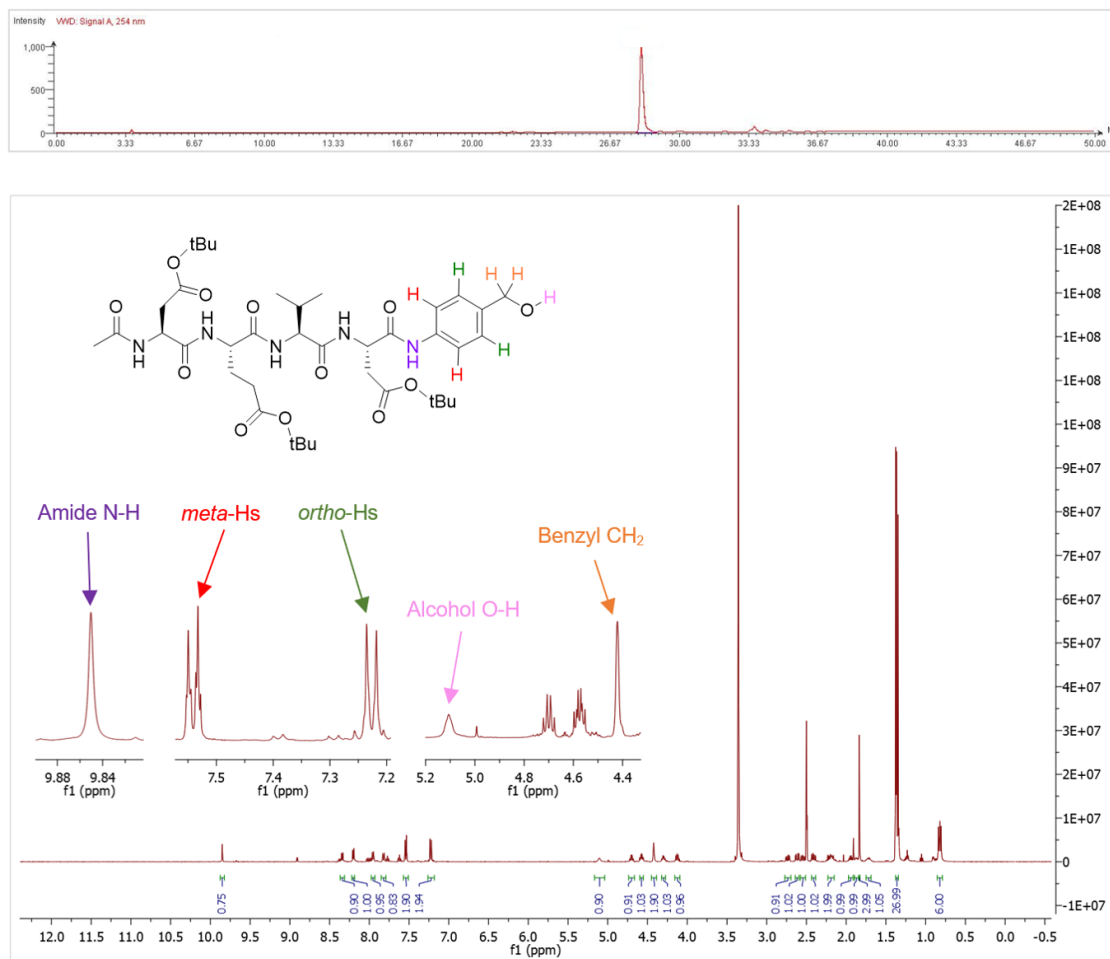
Figure 2.6: (Top) HPLC trace. (Bottom) ^{1}H NMR spectrum of peptide-linker intermediate **2.2** in DMSO-d_6.

Once the PABA-functionalised peptide was assembled and purified, the next step was to prepare the 1,8-naphthalimide fluorophore (**2.4**). 4-nitro-1,8-naphthalic anhydride (**2.0a**) was dissolved in ethanol (EtOH), with the addition of *N*-butylamine.[290] The reaction was then heated to reflux, which generated the nitro naphthalimide (**2.3**) in 84% yield. The newly formed **2.3** was then reduced to its amino derivative using Pd/C & H$_2$ (**Scheme 2.7**). The final 4-amino-*N*-butyl-1,8-naphthalimide (**2.4**) product was obtained as a deep orange solid with a 95% yield.
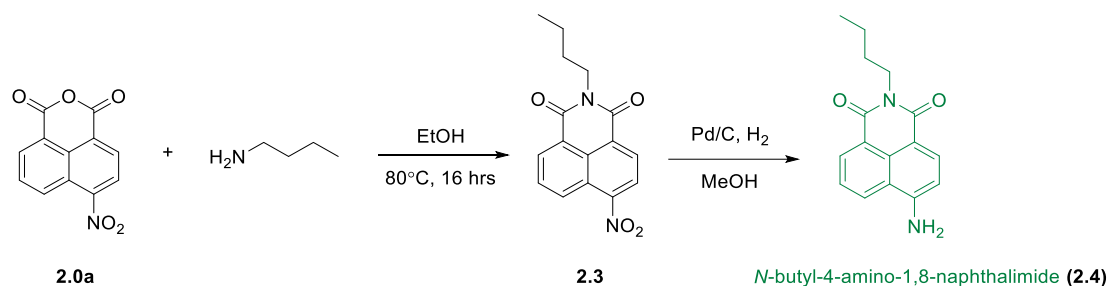
Scheme 2.7: Synthesising the Naph fluorophore (**2.4**) from 4-nitro naphthalic anhydride (**2.0a**).

A combination of LC-MS (ESI +/-) and NMR data confirmed the successful synthesis of **2.4**. The reverse-phase HPLC trace displays one sharp peak with a t_R = 25 minutes, informing us that only one UV-active component is present in the sample (**Figure 2.7**). The ion spectrum immediately below the HPLC trace tells us that all the $[M+H]^+$ species – with a target mass of 269.1 gmol^{-1} – appeared directly under the sharp UV-peak. This gave us strong evidence to suggest that the peak observed from the HPLC trace does indeed correspond to the compound. This is further correlated with the bottom two spectra, detailing all the mass ions present within that same UV-peak. Indeed, strong ionisation was observed in positive mode (ESI +) and negative mode (ESI -) for the target mass(es) of $[M+H]^+$ = 269.1 gmol^{-1} and $[M-H]^+$ = 267.0 gmol^{-1}, respectively. Several NMR experiments were used to characterise the nitro-intermediate and to further corroborate the LC-MS findings, such as; ^{1}H NMR, ^{13}C NMR, COSY, HSQC and HMBC – Figure S2.9 – 2.20 in the *Appendix.*
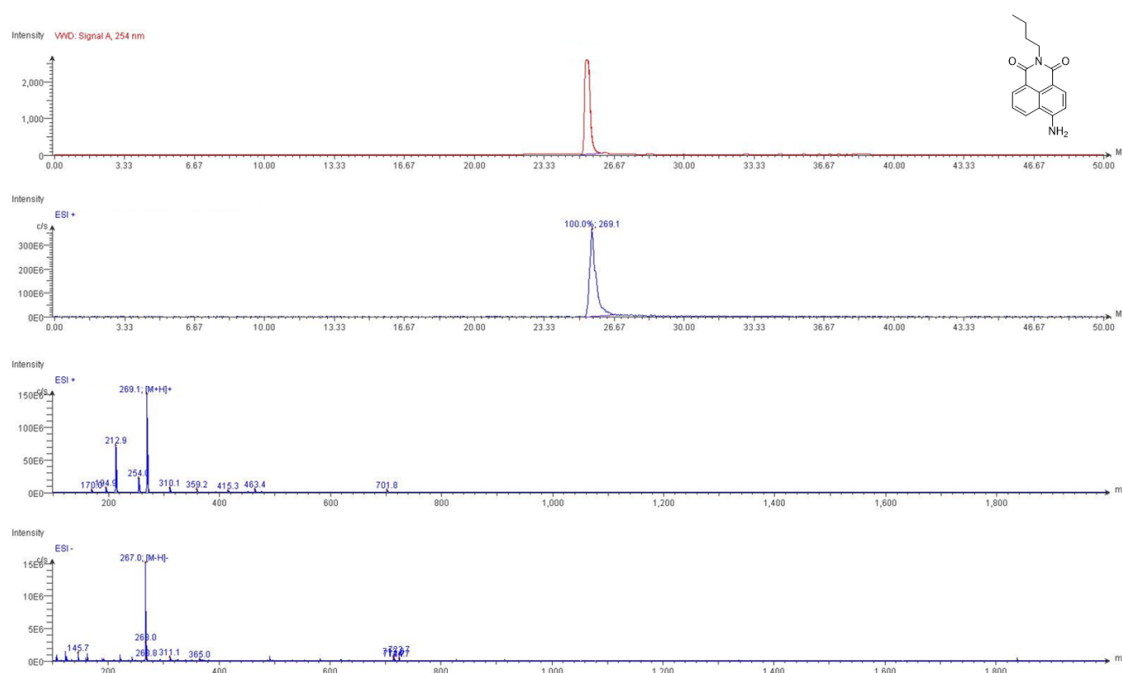
Figure 2.7: LC-MS data for naphthalimide fluorophore **2.4**.

The final step in the synthetic-pathway was to functionalise the peptide-linker intermediate **2.2** with the naphthalimide fluorophore (**2.4**), through a carbamate linkage. This carbamate functional group breaks down to release CO_2, and is a necessary component in the design strategy – as it allows the spontaneous release of the naphthalimide fluorophore after self-immolation of the PABC linker (**Scheme 2.2**). In order to couple the fluorophore to the parent peptide-linker, **2.4** was first converted to its corresponding carbamoyl chloride – which displayed a characteristic blue fluorescence – before reacting with the nucleophilic alcohol on the PABA moiety (**Scheme 2.8**). This transition in fluorescence can be attributed to the change in ICT-character around the 4-position. This reaction proceeded until a precipitate had formed, which was washed and filtered to afford the protected product Ac-DEVD(O*t*Bu)-PABC-Naph (**2.5**) with a yield of 66%.
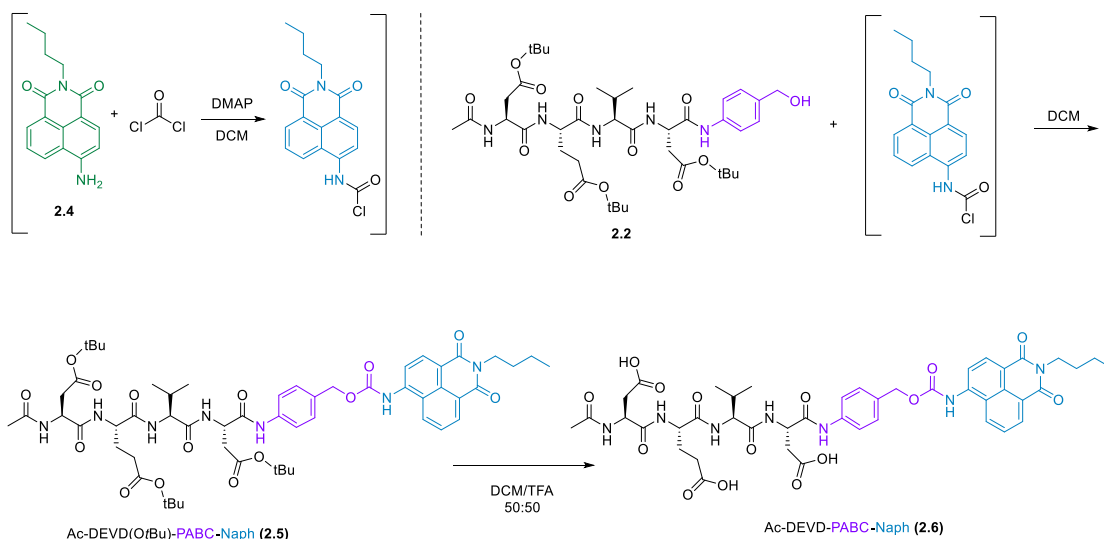
Scheme 2.8: Functionalisation of **2.2** with **2.4** via carbamate linkage, to form **2.5**.

The successful synthesis of the protected-peptide probe was identified and characterised by ^{1}H NMR, LC-MS and HRMS experiments (Figure S2.22). The ^{1}H NMR spectrum (**Figure 2.8**) displayed many peaks that were indicative

of the target compound. The amide N-H of the PABC linker and the Naph N-H on the carbamate functional group, appeared downfield at 10.0 ppm and 10.37 ppm, respectively. Both of these peaks resemble singlets, with integration for 1H each. The alcohol O-H that was present on the PABA before this reaction, has now disappeared (now carbamate), with the benzyl-CH_2 peak moving further downfield due to its proximity to the newly formed carbamate linkage. This peak now appears at 5.21 ppm, while still integrating for 2H – with no coupling now observed in the COSY spectrum (Figure S2.5). Other characteristic peaks are also present, like the aromatic protons on the naphthalimide core. These peaks appeared – in the same region as the peptide-backbone amide N-Hs – around 7.8 ppm to 8.7 ppm, all integrating for 1H. The remaining peaks within the spectrum correspond to the rest of the peptide-backbone and amino acid side-chains. Gratifyingly, the HPLC trace displays one single UV-peak with a $t_R = 44$ minutes, further attesting to the compound's purity. This peak elutes quite late from the system, indicating the compounds affinity for the column's C_{18} silica stationary-phase, and its over-all hydrophobicity. This was not unexpected, as the DEVD sequence currently remains fully-protected, and the -tBu groups tend to be rather lipophilic.
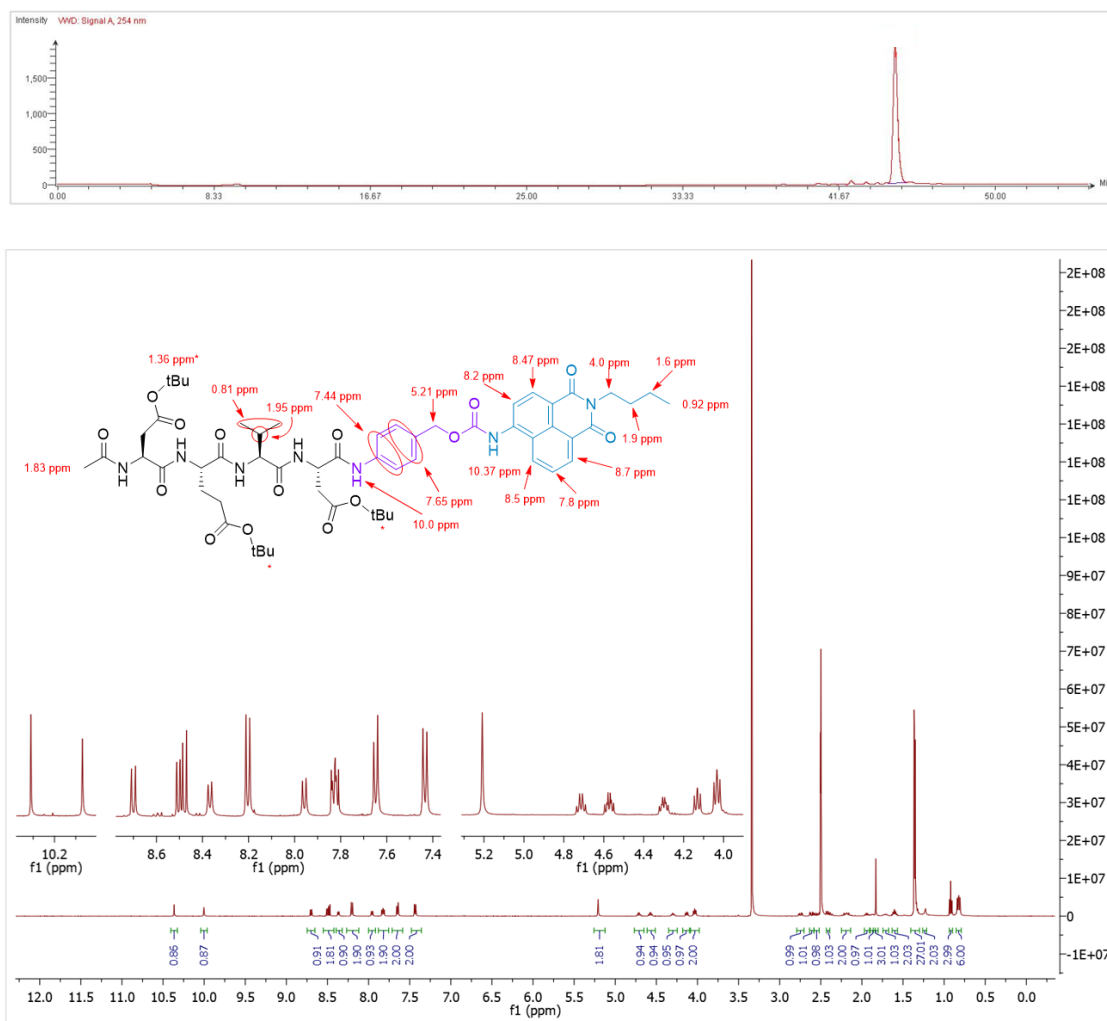
Figure 2.8: (Top) HPLC trace. (Bottom) ^{1}H NMR spectrum of protected compound **2.5** in DMSO-d_6.

The protected peptide-conjugate was dissolved in TFA/DCM to facilitate deprotection of the -*t*Bu side-chains. This afforded the deprotected final product Ac-DEVD-PABC-Naph (**2.6**) as a pale yellow solid with a yield of 81%. LC-MS and HRMS experiments were used to characterise the final compound, with the LC-MS data generating a UV-peak – that eluted much earlier than the protected precursor – at t_R = 32 minutes (**Figure 2.9**). In contrast to previous intermediates analysed via LC-MS, this deprotected compound displays strong ionisation in negative mode (ESI -) for the target mass of [M-H]$^+$ = 916.4 gmol^{-1}. This preference for the negative ionisation mode (-H$^+$) is mainly due to the (now) liberated carboxylic acid side-chains on the Asp and Glu residues, as these are acidic functional groups that readily undergo deprotonation. It is also worth noting that this HPLC trace is from a very dilute sample, with some small artifact-peaks

residing on the baseline of the C_{18}-column. However, the most intense peak corresponds to the product.
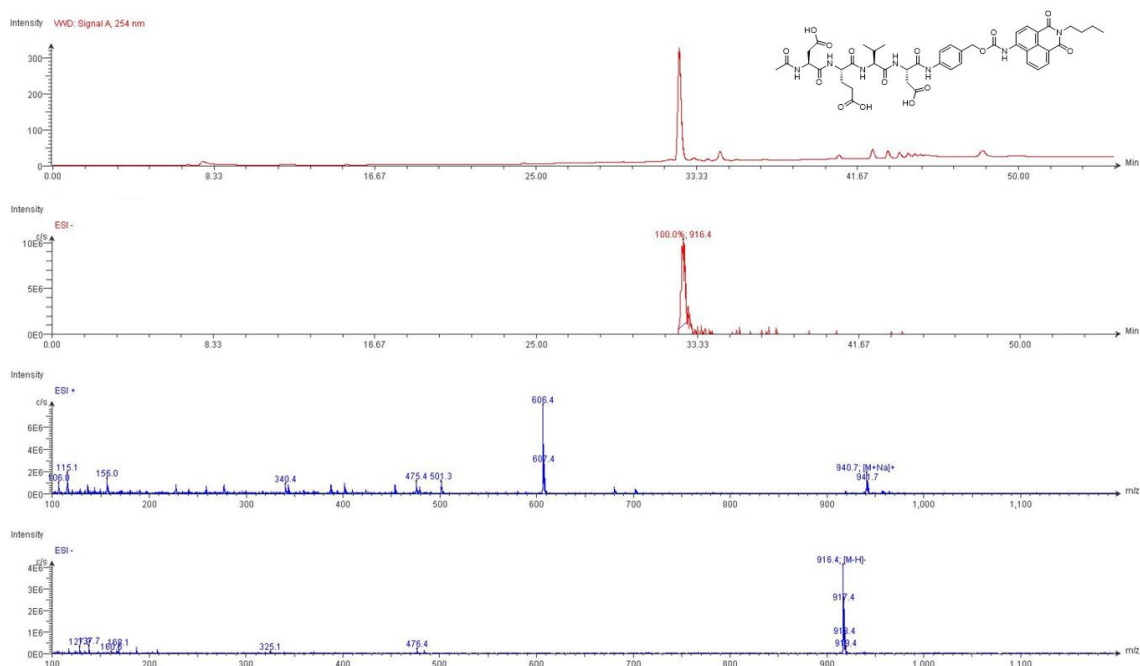
Figure 2.9: LC-MS data for the deprotected final compound **2.6**.

High-Res Mass Spec. (ESI +) was also used to determine molecular formula, with confirmation of the target mass $[M+H]^+$ = 918.3502 gmol^{-1} possessing an adequately low mass error value of -5.29 ppm (**Figure 2.10**).
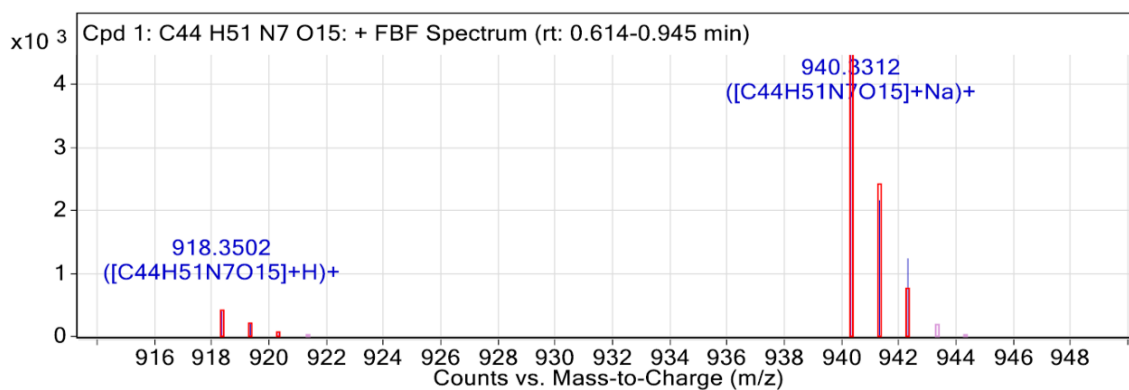
Figure 2.10: HRMS data for the deprotected final compound **2.6**.

With the above characterisation data in hand, we were satisfied that the target compound (**2.6**) was synthesized successfully and acceptably pure. The natural course of action was to conduct proof-of-principle experiments utilising our novel probe for the ratiometric visualisation of caspase-3.

2.4 Spectroscopic Response to Caspase-3

2.4.1 UV-vis and Fluorescence Studies

The spectroscopic response of Ac-DEVD-PABC-Naph (**2.6**) towards caspase-3 was investigated using a combination of UV-vis and fluorescence spectrophotometry. The changes in the absorbance spectrum (UV-vis) of **2.6** (10 µM) were observed upon addition of caspase-3 (**Figure 2.11**). The probe displayed a typical absorption peak at 372 nm before treatment with caspase-3 (200 ng/ml), which shifted to a peak maxima at 432 nm after 2 hours.
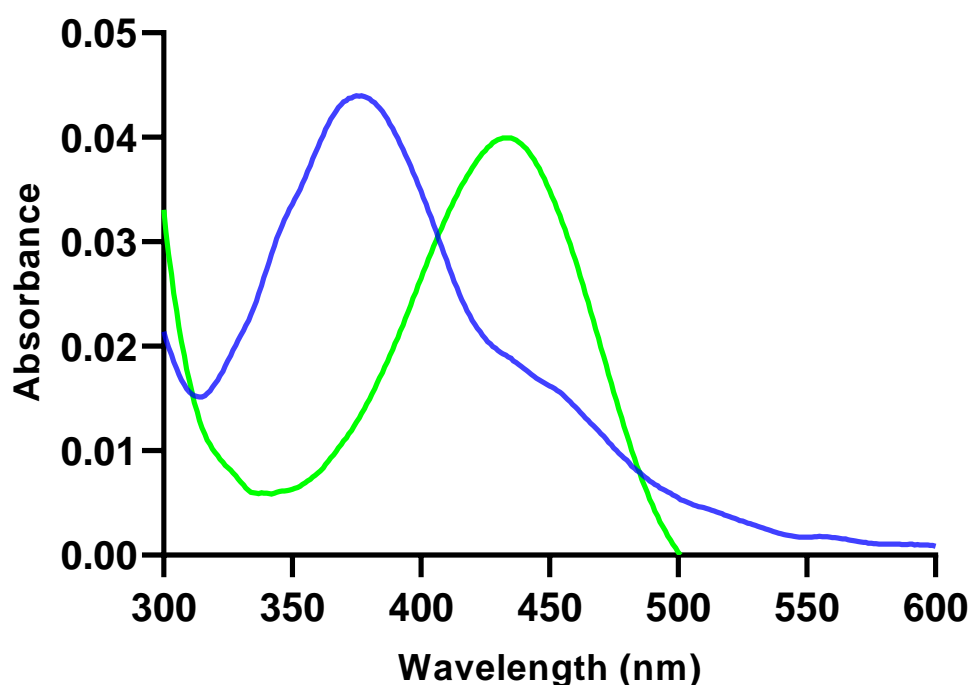
Figure 2.11: Absorbance spectra of **2.6** before and after Caspase-3.

To gain an enhanced understanding of the changes observed in this absorption spectrum, the absorbance intensities were monitored at 5-minute intervals for 2 hours (**Figure 2.12**). Although the absorption intensities appeared quite low – which can sometimes be the case with naphthalimides – there was still an obvious progression from the parent compound (**2.6**) to the free Naph (**2.4**) upon treatment with caspase-3 (200 ng/ml), with a clear isosbestic point at 402 nm.

76
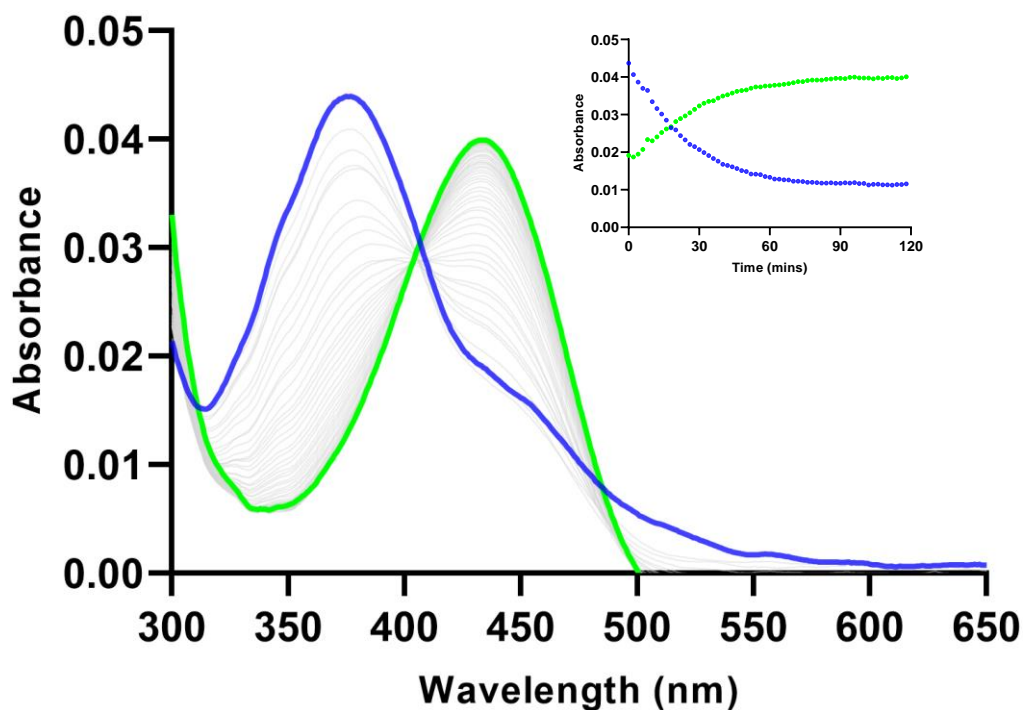
Figure 2.12: Changes observed in the absorbance spectrum of **2.6** (10 μM) upon addition of Caspase-3 (200 ng/ml) in assay buffer (0.28% DMSO) pH 7.4, over 120 min. *Inset*: Absorbance intensities at 372 nm and 432 nm versus time.

Using this isosbestic point (402 nm) as the excitation wavelength, the probe displayed a maximum fluorescence emission at 475 nm (**Figure 2.13**). After treatment with caspase-3, the fluorescent peak at 475 nm diminished almost completely. A new emission peak corresponding to **2.4** appeared at 535 nm, suggesting that the probe was cleaved by caspase-3 to release the naphthalimide fluorophore. The ratiometric fluorescence signal (I_{535} / I_{475}) had increased over 2-fold after the probe was totally hydrolysed by caspase-3 (200 ng/ml), demonstrating the considerable potential of **2.6** for the quantification of caspase-3.
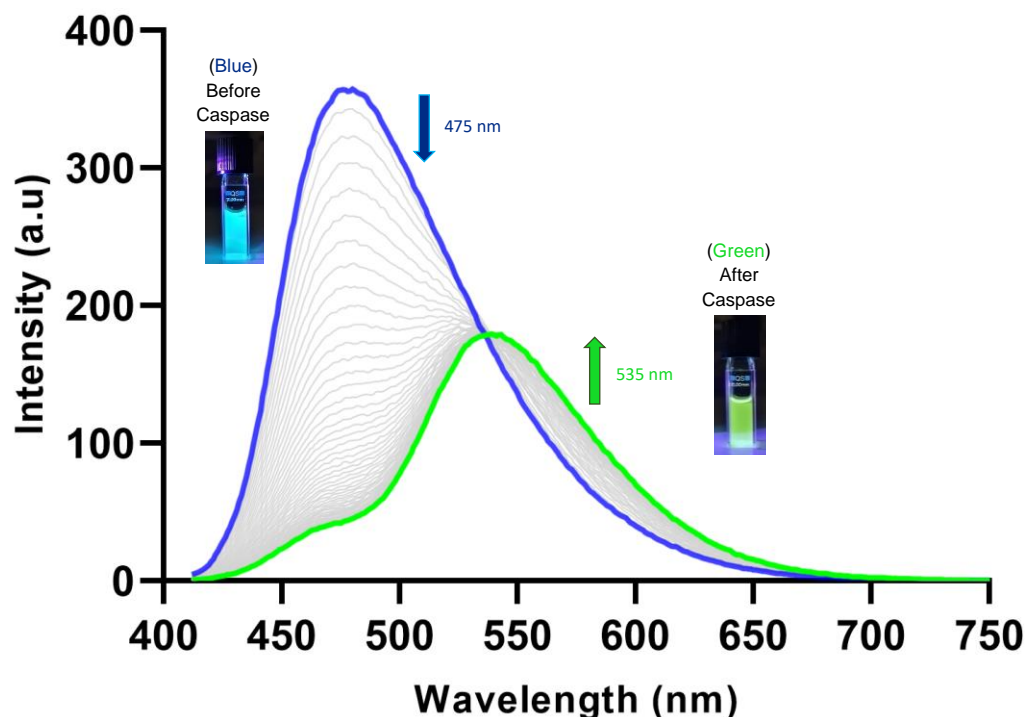
Figure 2.13: Changes observed in the fluorescence spectrum of **2.6** (10 μM) upon addition of Caspase-3 (200 ng/ml) in assay buffer (0.28% DMSO) pH 7.4 over 120 min (λ_{ex} = 402 nm). *Inset:* Pictures of probe solutions with and without treatment of Caspase-3 under illumination via UV lamp.

The changes in the fluorescence profile of **2.6** (10 μM) were then observed after treatment with known concentrations of caspase-3 (**Figure 2.14**). Increasing concentrations of caspase-3 (0 – 80 ng/ml) were used for this investigation, and a steady progression from the parent probe to the hydrolysed product was apparent. 10 ng of caspase-3 reduced the initial fluorescence output by roughly half. However, 10 & 20 ng/ml were unable to produce a ratiometric fluorescence signal (I_{535} / I_{475}) above 1.0. To achieve this, concentrations >40 ng/ml were required, with (unsurprisingly) the highest concentration of 80 ng/ml generating the best ratiometric response. This initial study gave us a brief insight into the enzyme kinetics associated with the reaction between caspase-3 and the probe. Further experiments concerning this enzyme-probe interaction will be conducted and analysed later on in the *Enzyme Kinetics* section, with various kinetic constants being calculated for **2.6** such as; Michaelis constant (K_m), Catalytic constant (k_{cat}), Catalytic efficiency (k_{cat}/K_m) and Limit of Detection (*LOD*).
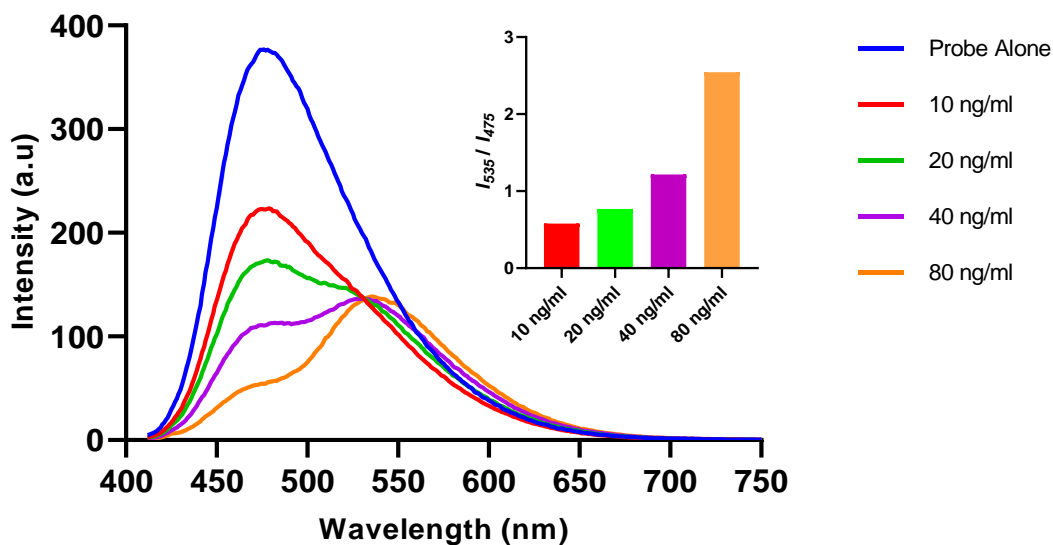
Figure 2.14: Fluorescence spectrum of **2.6** (10 μM, 0.28% DMSO) in assay buffer, with various concentrations of Caspase-3 (λ_{ex} = 402 nm). *Inset:* Bar chart representing the fluorescent ratio response at λ_{max} 535 nm versus 475 nm.

The changes observed in the fluorescence profile of the probe proved our initial design strategy – as depicted in **Figure 2.2** – of the self-immolative pathway undertaken by the compound after treatment with caspase-3. The ICT excited-state of **2.4** appeared to be affected by the aqueous environment to a greater extent than the parent (un-hydrolysed) probe. The green fluorescence intensity maximum (535 nm) was roughly half that of the initial blue fluorescence (475 nm), even after 120 minutes. Although it is well-recorded in literature that the ICT-character of the substituent on the 4-position of the naphthalimide-core is very sensitive to its solvent environment,[291,292] it is still worth noting that the carbamate functionality seems to provide some degree of *protection* in this regard. It's postulated that when the 4-amino (-NH$_2$) is functionalised with the carbamate linkage, its ICT to the rest of the naphthalimide fluorophore is modulated (Blue fluorescence in this case), but the intensity remains substantial – even in an aqueous environment.

This phenomenon was investigated by conducting Ionic Strength studies in aqueous media. As optical imaging is often done in buffered solutions, it is important to study the effect of ionic strength on the emission output of the probe. These experiments were performed with increasing additions of NaCl to an aqueous solution of **2.6** (5 μM). There was only a small change in the

fluorescence spectrum of the probe, with a slight decrease in fluorescence intensity observed when the concentration of NaCl was increased from 0 to 960 mM (**Figure 2.15**). This study indicates that ionic strength does not affect the fluorescence output of **2.6**.
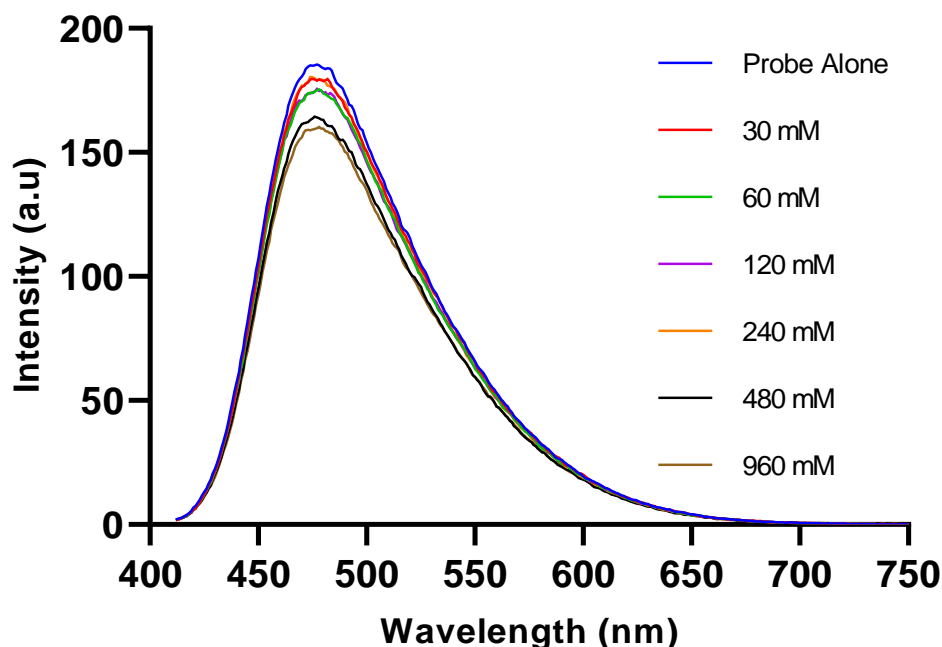
Figure 2.15: Fluorescence spectrum of **2.6** (5 μM) in H_2O (0.14% DMSO) with increasing concentrations of NaCl (aq.).

To investigate the role of caspase-3 in the fluorescence change of the probe, a potent reversible inhibitor for caspase-3 (Ac-DEVD-CHO) was added to the reaction mixture. As highlighted in **Figure 2.16**, the probe alone (Blue) showed no change in fluorescence over 1 hour. However, when incubated with an increasing concentration of inhibitor, a partial loss of caspase-3 activity was observed with 0.05 μM (Purple) up to almost complete inactivity at 0.5 μM (Red). After the addition of 0.5 μM of inhibitor, the fluorescence signal at 475 nm only decreased slightly. This can be attributed to the almost complete loss in enzymatic activity of caspase-3. These results demonstrate the essential role of caspase-3 activity in changing the fluorescent profile of **2.6**. Enzymatic cleavage of the probe by the active caspase-3 induces the ratiometric fluorescence response. Furthermore, the fluorescent ratio of the probe can be utilised for the visualisation of caspase-3 activity.
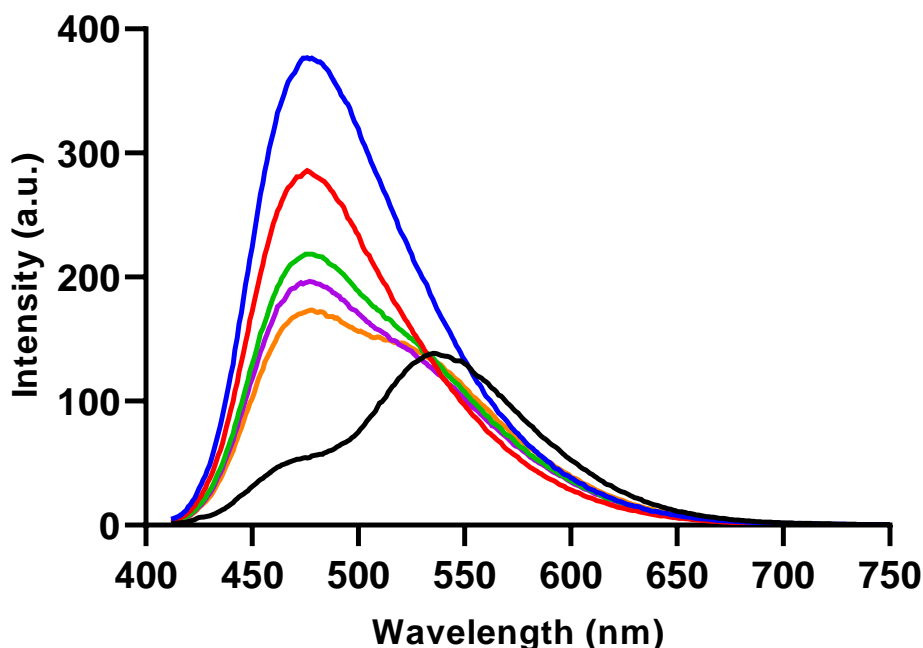
Figure 2.16: Fluorescence emission spectra (λ_{ex} = 402 nm) of reactions after incubation at 25°C for 1 hr. (Blue) 10 µM probe, (Red) 10 µM probe + 0.5 µM Inhib. + 40 ng Caspase-3, (Green) 10 µM probe + 0.05 µM Inhib. + 40 ng Caspase-3, (Purple) 10 µM probe + 0.01 µM Inhib. + 40 ng caspase-3, (Orange) 10 µM probe + 40 ng Caspase-3, (**Black**) 10 µM probe + 80 ng Caspase-3, 3 hrs.

2.4.2 Enzyme Kinetics

Kinetic data for the reaction between **2.6** (10 µM) and caspase-3 was generated by monitoring the changes in the ratiometric fluorescent signal (**Figure 2.17**). The fluorescence ratio (I_{535} / I_{475}) change, along with time, was documented with different known concentrations of caspase-3 (0 – 80 ng). In the absence of caspase-3 (Grey), the fluorescence ratio did not change over time, indicative of the probe's stability in aqueous media. When caspase-3 was added, the probe was gradually hydrolysed, and the fluorescent ratio increased over a period of 4 hours. Interestingly, it required upwards of 40 ng/ml (red & blue) concentrations of caspase-3 to achieve a complete plateau over the 4-hour time period. In the first 30 minutes, the ratiometric fluorescence response of the probe to various concentrations of caspase-3 showed good linearity. Going forward, 30 minutes was used for the quantification of caspase-3.
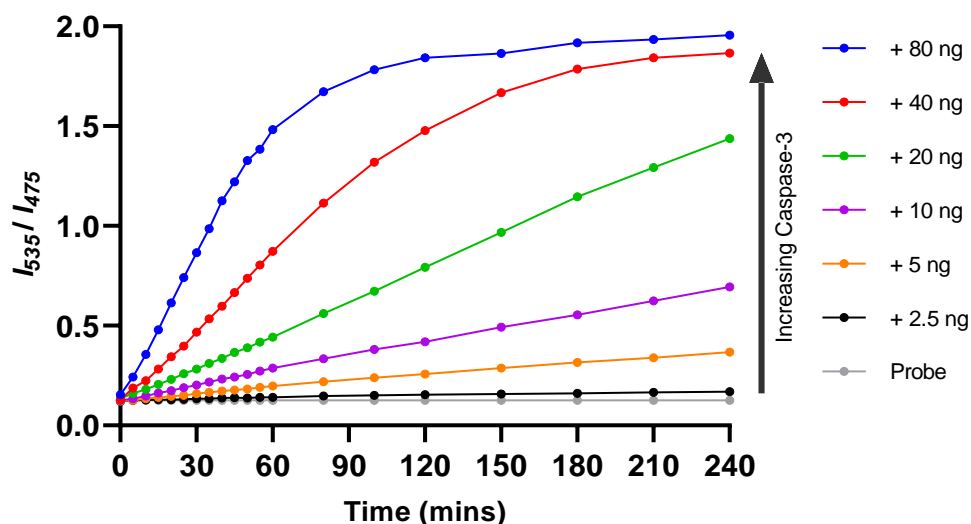
Figure 2.17: Response kinetics of **2.6** (10 μM) towards different concentrations of capase-3 over 4 hrs.

The fluorescence emission of **2.6** with different concentrations of caspase-3 at 30 minutes was then extracted. The scatterplot of the data showed what appeared to be a linear relationship between the fluorescence ratio (I_{535}/I_{475}) and concentration of caspase-3. Fitting a straight-line to this data – linear regression – provided us with a mathematical model of this relationship that can be used to find the concentration (ng/ml) of caspase-3 in (potentially) any sample by obtaining its fluorescence ratio output. The fluorescence ratio (I_{535} / I_{475}) was indeed observed to increase linearly in the concentration range of 0-80 ng/ml of caspase-3 (**Figure 2.18**), with a coefficient of determination (R^2) equal to 0.9983 suggesting that the model provides an appropriate fit to the data.

$$y = 0.00931x + 0.1099$$
$$R^2 = 0.9983$$
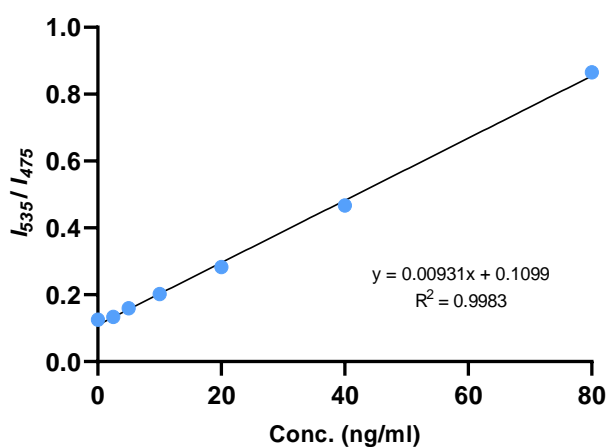
Figure 2.18: Linear fitting curve of fluorescence intensity ratio (I_{535}/I_{475}) to the concentration of caspase-3 (0-80 ng/ml). Reaction was incubated at 25°C for 30 min.

The limit of detection (*LOD*) for caspase-3 using **2.6** was calculated to be 4.96 ng/ml. This value was generated from a calibration curve (**Figure 2.19**) detailing the fluorescence intensities at λ_{max} = 535 nm at known concentrations of caspase-3 (5 – 80 ng/ml). The *LOD* for this probe was higher than others reported in literature.[183,286] Ratiometric probes for caspase-3 visualisation/quantification are rare, let alone naphthalimide-based ones, so direct comparison is difficult. The R^2-value of the linear regression was slightly below the 0.990 threshold,[293] thus may warrant some degree of caution when interpreting data. Nevertheless, these preliminary results demonstrate the potential of the probe for the quantification of caspase-3 in aqueous media with high sensitivity.

y = 0.7970x + 70.71
R^2 = 0.9879
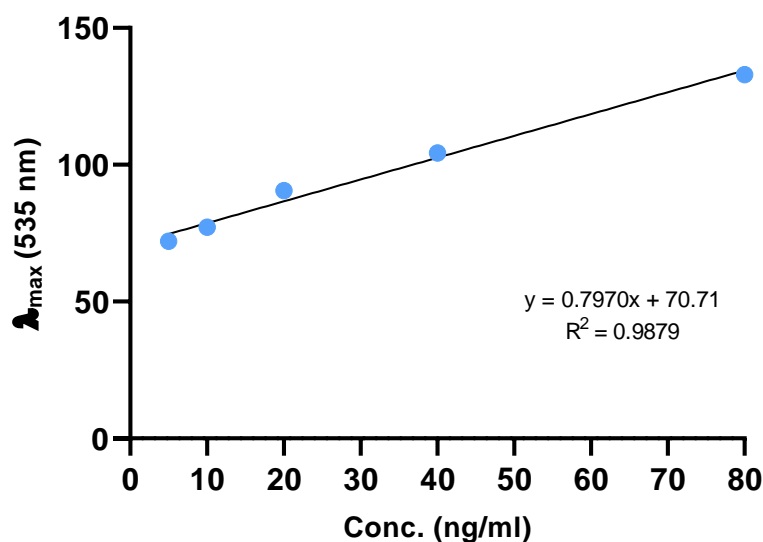
Figure 2.19: Calibration curve of fluorescence intensity (λ_{max} = 535 nm) at known concentrations of Caspase-3 (2.5 – 80 ng/ml).

The kinetic constants of caspase-3 toward **2.6** were then evaluated to determine the effectiveness of this new ratiometric probe. In accordance with Michaelis-Menten kinetics, the initial rates of product formation under varying probe concentrations (1 – 10 μM) were monitored (**Figure 2.20**). An expected trend was observed, with the lowest concentration (1 μM) requiring the least amount of time for complete hydrolysis – as evidenced by its quick time to plateau, compared to higher concentrations (10 μM) that took longer to reach complete hydrolysis of the substrate. This experiment was allowed to run for an extended period of 5 hours to allow an adequate plateau region to form – which is necessary when computing kinetic data.
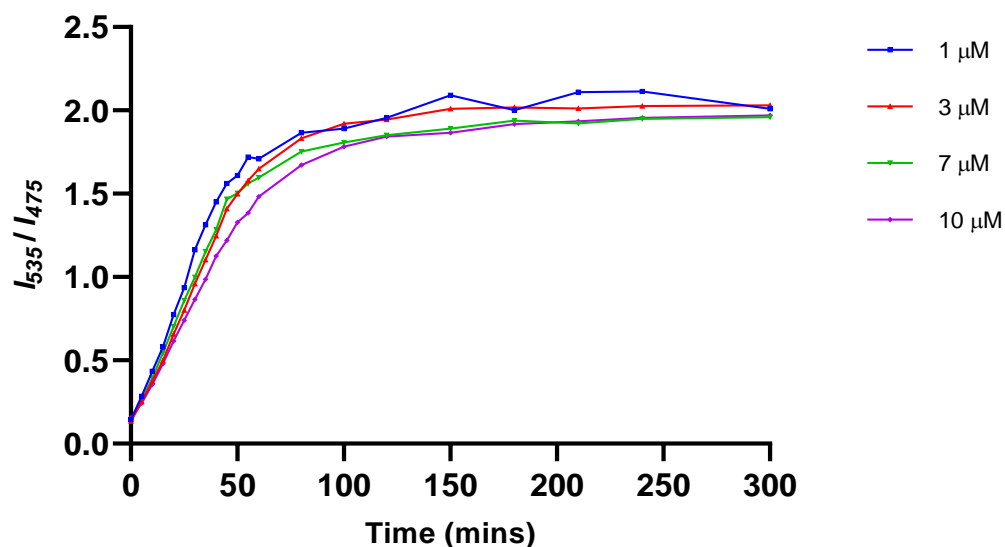
Figure 2.20: Response kinetics of Caspase-3 (80 ng/ml) towards different concentrations of **2.6** over 5 hrs at 25°C.

Once the data was fitted to the Michaelis-Menten equation $V_0 = k_{cat}[E]_0[S] / (K_M + [S])$, the kinetic constants were then calculated using a non-linear regression via *GraphPad™ Prism®* software.[294] In this equation, the K_M of an enzyme-substrate (*ES*) complex is a numerical estimate of the affinity of a substrate for an enzyme, with the k_{cat} representing the number of catalytic cycles that each active-site can yield per unit time (sec⁻¹). The K_M and k_{cat} values of caspase-3 for **2.6** were 46.4 µM and 0.51 sec⁻¹, respectively. These preliminary results suggests that the probe is slower to reach complete hydrolysis compared the literature standard Ac-DEVD-AFC (K_M = 12.7 µM, k_{cat} = 2.7 sec⁻¹).[183] This may be explained by the additional immolation process (of the PABC moiety) required by the probe once the *C*-terminal aspartic acid is hydrolysed by the enzyme. The larger K_M of the probe is not entirely unsurprising, as the bulky naphthalimide fluorophore may affect the substrate's affinity for the enzyme.

2.4.3 Selectivity Studies

Finally, the selectivity of **2.6** was explored to compare caspase-3 activity to other endogenous species, such as small biomolecules (cysteine, glucose, glutathione, glycine, and ascorbic acid) and proteins (lysozyme, trypsin, BSA, subtilisin, and pepsin). As depicted in **Figure 2.21**, none of the endogenous biomolecules could produce a fluorescence ratio change in the probe. Interestingly, none of the

enzymes like lysozyme, trypsin, BSA, subtilisin, and pepsin could induce a fluorescence change either.
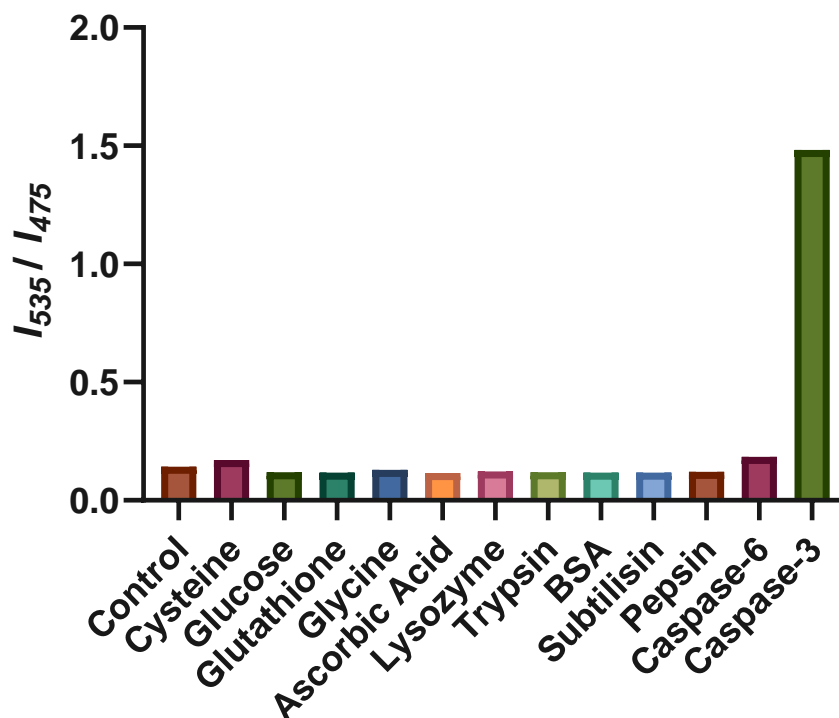
Figure 2.21: Fluorescence response of **2.6** to various species. The concentrations of cysteine, glucose, glutathione, glycine, and ascorbic acid were all 10 mM. The concentrations of lysozyme, trypsin, BSA, subtilisin, and pepsin were all 1 μg/ml. The concentrations of caspase-3, & -6 are 80 ng/ml. Reaction time was 1 hr at 25°C.

Only caspase-3 could induce a definite fluorescence ratio increase. Caspase-6, which is another member of the executioner caspases, was also investigated. Caspase-3 and -6 are believed to be responsible for the actual execution of cell death and often have short or absent pro-domains.[269] Caspase-6 has a preference for small hydrophobic side-chains like valine (V*E*X*D) within its inherent substrate specificity. However, caspase-3 has a nearly absolute requirement for aspartic acid (D*E*X*D), indicating its critical role in its enzymatic activity or substrate recognition. Indeed, the fluorescence ratio change observed for caspase-6 was far less than that produced by caspase-3. These results indicate the high selectivity of **2.6** for caspase-3, therefore the ratiometric fluorescence signal could be employed as an indicator for caspase-3 activity.

2.5 Potential NIR-Fluorescence with Augmented Naphthalimide

Near-infrared (NIR) fluorescent probes offer several advantages in various scientific and medical applications due to their unique properties. NIR light (typically in the 700 – 1000 nm range) has the advantage of deep tissue penetration compared to visible light. This allows NIR-fluorescent probes to be used for *in vivo* imaging and diagnostics, as they can penetrate tissues more effectively, reducing scattering and improving signal detection at greater depths within the body.[295] Tissues and biological samples often exhibit autofluorescence in the visible range, which can interfere with fluorescence measurements. NIR probes emit light in a spectral region with minimal autofluorescence, resulting in a higher signal-to-background ratio and improved sensitivity for imaging and detection. The longer wavelength of NIR light provides better spatial resolution in microscopy and imaging techniques, allowing for clearer and more detailed visualisation of biological structures and processes. NIR light is also less damaging to living cells and tissues than shorter wavelengths, reducing the risk of phototoxicity during prolonged imaging experiments. This is particularly important for long-term studies and live-cell imaging.[296]

The fluorescence output of the 1,8-naphthalimide can be modulated by introducing different (usually) conjugated structures onto the *head* or *tail* of the naphthalimide core. Fortunately for these fluorophores, this is synthetically feasible with many intriguing compounds being reported in literature (**Figure 2.22**).[297]

λ_{em} = 466 nm λ_{em} = 532 nm λ_{em} = 582 nm λ_{em} = 627 nm
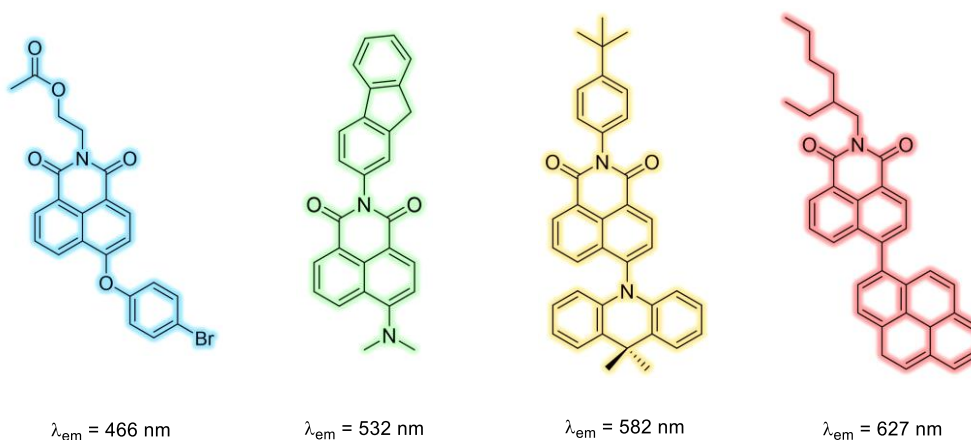
Figure 2.22: Examples of synthetically modified naphthalimide fluorophores, with their corresponding emission colour (blue/green/yellow/red) and wavelength (λ_{em}).[298]

Building on from the success of our previous naphthalimide-based peptide probe, the 4-position functionality was modified by extending the conjugation via a 4-amino styrene (**Scheme 2.9**).
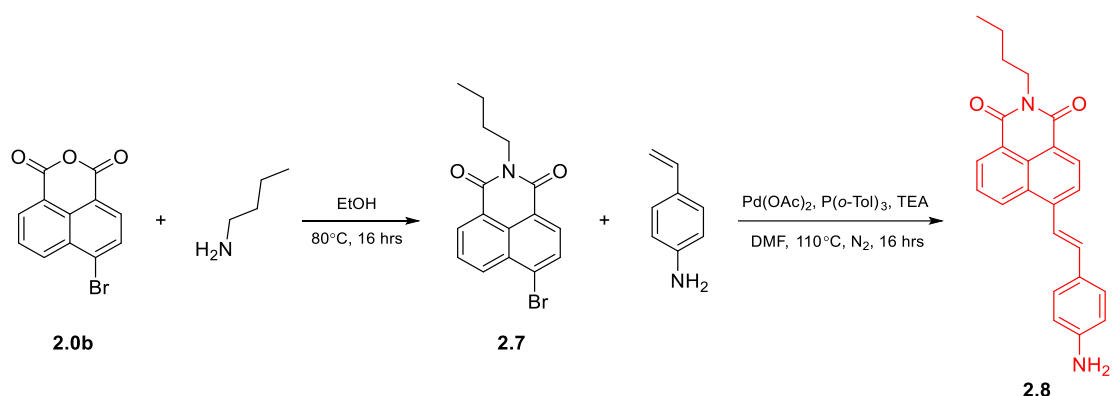
Scheme 2.9: Synthetic pathway for 4-amino styrylnaphthalimide fluorophore – **AS-Naph** (**2.8**).

This synthetic strategy was inspired by the work of Lee et. al. who designed a similar probe with a boronic acid trigger for the fluorescent detection of H_2O_2.[299] Amine condensation at the *head* of the naphthalimide was carried out under similar conditions as mentioned before. The 4-bromo-1,8-naphthalimide (**2.7**) was then subject to a *Heck* coupling reaction with 4-aminostyrene in the presence of catalyst Pd(OAc)$_2$, to afford the final 4-aminostyryl-*N*-butyl-1,8-naphthalimide (AS-Naph, **2.8**) fluorophore with a 62% yield. Evidence for the successful synthesis of this fluorophore is highlighted by the ^1H NMR spectrum and single-peak HPLC trace (**Figure 2.23**). For full-characterisation spectra (LC-MS, ^1H NMR, ^{13}C NMR, COSY, HSQC & HMBC), please see *Appendix* (Figure S2.36 – 2.41).
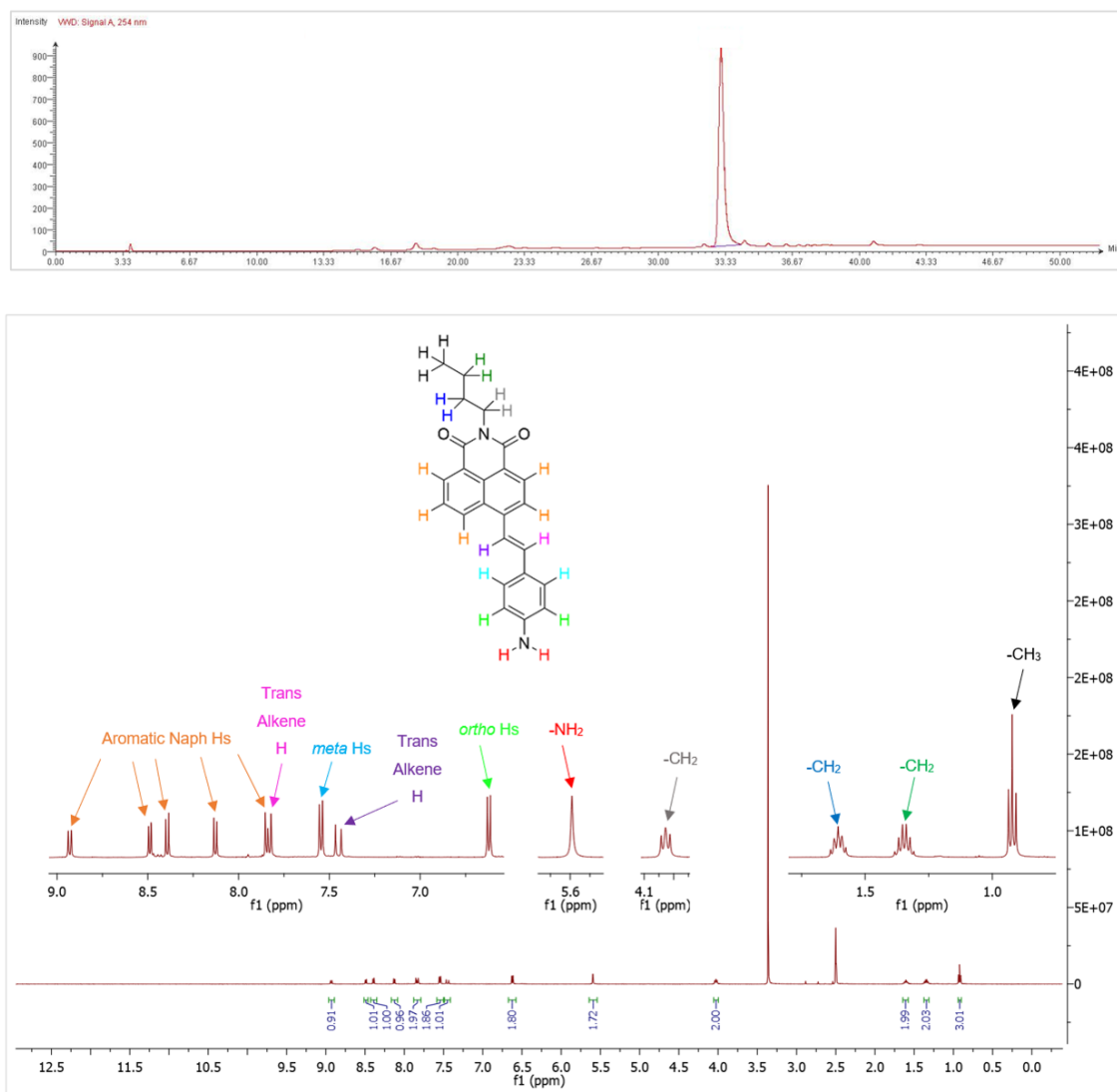
Figure 2.23: (Top) HPLC trace. (Bottom) ^{1}H NMR spectrum of **2.8** in DMSO-d_6.

Confirmation of the *trans* orientation around the alkene double-bond was obtained by calculating the coupling constant between the two vinylic protons (pink & purple), this was found to be 15.9 Hz. Typically, vicinal *cis* protons possess coupling constants around 10 Hz, with vicinal *trans* protons operating around 16 Hz.[300] This was further corroborated by the characteristic "U" shape splitting pattern (doublet) observed.

This naphthalimide fluorophore (**2.8**) displayed red fluorescence emission at λ_{max} = 630 nm in THF (**Figure 2.24**), which is almost a 100 nm shift compared to the previous Naph probe (λ_{max} = 535 nm).
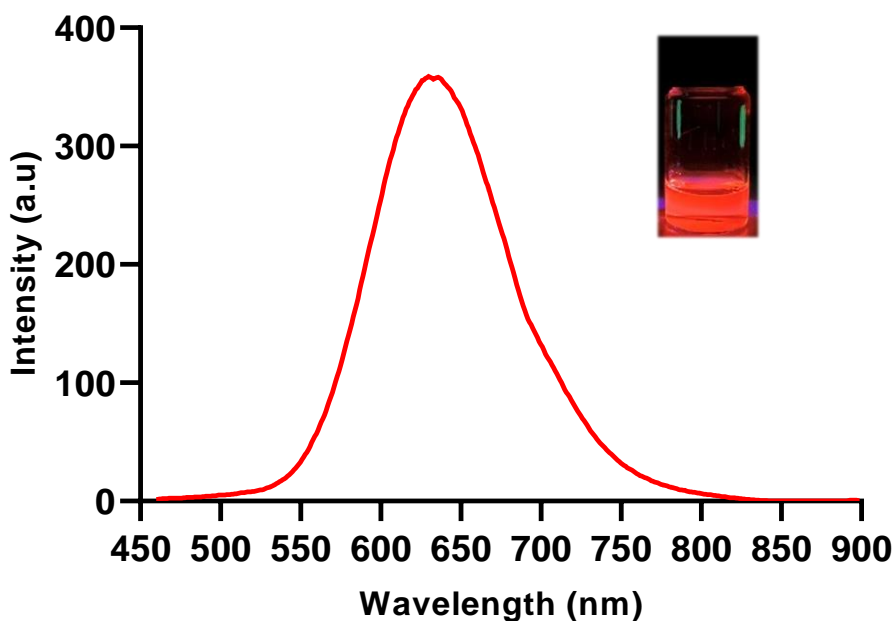
Figure 2.24: Fluorescence emission spectrum of **2.8** (λ_{ex} = 448 nm, 20 μM) in THF (0.73% DMSO). *Inset*: Picture of probe solution under illumination via UV lamp.

The *red-shift* (bathochromic) in fluorescence emission can be attributed to the extended ICT-pathway provided by the aminostyryl moiety. The ICT-character of **2.8** is depicted in **Figure 2.25**.
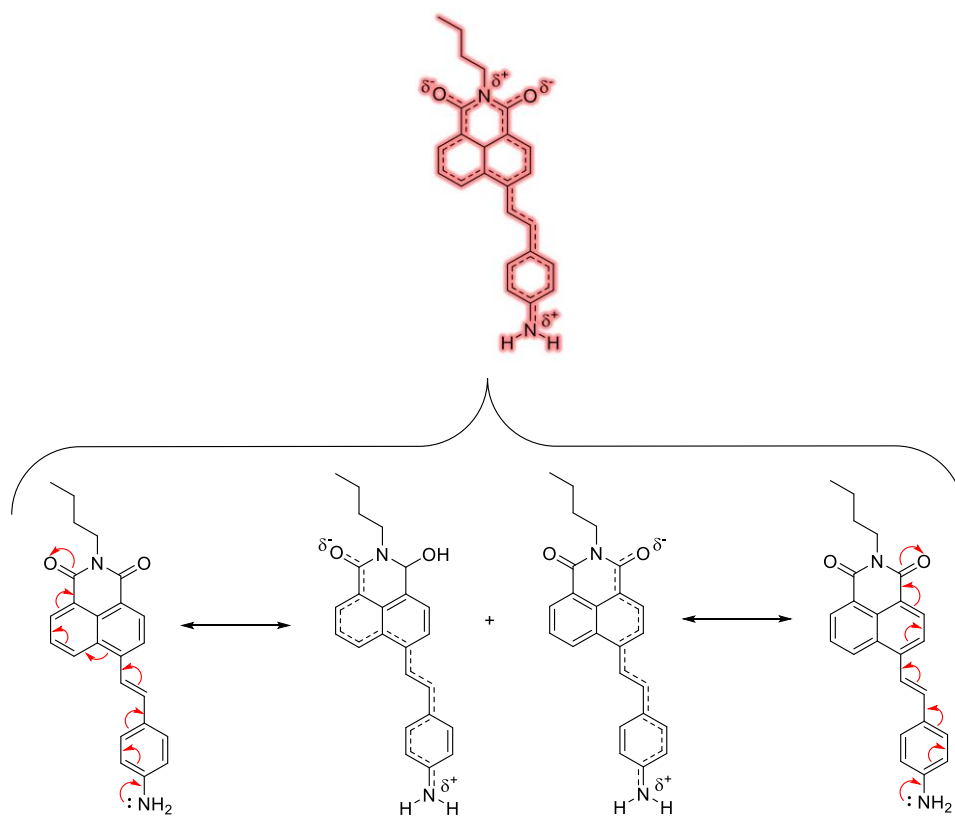
Figure 2.25: Illustration of the extended ICT within **2.8**.

The initial idea was to synthesize another caspase-3 peptide probe utilising this red-emitting naphthalimide, but this time with the advantages of NIR emission such as; minimal autofluorescence, reduced potential phototoxicity, and enhanced tissue penetration depth. We theorise that when **2.8** is functionalised to the parent peptide via carbamate linkage, the ICT-character of the fluorophore will follow the same *blue-shift* (hypsochromic) emission trend as the previous Naph. The new conjugate was expected to emit green fluorescence as the unhydrolysed parent peptide-probe. However, upon treatment with caspase-3, the released fluorophore would possess red emission (**Scheme 2.10**). This green-to-red fluorescent probe (Ac-DEVD-PABC-AS-Naph) has the potential to be an elegant step forward from the (already successful) blue-to-green probe.
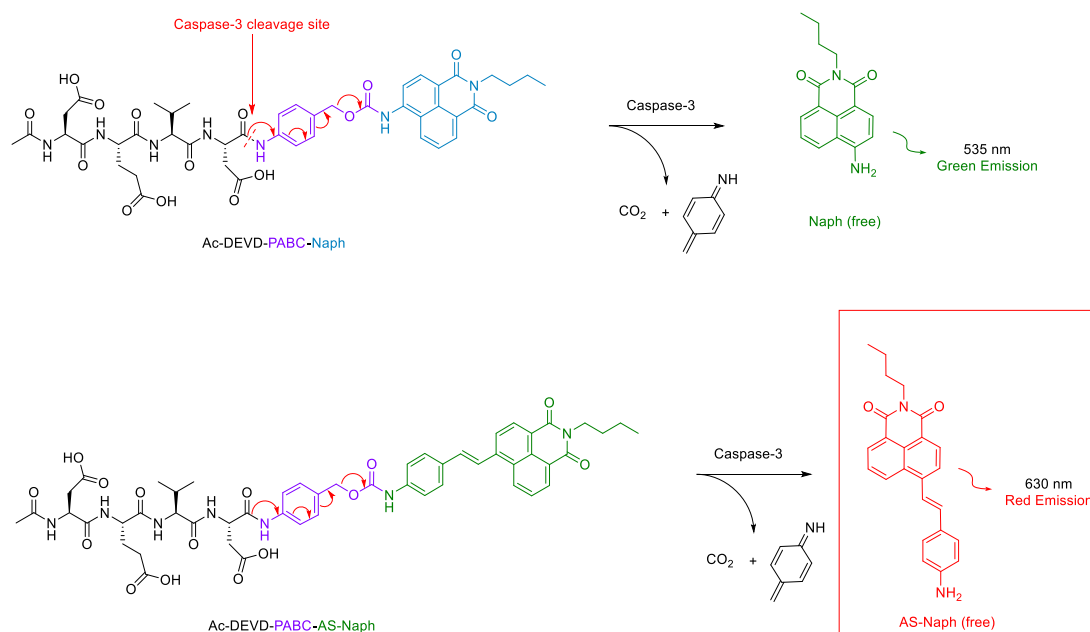
Scheme 2.10: Design strategy and schematic comparison of the potential green-to-red peptide probe (Ac-DEVD-PABC-AS-Naph) utilising the newly synthesized fluorophore (**2.8**).

However, grand expectations had to be appropriately managed, as initial fluorescence experiments indicated that **2.8**'s emission appeared to be quenched in aqueous environments. To further understand the emission profile of the fluorophore, a study was conducted to see if the fluorescence output would be affected by different solvent environments (**Figure 2.26**). A wide range of solvents with varying degrees of polarity were investigated for this study, as the polarity of the environment has been shown to impact the ICT of the naphthalimide fluorophore.[210]

90
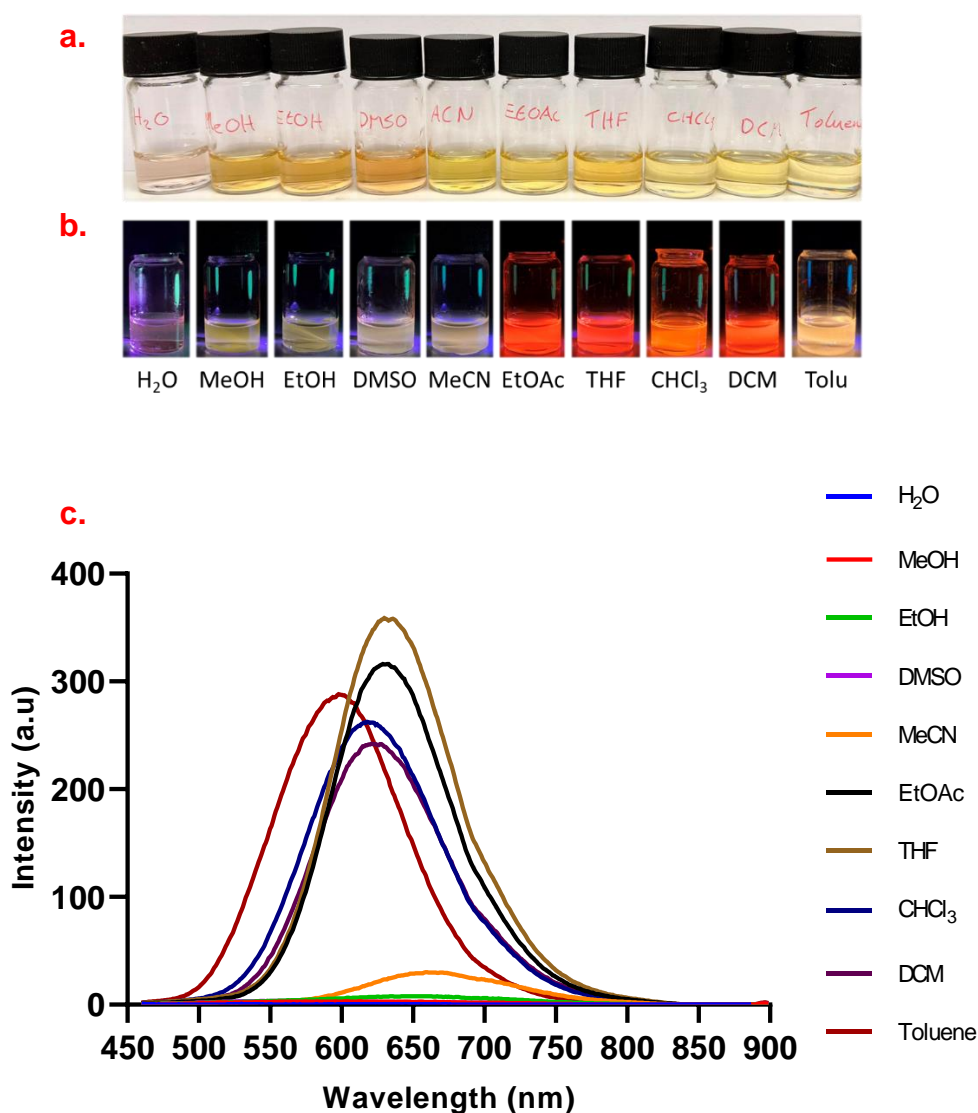
Figure 2.26: (a) Picture of probe solution(s) in various solvents. (b) Picture of probe solution(s) under illumination via UV lamp. (c) Fluorescence spectra of **2.8** (λ_{ex} = 448 nm, 20 µM) in different solvent environments (0.73% DMSO).

The solvents chosen for this study range from most polar (H_2O) to fairly non-polar (Toluene), with a gradient of polar/non-polar solvents in between. From the graph above (c), it is clearly observed that **2.8**'s fluorescent emission intensity is diminished in more polar solvents like H_2O and MeOH, with very weak to weak intensity observed for EtOH and MeCN, respectively. However, the situation dramatically changes when the probe operates in more non-polar aprotic environments, with the likes of EtOAc, THF, $CHCl_3$ and DCM displaying greatly enhanced fluorescence output. This can also be visualised by observing the probe solution(s) under a UV lamp (b). MeOH, EtOH, DMSO and MeCN display weak yellow fluorescence, whereas EtOAc, THF, $CHCl_3$ and DCM produce bright red/orange fluorescence. Toluene was noted as an unexpected result, as it did

not follow the same fluorescence trend displayed by other non-polar solvents. It did produce a comparable emission intensity however, but its fluorescence was surprisingly blue-shifted, with bright yellow fluorescence observed ($\lambda_{em} = 598$ nm). A roughly 25 nm hypsochromic shift is observed when comparing the λ_{max} of toluene to another non-polar solvent ($CHCl_3$). The H_2O sample also stood out as appreciably different to the rest of the cohort. Starting with the visual experiment (a), the probe dissolved in H_2O produced a pale-pink solution – the only sample that did not appear as a yellow/orange. Upon illumination via UV lamp, the H_2O sample displayed very weak pale-pink/red fluorescence – which was noted as uncharacteristic for the more-polar solvents (weak yellow fluorescence). However, it did keep in trend with the other polar solvents by generating an almost completely quenched fluorescence profile.

As the (potential) application of this probe will need to operate in aqueous environments – aqueous assay buffer for caspase-3 studies – it was important to understand if H_2O was responsible for the poor fluorescent output of **2.8**. To this end, the probe (20 µM) was dissolved in MeCN with increasing percentage (1 – 20%) of H_2O (**Figure 2.27**). MeCN was chosen for this experiment as it was the only solvent – from the solvent study – that displayed some sort of fluorescence while also being miscible with H_2O.
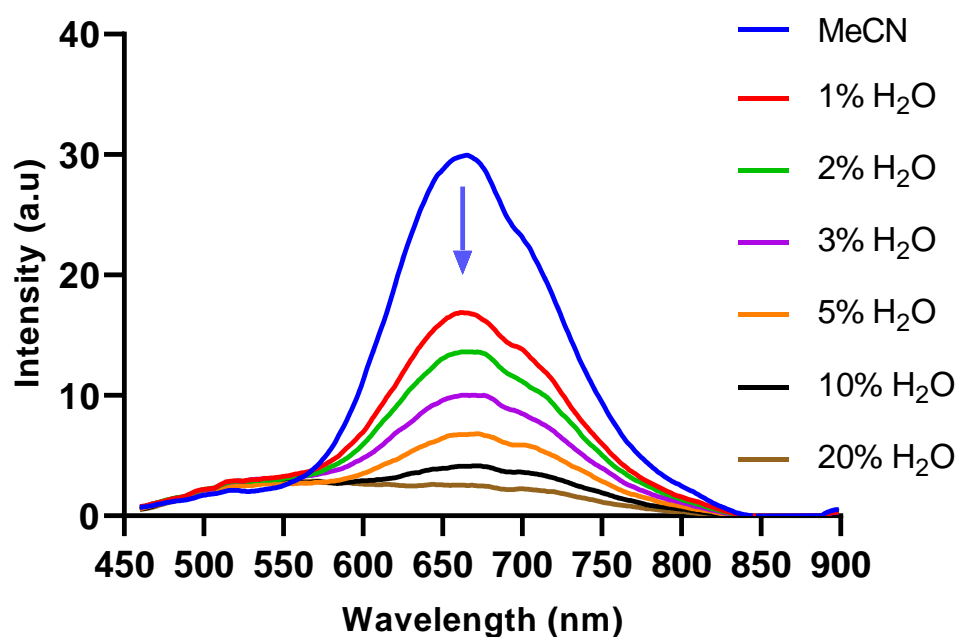
Figure 2.27: Fluorescence spectrum of **2.8** (20 µM) in MeCN (0.73% DMSO), with increasing amounts of H_2O ($\lambda_{ex} = 448$ nm).

The fluorescence intensity of the probe in neat MeCN is (expectedly) the same as it was in the initial solvent study. However, upon addition of (only) 1% H_2O, the fluorescence intensity (λ_{max} = 659 nm) decreased by almost 50%. This trend was further observed with increasing concentrations of H_2O, up to complete quenching at 20% H_2O. These results may indicate that fluorescent quenching is promoted by the presence of H_2O within the sample. Unfortunately, as the probe's fluorescent profile appears to be quenched in aqueous environments, this restricts its potential use within a caspase-3 probe. There may be other potential applications for **2.8** in the future, that utilise its fluorescent preference for hydrophobic environments. However, this probe was not expected to generate the required ratiometric response, thus, we did not venture to synthesize such a compound.

2.6 Conclusions

In conclusion, a versatile methodology for the synthesis of a caspase-3 selective ratiometric probe (**2.6**) has been developed. This strategy involved a cell-permeable naphthalimide fluorophore that was covalently bound to the peptide backbone via a PABC linker. A breakdown of our rationale is highlighted in **Scheme 2.2**. The 4-position on the naphthalimide core strongly governs its fluorescence profile. The amino-derivative (**2.4**) in the same position is "unrestricted" and elicits a "push-pull" ICT excited-state, resulting in broad absorption and emission bands around 432 and 535 nm. With this in mind, **2.2** was designed to connect to **2.4** via PABC. An amide bond was formed between the *C*-terminal aspartic acid on **2.1** and the amino group within PABA. Upon enzymatic hydrolysis, PABC underwent spontaneous degradation via a 1,6-elimination, with the loss of CO_2 and aza-quinone methide. The presence of H_2O leads to rapid quenching of this high energy, highly electrophilic intermediate.[301] This self-immolative process released **2.4**, which produced a ratiometric change in fluorescence. In contrast to quantification of enzyme activity by fluorescent change at only one emission wavelength, the ratiometric change at two distinct wavelengths can quantitatively measure enzyme activity with increased accuracy.

2.6 displayed an absorbance band at 372 nm before the addition of caspase-3 and 432 nm after treatment with caspase-3. Likewise, a fluorescence emission maxima was observed at 475 nm for the unhydrolysed probe, and 535 nm after incubation with caspase-3. Both of these spectra clearly demonstrate the time-dependant ratiometric fluorescent response generated by the probe for the visualisation of caspase-3. Enzyme kinetics such as K_m (46.4 μM), k_{cat} (0.51 sec^{-1}), and *LOD* (4.96 ng/ml) were obtained using a non-linear regression via *GraphPad™ Prism®* software. These results indicate that the probe possesses comparable kinetic data to other probes in literature, but with the added benefits of ratiometric detection. The selectivity of the probe was demonstrated to be extremely adequate, with none of the endogenous biomolecules or enzymes (including caspase-6) generating a fluorescence ratio change.

We tried to expand on the naphthalimide-based peptide probe idea by synthesizing a red-emitting naphthalimide fluorophore (**2.8**) for improved visualisation of caspase-3. This fluorophore consisted of a 4-aminostyryl group functionalised at the 4-position on the naphthalimide core, which increased its conjugation length and gave rise to an extended ICT-pathway. **2.8** displayed a NIR emission maxima (λ_{max}) around 630 nm, with bright red fluorescence. We had hoped to covalently bond the amino-NH_2 on the styrene to a carbamate linkage, in a similar fashion to our previous (blue-to-green) peptide probe. However, the compound's fluorescent output was found to be quenched in aqueous environments, thus hindering its application. It was anticipated that the fluorophore would not generate the necessary ratiometric response in aqueous assay buffer (for caspase-3 studies), therefore making the unfortunate decision to abandon synthesis regarding this red-emitting caspase-3 probe.

Future work will continue to investigate the spectroscopic properties of **2.6** by completing further iterations to gain an enhanced understanding of our probe and the role it plays in the fluorescent detection/visualisation of caspase-3. However, we are motivated by the selectivity and sensitivity of the probe in response to caspase-3, and we hope to apply the probe for measuring caspase-3 activity within living cells in the near future.

Chapter 3

Synthesis of Squaramide-based

DO3A Ligands and their potential for

Luminescent Ln^{3+} Complexes

3.Synthesis of Squaramide-based DO3A Ligands and their potential for Luminescent Ln^{3+} Complexes

3.1 Introduction

"Lanthanons, these elements perplex us in our research, baffle us in our speculations, and haunt us in our very dreams. They stretch like an unknown sea before us; mocking, mystifying, and murmuring strange revelations and possibilities" – Sir William Crookes

Crookes delivered this famous speech in an address to the Royal Society in February 1887, a time when all but three of the lanthanide elements had been successfully isolated.[302] Scientific discovery of the lanthanides followed an irregular pattern and did not emerge in order of atomic number. Surprisingly, cerium was discovered long before lanthanum, during the latter part of the eighteenth century. It wasn't until 1875 that cerium was successfully extracted from an ore and named in honour of *Ceres*, an asteroid found between Mars and Jupiter in 1801.[303] Subsequently, a few decades later, a mineral named ytterite was discovered near the town of Ytterby, Sweden, in 1787. Over the next century, most of the remaining lanthanides were isolated from ytterite, and the discovery of lutetium in 1907 marked the completion of isolating all the lanthanides.[304]

Luminescence has played a crucial role in the discovery of several lanthanide elements, and, reciprocally, these elements have consistently been central to lighting and light conversion technologies. These technologies include lasers, cathode-ray and plasma displays, light-emitting diodes, to name a few. More recently, it has become evident that the unique luminescent properties of lanthanide ions can be harnessed for applications spanning from biomedical and sensing fields to luminescence imaging. This realisation has prompted fascinating advancements in the coordination chemistry of these ions.[305]

The 15 elements across the lanthanide series feature electronic configurations ranging from [Xe] $4f^0\,5d^1\,6s^2$ for Lanthanum and [Xe] $4f^{14}\,5d^1\,6s^2$ for Lutetium. This specific electronic configuration of lanthanide elements is accountable for the consistency in their physical and chemical properties;

including oxidation states, redox potentials, and ionic radii.[306] This uniformity in chemistry makes their separation quite challenging. All lanthanide elements exhibit a stable +3 oxidation state (Ln^{3+}), which represents an optimal balance between the ionisation energy cost and the solvation-energy or lattice-energy stabilisation of the ion. The 4f electrons of lanthanide elements are shielded by the $5s^2$ and $5p^6$ orbitals, making them poorly available for covalent interactions with ligands. Consequently, interactions are mostly electrostatic in nature, and the geometry of Ln^{3+} complexes is influenced more by steric factors than electronic ones.[307] As a result, lanthanide complexes that possess the same ligand tend to exhibit the same structure. Lanthanide ions – due to their small size – possess a high positive surface-charge density, classifying them as similar to hard Lewis acids. Hence, they have a strong affinity for ligands with highly electronegative donor-sites (hard Lewis bases) – following the order: $F^- > HO^- > H_2O > NO_3^- > Cl^-$.

Lanthanide ions do not efficiently absorb light by themselves. The preferred method to sensitise their luminescence involves using chromophores as *antennas* to absorb light. In this scenario, the following sensitisation steps occur: population of the lowest-lying singlet excited state (*S*) of the organic chromophore, subsequent intersystem-crossing (*ISC*) to its triplet level (*T*), and finally, energy transfer (*en*) to the lanthanide centre (**Figure 3.1**).[308]
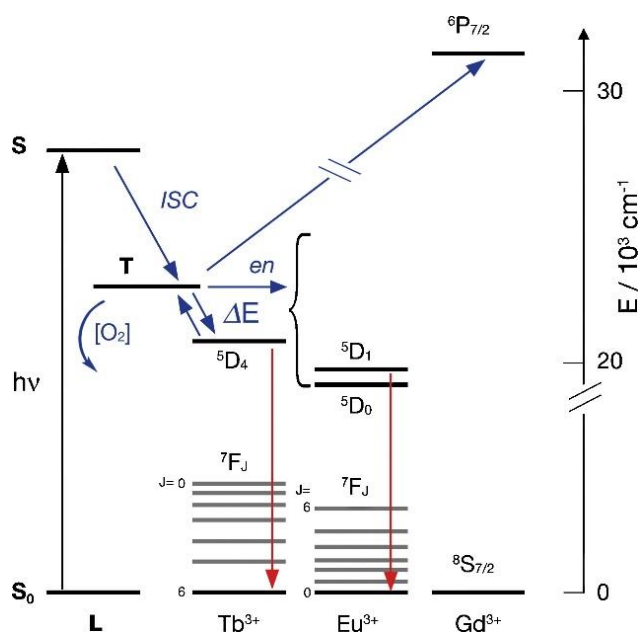
Figure 3.1: Jablonski diagram depicting the antenna effect for sensitisation of luminescence in popular lanthanide cations. Blue arrows indicate non-radiative processes, while red arrows indicate radiative processes.[308]

To prevent non-radiative deactivation caused by interactions with O-H oscillators in H_2O, it is necessary to effectively shield the 8-9 coordination sphere of the Ln^{3+} centre against the solvent environment. Therefore, the choice of ligand system for constructing lanthanide complexes must fulfil several criteria. These criteria pertain to the overall stability of the complex and the occupation of coordination positions, with the aim to maximise emission intensity. To enhance the thermodynamic stability of the complex, it is crucial to maximise the interaction between the Ln^{3+} centre and the ligand. Given the hard nature of Ln^{3+} cations, they exhibit a preference for hard binding sites with substantial electrostatic components. Therefore, anionic ligands like phosphonates, β-diketonates and carboxylates, are highly recommended for this purpose.

The structure of the ligand should possess enough flexibility to allow firm encapsulation of the Ln^{3+} cation, resulting in exceptionally high thermodynamic and kinetic stabilities and a complete shielding of the metal centre. The stability of the complex is enhanced when ligands incorporate binding groups with strong affinities for the cation, such as nitrogen and/or oxygen donor atoms.[309] A crucial category of acyclic ligands consists of polyaminopolycarboxylate systems, where four or more acetic groups are covalently linked to a polyamino framework like EDTA or DTPA. These ligands form anionic Ln^{3+} complexes that are both highly stable and soluble in aqueous solutions (**Figure 3.2A**).[310]

EDTA

DTPA

NOTA

DOTA
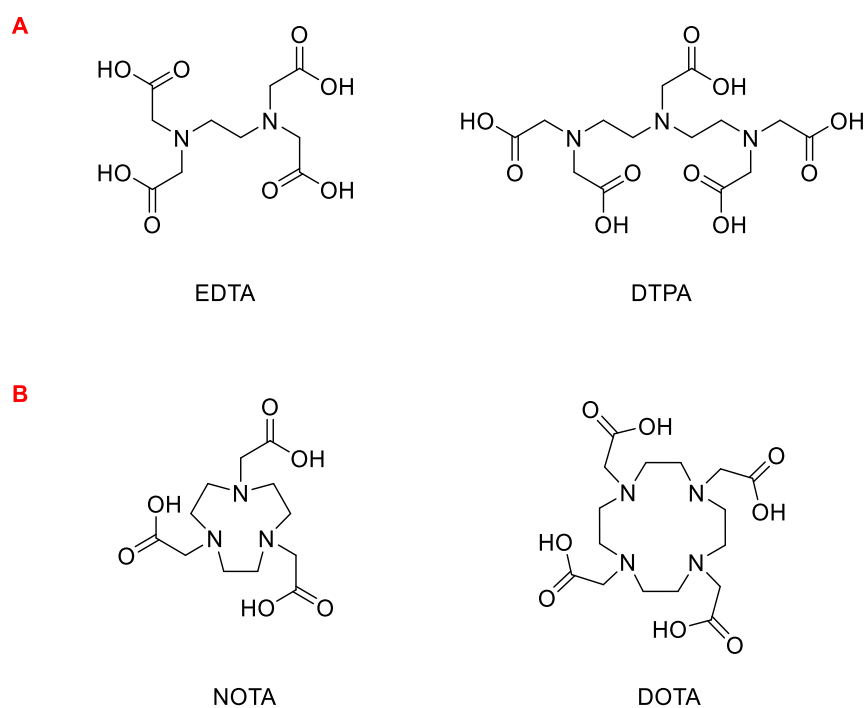
Figure 3.2: Examples of acyclic (A) and cyclic (B) ligands used to form Ln^{3+} complexes.

There also exists cyclic ligands, that often contain a polyaza-macrocycle with additional anionic binding sites attached to the secondary amine nitrogen atom of the ring (**Figure 3.2B**). The stability of these complexes can be fine-tuned by modifying the size of the ring (DOTA > NOTA) and varying the number and functionality of the lateral binding arms that surround the lanthanide cation. The DOTA ligand is up there as one of the best in literature for Ln^{3+} complexes, with some of the highest stability constants ever recorded.[311] The four nitrogen atoms of the cyclen ring collectively bind to the faces of the square anti-prism, mirroring a frequently observed crystal structure for complexes of DOTA-type ligands with Ln^{3+} cations. They maintain the same quadrangular conformation, whether in their free or complexed state.[312] Intuitively, the size of the chelating-ring also has an impact on the stability of the complex, with smaller ring-ligands (e.g. NOTA), and indeed larger ring-systems usually imparting a negative effect. These complexes are valuable for various applications, serving as contrast agents or luminescent labels in biological assays, depending on the specific Ln^{3+} cation used.

Luminescent Ln^{3+} complexes are multi-component systems in which the key elements, including the metal cation, the coordination site (ligand), and the antenna, are arranged in a supramolecular structure (**Figure 3.3**). Therefore, the selection of these elements and their arrangement within the overall structure are critical factors to be addressed during the molecular design process to maximise the overall sensitisation efficiency. The chromophore responsible for enhancing the sensitisation of lanthanide luminescence is commonly referred to as the *"antenna."* It plays a pivotal role in determining the emission intensity of the Ln^{3+} complex. Typically, the antenna can be any aromatic or hetero-aromatic, highly π-conjugated system with a high efficiency of light absorption and robust efficiencies in intersystem crossing and energy transfer processes.[313]
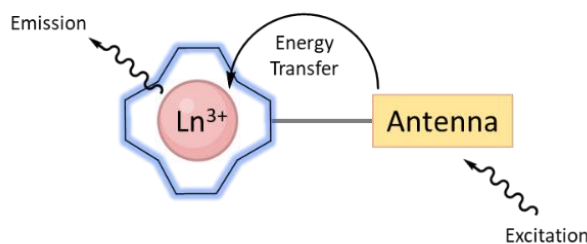
Figure 3.3: Cartoon schematic depicting the antenna effect for luminescence emission of Ln^{3+} complexes. *Note:* Blue structure = metal-bound ligand.

To ensure rapid energy transfer, having a short distance between the antenna and the Ln^{3+} cations is clearly advantageous. The most favourable outcomes are achieved when the antenna directly coordinates with the metal centre. This approach has been predominantly utilised with chromophores that incorporate binding sites for the Ln^{3+} cation (**Figure 3.4**), such as aza-aromatic compounds (phenanthroline, bipyridine, terpyridine, azatriphenylene) or phenolate aromatics (e.g. 1-hydroxypyridin-2-one and 2-hydroxyisophthalamide).
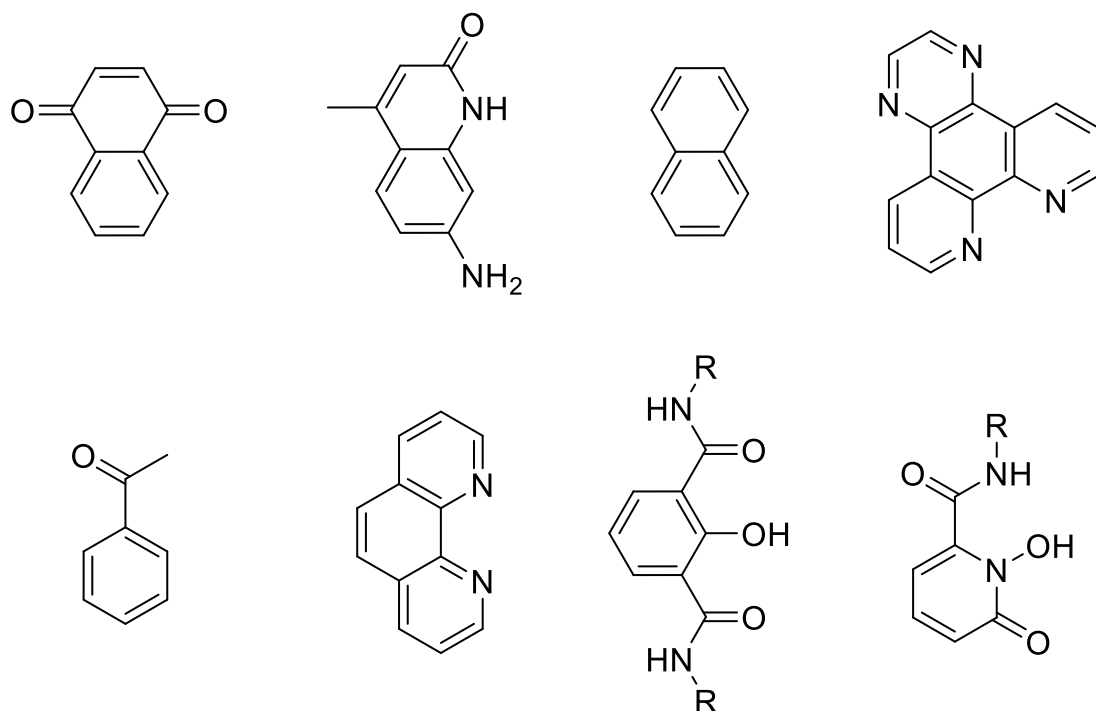
Figure 3.4: Examples of chromophores commonly used as Antennas for Ln^{3+} sensitisation.

The emission properties of lanthanide cations encompass a broad spectral range that extends from the UV (Gd^{3+}) to the visible; blue (Tm^{3+}), green (Tb^{3+}), yellow (Dy^{3+}), orange (Sm^{3+}), and red (Eu^{3+}) to the NIR (Yb^{3+}, Nd^{3+} and Er^{3+}). Compounds containing these Ln^{3+} complexes also possess narrow emission bands, long luminescence lifetimes, and resistance to photobleaching, making them promising candidates for use in biological imaging.

This chapter will focus on the use of the squaramide motif as an antenna for Ln^{3+} sensitisation and luminescence. Squaramides – a family of conformationally rigid cyclobutene ring derivatives (**Figure 3.5A**), have been rapidly gaining attention in various fields of the biological and chemical sciences.[314,315] These molecules consist of two N-H groups that can act as hydrogen-bond donors positioned close to two carbonyl groups, which function

as hydrogen-bond acceptors. This unique molecular structure imparts distinct chemical and physical properties, making it exceptionally valuable as a tool in diverse areas such as self-assembly, molecular recognition, catalysis, and bioconjugation. One of the most notable features of squaramides is their ability to delocalise a lone-pair into the cyclo-butenedione system, imparting aromatic character to the four-membered ring (**Figure 3.5B**).
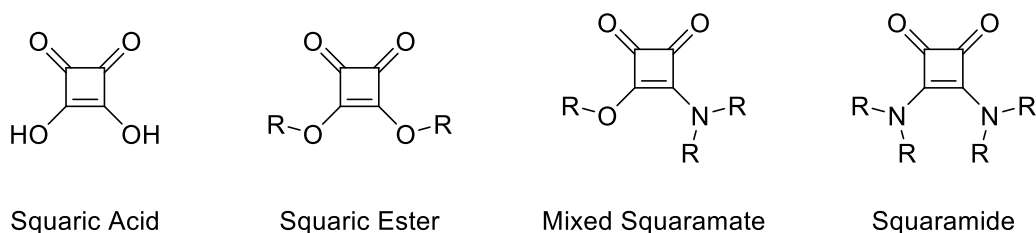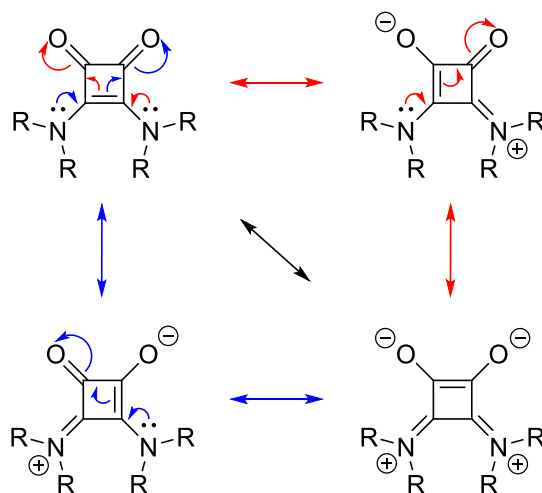
Figure 3.5: Common naming conventions for Squarate Derivatives (A),[316] and resonance structures for the Squaramide motif (B).[317]

Although the squaramide scaffold (and its derivatives) have been used extensively in studies regarding anion transport,[318] and bioisosteres in contemporary drug design,[319] only a few examples in the literature exist detailing the use of this moiety for the sensitisation of Ln^{3+} complexes.[320,321] Here at the Elmes group, we have a wealth of knowledge and synthetic experience regarding the squaramide scaffold,[322,323,324] and hope to utilise this to develop novel ligands with the incorporation of a squaramide – and its derivatives – as an (underappreciated) antenna for Ln^{3+} sensitisation and luminescence. In the first instance, we aim to create a synthetic analogue of DOTA, by functionalising the

cyclen ring-system directly with a squaramide motif. An illustration of our design strategy for potential lanthanide luminescence is depicted in **Figure 3.6**.
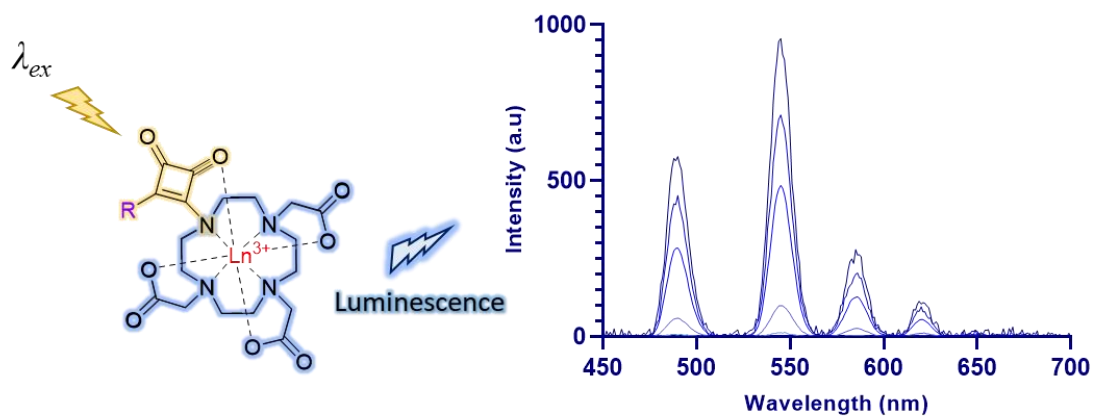
Figure 3.6: Illustration of Squaramide-based DO3A ligand for potential Ln^{3+} luminescence.

3.2 Chapter Objective(s)

The objective of this chapter is to generate structural analogues of DOTA for the purpose of forming novel Ln^{3+} complexes. The initial goal was to synthesize a family of squaramide-based DO3A ligands and investigate their potential use for Ln^{3+} luminescence. In our ligand design, we took several factors into consideration, including: (i) high structural simplicity – meaning it should consist of only essential components, specifically a chromophore and an efficient coordination site; (ii) ensuring excellent water solubility; (iii) achieving high chemical and thermal stability; and (iv) ease of synthetic accessibility. The first (proof of principle) probe design strategy was to synthesize a mono-substituted squaramic acid analogue of DOTA (**Figure 3.7**).

DOTA

DO3A-Sq-OH

pKa ~5
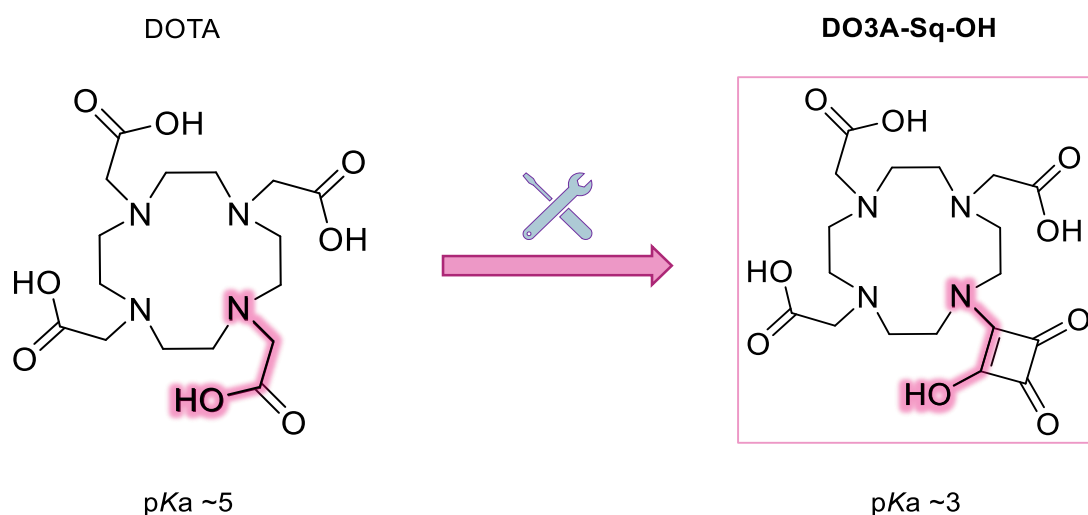
pKa ~3

Figure 3.7: Design strategy for the synthetic DOTA analogue (DO3A-Sq-OH), with key structural/chemical features highlighted.

We envisage that the squaramic acid-OH arm on DO3A-Sq-OH will possess a similar *pKa* (≈ 3) to that of the native DOTA (≈ 5), with the Sq-O$^-$ species being present at physiological pH.[314] The number of carbon atoms between the ring-nitrogen and -OH group remains the same at two, thus imparting a similar *arm-length* (for coordination). However, the squaramide motif should grant significant structural rigidity over the native carboxylic acid arm, while at the same time acting as an antenna for potential sensitisation. We hope that by trying to conserve the structural/chemical characteristics of the native DOTA, the new squaramide analogue(s) will possess similar stability constants. Our potential family of squaramide-based DO3A ligands are highlighted in **Figure 3.8**.

DO3A-ESq (**3.4**)   DO3A-Sq-OH (**3.5**)   DO3A-Sq-NH$_2$ (**3.6**)   DO3A-Sq-EDA (**3.7**)
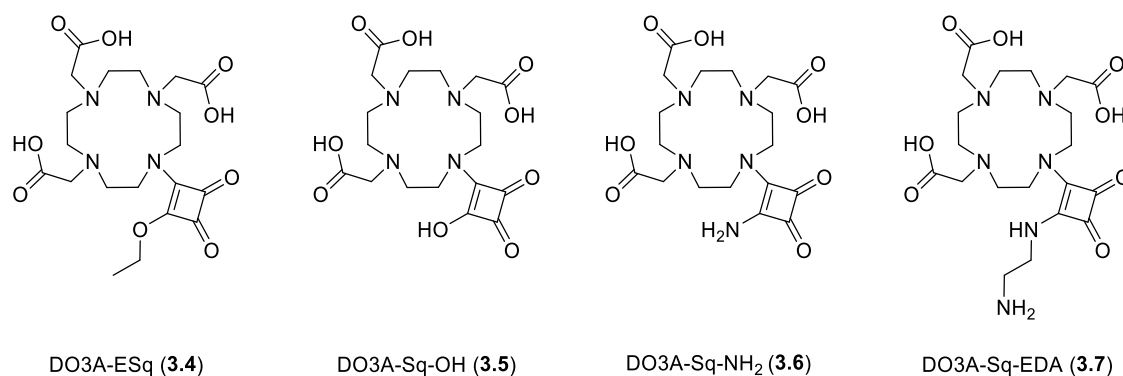
Figure 3.8: Structures of squaramide-based DO3A ligands.

From here, we wanted to investigate if it was possible to vary the substitution pattern of squaramide(s) around the cyclen ring-scaffold. The *naked* cyclen-ring contains four secondary (N-H) amino groups that can theoretically be functionalised, so we endeavoured to synthesize di-, tri-, and tetra-substituted squaramide-based cyclen ligands. An illustration of this design strategy – expanding on from the mono-substituted analogues – is depicted in **Figure 3.9**. The increase in squaramide substitution around the cyclen-ring we believe may have a cooperative effect in enhancing not only the stability constant(s) of the complexes, but also the sensitisation for Ln^{3+} luminescence. The structural rigidity bestowed onto the ligand with each additional squaramide substitution may generate highly stable *cage-like* complexes. Of course, the removal of one (or more) carboxylic acid binding site from DOTA, can have a detrimental effect on the stability of the complexes. However, this is partially offset by the squaramic acid antenna, which includes additional binding sites that are strategically positioned to complete the coordination sphere of the Ln^{3+} cation.

DOTA

DO3A-Sq-OH
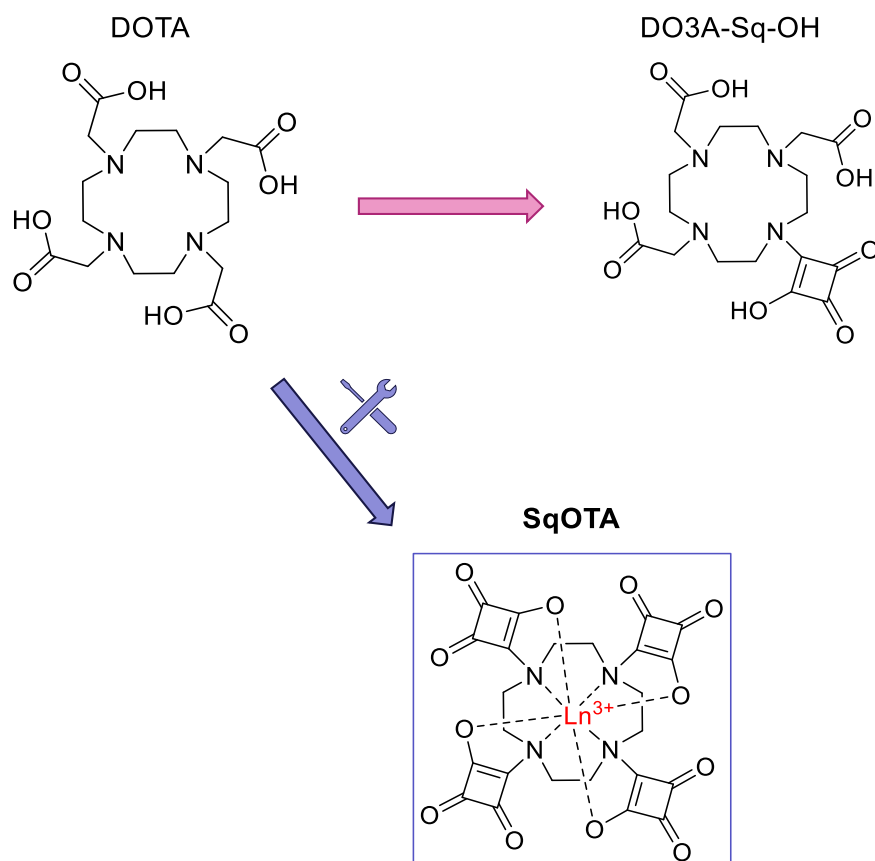
SqOTA

Figure 3.9: Design strategy for the tetra-substituted squaramic acid analogue (SqOTA).

Having the di-, tri-, and tetra-substituted squaramide-based cyclen ligands in hand (**Figure 3.10**), we foresee an interesting study regarding the substitution pattern for forming novel luminescent complexes with different Ln^{3+} centres (e.g. Eu^{3+}, Tb^{3+}, Gd^{3+}).

DO2A-2Sq-OH (**3.11**)   SqO3A-COOH (**3.15**)   SqOTA (**3.17**)
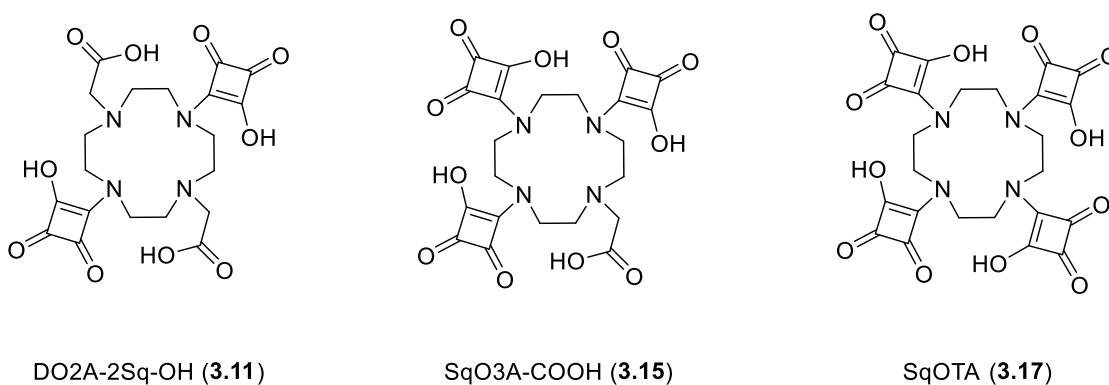
Figure 3.10: Structures of di-, tri-, and tetra-substituted squaramide-based cyclen ligands.

Herein, we report the synthesis of mono-, di-, tri- and tetra-substituted squaramide-based cyclen ligands, and a preliminary investigation into their potential use in forming luminescent Ln^{3+} complexes. We then tried to expand this idea further with the generation of a lanthanide-based caspase-3 probe

(**Figure 3.11**). It is postulated that this probe may undergo a change in luminescence after being hydrolysed by caspase-3 via two potential methods: (A) the squaramide antenna (as drawn) may not be efficiently coordinated to the Ln^{3+} centre until after enzymatic cleavage; (B) the ethylene diamine (EDA) linker confers a high degree of flexibility to this compound, thus, the Ln^{3+} coordination site may be affected by the potential overlapping peptide sequence (**Figure 3.11**). This Ln^{3+}-peptide probe will build on from our success with organic fluorophores – as demonstrated in Chapter 2 – while harnessing the numerous benefits offered by luminescent lanthanide complexes.

Ac-DEVD-EDA-Sq-DO3A (**3.19**)
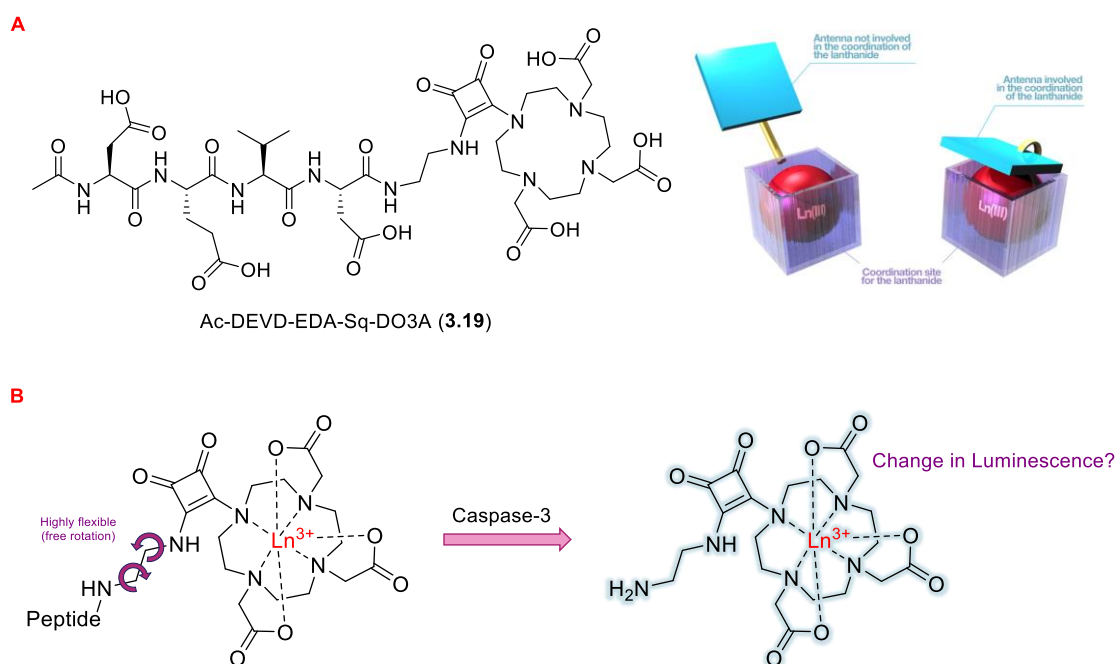
Figure 3.11: Structure of Ln^{3+}-based Caspase-3 probe, and potential methods for change in luminescence.

3.3 Synthesis and Characterisation of Squaramide-DO3A Ligands

The synthetic pathway to squaramide-based DO3A ligands is outlined in **Scheme 3.1**. The initial step involved synthesising 3,4-diethoxy-3-cyclobutene-1,2-dione (**3.1**), commonly known as diethyl squarate (DESq). Diethyl squarate is one of the most prevalent alkoxy derivatives of squaric acid and serves as the primary starting material for synthesising squaramide derivatives. **3.1** was synthesized using a method adapted from the one originally reported by Liu *et al.*[325] In this process, 3,4-diethoxy-3-cyclobutene-1,2-dione – squaric acid (**3.0a**) – was reacted with triethyl orthoformate to afford **3.1** with a yield of 85%.
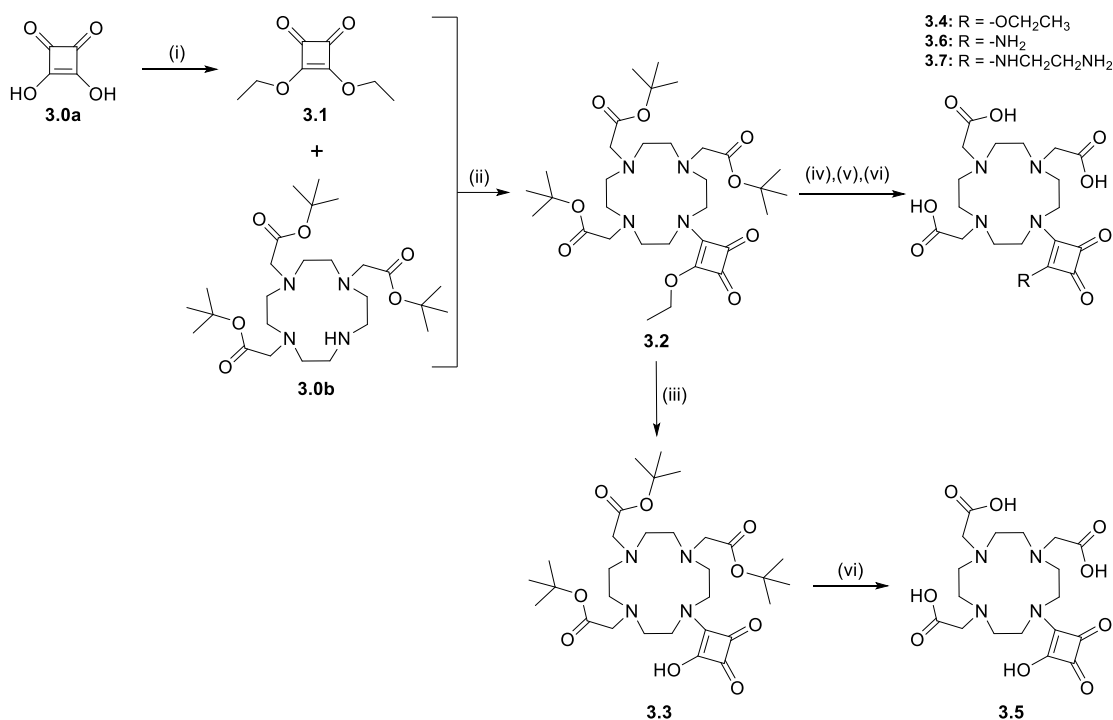
Scheme 3.1: Synthetic pathway to squaramide-based DO3A ligands (**3.4 – 3.7**). *Reagents and conditions:* (i) triethyl orthoformate, EtOH, 80°C, 72 hrs, 85%. (ii) DESq, TEA, EtOH, rt, 16 hrs, 87%. (iii) 1M NaOH (aq.), EtOH, rt, 2 hrs, 89%. (iv) NH₃/EtOH, EtOH, rt, 16 hrs, 90%. (v) EDA, EtOH, rt, 16 hrs, 91%. (vi) TFA, rt, 16 hrs, 95%.

This project was a joint venture between our collaborator Dr Celia Bonnet at the Centre de Biophysique Moléculaire (CBM/CNRS) – Orleans, France. I spent a short amount of time out in Orleans under the supervision of Dr Bonnet where the initial synthesis of the squaramide-based DO3A ligands was conducted. This project began with the attempted synthesis of the squaramic acid

ligand (**3.5**). Protected squaramate precursor (**3.2**) was generated using a method adapted from Corsi *et. al.*,[326] where tri-*tert*-butyl 2,2′,2"-(1,4,7,10-tetraazacyclododecane-1,4,7-triyl) triacetate (DO3A*t*Bu, **3.0b**) was treated with an excess of DESq (**3.1**) to afford the mono-substituted protected product with an 87% yield (**Scheme 3.2**). This reaction involved a nucleophilic substitution between DO3A*t*Bu and DESq (**3.1**), resulting in the formation of a tetrahedral intermediate. During this process, intramolecular proton transfer occurs between the protonated amine and the ethoxy ester, enabling the ester to serve as a good leaving group. The tetrahedral intermediate subsequently collapses, yielding the desired compound (**3.2**), and releasing ethanol as a byproduct.
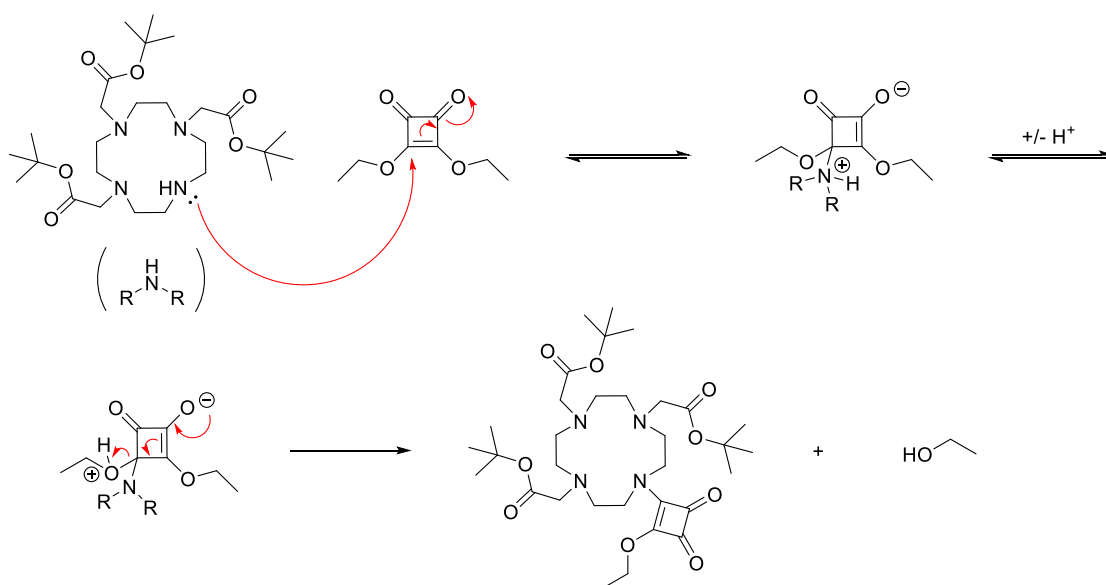
Scheme 3.2: Proposed mechanism of nucleophilic substitution with DO3A*t*Bu and DESq to form **3.2**.[322]

Evidence for the successful synthesis of **3.2** was confirmed by LC-MS and ¹H NMR analysis (**Figure 3.12**), with further experiments (¹³C NMR, COSY, HSQC, HMBC and HRMS) being documented in the *Appendix* (see Figure S3.9 – 3.13).
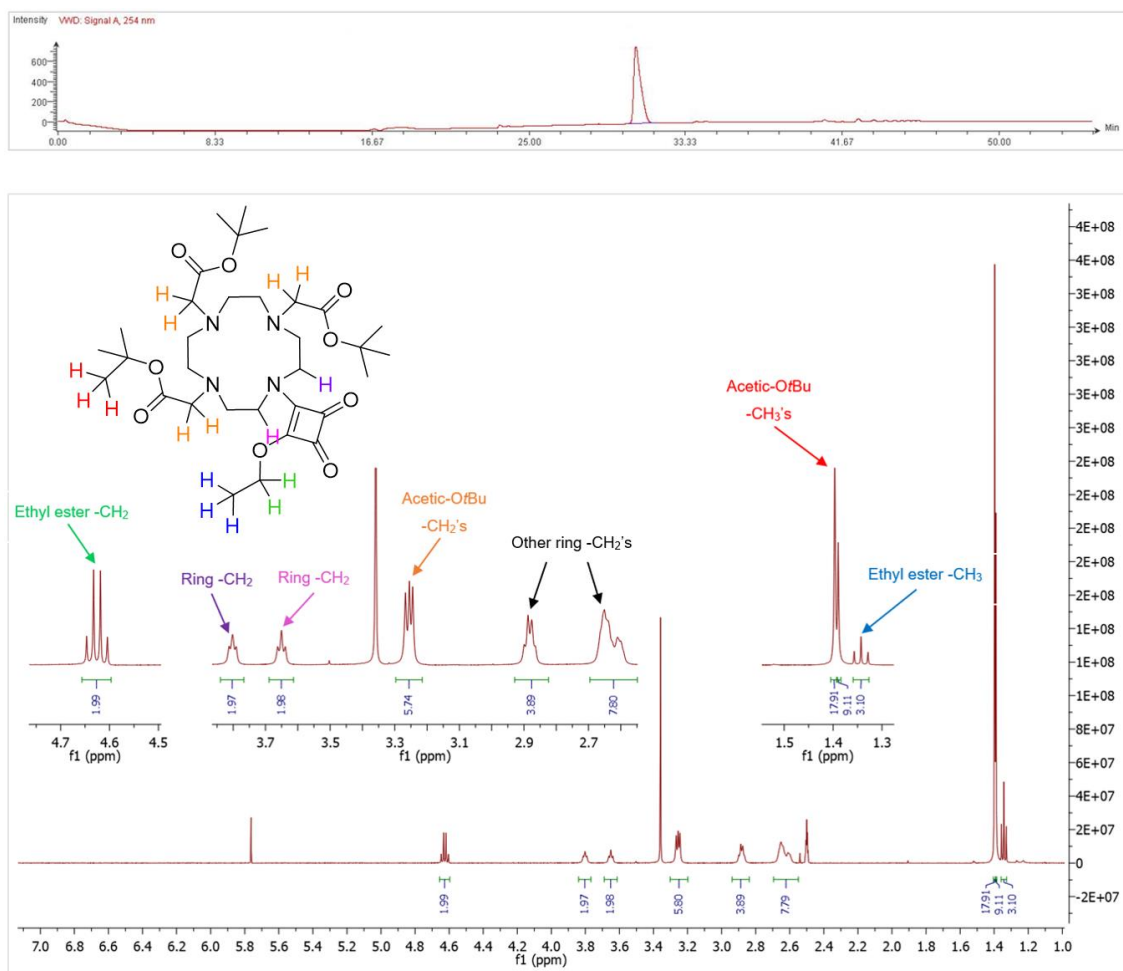
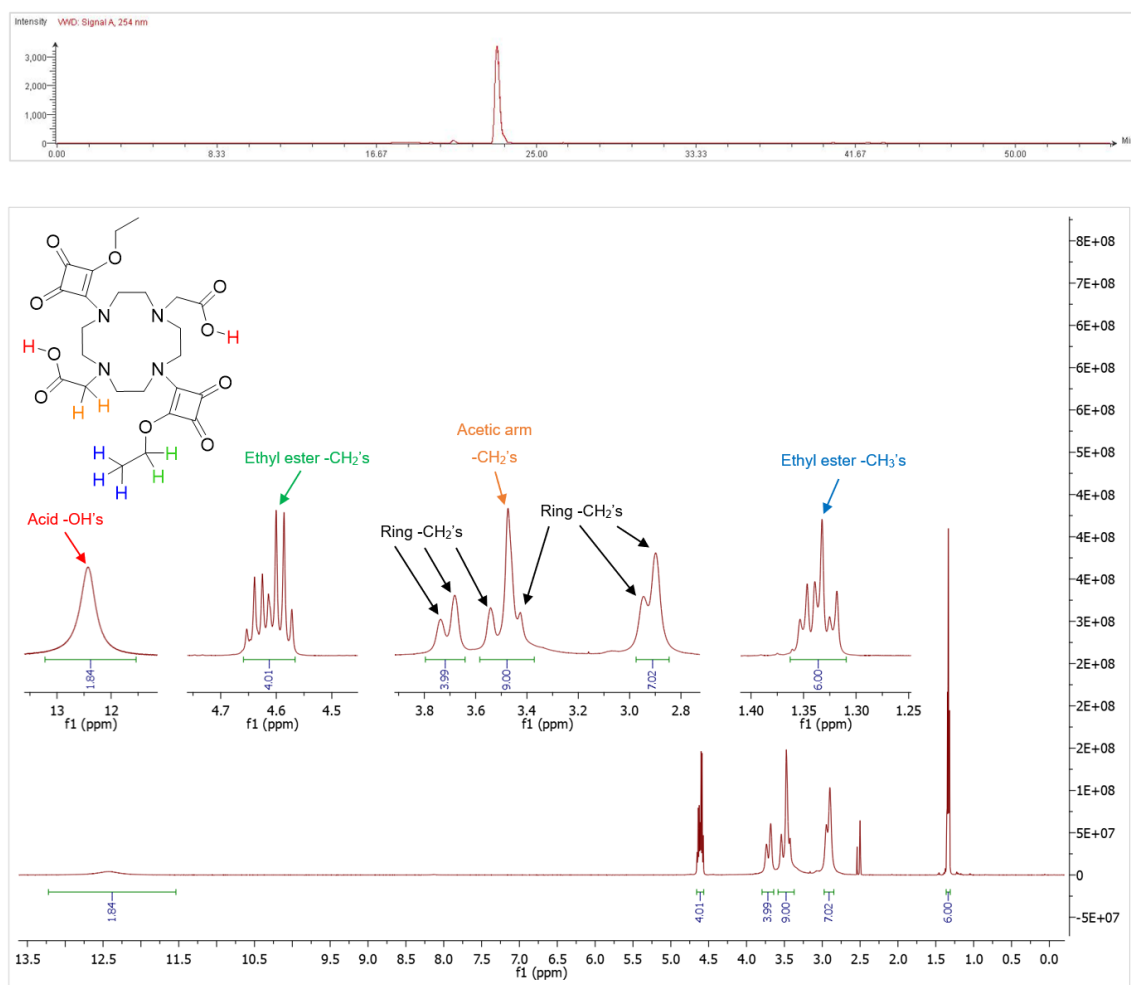**Figure 3.12:** (Top) HPLC trace. (Bottom) ^{1}H NMR spectrum of **3.2** in DMSO-d_6. Some ring-protons (on the structure) and peak annotations are removed for clarity, see Figure S3.8.

The HPLC trace of **3.2** displays a UV peak for the target compound with a t_R = 31 minutes. The ^{1}H NMR spectrum highlights the characteristic peaks of this fully protected compound. The -CH$_2$ protons on the cyclen-ring show up from 2.6 – 3.8 ppm, with the protons closest to the squaramate moiety displaying as triplets furthermost downfield at 3.65 ppm and 3.81 ppm, both integrating for 2H each. The -CH$_2$ singlets of the acetic-O*t*Bu arms appeared very close together at ~3.25 ppm, integrating for 6H in total. The *t*Bu-CH$_3$ protons appeared as singlets around ~1.39ppm, integrating for a total of 27H. Finally, the classic ethyl splitting pattern – representing the squaramate ester protons – was observed as a triplet (integrating for 3H) and a quartet (integrating for 2H) at 1.34 ppm and 4.63 ppm, respectively. Interestingly, this was the first, and last time that (somewhat) well-resolved triplets for the ring-CH$_2$ protons were observed. Perhaps, when the ligand is fully protected (as in this case) it possesses a certain degree of steric-bulk or rigidity, hindering the natural flexibility of the cyclen-ring, thus displaying

more resolved triplets. **3.2** was then subject to TFA deprotection of the -O*t*Bu arms to afford **3.4** with a 95% yield. LC-MS and ^{1}H NMR data is supplied in **Figure 3.13**. However, due to time limitations (only in France for a few weeks) and synthetic/purification difficulties, only the squaramate ethyl ester derivative (**3.4**) was synthesized successfully.
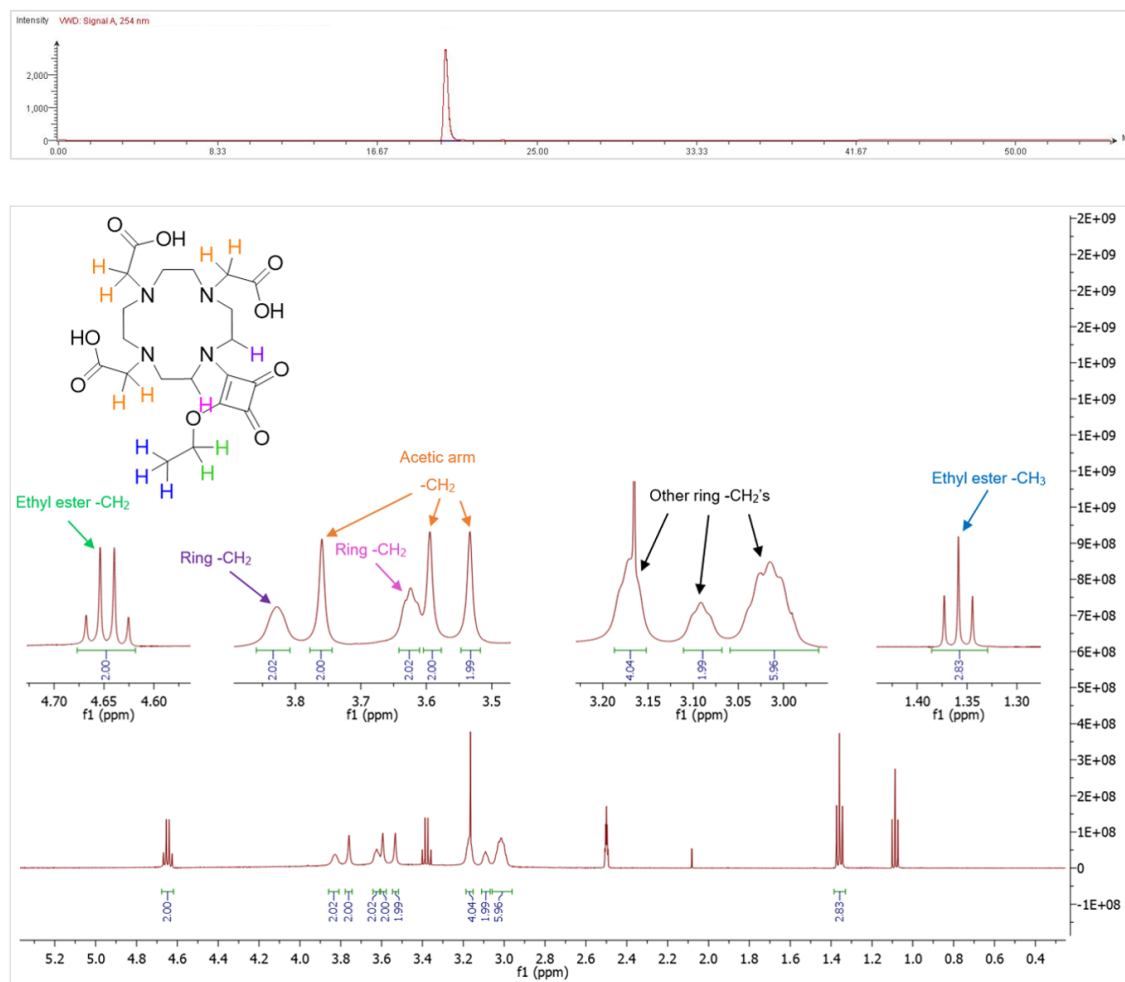
Figure 3.13: (Top) HPLC trace. (Bottom) ^{1}H NMR spectrum of **3.4** in DMSO-d_6.

The HPLC trace for **3.4** displays one UV peak with a t_R = 20 minutes. The ^{1}H NMR spectrum showed many peaks that were indicative of the target compound (**3.4**), with the -CH$_2$ protons on the acetic-arms showing up as three distinct singlets between 3.53 – 3.76 ppm each integrating for 2H. The cyclen-ring protons appeared as broad triplets from 3.01 – 3.83 ppm, with some of the more resolved (downfield) peaks integrating for 2H each. Finally, the classic ethyl splitting pattern remained the same, with a triplet at 1.34 ppm and a quartet at 4.63 ppm integrating for 3H and 2H, respectively.

111

Now back at Maynooth University, the first objective was to complete the synthesis of **3.5**. However, synthesis of this ligand was not as straight forward as initially perceived. The original synthetic approach was to subject compound **3.2** to acid hydrolysis via 1M HCl (aq.), as the -OtBu protecting groups and squaramate ethyl ester are acid sensitive. This unfortunately led to a crude mixture containing multiple UV signals at different retention times (HPLC trace) with no corresponding target mass observed, thus this synthetic approach was swiftly abandoned. However, LC-MS and HPLC data was employed to investigate this process further with the hopes of gaining some insight into this reaction (**Figure 3.14**).
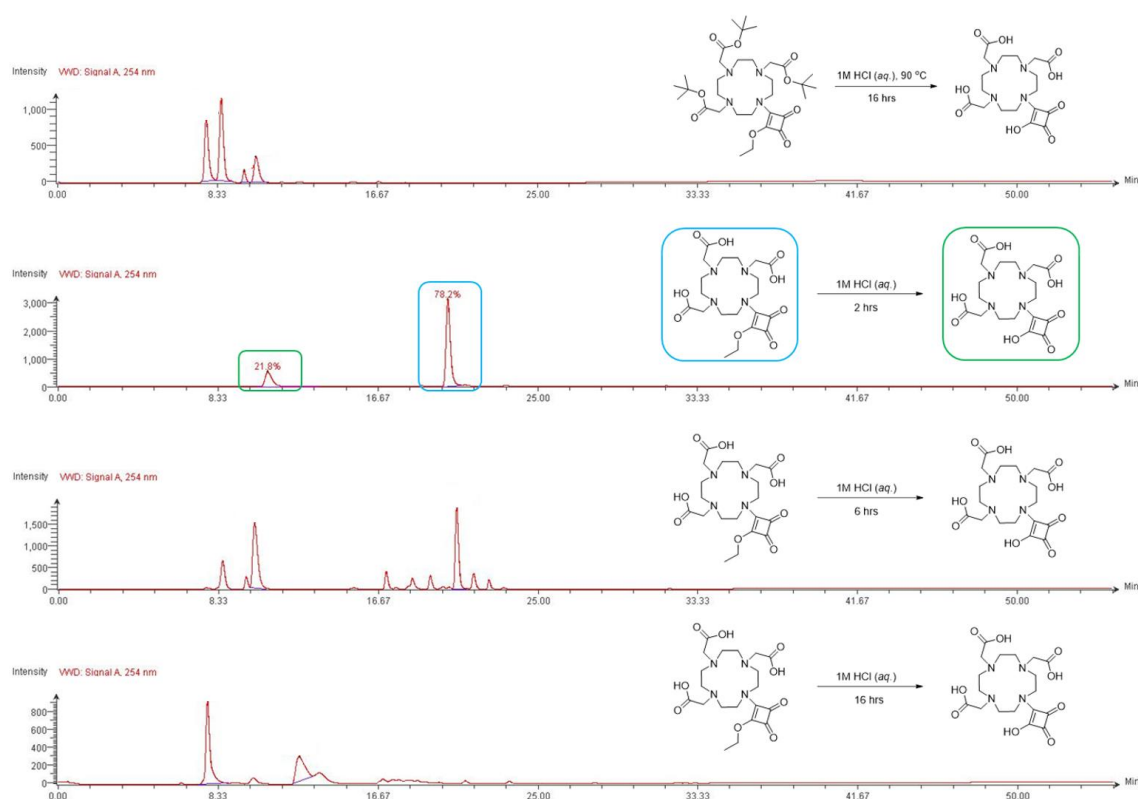
Figure 3.14: HPLC investigation into the suspected degradation via acid hydrolysis.

The next synthetic strategy attempted, was to reach compound **3.4** first, then hydrolyse the squaramate ethyl ester sequentially instead of global deprotection from **3.2** to **3.5**. This time, a much cleaner conversion from starting material **3.4** (blue box) to target squaramic acid product **3.5** (green box) was observed after 2 hours. From integrating the area under the curve (UV peak), it was observed that only a ~20% conversion was achieved in this time. Thus, the reaction was allowed to continue for a longer period of time. After 6 hours, multiple UV signals appeared alongside the starting material and product peaks.

The reaction was then left overnight, and after 16 hours the HPLC trace had completely changed baring no resemblance to the original chromatogram (after 2 hours). Although there is still UV signals after 16 hours, it is postulated that perhaps some rearrangement of the squaramide moiety had occurred,[327] but this was not confirmed nor was it investigated further.

A different approach was utilised, with the final synthetic work-around consisting of hydrolysing the protected squaramate ethyl ester (**3.2**) – via 1M NaOH – to the protected squaramic acid (**3.3**) before deprotecting the -O*t*Bu arms. By hydrolysing the ethyl ester first (**Scheme 3.1**), a very efficient conversion from **3.2** to **3.3** was observed, with a yield of 89%. Compound **3.3** was characterised via LC-MS data (Figure S3.14 – 3.17) which contained one UV peak with a t_R = 32 minutes – as outlined in **Figure 3.15**. From here, it was a standard TFA deprotection as before to afford **3.5** with a yield of 95%.
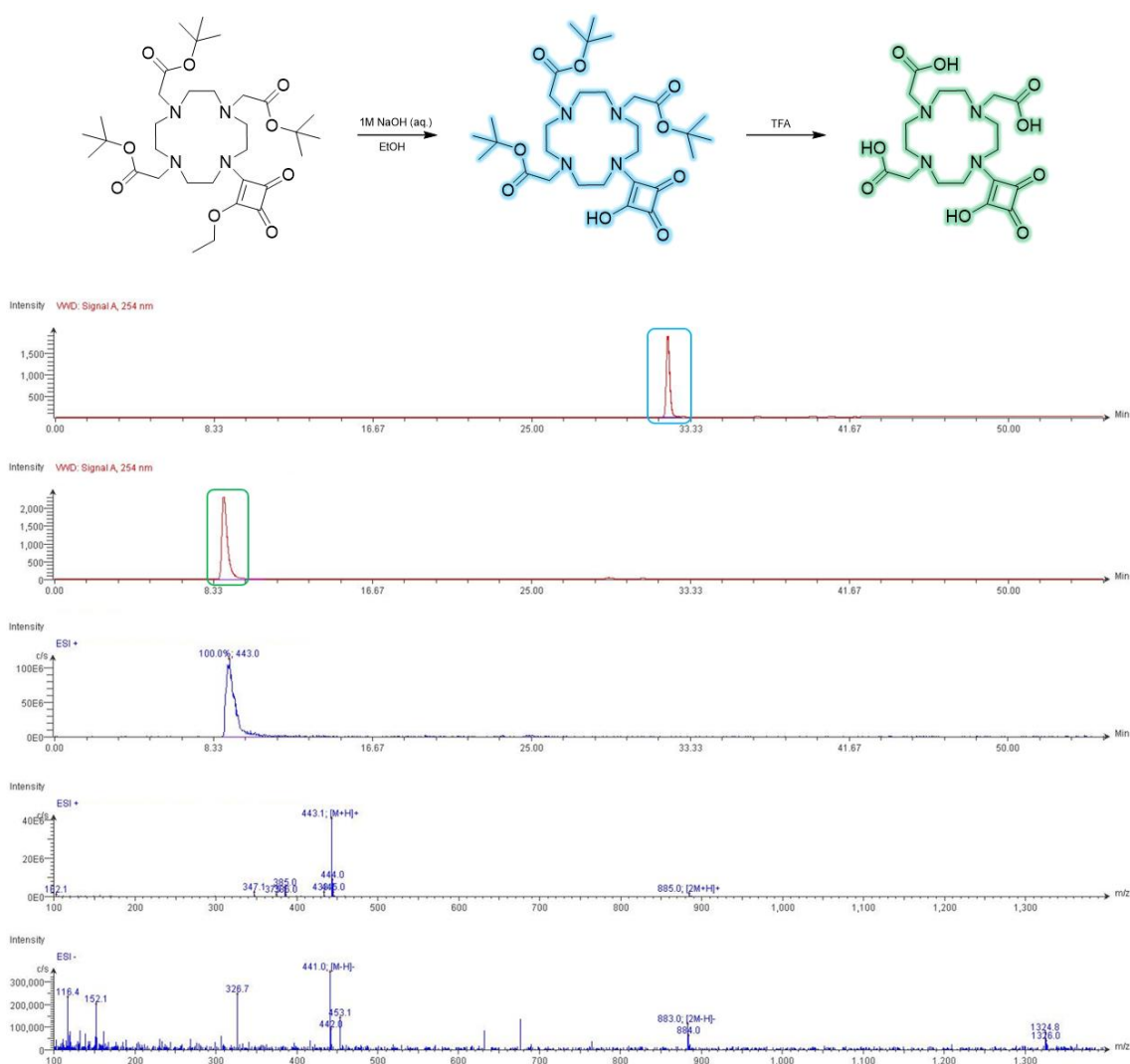
Figure 3.15: LC-MS data of conversion from **3.3** (blue) to product **3.5** (green).

Evidence for the successful synthesis of **3.5** was confirmed by LC-MS (**Figure 3.15**) and ^{1}H NMR analysis (**Figure 3.16**). Further experiments (^{13}C NMR, COSY, HSQC, HMBC and IR) were used to fully characterise the compound, see Figure S3.29 – 3.34. The HPLC trace of **3.5** displayed one sharp UV peak with a t_R = 9 min. Under this UV peak, strong ionisation was observed for the target mass of $[M+H]^+$ = 443.1 gmol^{-1} in positive mode (ESI+) and $[M-H]^+$ = 441.0 gmol^{-1} in negative mode (ESI-). The early elution time for this compound can be attributed to it being fully deprotected. Once the squaramic acid -OH and the carboxylic acid arms -COOH's are revealed (which are very polar in nature), it makes the overall molecule quite hydrophilic and have a strong preference for retention within the aqueous mobile-phase. The ^{1}H NMR displayed the cyclen-ring -CH$_2$ protons as broad triplets from 2.95 – 3.26 ppm integrating for 4H each. The remaining -CH$_2$ ring-protons closest to the squaramic acid moiety also appeared as broad triplets at 3.56 ppm and 3.76 ppm, both integrating for 2H each. The -CH$_2$ protons on the carbon adjacent to the carboxylic acid arms appeared as one sharp singlet around 3.78 ppm integrating for 6H. It is also worth noting that none of the -COOH protons were observed in their predicted region of 10 – 13 ppm, the same holds true for the squaramic acid -OH. These acidic O-H protons should be highly deshielded due to the electronegativity of oxygen and anisotropy from the C=O bond. Their disappearance may be due to intramolecular H-bonding, or very fast exchange (on the NMR timescale) with residual H$_2$O within the solvent (DMSO-d_6).
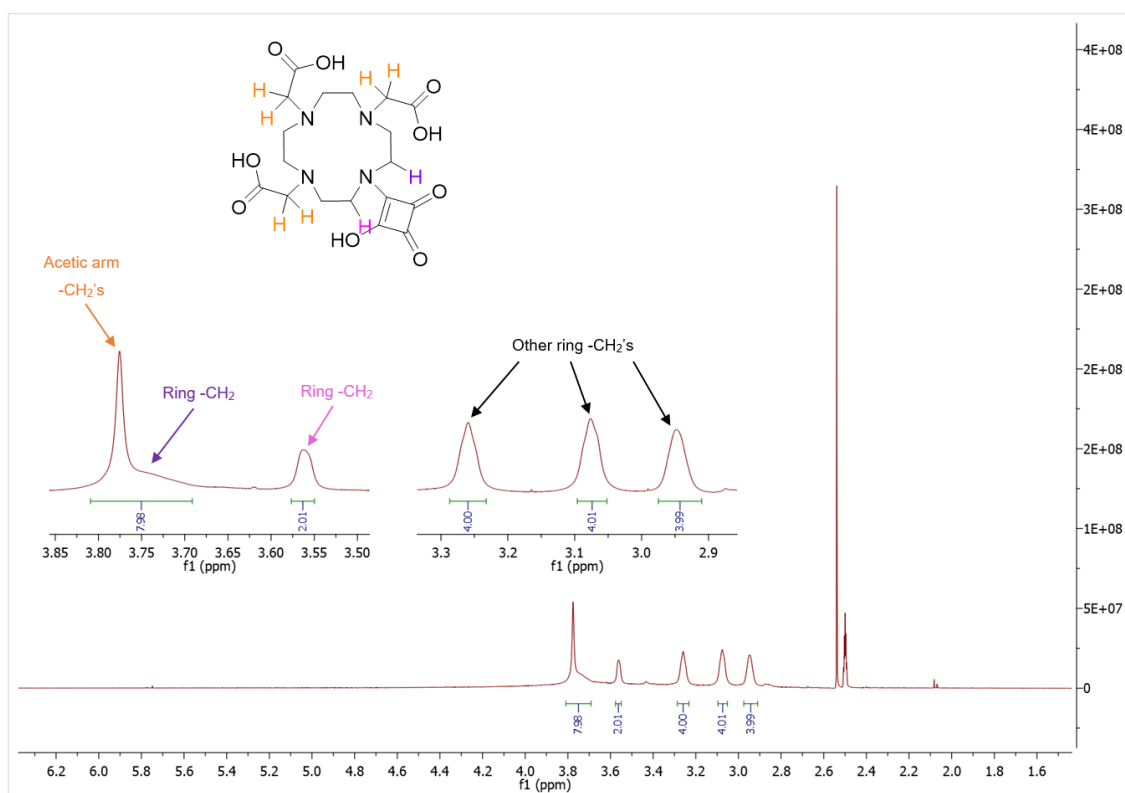
Figure 3.16: ^{1}H NMR spectrum of mono-substituted squaramic acid derivative **3.5** in DMSO-d_6.

Finally, HRMS was also used as a complimentary analysis to affirm the molecular formula of **3.5**, with confirmation of the target mass [M+H]$^+$ = 443.1780 gmol^{-1} possessing an acceptably low mass error value of 1.59 ppm (**Figure 3.17**).
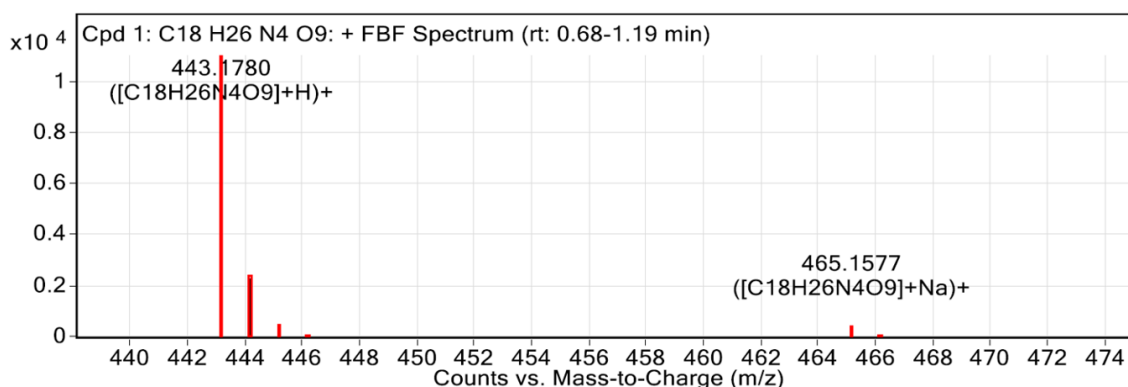
Figure 3.17: HRMS (ESI+) data for mono-substituted squaramic acid ligand **3.5**.

To complete the family of squaramide-based DO3A ligands, **3.6** and **3.7** were synthesized via a similar method as outlined in **Scheme 3.1**. The rationale for designing and synthesizing ligand **3.6** resolves around replacing the squaramic acid -OH group with a functionality far less acidic (-NH$_2$), to investigate the importance of this squaramide coordination-site for lanthanide luminescence. It is theorised that this new -NH$_2$ group will coordinate much more poorly to the

Ln^{3+} centre, than its -OH counterpart. Furthermore, lanthanides typically have relatively long-lived excited states, which can experience energy transfer to high-frequency vibrational oscillators, such as NH-groups.[328] Consequently, when these groups are in close proximity to the lanthanide, they promote the thermal dissipation of energy through a process known as vibronic coupling. This leads to the quenching of luminescence.[329] Ligand **3.7** was designed to act as a linker for further conjugate coupling, which is explored later on in this section. Full characterisation/synthesis data for **3.6** and **3.7** can be found in the relevant *Experimental* section, and supporting spectra can be viewed in the *Appendix* (see Figure S3.42 – 3.49 & S3.58 – 3.62, respectively).

3.3.1 Di-, Tri- & Tetra-substituted Squaramide-based Ligands

Building on from the mono-substituted squaramide-DO3A ligands, we aimed to explore the potential for increasing the squaramide substitution arrangement around the cyclen-ring scaffold. An illustration of our initial design strategy is highlighted in **Figure 3.9**. These ligands – with an increased number of squaramide moieties – will serve to investigate two distinct research questions; (i) will the addition of more than one antenna serve to enhance the ligands sensitisation ability for luminescent Ln^{3+} complexes (Tb^{3+} & Eu^{3+}), and (ii) will increasing the steric-profile (rigidity) and altering the symmetry characteristics lead to more effective/kinetically inert chelates (Gd^{3+})? A structural representation of the above research questions are illustrated in **Figure 3.18**.
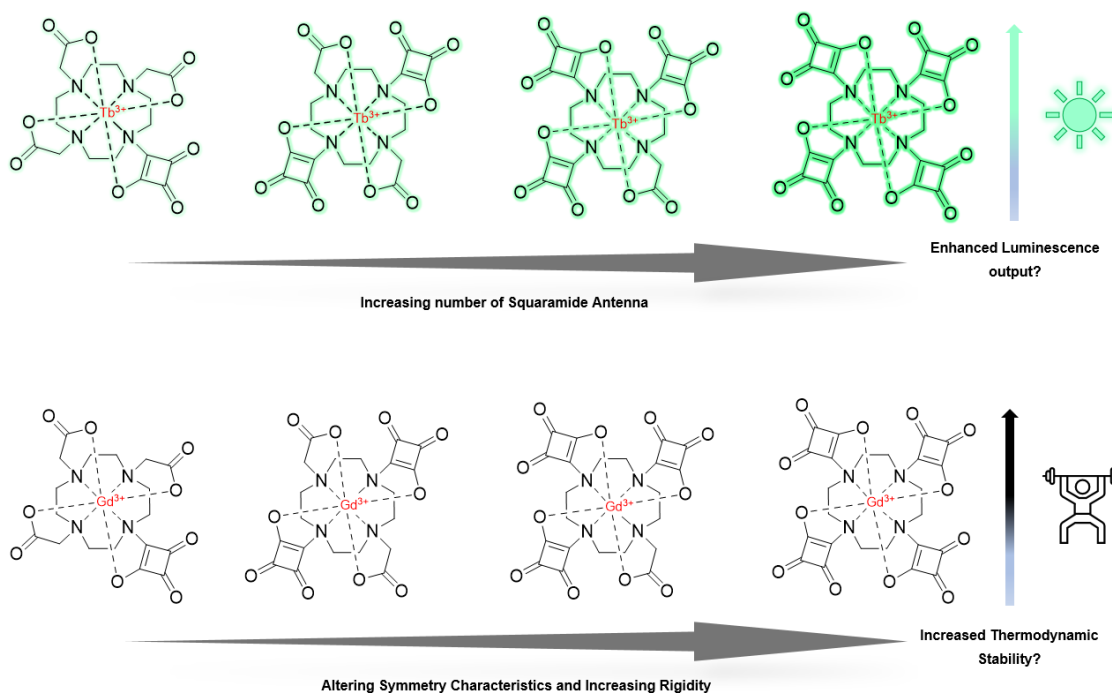
Figure 3.18: Potential of increased Squaramide-substitution for Luminescence Intensity and Complex Stability.

Increasing the number of antenna-ligands within the vicinity of the lanthanide ion may enhance the probability of energy transfer. This is because the more antennas that are present, the greater the chance that one of them will absorb an incident photon and subsequently transfer its energy to the lanthanide-centre. As a result of this increased energy transfer, the lanthanide ions receive more energy, which may promote their excitation and subsequent luminescence. In other words, having more antennas may potentially increase the efficiency of sensitising the lanthanide ions, leading to brighter and more intense luminescence.[330] Ln^{3+} complexes with increased stabilities are also of great importance, especially in clinical settings. Gadolinium-based probes are often used as contrast agents for magnetic resonance imaging (MRI). However, free-gadolinium (Gd^{3+}) is highly toxic (intravenous $LD_{50} \sim 0.2$ mmol/kg in mice). Thus, to minimise metal-leakage and unspecific deposition, the paramagnetic metal (Gd^{3+}) must be administered as a chelate with exceedingly high thermodynamic stability and kinetic inertia. This helps prevent unwanted interactions and ensures the metal remains biologically tolerable ($LD_{50} \sim 10$ mmol/kg).[331]

The synthetic pathway for the di-substituted squaramide ligand is outlined in **Scheme 3.3**. Synthesis was carried out in a similar fashion to the squaramide-DO3A ligands, with the first step involving a nucleophilic substitution reaction

between DESq (**3.1**) and di-*tert*-butyl 2,2′-(1,4,7,10-tetraazacyclododecane-1,7-diyl) diacetate (DO2AtBu, **3.0c**) to afford the di-substituted protected product (**3.8**) with an 92% yield.
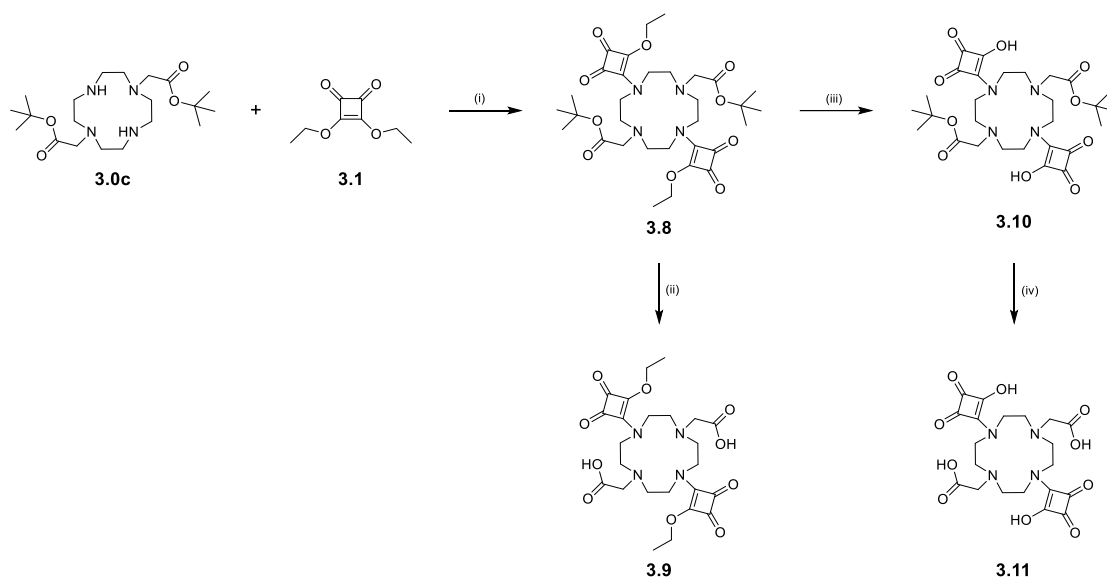
Scheme 3.3: Proposed synthetic pathway to di-substituted squaramide-based ligand (**3.11**). *Reagents and conditions:* (i) TEA, EtOH, rt, 16 hrs, 92%. (ii) TFA, 4 hrs, 95%.

Evidence for the successful synthesis of **3.8** was confirmed by LC-MS, ^{1}H NMR (**Figure 3.19**) and HMBC analysis, with further experiments (^{13}C NMR, COSY, HSQC and HRMS) being documented in the *Appendix* (see Figure S3.66 – 3.70).
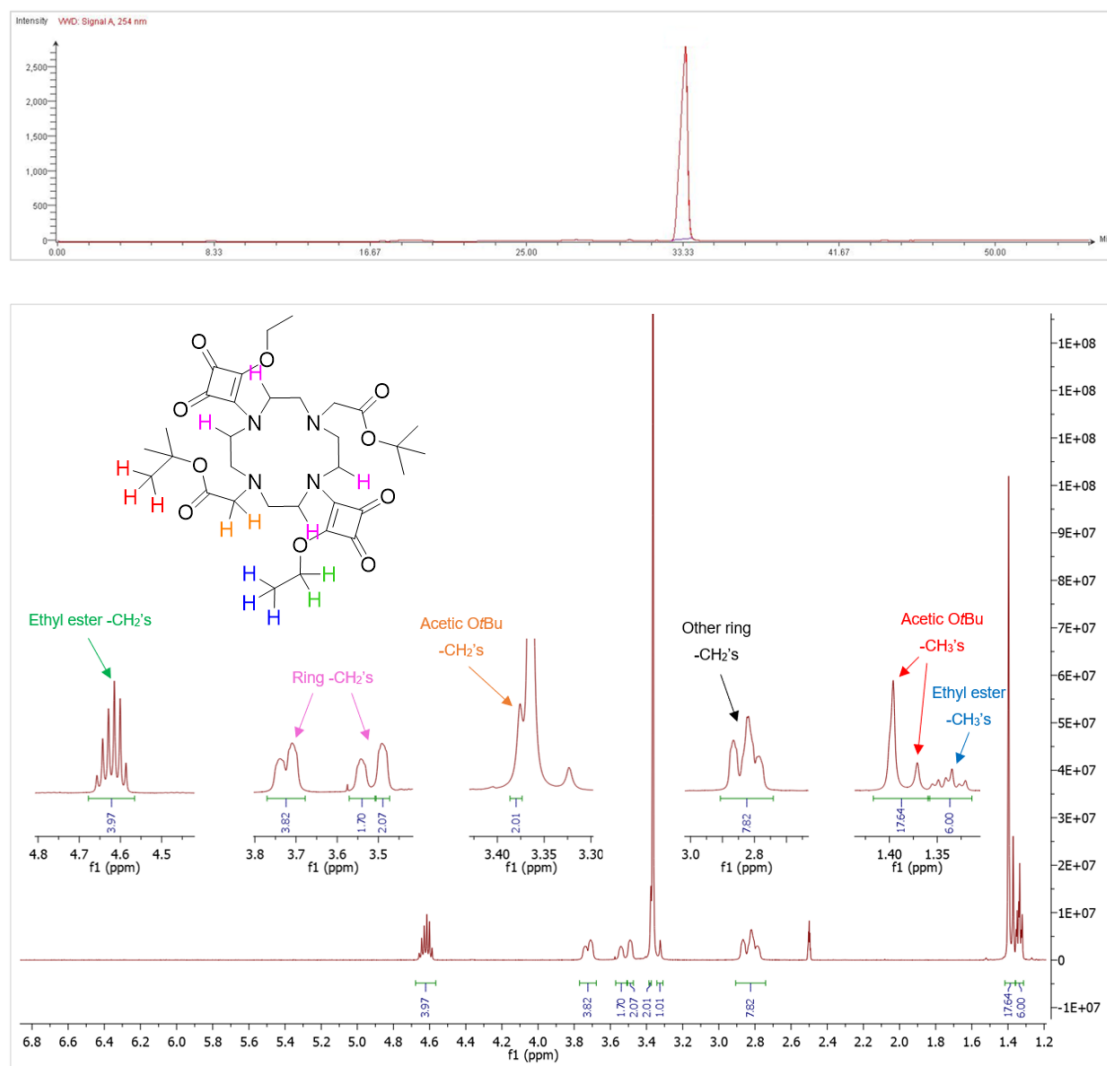
Figure 3.19: (Top) HPLC trace. (Bottom) ^{1}H NMR spectrum of **3.8** in DMSO-d_6.

The HPLC trace of **3.8** displayed one sharp UV peak with a t_R = 33 min. The ^{1}H NMR spectrum highlighted many peaks that were indicative of the target compound (**3.8**). The cyclen-ring -CH2 protons closest to each squaramate moiety appeared as broad triplets from 3.49 – 3.74 ppm integrating for a total of 8H, with the rest of the ring-protons showing up bunched together around 2.82 ppm integrating for another 8H. Interestingly, the squaramate ethyl ester protons were observed to be quite different from the mono-substituted ligands, with the -CH2 protons appearing as a *complex multiplet* (integrating for 4H) and the -CH3 protons forming a *multiplet* of overlapping peaks (integrating for 6H) at 1.33 ppm and 4.61 ppm, respectively. This unusual display of multiplicity could be due to an intermolecular π-stacking interaction or the slow exchange between conformational isomers.[332] The *t*Bu-CH3 protons were found to be two distinct singlets at 1.37 ppm and 1.40 ppm integrating for a total of 18H. However, the

other acetic-arm -CH_2 protons were obscured by the residual H_2O peak around 3.38 ppm. These were confirmed to be the acetic-CH_2's by a HMBC experiment (**Figure 3.20**). ^{1}H-^{13}C coupling was observed between the -CH_2 protons and the carbonyl carbons (170 ppm) on the acetic-OtBu arms. No other -CH_2 protons experienced this ^{1}H-^{13}C coupling, and the other ^{13}C peaks that far downfield (172 – 189 ppm) belong to the 4C's on the cyclobutene-ring (see Figure S3.66).
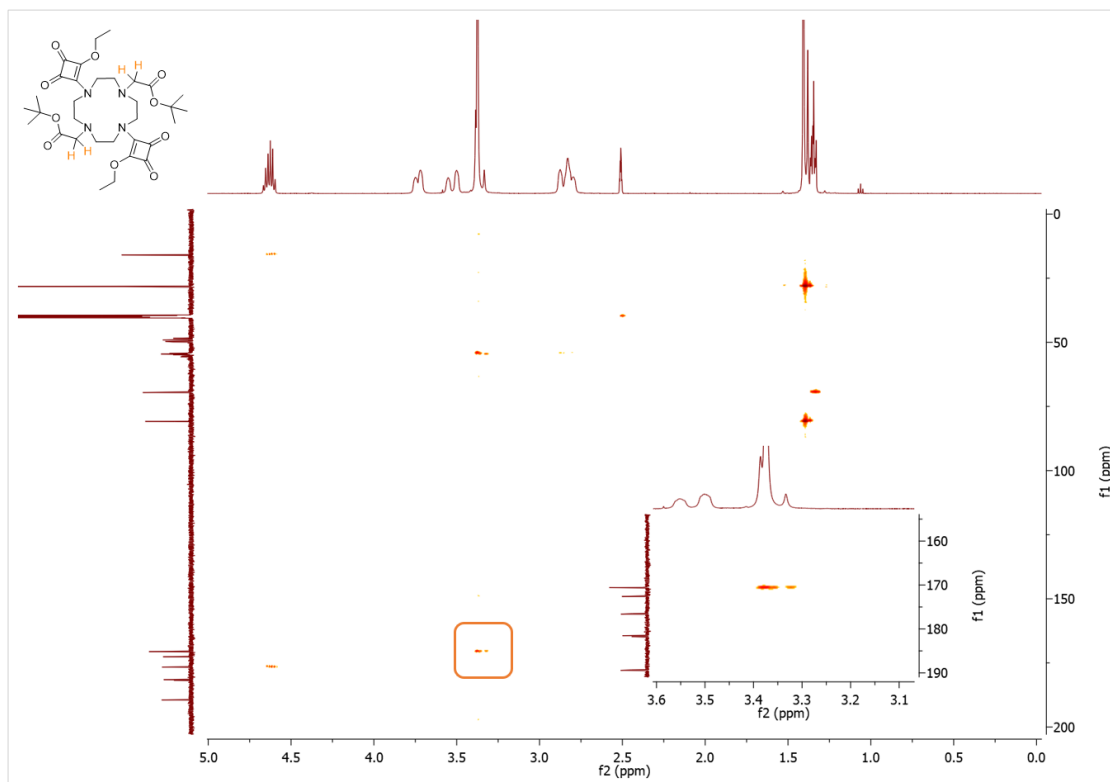
Figure 3.20: HMBC spectrum of compound **3.8** in DMSO-d_6. *Inset:* Zoomed-in portion (orange) of HMBC spectrum.

Unfortunately, due to synthetic/purification difficulties, di-substituted squaramic acid ligand **3.11** could not be obtained in appreciable amounts. However, the di-substituted squaramate ethyl ester derivative **3.9** was successfully generated from **3.8** with a 95% yield. LC-MS data and ^{1}H NMR experiments provided us with enough evidence to suggest that **3.9** was synthesized successfully (**Figure 3.21**), with further characterisation being documented in the *Appendix* (see Figure S3.73 – 3.77).

Figure 3.21: (Top) HPLC trace. (Bottom) ^{1}H NMR spectrum of **3.9** in DMSO-d_6.

The HPLC trace of **3.9** displayed one sharp UV peak with a t_R = 23 min, noting the clear change in retention time once the -OtBu groups were removed. The ^{1}H NMR spectrum was very similar to its precursor (**3.8**), with the ethyl ester -CH$_2$'s appearing as overlapping quartets around 4.61 ppm integrating for 4H, and the -CH$_3$'s also being observed as overlapping triplets at 1.33 ppm integrating for a total of 6H. The acetic arm -CH$_2$'s are again obscured by the residual H$_2$O peak at 3.47 ppm, and the ring-CH$_2$ protons range from 2.90 – 3.74 ppm.

The synthetic pathway for the further increased squaramide-substitution ligands in highlighted in **Scheme 3.4**. To generate the tri- and tetra-substituted squaramide ligands, the synthesis was carried out via the same route as the di-substituted squaramide ligands, with the first step involving a nucleophilic substitution reaction between DESq (**3.1**) and the naked 1,4,7,10-tetraazacyclododecane – cyclen ring (**3.0d**). This reaction produced the tri-substituted (with one free ring-NH) squaramide product (**3.12**) in a 96% yield.

121
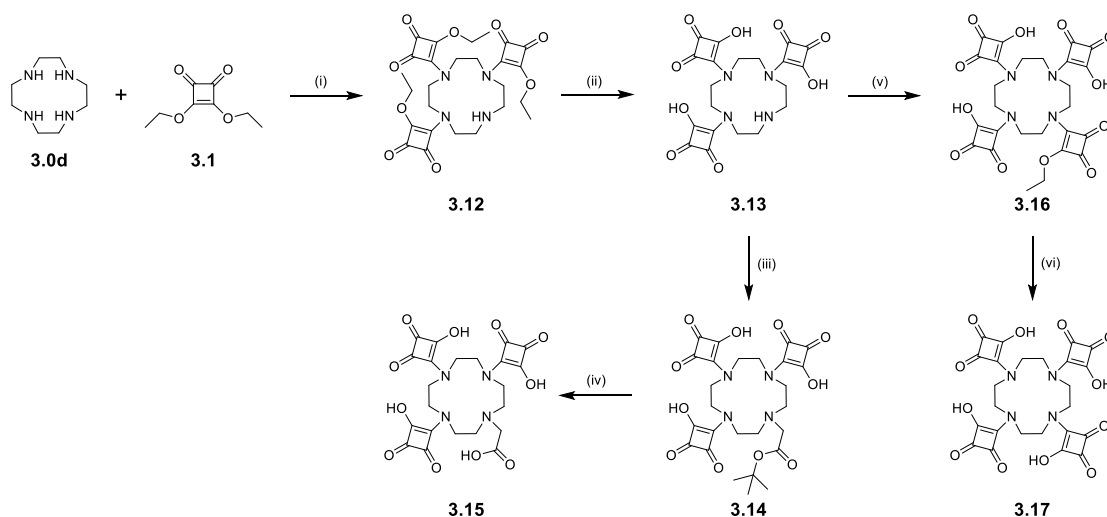
Scheme 3.4: Synthetic pathway to tri- (**3.15**) & tetra-substituted (**3.17**) squaramide-based ligands. *Reagents and conditions:* (i) TEA, EtOH, rt, 16 hrs, 96%. (ii) 1M HCl (aq.), 90°C, 16 hrs, 98%. (iii) BrOAcO*t*Bu, K$_2$CO$_3$, DMSO, 90°C, 10 days, 88%. (iv) TFA, 2 hrs, 90%. (v) DESq, TEA, EtOH, MW 100°C 2 hrs, 85%. (vi) 1M HCl (aq.), rt, 1 hr, 57%.

This synthetic pathway was not without its difficulties. However, after many such experimental manoeuvres, a novel methodology for the synthesis of these tri- and tetra-substituted squaramide-based ligands has been developed. An extensive road-map detailing the synthetic intricacies of this methodology is outlined in **Scheme 3.5**.
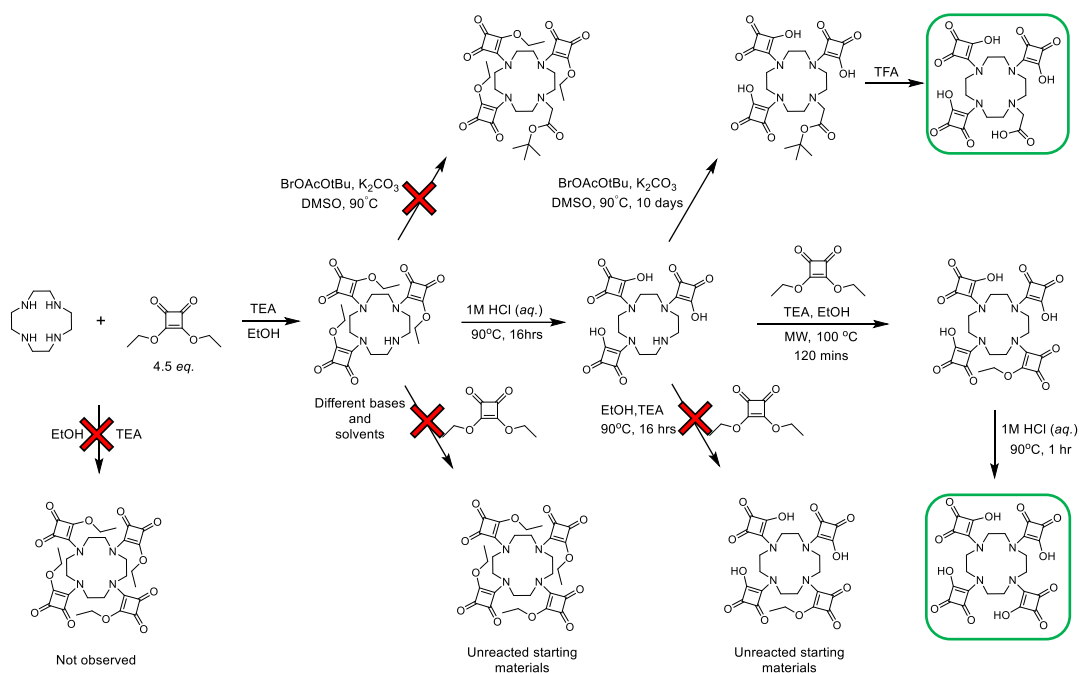
Scheme 3.5: Illustration of synthetic difficulties encountered and work-around employed to achieved tri- & tetra-substituted squaramide ligands. Red X indicating unsuccessful reaction pathway, and green Box highlighting alternate route to target compounds (**3.15** & **3.17**)

Although compound **3.12** was generated in a 96% yield, the ideal tetra-substituted squaramate ethyl ester product was not observed. Indeed, this product was never observed, even after utilising many different synthetic conditions (temperatures, solvents & bases). Perhaps the steric profile of **3.12** – especially around the ethyl ester arms – generates enough hindrance near the ring-NH that its nucleophilicity is effectively quenched under normal conditions.[333] Compound **3.12** was confirmed via LC-MS and ¹H NMR (**Figure 3.22**) – with further characterisation detailed in Figure S3.80 – 3.84.
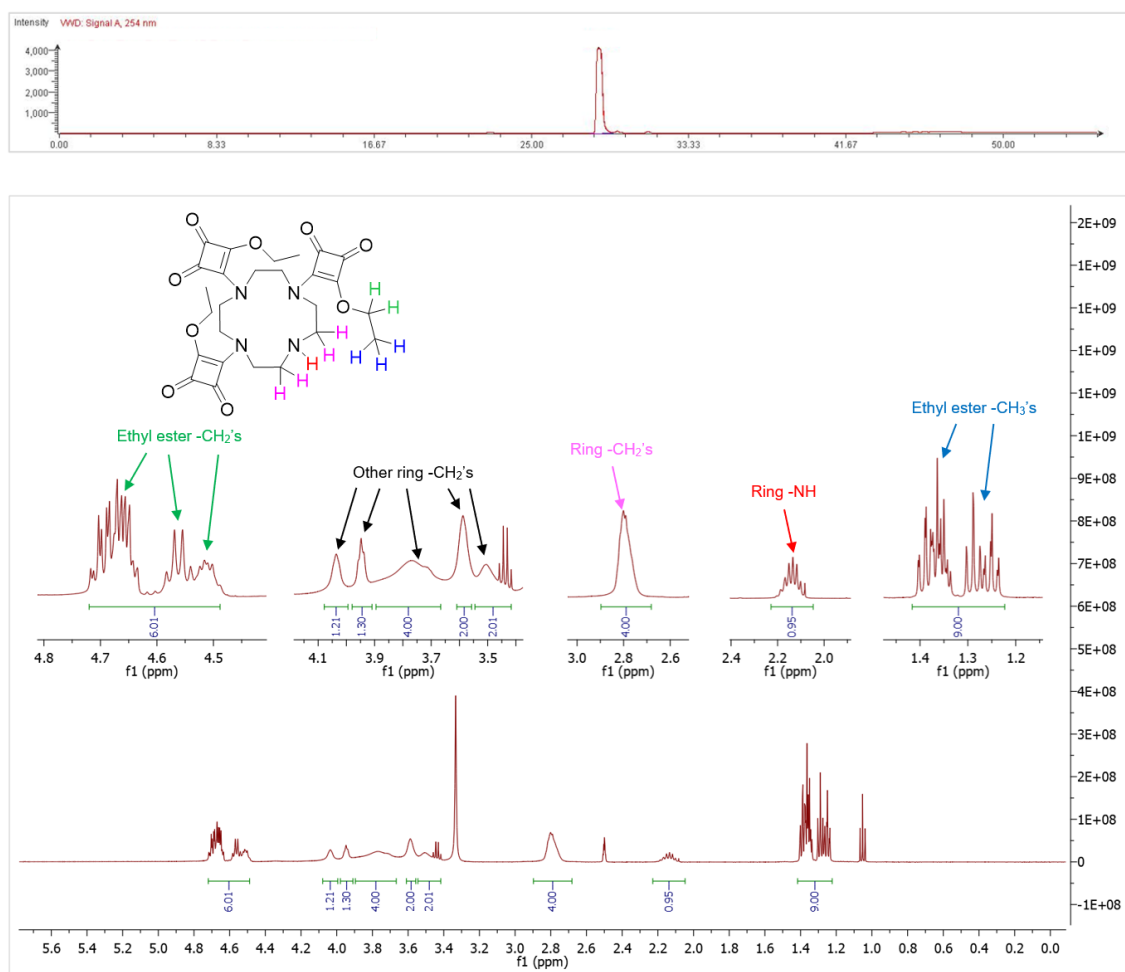
Figure 3.22: (Top) HPLC trace. (Bottom) ¹H NMR spectrum of **3.12** in DMSO-d_6.

The HPLC trace of **3.12** displayed one sharp UV peak with a t_R = 28 min. The ¹H NMR spectrum was similar to the di-substituted compound **3.8**, in the fact that numerous overlapping peaks corresponding to the squaramate ethyl ester -CH₂'s and -CH₃'s were observed. The -CH₂'s appeared as a multiplet (overlapping quartets) from 4.52 – 4.67 ppm integrating for a total of 6H, with the -CH₃'s being observed further upfield – again as overlapping triplets – around 1.25 – 1.36 ppm integrating for a total of 9H. The unsubstituted ring-NH appeared

as a septet nearby at 2.15 ppm, integrating for 1H. This was corroborated by the missing signal in the corresponding HSQC spectrum and coupling to adjacent ring-CH$_2$'s confirmed by COSY (see Figure S3.81). These adjacent ring-CH$_2$'s – furthest away from the squaramate moieties – appeared as a broad multiplet uncharacteristically upfield at 2.80 ppm, integrating for 4H. The remaining ring-protons appeared in the region of 3.51 – 4.04 ppm as broad signals integrating for a total of 12H.

With tri-substituted compound **3.12** in hand, the next synthetic step was to try use it to reach the target molecules. However, many different reaction conditions were employed, such as; temperatures (rt up to 100°C), solvents (MeCN, EtOH, EtOAc, DMSO & DMF) and bases (TEA, DIPEA, NMM & K$_2$CO$_3$) to try form the tri-substituted product (via *tert*-butyl bromoacetate) and the tetra-substituted product (via DESq) from **3.12**, but only unreacted starting materials were observed. Perhaps, again, the steric bulk around the ring-NH was too severe to facilitate any reactivity. As this was the second road-block that was encountered early on in the synthesis, a change in synthetic strategy was required. This involved removing some of the steric hindrance that was currently presumed to be the problem. The ethyl esters on compound **3.12** were hydrolysed via 1M HCl (aq.) to their corresponding -OH's, which formed compound **3.13** in an almost quantitative yield of 98%. LC-MS (**Figure 3.23**) and HRMS (Figure S3.90) was used to characterise compound **3.13**. The HPLC trace displayed one sharp UV peak with a t_R = 10 min. This dramatic change in retention time – reminiscent of going from **3.3** to **3.5** – can be attributed to the increased hydrophilic character of **3.13** compared to **3.12**. Strong ionisation was observed for the target mass of [M+H]$^+$ = 461.0 gmol^{-1} in positive mode and [M-H]$^+$ = 458.9 gmol^{-1} in negative mode, with HRMS confirming this target mass [M-H]$^+$ = 459.1151 gmol^{-1} possessing a mass error of -2.05 ppm.
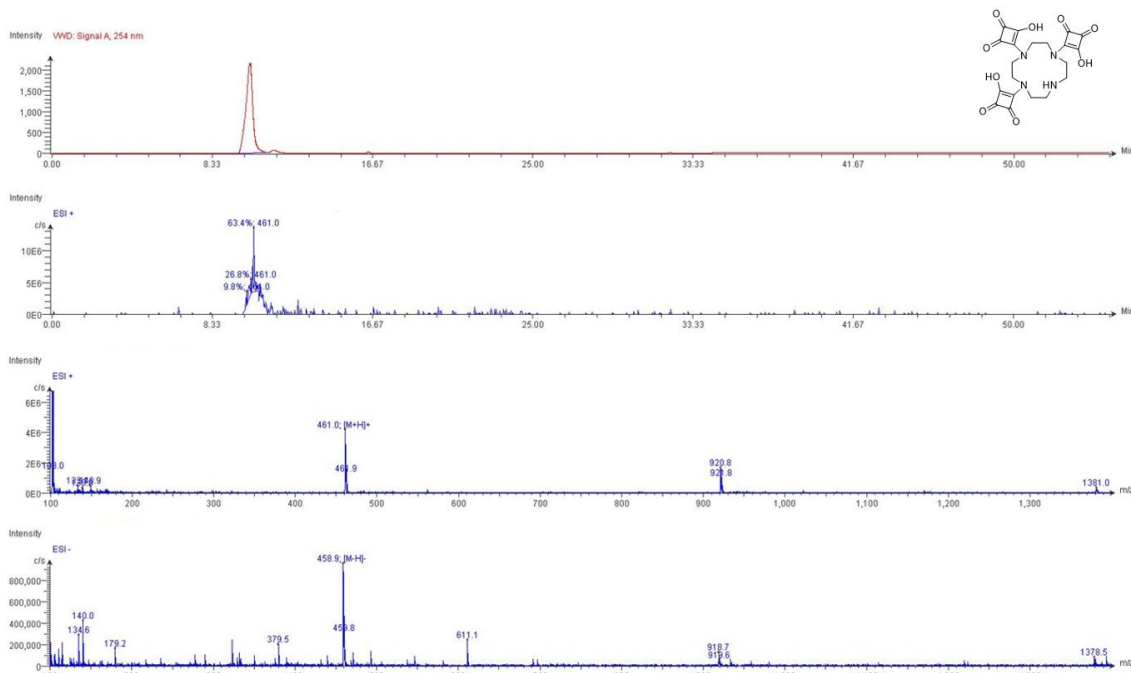
Figure 3.23: LC-MS data for the tri-substituted squaramic acid intermediate **3.13**.

Similar reaction conditions that were attempted with **3.12**, were then employed to **3.13**, with the hopes that the removal of the steric bulk may improve reactivity going forward. This proved fruitful, as tri-substituted compound **3.14** was synthesized in an 88% yield via conventional heating in DMSO. Once **3.14** was purified (see Figure S3.91 – 3.96), it was a standard TFA deprotection to yield the final tri-substituted squaramic acid ligand **3.15** with a yield of 90%. This compound was characterised by LC-MS (**Figure 3.24**) & Figure S3.98 – S3.102.
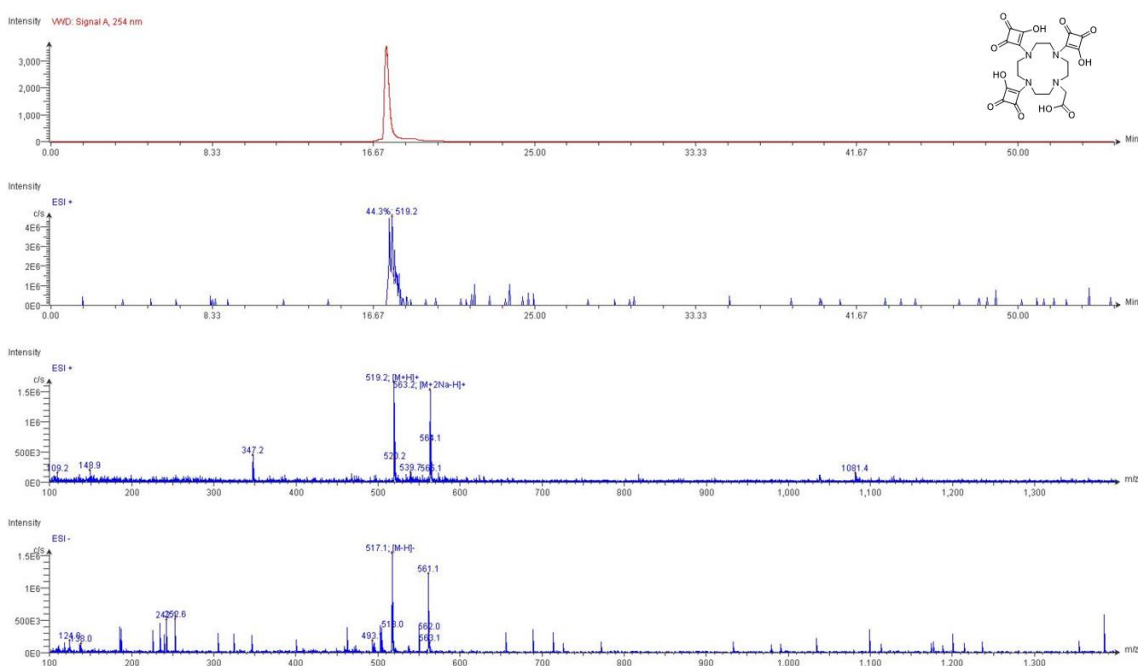
Figure 3.24: LC-MS data for tri-substituted squaramic acid ligand **3.15**.

125

The HPLC trace displayed one sharp UV peak with a t_R = 17 min, and strong ionisation was observed for the target mass of $[M+H]^+$ = 519.2 gmol^{-1} in positive mode and $[M-H]^+$ = 517.1 gmol^{-1} in negative mode.

Although compound **3.13** was able to facilitate the synthesis of **3.14** via alkylation, the same enhanced reactivity was not observed when substituting the final DESq onto the cyclen-ring (tetra-substituted). What first appeared to be a steric issue, may now pertain electronic difficulties too, or perhaps it is an unfortunate combination of both. Indeed, like previous attempts, many different experimental conditions were trialled, with unreacted starting materials consistently being observed. The synthetic breakthrough finally came via an unconventional approach. DESq and **3.13** were reacted together with the help of a microwave synthesizer, to produce the tetra-substituted compound **3.16** in a much-improved yield of 85%.

Note on Microwave Synthesis: From a practical and synthetic perspective, microwave irradiation results in the direct activation of either solvent or reactant molecules in a solution through localised superheating. Microwave energy is swiftly and directly transferred to any absorbing material, creating high instantaneous temperatures. This activates a significant portion of the reacting species above the required activation energy. In contrast, traditional conductive heating involves energy transfer from a heat source to an oil bath/crucible, which then heats the outer surface of the reaction flask (**Figure 3.25**). This energy gradually moves through the vessel and is dissipated throughout the reaction mixture, making it an inefficient process that leads to extended reaction times and potential side-reactions. Direct microwave heating not only reduces chemical reaction times from hours to minutes but is also known for reducing side reactions, enhancing yields, and improving reproducibility.[334]
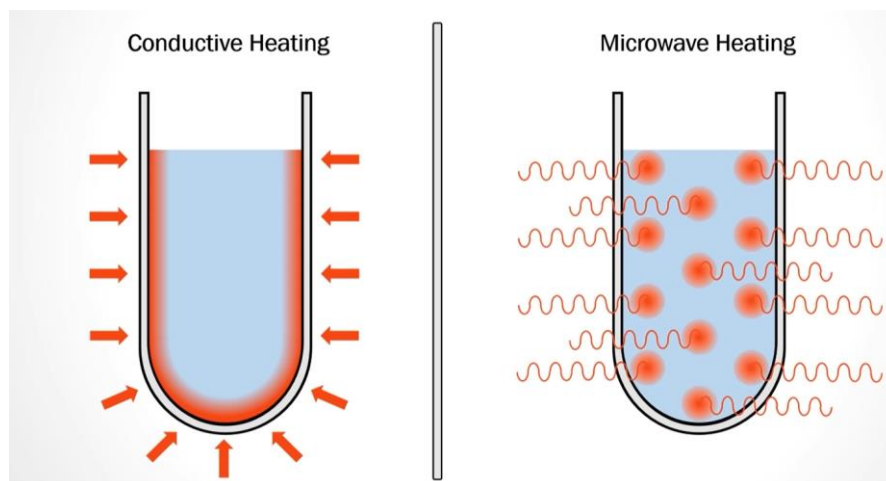
Figure 3.25: Comparison between conventional reflux and microwave heating.[335]

Perhaps it was the efficient microwave heating of the solution that overcame the activation energy barrier for nucleophilic substitution between DESq and **3.13**, or maybe it was the increase in pressure that provided the necessary conditions for reactivity. Regardless, it was a much-needed step towards generating the tetra-substituted compound. With this in mind, an in-depth investigation into the chemical/physical intricacies of this microwave reaction was not conducted. However, the reaction time was roughly optimised, as it was observed to take ~2 hours for complete consumption of starting material. Compound **3.16** was confirmed via LC-MS (**Figure 3.26**), HRMS (Figure S3.109) and ^{1}H NMR (**Figure 3.27**), with complete characterisation being documented in the *Appendix* (see Figure S3.104 – 3.112).
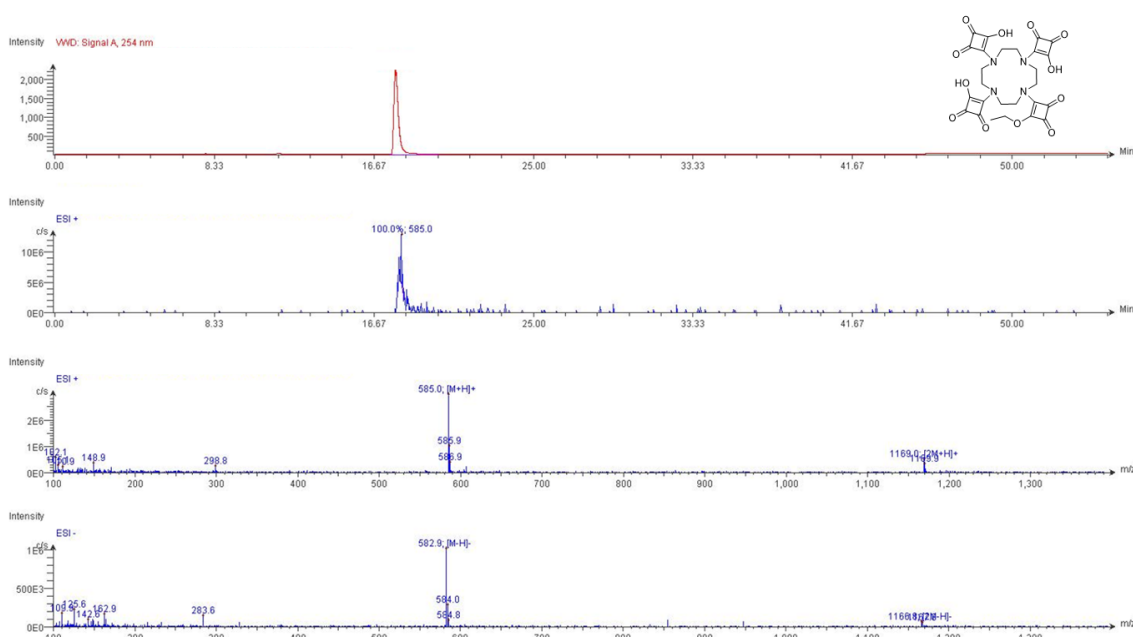
Figure 3.26: LC-MS data for **3.16**.

The HPLC trace displayed one sharp UV peak with a t_R = 17 min. Strong ionisation was observed for the target mass of $[M+H]^+$ = 585.0 gmol^{-1} in positive mode and $[M-H]^+$ = 582.9 gmol^{-1} in negative mode, with HRMS confirming this target mass $[M-H]^+$ = 583.1338 gmol^{-1} possessing a mass error of -3.50 ppm.
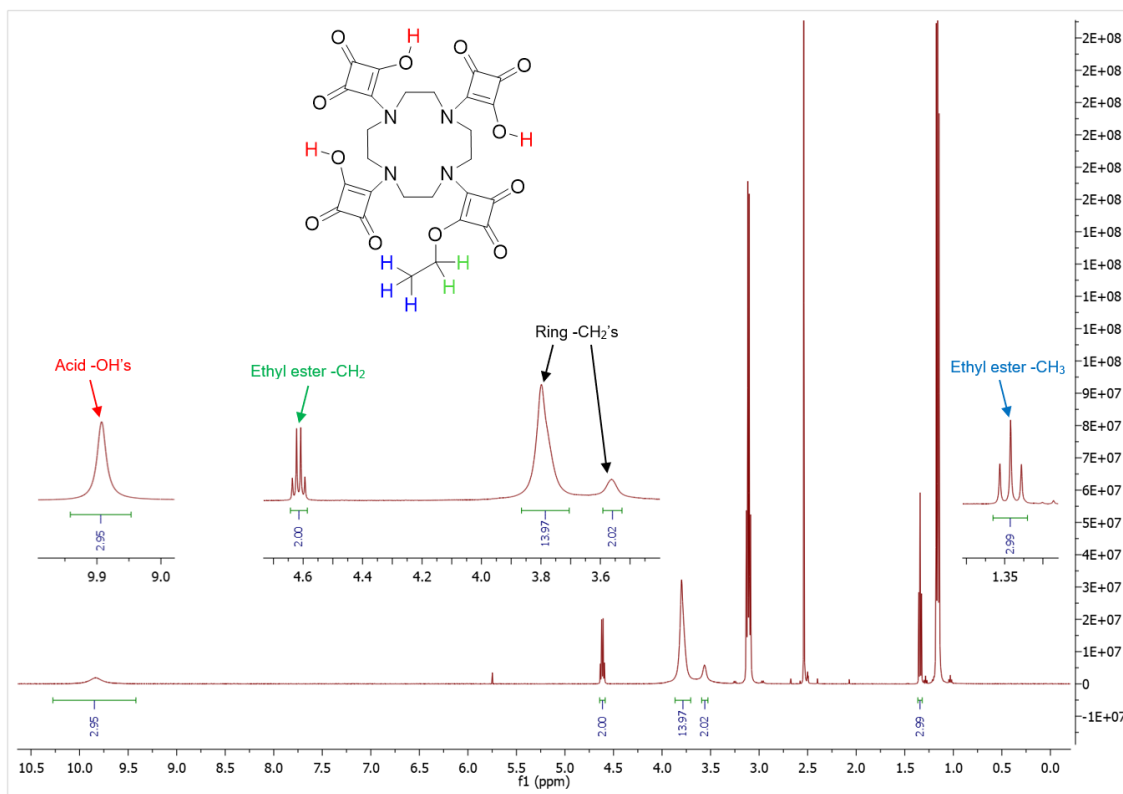
Figure 3.27: ^{1}H NMR spectrum of **3.16** in DMSO-d_6.

The ^{1}H NMR spectrum of **3.16** was interesting, because as the molecule became more symmetrical, the -CH$_2$ protons on the cyclen-ring appeared to almost merge together as (uncharacteristically) broad singlets in the region of 3.56 – 3.80 ppm, integrating for a total of 16H. This was indicative of the ring-CH$_2$'s being in a near identical environment upon substitution of the fourth DESq molecule. However, one ring-CH$_2$ was observed by itself as a distinctive peak integrating for 2H, suggesting that it may be experiencing a slightly different chemical environment, or some conformational bias may remain. In a rare display, the squaramic acid -OH's were observed as a broad singlet at 9.83 ppm integrating for 3H. Corresponding to the final DESq, the squaramate ethyl ester -CH$_2$ protons appeared as a quartet at 4.61 ppm integrating for 2H, with the -CH$_3$ protons appearing as a triplet at 1.34 ppm integrating for 3H. It was also noted that this compound was highly hygroscopic and appeared as a brown oil under

ambient conditions. Because of this, residual EtOH was very difficult to remove from the sample, as is quite apparent from the above spectrum.

The final step towards generating the tetra-substituted squaramic acid derivative, was to hydrolyse the remaining ethyl ester via 1M HCl (aq.) to its corresponding -OH, which produced compound **3.17** with a yield of 57%. The reduced yield for this final hydrolyses step was unfortunate, as it appeared to suffer from similar (potential) degradation pathways as compound **3.5**. However, HRMS (**Figure 3.28**) and ^{1}H NMR (**Figure 3.29**) data provided sufficient evidence to suggest that the compound was successfully synthesized.
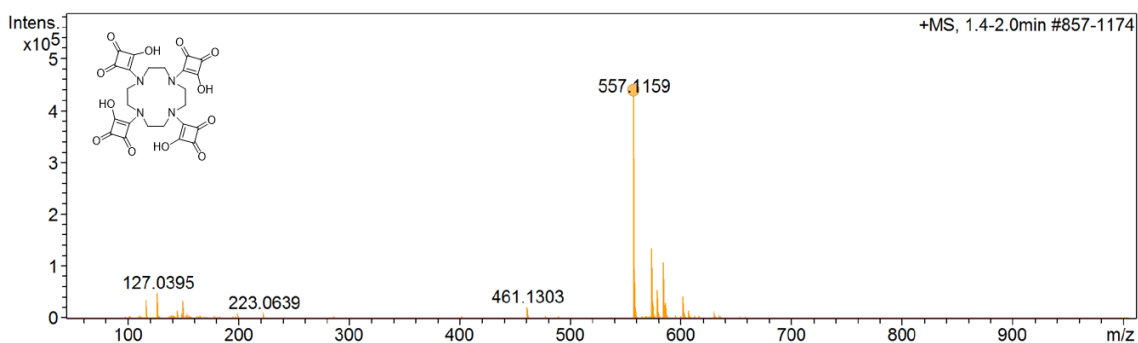
Figure 3.28: HRMS (ESI+) data for tetra-substituted squaramic acid ligand **3.17**.

HRMS data affirmed the molecular formula of **3.17**, with confirmation of the target mass $[M+H]^+$ = 557.1159 gmol^{-1} possessing an adequate mass error value of -1.60 ppm.
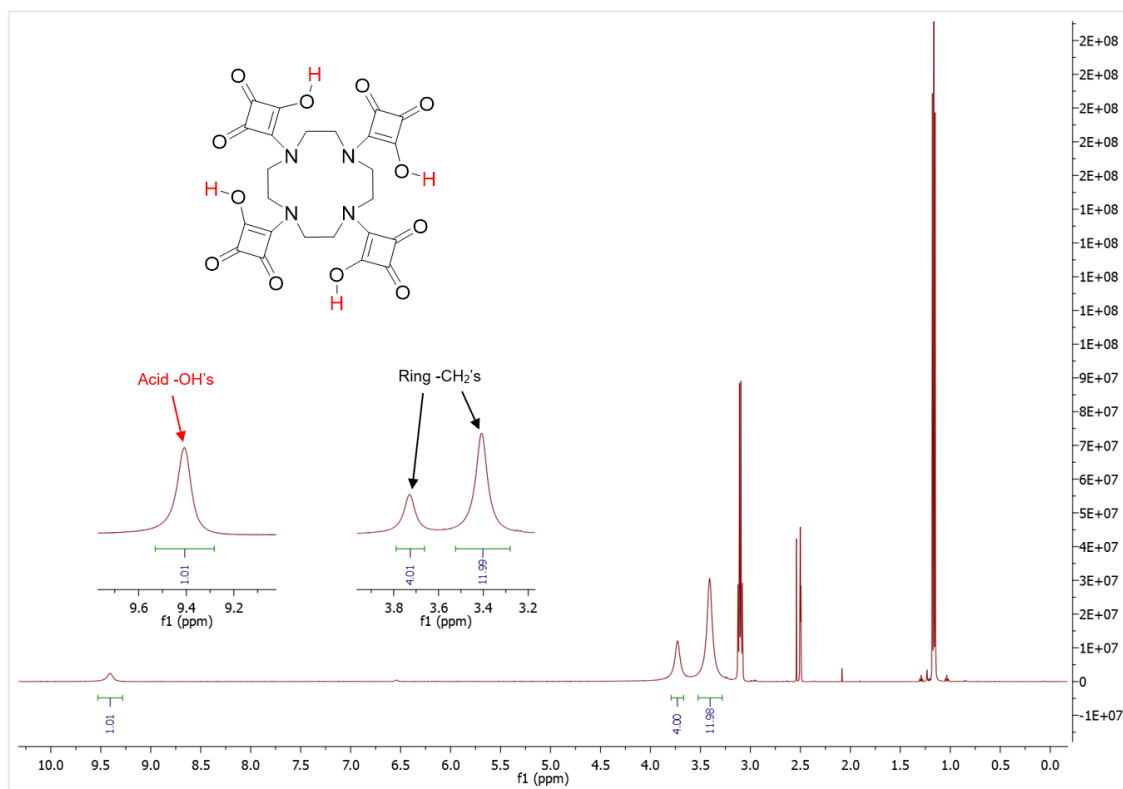
Figure 3.29: ^{1}H NMR spectrum of tetra-substituted squaramic acid ligand **3.17** in DMSO-d_6.

Similar to compound **3.16**, the ^{1}H NMR spectrum of **3.17** displays only a few peaks, likely owing to the symmetrical nature of the ligand. However (again), perhaps there is some asymmetry to the ligand, as the cyclen-ring -CH_2 protons appear as two distinct broad singlets at 3.41 ppm and 3.73 ppm integrating for 12H and 4H, respectively. The squaramic acid -OH's also appeared as a broad singlet, but much further downfield at 9.41 ppm integrating for 1H. This integration is a little off the mark from the expected 4H, but given the nature of labile protons such as these, accurate integration can often be difficult to obtain.[336] It is also noted that certain solvent peaks are present in the sample, as the triplet/quartet (at 1.17 ppm & 3.09 ppm, respectively) corresponds to the ethyl splitting pattern of EtOH. The NMR tubes are cleaned via sequential washing with EtOH and Acetone, so perhaps the hygroscopic nature of the ligand has sequestered some residual solvent in this sample.

With these novel multi-substituted squaramide-based ligands synthesized successfully, the possibility of a potential biological application was explored. By utilising our expertise and experience in peptide chemistry, we ventured to explore the idea of luminescent lanthanide-based peptide probes for enhanced visualisation of caspase-3.

3.3.2 Potential Lanthanide-based Caspase-3 Probe

Lanthanide complexes exhibit distinctive photophysical characteristics, such as luminescence lifetimes – lasting milliseconds, substantial Stokes shifts, extremely sharp emissions, and the capacity to engage in resonance energy transfer or photon up-conversion. Lanthanide-based probes can, therefore, be utilised to achieve exceptional detection sensitivity and enhanced imaging depth, enabling the exploration of biological systems in innovative ways. Still, lanthanide luminophores are not extensively employed in biological imaging. Compared to traditional fluorophores and fluorescent proteins, lanthanide probes have been hindered by their lower brightness, dependence on UV excitation, and reduced photon output. However, recent advancements in probe design, instrumentation, and imaging techniques have addressed many of these limitations, reigniting interest in the use of these rare-earth metals for biological imaging.

Lanthanide luminescence is inherently different from fluorescence. Fluorescence occurs when a molecule transitions between electronic states, while lanthanide metal ions luminesce due to parity-forbidden transitions within the 4f atomic orbitals. This unique photophysical process is responsible for the characteristic spectral properties of lanthanides. A consequence of this forbidden 4f-4f transition, is the slow decay of lanthanide excited-states – which produces very long emission lifetimes. In contrast to small organic fluorophores and fluorescent proteins – which emit light for only a few nanoseconds – lanthanide luminescence can persist for several milliseconds. Indeed, the luminescence lifetimes of frequently employed Tb^{3+} and Eu^{3+} complexes typically fall within the range of 0.5 to 2.5 milliseconds.[337]

In the pursuit of generating peptide-conjugates for the visualisation of caspase-3, we wanted to further expand on the success of our fluorogenic probe Ac-DEVD-PABC-Naph (Chapter 2) with the next (potential) generation of probes utilising lanthanide luminescence (**Figure 3.30**). In addition to the previously mentioned advantages that lanthanide luminescence possesses over traditional fluorescence, there is also a practical and modular advantage in that (theoretically) one probe/ligand can accommodate many different Ln^{3+} centres, each with their own photophysical characteristics. This could lead to the formation of caspase-3 probes with tuneable luminescence outputs, that may pave the way for new approaches in the detection/visualisation of apoptosis.
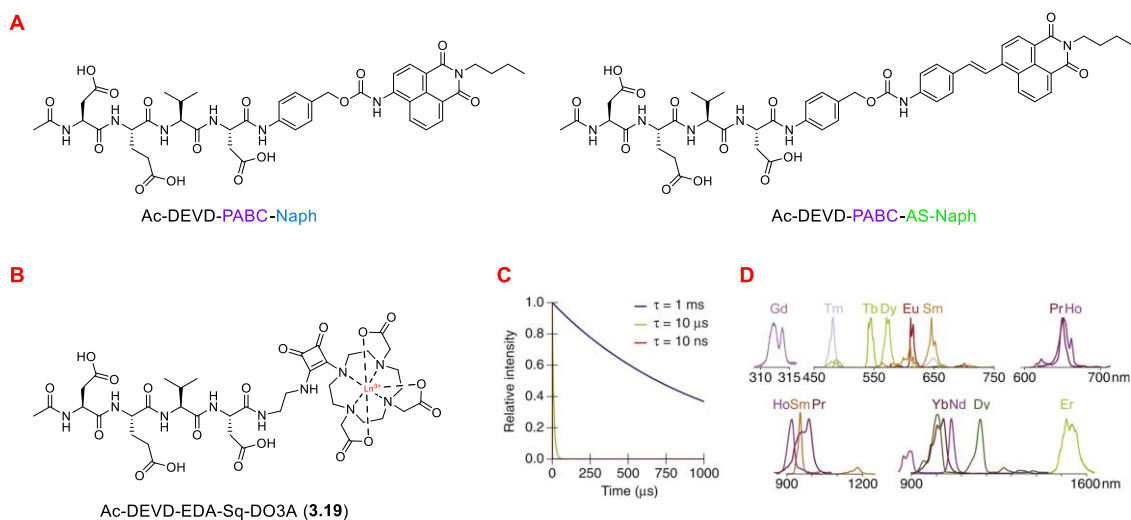
Figure 3.30: Illustration depicting the evolution of potential Caspase-3 probes discussed in this thesis. (A) Fluorogenic Peptide-probes. (B) Potential Lanthanide-based Peptide-probe. (C) Theoretical decay curves of luminophores with 10-ns (red), 10-µs (green), and 1-ms (blue) lifetimes. (D) Emission spectra of trivalent lanthanide ions (Ln³⁺).[338]

The initial design strategy for **3.19** and its potential mode-of-action is outlined in **Figure 3.11**. Synthesis of this peptide-probe started with the incorporation of the mono-substituted squaramide ligand **3.7**, which possesses an ethylene diamine (EDA) linker. This EDA moiety acts as a reactive handle for coupling to the Ac-DEVD(OtBu)-OH (**2.1**) peptide, while at the same time putting some distance between the bulky squaramide ligand and the capase-3 cleavage site. Protected ligand **3.7*** was coupled to **2.1** via EEDQ to afford **3.18** with a yield of 82%. This was then followed by a TFA deprotection to generate the peptide-ligand **3.19** in a yield of 91% (**Scheme 3.6**).
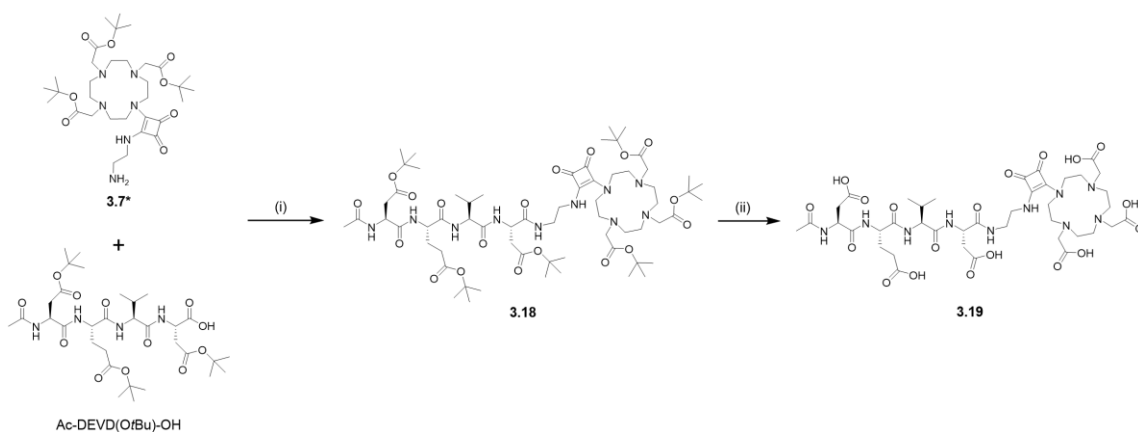
Scheme 3.6: Synthetic pathway to Ac-DEVD-EDA-Sq-DO3A ligand **3.19**. _Note:_ * denotes protected ligand. _Reagents and conditions:_ (i) EEDQ, DCM, rt, 16 hrs, 82%. (ii) DCM/TFA, rt, 6 hrs, 91%.

132

The final deprotected peptide-ligand (**3.19**) was characterised by LC-MS (**Figure 3.31**), with confirmation of molecular formula via HRMS (**Figure 3.32**). Full characterisation was documented in the *Appendix* (see Figure S3.124 – 3.131). The HPLC trace displayed one sharp UV peak with a t_R = 20 min. Strong ionisation was observed for the target mass of $[M+H]^+$ = 985.2 gmol^{-1} in positive mode and $[M-H]^+$ = 983.1 gmol^{-1} in negative mode.
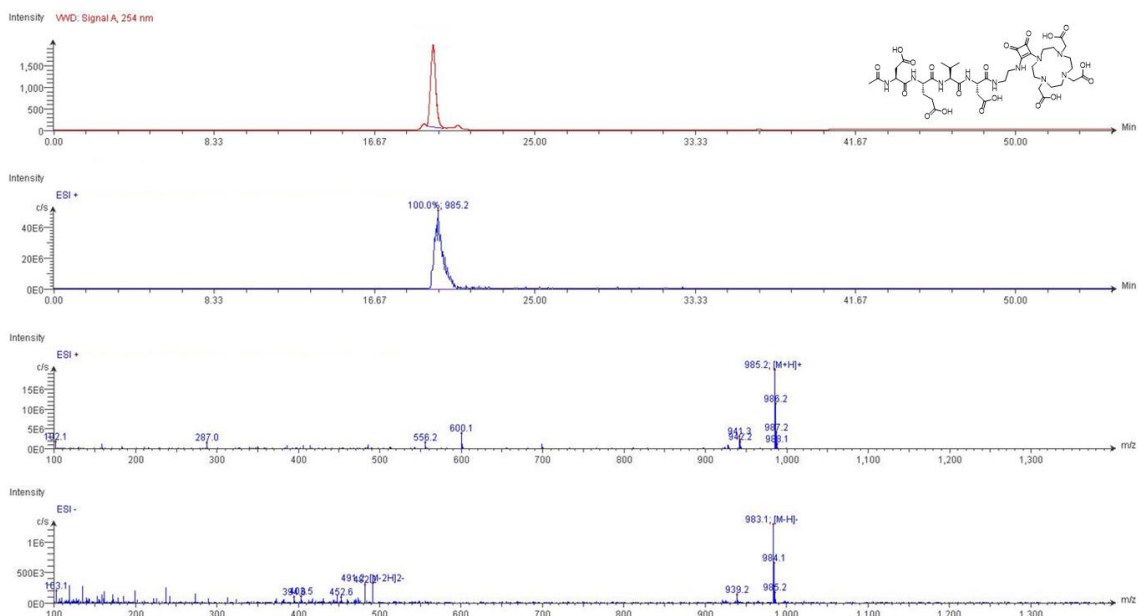
Figure 3.31: LC-MS data for Ac-DEVD-EDA-Sq-DO3A (**3.19**).

HRMS data affirmed the molecular formula of **3.19**, with confirmation of the target mass $[M+H]^+$ = 985.4115 gmol^{-1} possessing an excellent mass error value of 0.11 ppm.
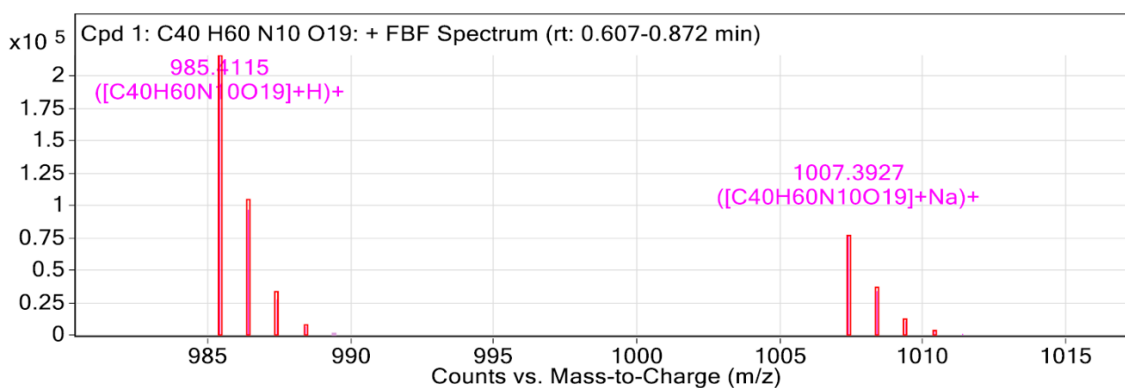
Figure 3.32: HRMS (ESI+) data for Ac-DEVD-EDA-Sq-DO3A (**3.19**).

With the successful synthesis of **3.19**, the initial family of squaramide-based cyclen-ligands was complete. We were satisfied that the characterisation data – to the best of our knowledge – was thorough and accurate, and the next

step was to conduct a preliminary investigation into the photophysical characteristics of each ligand and their subsequent Ln^{3+} complex(s).

3.4 Spectroscopic Studies

3.4.1 UV-vis Comparison of Ligands

The 4*f*-4*f* transitions in luminescent lanthanide ions are considered *disallowed* according to the Laporte selection rule. Consequently, the low transition probabilities lead to extinction coefficients that are several orders of magnitude lower than those of commonly used fluorophores. Because efficient and direct excitation of these Ln^{3+} ions would necessitate light intensities that can be harmful to biological samples, *antenna chromophores* are commonly employed to transfer energy to lanthanide ions. With this in mind, the first part of the investigation was to obtain the necessary excitation wavelengths (λ_{max}) of the ligands. This UV-vis comparison was limited to ligands that could potentially form Ln^{3+} complexes, thus, any protected* ligands were excluded from this study. Starting with the mono-substituted squaramide-DO3A ligands, the absorbance spectra were recorded for each ligand (20µM) in *Milli-Q®* H_2O (**Figure 3.33**).
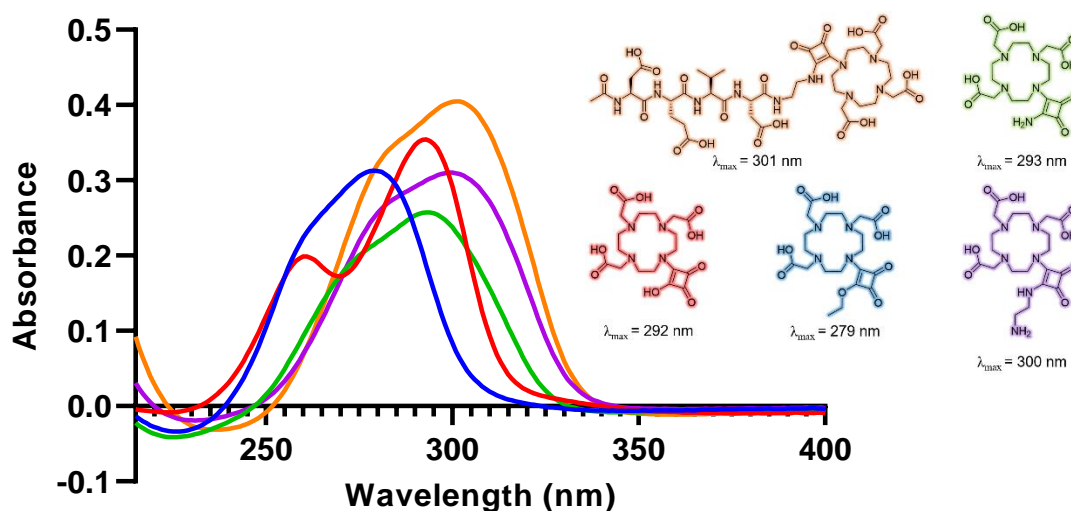
Figure 3.33: Absorbance spectra of Squaramide-DO3A ligands (20µM) in H_2O. *Inset:* Ligand structures and absorbance maxima (λ_{max}). <u>*Note:*</u> Colour corresponds to their respective absorbance spectrum.

From lowest wavelength – absorbance maxima (λ_{max}) – to highest: **3.4** (279 nm), **3.5** (292 nm), **3.6** (293 nm), **3.7** (300 nm) and **3.19** (301 nm). Ligands **3.4** and **3.5**, with substituents baring -OEt and -OH (respectively), possess the lowest λ_{max} values. Indeed, both of these ligands contain oxygen-based functional groups, which is interesting because when moving to the nitrogen-based

functional groups of **3.6** (-NH$_2$) and **3.7/3.19** (-NHCH$_2$R), a bathochromic shift and an increase in wavelength λ_{max} was observed. Perhaps this phenomenon can be related to the electron-donating (ED) characteristics of each functional group, with nitrogen-based functional groups providing increased ED abilities compared to oxygen-based functional groups. In this case, as oxygen is more electronegative it may be a poorer ED group compared to the corresponding nitrogen derivatives. From a molecular orbital point of view, the squaramide nitrogens can donate electron-density into the cyclobutene-ring more efficiently, thus making the arrangement more stable – through resonance (**Figure 3.5**). The energy level of the affected orbital is then subsequently lowered, causing a noticeable red-shift in the maximum wavelength (279 – 301 nm).[339]

The di-, tri-, and tetra-substituted squaramide-based ligands were only synthesized as their squaramic acid derivatives. As such, their corresponding maximum wavelength (λ_{max}) did not differ all that much. With the absorbance spectra recorded and the λ_{max} obtained for each squaramide-DO3A ligand, the next step was to try and form some Ln^{3+} complexes to conduct preliminary luminescence studies.

3.4.2 Preliminary Tb^{3+} & Eu^{3+} Luminescence Studies

The excited $4f$ states of Ln^{3+} ions are shielded by the filled 5s^2 and 5p^6 subshells, thus lanthanide emission spectra possess very narrow bandwidths and individual peaks that originate from different transitions are easily distinguishable. For instance, Tb^{3+} luminescence displays distinct line-like emissions at 490, 540, and 580 nm, while Eu^{3+} luminescence occurs at 590, 610, and 720 nm. Various other lanthanides exhibit ultrasharp emission peaks in the visible range, but their relatively low quantum yields – typically below 10% – have restricted their application as imaging probes.[247]
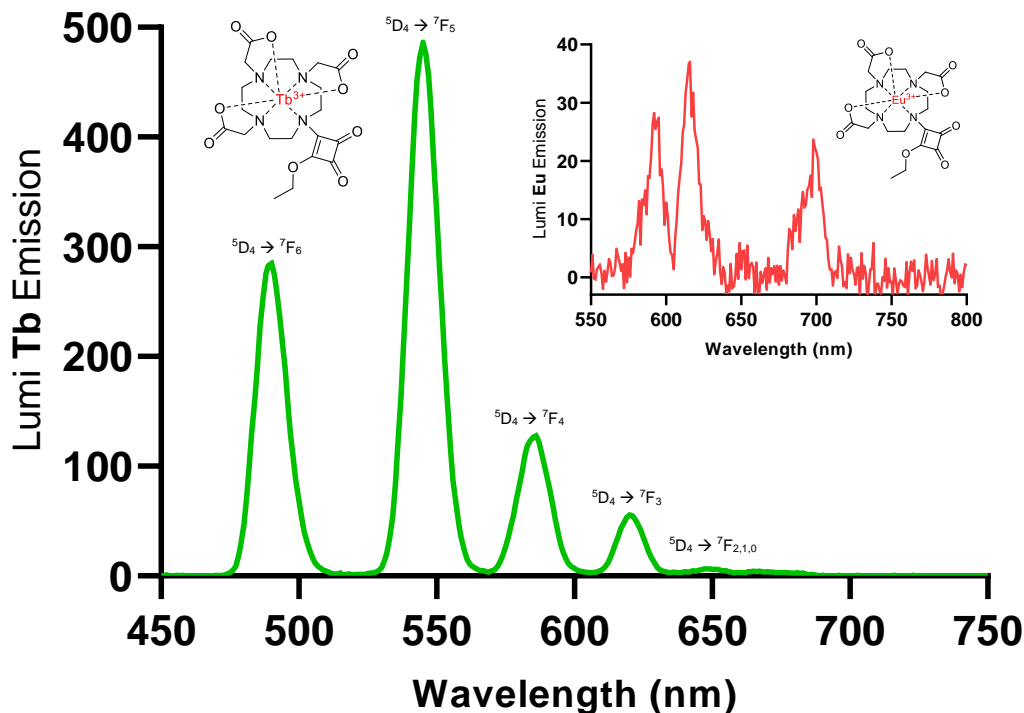
Figure 3.34: The delayed luminescence spectrum of **[Tb(3.4)]** (20µM) recorded in *Milli-Q® *H_2O (λ_{ex} = 279 nm), showing the characteristic Tb^{3+} transitions $^5D_4 \rightarrow {}^7F_{6,5,4,3,2,1,0}$. *Inset:* **[Eu(3.4)]** (20µM) recorded under the same conditions.

The delayed Tb^{3+}-centred emission was recorded upon excitation of **[Tb(3.4)]** at λ_{ex} = 279 nm in H_2O. **Figure 3.34** highlights the Tb^{3+}-centred transitions at λ_{max} = 490, 545, 584, 622, 648, 667 and 679 nm, upon deactivation of the $^5D_4$ state to the ^7F_x (x = 6-0) states, respectively. The same luminescence intensity was not observed for **[Eu(3.4)]**. Although weakly intense Eu^{3+}-centred transitions at λ_{max} = 590, 610 and 700 nm were observed, perhaps the coordination-sphere of the Eu^{3+} centre was not fully satisfied. Indeed, if there was bound H_2O molecules, it could potentially result in the $^5D_4$ excited state of Eu^{3+} being quenched by O-H oscillators.[340] As the squaramic acid derivative **3.5** possesses an extra coordination-site (compared to **3.4**), in theory this may result in a more complete Ln^{3+} coordination-sphere and potentially expel any remaining H_2O molecules.

This work was carried out in CNRS – Orleans (France), under the supervision of Dr. Celia Bonnet and with the help of her team. However, due to time constraints, only preliminary luminescence data for ligand **3.4** was obtained. All ligands have been sent back to CNRS for more complete luminescence

measurements. Unfortunately, those results were not available at the time of writing this thesis, but may be inserted in the near future or compiled into a publication. Be that as it may, we are excited that even one of the squaramide-based ligands (**3.4**) was able to produce a novel luminescent complex, and we look forward to exploring the potential use of these ligands in the future.

3.5 Conclusions

In conclusion, an extensive family of novel, water-soluble squaramide-based cyclen ligands with varying symmetry and substitution patterns (**3.4** – **3.17**) have been synthesized, including one ligand that may have the potential to act as a lanthanide-based caspase-3 probe (**3.19**). UV-vis absorbance spectra were recorded for each ligand, with the mono-substituted squaramide-DO3A ligands displaying a wavelength maximum (λ_{max}) in the range of 279 – 301 nm. It was observed that ligands containing nitrogen-based electron-donating substituents displayed red-shifted λ_{max} values. This was postulated to arise from the lowered orbital energy-level due to resonance stability from the donated electron-density. Higher excitation wavelengths (λ_{ex}) are advantageous, as lower wavelengths (like those required for direct excitation) can be damaging to biological samples. Ligand **3.4** was then complexed to form **[Tb(3.4)]** and **[Eu(3.4)]**. Preliminary luminescence spectra were then recorded for each complex (20μM) in H_2O. **[Tb(3.4)]** displayed intense line-like Tb^{3+}-centred transitions at λ_{max} = 490, 545, 584, 622, 648, 667 and 679 nm, corresponding to the deactivation of the $^5D_4$ state to the ^7F_x (x = 6-0) states. **[Eu(3.4)]** only produced weak Eu^{3+}-centred transitions at λ_{max} = 590, 610 and 700 nm. More experiments are required to understand photophysical mechanisms between the lanthanide metal-centres and our squaramide-based ligands for potential luminescent complexes. Future work will include more in depth and complete luminescent studies for all the ligands.

We hope to explore the potential of **3.19** to act as a caspase-3 probe in the future, via complexation to various Ln^{3+} centres and observing their response to caspase-3. The synthetic scope for potential caspase-3 probes is rather extensive, as many more versions of **3.19** could potentially be synthesized. Utilising a similar design strategy, and incorporating the previously synthesized di-, tri- and tetra-substituted squaramide-based ligands (**3.11**, **3.15** & **3.17**), capase-3 probes with increasing number of antenna-ligands could be synthesized (**Figure 3.35**). Increasing the number of antenna-ligands within the vicinity of the Ln^{3+} ion may lead to brighter and more intense luminescent probes.
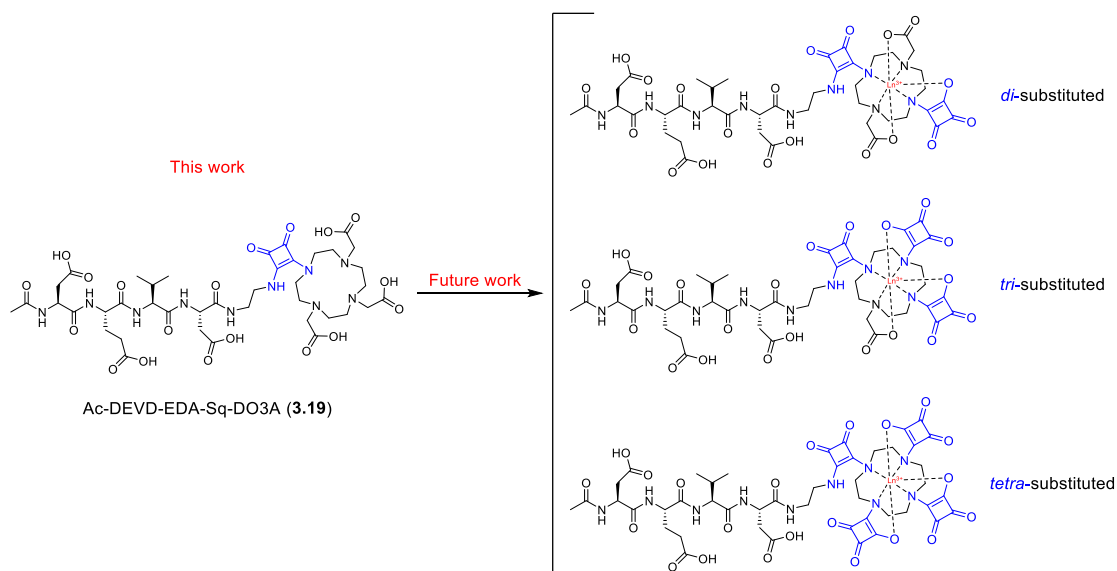
Figure 3.35: Illustration depicting potential lanthanide-based caspase-3 probes utilising mono-, di-, tri- and tetra-substituted squaramide ligands.

We are motivated and excited by the preliminary luminescence studies conducted on **3.4**, and the synthetic/spectroscopic potential of this family of squaramide-based ligands for generating luminescent Ln^{3+} complexes. We will conduct further experiments regarding this family of ligands, with the hope to apply them to a biological application via caspase-3 or otherwise. There may be other numerous potential applications for this family of ligands, not just for luminescent complexes, but perhaps, also, for generating highly stable Gd^{3+}-based MRI contrast agents. With the aid of our collaborators at CNRS in Orleans, I believe many exciting results are soon to follow.

Chapter 4

Towards the Synthesis of

Squaramide-based Peptidomimetics

4. Towards the Synthesis of Squaramide-based Peptidomimetics

4.1 Introduction

"Even in the dark times between experimental breakthroughs, there always continues a steady evolution of theoretical ideas, leading almost imperceptibly to changes in previous beliefs" – Prof. Steven Weinberg (Nobel Lecture 1989)

The term "isosterism" was initially coined by Langmuir in 1919, and it pertains to the physicochemical properties of the components of organic molecules.[341] This concept was further developed by Grimm, who utilised the hypothesis of the "hydride displacement law" to elucidate the capacity of specific functional groups to imitate or resemble other molecules.[342] Erlenmeyer provided further rationalisation of these concepts and categorised isosteres into atoms, ions, and molecules based on their valence electrons.[343] Friedman contributed a deeper understanding of this concept and introduced the term "bioisosterism" to encompass all atoms and molecules that fall under the broadest definition of isosteres.[344] This approach was not dependent on whether the drug acted as an agonist or an antagonist in terms of its biological activity. Thornber then extended the application of the term bioisosterism to incorporate subunits, groups, or molecules that share physicochemical properties leading to similar biological effects.[345] This conceptualisation of bioisosterism would remain undisputed for another twelve years, until 1991 when Burger expanded the definition of bioisosteres to encompass compounds – or functional groups – that share similar molecular shapes and volumes, regardless of their role as agonists or antagonists.[346] These bioisosteres would necessitate an approximately equal distribution of electrons, which in turn would result in a high likelihood of producing similar physical properties (**Figure 4.1**).[347]
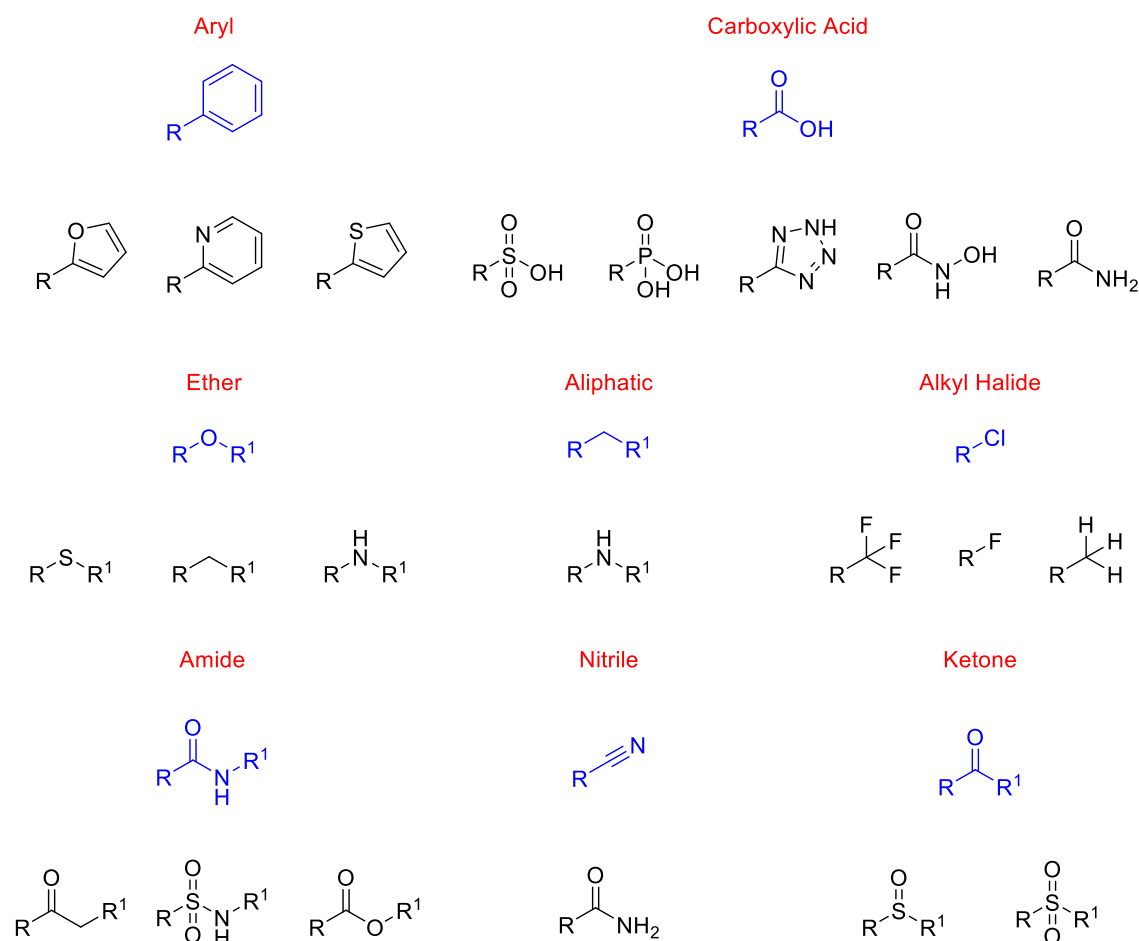
Figure 4.1: Examples of potential Isosteres for various functional groups.[348]

Presently, bioisosterism stands as one of the most valuable tools for medicinal chemists in rational drug design, especially with regard to carboxylic acid bioisosteres.[349] The carboxylic acid functional group is a component of the pharmacophore in numerous commercial drugs, spanning from anticoagulants, statins, β-lactam antibiotics, and non-steroidal anti-inflammatory drugs (NSAIDs).[350] The significance of the carboxylic acid group lies in its contribution to biomolecular recognition at the receptor site, facilitated by its capability to form strong hydrogen bonds.[351] A valuable lesson learned from drug discovery is that structures with similar bond connectivity and (overall) shape – compared to the naturally occurring functional group – are not always the most potent replacements.[352] Certain replacements may exhibit similar structures but possess distinct molecular recognition patterns. Hence, the critical factor for molecular recognition in biological systems may be the charge distribution of the substrate in space, rather than its molecular shape and volume.

Following the remarkable achievements of the last century, medicinal chemistry and the pharmaceutical industry are faced with the challenge of developing drugs for progressively challenging target classes. One potential solution lies in the application of bioisosterism, by leveraging the mimicry of the interaction surfaces themselves. This necessitates the capability to replicate not only the primary structure of biomacromolecules, but also their secondary and possibly tertiary structure.

Peptidomimetics are synthetic compounds designed to mimic the structural and functional features of peptides, offering the potential to retain their biological activity while overcoming some of their inherent drawbacks. The need for novel peptidomimetics has gained prominence in recent years as researchers seek to harness the therapeutic potential of peptides, ranging from traditional signalling peptides to complex protein-protein interaction disruptors, with enhanced drug-like properties.[353] This shift in focus has been driven by the recognition that peptidomimetics may provide a critical bridge between the world of peptides and small molecules, enabling the development of more effective and clinically viable drugs.

One category of peptidomimetic compounds designed to tackle this challenge is, *foldamers*.[354] The development of peptide-foldamers is founded on the similarity of their folding characteristics to biopolymers and involves peptides that contain β-, γ-, and δ-amino acids (**Figure 4.2**).[355]
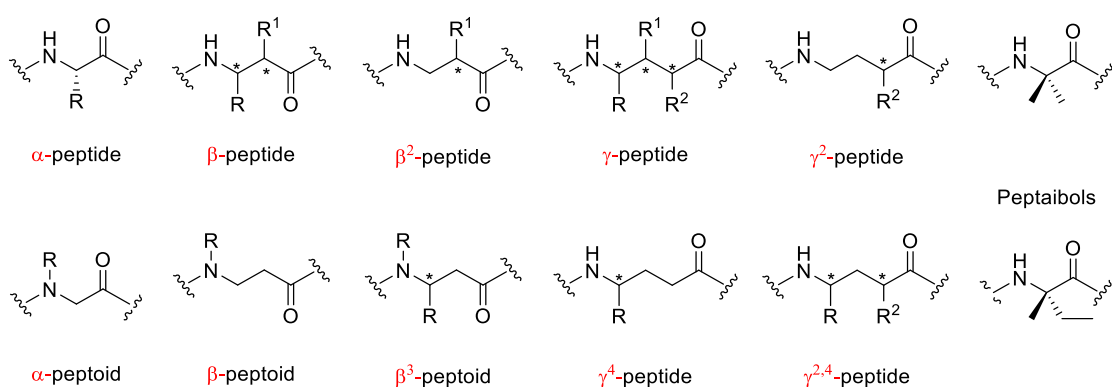
Figure 4.2: Structure and substitution patterns of peptide backbone monomers.

The initial class of foldamers emerged from the substitution of α-amino acids in helical peptides with β-amino acid building blocks.[356] β-amino acids are analogues of α-amino acids, in which an additional methylene group is introduced between the *N*-terminal amine and *C*-terminal carboxylic acid. These amino acids

can be categorised into three types; β, β^2 and β^3, depending on their substitution pattern at the carbon atoms in positions 2 and 3. To enhance folding and entropic gain, additional variations of β-amino acids involving conformationally constrained cycloalkane rings have been developed for helical foldamers (**Figure 4.3**). These monomers can exist in both cis and trans conformations.[357] The stabilised helix-forming characteristics of cyclic β-amino acid oligomers are primarily determined by their backbone torsional angle, which is influenced by the ring size and stereochemistry.[358]
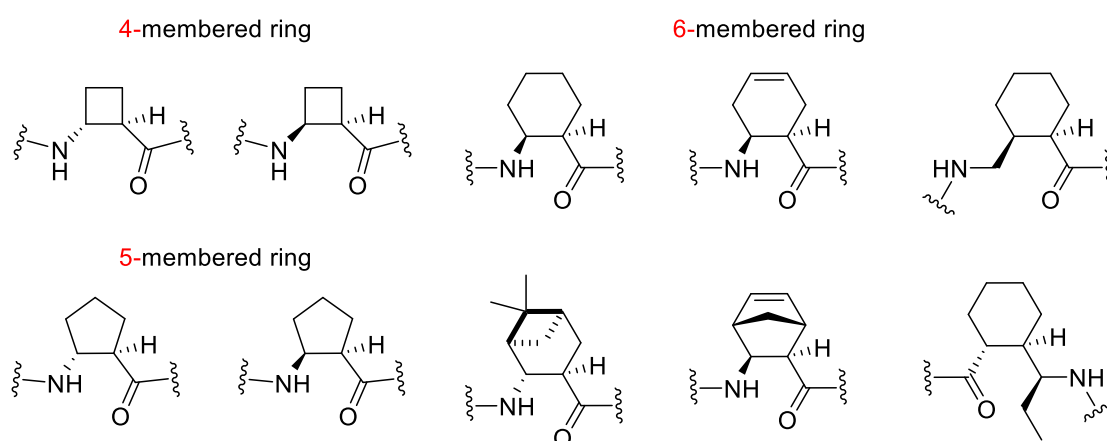
Figure 4.3: Examples of ring-constrained β- and γ- monomers utilised in peptide foldamers.[354]

Isosteres of γ-amino acids – such as aliphatic oligourea monomers – have also been created. These compounds are produced by substituting the α-carbon of γ-amino acids with a nitrogen atom.[359] Oligoureas are intriguing peptide-mimetics due to their capacity to mimic three-dimensional space, water solubility, synthetic flexibility, and metabolic stability.[360] Similar to traditional peptides, oligoureas can be readily synthesized through sequential coupling on resin and exhibit secondary, tertiary, and quaternary structures based on their sequences.[361] Crucially, the oligourea backbone is protease-resistant and can be integrated with peptide α-helices,[362] as it adopts a helical conformation that does not interfere with the propagation of the peptide α-helix.[363] This is rather significant, as many biologically active peptides contain α-helical structures. Substituting or partially replacing these helical regions with oligoureas could enhance the proteolytic resistance of the peptide without substantially affecting its binding properties.

Guichard and colleagues utilised this oligourea motif to design peptide therapeutics with improved pharmacokinetic properties. The essence of their

strategy involved replacing four consecutive AA's on Glucagon-like Peptide-1 (GLP-1) with three ureido residues, which capitalised on the structural resemblance of oligourea and α-peptide helices.[364] GLP-1 is an endocrine peptide hormone produced by the pancreas and several other organs, such as the gastrointestinal tract, heart, and brain.[365] It plays a crucial role in regulating blood sugar levels and various metabolic processes.[366] However, the therapeutic utilisation of GLP-1 can be challenging due to various factors, including its rapid degradation and short half-life in the body (2 – 3 minutes).[367] Various strategies have been used to improve the half-life in GLP-1 (**Figure 4.4**) including; coupling to large proteins (Efpeglenatide, Albiglutide & Dulaglutide),[368] conjugation to albumin-binding molecules (Semaglutide & Liraglutide),[369] sequence modifications (Lixisenatide & Exenatide),[368] α- to β-peptide substitution,[370] and cross-linking of AA side-chains.[371]
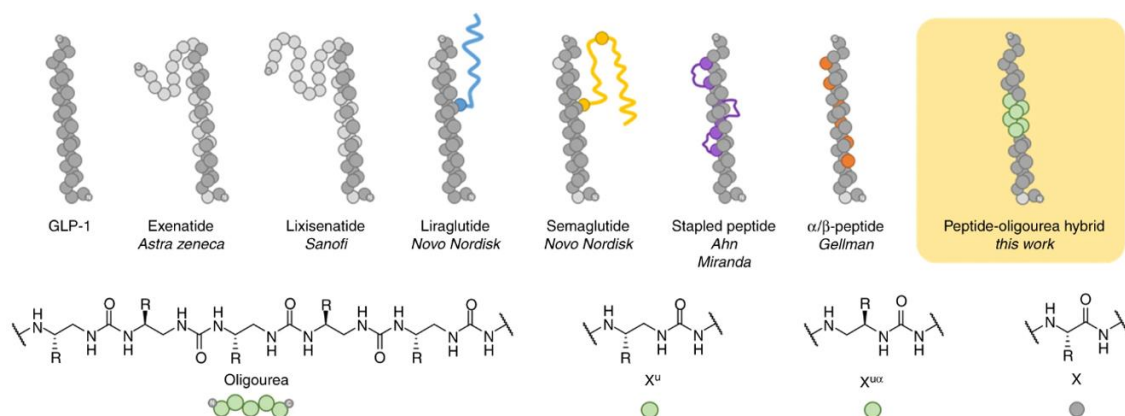
Figure 4.4: Illustration of the different GLP-1 analogues previously reported, and the current strategy based on peptide-oligourea hybrids.[364]

Three of Guichard's oligourea-peptide hybrids – out of the eight tested in mice – displayed a significantly prolonged duration of action. This enhanced effect was observed in correlation with studies on Neutral Endopeptidase 24.11 (NEP 24.11) – a peptidase involved in peptide degradation – and mouse plasma degradation. These findings suggest that the oligourea hybrids exhibit increased resistance against various peptidases present in the organism, contributing to their extended duration of action. Guichard's oligourea strategy was then applied to Semaglutide – an FDA-approved GLP-1 analogue – to generate a novel peptidomimetic. The results demonstrated that not only was the *in vivo* activity preserved, but the stability toward pancreatin (an enzyme mixture involved in the

digestion of proteins in the pancreas) was improved. This improvement in stability suggests a potential pathway for enhancing oral administration of the hybrid.

The conclusion of this study highlights the effectiveness of replacing four consecutive amino acid residues with a ureido triad of similar dimension and geometry in a peptide α-helix as a strategy to enhance pharmaceutical properties. The researchers anticipate that this approach will be valuable for the development of peptide therapeutics. Ongoing evaluations are being conducted to explore the application of this strategy to other peptide sequences and protein targets with therapeutic significance.

Another interesting peptidomimetic approach is the use of Retro-Inverso (RI) peptides. These peptides utilise *D*-amino acids as robust substitutes for *L*-amino acids, but are arranged in a reversed (retro) sequence relative to the original molecule.[372] RI analogues of all *L*-peptides are therefore peptides comprised of *D*-amino acids arranged in a reversed sequence. This subclass of peptides is significant because, when examined in a fully extended conformation, their side-chains align perfectly with those of the original *L*-peptide, albeit with reversed amide bonds and *N-/C*-terminal groups.[373] Hence, in situations where activity primarily stems from the arrangement of side chains without substantial involvement from the backbone chemical groups or the three-dimensional structure, a RI analogue may possess similar functionality as the all-*L* parent peptide – while exhibiting enhanced stability against proteolytic degradation.[374]

This chapter will document the use of a peptidomimetic strategy to try and improve the enzymatic stability of a pharmaceutical compound called *Cilengitide®*, via insertion of a *Squaramide* moiety.

Glioblastoma multiforme (GBM) is a highly aggressive and malignant brain tumour (**Figure 4.5**). Despite the use of current multimodality therapy involving surgery, X-ray therapy (XRT), and chemotherapy, the prognosis for patients with GBM remains challenging. The median progression-free survival (PFS) and overall survival (OS) for newly diagnosed patients are reported to be only 6.9 and 14.6 months, respectively.[375] The aggressiveness and infiltrative nature of GBM, along with its resistance to standard treatments, contribute to the difficulty in achieving favourable outcomes for patients. Continued research and innovative

therapeutic approaches are essential for improving the prognosis and quality of life for individuals diagnosed with GBM.
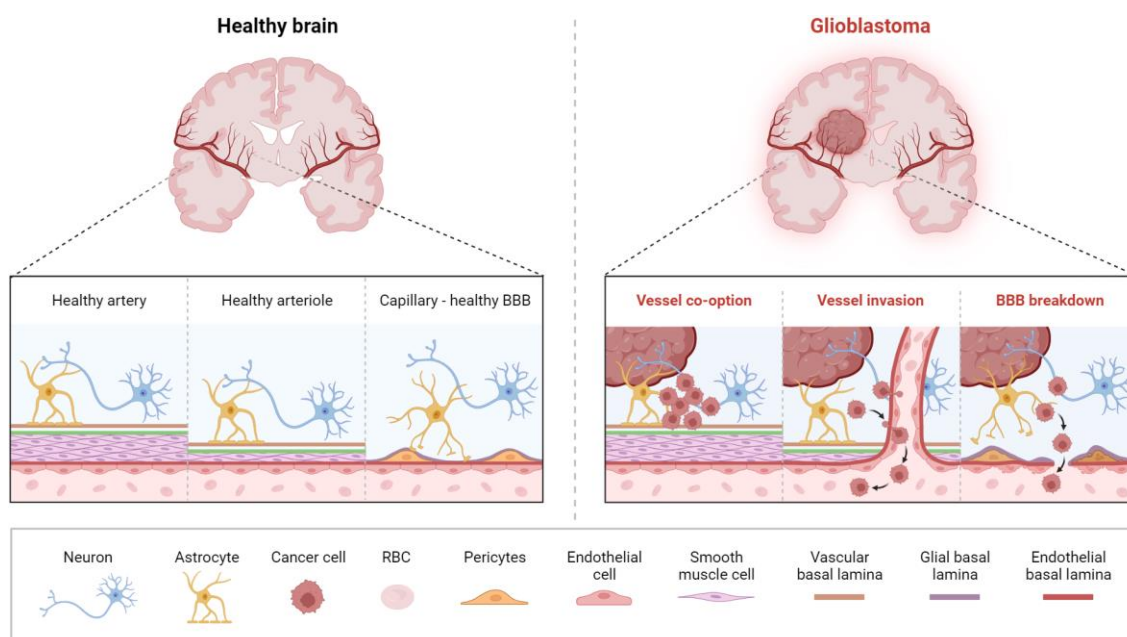
Figure 4.5: Healthy brain vs Glioblastoma, denoting vascular architecture.[376]

Integrins, consisting of dimerised α- and β- domains, are transmembrane receptors that interact with various extracellular ligands through an arginine-glycine-aspartic acid (RGD) peptide. The binding of ligands to integrins activates these receptors, influencing processes such as tumour cell invasion, migration, proliferation, survival, and angiogenesis.[377] GBM cells and the vascular components of tumours commonly express integrins.[378] Cilengitide – a cyclic RGD peptide (**Figure 4.6**) – competitively binds to the $\alpha v\beta 3$ and $\alpha v\beta 5$ integrin receptors.[379] Cilengitide has been shown to be active against pre-clinical GBM models, and clinical studies has also demonstrated promising anti-tumour results.[380] Cilengitide also demonstrated an exceptional safety profile, with no observed dose-limiting toxicities in phase I clinical studies. Indeed, it was the first integrin inhibitor to have reached phase III clinical development. However, this was the end of the road for Cilengitide, as the results were unfortunately, disappointing. 545 patients were enrolled in the phase III trial, with a median overall survival-rate of 26.3 months in the Cilengitide group, and 26.3 months in the placebo group.[381] The decision to abandon the development of Cilengitide as an anticancer drug was made following this registration trial, where the failure to demonstrate a survival advantage in patients most likely to benefit from the addition of Cilengitide to standard initial therapy, led to this conclusion.
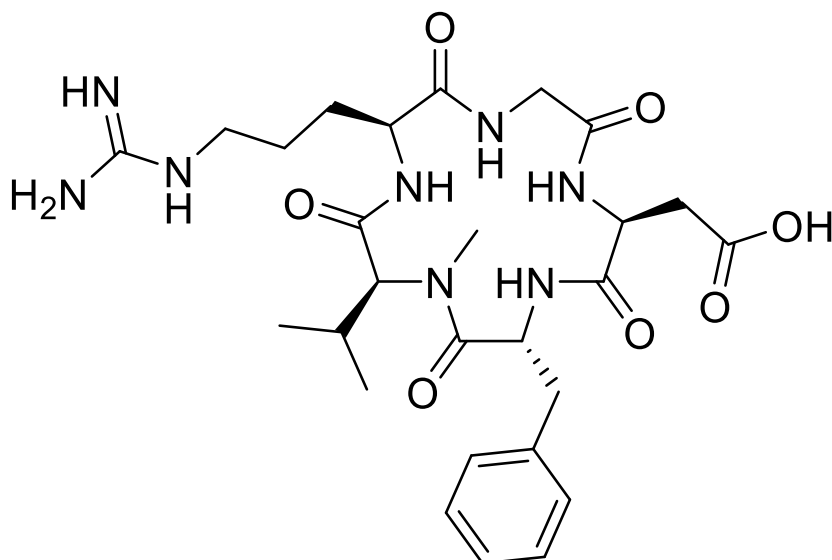
Figure 4.6: The structure of Cilengitide.

Roger Stupp – the lead researcher of the ten-year clinical development programme for Cilengitide responded to the disappointing results of the phase III clinical trial in 2014, suggesting that Cilengitide may deserve another chance in the future, *"The short half-life of only a few hours (2 – 4) may have been suboptimal… with formulations evoking longer half-lives potentially being more appropriate for future approaches".*[382] We believe that insertion of a squaramide moiety into the Cilengitide backbone may be an interesting approach for improving the drug's half-life and duration of action. Rationale for this hypothesis can be found in the ability of squaramides to act as both hydrogen-bond donors and acceptors – supporting the types of non-covalent interactions available to peptides. Many of the *squaryl*-analogues documented in literature are chemically derived from the squaric acid building block. Squaric acid possesses a high-degree of potential synthetic versatility, as it can readily undergo functional group inter-change to produce a wide range of derivatives.[322] These derivatives consist of squaramides, squaramic acids, squarates and semi-squarates (amongst others, see **Figure 3.5**), and have been shown to act as bio-isosteric replacements for carboxylic esters,[314] carboxylic acids,[383] amino acids,[384] and peptides (**Figure 4.7**).[385]

A

B

C

D
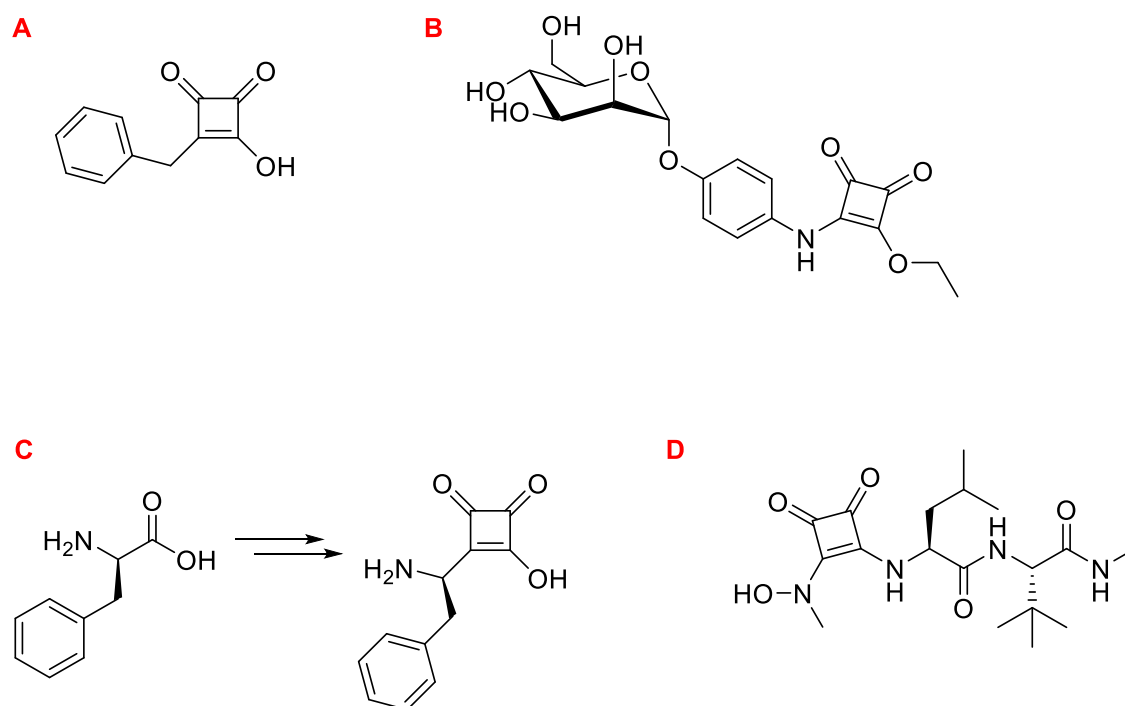
Figure 4.7: Select examples of squaryl-derivatives previously reported to act as bio-isosteric replacements for (A) Carboxylic Acids, (B) Esters, (C) Amino Acids, and (D) Peptides.

The substitution of a squaramide moiety into the Cilengitide backbone may improve the molecule's half-life through increased stability to proteases, while still retaining bio-activity. Another interesting facet of this hypothesis is that the inherent conformational bias around the squaramide motif may provide a novel insight into the complex binding pocket of the $\alpha v \beta 3/5$ integrin. This potential squaramide-peptidomimetic (*Squaratide*) may prove to be an elegant solution to the (current) poor pharmacokinetic profile of Cilengitide.

4.2 Chapter Objective

The discovery and development of new therapeutic agents has long been at the forefront of medicinal chemistry research. Among the vast array of molecules with pharmacological potential, peptides have garnered significant attention due to their ability to modulate intricate biological processes and exhibit high specificity. However, despite their many advantages, peptides are not without limitations, including susceptibility to enzymatic degradation, poor oral bioavailability, and difficulties in crossing cellular membranes. These shortcomings have spurred a growing demand for innovative approaches that help close the gap between the unique attributes of peptides and the favourable properties of small molecules. In response to these challenges, the field of peptidomimetics has emerged as a promising avenue for drug discovery.[386]

The objective of this chapter is to (again) utilise the many synthetic applications of squaramides. However, this time we build on our current expertise in peptide synthesis and venture into the realm of peptidomimetics. As mentioned in the above introduction section, the aim is to generate a synthetic analogue of a previous pharmaceutical drug – *Cilengitide* – that (unfortunately) failed at phase III clinical trials. This potential peptidomimetic contained a non-natural squaramide residue within the peptide backbone of Cilengitide. The initial design strategy consisted of replacing one amino acid, namely glycine, with the squaramide moiety (**Figure 4.8**).

Cilengitide - *c*RGDf*N*MeV   Squaratide - *c*R-Sq-Df*N*MeV
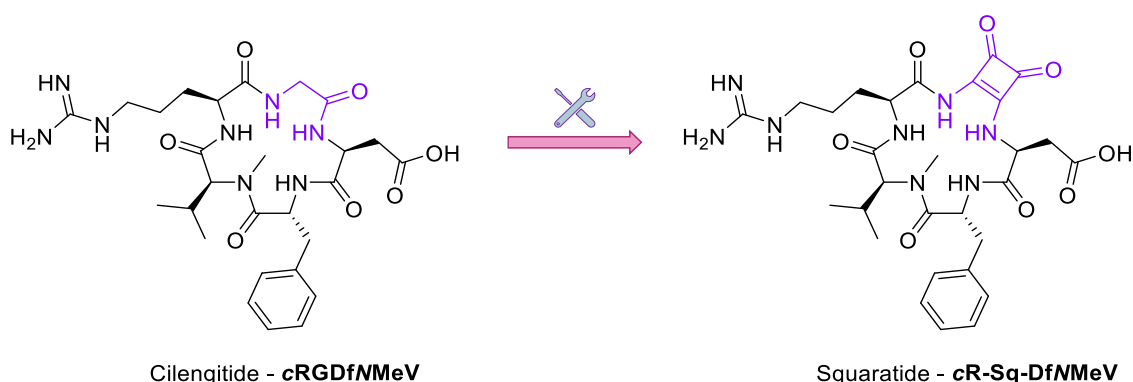
Figure 4.8: Design strategy for the Squaramide-based Cilengitide peptidomimetic (*c*R-Sq-DfV).

Glycine was chosen as the preliminary amino acid to be replaced, as it was envisioned that the squaramide would possess a similar residue charge-

distribution in space. This replacement would allow us to preserve the important interacting side-chains of the other amino acids within the peptide (**Figure 4.9**).
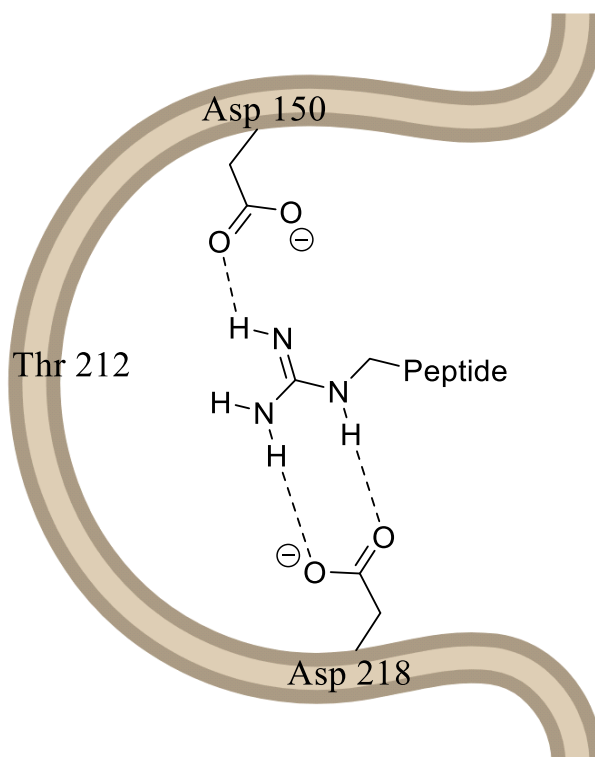
Figure 4.9: Example interactions in the αvβ3 integrin binding pocket.[387]

4.3 Synthesis and Characterisation of Cilengitide Peptidomimetics.

In a similar fashion to the peptide synthesis carried out in Chapter 2, the first step was to assemble the linear sequence using SPPS. This was done using 2-Chlorotrityl Chloride resin, with sequential coupling via the Fmoc/*t*Bu strategy (**Scheme 4.1**).
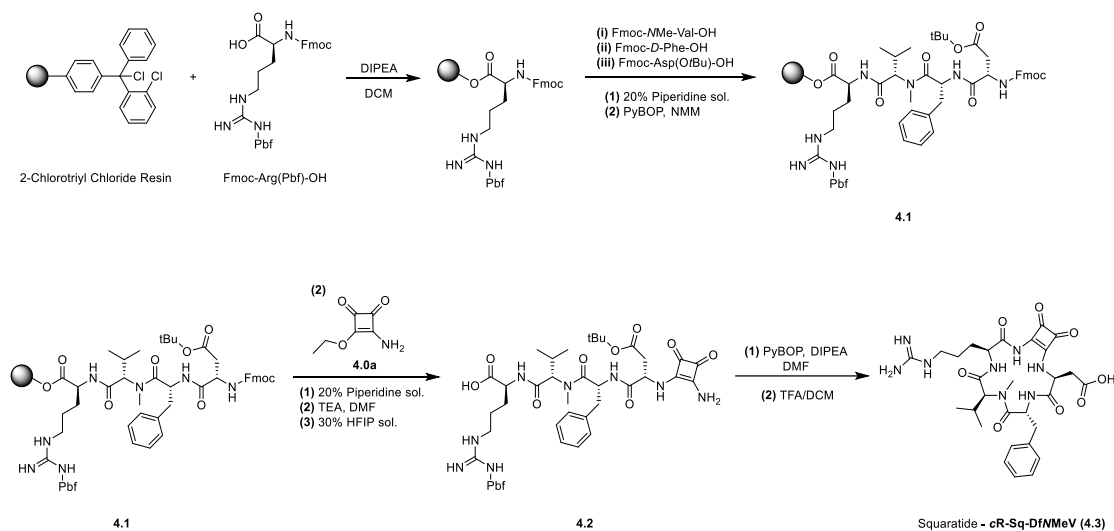
Scheme 4.1: Initial proposed pathway for the synthesis of *Squaratide* – **cR-Sq-Df*N*MeV (4.3)**.

After initial loading of the arginine residue onto the resin, SPPS will be used to assemble the tetra-peptide (Fmoc-D(O*t*Bu)-f-*N*MeV-R(Pbf)-OH, **4.1**) with PyBOP – as the coupling reagent – in the presence of NMM, before squaramide functionalisation, then cleavage from the resin, cyclisation, and finally global deprotection. The first two amino acids of the sequence Fmoc-*N*Me-Val-Arg(Pbf)-OH were successfully coupled using PyBOP/NMM coupling conditions. The HPLC trace of the test cleavage displayed one sharp UV peak with a t_R = 41 min. Strong ionisation was observed for the target mass of $[M+H]^+$ = 762.8 gmol^{-1} in positive mode and $[M-H]^+$ = 760.6 gmol^{-1} in negative mode (**Figure 4.10**).
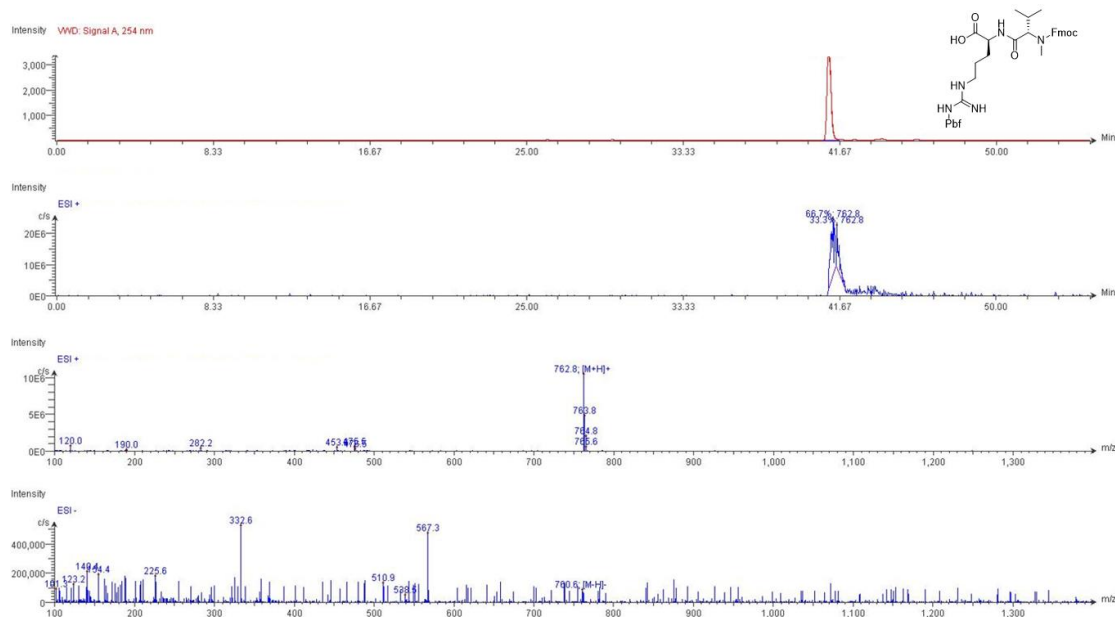
Figure 4.10: LC-MS data for **Fmoc-*N*Me-Val-Arg(Pbf)-OH**.

As the peptide sequence progressed, PyBOP and NMM were found to be inefficient for coupling to the *N*-methylated valine residue. Initial attempts using these coupling conditions resulted in a large amount of unreacted starting material (NH$_2$-*N*MeV-R(Pbf)-OH), even after multiple couplings (**Figure 4.11**).
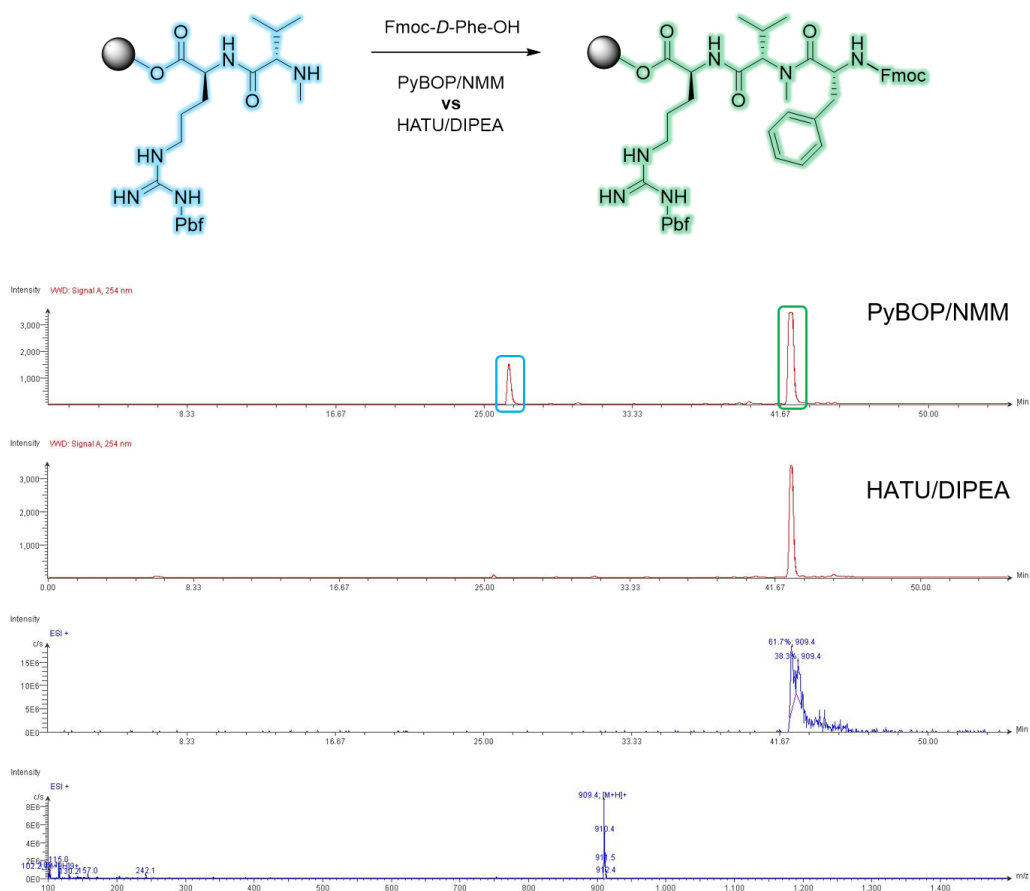
Figure 4.11: LC-MS data comparing PyBOP/NMM and HATU/DIPEA coupling conditions.

The coupling efficiency of PyBOP/NMM for this step in the synthesis was unsatisfactory, and a change in reaction conditions was required. This was likely due to the increased sterics around the *N*-terminal nitrogen of the valine residue, which possessed an extra methyl group. Hexafluorophosphate Azabenzotriazole Tetramethyl Uronium (HATU) – a popular reagent within peptide literature[89] – was employed alongside DIPEA to increase product formation. The HATU/DIPEA combination produced greatly enhanced coupling yields for this specific reaction compared to PyBOP/NMM, as highlighted above.
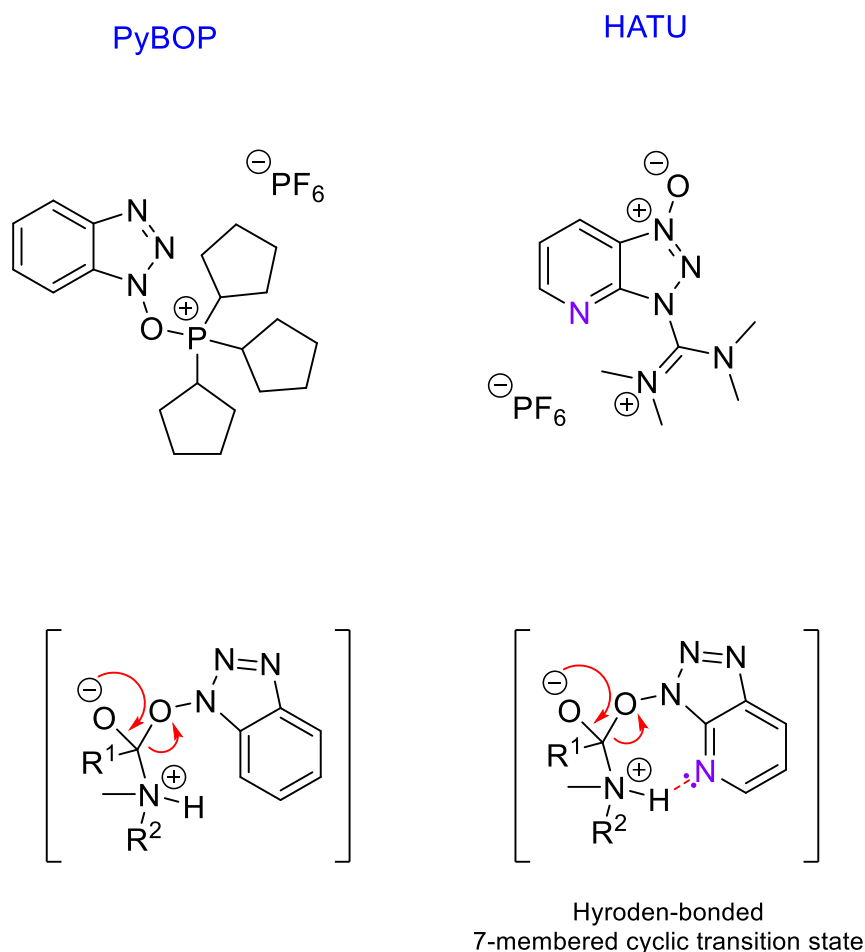
Figure 4.12: HATU-mediated (right) amide-bond formation compared to PyBOP (left).[388]

The ring-nitrogen - present within HATU - stabilises the incoming amine (neighbouring group effect) through a hydrogen-bonded 7-membered cyclic transition state (**Figure 4.12**).[388] This resulted in a dramatic increase in coupling efficiency. The hydroxy benzotriazole (HOBt) group (of PyBOP) does not contain this nitrogen atom, thus losing this advantage. The first step in this mechanism involves nucleophilic attack from the carboxylate anion of Fmoc-*D*-Phe-OH (formed by deprotonation via DIPEA) with the imine carbon of HATU, to form the

unstable *O*-acyl (tetramethyl)isouronium salt. The previously released hydroxy Azabenzotriazole (HOAt) then attacks the isouronium carbonyl carbon to yield the HOAt-activated ester, while also producing tetramethyl urea as a by-product. The *N*-terminal amine of Fmoc-*N*Me-Val-OH then reacts with the HOAt-activated ester to produce the desired peptide-bond through a nucleophilic substitution reaction (**Scheme 4.2**).

R¹ = Fmoc-*D*-Phe-OH
R² = HN-*N*Me-Val-Peptide
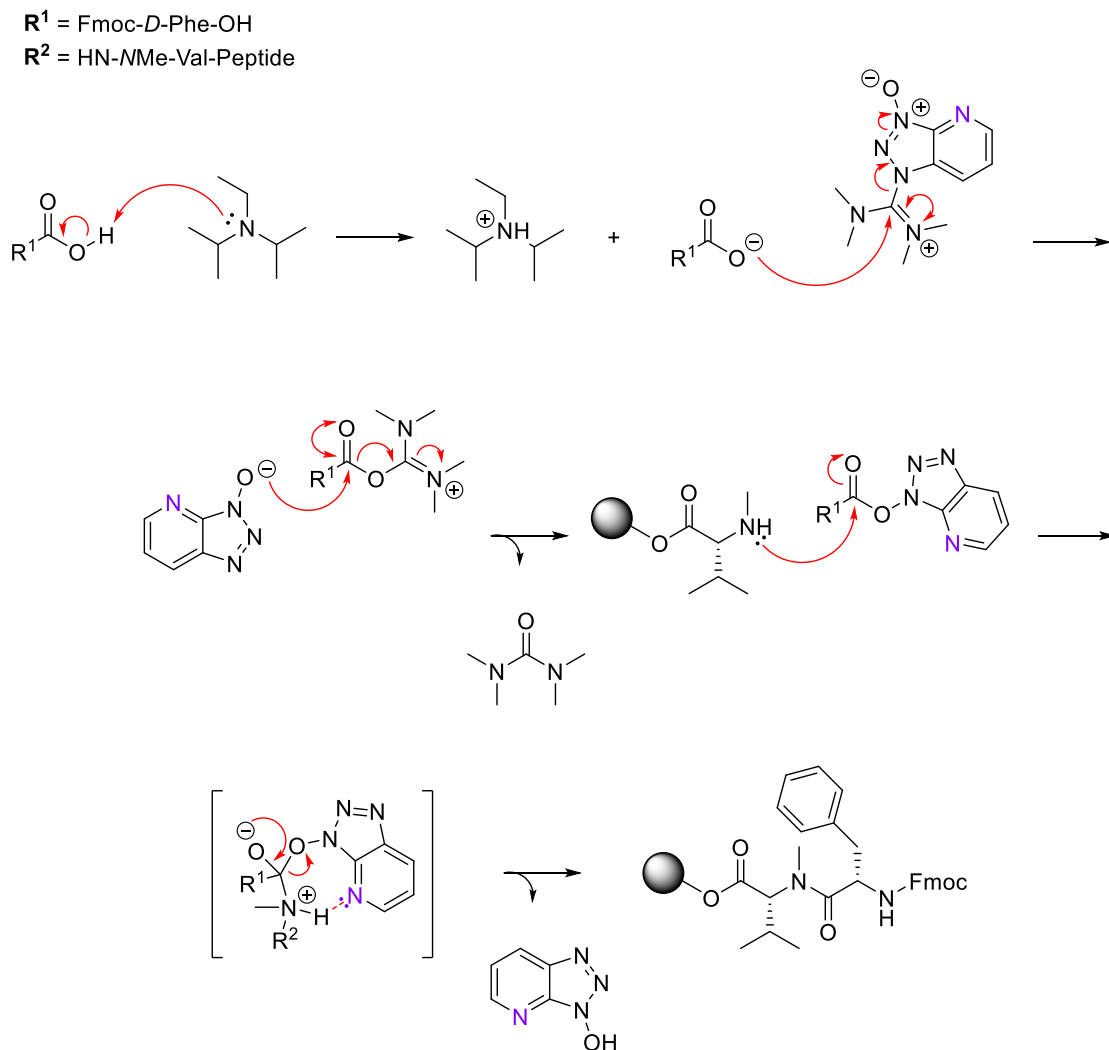
Scheme 4.2: Proposed mechanism for HATU/DIPEA mediated AA coupling.

Once the Fmoc-*D*-Phe-Oh residue was successfully attached to the peptide-on-resin, the next step was to couple the final natural amino acid – Fmoc-Asp(O*t*Bu)-OH. Previous coupling conditions (PyBOP/NMM) were re-employed, as there was no steric considerations regarding the *N*-terminus this time. The last step towards obtaining the *squaratide* linear sequence involved a conjugate addition–elimination type reaction with the amino-group on Asp and Amino Squarate (**4.0a**) or 3-amino-4-ethoxycyclobut-3-ene-1,2-dion. **4.0a** was

synthesized by adapting a procedure first reported by Roth & Sporleder in 1970.[389] Characterisation available in the *Appendix*, see Figure S4.112 – S4.115. However, this conjugate addition reaction did not appear to proceed, as only starting materials were observed. Perhaps the poor reactivity was not too unsurprising, as the potential electron-donating ability of the -NH$_2$ group can reduce the rate-of-reaction towards ethyl ester elimination. Indeed, mono-squaramides – or mixed squaramates – tend to only be mildly electrophilic.[390] This combined with the *pseudo high-dilution* conditions of SPPS (afforded by the resin), may explain the poor reactivity.

DESq (**3.1**) – a di-ester – is much more electrophilic, and was used to try circumvent the poor reactivity observed above. Successful substitution of **3.1** onto the peptide-resin was achieved under the same reaction conditions, to produce intermediate **4.4**. The HPLC trace displayed one sharp UV peak with a t_R = 39 min. Strong ionisation was observed for the target mass of [M+H]$^+$ = 982.1 gmol^{-1} in positive mode and [M-H]$^+$ = 980.0 gmol^{-1} in negative mode (**Figure 4.13**).
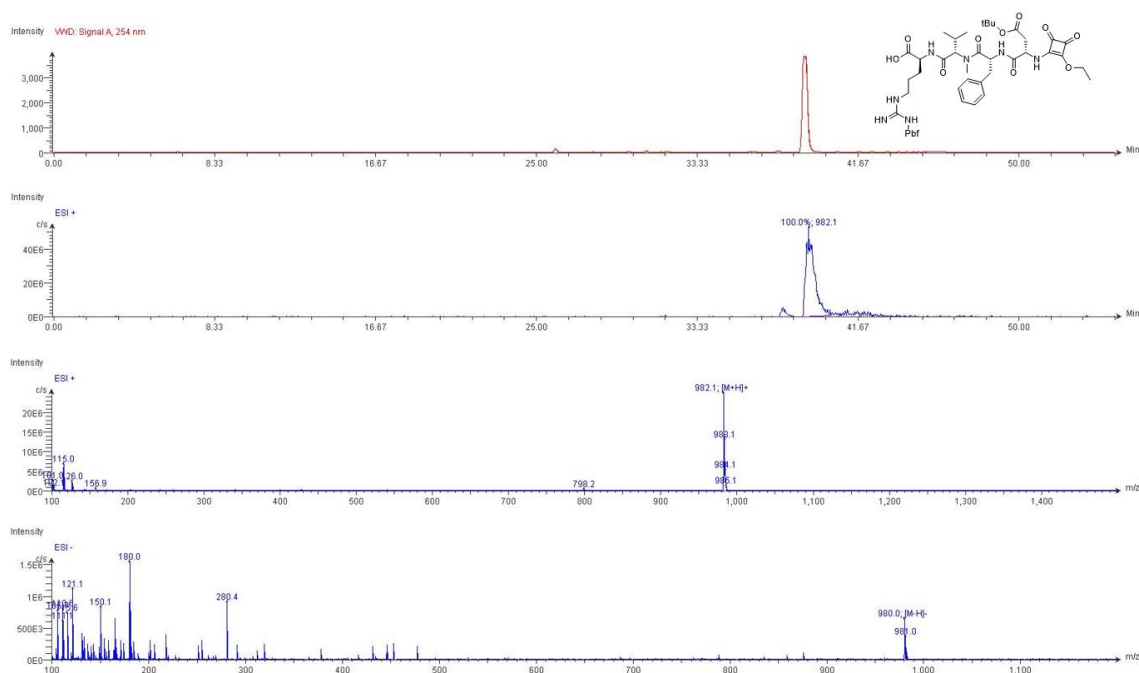
Figure 4.13: LC-MS data for **ESq-D(O*t*Bu)-f-*N*MeV-R(Pbf)-OH (4.4)**.

The mixed squaramate was then converted to its squaramide (-NH$_2$) derivative (**4.2**) via ethanolic ammonia. This synthetic work-around is highlighted below in **Scheme 4.3**.
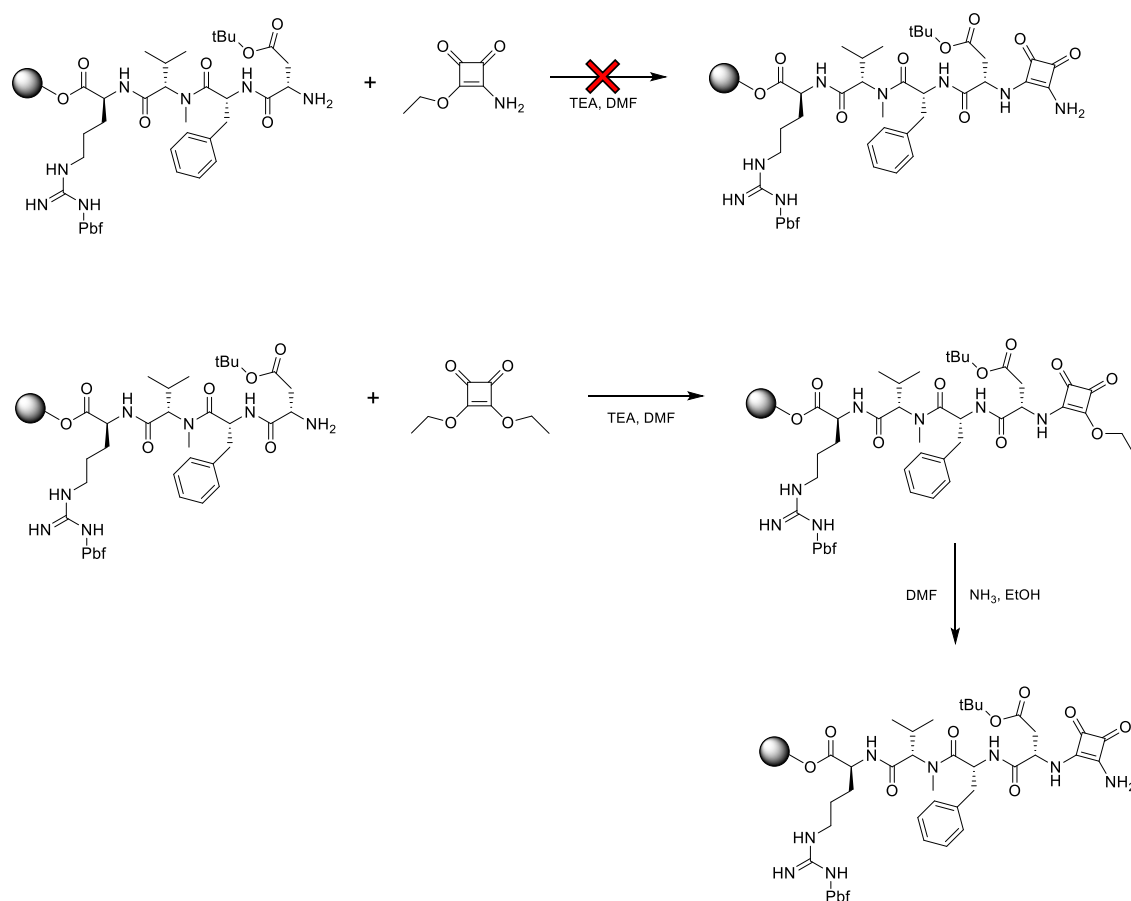
Scheme 4.3: Alternate synthetic route to achieve **ASq-D(O*t*Bu)-f-*N*MeV-R(Pbf)-OH (4.2)**.

The protected linear peptide was then cleaved from the resin using HFIP, and lyophilised prior to cyclisation via high-dilution conditions. However, the cyclisation reaction did not proceed, only the unreacted linear peptide was observed. This cyclisation reaction was carried out in different solvents (DMF, DCM & MeCN), different coupling reagents (PyBOP, HATU, EEDQ & EDCI) and bases (NMM, DIPEA & TEA), but unreacted starting material was observed each time. Electron density around the amino-nitrogen is withdrawn into the cyclobutene-ring by the highly electronegative carbonyl oxygens. Thus, the squaramide -NH$_2$ may be too poor a nucleophile to facilitate intramolecular cyclisation. A different approach was required, one that utilised a more reactive amine for cyclisation. This strategy involved coupling the squaramide -NH$_2$ to the *C*-terminus of arginine, and using its aliphatic *N*-terminal amino-group for intramolecular cyclisation. Unfortunately, similar poor reactivity was observed for this reaction, with no evidence for the target product being observed. These attempted synthesis are outlined in **Scheme 4.4**.
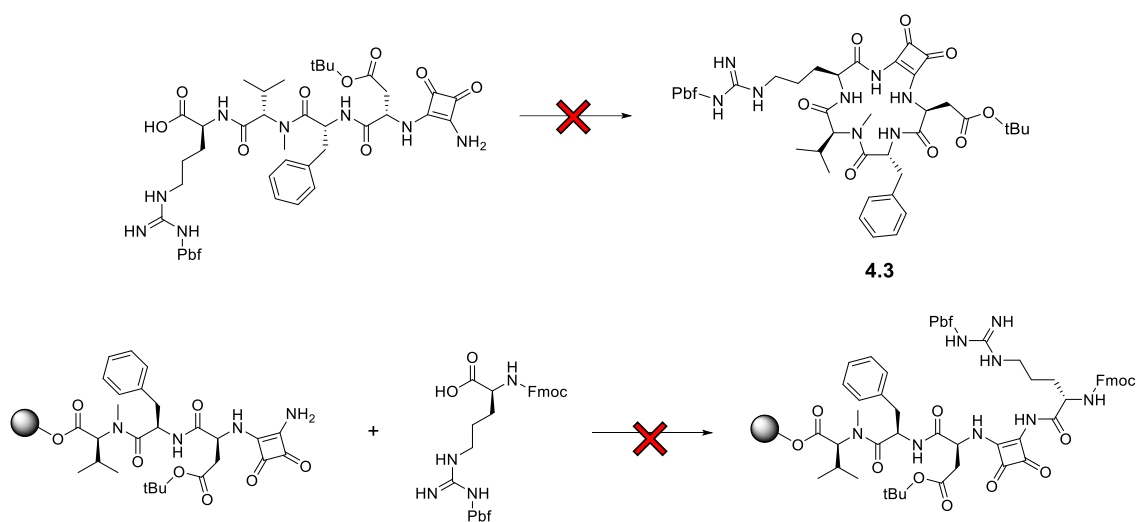
Scheme 4.4: Unsuccessful attempted synthesis to generate *Squaratide* – **4.3**.

The lessons learned from the above unsuccessful attempts prompted a rethinking of design strategy and a shift toward alternative approaches for this squaramide peptidomimetic. This synthetic compromise is discussed in more detail in the next section.

4.3.1 Alternate Design Strategy

This synthetic pathway involved modifying the natural amino acids to make them more reactive for inclusion into the *Squaratide backbone*, while retaining the important binding interactions afforded by their side-chain functionalities. *Amide-bond* formation between the squaramide-NH_2 group and the respective AA *C-*terminus proved to be synthetically challenging. To combat this, a different strategy was employed, where the carboxylic acid (of the amino acid) was converted to an alkyl-amino group. This primary amine can undergo (a traditional) nucleophilic substitution/elimination reaction without the need for coupling reagents. Although the native peptide (amide) bond is lost between the AA and the squaramide, this new bond was more synthetically achievable and perhaps, may be even more resistant to enzymatic degradation.

The first augmented AA employed was glycine, as this alkyl di-amine was commercially available (ethylene diamine). A schematic representation of the new design strategy is outlined in **Figure 4.14**.

Cilengitide - *c*RGDf*N*MeV

Squaratide - *c*R-Sq-Df*N*MeV (4.3)

Squaratide - *c*RG(*Ψ*)-Sq-f*N*MeV (4.8)
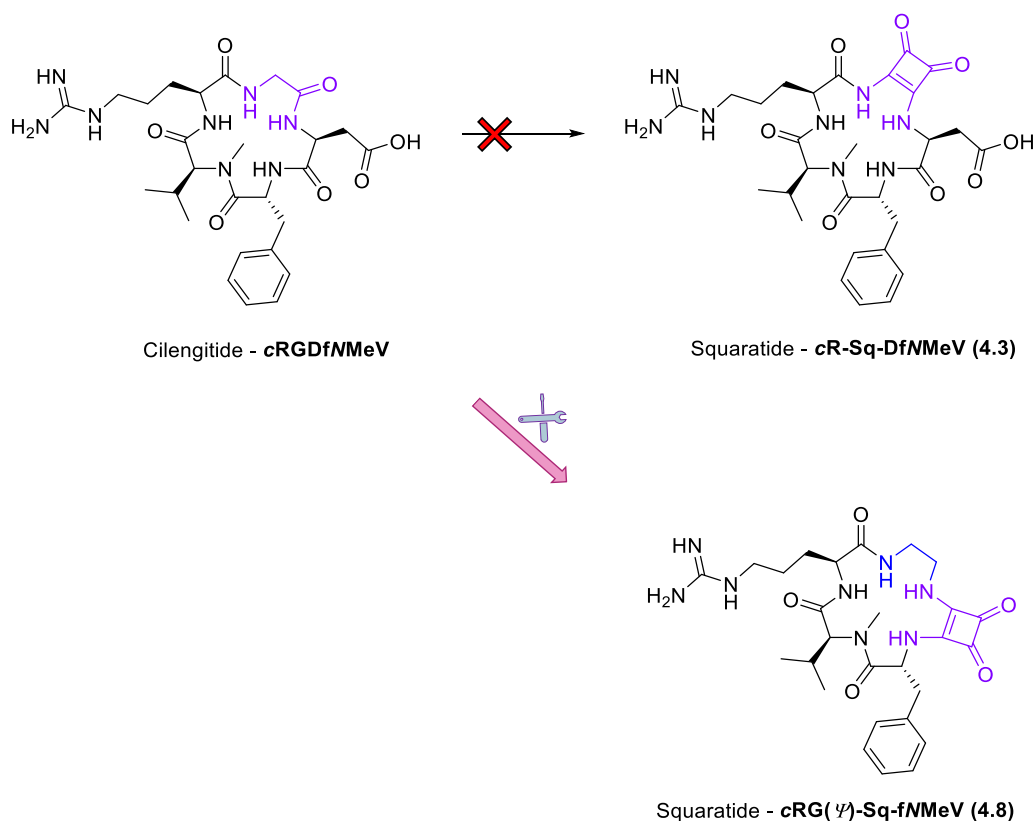
Figure 4.14: Synthetic alternative utilising Amino Acid alkyl di-amines. *Note:* (*ψ*) denotes the modified *C*-terminal Amino Acid.

The linear peptide (again) was assembled on 2-chlorotrityl chloride resin using the Fmoc/*t*Bu strategy. Learning from the lessons of the previous synthesis, DESq was functionalised directly onto the peptide sequence before the next reaction (**Scheme 4.5**).
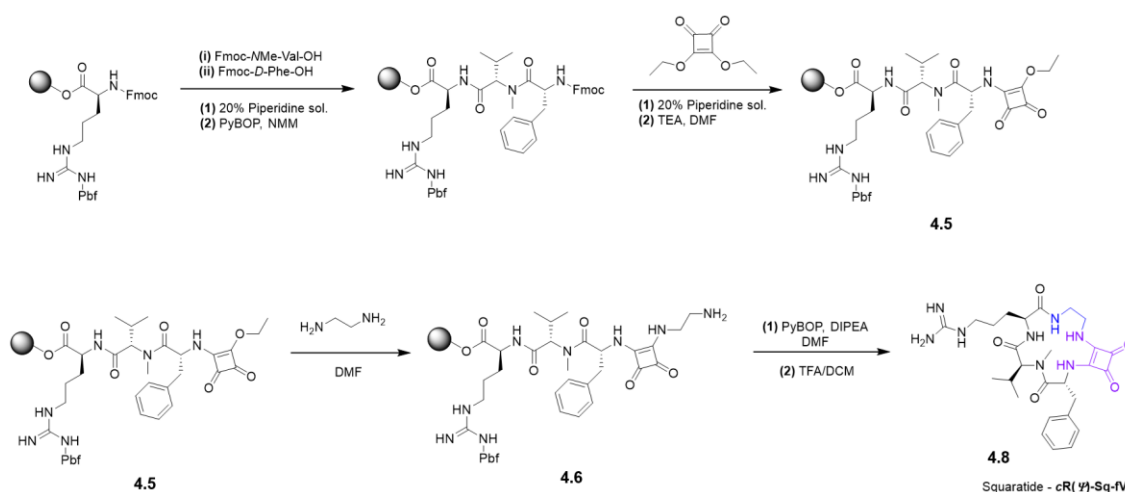
Scheme 4.5: Successful synthetic pathway for *Squaratide – c*RG(*ψ*)-Sq-f*N*MeV (4.8).

The last step towards completing the protected linear *squaratide* (**NH₂-G(*ψ*)-Sq-f-*N*MeV-R(Pbf)-OH, 4.6**) was to functionalise the sequence with

ethylene diamine (EDA) – the *C*-terminus removed, alkyl di-amine derivative of glycine. EDA is a very reactive molecule, and can even act as its own base. Thus, the use of additional organic bases (like before) was unnecessary for complete reaction. Characterisation of **4.6** was completed using LC-MS (**Figure 4.15**) and HRMS (Figure S4.8) data. The HPLC trace displayed one sharp UV peak with a t_R = 27 min, and strong ionisation was observed for the target mass of $[M+H]^+$ = 825.9 gmol^{-1} in positive mode and $[M-H]^+$ = 823.8 gmol^{-1} in negative mode, with HRMS confirming the target mass $[M+H]^+$ = 825.3961 gmol^{-1} possessing a mass error of -0.22 ppm.
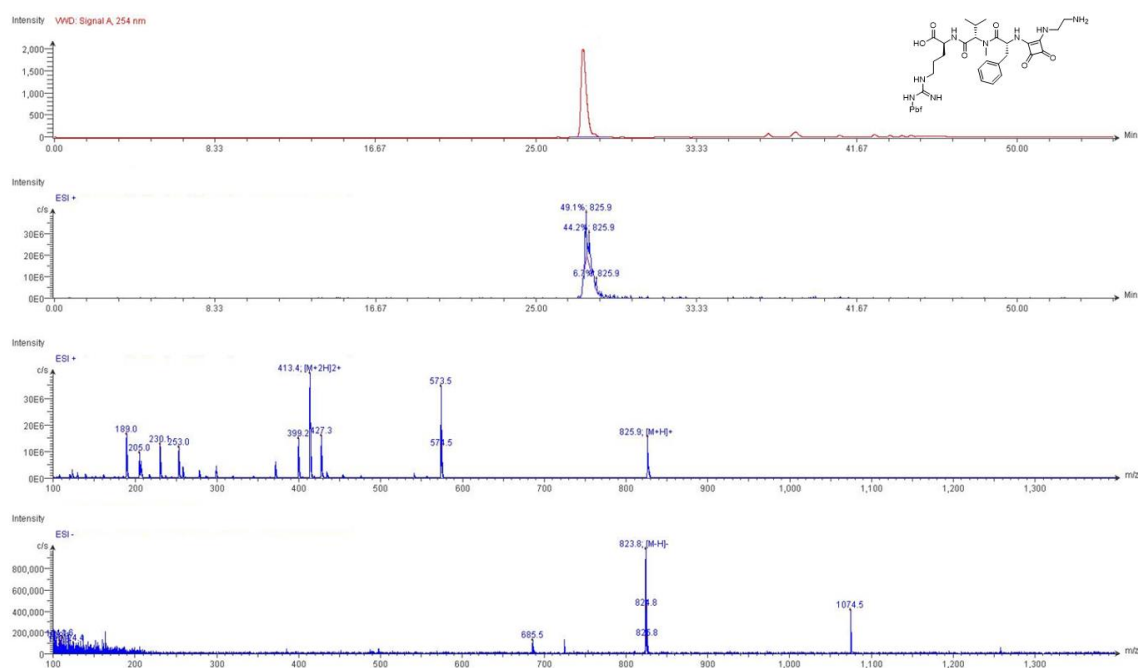
Figure 4.15: LC-MS data for linear squaratide – **NH$_2$-G(ψ)-Sq-*f-N*MeV-R(Pbf)-OH (4.6)**.

The intramolecular cyclisation was carried out under high-dilution conditions, to afford the *protected* cyclised product (***c*(RG(ψ)-Sq-f*N*MeV), 4.7**) as an off-white solid with a yield of 46%. Evidence for this successful cyclisation reaction was obtained from LC-MS (**Figure 4.16**) and HRMS (Figure S4.16) experiments. **4.7** possessed a larger retention time of t_R = 34 min, indicating that the previously free *C*-terminus and -NH$_2$ group (**4.6**) are no longer present and have likely been (intramolecularly) coupled together. The HPLC trace displayed one sharp UV peak, with ionisation observed for the target mass of $[M+H]^+$ = 807.2 gmol^{-1} in positive mode and $[M-H]^+$ = 805.1 gmol^{-1} in negative mode, with HRMS confirming this target mass $[M+H]^+$ = 807.3859 gmol^{-1} possessing a mass error of -0.05 ppm.
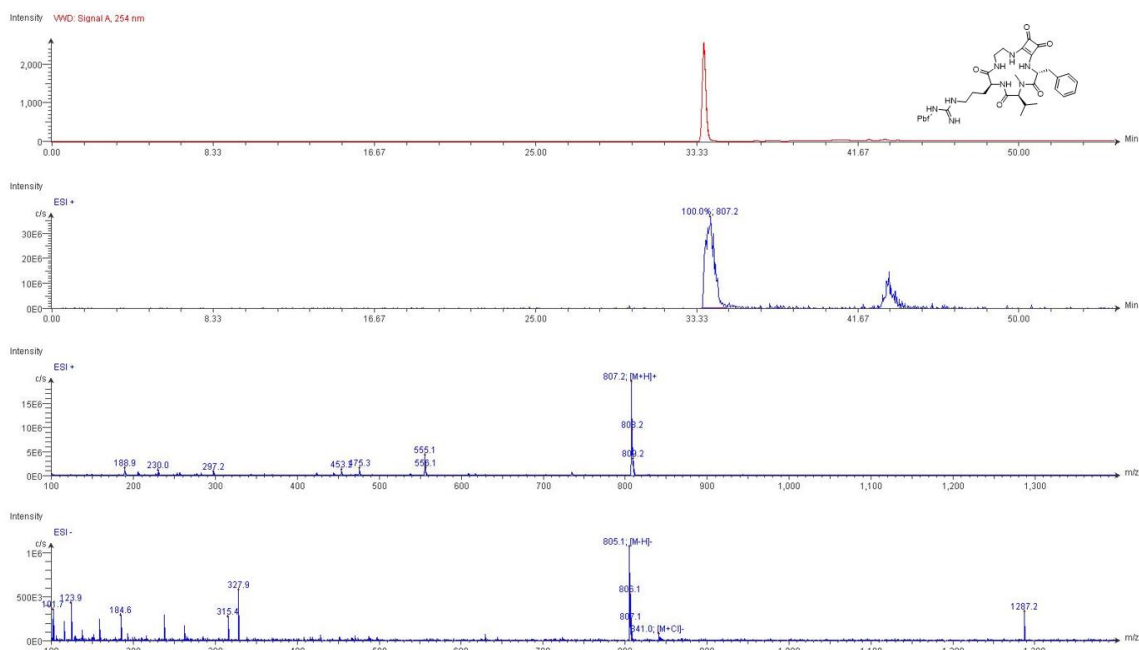
Figure 4.16: LC-MS data for the protected cyclic squaratide – *c*(**RG(ψ)-Sq-f*N*MeV) (4.6)**.

The final step was to deprotect the Pbf protecting-group on the arginine residue. This afforded the *deprotected* final product *c*(**RG(ψ)-Sq-f*N*MeV)** (**4.8**) as a white solid with a yield of 87%. The most intense UV peak on the HPLC trace corresponded to the product with a t_R = 24 min. Strong ionisation was also observed for the target mass of [M+H]$^+$ = 555.5 gmol^{-1} in positive mode, and [M-H]$^+$ = 553.4 gmol^{-1} in negative mode (**Figure 4.17**).
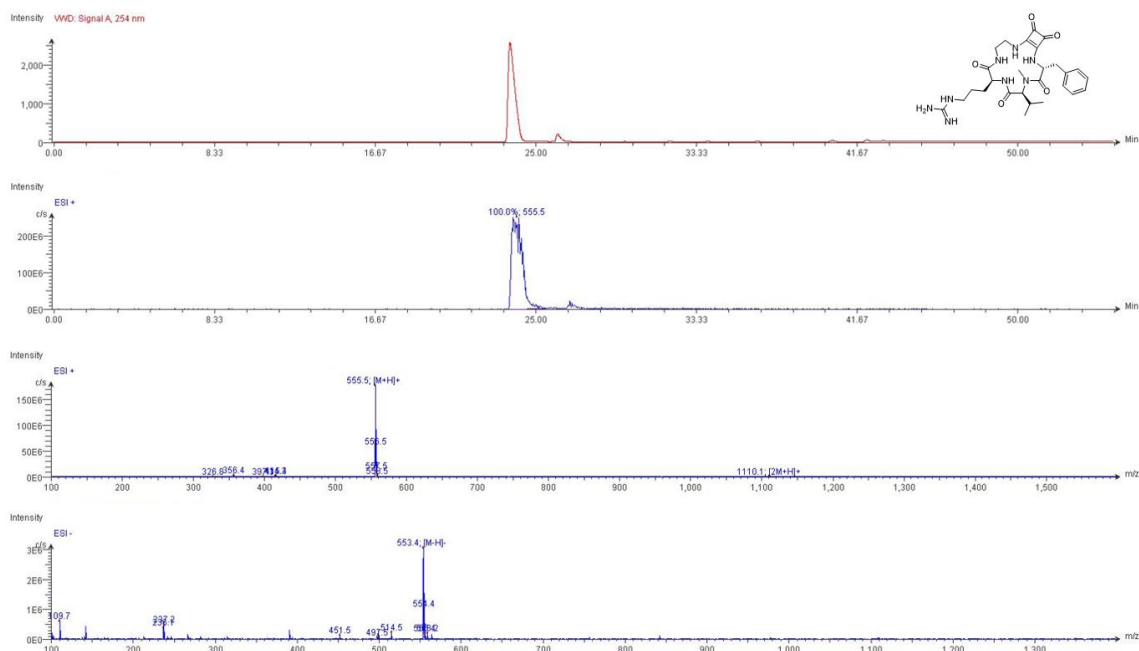
Figure 4.17: LC-MS data for the deprotected final cyclic squaratide – *c*(**RG(ψ)-Sq-f*N*MeV) (4.8)**.

Finally, HRMS was also used as a complimentary analysis to affirm the molecular formula of **4.8**, with confirmation of the target mass [M+H]$^+$ = 555.3038 gmol^{-1} possessing a low mass error value of 0.18 ppm (**Figure 4.18**).
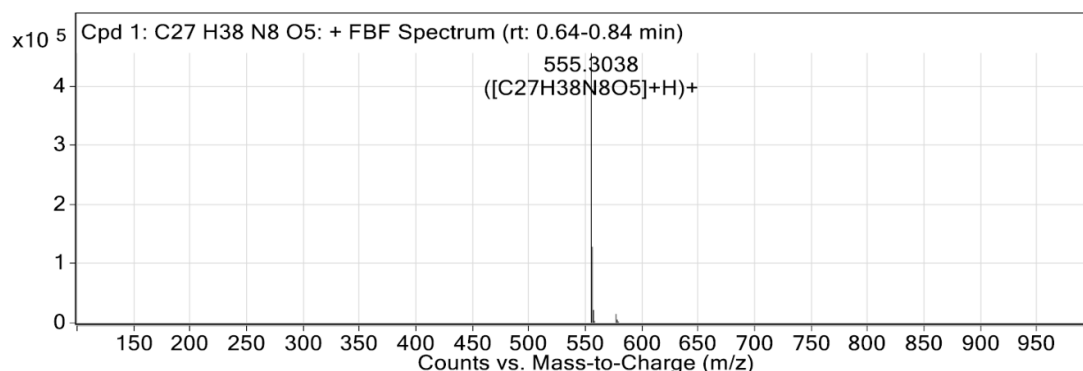
Figure 4.18: HRMS data for the deprotected cyclic squaratide **4.8**.

The above characterisation data provided enough evidence to suggest that the target compound **4.8**, was synthesized successfully. The next step was to try synthesize the other squaratide derivatives containing the modified alkyl di-amine amino acids. The aim was to replace each natural AA (five in total) with their di-amine counterpart, to produce 5 squaratide analogues (**Figure 4.19**).
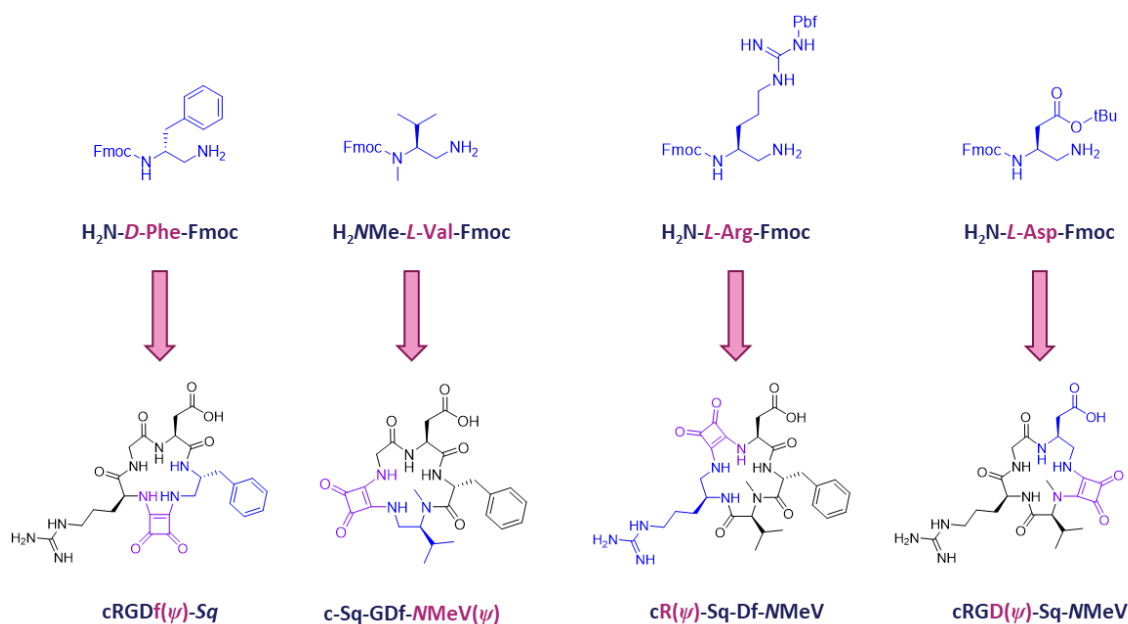
Figure 4.19: Four (future) target Squaratide analogues, depicting each alkyl di-amine amino acid.

4.3.2 Alkyl Di-amine Synthesis

The synthetic route to each alkyl di-amine is a multi-step pathway involving several AA-based intermediates before obtaining the final building block. A general scheme for the overall synthetic pathway is outlined in **Scheme 4.6**.
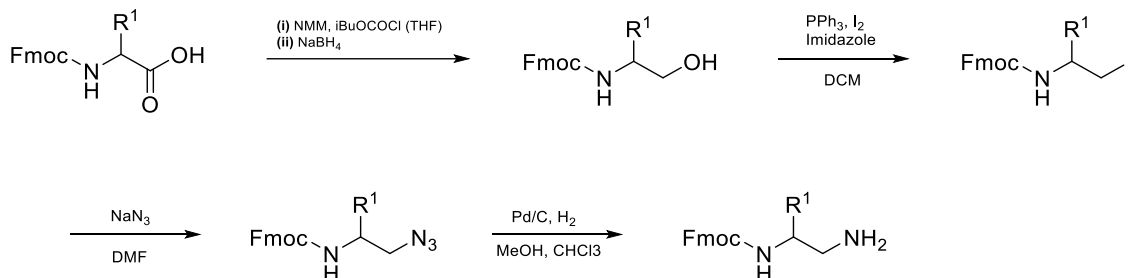
Scheme 4.6: General scheme for the synthesis of AA alkyl di-amines.

The above synthetic pathway has been adapted from that reported by Boeijen and coworkers.[391] The first step involved the reduction of the *C*-terminal carboxylic acid to its corresponding alcohol.[392] This hydroxy-group was then converted to an iodo-group via an S_N2-style *Appel* reaction.[393] The newly formed alkyl-iodide was then treated with NaN$_3$ to generate an alkyl-azide,[394] which was reduced (via Pd/C) to afford the N^β-Fmoc alkyl-amine product. Indeed, this procedure followed very similar reaction conditions for transforming each amino acid into its corresponding N^β-Fmoc alkyl-amine. With this in mind – and to avoid repetition – the synthesis described herein will focus on the pathway for only Fmoc-*D*-Phe-OH (**4.9a**). Characterisation and detailed experimental methods for the other amino acids can be found in the relevant *Procedure(s)* section and *Appendix*.

Commercially available **4.9a** (acid) was reduced to its corresponding alcohol (**Fmoc-*D*-Phe-ψ[CH₂OH], 4.9b**). This afforded the β-amino alcohol as white solid with a yield of 75%. This reaction was monitored via ^{1}H NMR (**Figure 4.20**) and DEPT 135 experiments. The ^{1}H NMR spectra of the commercial starting material (**4.9a**) and **4.9b** were overlayed to highlight the proton-peaks of interest. **4.9a** starting material (blue spectrum) displayed the -COOH proton of interest at 12.73 ppm integrating for 1H. This vastly downfield signal is characteristic of carboxylic acid protons, due to the electronegative nature of the carboxylate oxygen atoms. The red spectrum details the proton signals observed for **4.9b**, with the new -OH proton being observed as a broad triplet at 4.77 ppm integrating for 1H. In both cases we can see the appearance/disappearance of

certain characteristic peaks. Indeed, the -COOH signal that is present in the starting material is no longer observed in the product spectrum. Instead, a new peak corresponding to the reduced (alcohol) functionality is observed.
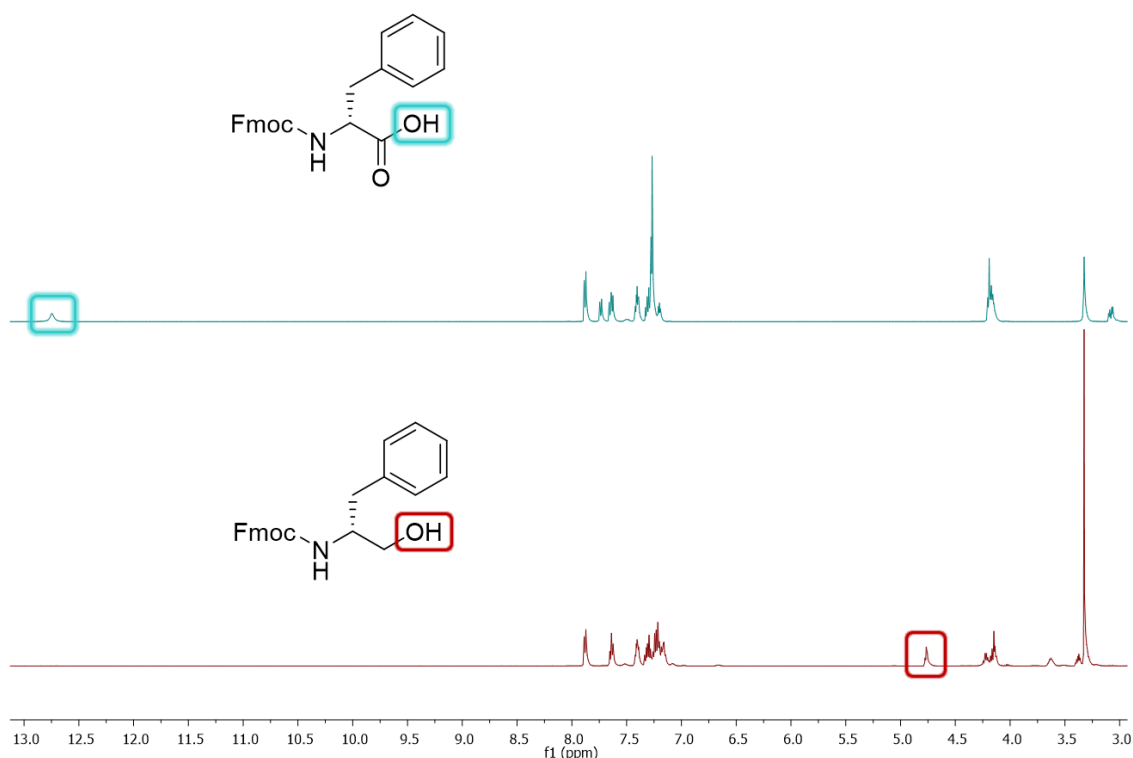
Figure 4.20: ^{1}H NMR spectra of (Top) Fmoc-*D*-Phe-OH starting material (**4.9a**), and (Bottom) β-amino alcohol (**4.9b**) in DMSO-*d$_6$*.

This colour scheme; blue spectrum = starting material and red spectrum = product, will be used throughout the characterisation. Another method to track the reduction of -COOH to -OH is to monitor the newly formed -CH$_2$ functionality. An elegant way to view this is to distinguish the ^{13}C signals via DEPT 135. The DEPT (Distortionless Enhancement by Polarisation Transfer) experiments gracefully combine the coherence-transfer techniques from the Insensitive Nuclei Enhanced by Polarisation Transfer (INEPT) experiment with the *spin-echo* protocol of the Attached-proton Test (APT). This strategic manipulation of nuclear spins produces spectra featuring both signal enhancement and distinct separation of methine (-CH), methylene (-CH$_2$), and methyl (-CH$_3$) resonances (**Figure 4.21**).[395] DEPT 45 produces a spectrum with all positive signals – similar to a traditional 1D-^{13}C NMR, except the quaternary carbons are omitted. DEPT 90 only displays -CH signals, and DEPT 135 displays -CH & -CH$_3$ signals in the positive, with -CH$_2$'s in the negative.
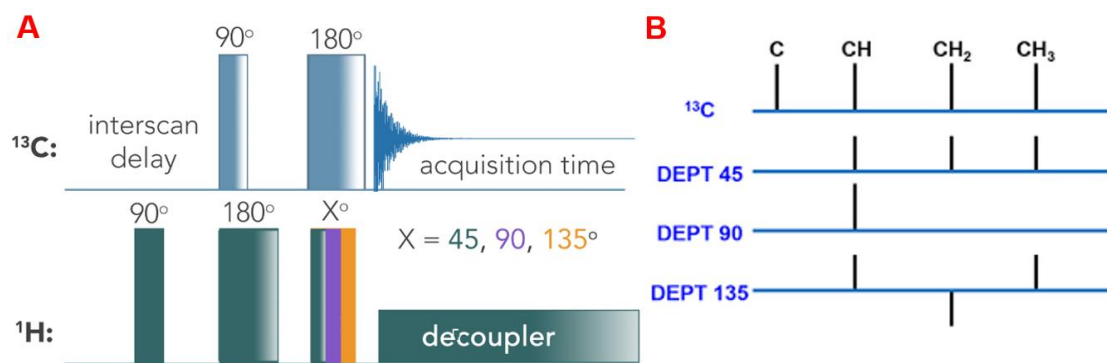
Figure 4.21: (A) DEPT experiments differing in flip-angle (45°, 90° & 135°) magnitude of the ^{1}H selection pulse. (B) Example DEPT spectra highlighting signal variation.

DEPT 135 was used for this analysis as it would very obviously highlight the new -CH$_2$ peak of interest. Like before, the DEPT 135 spectra of **4.9a** and **4.9b** were overlayed (**Figure 4.22**). The starting material spectrum produced two *negative-phase* peaks at 36.36 & 64.89 ppm, corresponding to the -CH$_2$ group on the side-chain and the -CH$_2$ beside the Fmoc-carbamate linkage, respectively. Upon reduction of the carboxylic acid, a -CH$_2$ signal appeared at 62.76 ppm, indicative of the newly formed hydroxy-group.
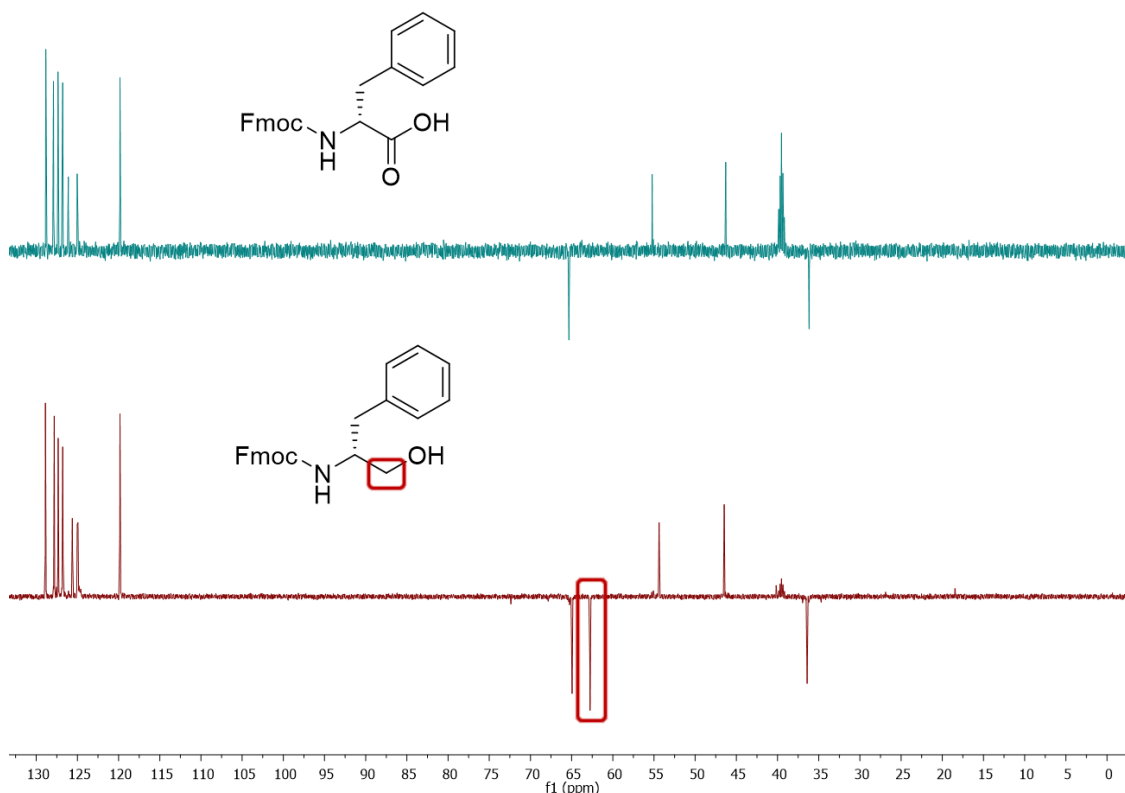
Figure 4.22: DEPT 135 spectra of (Top) **4.9a**, and (Bottom) **4.9b** in DMSO-d_6.

The ability of DEPT 135 to track the backbone (*) β-CH$_2$ chemical shift is a great way to monitor reaction progress and provide evidence of successful

synthesis. Indeed, this technique will be employed throughout the N^β-Fmoc alkyl-amine synthesis. The next step was to replace the hydroxy-group with an iodo-functionality, via a modified *Appel* reaction. ^{1}H NMR (**Figure 4.23**) and DEPT 135 experiments were again used track reaction progress and characterise the β-amino iodide product (**Fmoc-D-Phe-ψ[CH$_2$I], 4.9c**).
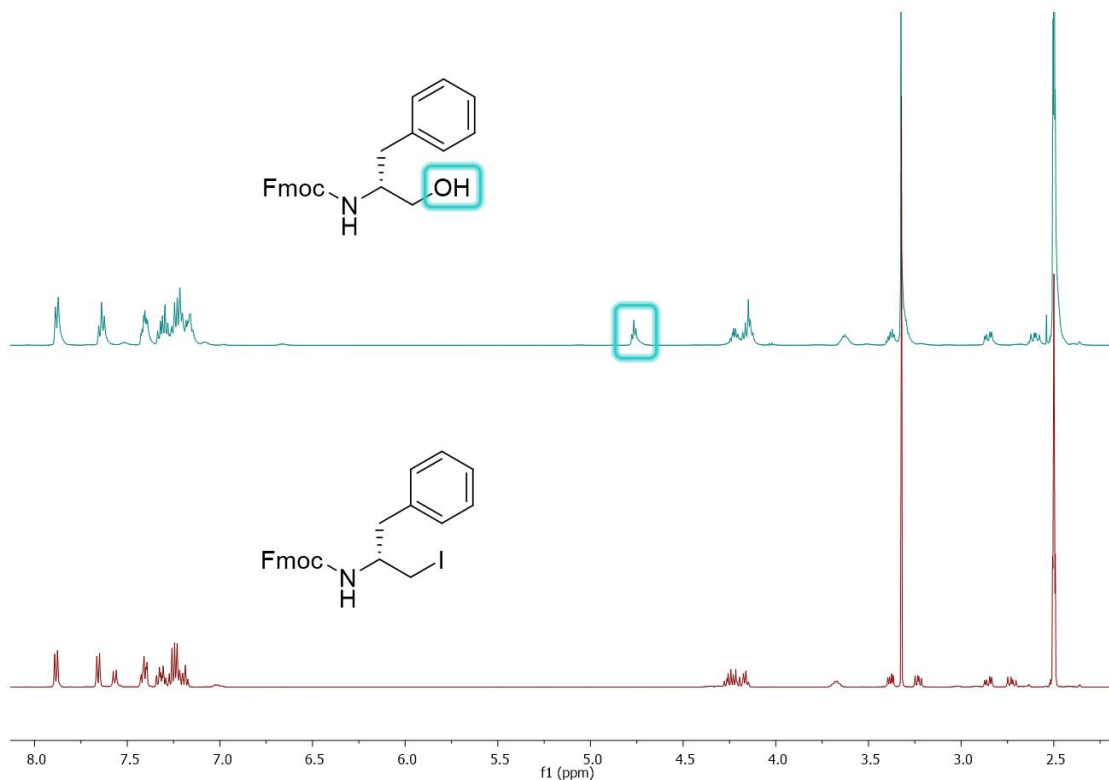
Figure 4.23: ^{1}H NMR spectra of (Top) Fmoc-D-Phe-ψ[CH$_2$OH] starting material (**4.9b**), and (Bottom) β-amino iodide (**4.9c**) in DMSO-d_6.

The ^{1}H NMR spectrum of **4.9c** remained unchanged for the most part. However, the previous (**4.9b**) -OH triplet at 4.77 ppm has now disappeared, as was replaced by the iodo-group. To confirm this, DEPT 135 experiments were carried about to observe the chemical-shift change of the β-CH$_2$ signal (**Figure 4.24**). Interestingly, β^*-CH$_2$ signal had shifted dramatically upfield from 62.76 ppm (-CH$_2$OH) to 12.61 ppm (-CH$_2$I), resulting in a chemical-shift change of -50.15 ppm. The β^*-CH$_2$ signal for **4.9b** was not observed in the spectrum for **4.9c** (Red), suggesting an efficient conversion from starting material to product.
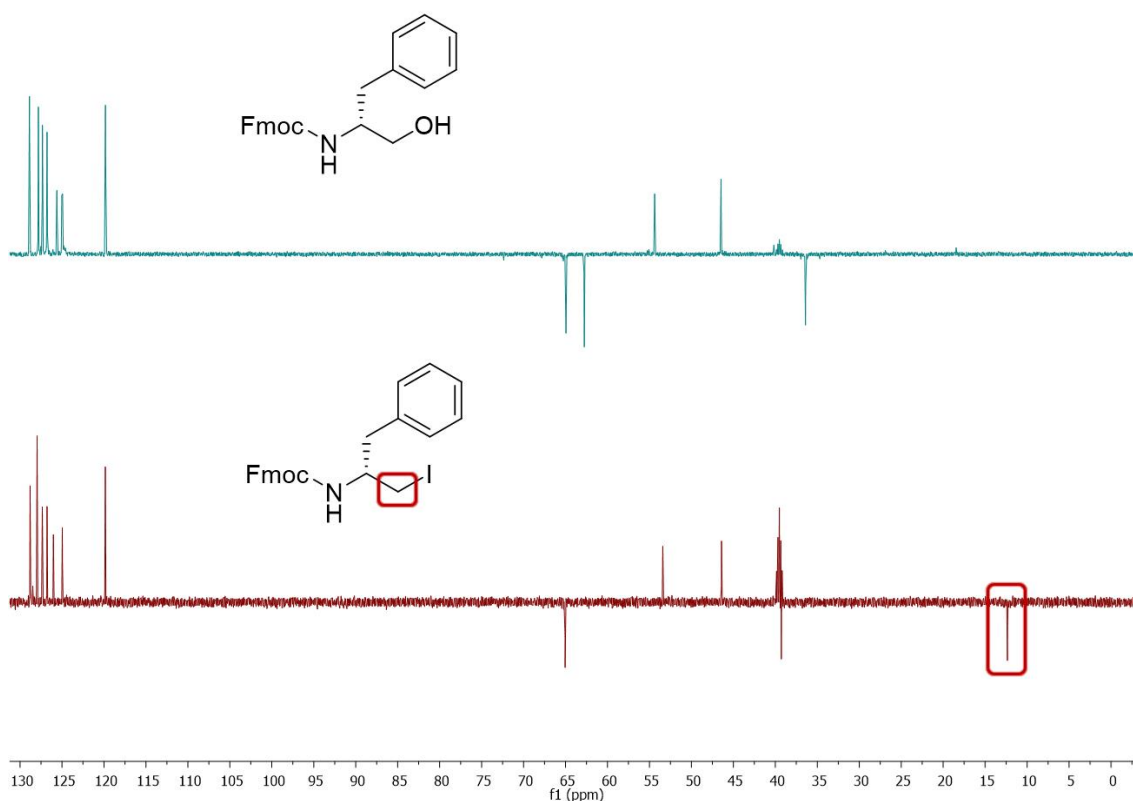
Figure 4.24: DEPT 135 spectra of (Top) **4.9b**, and (Bottom) **4.9c** in DMSO-d_6.

When an atom beyond the third period of the Periodic Table is bonded to the nucleus of interest, relativistic terms need to be taken into account. These atoms – often referred to as heavy atoms (HA) – exert significant effects on the shielding constant of light atoms (LA), which in turn, impacts the chemical shift, particularly at a one-bond distance (**Figure 4.25**).[396]
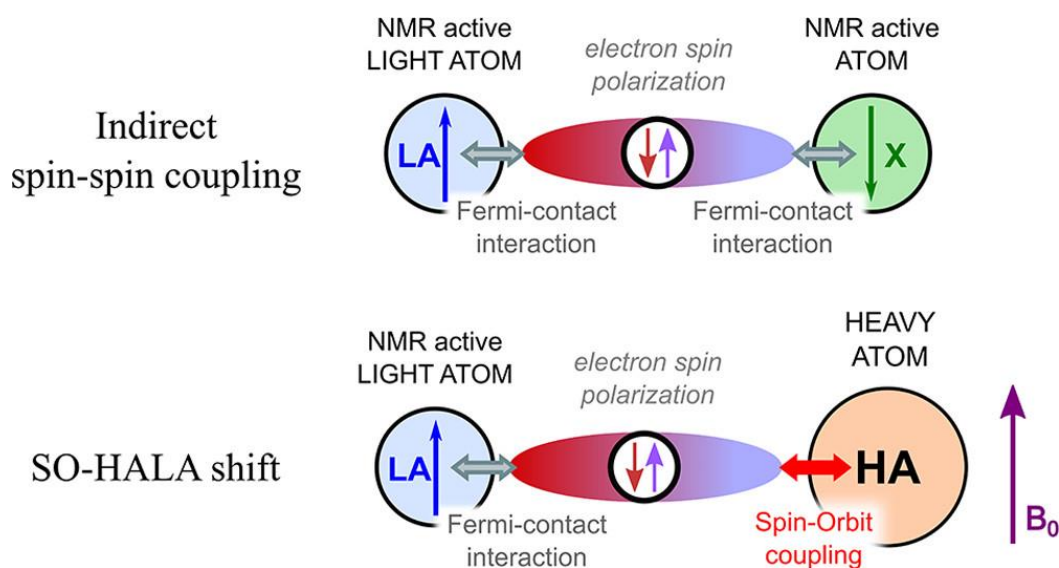
Figure 4.25: Cartoon illustration of the interactions between the Fermi-contact mechanism of the indirect spin-spin coupling constant and that of the spin-orbit coupling HALA shift.[396]

169

This is a good example of the profound shielding effect imposed on ^{13}C nuclei by iodo-groups.[397] This HA-LA phenomenon can be explained by the spin-orbit coupling (SO) of the heavy atom. The presence of the SO contribution results in a non-zero electron-spin density being induced at the heavy atom when a magnetic-field (B_0) is applied, and this spin-polarisation extends to the adjacent light atom.[398] Subsequently, the spin density interacts with the nuclear magnetic moment of the light atom (^{13}C in this case) through a Fermi-contact (FC) mechanism,[399] this resulted in a chemical-shift change of the β^*-CH$_2$ signal.

The newly formed **4.9c** was then treated with NaN$_3$ to generate the alkyl-azide product (**4.9d**) with a yield of 51%. The β^*-CH$_2$ signal of **4.9d** – from the DEPT 135 spectrum (**Figure 4.26**) – had shifted downfield from 12.61 ppm (-CH$_2$I) to 53.56 ppm (+40.95 ppm), an almost complete chemical-shift reversal from the previous reaction. It is also noted that there are other negative-phase signals observed in this region. However, this sample is rather dilute, thus these are suspected to be baseline artifacts, as the sample appeared to be pure (see Figure S4.20 – 4.23).
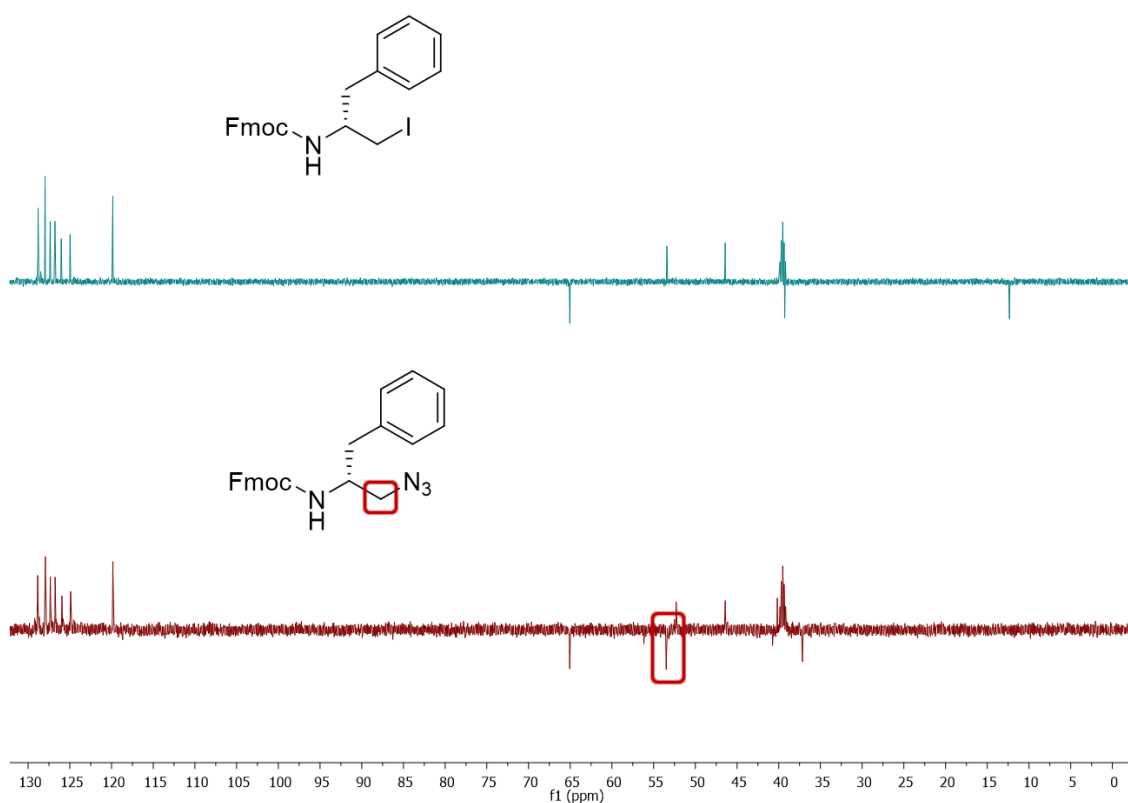
Figure 4.26: DEPT 135 spectra of (Top) Fmoc-D-Phe-ψ[CH$_2$I] starting material (**4.9c**), and (Bottom) alkyl-azide (**4.9d**) in DMSO-d_6.

Another visually appealing way to track this alkyl-azide formation is via IR Spectroscopy (**Figure 4.27**). The new azide-stretch (red spectrum) appeared as a strong, sharp band at 2096 wavenumbers (cm^{-1}), which was not present in the β-amino iodide starting material (blue spectrum), thus providing more evidence for the successful synthesis of **4.9d**.
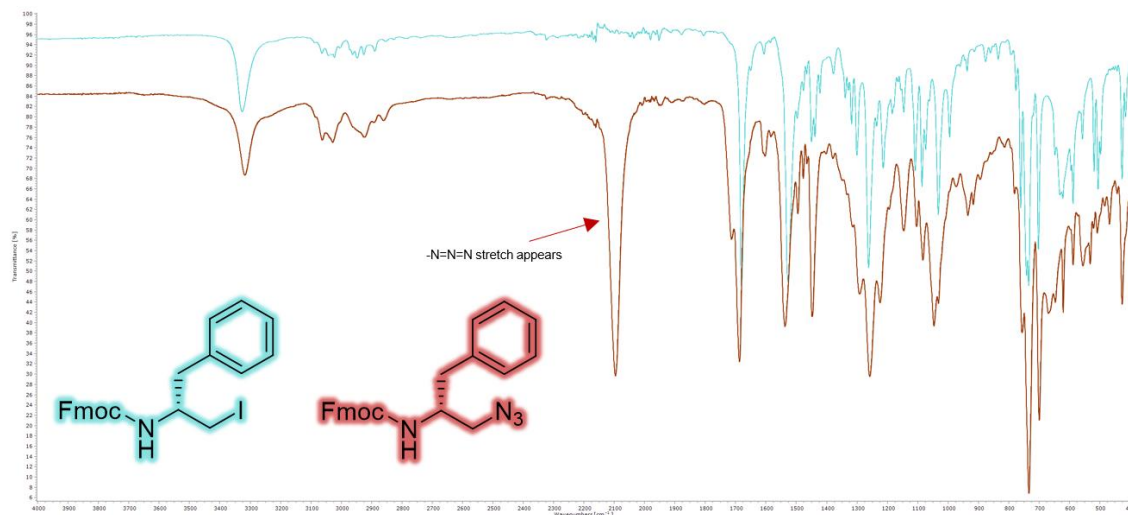
Figure 4.27: FTIR-ATR spectra of (Top) **4.9c**, and (Bottom) **4.9d**.

The last step was to reduce the alkyl-azide to its corresponding N^{β}-Fmoc alkyl-amine (**4.9e**) via Pd/C, this reaction proceeded with an 83% yield. This time the IR spectrum of the alkyl-amine product possessed no azide-stretch, indicating the complete reduction of the alkyl-azide starting material (**Figure 4.28**).
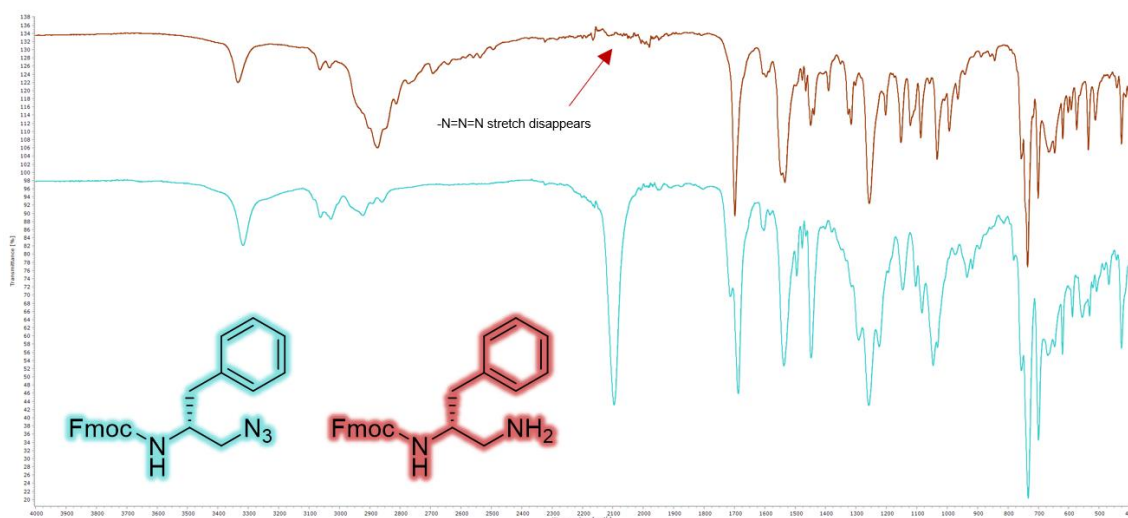
Figure 4.28: FTIR-ATR spectra of (Top) N^{β}-Fmoc alkyl-amine (**4.9e**), and (Bottom) Fmoc-*D*-Phe-ψ[CH$_2$N$_3$] starting material (**4.9d**).

Again, the DEPT 135 spectrum for **4.9e** highlighted the β^*-CH$_2$ signal at 41.88 ppm (**Figure 4.29**), a -11.68 ppm upfield-shift from **4.9d** (53.56 ppm). This upfield-shift is due to the *shielding ability* of the amino-NH$_2$ group. However, it does not shield the β^*-CH$_2$ as strongly as the iodo-functionality.
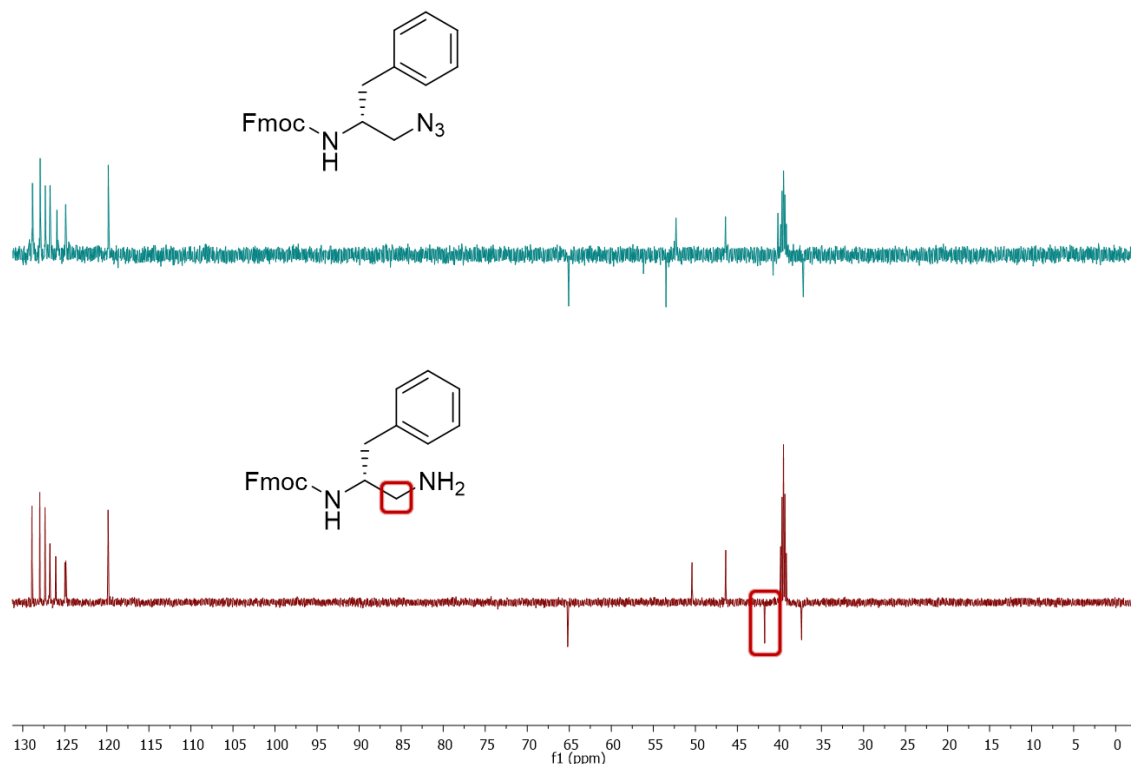
Figure 4.29: DEPT 135 spectra of (Top) **4.9d**, and (Bottom) **4.9e** in DMSO-d_6.

After each sequential stage of the synthesis, the corresponding β^*-CH$_2$ signal of the starting material was not observed in the product. This was a key indicator that each functional-group had been changed successfully (**Figure 4.30**). This was further corroborated by ^{1}H NMR and IR analysis – with LC-MS, ^{13}C NMR, COSY, HSQC and HMBC experiments being documented in the *Appendix* (see Figure S4.33 – 4.40). Similar characterisation was carried out for **Fmoc-Val-ψ[CH$_2$NH$_2$] (4.10e)** (Figure S4.62 – 4.72), **Fmoc-Asp(OtBu)-ψ[CH$_2$NH$_2$] (4.11e)** (Figure S4.84 – 4.91) and **Fmoc-Arg(Pbf)-ψ[CH$_2$N$_3$] (4.12d)** (Figure S4.105 – 4.111).
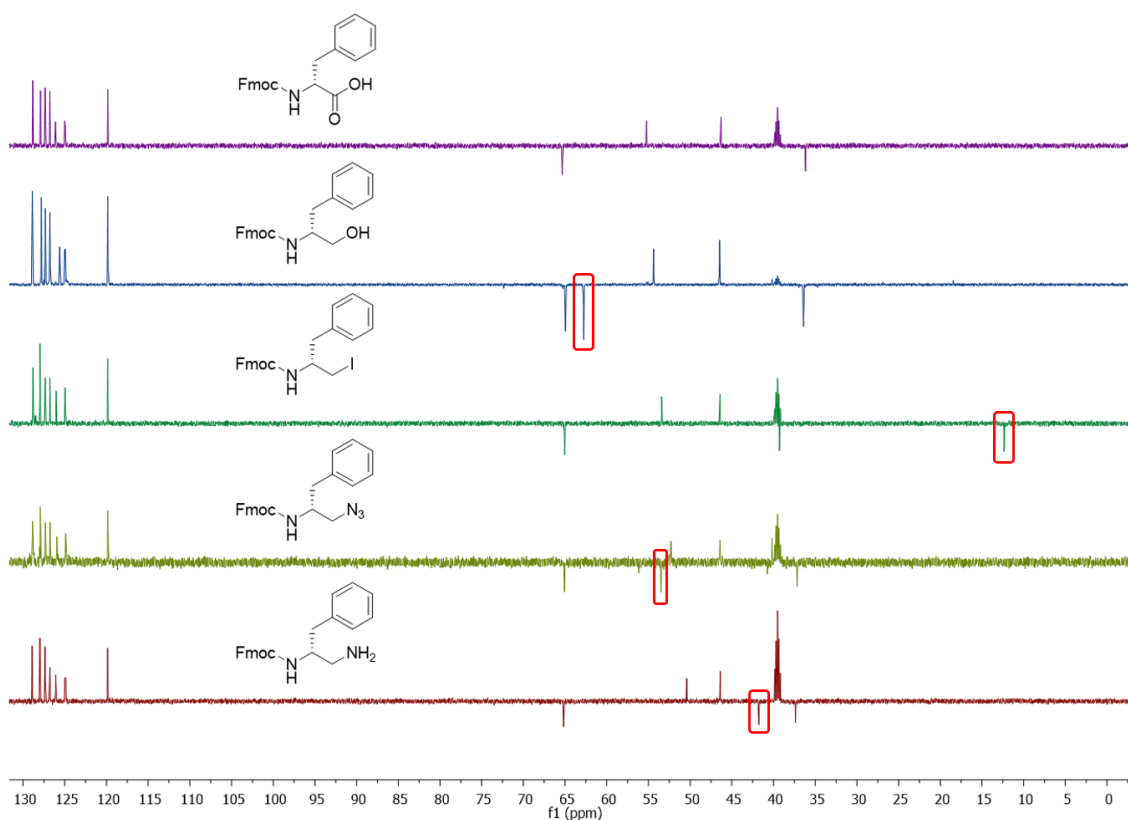
Figure 4.30: DEPT 135 comparison of the different β*-CH$_2$ chemical shifts, from the Fmoc-*D*-Phe-OH starting material (purple) to the N^β-Fmoc alkyl-amine product (red).

To synthesize the protected linear Squaratides on resin, each newly synthesized N^β-Fmoc alkyl-amine amino acid would be reacted under similar conditions for that used to produce the linear Gly derivative (**4.6**). Unfortunately, due to synthetic and purification difficulties, there was not enough time left to attempt this synthesis. Even the synthesis of one N^β-Fmoc alkyl-amine amino acid was a time-consuming, multi-step pathway that required multiple purification runs, with poor yields being observed for some steps.

4.4 Conclusions

In conclusion, initial attempts to synthesis the glycine-substituted Squaratide derivative (**4.3**) of Cilengitide were unsuccessful. Many different synthetic routes were explored to potentially overcome these synthetic difficulties. In the first case, the -NH$_2$ group on **4.0a** was not reactive enough to facilitate intramolecular cyclisation, as no cyclic product was observed. This cyclisation reaction was carried out in different solvents (DMF, DCM & MeCN), different coupling reagents (PyBOP, HATU, EEDQ & EDCI) and bases (NMM, DIPEA & TEA), but unreacted linear peptide (**4.2**) was observed each time. Indeed, this poor nucleophilicity was encountered again, with traditional (on resin) coupling between **4.0a** and Asp(O*t*Bu)-COOH resulting in unreacted starting material. A different strategy was required, as the amide-bond between the squaramide residue and the *C*-terminal amino-acid proved to be synthetically challenging.

A synthetic compromise was achieved with a slightly different design strategy. This involved the removal of the Squaramide-amide target functionality, and replacing it with a regular squaramide motif (on the linear sequence). This strategy reversed the reactivity of the system, with the squaramate now acting as the electrophile instead of the nucleophile (**4.2** in the first attempt), and vice versa – the amino acid operating as the nucleophile instead of the electrophile. This was done by converting the (commercially available) amino-acid *C*-terminus (-COOH) to an aliphatic amino-group (-NH$_2$) through a multi-step functional-group interchange pathway (**Scheme 4.6**). This synthetic conversion retained the natural side-chain functionality of the respective amino acid(s), but greatly increased their reactivity towards nucleophilic substitution with the linear squaramate-sequence on resin.

The first *Squaratide* to be synthetically attempted – featuring this alkyl-amine amino-acid derivative – was **4.8**. This molecule featured a *C*-terminal modified glycine – which was conveniently available as ethylene di-amine, and was chosen as the starting point to trial this new synthetic design strategy (**Figure 4.31**).

Cilengitide - *c*RGDfV

Squaratide - *c*R-Sq-DfV (4.3)

Squaratide - *c*RG(*ψ*)-Sq-fV (4.8)
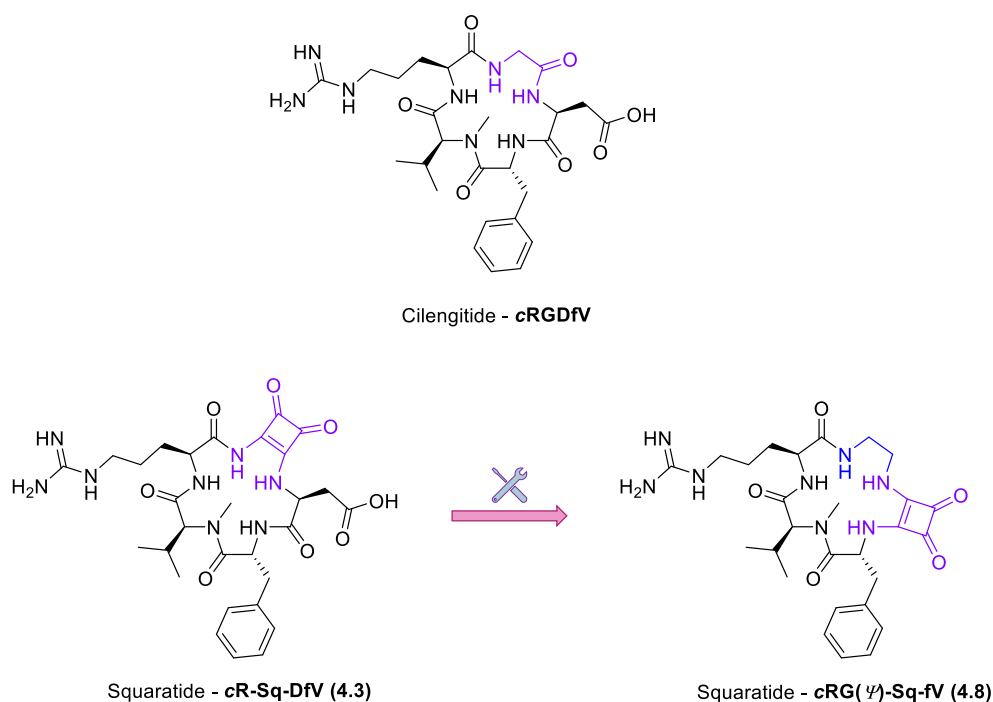
Figure 4.31: Structural comparison of (Top) Native Cilengitide, (Bottom left) Initial synthetic attempt, and (Bottom right) Synthetic compromise via alkyl-amine design strategy. <u>*Note:*</u> **(*ψ*)** denotes the modified *C*-terminal Amino Acid.

This design strategy proved to be effective, as the successful synthesis of **4.8** was evidenced by LC-MS analysis and molecular formula was confirmed via HRMS. Although we ran out of time to apply this strategy for the synthesis of other Squaratides, a versatile methodology was developed for the synthesis of their respective N^β-Fmoc alkyl-amine amino acids. Future work will involve using these modified amino acids to produce the other 4 cyclic squaratide derivatives (**Figure 4.19**). Once sufficient amounts of these cyclic compounds have been generated, their metabolic stability – compared to native Cilengitide – will be investigated.

Future work will also involve investigating if the chirality of the alkyl-amines (and peptide intermediates) has been compromised (racemisation). Spectroscopic and chromatographic methods are commonly employed to assess enantiomeric purity, differentiate between stereoisomers, and establish absolute configuration.[400] ^{1}H NMR may be an efficient technique for this investigation. Determining enantiomeric purity via NMR necessitates employing a chiral auxiliary to transform the enantiomeric mixture into a diastereoisomeric one. Provided there is a significant chemical shift change to achieve proper signal separation, integration yields a straightforward assessment of diastereoisomeric

composition, directly correlating with the original mixture's enantiomeric composition.[401] Another effective technique that could also be used for this analysis, is chiral HPLC. Chiral HPLC separates enantiomers based on their differential interactions with a chiral stationary phase. The stationary phase is typically composed of a chiral molecule, or a chiral additive bonded to a solid support (e.g. polysaccharides, cyclodextrins).[402] Enantiomers with stronger interactions with the chiral stationary phase will have longer retention times in the column compared to enantiomers with weaker interactions. As a result, the enantiomers elute from the column at different times, achieving separation.

This chapter was synthetically very challenging, with many unsuccessful reactions. However, an equally-exciting synthetic workaround was generated that allowed us to produce a cyclic Squaratide derivative of Cilengitide. This novel design strategy will potentially pave the way for more squaramide-based Cilengitide derivatives in the future, and investigate if squaramides can be used for the generation of peptidomimetics.

Chapter 5

Thesis Summary

5. Thesis Summary

The importance of luminescent peptide sensors and peptidomimetics lies in their ability to address challenges in detection, imaging, drug development, and various other fields. The overarching aim of this thesis was to highlight the potential of peptide-based technologies to offer innovative solutions towards a broad area of application, such as, advancing research and contributing to improvements in healthcare, environmental monitoring, and materials science.

Chapter 2 detailed a versatile methodology for the synthesis of a caspase-3 selective ratiometric probe (Ac-DEVD-PABC-Naph). This probe underwent a self-immolative process that released the free Naph fluorophore, which produced a ratiometric change in fluorescence. Quantification of enzyme activity by the ratiometric change at two distinct wavelengths can quantitatively measure enzyme activity with increased accuracy. Indeed, Ac-DEVD-PABC-Naph displayed an absorbance band at 372 nm before the addition of caspase-3 and 432 nm after treatment with caspase-3. Likewise, a fluorescence emission maxima was observed at 475 nm for the unhydrolysed probe, and 535 nm after incubation (120 min) with caspase-3. This clearly demonstrate the time-dependant ratiometric fluorescent response generated by the probe for the visualisation of caspase-3. Enzyme kinetics such as K_m (46.4 μM), k_{cat} (0.51 sec^{-1}), and *LOD* (4.96 ng/ml) were obtained using a non-linear regression via *GraphPad™ Prism®* software. The selectivity of the probe was also found to satisfactory, with none of the endogenous biomolecules or enzymes tested (including caspase-6) generating a fluorescence ratio change.

Building on this design strategy, a red-emitting naphthalimide fluorophore (AS-Naph) was synthesized for the (potential) enhanced visualisation of caspase-3. This fluorophore displayed a NIR emission maxima (λ_{max}) around 630 nm, with bright red fluorescence. The idea was to functionalise AS-Naph in a similar fashion to our previous (blue-to-green) peptide probe. However, the compound's fluorescent output was found to be quenched in aqueous environments, thus hindering its application.

Chapter 3 ventured to utilise a different kind of luminescence – analogous to organic fluorophores – from lanthanide metal-centres. The prolonged

luminescence lifetimes of emissive Ln^{3+} complexes facilitates the use of time-gated detection techniques to remove the inherent autofluorescence present biological fluorophores, thus enhancing the signal-to-noise ratio of the luminescence output. Additionally, their ability to tune emission colours, and their high quantum yields make them an attractive alternative to traditional organic fluorophores. With this in mind, an extensive family of novel, water-soluble squaramide-based cyclen ligands with varying symmetry and substitution patterns (**3.4** – **3.17**) were synthesized, including one ligand that may have the potential to act as a lanthanide-based caspase-3 probe (**3.19**).

UV-vis absorbance spectra were recorded for each ligand, with the mono-substituted squaramide-DO3A ligands displaying a wavelength maximum (λ_{max}) in the range of 279 – 301 nm. Ligand **3.4** was then complexed to form **[Tb(3.4)]** and **[Eu(3.4)]**. Preliminary luminescence spectra were then recorded for each complex (20μM) in H_2O. **[Tb(3.4)]** displayed intense line-like Tb^{3+}-centred transitions at λ_{max} = 490, 545, 584, 622, 648, 667 and 679 nm, corresponding to the deactivation of the $^5D_4$ state to the ^7F_x (x = 6-0) states. **[Eu(3.4)]** only produced weak Eu^{3+}-centred transitions at λ_{max} = 590, 610 and 700 nm.

Chapter 4 combined our experience with peptide synthesis (from chapter 2) and squaramide synthesis (from chapter 3) to investigate the use of squaramides as potential peptidomimetics. The aim was to generate a synthetic analogue of a previous pharmaceutical drug – *Cilengitide* – that (unfortunately) failed at phase III clinical trials. Insertion of a squaramide moiety into the Cilengitide-backbone may be an interesting approach for improving the drug's half-life and duration of action. Rationale for this hypothesis can be found in the ability of squaramides to act as both hydrogen-bond donors and acceptors – supporting the types of non-covalent interactions available to peptides.

Initial attempts to synthesis the glycine-substituted Squaratide derivative (**cR-Sq-DfV**) of Cilengitide were unsuccessful. Many different synthetic routes were explored to potentially overcome these synthetic difficulties, but ultimately, a redesign of synthetic strategy was required. This involved the removal of the Squaramide-amide target functionality, and replacing it with a regular squaramide motif (on the linear sequence). This synthetic conversion retained the natural side-chain functionality of the respective amino acid(s), but greatly increased their reactivity towards nucleophilic substitution with the linear squaramate-sequence

on resin. This design strategy proved to be effective, as the successful synthesis of *c*(**RG(ψ)-Sq-f*N*MeV)** was evidenced by LC-MS analysis and molecular formula was confirmed via HRMS. Although we ran out of time to apply this strategy for the synthesis of other Squaratides, a versatile methodology was developed for the synthesis of their respective N^β-Fmoc alkyl-amine amino acids.

5.1 Future Work

For chapter 2, future work will continue to investigate the spectroscopic properties of Ac-DEVD-PABC-Naph by completing further iterations to gain an enhanced understanding of our probe and the role it plays in the fluorescent detection/visualisation of caspase-3. However, we are motivated by the selectivity and sensitivity of the probe in response to caspase-3, and we hope to apply the probe for measuring caspase-3 activity within living cells in the near future.

Future work regarding chapter 3 will involve completing Tb^{3+} and Eu^{3+} luminescence studies, and thermodynamic/kinetic stability (Gd^{3+}) investigations for all ligands. Chemical Exchange Saturation Transfer (CEST) analysis will also be conducted for ligands **3.6** and **3.7**. We will also explore the potential of **3.19** to act as a caspase-3 probe in the future, via complexation to various Ln^{3+} centres and observing their response to caspase-3. Utilising a similar design strategy, and incorporating the previously synthesized di-, tri- and tetra-substituted squaramide-based ligands (**3.11**, **3.15** & **3.17**), capase-3 probes with increasing number of antenna-ligands could be synthesized (**Scheme 5.1**). Increasing the number of antenna-ligands within the vicinity of the Ln^{3+} ion may lead to brighter and more intense luminescent probes.
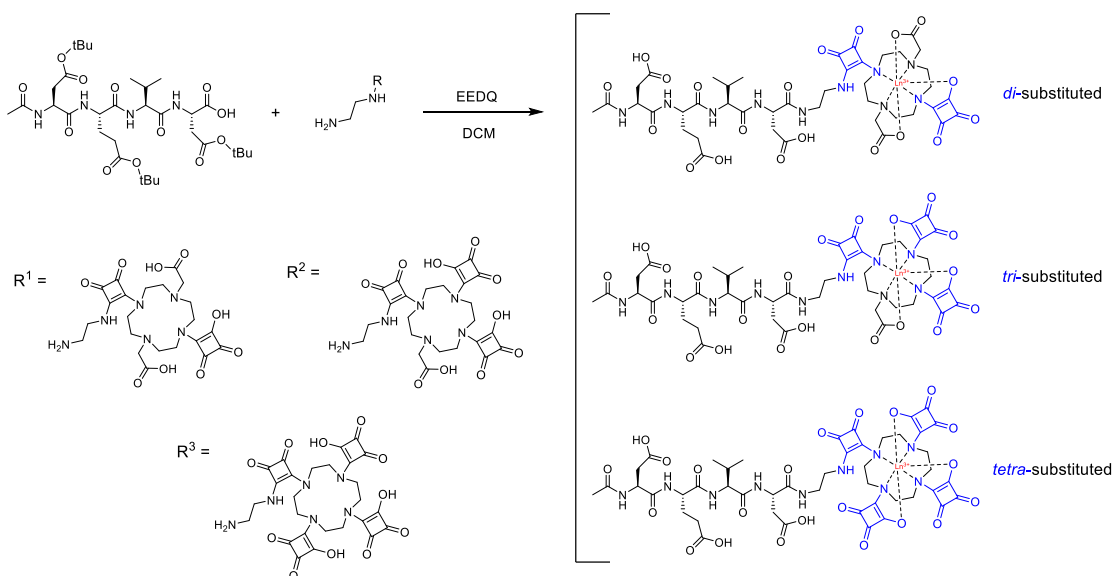
Scheme 5.1: Proposed synthetic pathway to potential caspase-3 probes with increased squaramide substitution.

Chapter 4 was synthetically very challenging, with many unsuccessful reactions. However, an interesting synthetic workaround was generated that allowed us to produce a cyclic Squaratide derivative of Cilengitide. Future work will continue this synthetic strategy to produce sufficient amounts of N^β-Fmoc alkyl-amine amino acids, and use these to generate the remaining squaratide derivatives (**Scheme 5.2**). These compounds will then be subject to enzymatic assays to investigate their metabolic stability – compared to the native Cilengitide.
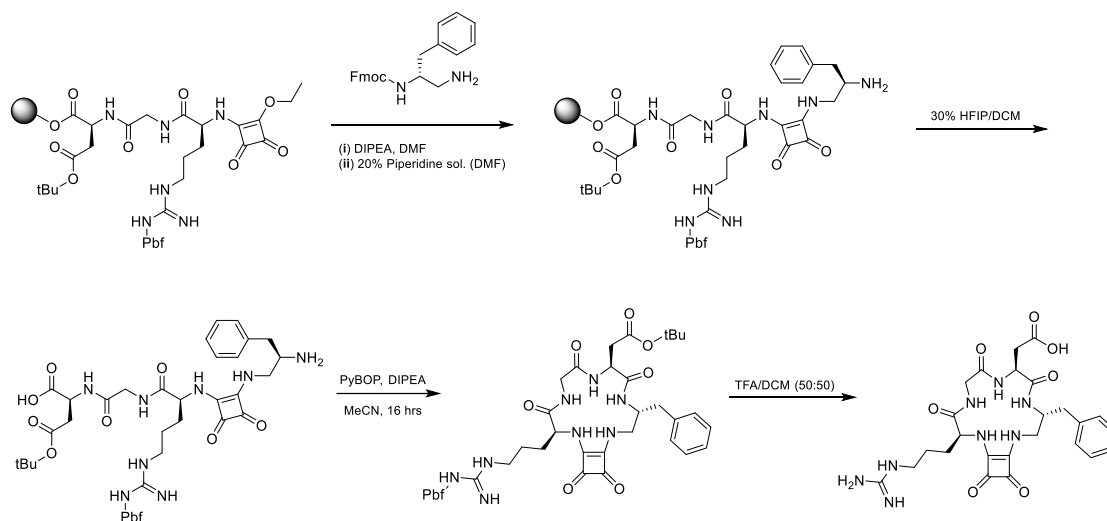
Scheme 5.2: Proposed route towards the synthesis of *Squaratides*, using *c*(**RGDf(ψ)-Sq**) as an example.

5.2 Publications

Conor Wynne, Robert B.P. Elmes, Modified Synthetic Peptides: From Therapeutics to Chemosensors, *Sensors & Diagnostics*, (**2024**), Advance Article.

Luke E. Brennan, Lokesh K. Kumawat, Magdalena E. Piatek, Airlie J. Kinross, Daniel A. McNaughton, Luke Marchetti, Conor Geraghty, **Conor Wynne**, Hua Tong, Oisin N. Kavanagh, Finbarr O'Sullivan, Chris S. Hawes, Philip A. Gale, Kevin Kavanagh, and Robert B.P. Elmes, Potent antimicrobial effect induced by disruption of chloride homeostasis, *Chem*, 9, (**2023**), 3138–3158.

Conor Geraghty, **Conor Wynne**, Robert B.P. Elmes, 1,8-Naphthalimide based fluorescent sensors for enzymes, *Coordination Chemistry Reviews*, 437 (**2021**), 213713.

L. K. Kumawat, **C. Wynne**, E. Cappello, P. Fisher, L. E. Brennan, A. Strofaldi, J. J. McManus, C. S. Hawes, K. A. Jolliffe, T. Gunnlaugsson, R. B. P. Elmes, Squaramide-Based Self-Associating Amphiphiles for Anion Recognition, *ChemPlusChem*, 86, (**2021**), 1058.

Chapter 6

Experimental Procedures

6. Experimental Procedures

6.1 General Procedures and Instrumentation

All reagents were of commercial quality. Solvents were dried and purified by standard methods – DCM was distilled over CaH_2 and MeCN was dried over 3 Å molecular sieves. Anhydrous DMF was purchased from Sigma Aldrich. Analytical TLC was performed on aluminium sheets coated with a 0.2 mm layer of silica gel 60 F254. Silica gel 60 (230-400 mesh) was used for flash chromatography. Compounds were lyophilised on a Labconco Freezone 1 Dry system. LC-MS was performed on an Agilent Technologies 1200 series setup, utilising an Agilent Eclipse XDB-C18 (5μm, 4.6 x 150mm) column at 40°C. A flow rate of 0.2 ml min^{-1} and gradient of 0.1% of formic acid in CH_3CN (solvent A) in 0.1% of formic acid in H_2O (solvent B) was used as mobile phase. Electrospray in positive & negative mode(s) was used for ionisation. NMR spectra were recorded using a Bruker Ascend 500 spectrometer, operated at 500 MHz for ^{1}H NMR analysis and 126 MHz for ^{13}C analysis, both at 293 K. The residual solvent peak was used as an internal standard for DMSO-d_6 and TMS for CDCl$_3$. Chemical shifts (δ) were reported in ppm. NMR spectra were processed, and stack plots produced using MestReNova 6.0.2 software. The NMR spectra assignments were based on ^{1}H, ^{13}C, COSY, HSQC, and HMBC spectra. Multiplicity is given as s = singlet, bs = broad singlet, d = doublet, brd = broad doublet, dd = doublet of doublets, ddd= doublet of doublet of doublets, t = triplet, q = quartet, m = multiplet as appropriate, and *J* values are given in Hz. Infrared (IR) spectra were obtained *via* ATR as a solid on a zinc selenide crystal in the region of 4000 – 400 cm^{-1} using a Perkin Elmer Spectrum 100 FT-IR spectrophotometer. High resolution mass spectra (HRMS) were recorded – courtesy of Bath University – on an Agilent 6200 series TOF/6500 series Q-TOF instrument with an ESI source. Microwave (MW) experiments were carried out in sealed vessels in a CEM Discovery MW, with transversal IR sensor for reaction temperature monitoring. UV-visible spectroscopy measurements were made at 25 °C on a Lambda 365 Perkin Elmer UV-vis spectrophotometer. Fluorescence emission spectra were performed at 25 °C and 37 °C on an Agilent Spectrofluorometer equipped with a 450 W xenon lamp for excitation. Starna and Hellma quartz cuvettes of 1 cm path length and several volumes were employed.

6.2 Synthetic Procedures for Chapter 2

6.2.1 Sequential Amino Acid Coupling

The Fmoc amino-acid resin was swelled in DCM for ~30 minutes prior to Fmoc-deprotection. At the end of this time, the resin was treated with *3x* 20% Piperidine sol. (DMF) for ~5 minutes, then subsequent washing with *3x* DMF, *3x* DCM and *3x* DMF. A solution of Fmoc-AA, PyBOP and NMM in DMF was added to the resin and allowed to shake for 90 minutes. The new AA-resin was then washed with *3x* DCM, *3x* DMF and *3x* DCM, before being dried *in vacuo*.

6.2.2 Cleavage of Amino Acid Sequence from Resin

A very small spatula tip amount of dry Fmoc-AA resin was placed into a suitable vial, and then treated with a 30% HFIP/DCM solution (1 ml) for 90 minutes (with gentle agitation). After this time, the *cleavage solution* and resin were filtered through a glass pasteur pipette fitted with cotton wool. The HFIP/DCM was removed from the filtrate via evaporation with compressed air. The residue that remained was redissolved in MeCN prior to LC-MS analysis.

6.2.3 Synthetic Methods

Fmoc-VD(O*t*Bu)-2-Cl-Trt
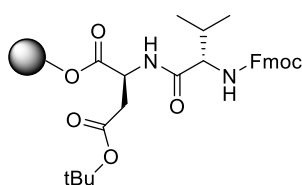
A solution of Fmoc-Val-OH (390 mg, 1.14 mmol, 3 eq.), PyBOP (1.19 g, 2.28 mmol) and NMM (376 µl, 3.42 mmol) in DMF (8 ml) was stirred in a small beaker for 15 min. After this time, the Fmoc-AA solution was added to the resin and allowed to shake for 90 min. The new peptide resin was then washed with *3x* DCM, *3x* DMF and *3x* DCM. **LC-MS** (0-100%) gradient of A in B, 55 min) t_R = 38 min.

Fmoc-DEVD(OtBu)-2-Cl-Trt
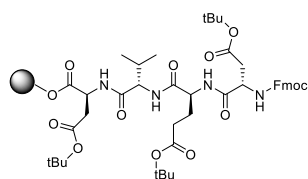
Fmoc deprotection and test cleavage as before. A solution of Fmoc-Asp(OtBu)-OH (470 mg, 1.14 mmol, 3 eq.), PyBOP (1.19 g, 2.28 mmol) and NMM (376 µl, 3.42 mmol) in DMF (8 ml) was stirred in a small beaker for 15 min. After this time, the Fmoc-AA solution was added to the resin and allowed to shake for 90 min. The new peptide resin was then washed with *3x* DCM, *3x* DMF and *3x* DCM. **LC-MS** (0-100%) gradient of A in B, 55 min) t_R = 42 min.

Ac-DEVD(OtBu)-OH (2.1)

(2*S*,5*S*,8*S*,11*S*)-11-acetamido-2-(2-(*tert*-butoxy)-2-oxoethyl)-8-(3-(*tert*-butoxy)-3-oxopropyl)-5-isopropyl-15,15-dimethyl-4,7,10,13-tetraoxo-14-oxa-3,6,9-triazahexadecanoic acid
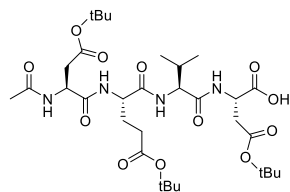
Fmoc deprotection as before. The peptide resin was treated with a solution of Pyridine/Acetic Anhydride (2:8, 8 ml) and allowed to shake for 30 min. The new resin was washed with *3x* DCM, *3x* DMF and *3x* DCM. LC-MS indicated complete consumption of starting material, with the complete loss of UV activity (loss of chromophore). Ninhydrin Test was used to confirm that the *N*-Terminus was completely acetylated (no primary amine present). The product was then removed from the resin via 30% HFIP/DCM (as before), to afford the *N*-Terminal *protected linear peptide* **Ac-DEVD(OtBu)-OH (2.1)** as an off-white solid – without further purification (227 mg, 87 %). **¹H NMR** (500 MHz, CDCl₃) δ 8.20 (d, *J* = 8.2 Hz, 1H), 8.09 (d, *J* = 7.2 Hz, 1H), 7.90 (d, *J* = 8.1 Hz, 1H), 7.78 (d, *J* = 9.0 Hz, 1H), 4.62 – 4.53 (m, 1H), 4.52 – 4.42 (m, 1H), 4.35 – 4.25 (m, 1H), 4.20 – 4.10 (m, 1H), 2.65 – 2.58 (m, 1H), 2.40 (d, *J* = 7.4 Hz, 2H), 2.23 – 2.10 (m, 2H), 1.99 – 1.91 (m, 1H), 1.91 – 1.84 (m, 1H), 1.83 (s, 3H), 1.76 – 1.63 (m, 1H), 1.37 (s, 27H), 0.82 (d, *J* = 6.8 Hz, 6H).

Ac-DEVD(OtBu)-PABA-OH (2.2)

tert-butyl-(4*S*,7*S*,10*S*,13*S*)-4-(2-(*tert*-butoxy)-2-oxoethyl)-7-(3-(*tert*-butoxy)-3-oxopropyl)-13-((4-(hydroxymethyl)phenyl)carbamoyl)-10-isopropyl-2,5,8,11-tetraoxo-3,6,9,12-tetraazapentadecan-15-oate
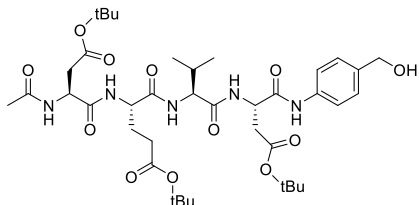
The *protected linear peptide* (150 mg, 0.22 mmol) was dissolved in a solution of DCM (10 ml) containing EEDQ (163 mg, 0.66 mmol). A few drops of DMSO were added to aid dissolution, along with 10 min of sonication. This mixture was then allowed to stir for 20 min under N_2-atmosphere at room temp. After this time, PABA (54 mg, 0.44 mmol) was added, and the new solution was stirred for 16 hrs. Reaction progress was monitored via LC-MS, with the appearance of a UV-peak resembling the product. The organic layer was extracted from subsequent washes with 5% Acetic Acid (aq.) & H_2O. The crude mixture was then re-dissolved in a minimum amount of MeCN before being purified via reverse-phase flash chromatography using a 0-50% gradient of MeCN in H_2O as eluent, to afford **2.2** as a pale-yellow solid (136 mg, 78 %). **LC-MS** (0-100%) gradient of A in B, 55 min) t_R = 28 min. **^{1}H NMR** (500 MHz, DMSO) δ 9.85 (s, 1H), 8.34 (d, *J* = 7.0 Hz, 1H), 8.20 (d, *J* = 8.1 Hz, 1H), 7.95 (d, *J* = 7.5 Hz, 1H), 7.82 (d, *J* = 8.5 Hz, 1H), 7.54 (d, *J* = 8.6 Hz, 2H), 7.23 (d, *J* = 8.6 Hz, 2H), 5.11 (t, *J* = 6.9 Hz, 1H), 4.73 – 4.67 (m, 1H), 4.60 – 4.55 (m, 1H), 4.42 (s, 2H), 4.33 – 4.26 (m, 1H), 4.15 – 4.10 (m, 1H), 2.74 (dd, *J* = 15.8, 6.4 Hz, 1H), 2.62 (dd, *J* = 16.0, 5.6 Hz, 1H), 2.54 (dd, *J* = 15.8, 8.1 Hz, 1H), 2.41 (dd, *J* = 16.0, 8.6 Hz, 2H), 2.24 – 2.14 (m, 2H), 1.97 – 1.92 (m, 1H), 1.89 – 1.85 (m, 1H), 1.83 (s, 3H), 1.76 – 1.67 (m, 1H), 1.36 (s, 27H), 0.82 (d, *J* = 6.8 Hz, 6H). **^{13}C NMR** (126 MHz, DMSO) δ 171.8, 171.0, 170.7, 170.6, 169.4, 169.3, 169.0, 168.7, 150.5, 137.6, 137.4, 136.1, 129.5, 128.9, 128.1, 127.9, 127.0, 126.9, 126.6, 121.5, 119.1, 80.3, 80.15, 79.6, 62.6, 57.8, 51.9, 50.5, 49.4, 39.5, 37.3, 31.2, 30.5, 27.8, 27.7, 27.7, 27.3, 22.5, 19.1, 18.1.

Nitro Naphthalimide (2.3)

2-butyl-6-nitro-1*H*-benzo[*de*]isoquinoline-1,3(2*H*)-dione
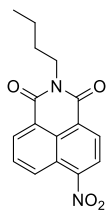
N-butyl amine (794 μl, 8.04 mmol) was added to a solution of 4-nitro naphthalic anhydride (**2.0a**) (1.63 g, 6.70 mmol) in EtOH (15 ml). The reaction was heated to reflux and allowed to stir for 16 hrs. TLC indicated complete consumption of starting material. The EtOH was removed under reduced pressure and the crude mixture was re-dissolved in a minimum amount of DCM, before being purified via flash chromatography using a 0-10% gradient of MeOH in DCM as eluent, to afford **2.3** as a light-brown solid (1.68 g, 84 %). **LC-MS** (0-100%) gradient of A in B, 55 min) t_R = 32 min. **^{1}H NMR** (500 MHz, DMSO) δ 8.69 (d, *J* = 8.7 Hz, 1H), 8.63 – 8.61 (m, 1H), 8.59 (d, *J* = 8.0 Hz, 1H), 8.54 (d, *J* = 8.0 Hz, 1H), 8.08 (dd, *J* = 8.6, 7.4 Hz, 1H), 4.07 – 4.01 (m, 2H), 1.67 – 1.59 (m, 2H), 1.41 – 1.32 (m, 2H), 0.93 (t, *J* = 7.4 Hz, 3H). **^{13}C NMR** (126 MHz, DMSO) δ 162.9, 162.1, 149.1, 131.7, 130.1, 129.6, 128.7, 128.4, 126.7, 124.2, 122.8, 122.7, 39.5, 29.5, 19.8, 13.7.

Amino Naphthalimide (2.4)

6-amino-2-butyl-1*H*-benzo[*de*]isoquinoline-1,3(2*H*)-dione
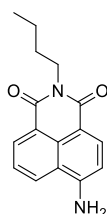
2.3 (1.68g, 5.63 mmol) was added to a suspension of Pd/C (120 mg, 1.13 mmol) in MeOH (25 ml). The mixture was bubbled through with H$_2$ gas for 10 min before leaving to stir under a H$_2$-atmosphere for 16 hours. TLC indicated complete consumption of starting material. After this time, the reaction mixture was filtered through a pad of *Celite®* (SiO$_2$) and washed with excess MeOH to remove the Pd/C. The MeOH filtrate was then removed under reduced pressure to yield **2.4** – without further purification – as a deep orange solid (1.43 g, 95 %). **LC-MS** (0-100%) gradient of A in B, 55 min) t_R = 25 min. **^{1}H NMR** (500 MHz, DMSO) δ 8.60 (d, *J* = 8.4 Hz, 1H), 8.41 (d, *J* = 7.2 Hz, 1H), 8.18 (d, *J* = 8.4 Hz, 1H), 7.66 – 7.61 (m, 1H), 7.42 (s, 2H), 6.83 (d, *J* = 8.4 Hz, 1H), 4.03 – 3.97 (m, 2H), 1.61 – 1.53 (m, 2H), 1.37 – 1.27 (m, 2H), 0.91 (t, *J* = 7.4 Hz, 3H). **^{13}C NMR** (126 MHz, DMSO) δ 163.8, 162.9, 152.7, 133.9, 131.0, 129.7, 129.3, 124.0, 121.8, 119.4, 108.1, 107.6, 39.5, 29.8, 19.8, 13.7.

Ac-DEVD(OtBu)-PABC-Naph (2.5)

tert-butyl-(4*S*,7*S*,10*S*,13*S*)-4-(2-(*tert*-butoxy)-2-oxoethyl)-7-(3-(*tert*-butoxy)-3-oxopropyl)-13-((4-(((((2-butyl-1,3-dioxo-2,3-dihydro-1*H*-benzo[*de*]isoquinolin-6-yl)carbamoyl)oxy)methyl)phenyl)carbamoyl)-10-isopropyl-2,5,8,11-tetraoxo-3,6,9,12-tetraazapentadecan-15-oate
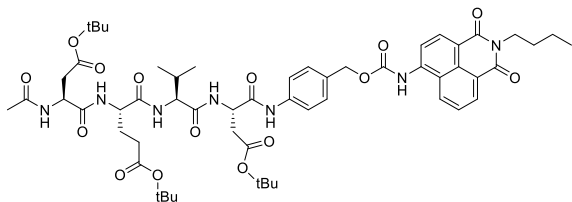
2.4 (9.6 mg, 0.036 mmol) was added to a solution of DMAP (11 mg, 0.09 mmol) in dry DCM (30 ml), and the solution was stirred at -10 °C in a salt/ice bath for 15 min under a N_2-atmosphere. A 15% Phosgene in Toluene sol. (12.9 μl, 0.18 mmol) was added dropwise – using a glass syringe and needle – over the course of 10 min. Once all the phosgene solution had been added, the reaction mixture was allowed to stir for 30 min in the ice-bath, then another 4 hrs at room temperature while still under N_2-atmosphere. After this time, a complete change in fluorescence – from green to blue – was observed (UV torch). The DCM was then removed via compressed N_2 gas, until complete dryness. A solution of **2.2** (25 mg, 0.03 mmol) in DCM (15 ml) was added dropwise via syringe over the (now dry) reaction mixture, and was allowed to stir at room temp. under N_2-atmosphere for 16 hrs. The precipitate that formed was filtered and washed with excess DCM to yield the protected product **2.5** – without further purification – as a light yellow solid (21.8 mg, 66 %). **LC-MS** (0-100%) gradient of A in B, 55 min) t_R = 44 min. **¹H NMR** (500 MHz, DMSO) δ 10.37 (s, 1H), 10.00 (s, 1H), 8.70 (d, *J* = 8.7 Hz, 1H), 8.49 (dd, *J* = 13.7, 7.3 Hz, 2H), 8.37 (d, *J* = 7.7 Hz, 1H), 8.20 (d, *J* = 8.2 Hz, 2H), 7.96 (d, *J* = 7.9 Hz, 1H), 7.85 – 7.80 (m, 2H), 7.65 (d, *J* = 8.6 Hz, 2H), 7.43 (d, *J* = 8.6 Hz, 2H), 5.21 (s, 2H), 4.75 – 4.68 (m, 1H), 4.60 – 4.54 (m, 1H), 4.33 – 4.27 (m, 1H), 4.16 – 4.11 (m, 1H), 4.03 (t, *J* = 7.4 Hz, 2H), 2.75 (dd, *J* = 15.8, 6.3 Hz, 1H), 2.61 (dd, *J* = 16.1, 5.6 Hz, 1H), 2.58 – 2.53 (m, 1H), 2.41 (dd, *J* = 15.9, 8.6 Hz, 1H), 2.26 – 2.11 (m, 2H), 1.98 – 1.90 (m, 1H), 1.90 – 1.85 (m, 1H), 1.83 (s, 3H), 1.76 – 1.67 (m, 1H), 1.64 – 1.57 (m, 2H), 1.36 (s, 27H), 1.23 (s, 2H), 0.92 (t, *J* = 7.4 Hz, 3H), 0.82 (d, *J* = 6.9 Hz, 6H). **¹³C NMR** (126 MHz, DMSO) δ 171.8, 171.0, 170.7, 170.6, 169.3, 168.99, 168.9, 163.5, 163.0, 154.0, 140.7, 138.8, 131.7, 131.1, 130.9, 129.3, 129.1, 128.4, 126.4, 123.9, 122.3, 119.2, 118.2, 117.1, 80.4, 80.1, 79.6, 66.4, 57.8, 51.9, 50.5, 49.4, 39.5, 37.3, 31.2, 30.5, 29.7, 27.8, 27.7, 27.7, 27.3, 22.5, 19.8, 19.0, 18.1,

13.7. HRMS (ESI) *m/z:* Calc. for $C_{56}H_{75}N_7O_{15}$ ([M+H]$^+$): 1086.5321, Found: 1086.5361

Ac-DEVD-PABC-Naph deprotected (2.6)

(4*S*,7*S*,10*S*,13*S*)-13-((4-(((((2-butyl-1,3-dioxo-2,3-dihydro-1*H*-benzo[*de*]isoquinolin-6-yl)carbamoyl)oxy)methyl)phenyl)carbamoyl)-7-(2-carboxyethyl)-4-(carboxymethyl)-10-isopropyl-2,5,8,11-tetraoxo-3,6,9,12-tetraazapentadecan-15-oic acid
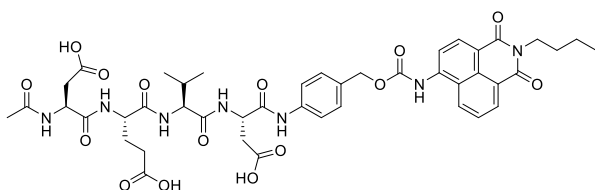
2.5 (21 mg, 0.02 mmol) was dissolved in 50:50 TFA/DCM (4 ml) and allowed to stir at r.t.p for 1 hour. LC-MS indicated the complete consumption of starting material. Thus, the TFA/DCM was evaporated using compressed air. The resulting oil was re-dissolved in a minimum amount of MeCN before being purified via reverse-phase flash chromatography using a 0-5% gradient of MeCN in H_2O as eluent, to afford **2.6** as a pale yellow solid (15 mg, 81 %). **LC-MS** (0-100%) gradient of A in B, 55 min) t_R = 32 min. **HRMS** (ESI) *m/z:* Calc. for $C_{44}H_{51}N_7O_{15}$ ([M+H]$^+$): 918.3443, Found: 918.3502

4-bromo-*N*-butyl-1,8-naphthalimide (2.7)

6-bromo-2-butyl-1*H*-benzo[*de*]isoquinoline-1,3(2*H*)-dione
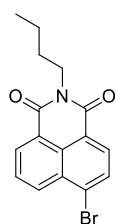
N-butyl amine (776 μl, 7.85 mmol) was added to a solution of 4-bromo naphthalic anhydride (**2.0b**) (1.98 g, 7.14 mmol) in EtOH (100 ml). The reaction was heated to reflux and allowed to stir for 16 hrs. TLC indicated complete consumption of starting material. The EtOH was removed under reduced pressure and the crude mixture was re-dissolved in a minimum amount of Hot EtOH for re-crystallisation. This yielded **2.7** as yellow needle-like crystals (2.08 g, 88 %). **LC-MS** (0-100%) gradient of A in B, 55 min) t_R = 35 min. **^{1}H NMR** (500 MHz, DMSO) δ 8.50 (d, *J* = 7.2 Hz, 1H), 8.46 (d, *J* = 8.5 Hz, 1H), 8.25 (d, *J* = 7.8 Hz, 1H), 8.15 (d, *J* = 7.9 Hz, 1H), 7.96 – 7.91 (m, 1H), 3.99 (t, *J* = 7.4 Hz, 2H), 1.63 – 1.55 (m, 2H), 1.39 – 1.30 (m, 2H), 0.92 (t, *J*

= 7.4 Hz, 3H). **¹³C NMR** (126 MHz, DMSO) δ 162.8, 162.8, 132.5, 131.5, 131.3, 130.9, 129.8, 129.1, 128.8, 128.2, 122.7, 121.9, 39.5, 29.6, 19.8, 13.7.

4-aminostyryl *N*-butyl-1,8-naphthalimide (2.8)

(*E*)-6-(4-aminostyryl)-2-butyl-1*H*-benzo[*de*]isoquinoline-1,3(2*H*)-dione
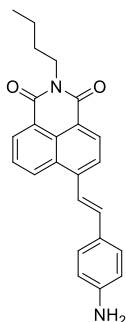
4-amino styrene (0.043 g, 0.36 mmol) was dissolved in anhydrous DMF (10 ml). This solution was then added to a 25 ml round-bottom flask containing **2.7** (0.1 g, 0.3 mmol), Pd(OAc)$_2$ (catalytic amount) and P(*o*-Tol)$_3$ (5.02 mg, 0.016 mmol). TEA (600 μl, 0.004 mmol) was added, and the reaction was placed under an N$_2$ atmosphere. The reaction was allowed to stir at 110°C for 16 hrs. The reaction mixture was then cooled to room temperature, diluted with H$_2$O (3 ml) and extracted with CHCl$_3$. The organic layer was dried with Na$_2$SO$_4$ and concentrated *in vacuo*. The product was precipitated out of Hot EtOH and filtered – with subsequent washes with cold EtOH – to yield the **2.8** as a dark red solid (0.69 g, 62 %) – without further purification. **LC-MS** (0-100%) gradient of A in B, 55 min) t_R = 33 min. **¹H NMR** (500 MHz, DMSO) δ 8.93 (d, *J* = 8.0 Hz, 1H), 8.49 (d, *J* = 6.5 Hz, 1H), 8.39 (d, *J* = 7.9 Hz, 1H), 8.13 (d, *J* = 8.0 Hz, 1H), 7.87 – 7.80 (m, 2H), 7.55 (d, *J* = 8.5 Hz, 2H), 7.45 (d, *J* = 15.9 Hz, 1H), 6.62 (d, *J* = 8.5 Hz, 2H), 5.60 (s, 2H), 4.03 (t, *J* = 7.4 Hz, 2H), 1.65 – 1.56 (m, 2H), 1.39 – 1.30 (m, 2H), 0.92 (t, *J* = 7.4 Hz, 3H). **¹³C NMR** (126 MHz, DMSO) δ 163.5, 163.2, 150.1, 142.2, 136.2, 130.8, 130.7, 130.7, 129.2, 128.7, 128.3, 126.6, 124.3, 122.3, 122.1, 119.2, 116.7, 113.8, 39.5, 29.7, 19.9, 13.8.

6.3 Synthetic Procedures for Chapter 3

6.3.1 Synthetic Methods

Diethyl squarate (3.1, DESq)

3,4-Diethoxy-3-cyclobutene-1,2-dione
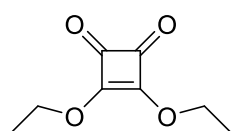
Triethyl orthoformate (24 ml, 144 mmol) was added to a suspension of 3,4-Dihydroxy-3-cyclobutene-1,2-dione – squaric acid (5.5 g, 48 mmol) in EtOH (120 ml), and the suspension was refluxed at 80°C for 72 hrs. TLC indicated the complete consumption of starting material. Thus, the EtOH was removed under reduced pressure and the resulting oil was re-dissolved in a minimum amount of DCM, before being purified via flash chromatography using a 0-5% gradient of MeOH in DCM as eluent, to afford **DESq** as a yellow/orange oil (6.9 g, 85 %). **LC-MS** (0-100%) gradient of A in B, 55 min) t_R = 30 min. **¹H NMR** (500 MHz, DMSO) δ 4.65 (q, J = 7.1 Hz, 4H), 1.37 (t, J = 7.1 Hz, 6H). **¹³C NMR** (126 MHz, DMSO) δ 189.1, 183.7, 70.2, 54.9, 39.5, 15.3. **IR** (ATR): v_{max} (cm⁻¹) = 2986, 1811, 1730, 1592, 1482, 1421, 1330, 1187.

DO3A*t*Bu-ESq (3.2)

tri-*tert*-butyl-2,2',2''-(10-(2-ethoxy-3,4-dioxocyclobut-1-en-1-yl)-1,4,7,10-tetraazacyclododecane-1,4,7-triyl)triacetate
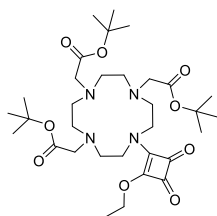
DESq (215 µl, 1.45 mmol) was added to a solution of DO3A*t*Bu (**3.0b**) (250 mg, 0.49 mmol) and TEA (203 µl, 1.45 mmol) in EtOH (5 ml) and the solution was stirred for 16 hrs at r.t.p. After this time, the EtOH was removed under reduced pressure and the resulting oil was re-dissolved in a minimum amount of DCM, before being purified via flash chromatography using a 0-10% gradient of MeOH in DCM as eluent, to afford **3.2** as a brown oil (272 mg, 87 %). **LC-MS** (0-100%) gradient of A in B, 55 min) t_R = 31 min. **¹H NMR** (500 MHz, DMSO) δ 4.63 (q, J = 7.0 Hz, 4H), 3.80 (t, J = 5.4 Hz, 2H), 3.65 (t, J = 5.9 Hz, 2H), 3.25 (t, J = 5.9 Hz, 6H), 2.91 –

2.85 (m, J = 11.2, 5.5 Hz, 4H), 2.69 – 2.58 (m, J = 5.9 Hz, 8H), 1.40 (s, 18H), 1.39 (s, 9H), 1.34 (t, J = 7.1 Hz, 3H).**¹³C NMR** (126 MHz, DMSO) δ 189.1, 181.1, 175.9, 171.7, 170.5, 170.4, 170.4, 80.1, 80.1, 68.8, 57.3, 57.1, 54.9, 54.5, 53.9, 53.2, 52.0, 51.4, 51.4, 51.3, 49.5, 48.6, 39.5, 27.9, 27.8, 27.8, 15.6. **HRMS** (ESI) *m/z:* Calc. for $C_{32}H_{54}N_4O_9$ ([M+H]⁺): 639.3891, Found: 639.3968

DO3A*t*Bu-Sq-OH (3.3)

tri-*tert*-butyl-2,2',2''-(10-(2-hydroxy-3,4-dioxocyclobut-1-en-1-yl)-1,4,7,10-tetraazacyclododecane-1,4,7-triyl)triacetate
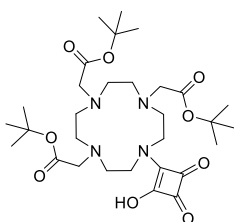
Tri-protected compound **3.2** (102 mg, 0.16 mmol) was dissolved in EtOH (0.5 ml) and added (dropwise) to a solution of aqueous 1M NaOH (3 ml). The mixture was then allowed to stir at r.t.p for 2 hours. LC-MS indicated the complete consumption of starting material (**3.2**); thus, the reaction mixture was diluted with DCM and the aqueous layer washed with *3x* DCM. The organic layers were combined, and the solvent was removed under reduced pressure. The crude product was re-dissolved in a minimum amount of DCM, before being purified via flash chromatography using a 0-25% gradient of MeOH in DCM as eluent, to afford **3.3** as a (hygroscopic) off-white solid (88 mg, 89 %). **LC-MS** (0-100%) gradient of A in B, 55 min) t_R = 32 min. **¹H NMR** (500 MHz, DMSO) δ 3.45 – 3.19 (m, J = 53.9 Hz, 12H), 2.99 – 2.80 (m, 2H), 2.72 – 2.55 (m, J = 1.8 Hz, 2H), 1.41 (s, 27H). **HRMS** (ESI) *m/z:* Calc. for $C_{30}H_{50}N_4O_9$ ([M+H]⁺): 611.3578, Found: 611.3645

DO3A-ESq (3.4)

2,2',2''-(10-(2-ethoxy-3,4-dioxocyclobut-1-en-1-yl)-1,4,7,10-tetraazacyclododecane-1,4,7-triyl)triacetic acid
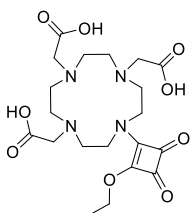
Tri-protected compound **3.2** (135 mg, 0.21 mmol) was dissolved in neat TFA (4 ml) and allowed to stir at r.t.p for 4 hours. TLC indicated the complete consumption of starting material (**3.2**). Thus, the TFA was evaporated using pressurised N_2 gas. The resulting oil was re-dissolved in a minimum amount of MeOH, before being added

dropwise to cold diethyl ether. The mixture was filtered to yield **3.4** as an off-white solid (94 mg, 95 %). **LC-MS** (0-100%) gradient of A in B, 55 min) t_R = 20 min. **¹H NMR** (500 MHz, DMSO) δ 4.65 (q, J = 7.1 Hz, 2H), 3.83 (t, J = 6.1 Hz, 2H), 3.76 (s, 2H), 3.62 (t, J = 5.9 Hz, 2H), 3.59 (s, 2H), 3.53 (s, 2H), 3.20 – 3.14 (m, 4H), 3.09 (t, J = 5.9 Hz, 2H), 3.05 – 2.97 (m, J = 11.2, 6.5 Hz, 6H), 1.35 (t, J = 7.0 Hz, 3H). **¹³C NMR** (126 MHz, DMSO) δ 188.8, 181.9, 176.7, 173.0, 171.4, 171.3, 169.6, 69.2, 64.9, 54.3, 53.4, 52.9, 52.6, 52.3, 50.3, 50.2, 49.5, 49.1, 48.6, 48.0, 39.5, 15.5, 15.2. **IR** (ATR): v_{max} (cm⁻¹) = 2979, 2863, 1800, 1697, 1586, 1489, 1432, 1386, 1354, 1311, 1183, 1130, 1091, 1043, 988, 871, 797, 719, 677, 597, 518, 471, 442, 414. **HRMS** (ESI) *m/z:* Calc. for $C_{20}H_{30}N_4O_9$ ([M+H]⁺): 471.2013, Found: 471.2088

DO3A-Sq-OH (3.5)

2,2',2''-(10-(2-hydroxy-3,4-dioxocyclobut-1-en-1-yl)-1,4,7,10-tetraazacyclododecane-1,4,7-triyl)triacetic acid
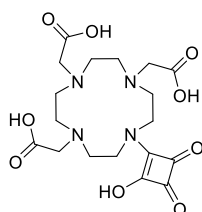
Compound **3.3** (88 mg, 0.15 mmol) was dissolved in neat TFA (4 ml) and allowed to stir at r.t.p for 4 hours. TLC indicated the complete consumption of starting material (**3.3**). Thus, the TFA was evaporated using pressurised N_2 gas. The resulting oil was re-dissolved in a minimum amount of MeOH, before being added dropwise to cold diethyl ether. The mixture was filtered to yield **3.5** as an off-white solid (63 mg, 95 %). **LC-MS** (0-100%) gradient of A in B, 55 min) t_R = 9 min. **¹H NMR** (500 MHz, DMSO) δ 3.81 – 3.74 (m, 8H), 3.58 – 3.54 (m, 2H), 3.26 (t, J = 6.1 Hz, 4H), 3.08 (t, J = 5.9 Hz, 4H), 2.95 (t, J = 6.2 Hz, 4H). **¹³C NMR** (126 MHz, DMSO) δ 188.1, 180.0, 172.8, 171.6, 170.4, 54.3, 54.2, 52.9, 52.2, 48.6, 48.4, 45.8, 40.4, 39.5. **IR** (ATR): v_{max} (cm⁻¹) = 3002, 2860, 1779, 1720, 1637, 1541, 1502, 1432, 1374, 1291, 1200, 1125, 1082, 1023, 987, 879, 828, 799, 675, 607, 466, 400. **HRMS** (ESI) *m/z:* Calc. for $C_{18}H_{26}N_4O_9$ ([M+H]⁺): 443.1700, Found: 443.1780

DO3A*t*Bu-Sq-NH₂ (3.6*)

tri-*tert*-butyl-2,2',2''-(10-(2-amino-3,4-dioxocyclobut-1-en-1-yl)-1,4,7,10-tetraazacyclododecane-1,4,7-triyl)triacetate
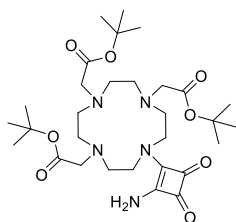
Tri-protected compound **3.2** (132 mg, 0.2 mmol) was dissolved in EtOH (2 ml), to which a solution of Ethanolic Ammonia (1.03 ml, 2.0 mmol) was added, and the combined solution was stirred for 16 hrs at r.t.p. LC-MS indicated the complete consumption of starting material (**3.2**). After this time, the EtOH was removed under reduced pressure and the crude product was re-dissolved in DCM. The organic layer was washed with H_2O to remove any residual ammonia. The DCM was then removed under reduced pressure to yield **3.6*** as a yellow oil (110 mg, 90 %). **LC-MS** (0-100%) gradient of A in B, 55 min) t_R = 29 min. **¹H NMR** (500 MHz, DMSO) δ 7.51 (s, 2H), 3.87 (t, *J* = 5.9 Hz, 2H), 3.62 (t, *J* = 6.2 Hz, 2H), 3.32 – 3.23 (m, *J* = 16.8 Hz, 6H), 2.87 (t, *J* = 6.1 Hz, 4H), 2.71 – 2.59 (m, *J* = 7.2, 5.7 Hz, 8H), 1.40 (s, 9H), 1.39 (s, 18H). **¹³C NMR** (126 MHz, DMSO) δ 183.2, 182.4, 170.8, 170.5, 170.4, 168.8, 168.2, 80.2, 80.0, 57.7, 56.5, 55.1, 54.1, 51.7, 51.6, 50.1, 48.2, 40.4, 39.5, 27.9, 27.8.

DO3A-Sq-NH₂ (3.6)

2,2',2''-(10-(2-amino-3,4-dioxocyclobut-1-en-1-yl)-1,4,7,10-tetraazacyclododecane-1,4,7-triyl)triacetic acid
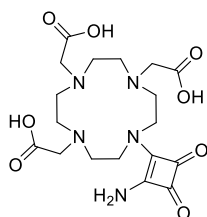
Tri-protected compound **3.6*** (110 mg, 0.18 mmol) was dissolved in neat TFA (4 ml) and allowed to stir at r.t.p for 4 hours. TLC indicated the complete consumption of starting material (**3.6***). Thus, the TFA was evaporated using pressurised N_2 gas. The resulting oil was re-dissolved in a minimum amount of MeOH, before being added dropwise to cold diethyl ether. The mixture was filtered to yield **3.6** as an off-white solid (75 mg, 95 %). **LC-MS** (0-100%) gradient of A in B, 55 min) t_R = 17 min. **¹H NMR** (500 MHz, DMSO) δ 7.68 (s, 2H), 3.78 (t, *J* = 6.2 Hz, 4H), 3.68 (s, 2H), 3.63 (s, 4H), 3.15 – 3.00 (m, 12H).**¹³C NMR** (126 MHz, DMSO) δ 183.3, 183.2, 171.1, 171.0, 170.3, 169.3, 168.3, 64.9, 54.5, 54.3, 53.4, 50.6, 49.0, 47.7, 39.5, 15.2. **IR** (ATR): ν_max (cm⁻¹) = 3325, 3169, 2975, 2864, 1799, 1718, 1637, 1565, 1500,

1437, 1351, 1318, 1193, 1126, 982, 893, 833, 798, 720, 677, 596, 565, 518, 477, 446, 416. **HRMS** (ESI) *m/z:* Calc. for $C_{18}H_{27}N_5O_8$ ([M+H]$^+$): 442.1860, Found: 442.1935

DO3A*t*Bu-Sq-EDA (3.7*)

tri-*tert*-butyl-2,2',2''-(10-(2-((2-aminoethyl)amino)-3,4-dioxocyclobut-1-en-1-yl)-1,4,7,10-tetraazacyclododecane-1,4,7-triyl)triacetate
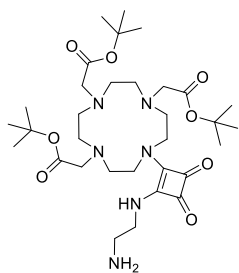
Tri-protected compound **3.2** (93 mg, 0.15 mmol) was dissolved in EtOH (3 ml), to which Ethylene diamine (100 μl, 1.5 mmol) was added and stirred for 16 hrs at r.t.p. LC-MS indicated the complete consumption of starting material (**3.2**). After this time, the EtOH was removed under reduced pressure to yield the crude product as a yellow oil. This oil was then re-dissolved in a minimum amount of DCM, before being purified via flash chromatography using a 0-10% gradient of MeOH in DCM as eluent, to afford **3.7*** as a (hygroscopic: yellow oil) pale yellow solid (89 mg, 91 %). **LC-MS** (0-100%) gradient of A in B, 55 min) t_R = 25 min. **^{1}H NMR** (500 MHz, DMSO) δ 3.85 (t, *J* = 5.5 Hz, 2H), 3.58 (t, *J* = 5.8 Hz, 2H), 3.52 (t, *J* = 5.8 Hz, 2H), 3.34 (s, 2H), 3.32 (s, 2H), 3.30 (s, 2H), 3.01 – 2.77 (m, *J* = 5.9 Hz, 4H), 2.74 – 2.56 (m, *J* = 7.1, 5.5 Hz, 10H), 1.40 (s, 27H). **^{13}C NMR** (126 MHz, DMSO) δ 182.6, 181.9, 171.0, 170.5, 170.3, 167.9, 167.8, 80.0, 57.7, 55.8, 55.3, 54.9, 54.1, 53.2, 52.2, 52.1, 51.7, 51.4, 48.9, 46.5, 42.9, 27.8, 27.8. **HRMS** (ESI) *m/z:* Calc. for $C_{32}H_{56}N_6O_8$ ([M+H]$^+$): 653.4160, Found: 653.4237

DO3A-Sq-EDA (3.7)

2,2',2''-(10-(2-((2-aminoethyl)amino)-3,4-dioxocyclobut-1-en-1-yl)-1,4,7,10-tetraazacyclododecane-1,4,7-triyl)triacetic acid
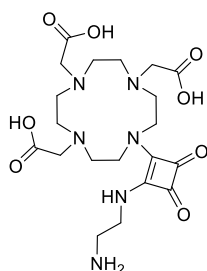
Tri-protected compound **3.7*** (89 mg, 0.14 mmol) was dissolved in neat TFA (4 ml) and allowed to stir at r.t.p for 4 hours. LC-MS indicated the complete consumption of starting material (**3.7***). Thus, the TFA was evaporated using pressurised N$_2$ gas. The resulting oil was re-dissolved in a minimum amount of MeOH, before being added dropwise to cold diethyl ether. The mixture was filtered to

yield the crude product. This solid was then re-dissolved in a minimum amount of H_2O, before being purified via reverse-phase flash chromatography using a 0-5% gradient of MeCN in H_2O as eluent, to afford **3.7** as a pale-yellow solid (63 mg, 95 %). **LC-MS** (0-100%) gradient of A in B, 55 min) t_R = 17 min. **^{1}H NMR** (500 MHz, DMSO) δ 8.39 (s, 3H), 7.46 (s, 1H), 3.58 (s, 9H), 3.49 – 3.20 (m, 4H), 3.06 – 2.90 (m, 13H). **^{13}C NMR** (126 MHz, DMSO) δ 182.6, 182.4, 171.6, 168.0, 158.0, 157.7, 116.1, 49.1, 41.1, 39.5. **IR** (ATR): v_{max} (cm^{-1}) = 2976, 2867, 1793, 1664, 1570, 1514, 1429, 1353, 1282, 1177, 1125, 1083, 1018, 983, 887, 831, 797, 719, 679, 596, 517, 482, 401. **HRMS** (ESI) *m/z:* Calc. for $C_{20}H_{32}N_6O_8$ ([M+H]$^+$): 485.2282, Found: 485.2357

DO2A*t*Bu-2ESq (3.8)

di-*tert*-butyl-2,2'-(4,10-bis(2-ethoxy-3,4-dioxocyclobut-1-en-1-yl)-1,4,7,10-tetraazacyclododecane-1,7-diyl)diacetate
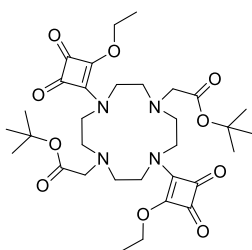
DESq (**3.1**) (66.5 μl, 0.45 mmol) was added to a solution of DO2A*t*Bu (**3.0c**) (100 mg, 0.15 mmol) and TEA (62.7 μl, 0.45 mmol) in EtOH (3 ml) and the solution was stirred for 16 hrs at r.t.p. After this time, the EtOH was concentrated under reduced pressure until a precipitate formed. The precipitate was filtered and washed with cold to afford **3.8** as a light-brown solid (89 mg, 92 %) – without further purification. **LC-MS** (0-100%) gradient of A in B, 55 min) t_R = 33 min. **^{1}H NMR** (500 MHz, DMSO) δ 4.67 – 4.57 (m, 4H), 3.76 – 3.68 (m, 4H), 3.54 (t, *J* = 7.8 Hz, 2H), 3.49 (t, *J* = 7.9 Hz, 2H), 3.38 (s, 2H), 2.87 (t, *J* = 7.8 Hz, 2H), 2.84 – 2.76 (m, 6H), 1.40 (s, 18H), 1.36 – 1.31 (m, 6H). **^{13}C NMR** (126 MHz, DMSO) δ 189.0, 188.9, 181.3, 181.1, 176.2, 176.1, 172.2, 172.1, 170.2, 80.5, 80.4, 80.3, 69.1, 69.0, 55.2, 55.0, 54.4, 54.3, 54.1, 54.0, 53.9, 49.5, 49.2, 48.6, 48.0, 39.5, 27.8, 27.7, 15.6, 15.5. **HRMS** (ESI) *m/z:* Calc. for $C_{32}H_{48}N_4O_{10}$ ([M+H]$^+$): 649.3370, Found: 649.3439

DO2A-2ESq (3.9)

2,2'-(4,10-bis(2-ethoxy-3,4-dioxocyclobut-1-en-1-yl)-1,4,7,10-
tetraazacyclododecane-1,7-diyl)diacetic acid
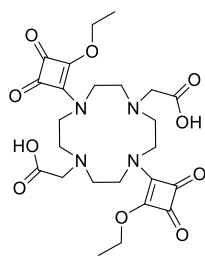
Di-protected compound **3.8** (50 mg, 0.08 mmol) was dissolved in neat TFA (4 ml) and allowed to stir at r.t.p for 4 hours. TLC indicated the complete consumption of starting material (**3.8**). Thus, the TFA was evaporated using pressurised N_2 gas. The resulting oil was re-dissolved in a minimum amount of MeOH, before being added dropwise to cold diethyl ether. The mixture was filtered to yield **3.9** as an off-white solid (41 mg, 95 %). **LC-MS** (0-100%) gradient of A in B, 55 min) t_R = 23 min. **^{1}H NMR** (500 MHz, DMSO) δ 12.43 (s, 2H), 4.70 – 4.53 (m, 4H), 3.74 (s, 2H), 3.68 (s, 2H), 3.54 (s, 2H), 3.51 – 3.39 (m, 7H), 2.95 (s, 2H), 2.90 (s, 5H), 1.40 – 1.28 (m, 6H). **^{13}C NMR** (126 MHz, DMSO) δ 189.1, 189.0, 181.4, 181.1, 176.4, 172.3, 69.2, 69.1, 54.4, 54.1, 53.9, 53.0, 52.0, 49.4, 48.7, 39.5, 15.6, 15.5. **HRMS** (ESI) *m/z:* Calc. for $C_{24}H_{32}N_4O_{10}$ ([M+H]$^+$): 537.2118, Found: 537.2187

ESqO3A-NH (3.12)

4,4',4''-(1,4,7,10-tetraazacyclododecane-1,4,7-triyl)tris(3-ethoxycyclobut-3-ene-
1,2-dione)
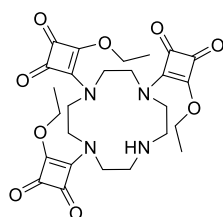
DESq (**3.1**) (386 μl, 2.6 mmol) was added to a solution of Cyclen (**3.0d**) (100 mg, 0.58 mmol) and TEA (243 μl, 1.74 mmol) in EtOH (5 ml) and the solution was stirred for 16 hrs at r.t.p. The resulting precipitate was filtered and washed with EtOH – without further purification – to yield (**3.12**) as a pale brown solid (303 mg, 96%). **LC-MS** (0-100%) gradient of A in B, 55 min) t_R = 28 min. **^{1}H NMR** (500 MHz, DMSO) δ 4.73 – 4.63 (m, 2H), 4.59 – 4.53 (m, 2H), 4.53 – 4.48 (m, 2H), 4.04 (t, *J* = 7.7 Hz, 2H), 3.95 (t, *J* = 7.6 Hz, 2H), 3.84 – 3.69 (m, 4H), 3.59 (s, 2H), 3.54 – 3.47 (m, 2H), 2.85 – 2.74 (m, 4H), 1.41 – 1.32 (m, 6H), 1.32 – 1.23 (m, 3H). **^{13}C NMR** (126 MHz, DMSO) δ 189.2, 189.1, 188.8, 188.7, 188.7, 188.4, 188.4, 188.3, 188.3, 182.0, 181.8, 181.8, 181.8, 181.6, 181.6, 181.5, 177.1, 177.0, 176.9, 176.8, 176.7, 176.2, 176.1, 176.1, 176.0, 173.0, 173.0, 172.7,

172.6, 172.3, 172.3, 172.1, 69.4, 69.3, 69.2, 69.0, 56.0, 53.4, 53.2, 52.8, 52.6, 52.4, 52.4, 52.3, 51.9, 51.5, 50.8, 48.4, 48.2, 48.0, 47.7, 47.5, 47.4, 46.9, 46.9, 46.7, 46.5, 46.3, 39.5, 18.6, 15.8, 15.7, 15.7, 15.6, 15.4, 15.4, 15.4. **HRMS** (ESI) *m/z:* Calc. for $C_{26}H_{32}N_4O_9$ ([M+H]$^+$): 545.2169, Found: 545.2252

SqO3A-NH (3.13)

4,4',4''-(1,4,7,10-tetraazacyclododecane-1,4,7-triyl)tris(3-hydroxycyclobut-3-ene-1,2-dione)
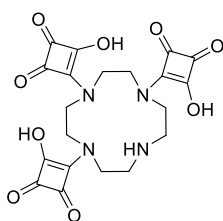
Tri-substituted Cyclen **3.12** (120 mg, 0.22 mmol) was dissolved in aqueous 1M HCl (10 ml) and allowed to stir at 90°C for 16 hrs. TLC indicated the complete consumption of starting material (**3.12**); thus, the solvent was removed under reduced pressure, and the crude product was re-suspended in a minimum amount of MeOH before being added dropwise to cold diethyl ether. The mixture was then centrifuged and washed with more cold diethyl ether to yield **3.13** as an off-white solid (99 mg, 98%). **LC-MS** (0-100%) gradient of A in B, 55 min) t_R = 10 min. **^{1}H NMR** (400 MHz, DMSO) δ 4.40 (s, 8H), 3.87 (s, 2H), 3.79 (s, 2H), 3.69 (s, 2H), 3.13 (s, 2H). **^{13}C NMR** (101 MHz, DMSO) δ 185.5, 184.8, 176.1, 174.9, 51.1, 49.5, 48.6, 48.0, 45.1, 39.5. **IR** (ATR): v_{max} (cm^{-1}) = 3544, 3415, 1796, 1671, 1558, 1515, 1488, 1427, 1384, 1306, 1224, 1164, 1102, 1073, 1040, 998, 964, 921, 863, 831, 808, 673, 635, 603, 492, 409. **HRMS** (ESI) *m/z:* Calc. for $C_{20}H_{20}N_4O_9$ ([M-H]$^+$): 459.1230, Found: 459.1151

SqO3A-O*t*Bu (3.14)

tert-butyl-2-(4,7,10-tris(2-hydroxy-3,4-dioxocyclobut-1-en-1-yl)-1,4,7,10-tetraazacyclododecan-1-yl)acetate
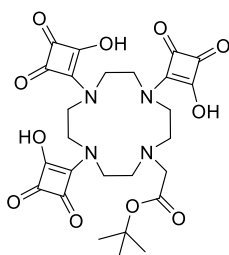
tert-butyl bromoacetate (173 µl, 1.17 mmol) was added to a suspension of **3.13** (90 mg, 0.19 mmol) and K_2CO_3 (162 mg, 1.17 mmol) in DMSO (15 ml). The reaction mixture was allowed to stir at 90°C for 10 days, and the reaction progress was monitored via LC-MS. After this time, the solvent was removed and the crude mixture was re-dissolved in a minimum amount of H_2O,

before being purified via reverse-phase flash chromatography using a 0-5% gradient of MeCN in H_2O as eluent, to afford **3.14** as an off-white solid (96 mg, 88 %). **LC-MS** (0-100%) gradient of A in B, 55 min) t_R = 24 min. **^{1}H NMR** (500 MHz, DMSO) δ 3.78 (s, 6H), 3.57 (s, 2H), 3.46 (s, 2H), 3.38 (s, 6H), 2.80 (s, 2H), 1.41 (s, 9H). **^{13}C NMR** (126 MHz, DMSO) δ 199.0, 198.3, 188.1, 187.9, 180.9, 180.6, 170.2, 163.5, 80.4, 78.3, 55.0, 53.7, 49.7, 46.4, 39.5, 27.9, 27.9, 27.8.

SqO3A-COOH (3.15)

2-(4,7,10-tris(2-hydroxy-3,4-dioxocyclobut-1-en-1-yl)-1,4,7,10-tetraazacyclododecan-1-yl)acetic acid
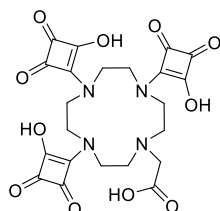
3.14 (89 mg, 0.16 mmol) was dissolved in neat TFA (4 ml) and allowed to stir at r.t.p for 2 hours. LC-MS indicated the complete consumption of starting material (**3.14**). Thus, the TFA was evaporated using pressurised N_2 gas. The resulting oil was re-dissolved in a minimum amount of MeOH, before being added dropwise to cold diethyl ether. The mixture was filtered and washed again to afford **3.15** as a white solid (75 mg, 90 %) – without further purification. **LC-MS** (0-100%) gradient of A in B, 55 min) t_R = 17 min. **^{1}H NMR** (500 MHz, DMSO) δ 4.53 (s, 2H), 3.64 (br m, 14H), 2.98 (s, 2H). *Note:* Signals not well-resolved for this compound and satisfactory **^{13}C NMR** could not be obtained. See attached spectra in *Appendix – Chapter 3*. **IR** (ATR): v_{max} (cm^{-1}) = 3417, 1783, 1676, 1624, 1507, 1426, 1350, 1306, 1202, 1176, 1121, 1039, 979, 916, 834, 801, 721, 591, 515, 442, 404.

SqO3A-ESq (3.16)

4,4',4''-(10-(2-ethoxy-3,4-dioxocyclobut-1-en-1-yl)-1,4,7,10-tetraazacyclododecane-1,4,7-triyl)tris(3-hydroxycyclobut-3-ene-1,2-dione)
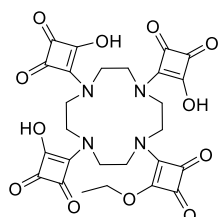
3.13 (99 mg, 0.22 mmol) was suspended in a solution of EtOH (3 ml) containing DESq (**3.1**) (98 μl, 0.66 mmol) and TEA (184 μl, 1.32 mmol) in a boiling tube and was subjected to microwave (MW) irradiation for 120 min at 100 °C. After this time, the EtOH was removed under reduced pressure and the resulting oil was re-dissolved in a minimum amount of MeOH, before being added dropwise to cold diethyl ether.

The mixture was centrifuged and washed with more cold diethyl ether to yield the crude product (**3.16**) as a brown oil. This oil was then re-dissolved in a minimum amount of H_2O, before being purified via reverse-phase flash chromatography using a 0-5% gradient of MeCN in H_2O as eluent, to afford **3.16** as a brown oil (107 mg, 85 %). **LC-MS** (0-100%) gradient of A in B, 55 min) t_R = 17 min. **¹H NMR** (500 MHz, DMSO) δ 9.83 (s, 3H), 4.62 (q, J = 7.1 Hz, 2H), 3.80 (t, J = 5.9 Hz, 14H), 3.56 (t, J = 6.1 Hz, 2H), 1.34 (t, J = 7.1 Hz, 3H). **¹³C NMR** (126 MHz, DMSO) δ 199.8, 198.8, 198.7, 188.7, 188.5, 188.3, 188.2, 188.0, 182.1, 181.8, 180.8, 180.5, 176.6, 172.4, 69.2, 55.0, 50.6, 50.4, 48.9, 48.4, 48.3, 48.0, 45.7, 40.4, 39.5, 15.5, 8.6. **IR** (ATR): v_{max} (cm⁻¹) = 3399, 3249, 2986, 2675, 2505, 1774, 1701, 1636, 1594, 1537, 1501, 1427, 1387, 1347, 1278, 1227, 1174, 1093, 1027, 950, 836, 793, 547, 421. **HRMS** (ESI) *m/z:* Calc. for $C_{26}H_{24}N_4O_{12}$ ([M-H]⁺): 583.1391, Found: 583.1338

SqOTA (3.17)

4,4',4'',4'''-(1,4,7,10-tetraazacyclododecane-1,4,7,10-tetrayl)tetrakis(3-hydroxycyclobut-3-ene-1,2-dione)
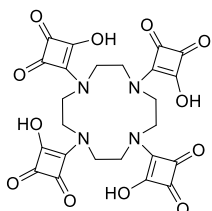
Tetra-substituted Cyclen **3.16** (30 mg, 0.05 mmol) was dissolved in aqueous 1M HCl (10 ml) and allowed to stir at room temperature and pressure for 1 hr. LC-MS indicated the complete consumption of starting material (**3.16**); thus, the solvent was removed under reduced pressure, and the crude product was re-suspended in a minimum amount of MeOH before being added dropwise to cold diethyl ether. The suspension was centrifuged and washed before being re-dissolved in a minimum amount of H_2O for purification via reverse-phase flash chromatography using a 0-5% gradient of MeCN in H_2O. This yielded **3.17** as an off-white solid (16 mg, 57%). **LC-MS** (0-100%) gradient of A in B, 55 min) t_R = 16 min. **¹H NMR** (500 MHz, DMSO) δ 9.41 (s, 1H), 3.73 (s, 4H), 3.41 (s, 12H). **HRMS** (ESI) *m/z:* Calc. for $C_{24}H_{20}N_4O_{12}$ ([M+H]⁺): 557.1078, Found: 557.1159

Ac-DEVD(O*t*Bu)-EDA-Sq-DO3A*t*Bu (3.18)

tri-*tert*-butyl-2,2',2''-(10-(2-(((5*S*,8*S*,11*S*,14*S*)-14-acetamido-5-(2-(*tert*-butoxy)-2-oxoethyl)-11-(3-(*tert*-butoxy)-3-oxopropyl)-8-isopropyl-18,18-dimethyl-4,7,10,13,16-pentaoxo-17-oxa-3,6,9,12-tetraazanonadecyl)amino)-3,4-dioxocyclobut-1-en-1-yl)-1,4,7,10-tetraazacyclododecane-1,4,7-triyl)triacetate
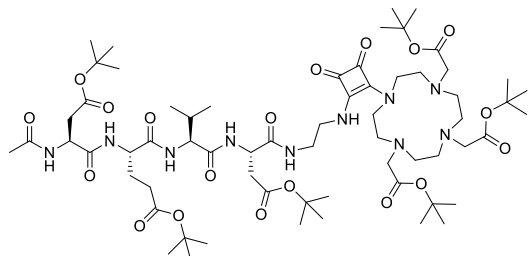
Ac-DEVD(O*t*Bu)-OH (**2.1**) was synthesised on 2-chlorotrityl chloride resin via Fmoc/*t*Bu SPPS. EEDQ (74 mg, 0.30 mmol) was added to a solution of **2.1** (70 mg, 0.10 mmol) in DCM (10 ml + few drops of DMSO to facilitate dissolution) and allowed to stir for 1 hour. After this time, tri-protected amine **3.7*** (130 mg, 0.20 mmol) was added and the resulting solution was stirred for 16 hours at r.t.p. The reaction mixture was then added to a separating funnel and washed with *3x* 15% Citric Acid (aq.) and *2x* H_2O. The organic layer was separated, and solvent was removed under reduced pressure. The crude product was then purified via flash chromatography using a 0-20% gradient of MeOH in DCM as eluent, to afford **3.18** as a (hygroscopic) off-white solid (110 mg, 82 %). **LC-MS** (0-100%) gradient of A in B, 55 min) t_R = 33 min.
¹H NMR (500 MHz, DMSO) δ 8.22 – 8.16 (m, 2H), 7.96 – 7.91 (m, 2H), 7.88 (t, *J* = 7.1 Hz, 1H), 7.80 (d, *J* = 8.2 Hz, 1H), 4.61 – 4.46 (m, 2H), 4.35 – 4.27 (m, 1H), 4.09 (dd, *J* = 11.0, 4.0 Hz, 1H), 3.96 (t, *J* = 7.1 Hz, 1H), 3.88 (t, *J* = 5.8 Hz, 2H), 3.66 – 3.51 (m, 4H), 3.32 (s, 4H), 3.28 (s, 4H), 3.26 (s, 4H), 2.96 – 2.81 (m, 4H), 2.74 – 2.58 (m, 10H), 2.25 – 2.12 (m, 2H), 1.96 – 1.88 (m, 1H), 1.83 (s, 3H), 1.42 – 1.34 (m, 54H), 0.87 – 0.79 (m, 6H). **¹³C NMR** (126 MHz, DMSO) δ 182.7, 182.6, 181.7, 171.8, 171.8, 171.4, 171.0, 170.9, 170.6, 170.5, 170.4, 170.2, 169.4, 169.3, 169.3, 169.2, 168.0, 168.0, 167.3, 167.1, 150.5, 147.7, 136.0, 130.2, 129.6, 129.5, 128.9, 128.1, 127.9, 126.5, 121.4, 119.9, 80.4, 80.1, 80.1, 80.1, 80.0, 79.6, 79.5, 58.8, 57.8, 57.7, 55.7, 55.5, 54.1, 51.8, 51.7, 51.6, 49.7, 49.6, 49.5, 49.5, 48.8, 42.8, 40.4, 39.5, 37.3, 35.1, 31.3, 31.2, 31.0, 30.7, 30.4, 29.8, 29.0, 28.8, 28.7, 28.6, 27.8, 27.8, 27.7, 27.6, 27.3, 22.5, 22.1, 19.1, 19.0, 18.5, 18.1, 13.9. **HRMS** (ESI) *m/z:* Calc. for $C_{64}H_{108}N_{10}O_{19}$ ([M+H]⁺): 1321.7792, Found: 1321.7888

Ac-DEVD-EDA-Sq-DO3A (3.19)

2,2',2''-(10-(2-(((5S,8S,11S,14S)-11-(2-carboxyethyl)-5,14-bis(carboxymethyl)-8-isopropyl-4,7,10,13,16-pentaoxo-3,6,9,12,15-pentaazaheptadecyl)amino)-3,4-dioxocyclobut-1-en-1-yl)-1,4,7,10-tetraazacyclododecane-1,4,7-triyl)triaceticacid
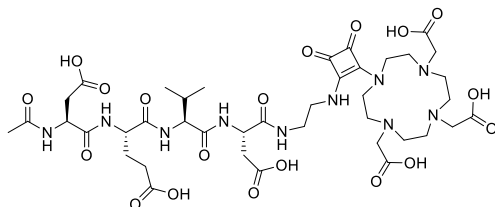
Protected peptide-conjugate **3.18** (110 mg, 0.08 mmol) was dissolved in 50:50 TFA/DCM (4 ml) and allowed to stir at r.t.p for 6 hours. LC-MS indicated the complete consumption of starting material (**3.18**). Thus, the TFA/DCM was evaporated using pressurised N_2 gas. The resulting oil was re-dissolved in a minimum amount of MeOH, before being added dropwise to cold diethyl ether. The precipitate was filtered, then re-dissolved in a minimum amount of H_2O before being purified via reverse-phase flash chromatography using a 0-5% gradient of MeCN in H_2O as eluent, to afford **3.19** as an off-white solid (75 mg, 91 %). **LC-MS** (0-100%) gradient of A in B, 55 min) t_R = 20 min. **^{1}H NMR** (500 MHz, DMSO) δ 8.36 (d, J = 8.0 Hz, 1H), 8.23 (d, J = 7.6 Hz, 1H), 8.16 (d, J = 7.4 Hz, 1H), 7.99 (d, J = 7.8 Hz, 1H), 7.95 (d, J = 7.8 Hz, 1H), 7.87 (t, J = 5.7 Hz, 1H), 7.83 (d, J = 7.1 Hz, 1H), 7.70 (d, J = 8.0 Hz, 1H), 7.62 – 7.53 (m, 1H), 4.58 – 4.49 (m, 2H), 4.48 – 4.41 (m, 1H), 4.33 – 4.24 (m, 1H), 4.09 – 4.03 (m, 1H), 3.98 (t, J = 7.1 Hz, 1H), 3.80 (s, 4H), 3.67 (s, 4H), 3.64 – 3.51 (m, 3H), 3.33 – 3.22 (m, 2H), 3.16 (s, 4H), 3.06 (s, 3H), 2.75 – 2.61 (m, 2H), 2.49 – 2.42 (m, 1H), 2.30 – 2.15 (m, 2H), 2.01 – 1.86 (m, 2H), 1.84 (s, 3H), 1.75 (m, 1H), 0.88 – 0.77 (m, 6H). **^{13}C NMR** (126 MHz, DMSO) δ 182.8, 182.7, 182.7, 174.2, 171.8, 171.8, 171.5, 171.3, 171.3, 171.2, 171.1, 171.0, 171.0, 170.9, 170.9, 170.8, 170.7, 170.7, 170.3, 169.8, 169.7, 168.1, 168.0, 167.7, 158.7, 158.5, 158.2, 157.9, 65.0, 58.7, 58.0, 54.2, 53.1, 52.2, 51.8, 49.8, 49.7, 48.8, 47.8, 42.9, 40.4, 39.5, 36.3, 36.0, 30.4, 30.1, 30.0, 27.2, 27.0, 22.5, 19.1, 19.0, 18.5, 18.1, 15.2. **IR** (ATR): v_{max} (cm^{-1}) = 3290, 2966, 2546, 1793, 1717, 1651, 1579, 1519, 1428, 1351, 1200, 1136, 1091, 990, 891, 824, 798, 765, 678, 599, 516, 474, 412. **HRMS** (ESI) *m/z:* Calc. for $C_{40}H_{60}N_{10}O_{19}$ ([M+H]$^+$): 985.4036, Found: 985.4115

6.4 Synthetic Procedures for Chapter 4

6.4.1 Alkyl Di-amine Synthesis

N^β-Fmoc amino acid (1.47 mmol) was added to a solution of NMM (4.42 mmol) in THF and the solution was stirred for 15 min at -10°C. Isobutyl chloroformate (2.94 mmol) was added dropwise and left to stir for another 60 min. After this time, the inorganic salts were filtered off and washed with excess THF. The resulting filtrate was added dropwise to a suspension of $NaBH_4$ (2.94 mmol) in a minimal amount of H_2O at 0°C. This reaction was stirred for 3 hrs at room temperature. The solvents were removed *in vacuo*, and the reaction mixture was redissolved in EtOAc. The organic layer was washed and extracted before being purified via flash chromatography – to afford the β-amino alcohol.

In the next step, the β-amino alcohol (1.0 mmol) was pre-dissolved in anhydrous DCM before being added – dropwise – to a stirred mixture of PPh_3 (3.0 mmol), imidazole (5.0 mmol) and iodine (3.0 mmol) in anhydrous DCM. The reaction mixture was placed under a N_2-atmosphere and was allowed to stir for 16 hrs at room temperature. After this time, the DCM concentrated *in vacuo* before being purified via flash chromatography – to afford the β-amino iodide.

The β-amino iodide (**2**) (1.0 mmol) was added to a solution of NaN_3 (5.0 mmol) in DMF. The reaction mixture was placed under a N_2-atmosphere and was allowed to stir for 16 hrs at room temperature. After this time, H_2O was added to the mixture and the crude compound was extracted with EtOAc. Organic phases were combined, dried with $MgSO_4$ and solvent concentrated *in vacuo* before being purified via flash chromatography – to afford the alkyl-azide.

In the following step, the alkyl-azide (1.0 mmol) was added to a suspension of Pd/C (0.25 mmol) in $CHCl_3$/MeOH (1:5), and was allowed to stir for 16 hrs at room temperature. After this time, the reaction mixture was filtered and washed with excess $CHCl_3$/MeOH (1:5). The filtrate solvent was reduced before being added dropwise to cold deionised H_2O. The resulting precipitate was then filtered and dried to afford the N^β-Fmoc alkyl-amine product.

6.3.1 Synthetic Methods

Fmoc-/MeVal-Arg(Pbf)-2-Cl-Trt
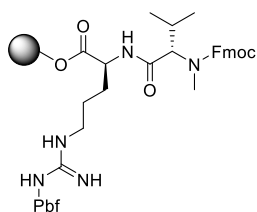
First residue loading (Fmoc-Arg(Pbf)-OH) was performed as outlined in the general methods above. A solution of Fmoc-*N*Me-Val-OH (270 mg, 0.77 mmol, 3 eq.), PyBOP (800 mg, 1.54 mmol) and NMM (255 µl, 2.31 mmol) in DMF (8 ml) was stirred in a small beaker for 15 min. After this time, the Fmoc-AA solution was added to the resin and allowed to shake for 90 min. The new peptide resin was then washed with *3x* DCM, *3x* DMF and *3x* DCM. **LC-MS** (0-100%) gradient of A in B, 55 min) t_R = 41 min.

Fmoc-D-Phe-/MeVal-Arg(Pbf)-2-Cl-Trt
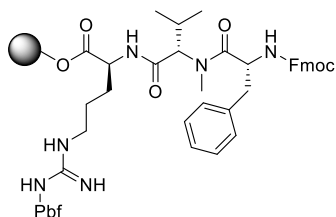
A solution of Fmoc-*D*-Phe-OH (300 mg, 0.77 mmol, 3 eq.), HATU (587 mg, 1.54 mmol) and DIPEA (382 µl, 2.31 mmol) in DMF (8 ml) was stirred in a small beaker for 15 min. After this time, the Fmoc-AA solution was added to the resin and allowed to shake for 90 min. The resin was washed with *3x* DMF, *3x* DCM, and *3x* DMF. An additional coupling step was required using the same conditions for another 30 min. LC-MS indicated the complete consumption of starting material after this time. The new peptide resin was then washed with *3x* DCM, *3x* DMF and *3x* DCM. **LC-MS** (0-100%) gradient of A in B, 55 min) t_R = 42 min.

ESq-D-Phe-/MeVal-Arg(Pbf)-2-Cl-Trt (4.5)
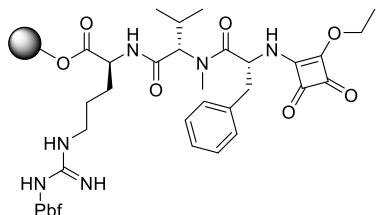
Fmoc-deprotection (as before). The peptide resin was treated with a solution of DESq (190 µl, 1.28 mmol, 5 eq.) and TEA (174 µl, 1.28 mmol) in DMF (10 ml) for 16 hrs. LC-MS indicated complete consumption of starting material. The new resin was washed with *3x* DCM, *3x* DMF and *3x* DCM. **LC-MS** (0-100%) gradient of A in B, 55 min) t_R = 35 min.

NH$_2$-G(ψ)-Sq-*D*-Phe-*N*MeVal-Arg(Pbf)-OH (4.6)

N^2-(N-((2-((2-aminoethyl)amino)-3,4-dioxocyclobut-1-en-1-yl)-D-phenylalanyl)-
N-methyl-L-valyl)-N^ω-((2,2,4,6,7-pentamethyl-2,3-dihydrobenzofuran-5-
yl)sulfonyl)-L-arginine
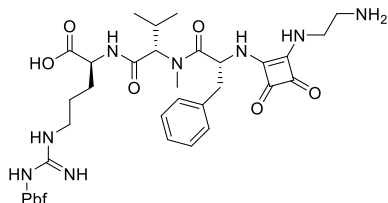
The peptide resin (**4.5**) was treated with a solution of EDA (256 µl, 3.84 mmol, 15 eq.) in DMF (10 ml) for 5 hrs. LC-MS indicated complete consumption of starting material. The new resin was washed with 3x DCM, 3x DMF and 3x DCM. The product was then removed from the resin via 30% HFIP/DCM (as before), to afford the linear peptide (**4.6**) as a pale-yellow solid (156 mg, 71 %). **LC-MS** (0-100%) gradient of A in B, 55 min) t_R = 27 min. **^{1}H NMR** (600 MHz, DMSO) δ 8.35 (s, 1H), 7.78 (s, 1H), 7.33 – 7.20 (m, 5H), 6.62 (s, 1H), 6.41 (s, 1H), 5.48 (s, 1H), 5.06 (s, 1H), 4.04 (s, 2H), 3.74 (s, 2H), 3.07 – 2.92 (m, 8H), 2.87 (s, 2H), 2.80 (s, 3H), 2.54 (s, 6H), 2.44 (s, 3H), 2.40 (s, 3H), 1.99 (s, 3H), 1.68 – 1.60 (m, 1H), 1.40 (s, 8H), 1.29 (s, 2H), 0.96 (d, *J* = 6.3 Hz, 3H), 0.57 (d, *J* = 6.0 Hz, 3H). **HRMS** (ESI) *m/z:* Calc. for C$_{40}$H$_{56}$N$_8$O$_9$S ([M+H]$^+$): 825.3891, Found: 825.3961

Note: (**ψ**) *denotes the modified C-terminal Amino Acid*

c(RG(ψ)-Sq-f*N*MeV) protected (4.7)

N-(N-(3-((7R,10S,13S)-13-benzyl-10-isopropyl-11-methyl-6,9,12,16,17-
pentaoxo-2,5,8,11,14-pentaazabicyclo[13.2.0]heptadec-1(15)-en-7-
yl)propyl)carbamimidoyl)-2,2,4,6,7-pentamethyl-2,3-dihydrobenzofuran-5-
sulfonamide
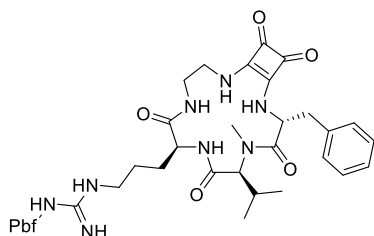
4.6 (21 mg, 0.025 mmol) was dissolved in a solution containing DIPEA (27 µl, 0.15 mmol) and 4 ml of DMF. Once the starting material was dissolved, the solvent volume was increased to 10 ml to give a final concentration of 2.5 mM. To this solution, PyBOP (39 mg, 0.075 mmol) was added and allowed to stir under N$_2$-atmosphere for 4 days. Reaction progress was monitored via LC-MS, with the appearance of a more non-polar (increased retention time) UV-peak resembling the cyclised product. At the

end of this time, the DMF was removed *in vacuo*, the crude mixture was redissolved in DCM and the organic layer was extracted from subsequent washes with 10% Citric Acid (aq.) & H_2O. The crude mixture was then dissolved in a minimum amount of MeCN before being purified via flash chromatography using a 0-5% gradient of MeOH in DCM as eluent, to afford the *protected product* (**4.7**) as an off-white solid (9.2 mg, 46 %). **LC-MS** (0-100%) gradient of A in B, 55 min) t_R = 34 min. **¹H NMR** (600 MHz, DMSO) δ 7.99 (d, *J* = 8.5 Hz, 1H), 7.35 – 7.25 (m, 5H), 7.25 – 7.17 (m, 2H), 6.65 (s, 2H), 6.36 (s, 2H), 5.32 (t, *J* = 7.0 Hz, 1H), 4.47 (d, *J* = 11.0 Hz, 1H), 3.90 – 3.78 (m, 1H), 3.51 (s, 1H), 3.49 – 3.41 (m, 2H), 3.09 – 2.98 (m, 6H), 2.96 (s, 3H), 2.47 (s, 3H), 2.42 (s, 3H), 2.20 – 2.13 (m, 1H), 2.04 – 1.95 (m, 4H), 1.77 (s, 2H), 1.41 (s, 6H), 1.23 (s, 2H), 0.86 (d, *J* = 6.8 Hz, 3H), 0.75 (s, 3H). **¹³C NMR** (151 MHz, DMSO) δ 183.7, 171.6, 157.4, 156.0, 137.3, 131.4, 129.6, 129.3, 128.2, 126.5, 124.3, 116.3, 86.3, 69.8, 42.5, 39.5, 38.7, 35.1, 31.3, 30.0, 29.1, 29.1, 29.0, 28.8, 28.7, 28.7, 28.6, 28.6, 28.3, 26.6, 26.6, 25.1, 22.1, 19.4, 18.9, 17.6, 13.9, 12.3. **HRMS** (ESI) *m/z:* Calc. for $C_{40}H_{54}N_8O_8S$ ([M+H]⁺): 807.3785, Found: 807.3859

c(RG(ψ)-Sq-f*N*MeV) (4.8)

1-(3-((7*R*,10*S*,13*S*)-13-benzyl-10-isopropyl-11-methyl-6,9,12,16,17-pentaoxo-2,5,8,11,14-pentaazabicyclo[13.2.0]heptadec-1(15)-en-7-yl)propyl)guanidine
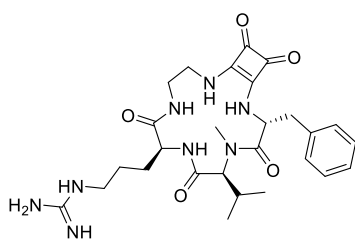
4.7 (9 mg, 0.011 mmol) was dissolved in 50:50 TFA/DCM (2 ml) and allowed to stir at r.t.p for 2 hours. LC-MS indicated the complete consumption of starting material. Thus, the TFA/DCM was evaporated using compressed air. The resulting oil was re-dissolved in a minimum amount of MeOH, before being added dropwise to cold diethyl ether. The precipitate was filtered, then re-dissolved in a minimum amount of MeCN before being purified via reverse-phase flash chromatography using a 0-5% gradient of MeCN in H_2O as eluent, to afford the *deprotected final product* (**4.8**) as a white solid (5.3 mg, 87 %). **LC-MS** (0-100%) gradient of A in B, 55 min) t_R = 24 min. **HRMS** (ESI) *m/z:* Calc. for $C_{27}H_{38}N_8O_5$ ([M+H]⁺): 555.2965, Found: 555.3038

Fmoc-Gly-Asp(O*t*Bu)-2-Cl-Trt
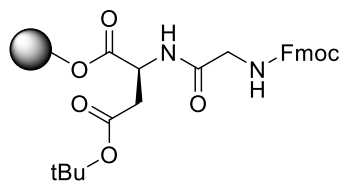
First residue loading (Fmoc-Asp(O*t*Bu)-OH) was performed as outlined in the general methods above. A solution of Fmoc-Gly-OH (340 mg, 1.14 mmol, 3 eq.), PyBOP (1.19 g, 2.29 mmol) and NMM (376 µl, 3.41 mmol) in DMF (8 ml) was stirred in a small beaker for 15 min. After this time, the Fmoc-AA solution was added to the resin and allowed to shake for 90 min. The new peptide resin was then washed with *3x* DCM, *3x* DMF and *3x* DCM. **LC-MS** (0-100%) gradient of A in B, 55 min) t_R = 35 min.

Fmoc-Arg(Pbf)-Gly-Asp(O*t*Bu)-2-Cl-Trt
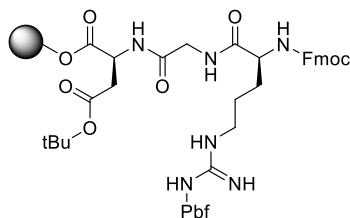
A solution of Fmoc-Arg(Pbf)-OH (740 mg, 1.14 mmol, 3 eq.), PyBOP (1.19 g, 2.29 mmol) and NMM (376 µl, 3.41 mmol) in DMF (8 ml) was stirred in a small beaker for 15 min. After this time, the Fmoc-AA solution was added to the resin and allowed to shake for 90 min. The new peptide resin was then washed with *3x* DCM, *3x* DMF and *3x* DCM. **LC-MS** (0-100%) gradient of A in B, 55 min) t_R = 39 min.

ESq-Arg(Pbf)-Gly-Asp(O*t*Bu)-2-Cl-Trt
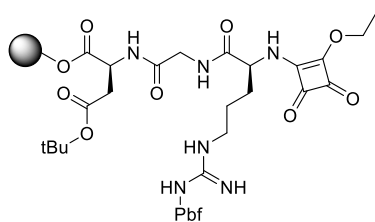
Fmoc-deprotection (as before). The peptide resin was treated with a solution of DESq (281 µl, 1.89 mmol, 5 eq.) and TEA (265 µl, 1.89 mmol) in DMF (10 ml) for 16 hrs. LC-MS indicated complete consumption of starting material. The new resin was washed with *3x* DCM, *3x* DMF and *3x* DCM. **LC-MS** (0-100%) gradient of A in B, 55 min) t_R = 32 min.

Fmoc-*D*-Phe-ψ[CH$_2$OH] (4.9b)

(9*H*-fluoren-9-yl)methyl (*R*)-(1-hydroxy-3-phenylpropan-2-yl)carbamate
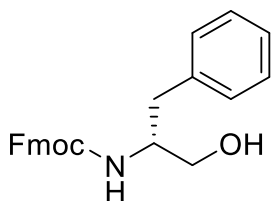
Fmoc-*D*-Phe-OH (**4.9a**) (500 mg, 1.29 mmol) was added to a solution of NMM (426 µl, 3.87 mmol) in THF (5 ml) and the solution was stirred for 15 min at -10°C. Isobutyl chloroformate (335 µl, 2.58 mmol) was added dropwise (over 10 min) and left to stir for another 60 min. After this time, the newly formed white precipitate was filtered off and washed with excess THF. The resulting filtrate was added dropwise to a suspension of NaBH$_4$ (98 mg, 2.58 mmol) in a minimal amount of H$_2$O at 0°C. This reaction was stirred for 3 hrs at room temperature. The crude reaction mixture was then decanted into cold H$_2$O (200 ml), filtered, washed with excess H$_2$O, and dried, to afford the *β*-amino alcohol (**4.9b**) as a white solid (361 mg, 75 %) – without further purification. **LC-MS** (0-100%) gradient of A in B, 55 min) t_R = 38 min. **^{1}H NMR** (500 MHz, DMSO) δ 7.88 (d, *J* = 7.5 Hz, 2H), 7.64 (t, *J* = 7.4 Hz, 2H), 7.44 – 7.36 (m, 2H), 7.34 – 7.27 (m, 2H), 7.27 – 7.19 (m, 4H), 7.19 – 7.12 (m, 2H), 4.77 (t, *J* = 5.6 Hz, 1H), 4.26 – 4.19 (m, 1H), 4.19 – 4.10 (m, 2H), 3.68 – 3.58 (m, 1H), 3.42 – 3.35 (m, 1H), 2.85 (dd, *J* = 13.6, 5.0 Hz, 1H), 2.65 – 2.56 (m, 1H). **IR** (ATR): v_{max} (cm^{-1}) = 3323, 3060, 3025, 2948, 2888, 1686, 1601, 1533, 1445, 1381, 1318, 1258, 1147, 1085, 1015, 935, 900, 866, 733, 700, 646, 620, 587, 536, 503, 426.

Note: (*ψ*) *denotes the modified C-terminal Amino Acid*

Fmoc-*D*-Phe-ψ[CH$_2$I] (4.9c)

(9*H*-fluoren-9-yl)methyl (*R*)-(1-iodo-3-phenylpropan-2-yl)carbamate
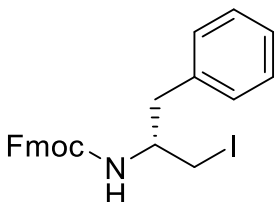
4.9b (250 mg, 0.67 mmol) was pre-dissolved in anhydrous DCM (5 ml, few drops DMSO) before being added – dropwise – to a solution of PPh$_3$ (526 mg, 2.01 mmol), imidazole (227 mg, 3.34 mmol) and iodine (507 mg, 2.01 mmol) in anhydrous DCM (20 ml). The reaction mixture was placed under a N$_2$-atmosphere and was allowed to stir for 16 hrs at room temperature. After this time, the DCM concentrated *in vacuo* before being purified via flash chromatography using a 0-10% gradient of EtOAc in Cyclohexane as eluent, to

afford the β-amino iodide (**4.9c**) as an off-white solid (272 mg, 84 %). **LC-MS** (0-100%) gradient of A in B, 55 min) t_R = 44 min. **^{1}H NMR** (500 MHz, DMSO) δ 7.88 (d, J = 7.5 Hz, 2H), 7.66 (d, J = 7.5 Hz, 2H), 7.57 (d, J = 8.2 Hz, 1H), 7.44 – 7.38 (m, 2H), 7.35 – 7.28 (m, 2H), 7.28 – 7.21 (m, 4H), 7.21 – 7.16 (m, 1H), 4.29 – 4.13 (m, 3H), 3.72 – 3.62 (m, 1H), 3.38 (dd, J = 10.0, 4.8 Hz, 1H), 3.23 (dd, J = 10.0, 6.9 Hz, 1H), 2.85 (dd, J = 13.6, 5.3 Hz, 1H), 2.73 (dd, J = 13.6, 8.7 Hz, 1H). **IR** (ATR): v_{max} (cm^{-1}) = 3326, 3022, 2947, 2889, 2852, 2160, 1681, 1606, 1527, 1450, 1377, 1300, 1261, 1213, 1146, 1108, 1085, 1032, 994, 937, 875, 834, 734, 702, 621, 587, 557, 505, 426.

Fmoc-*D*-Phe-ψ[CH$_2$N$_3$] (4.9d)

(9*H*-fluoren-9-yl)methyl (*R*)-(1-azido-3-phenylpropan-2-yl)carbamate
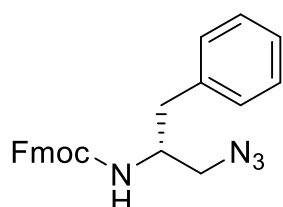
4.9c (250 mg, 0.52 mmol) was added to a solution of NaN$_3$ (168 mg, 2.56 mmol) in DMF (15 ml). The reaction mixture was placed under a N$_2$-atmosphere and was allowed to stir for 16 hrs at room temperature. After this time, H$_2$O was added to the mixture and the crude compound was extracted with *3x* EtOAc. Organic phases were combined, dried with MgSO$_4$ and solvent concentrated *in vacuo* before being purified via flash chromatography using a 0-20% gradient of EtOAc in Cyclohexane as eluent, to afford the alkyl-azide (**4.9d**) as an off-white solid (106 mg, 51 %). **LC-MS** (0-100%) gradient of A in B, 55 min) t_R = 43 min. **IR** (ATR): v_{max} (cm^{-1}) = 3317, 3062, 3028, 2923, 2096, 1687, 1603, 1537, 1495, 1448, 1258, 1146, 1082, 1046, 934, 813, 733, 699, 668, 620, 587, 555, 531, 508, 468, 426.

Fmoc-*D*-Phe-ψ[CH$_2$NH$_2$] (4.9e)

(9*H*-fluoren-9-yl)methyl (*R*)-(1-amino-3-phenylpropan-2-yl)carbamate
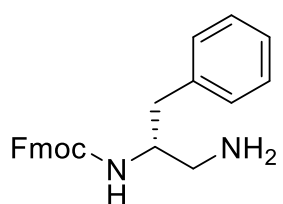
4.9d (50 mg, 0.13 mmol) was added to a suspension of Pd/C (4.3 mg, 0.026 mmol) in CHCl$_3$/MeOH (1:5, 10 ml). The reaction mixture was bubbled through with H$_2$ gas before being placed under a H$_2$-atmosphere, and was allowed to stir for 16 hrs at room temperature. After this time, the reaction mixture

was filtered through a pad of *Ceilite®* and washed with excess CHCl$_3$/MeOH (1:5). The filtrate solvent was reduced by ~95% before being added dropwise to cold deionised H$_2$O. The resulting precipitate was then filtered and dried to afford the alkyl-amine product (**4.9e**) as an off-white solid (40 mg, 83 %). **LC-MS** (0-100%) gradient of A in B, 55 min) t_R = 28 min. **^{1}H NMR** (500 MHz, DMSO) δ 8.10 (s, 2H), 7.89 (d, *J* = 7.5 Hz, 2H), 7.66 – 7.61 (m, 2H), 7.45 – 7.38 (m, 3H), 7.36 – 7.29 (m, 2H), 7.29 – 7.22 (m, 2H), 7.20 (d, *J* = 7.3 Hz, 2H), 4.35 – 4.27 (m, 1H), 4.21 – 4.12 (m, 2H), 3.96 – 3.85 (m, 1H), 2.87 – 2.79 (m, 2H), 2.76 – 2.68 (m, 1H). **^{13}C NMR** (126 MHz, DMSO) δ 155.8, 143.8, 143.7, 140.7, 140.7, 137.8, 129.2, 128.2, 127.6, 127.1, 127.0, 126.3, 125.3, 125.1, 120.1, 65.5, 50.7, 46.7, 42.0, 39.5, 37.6, 30.7. **IR** (ATR): v_{max} (cm^{-1}) = 3333, 3064, 3032, 2875, 2772, 2692, 2642, 1698, 1596, 1534, 1449, 1390, 1316, 1256, 1202, 1152, 1121, 1087, 1033, 993, 843, 735, 700, 646, 619, 573, 535, 466, 426.

Fmoc-Asp(O*t*Bu)-*D*-Phe
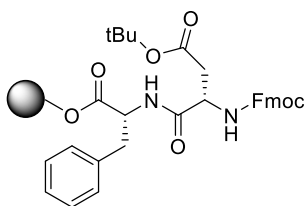
First residue loading (Fmoc-*D*-Phe-OH) was performed as outlined in the general methods above. A solution of Fmoc-Asp(O*t*Bu)-OH (570 mg, 1.39 mmol, 3 eq.), PyBOP (1.45 g, 2.78 mmol) and NMM (460 μl, 4.18 mmol) in DMF (8 ml) was stirred in a small beaker for 15 min. After this time, the Fmoc-AA solution was added to the resin and allowed to shake for 90 min. The new peptide resin was then washed with *3x* DCM, *3x* DMF and *3x* DCM. **LC-MS** (0-100%) gradient of A in B, 55 min) t_R = 40 min.

Fmoc-Gly-Asp(O*t*Bu)-*D*-Phe-2-Cl-Trt
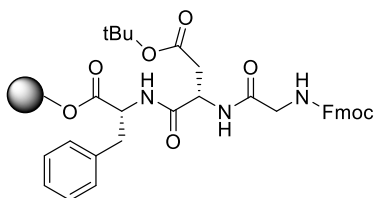
A solution of Fmoc-Gly-OH (410 mg, 1.38 mmol, 3 eq.), PyBOP (1.45 g, 2.78 mmol) and NMM (460 μl, 4.18 mmol) in DMF (8 ml) was stirred in a small beaker for 15 min. After this time, the Fmoc-AA solution was added to the resin and allowed to shake for 90 min. The new peptide resin was then washed with *3x* DCM, *3x* DMF and *3x* DCM. **LC-MS** (0-100%) gradient of A in B, 55 min) t_R = 38 min.

Synthesis of ESq-Gly-Asp(OtBu)-D-Phe-2-Cl-Trt
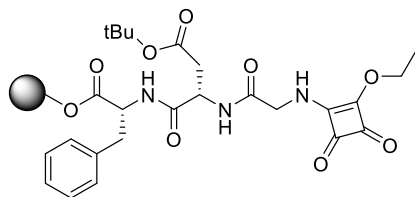
Fmoc-deprotection (as before). The peptide resin was treated with a solution of DESq (340 μl, 2.30 mmol, 5 eq.) and TEA (321 μl, 2.30 mmol) in DMF (10 ml) for 16 hrs. LC-MS indicated complete consumption of starting material. The new resin was washed with *3x* DCM, *3x* DMF and *3x* DCM. **LC-MS** (0-100%) gradient of A in B, 55 min) t_R = 30 min.

Fmoc-Val-ψ[CH₂OH] (4.10b)

(9*H*-fluoren-9-yl)methyl (*S*)-(1-hydroxy-3-methylbutan-2-yl)carbamate
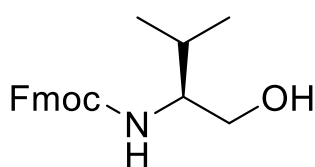
Synthesized via general procedure… to afford the *β*-amino alcohol (**4.10b**) as a white solid (312 mg, 65 %) – without further purification. **LC-MS** (0-100%) gradient of A in B, 55 min) t_R = 36 min. **¹H NMR** (500 MHz, DMSO) δ 7.89 (d, *J* = 7.5 Hz, 2H), 7.72 (d, *J* = 7.4 Hz, 2H), 7.41 (td, *J* = 7.4 Hz, 2H), 7.35 – 7.29 (m, 2H), 6.99 (d, *J* = 9.0 Hz, 1H), 4.51 (d, *J* = 7.2 Hz, 1H), 4.31 (dd, *J* = 13.0, 9.8 Hz, 1H), 4.24 – 4.18 (m, 2H), 3.43 – 3.34 (m, 2H), 1.84 – 1.75 (m, 1H), 0.85 (d, *J* = 6.7 Hz, 3H), 0.82 (d, *J* = 6.8 Hz, 3H). **IR** (ATR): v_{max} (cm^{-1}) = 3464, 3343, 3067, 3041, 2964, 2872, 1664, 1541, 1447, 1402, 1312, 1251, 1228, 1123, 1071, 1043, 976, 929, 882, 825, 762, 735, 670, 642, 621, 589, 532, 428.

Note: (**ψ**) *denotes the modified C-terminal Amino Acid*

Fmoc-Val-ψ[CH₂I] (4.10c)

(9*H*-fluoren-9-yl)methyl (*S*)-(1-iodo-3-methylbutan-2-yl)carbamate
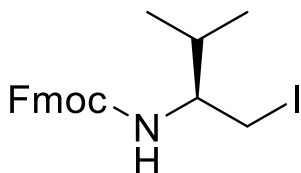
Synthesized via general procedure… to afford the *β*-amino iodide (**4.10c**) as an off-white solid (337 mg, 87 %). **LC-MS** (0-100%) gradient of A in B, 55 min) t_R = 44 min. **¹H NMR** (500 MHz, CDCl₃) δ 7.89 (d, *J* = 7.4 Hz, 2H), 7.73 (t, *J* = 7.9 Hz, 2H), 7.44 – 7.35 (m, 3H), 7.35 – 7.28 (m, 2H), 4.37 – 4.26 (m, 2H), 4.23 (t, *J* = 7.0 Hz, 1H), 3.43 (dd, *J* = 10.0, 3.5 Hz, 1H), 3.22 (d, *J* = 7.2 Hz, 1H), 1.81 – 1.71 (m, 1H), 0.88 – 0.78 (m, 6H). **IR** (ATR): v_{max} (cm^{-1}) = 3300,

3048, 3020, 2961, 2871, 2161, 1686, 1610, 1526, 1449, 1369, 1312, 1283, 1251, 1179, 1150, 1118, 1088, 1031, 979, 936, 862, 817, 735, 691, 645, 620, 531, 497, 427.

Fmoc-Val-ψ[CH$_2$N$_3$] (4.10d)

(9*H*-fluoren-9-yl)methyl (*S*)-(1-azido-3-methylbutan-2-yl)carbamate
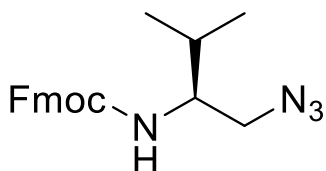
Synthesized via general procedure… to afford the alkyl-azide (**4.10d**) as an off-white solid (87 mg, 39 %). **LC-MS** (0-100%) gradient of A in B, 55 min) t_R = 42 min. **IR** (ATR): v_{max} (cm^{-1}) = 3318, 2961, 2874, 2094, 1688, 1532, 1445, 1295, 1243, 1157, 1117, 1079, 1031, 980, 933, 889, 843, 734, 664, 573, 534, 509, 461, 427.

Fmoc-Val-ψ[CH$_2$NH$_2$] (4.10e)

(9*H*-fluoren-9-yl)methyl (*S*)-(1-amino-3-methylbutan-2-yl)carbamate
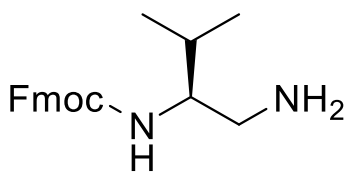
Synthesized via general procedure… to afford the alkyl-amine product (**4.10e**) as an off-white solid (38 mg, 74 %). **LC-MS** (0-100%) gradient of A in B, 55 min) t_R = 27 min. **^{1}H NMR** (500 MHz, DMSO) δ 8.00 (s, 2H), 7.90 (d, *J* = 7.5 Hz, 2H), 7.73 (dd, *J* = 7.8 Hz, 2H), 7.42 (dd, *J* = 7.5 Hz, 2H), 7.33 (dd, *J* = 7.4 Hz, 2H), 7.28 (d, *J* = 9.1 Hz, 1H), 4.45 (dd, *J* = 13.3, 9.8 Hz, 1H), 4.26 – 4.20 (m, 2H), 3.55 – 3.47 (m, 1H), 2.91 (d, *J* = 11.9 Hz, 1H), 2.73 (t, *J* = 10.9 Hz, 1H), 1.78 – 1.69 (m, 1H), 0.84 (d, *J* = 6.8 Hz, 3H), 0.81 (d, *J* = 6.8 Hz, 3H). **^{13}C NMR** (126 MHz, DMSO) δ 156.3, 144.0, 143.7, 140.8, 127.6, 127.6, 127.0, 125.3, 125.2, 120.1, 120.1, 65.4, 54.2, 46.8, 40.4, 39.5, 30.2, 18.9, 17.9. **IR** (ATR): v_{max} (cm^{-1}) = 3352, 3022, 2962, 2867, 2687, 2621, 2578, 2456, 2323, 2022, 1980, 1681, 1598, 1527, 1448, 1405, 1357, 1309, 1255, 1194, 1121, 1072, 1020, 978, 860, 737, 644, 620, 563, 535, 470, 424.

Fmoc-Arg(Pbf)-Gly-2-Cl-Trt
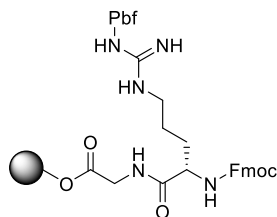
First residue loading (Fmoc-*Gly*-OH) was performed as outlined in the general methods above. A solution of Fmoc-Arg(Pbf)-OH (860 mg, 1.32 mmol, 3 eq.), PyBOP (1.37 g, 2.63 mmol) and NMM (436 µl, 3.87 mmol) in DMF (8 ml) was stirred in a small beaker for 15 min. After this time, the Fmoc-AA solution was added to the resin and allowed to shake for 90 min. The new peptide resin was then washed with *3x* DCM, *3x* DMF and *3x* DCM. **LC-MS** (0-100%) gradient of A in B, 55 min) t_R = 37 min.

Fmoc-*N*MeVal-Arg(Pbf)-Gly-2-Cl-Trt
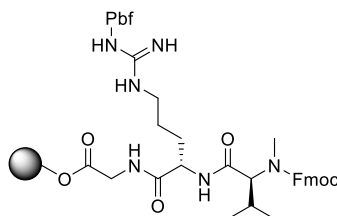
A solution of Fmoc-*N*MeVal-OH (470 mg, 1.32 mmol, 3 eq.), PyBOP (1.37 g, 2.63 mmol) and NMM (436 µl, 3.87 mmol) in DMF (8 ml) was stirred in a small beaker for 15 min. After this time, the Fmoc-AA solution was added to the resin and allowed to shake for 90 min. The new peptide resin was then washed with *3x* DCM, *3x* DMF and *3x* DCM. **LC-MS** (0-100%) gradient of A in B, 55 min) t_R = 40 min.

Fmoc-Asp(O*t*Bu)-ψ[CH$_2$OH] (4.11b)

tert-butyl (*S*)-3-(((((9H-fluoren-9-yl)methoxy)carbonyl)amino)-4-hydroxybutanoate
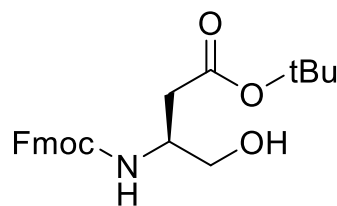
Synthesised via general procedure… to afford the β-amino alcohol (**4.11b**) as an off-white solid (294 mg, 61 %). **LC-MS** (0-100%) gradient of A in B, 55 min) t_R = 39 min. **¹H NMR** (500 MHz, DMSO) δ 7.88 (d, *J* = 7.5 Hz, 2H), 7.72 – 7.65 (m, 2H), 7.44 – 7.38 (m, 2H), 7.35 – 7.29 (m, 2H), 7.14 (d, *J* = 8.7 Hz, 1H), 4.79 (d, *J* = 6.9 Hz, 1H), 4.33 – 4.22 (m, 2H), 4.19 (t, *J* = 6.8 Hz, 1H), 3.88 – 3.78 (m, 1H), 3.38 – 3.34 (m, 1H), 3.25 – 3.18 (m, 1H), 2.46 (d, *J* = 5.0 Hz, 1H), 2.21 (dd, *J* = 15.1, 9.1 Hz, 1H), 1.35 (s, 9H).

Note: (*ψ*) *denotes the modified C-terminal Amino Acid*

Fmoc-Asp(O*t*Bu)-ψ[CH₂I] (4.11c)

tert-butyl (*S*)-3-((((9H-fluoren-9-yl)methoxy)carbonyl)amino)-4-iodobutanoate
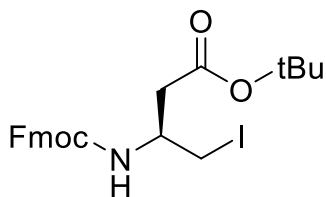
*Synthesised via general procedure… to afford the β-amino iodide (**4.11c**) as an off-white solid (269 mg, 77 %).* **LC-MS** (0-100%) gradient of A in B, 55 min) t_R = 44 min.

Fmoc-Asp(O*t*Bu)-ψ[CH₂N₃] (4.11d)

tert-butyl (*S*)-3-((((9H-fluoren-9-yl)methoxy)carbonyl)amino)-4-azidobutanoate
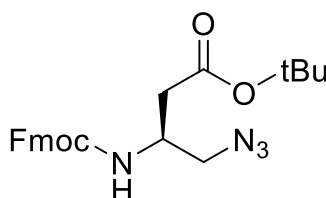
*Synthesised via general procedure… to afford the alkyl-azide (**4.11d**) as an off-white solid (109 mg, 39 %).* **LC-MS** (0-100%) gradient of A in B, 55 min) t_R = 43 min. **¹H NMR** (500 MHz, DMSO) δ 7.89 (d, *J* = 7.5 Hz, 2H), 7.71 – 7.65 (m, 2H), 7.49 (d, *J* = 8.6 Hz, 1H), 7.44 – 7.38 (m, 2H), 7.34 – 7.29 (m, 2H), 4.35 – 4.28 (m, 2H), 4.21 (t, *J* = 6.8 Hz, 1H), 4.02 – 3.93 (m, 1H), 3.32 – 3.27 (m, 2H), 2.43 (dd, *J* = 15.4, 5.7 Hz, 1H), 2.35 (dd, *J* = 15.4, 8.6 Hz, 1H), 1.36 (s, 9H).

Fmoc-Asp(O*t*Bu)-ψ[CH₂NH₂] (4.11e)

tert-butyl (*S*)-3-((((9H-fluoren-9-yl)methoxy)carbonyl)amino)-4-aminobutanoate
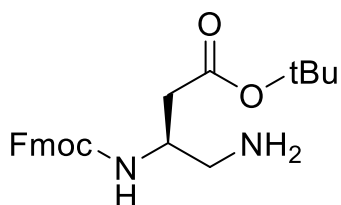
*Synthesised via general procedure… to afford the alkyl-amine product (**4.11e**) as an off-white solid (64 mg, 87 %).* **LC-MS** (0-100%) gradient of A in B, 55 min) t_R = 27 min. **¹H NMR** (500 MHz, DMSO) δ 8.10 (s, 2H), 7.89 (d, *J* = 7.8 Hz, 2H), 7.72 – 7.65 (m, 2H), 7.45 – 7.38 (m, 3H), 7.35 – 7.30 (m, 2H), 4.37 (dd, *J* = 10.4, 6.3 Hz, 1H), 4.29 – 4.19 (m, 2H), 4.11 – 4.02 (m, 1H), 2.92 – 2.83 (m, 1H), 2.83 – 2.74 (m, 1H), 2.55 (dd, *J* = 15.5, 4.9 Hz, 1H), 2.37 (dd, *J* = 15.5, 9.0 Hz, 1H), 1.36 (s, 9H). **¹³C NMR** (126 MHz, DMSO) δ 169.3, 155.7, 143.9, 143.7, 140.8, 127.7, 127.1, 125.2, 125.2, 120.2, 80.3, 65.7, 46.6, 46.5, 42.1, 39.5, 38.1, 27.7.

Fmoc-*D*-Phe-*N*MeVal-2-Cl-Trt
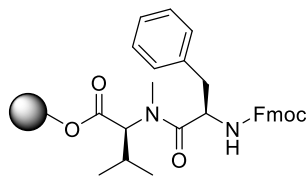
First residue loading (Fmoc-*N*MeVal-OH) was performed as outlined in the general methods above. A solution of Fmoc-D-Phe-OH (420 mg, 1.07 mmol, 3 eq.), HATU (817 mg, 2.15 mmol) and DIPEA (531 μl, 3.22 mmol) in DMF (8 ml) was stirred in a small beaker for 15 min. After this time, the Fmoc-AA solution was added to the resin and allowed to shake for 90 min. The new peptide resin was then washed with *3x* DCM, *3x* DMF and *3x* DCM. **LC-MS** (0-100%) gradient of A in B, 55 min) t_R = 40 min.

Fmoc-Arg(Pbf)-ψ[CH$_2$OH] (4.12b)

(9*H*-fluoren-9-yl)methyl-(*S*)-(1-hydroxy-5-(3-((2,2,4,6,7-pentamethyl-2,3-dihydrobenzofuran-5-yl)sulfonyl)guanidino)pentan-2-yl)carbamate
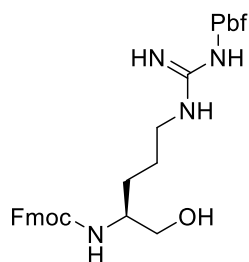
Synthesised via general procedure… to afford the *β*-amino alcohol (**4.12b**) as an off-white solid (254 mg, 52 %). **LC-MS** (0-100%) gradient of A in B, 55 min) t_R = 39 min. **^{1}H NMR** (500 MHz, DMSO) δ 7.88 (d, *J* = 7.5 Hz, 2H), 7.70 (d, *J* = 7.5 Hz, 2H), 7.43 – 7.37 (m, 2H), 7.34 – 7.28 (m, 2H), 7.04 (d, *J* = 8.6 Hz, 1H), 4.66 (t, *J* = 5.5 Hz, 1H), 4.32 – 4.22 (m, 2H), 4.22 – 4.17 (m, 1H), 3.33 – 3.29 (m, 1H), 3.26 – 3.19 (m, 1H), 3.05 – 2.98 (m, 2H), 2.93 (s, 2H), 2.48 (s, 3H), 2.42 (s, 3H), 1.99 (s, 2H), 1.99 (s, 3H), 1.38 (s, 6H). **IR** (ATR): v_{max} (cm^{-1}) = 3436, 3328, 3157, 3067, 2933, 2874, 1698, 1615, 1544, 1449, 1406, 1369, 1240, 1152, 1087, 1034, 993, 901, 851, 807, 739, 659, 566, 506, 424.

Note: (*ψ*) *denotes the modified C-terminal Amino Acid*

Fmoc-Arg(Pbf)-ψ[CH$_2$I] (4.12c)

(9*H*-fluoren-9-yl)methyl-(*S*)-(1-iodo-5-(3-((2,2,4,6,7-pentamethyl-2,3-dihydrobenzofuran-5-yl)sulfonyl)guanidino)pentan-2-yl)carbamate
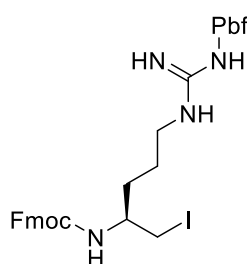
Synthesised via general procedure… to afford the β-amino iodide (**4.12c**) as an off-white solid (213 mg, 67 %). **LC-MS** (0-100%) gradient of A in B, 55 min) t_R = 44 min. **^{1}H NMR** (500 MHz, DMSO) δ 7.89 (d, *J* = 7.9 Hz, 2H), 7.73 – 7.68 (m, 2H), 7.43 – 7.37 (m, 3H), 7.35 – 7.29 (m, 2H), 4.38 – 4.26 (m, 2H), 4.22 (t, *J* = 6.4 Hz, 1H), 3.44 – 3.36 (m, 1H), 3.32 – 3.25 (m, 1H), 3.21 – 3.13 (m, 1H), 3.04 – 2.98 (m, 2H), 2.94 (s, 2H), 2.48 (s, 3H), 2.42 (s, 3H), 2.00 (s, 3H), 1.99 (s, 2H), 1.53 – 1.45 (m, 1H), 1.39 (s, 6H), 1.36 – 1.30 (m, 2H). **IR** (ATR): v_{max} (cm^{-1}) = 3440, 3332, 2968, 2934, 1703, 1615, 1545, 1449, 1405, 1370, 1334, 1239, 1153, 1089, 1043, 993, 903, 851, 805, 783, 734, 659, 619, 566, 505, 425.

Fmoc-Arg(Pbf)-ψ[CH$_2$N$_3$] (4.12d)

(9*H*-fluoren-9-yl)methyl-(*S*)-(1-azido-5-(3-((2,2,4,6,7-pentamethyl-2,3-dihydrobenzofuran-5-yl)sulfonyl)guanidino)pentan-2-yl)carbamate
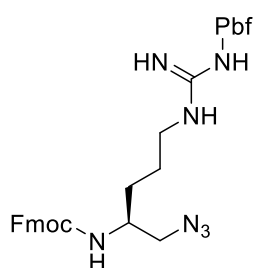
Synthesised via general procedure… to afford the alkyl-azide (**4.12d**) as an off-white solid (93 mg, 49 %). **LC-MS** (0-100%) gradient of A in B, 55 min) t_R = 42 min. **^{1}H NMR** (500 MHz, DMSO) δ 7.89 (d, *J* = 7.1 Hz, 2H), 7.69 (d, *J* = 7.4 Hz, 2H), 7.43 – 7.35 (m, 3H), 7.34 – 7.28 (m, 2H), 4.36 – 4.29 (m, 2H), 4.21 (t, *J* = 6.8 Hz, 1H), 3.60 – 3.51 (m, 1H), 3.28 – 3.18 (m, 2H), 3.05 – 2.97 (m, 2H), 2.94 (s, 2H), 2.48 (s, 3H), 2.42 (s, 3H), 2.00 (s, 3H), 1.99 (s, 1H), 1.39 (s, 7H), 1.34 – 1.25 (m, 2H). **IR** (ATR): v_{max} (cm^{-1}) = 3432, 3329, 2971, 2933, 2868, 2098, 1699, 1615, 1545, 1448, 1406, 1369, 1240, 1152, 1087, 1034, 993, 903, 851, 806, 738, 659, 565, 506, 425.

Amino squarate (ASq, 4.0a)

3-amino-4-ethoxycyclobut-3-ene-1,2-dione
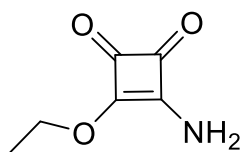
2M ethanolic-ammonia (24.2 ml, 48.5 mmol) was added drop-wise over 5 hours via syringe pump to a solution of DESq (**3.1**) (3.3 g, 19.4 mmol) in EtOH (60 ml), and the solution was stirred for 16 hrs at r.t.p. The resulting precipitate was filtered and washed with cold EtOH to yield the crude product. The crude product was then re-dissolved in a minimum amount of DCM, before being purified via flash chromatography using a 0-30% gradient of MeOH in DCM as eluent, to afford **4.0a** as a pale-yellow solid (2.12 g, 77 %). **LC-MS** (0-100%) gradient of A in B, 55 min) t_R = 20 min. **^{1}H NMR** (400 MHz, DMSO) δ 8.31 (s, 2H), 4.64 (q, J = 7.1 Hz, 2H), 1.36 (t, J = 7.1 Hz, 3H). **^{13}C NMR** (101 MHz, DMSO) δ 190.1, 183.1, 177.8, 174.3, 68.6, 39.5, 15.6. **IR** (ATR): v_{max} (cm^{-1}) = 3330, 3073, 2970, 2928, 1809, 1697, 1642, 1547, 1477, 1437, 1375, 1351, 1263, 1185, 1147, 1090, 1033, 873, 775, 659, 579, 454, 418.

6.5 Interpreting LC-MS Data

This section will briefly outline how to interpret the LC-MS data using **2.4** as an example (spectra below).
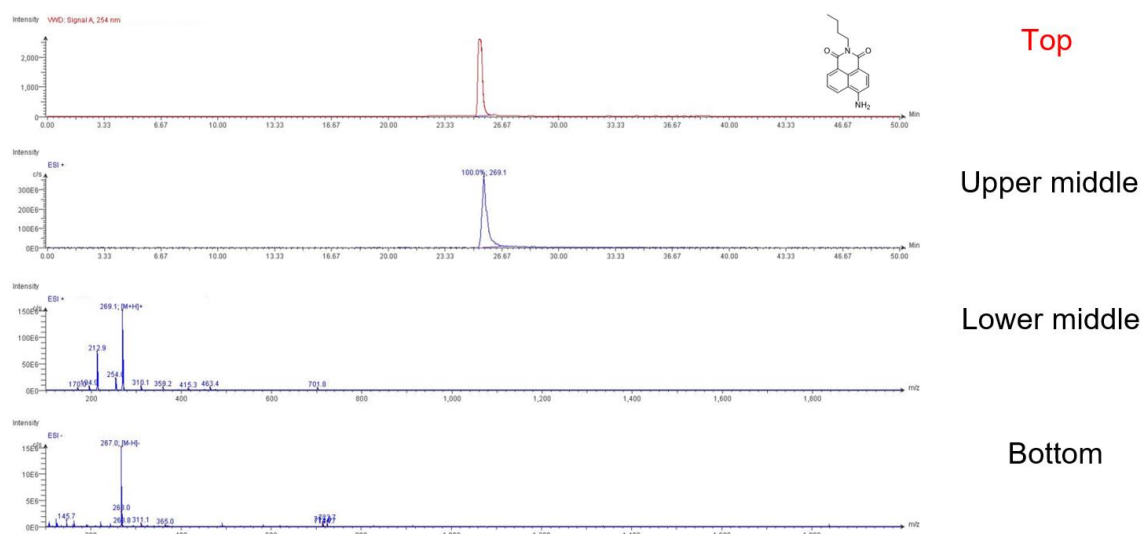
The **Top** spectrum is a HPLC chromatogram generated by a deuterium lamp at 254 nm. There is only one UV peak present, indicating that there is only one UV-active molecule in the sample. This particular compound has a retention time (t_R) = 25 minutes.

The spectrum immediately below (**Upper middle**) is an Extracted Ion Chromatogram (XIC) in positive mode (ESI+), and plots the intensity of the signal observed at a chosen m/z value (target mass $[M+H]^+$ = 269.1 gmol^{-1} in this case) as a function of t_R. This tells us that all the $[M+H]^+$ species – with a target mass of 269.1 gmol^{-1} – appeared directly under the sharp UV-peak, giving us strong evidence to suggest that the peak observed from the HPLC trace does indeed correspond to the compound.

The final two spectra – **Lower middle** and **Bottom** – detail the full-view mass spectrum under the observed UV-signal (at t_R = 25 min) for both ESI+ and ESI-, respectively. These spectra give us an idea of all the mass-ions that are present when we "look under" the UV-signal of interest, usually highlighting target mass and potential adducts. Indeed, in this example strong ionisation was observed in positive mode (ESI +) and negative mode (ESI -) for the target mass(es) of $[M+H]^+$ = 269.1 gmol^{-1} and $[M-H]^+$ = 267.0 gmol^{-1}, respectively.

6.6 Loading of First Amino Acid Residue

2-chlorotrityl chloride resin (*FluoroChem*) was weighed out into a 20 ml fritted-syringe. The resin was suspended in 10 ml of DCM and allowed to swell for ~1 hour. After this time, a solution of Fmoc amino-acid and DIPEA in DCM was added to the resin. The resin was agitated gently for 2 hours, then washed consecutively with *3x* DCM/MeOH/DIPEA (17:2:1), *3x* DCM, *3x* DMF, *3x* DCM, before being dried *in vacuo.*

Dry Fmoc amino-acid resin (approx. 5 µmol with respect to Fmoc) was weighed into two separate 10 ml volumetric flasks. 2 ml of 10% Piperidine sol. (in DMF) was added and agitated gently for 30 minutes. The solution(s) were diluted to 10 ml with MeCN. 2 ml of each solution was transferred to two individual 25 ml volumetric flasks and diluted to the mark again with MeCN (solution 1 and solution 2, i.e. Duplicate). A reference solution was prepared in a similar manner as above, but without the addition of resin. Each cuvette was filled by taking 2.5 ml of each sample (Sol. 1, Sol. 2 & Ref.), before being placed into the spectrophotometer. The absorbance of each sample was recorded at 304 nm, and an estimate of first residue attachment was obtained from the following equation:

$$Fmoc\ Loading: mmol\ g^{-1} = \left(Abs_{sample(average)} - Abs_{Ref}\right) x \left(\frac{16.4}{mg\ of\ resin_{(average)}}\right)$$

6.7 Caspase-3 Enzymatic Assay in Solution

The enzymatic analysis was carried out with human recombinant caspase-3 *in vitro*. A stock solution of **2.6** was prepared in dimethyl sulfoxide (DMSO). Ac-DEVD-PABC-Naph (10 µM) and caspase-3 were dissolved in assay buffer (50 mM HEPES, pH 7, 0.1% CHAPS, 10 mM DTT, 100 mM NaCl, 1 mM EDTA and 10% Sucrose) and 18 megohm water at 25°C in a quartz cuvette. The cuvette was placed into the cell holder, and fluorescence signals were measured with an excitation wavelength of 402 nm. The emission was collected from 410 to 750 nm. A blank solution without caspase-3 was also measured for comparison, under the same conditions.

6.8 Preparing the Ln^{3+} Complexes

Chloride salts of lanthanide complexes were prepared by combining an appropriate standardised lanthanide chloride solution with an equal amount of ligand in an aqueous solution. The pH of the solution was adjusted to 5.5 using 1M NaOH and 1M HCl as needed. The reaction mixture was stirred at 50°C. The reaction pH was maintained in the range of 5.0 - 5.5 by adding 1M NaOH solution. The progress of the reaction was monitored using xylenol orange indicator (0.15M acetic acid/sodium acetate buffer, pH 5.5). When the indicator showed that no free Ln^{3+} remained, the pH was raised to 7 using 1M NaOH, and the mixture was filtered and then lyophilised to obtain the complex, which was used without further purification.

Bibliography

Bibliography

(1) Plimmer, R. H. A. *The Chemical Constitution of the Proteins Part II*; Read Books, 2008.

(2) Scott, D. A.; Best, C. H. The Preparation of Insulin. *Industrial & Engineering Chemistry* **1925**, *17* (3), 238-240. DOI: 10.1021/ie50183a004.

(3) Bliss, M.; Banting, F. G.; Best, C. H.; Collip, J. B. BANTING'S, BEST'S, and COLLIP'S ACCOUNTS OF THE DISCOVERY OF INSULIN. *Bulletin of the History of Medicine* **1982**, *56* (4), 554-568. (acccessed 2022/10/05/).JSTOR.

(4) du Vigneaud, V.; Ressler, C.; Swan, J. M.; Roberts, C. W.; Katsoyannis, P. G. The Synthesis of Oxytocin1. *Journal of the American Chemical Society* **1954**, *76* (12), 3115-3121. DOI: 10.1021/ja01641a004.

(5) Merrifield, B. Solid Phase Synthesis. *Science* **1986**, *232* (4748), 341-347. DOI: 10.1126/science.3961484 (acccessed 2022/10/04).

(6) Muttenthaler, M.; King, G. F.; Adams, D. J.; Alewood, P. F. Trends in peptide drug discovery. *Nature Reviews Drug Discovery* **2021**, *20* (4), 309-325. DOI: 10.1038/s41573-020-00135-8.

(7) Steiner, D. F. Peptide Hormones, Biosynthesis and Posttranslational Processing of. In *Encyclopedia of Endocrine Diseases*, Martini, L. Ed.; Elsevier, 2004; pp 545-555.

(8) Gonzalez-Lozano, M. A.; Li, K. W. Peptide Neurotransmitters and Hormones. In *eLS*, 2020; pp 1-9.

(9) Dignass, A. U.; Sturm, A. Peptide growth factors in the intestine. *European Journal of Gastroenterology & Hepatology* **2001**, *13* (7).

(10) Lau, J. L.; Dunn, M. K. Therapeutic peptides: Historical perspectives, current development trends, and future directions. *Bioorg Med Chem* **2018**, *26* (10), 2700-2707. DOI: 10.1016/j.bmc.2017.06.052.

(11) Muheem, A.; Shakeel, F.; Jahangir, M. A.; Anwar, M.; Mallick, N.; Jain, G. K.; Warsi, M. H.; Ahmad, F. J. A review on the strategies for oral delivery of proteins and peptides and their clinical perspectives. *Saudi Pharmaceutical Journal* **2016**, *24* (4), 413-428. DOI: https://doi.org/10.1016/j.jsps.2014.06.004.

(12) Zizzari, A. T.; Pliatsika, D.; Gall, F. M.; Fischer, T.; Riedl, R. New perspectives in oral peptide delivery. *Drug Discovery Today* **2021**, *26* (4), 1097-1105. DOI: https://doi.org/10.1016/j.drudis.2021.01.020.

(13) Usmani, S. S.; Bedi, G.; Samuel, J. S.; Singh, S.; Kalra, S.; Kumar, P.; Ahuja, A. A.; Sharma, M.; Gautam, A.; Raghava, G. P. S. THPdb: Database of FDA-approved peptide and protein therapeutics. *PLOS ONE* **2017**, *12* (7), e0181748. DOI: 10.1371/journal.pone.0181748.

(14) Research, T. M. *Peptide Therapeutics Market Outlook 2031*. N/A, 2022. https://www.transparencymarketresearch.com/peptide-therapeutics-market.html (accessed 2022 October).

(15) Shah, J. N.; Guo, G.-Q.; Krishnan, A.; Ramesh, M.; Katari, N. K.; Shahbaaz, M.; Abdellattif, M. H.; Singh, S. K.; Dua, K. Peptides-based therapeutics: Emerging potential therapeutic agents for COVID-19. *Therapies* **2022**, *77* (3), 319-328. DOI: https://doi.org/10.1016/j.therap.2021.09.007.

(16) Park, J. H.; Moon, J. H.; Kim, H. J.; Kong, M. H.; Oh, Y. H. Sedentary Lifestyle: Overview of Updated Evidence of Potential Health Risks. *Korean J Fam Med* **2020**, *41* (6), 365-373. DOI: 10.4082/kjfm.20.0165.

(17) Imai, K.; Takaoka, A. Comparing antibody and small-molecule therapies for cancer. *Nature Reviews Cancer* **2006**, *6* (9), 714-727. DOI: 10.1038/nrc1913.

(18) Fosgerau, K.; Hoffmann, T. Peptide therapeutics: current status and future directions. *Drug Discovery Today* **2015**, *20* (1), 122-128. DOI: https://doi.org/10.1016/j.drudis.2014.10.003.

(19) Davda, J.; Declerck, P.; Hu-Lieskovan, S.; Hickling, T. P.; Jacobs, I. A.; Chou, J.; Salek-Ardakani, S.; Kraynov, E. Immunogenicity of immunomodulatory, antibody-based, oncology therapeutics. *Journal for ImmunoTherapy of Cancer* **2019**, *7* (1), 105. DOI: 10.1186/s40425-019-0586-0.

(20) Smith, A. J. New Horizons in Therapeutic Antibody Discovery: Opportunities and Challenges versus Small-Molecule Therapeutics. *SLAS Discovery* **2015**, *20* (4), 437-453. DOI: https://doi.org/10.1177/1087057114562544.

(21) Diao, L.; Meibohm, B. Pharmacokinetics and Pharmacokinetic–Pharmacodynamic Correlations of Therapeutic Peptides. *Clinical Pharmacokinetics* **2013**, *52* (10), 855-868. DOI: 10.1007/s40262-013-0079-0.

(22) Wang, L.; Wang, N.; Zhang, W.; Cheng, X.; Yan, Z.; Shao, G.; Wang, X.; Wang, R.; Fu, C. Therapeutic peptides: current applications and future directions. *Signal Transduction and Targeted Therapy* **2022**, *7* (1), 48. DOI: 10.1038/s41392-022-00904-4.

(23) Chandrudu, S.; Simerska, P.; Toth, I. Chemical methods for peptide and protein production. In *Molecules (Basel, Switzerland)*, 2013; Vol. 18, pp 4373-4388.

(24) Anderson, G. W.; McGregor, A. C. t-Butyloxycarbonylamino Acids and Their Use in Peptide Synthesis. *Journal of the American Chemical Society* **1957**, *79* (23), 6180-6183. DOI: 10.1021/ja01580a020.

(25) Kemp, D. S.; Leung, S.-L.; Kerkman, D. J. Models that demonstrate peptide bond formation by prior thiol capture I. Capture by disulfide formation. *Tetrahedron Letters* **1981**, *22* (3), 181-184. DOI: https://doi.org/10.1016/0040-4039(81)80049-4.

(26) Dawson, P. E.; Muir, T. W.; Clark-Lewis, I.; Kent, S. B. H. Synthesis of Proteins by Native Chemical Ligation. *Science* **1994**, *266* (5186), 776-779. DOI: 10.1126/science.7973629 (acccessed 2022/10/11).

(27) Muir, T. W.; Sondhi, D.; Cole, P. A. Expressed protein ligation: A general method for protein engineering. *Proceedings of the National Academy of Sciences* **1998**, *95* (12), 6705-6710. DOI: 10.1073/pnas.95.12.6705 (acccessed 2022/10/11).

(28) Nilsson, B. L.; Kiessling, L. L.; Raines, R. T. Staudinger Ligation: A Peptide from a Thioester and Azide. *Organic Letters* **2000**, *2* (13), 1939-1941. DOI: 10.1021/ol0060174.

(29) Skwarczynski, M.; Kiso, Y. Application of the O-N Intramolecular Acyl Migration Reaction in Medicinal Chemistry. *Current Medicinal Chemistry* **2007**, *14* (26), 2813-2823. DOI: http://dx.doi.org/10.2174/092986707782360123.

(30) Bergmann, M.; Zervas, L. Über ein allgemeines Verfahren der Peptid-Synthese. *Berichte der deutschen chemischen Gesellschaft (A and B Series)* **1932**, *65* (7), 1192-1201, https://doi.org/10.1002/cber.19320650722. DOI: https://doi.org/10.1002/cber.19320650722 (acccessed 2022/10/12).

(31) Conda-Sheridan, M.; Krishnaiah, M. Protecting Groups in Peptide Synthesis. In *Peptide Synthesis: Methods and Protocols*, Hussein, W. M., Skwarczynski, M., Toth, I. Eds.; Springer US, 2020; pp 111-128.

(32) Zinieris, N.; Leondiadis, L.; Ferderigos, N. Nα-Fmoc Removal from Resin-Bound Amino Acids by 5% Piperidine Solution. *Journal of Combinatorial Chemistry* **2005**, *7* (1), 4-6. DOI: 10.1021/cc049872d.

(33) Lundt, B. F.; Johansen, N. L.; Vølund, A.; Markussen, J. REMOVAL OF t-BUTYL AND t-BUTOXYCARBONYL PROTECTING GROUPS WITH TRIFLUOROACETIC ACID. *International Journal of Peptide and Protein Research* **1978**, *12* (5), 258-268, https://doi.org/10.1111/j.1399-3011.1978.tb02896.x. DOI: https://doi.org/10.1111/j.1399-3011.1978.tb02896.x (acccessed 2022/10/14).

(34) Xu, Y.; Wang, T.; Guan, C.-J.; Li, Y.-M.; Liu, L.; Shi, J.; Bierer, D. Dmab/ivDde protected diaminodiacids for solid-phase synthesis of peptide

disulfide-bond mimics. *Tetrahedron Letters* **2017**, *58* (17), 1677-1680. DOI: https://doi.org/10.1016/j.tetlet.2017.03.024.

(35) Gatos, D.; Athanassopoulos, P.; Tzavara, C.; Barlos, K. Peptides 1998: Proceedings of the 25th European Peptide Symposium. Bajusz, S., Hudecz, F., Eds: 1999.

(36) Hojo, K.; Maeda, M.; Smith, T. J.; Kita, E.; Yamaguchi, F.; Yamamoto, S.; Kawasaki, K. Peptide Synthesis in Water IV.
Preparation of <i>N</i>-Ethanesulfonylethoxycarbonyl (Esc) Amino Acids and Their Application to Solid Phase Peptide Synthesis. *Chemical and Pharmaceutical Bulletin* **2004**, *52* (4), 422-427. DOI: 10.1248/cpb.52.422.

(37) McMurray, J. S. Solid phase synthesis of a cyclic peptide using fmoc chemistry. *Tetrahedron Letters* **1991**, *32* (52), 7679-7682. DOI: https://doi.org/10.1016/0040-4039(91)80563-L.

(38) Chan, W. C. Bycroft, BW; Evans, DJ; White, PDJ Chem. Soc. *Chem. Commun* **1995**, 2209-2210.

(39) Wang, S. S.; Yang, C. C.; Kulesha, I. D.; Sonenberg, M.; Merrifield, R. B. SOLID PHASE SYNTHESIS OF BOVINE PITUITARY GROWTH HORMONE-(123–131) NONAPEPTIDE. *International Journal of Peptide and Protein Research* **1974**, *6* (2), 103-109, https://doi.org/10.1111/j.1399-3011.1974.tb02367.x. DOI: https://doi.org/10.1111/j.1399-3011.1974.tb02367.x (acccessed 2022/10/14).

(40) Bodanszky, M. Alkyl Esters of Amino Acids. *International Journal of Peptide and Protein Research* **1984**, *23* (1), 111-111, https://doi.org/10.1111/j.1399-3011.1984.tb02699.x. DOI: https://doi.org/10.1111/j.1399-3011.1984.tb02699.x (acccessed 2022/10/14).

(41) Birr, C.; Lochinger, W.; Stahnke, G.; Lang, P. Der α.α-Dimethyl-3.5-dimethoxybenzyloxycarbonyl (Ddz)-Rest, eine photo- und säurelabile Stickstoff-Schutzgruppe für die Peptidchemie. *Justus Liebigs Annalen der Chemie* **1972**, *763* (1), 162-172, https://doi.org/10.1002/jlac.19727630118. DOI: https://doi.org/10.1002/jlac.19727630118 (acccessed 2022/10/14).

(42) Martinez, J.; Laur, J.; Castro, B. Carboxamidomethyl esters (CAM esters) as carboxyl protecting groups. *Tetrahedron Letters* **1983**, *24* (47), 5219-5222. DOI: https://doi.org/10.1016/S0040-4039(00)88401-4.

(43) Carpino, L. A. Oxidative Reactions of Hydrazines. IV. Elimination of Nitrogen from 1,1-Disubstituted-2-arenesulfonhydrazides1-4. *Journal of the American Chemical Society* **1957**, *79* (16), 4427-4431. DOI: 10.1021/ja01573a050.

(44) Barany, G.; Albericio, F. Three-dimensional orthogonal protection scheme for solid-phase peptide synthesis under mild conditions. *Journal of the American Chemical Society* **1985**, *107* (17), 4936-4942. DOI: 10.1021/ja00303a019.

(45) Barany, G.; Merrifield, R. B. A new amino protecting group removable by reduction. Chemistry of the dithiasuccinoyl (Dts) function. *Journal of the American Chemical Society* **1977**, *99* (22), 7363-7365. DOI: 10.1021/ja00464a050.

(46) Isidro-Llobet, A.; Álvarez, M.; Albericio, F. Amino Acid-Protecting Groups. *Chemical Reviews* **2009**, *109* (6), 2455-2504. DOI: 10.1021/cr800323s.

(47) Roeske, R. Preparation of t-Butyl Esters of Free Amino Acids1. *The Journal of Organic Chemistry* **1963**, *28* (5), 1251-1253. DOI: 10.1021/jo01040a022.

(48) Luna, O. F.; Gomez, J.; Cárdenas, C.; Albericio, F.; Marshall, S. H.; Guzmán, F. Deprotection Reagents in Fmoc Solid Phase Peptide Synthesis: Moving Away from Piperidine? In *Molecules*, 2016; Vol. 21.

(49) Hermanson, G. T. Chapter 3 - The Reactions of Bioconjugation. In *Bioconjugate Techniques (Third Edition)*, Hermanson, G. T. Ed.; Academic Press, 2013; pp 229-258.

(50) Pál, G.; Santamaria, F.; Kossiakoff, A. A.; Lu, W. The first semi-synthetic serine protease made by native chemical ligation. *Protein Expression and Purification* **2003**, *29* (2), 185-192. DOI: https://doi.org/10.1016/S1046-5928(03)00022-6.

(51) Low, D. W.; Hill, M. G.; Carrasco, M. R.; Kent, S. B. H.; Botti, P. Total synthesis of cytochrome b562 by native chemical ligation using a removable auxiliary. *Proceedings of the National Academy of Sciences* **2001**, *98* (12), 6554-6559. DOI: 10.1073/pnas.121178598 (acccessed 2022/10/17).

(52) Lu, W.; Starovasnik, M. A.; Kent, S. B. H. Total chemical synthesis of bovine pancreatic trypsin inhibitor by native chemical ligation. *FEBS Letters* **1998**, *429* (1), 31-35, https://doi.org/10.1016/S0014-5793(98)00547-X. DOI: https://doi.org/10.1016/S0014-5793(98)00547-X (acccessed 2022/10/17).

(53) Hermanson, G. T. Chapter 17 - Chemoselective Ligation; Bioorthogonal Reagents. In *Bioconjugate Techniques (Third Edition)*, Hermanson, G. T. Ed.; Academic Press, 2013; pp 757-785.

(54) Chong, S.; Mersha, F. B.; Comb, D. G.; Scott, M. E.; Landry, D.; Vence, L. M.; Perler, F. B.; Benner, J.; Kucera, R. B.; Hirvonen, C. A.; et al. Single-column purification of free recombinant proteins using a self-cleavable affinity tag derived from a protein splicing element. *Gene* **1997**, *192* (2), 271-281. DOI: https://doi.org/10.1016/S0378-1119(97)00105-4.

(55) Staudinger, H.; Meyer, J. Über neue organische Phosphorverbindungen III. Phosphinmethylenderivate und Phosphinimine. *Helvetica Chimica Acta* **1919**, *2* (1), 635-646, https://doi.org/10.1002/hlca.19190020164. DOI: https://doi.org/10.1002/hlca.19190020164 (acccessed 2022/10/17).

(56) Saxon, E.; Bertozzi, C. R. Cell Surface Engineering by a Modified Staudinger Reaction. *Science* **2000**, *287* (5460), 2007-2010. DOI: 10.1126/science.287.5460.2007 (acccessed 2022/10/17).

(57) Köhn, M.; Breinbauer, R. The Staudinger Ligation—A Gift to Chemical Biology. *Angewandte Chemie International Edition* **2004**, *43* (24), 3106-3116, https://doi.org/10.1002/anie.200401744. DOI: https://doi.org/10.1002/anie.200401744 (acccessed 2022/10/17).

(58) Tian, J.; Li, Y.; Ma, B.; Tan, Z.; Shang, S. Automated Peptide Synthesizers and Glycoprotein Synthesis. *Frontiers in Chemistry* **2022**, *10*, Review.

(59) Petrou, C.; Sarigiannis, Y. 1 - Peptide synthesis: Methods, trends, and challenges. In *Peptide Applications in Biomedicine, Biotechnology and Bioengineering*, Koutsopoulos, S. Ed.; Woodhead Publishing, 2018; pp 1-21.

(60) Songster, M. F.; Barany, G. [8] Handles for solid-phase peptide synthesis. In *Methods in Enzymology*, Vol. 289; Academic Press, 1997; pp 126-174.

(61) Booth, S.; Hermkens, P. H. H.; Ottenheijm, H. C. J.; Rees, D. C. Solid-phase organic reactions III: A review of the literature Nov 96–Dec 97. *Tetrahedron* **1998**, *54* (51), 15385-15443. DOI: https://doi.org/10.1016/S0040-4020(98)00968-5.

(62) Auzanneau, F.-I.; Christensen, M. K.; Harris, S. L.; Meldal, M.; Pinto, B. M. Synthesis and characterization of polyethylene glycol polyacrylamide copolymer (PEGA) resins containing carbohydrate ligands. Evaluation as supports for affinity chromatography. *Canadian Journal of Chemistry* **1998**, *76* (8), 1109-1118. DOI: 10.1139/v98-118 (acccessed 2022/10/18).

(63) Merrifield, R. B. Solid Phase Peptide Synthesis. I. The Synthesis of a Tetrapeptide. *Journal of the American Chemical Society* **1963**, *85* (14), 2149-2154. DOI: 10.1021/ja00897a025.

(64) Park, B.-D.; Lee, Y.-S. The effect of PEG groups on swelling properties of PEG-grafted-polystyrene resins in various solvents. *Reactive and Functional Polymers* **2000**, *44* (1), 41-46. DOI: https://doi.org/10.1016/S1381-5148(99)00075-9.

(65) Shelton, P. T.; Jensen, K. J. Linkers, Resins, and General Procedures for Solid-Phase Peptide Synthesis. In *Peptide Synthesis and Applications*, Jensen, K. J., Tofteng Shelton, P., Pedersen, S. L. Eds.; Humana Press, 2013; pp 23-41.

(66) Bayer, E. Towards the Chemical Synthesis of Proteins. *Angewandte Chemie International Edition in English* **1991**, *30* (2), 113-129, https://doi.org/10.1002/anie.199101133. DOI: https://doi.org/10.1002/anie.199101133 (acccessed 2022/10/20).

(67) Kempe, M.; Barany, G. CLEAR: A Novel Family of Highly Cross-Linked Polymeric Supports for Solid-Phase Peptide Synthesis1,2. *Journal of the American Chemical Society* **1996**, *118* (30), 7083-7093. DOI: 10.1021/ja954196s.

(68) Mazzini, S. Solid-phase synthesis and NMR studies of modified oligonucleotides forming triplex helix and of oligonucleopeptides mimicking the topoisomerase I-DNA covalent complex. **2009**.

(69) García-Ramos, Y.; Paradís-Bas, M.; Tulla-Puche, J.; Albericio, F. ChemMatrix® for complex peptides and combinatorial chemistry. *Journal of Peptide Science* **2010**, *16* (12), 675-678, https://doi.org/10.1002/psc.1282. DOI: https://doi.org/10.1002/psc.1282 (acccessed 2022/10/20).

(70) Guillier, F.; Orain, D.; Bradley, M. Linkers and Cleavage Strategies in Solid-Phase Organic Synthesis and Combinatorial Chemistry. *Chemical Reviews* **2000**, *100* (6), 2091-2158. DOI: 10.1021/cr980040+.

(71) Kassem, T.; Sabatino, D.; Jia, X.; Zhu, X. X.; Lubell, W. D. To Rink or Not to Rink Amide Link, that is the Question to Address for More Economical and Environmentally Sound Solid-Phase Peptide Synthesis. *International Journal of Peptide Research and Therapeutics* **2009**, *15* (3), 211-218. DOI: 10.1007/s10989-009-9177-0.

(72) Sieber, P. A new acid-labile anchor group for the solid-phase synthesis of C-terminal peptide amides by the Fmoc method. *Tetrahedron Letters* **1987**, *28* (19), 2107-2110. DOI: https://doi.org/10.1016/S0040-4039(00)96055-6.

(73) Hoekstra, J. W. The 2-Chlorotrityl Resin a Worthy Addition to the Medicinal Chemists Toolbox. *Current Medicinal Chemistry* **2001**, *8* (6), 715-719. DOI: http://dx.doi.org/10.2174/0929867013373192.

(74) Bunin, B. A. 3 - LINKERS FOR SOLID-PHASE SYNTHESIS. In *The Combinatorial Index*, Bunin, B. A. Ed.; Academic Press, 2012; pp 9-76.

(75) Woo, Y.-H.; Mitchell, A. R.; Camarero, J. A. The Use of Aryl Hydrazide Linkers for the Solid Phase Synthesis of Chemically Modified Peptides. *International Journal of Peptide Research and Therapeutics* **2007**, *13* (1), 181-190. DOI: 10.1007/s10989-006-9064-x.

(76) Boas, U.; Brask, J.; Christensen, J. B.; Jensen, K. J. The Ortho Backbone Amide Linker (o-BAL) Is an Easily Prepared and Highly Acid-Labile Handle for Solid-Phase Synthesis. *Journal of Combinatorial Chemistry* **2002**, *4* (3), 223-228. DOI: 10.1021/cc010070h.

(77) Barlos, K.; Gatos, D.; Kallitsis, J.; Papaphotiu, G.; Sotiriu, P.; Wenqing, Y.; Schäfer, W. Darstellung geschützter peptid-fragmente unter einsatz substituierter triphenylmethyl-harze. *Tetrahedron Letters* **1989**, *30* (30), 3943-3946. DOI: https://doi.org/10.1016/S0040-4039(00)99290-6.

(78) Fields, C. G.; VanDrisse VI Fau - Fields, G. B.; Fields, G. B. Edman degradation sequence analysis of resin-bound peptides synthesized by 9-fluorenylmethoxycarbonyl chemistry. (1040-5704 (Print)). From 1993 Jan-Feb.

(79) Yang, Y. Chapter 11 - Peptide Racemization. In *Side Reactions in Peptide Synthesis*, Yang, Y. Ed.; Academic Press, 2016; pp 257-292.

(80) Arbour, C. A.; Kondasinghe, T. D.; Saraha, H. Y.; Vorlicek, Teanna L.; Stockdill, J. L. Epimerization-free access to C-terminal cysteine peptide acids, carboxamides, secondary amides, and esters via complimentary strategies. *Chemical Science* **2018**, *9* (2), 350-355, 10.1039/C7SC03553E. DOI: 10.1039/C7SC03553E.

(81) Behrendt, R.; White, P.; Offer, J. Advances in Fmoc solid-phase peptide synthesis. *Journal of Peptide Science* **2016**, *22* (1), 4-27, https://doi.org/10.1002/psc.2836. DOI: https://doi.org/10.1002/psc.2836 (acccessed 2022/10/22).

(82) Mäde, V.; Els-Heindl, S.; Beck-Sickinger, A. G. Automated solid-phase peptide synthesis to obtain therapeutic peptides. *Beilstein Journal of Organic Chemistry* **2014**, *10*, 1197-1212. DOI: 10.3762/bjoc.10.118.

(83) Veber, D.; Milkowski, J.; Varga, S.; Denkewalter, R.; Hirschmann, R. Acetamidomethyl. A Novel Thiol Protecting Group for Cysteine. *Journal of the American Chemical Society* **1972**, *94* (15), 5456-5461. DOI: 10.1021/ja00770a600.

(84) Díaz-Mochón, J. J.; Bialy, L.; Bradley, M. Full Orthogonality between Dde and Fmoc: The Direct Synthesis of PNA−Peptide Conjugates. *Organic Letters* **2004**, *6* (7), 1127-1129. DOI: 10.1021/ol049905y.

(85) Jursic, B. S.; Zdravkovski, Z. A Simple Preparation of Amides from Acids and Amines by Heating of Their Mixture. *Synthetic Communications* **1993**, *23* (19), 2761-2770. DOI: 10.1080/00397919308013807.

(86) Montalbetti, C. A. G. N.; Falque, V. Amide bond formation and peptide coupling. *Tetrahedron* **2005**, *61* (46), 10827-10852. DOI: https://doi.org/10.1016/j.tet.2005.08.031.

(87) Nájera, C. From α-Amino Acids to Peptides: All You Need for the Journey. *Synlett* **2002**, *2002* (09), 1388-1404.

(88) Hegarty, A. F.; McCormack, M. T.; Brady, K.; Ferguson, G.; Roberts, P. J. Competing acyl transfer and intramolecular O → N acyl group migration from an isolable O-acylisourea. *Journal of the Chemical Society, Perkin Transactions 2* **1980**, (6), 867-875, 10.1039/P29800000867. DOI: 10.1039/P29800000867.

(89) Carpino, L. A. 1-Hydroxy-7-azabenzotriazole. An efficient peptide coupling additive. *Journal of the American Chemical Society* **1993**, *115* (10), 4397-4398. DOI: 10.1021/ja00063a082.

(90) Subirós-Funosas, R.; Prohens, R.; Barbas, R.; El-Faham, A.; Albericio, F. Oxyma: An Efficient Additive for Peptide Synthesis to Replace the Benzotriazole-Based HOBt and HOAt with a Lower Risk of Explosion[1]. *Chemistry – A European Journal* **2009**, *15* (37), 9394-9403, https://doi.org/10.1002/chem.200900614. DOI: https://doi.org/10.1002/chem.200900614 (acccessed 2022/11/01).

(91) Gawne, G.; Kenner, G. W.; Sheppard, R. C. Acyloxyphosphonium salts as acylating agents. Synthesis of peptides. *Journal of the American Chemical Society* **1969**, *91* (20), 5669-5671. DOI: 10.1021/ja01048a057.

(92) Dourtoglou, V.; Gross, B.; Lambropoulou, V.; Zioudrou, C. O-Benzotriazolyl-N,N,N′,N′-tetramethyluronium Hexafluorophosphate as Coupling Reagent for the Synthesis of Peptides of Biological Interest. *Synthesis* **1984**, *1984* (07), 572-574.

(93) del Fresno, M.; El-Faham, A.; Carpino, L. A.; Royo, M.; Albericio, F. Substituted Guanidines: Introducing Diversity in Combinatorial Chemistry. *Organic Letters* **2000**, *2* (23), 3539-3542. DOI: 10.1021/ol006322p.

(94) Mehta, A.; Jaouhari, R.; Benson, T. J.; Douglas, K. T. Improved efficiency and selectivity in peptide synthesis: Use of triethylsilane as a carbocation scavenger in deprotection of t-butyl esters and t-butoxycarbonyl-protected sites. *Tetrahedron Letters* **1992**, *33* (37), 5441-5444. DOI: https://doi.org/10.1016/S0040-4039(00)79116-7.

(95) Dick, F. Acid Cleavage/Deprotection in Fmoc/tBiu Solid-Phase Peptide Synthesis. In *Peptide Synthesis Protocols*, Pennington, M. W., Dunn, B. M. Eds.; Humana Press, 1995; pp 63-72.

(96) King, D. S.; Fields, C. G.; Fields, G. B. A cleavage method which minimizes side reactions following Fmoc solid phase peptide synthesis. *International Journal of Peptide and Protein Research* **1990**, *36* (3), 255-266, https://doi.org/10.1111/j.1399-3011.1990.tb00976.x. DOI: https://doi.org/10.1111/j.1399-3011.1990.tb00976.x (acccessed 2022/11/03).

(97) Di, L. Strategic Approaches to Optimizing Peptide ADME Properties. *The AAPS Journal* **2015**, *17* (1), 134-143. DOI: 10.1208/s12248-014-9687-3.

(98) Schaller, A. Bioactive peptides as signal molecules in plant defense, growth, and development. In *Studies in Natural Products Chemistry*, Atta ur, R. Ed.; Vol. 25; Elsevier, 2001; pp 367-411.

(99) Davidson, B. S. Ascidians: producers of amino acid-derived metabolites. *Chemical Reviews* **1993**, *93* (5), 1771-1791. DOI: 10.1021/cr00021a006.

(100) Fusetani, N.; Matsunaga, S. Bioactive sponge peptides. *Chemical Reviews* **1993**, *93* (5), 1793-1806. DOI: 10.1021/cr00021a007.

(101) Hamada, Y.; Shioiri, T. Recent Progress of the Synthetic Studies of Biologically Active Marine Cyclic Peptides and Depsipeptides. *Chemical Reviews* **2005**, *105* (12), 4441-4482. DOI: 10.1021/cr0406312.

(102) Kazmaier, U.; Deska, J. Peptide Backbone Modifications. *Current Organic Chemistry* **2008**, *12* (5), 355-385. DOI: 10.2174/138527208783743697.

(103) Pelay-Gimeno, M.; Glas, A.; Koch, O.; Grossmann, T. N. Structure-Based Design of Inhibitors of Protein–Protein Interactions: Mimicking Peptide Binding Epitopes. *Angewandte Chemie International Edition* **2015**, *54* (31), 8896-8927, https://doi.org/10.1002/anie.201412070. DOI: https://doi.org/10.1002/anie.201412070 (acccessed 2023/01/08).

(104) Lenci, E.; Trabocchi, A. Peptidomimetic toolbox for drug discovery. *Chemical Society Reviews* **2020**, *49* (11), 3262-3277, 10.1039/D0CS00102C. DOI: 10.1039/D0CS00102C.

(105) Pasco, M.; Dolain, C.; Guichard, G. 5.05 - Foldamers in Medicinal Chemistry. In *Comprehensive Supramolecular Chemistry II*, Atwood, J. L. Ed.; Elsevier, 2017; pp 89-125.

(106) Henninot, A.; Collins, J. C.; Nuss, J. M. The Current State of Peptide Drug Discovery: Back to the Future? *Journal of Medicinal Chemistry* **2018**, *61* (4), 1382-1414. DOI: 10.1021/acs.jmedchem.7b00318.

(107) Masri, E.; Ahsanullah; Accorsi, M.; Rademann, J. Side-Chain Modification of Peptides Using a Phosphoranylidene Amino Acid. *Organic Letters* **2020**, *22* (8), 2976-2980. DOI: 10.1021/acs.orglett.0c00713.

(108) Wiśniewski, K.; Galyean, R.; Tariga, H.; Alagarsamy, S.; Croston, G.; Heitzmann, J.; Kohan, A.; Wiśniewska, H.; Laporte, R.; Rivière, P. J. M.; et al. New, Potent, Selective, and Short-Acting Peptidic V1a Receptor Agonists. *Journal of Medicinal Chemistry* **2011**, *54* (13), 4388-4398. DOI: 10.1021/jm200278m.

(109) Noisier, A. F. M.; Brimble, M. A. C–H Functionalization in the Synthesis of Amino Acids and Peptides. *Chemical Reviews* **2014**, *114* (18), 8775-8806. DOI: 10.1021/cr500200x.

(110) Gong, W.; Zhang, G.; Liu, T.; Giri, R.; Yu, J.-Q. Site-Selective C(sp3)–H Functionalization of Di-, Tri-, and Tetrapeptides at the N-Terminus. *Journal of the American Chemical Society* **2014**, *136* (48), 16940-16946. DOI: 10.1021/ja510233h.

(111) Popp, B. V.; Ball, Z. T. Proximity-driven metallopeptide catalysis: Remarkable side-chain scope enables modification of the Fos bZip domain. *Chemical Science* **2011**, *2* (4), 690-695, 10.1039/C0SC00564A. DOI: 10.1039/C0SC00564A.

(112) Brot, N.; Weissbach, H. The biochemistry of methionine sulfoxide residues in proteins. *Trends in Biochemical Sciences* **1982**, *7* (4), 137-139. DOI: https://doi.org/10.1016/0968-0004(82)90204-3.

(113) Jones, J. B.; Hysert, D. W. Alkylations of the Side-chain Nucleophiles of Cysteine, Methionine, Histidine, and Lysine Derivatives with Allyl Bromide, 1-Bromo-2-butyne, and 2-Bromoacetophenone. *Canadian Journal of Chemistry* **1971**, *49* (18), 3012-3019. DOI: 10.1139/v71-502 (acccessed 2022/11/10).

(114) Frey, V.; Viaud, J.; Subra, G.; Cauquil, N.; Guichou, J.-F.; Casara, P.; Grassy, G.; Chavanieu, A. Structure–activity relationships of Bak derived peptides: Affinity and specificity modulations by amino acid replacement. *European Journal of Medicinal Chemistry* **2008**, *43* (5), 966-972. DOI: https://doi.org/10.1016/j.ejmech.2007.06.008.

(115) Haskell-Luevano, C.; Toth, K.; Boteju, L.; Job, C.; Castrucci, A. M. d. L.; Hadley, M. E.; Hruby, V. J. β-Methylation of the Phe7 and Trp9 Melanotropin Side Chain Pharmacophores Affects Ligand−Receptor Interactions and Prolonged Biological Activity. *Journal of Medicinal Chemistry* **1997**, *40* (17), 2740-2749. DOI: 10.1021/jm970018t.

(116) Ban, H.; Gavrilyuk, J.; Barbas, C. F., III. Tyrosine Bioconjugation through Aqueous Ene-Type Reactions: A Click-Like Reaction for Tyrosine. *Journal of the American Chemical Society* **2010**, *132* (5), 1523-1525. DOI: 10.1021/ja909062q.

(117) Ban, H.; Nagano, M.; Gavrilyuk, J.; Hakamata, W.; Inokuma, T.; Barbas, C. F., III. Facile and Stabile Linkages through Tyrosine: Bioconjugation Strategies with the Tyrosine-Click Reaction. *Bioconjugate Chemistry* **2013**, *24* (4), 520-532. DOI: 10.1021/bc300665t.

(118) Chalker, J. M.; Bernardes, G. J. L.; Lin, Y. A.; Davis, B. G. Chemical Modification of Proteins at Cysteine: Opportunities in Chemistry and Biology. *Chemistry – An Asian Journal* **2009**, *4* (5), 630-640, https://doi.org/10.1002/asia.200800427. DOI: https://doi.org/10.1002/asia.200800427 (acccessed 2022/11/10).

(119) Bernardim, B.; Cal, P. M. S. D.; Matos, M. J.; Oliveira, B. L.; Martínez-Sáez, N.; Albuquerque, I. S.; Perkins, E.; Corzana, F.; Burtoloso, A. C. B.; Jiménez-Osés, G.; et al. Stoichiometric and irreversible cysteine-selective protein modification using carbonylacrylic reagents. *Nature Communications* **2016**, *7* (1), 13128. DOI: 10.1038/ncomms13128.

(120) Abbas, A.; Xing, B.; Loh, T.-P. Allenamides as Orthogonal Handles for Selective Modification of Cysteine in Peptides and Proteins. *Angewandte Chemie*

International Edition **2014**, *53* (29), 7491-7494, https://doi.org/10.1002/anie.201403121. DOI: https://doi.org/10.1002/anie.201403121 (acccessed 2022/11/10).

(121) Vinogradova, E. V.; Zhang, C.; Spokoyny, A. M.; Pentelute, B. L.; Buchwald, S. L. Organometallic palladium reagents for cysteine bioconjugation. *Nature* **2015**, *526* (7575), 687-691. DOI: 10.1038/nature15739.

(122) Kumari, S.; Carmona, A. V.; Tiwari, A. K.; Trippier, P. C. Amide Bond Bioisosteres: Strategies, Synthesis, and Successes. *Journal of Medicinal Chemistry* **2020**, *63* (21), 12290-12358. DOI: 10.1021/acs.jmedchem.0c00530. Houben−Weyl: Methods of Organic Chemistry. Additional and Supplementary Volumes to the 4th Edition. Volume E 22A. Synthesis of Peptides and Peptidomimetics Editor-in-Chief, Murray Goodman (San Diego, CA). Georg Thieme Verlag: Stuttgart and New York. 2002. xxviii + 902 pp. $1895.00. ISBN 3-13-219604-5. *Journal of the American Chemical Society* **2002**, *124* (26), 7874-7874. DOI: 10.1021/ja025221e.

(123) Chatterjee, J.; Rechenmacher, F.; Kessler, H. N-Methylation of Peptides and Proteins: An Important Element for Modulating Biological Functions. *Angewandte Chemie International Edition* **2013**, *52* (1), 254-269, https://doi.org/10.1002/anie.201205674. DOI: https://doi.org/10.1002/anie.201205674 (acccessed 2022/11/15).

(124) Cheloha, R. W.; Watanabe, T.; Dean, T.; Gellman, S. H.; Gardella, T. J. Backbone Modification of a Parathyroid Hormone Receptor-1 Antagonist/Inverse Agonist. *ACS Chemical Biology* **2016**, *11* (10), 2752-2762. DOI: 10.1021/acschembio.6b00404.

(125) Schneider, J. A.; Craven, T. W.; Kasper, A. C.; Yun, C.; Haugbro, M.; Briggs, E. M.; Svetlov, V.; Nudler, E.; Knaut, H.; Bonneau, R.; et al. Design of Peptoid-peptide Macrocycles to Inhibit the β-catenin TCF Interaction in Prostate Cancer. *Nature Communications* **2018**, *9* (1), 4396. DOI: 10.1038/s41467-018-06845-3.

(126) Wei, X.; Zhan, C.; Chen, X.; Hou, J.; Xie, C.; Lu, W. Retro-Inverso Isomer of Angiopep-2: A Stable d-Peptide Ligand Inspires Brain-Targeted Drug Delivery. *Molecular Pharmaceutics* **2014**, *11* (10), 3261-3268. DOI: 10.1021/mp500086e.

(127) Laporte, R.; Kohan, A.; Heitzmann, J.; Wiśniewska, H.; Toy, J.; La, E.; Tariga, H.; Alagarsamy, S.; Ly, B.; Dykert, J.; et al. Pharmacological Characterization of FE 202158, a Novel, Potent, Selective, and Short-Acting Peptidic Vasopressin V$_{1a}$ Receptor Full Agonist for the Treatment of Vasodilatory Hypotension. *Journal of Pharmacology and Experimental Therapeutics* **2011**, *337* (3), 786. DOI: 10.1124/jpet.111.178848.

(128) Laterre, P.-F.; Berry, S. M.; Blemings, A.; Carlsen, J. E.; François, B.; Graves, T.; Jacobsen, K.; Lewis, R. J.; Opal, S. M.; Perner, A.; et al. Effect of Selepressin vs Placebo on Ventilator- and Vasopressor-Free Days in Patients

With Septic Shock: The SEPSIS-ACT Randomized Clinical Trial. *JAMA* **2019**, *322* (15), 1476-1485. DOI: 10.1001/jama.2019.14607 (acccessed 11/15/2022).

(129) Bossler, H. G.; Seebach, D. Peptide Enolates. C-Alkylation of Glycine Residues in linear tri-, tetra-, and pentapeptides via dilithium azadienediolates. *Helvetica Chimica Acta* **1994**, *77* (4), 1124-1165, https://doi.org/10.1002/hlca.19940770424. DOI: https://doi.org/10.1002/hlca.19940770424 (acccessed 2022/11/15).

(130) Seebach, D.; Beck, A. K.; Bossler, H. G.; Gerber, C.; Ko, S. Y.; Murtiashaw, C. W.; Naef, R.; Shoda, S.-I.; Thaler, A.; Krieger, M.; et al. Modification of Cyclosporin A (CS): Generation of an enolate at the sarcosine residue and reactions with electrophiles. *Helvetica Chimica Acta* **1993**, *76* (4), 1564-1590, https://doi.org/10.1002/hlca.19930760415. DOI: https://doi.org/10.1002/hlca.19930760415 (acccessed 2022/11/15).

(131) Datta, S.; Bayer, A.; Kazmaier, U. Highly stereoselective modifications of peptides via Pd-catalyzed allylic alkylation of internal peptide amide enolates. *Organic & Biomolecular Chemistry* **2012**, *10* (41), 8268-8275, 10.1039/C2OB26351C. DOI: 10.1039/C2OB26351C.

(132) Zhao, L.; Baslé, O.; Li, C.-J. Site-specific C-functionalization of free-(NH) peptides and glycine derivatives via direct C–H bond functionalization. *Proceedings of the National Academy of Sciences* **2009**, *106* (11), 4106-4111. DOI: 10.1073/pnas.0809052106 (acccessed 2022/11/16).

(133) Osberger, T. J.; Rogness, D. C.; Kohrt, J. T.; Stepan, A. F.; White, M. C. Oxidative diversification of amino acids and peptides by small-molecule iron catalysis. *Nature* **2016**, *537* (7619), 214-219. DOI: 10.1038/nature18941.

(134) White, C. J.; Yudin, A. K. Contemporary strategies for peptide macrocyclization. *Nature Chemistry* **2011**, *3* (7), 509-524. DOI: 10.1038/nchem.1062.

(135) Heinis, C. Tools and rules for macrocycles. *Nature Chemical Biology* **2014**, *10* (9), 696-698. DOI: 10.1038/nchembio.1605.

(136) Veber, D. F.; Freidinger, R. M.; Perlow, D. S.; Paleveda, W. J.; Holly, F. W.; Strachan, R. G.; Nutt, R. F.; Arison, B. H.; Homnick, C.; Randall, W. C.; et al. A potent cyclic hexapeptide analogue of somatostatin. *Nature* **1981**, *292* (5818), 55-58. DOI: 10.1038/292055a0.

(137) Kessler, H. Conformation and Biological Activity of Cyclic Peptides. *Angewandte Chemie International Edition in English* **1982**, *21* (7), 512-523, https://doi.org/10.1002/anie.198205121. DOI: https://doi.org/10.1002/anie.198205121 (acccessed 2022/11/18).

(138) Wang, C. K.; Craik, D. J. Designing macrocyclic disulfide-rich peptides for biotechnological applications. *Nature chemical biology* **2018**, *14* (5), 417-427. DOI: 10.1038/s41589-018-0039-y PubMed.

(139) Korsinczky, M. L. J.; Schirra, H. J.; Rosengren, K. J.; West, J.; Condie, B. A.; Otvos, L.; Anderson, M. A.; Craik, D. J. Solution structures by 1H NMR of the novel cyclic trypsin inhibitor SFTI-1 from sunflower seeds and an acyclic permutant11Edited by M. F. Summers. *Journal of Molecular Biology* **2001**, *311* (3), 579-591. DOI: https://doi.org/10.1006/jmbi.2001.4887.

(140) Colgrave, M. L.; Korsinczky, M. J. L.; Clark, R. J.; Foley, F.; Craik, D. J. Sunflower trypsin inhibitor-1, proteolytic studies on a trypsin inhibitor peptide and its analogs. *Peptide Science* **2010**, *94* (5), 665-672, https://doi.org/10.1002/bip.21415. DOI: https://doi.org/10.1002/bip.21415 (acccessed 2022/11/28).

(141) Parenty, A.; Moreau, X.; Campagne, J. M. Macrolactonizations in the Total Synthesis of Natural Products. *Chemical Reviews* **2006**, *106* (3), 911-939. DOI: 10.1021/cr0301402.

(142) Albericio, F.; Hammer, R. P.; GarcÍA-EcheverrÍA, C.; Molins, M. A.; Chang, J. L.; Munson, M. C.; Pons, M.; Giralt, E.; Barany, G. Cyclization of disulfide-containing peptides in solid-phase synthesis†. *International Journal of Peptide and Protein Research* **1991**, *37* (5), 402-413, https://doi.org/10.1111/j.1399-3011.1991.tb00755.x. DOI: https://doi.org/10.1111/j.1399-3011.1991.tb00755.x (acccessed 2022/11/29).

(143) McCusker, C. F.; Kocienski, P. J.; Boyle, F. T.; Schätzlein, A. G. Solid-phase synthesis of c(RGDfK) derivatives: on-resin cyclisation and lysine functionalisation. *Bioorganic & Medicinal Chemistry Letters* **2002**, *12* (4), 547-549. DOI: https://doi.org/10.1016/S0960-894X(01)00799-5.

(144) Kates, S. A.; Solé, N. A.; Johnson, C. R.; Hudson, D.; Barany, G.; Albericio, F. A novel, convenient, three-dimensional orthogonal strategy for solid-phase synthesis of cyclic peptides. *Tetrahedron Letters* **1993**, *34* (10), 1549-1552. DOI: https://doi.org/10.1016/0040-4039(93)85003-F.

(145) Bechtler, C.; Lamers, C. Macrocyclization strategies for cyclic peptides and peptidomimetics. *RSC Medicinal Chemistry* **2021**, *12* (8), 1325-1351, 10.1039/D1MD00083G. DOI: 10.1039/D1MD00083G.

(146) B:urgi, H. B.; Dunitz, J. D.; Lehn, J. M.; Wipff, G. Stereochemistry of reaction paths at carbonyl centres. *Tetrahedron* **1974**, *30* (12), 1563-1572. DOI: https://doi.org/10.1016/S0040-4020(01)90678-7.

(147) Martí-Centelles, V.; Pandey, M. D.; Burguete, M. I.; Luis, S. V. Macrocyclization Reactions: The Importance of Conformational, Configurational, and Template-Induced Preorganization. *Chemical Reviews* **2015**, *115* (16), 8736-8834. DOI: 10.1021/acs.chemrev.5b00056.

(148) Schmidt, U.; Langner, J. Cyclotetrapeptides and cyclopentapeptides: occurrence and synthesis*. *The Journal of Peptide Research* **1997**, *49* (1), 67-73, https://doi.org/10.1111/j.1399-3011.1997.tb01122.x. DOI: https://doi.org/10.1111/j.1399-3011.1997.tb01122.x (acccessed 2022/11/30).

(149) Hardy, P. M.; Kenner, G. W.; Sheppard, R. C. Peptides—XIII: Effects of configuration on dielectric increments and cyclization of some simple peptides. *Tetrahedron* **1963**, *19* (1), 95-105. DOI: https://doi.org/10.1016/0040-4020(63)80009-5.

(150) Hoffmann, R. W. Flexible Molecules with Defined Shape—Conformational Design. *Angewandte Chemie International Edition in English* **1992**, *31* (9), 1124-1134, https://doi.org/10.1002/anie.199211241. DOI: https://doi.org/10.1002/anie.199211241 (acccessed 2022/12/01).

(151) Daidone, I.; Neuweiler, H.; Doose, S.; Sauer, M.; Smith, J. C. Hydrogen-Bond Driven Loop-Closure Kinetics in Unfolded Polypeptide Chains. *PLOS Computational Biology* **2010**, *6* (1), e1000645. DOI: 10.1371/journal.pcbi.1000645.

(152) Smith, J. A.; Pease, L. G.; Kopple, K. D. Reverse Turns in Peptides and Protein. *Critical Reviews in Biochemistry* **1980**, *8* (4), 315-399. DOI: 10.3109/10409238009105470.

(153) Rothe, M.; Steffen, K. D.; Rothe, I. Synthesis of Cyclotri-L-prolyl, a Cyclotripeptide Having a Nine-Membered Ring. *Angewandte Chemie International Edition in English* **1965**, *4* (4), 356-356, https://doi.org/10.1002/anie.196503561. DOI: https://doi.org/10.1002/anie.196503561 (acccessed 2022/12/02).

(154) Favre, M.; Moehle, K.; Jiang, L.; Pfeiffer, B.; Robinson, J. A. Structural Mimicry of Canonical Conformations in Antibody Hypervariable Loops Using Cyclic Peptides Containing a Heterochiral Diproline Template. *Journal of the American Chemical Society* **1999**, *121* (12), 2679-2685. DOI: 10.1021/ja984016p.

(155) Takeuchi, Y.; Marshall, G. R. Conformational Analysis of Reverse-Turn Constraints by N-Methylation and N-Hydroxylation of Amide Bonds in Peptides and Non-Peptide Mimetics. *Journal of the American Chemical Society* **1998**, *120* (22), 5363-5372. DOI: 10.1021/ja970855k.

(156) Kessler, H.; Haase, B. Cyclic hexapeptides derived from the human thymopoietin III. *International Journal of Peptide and Protein Research* **1992**, *39* (1), 36-40, https://doi.org/10.1111/j.1399-3011.1992.tb01553.x. DOI: https://doi.org/10.1111/j.1399-3011.1992.tb01553.x (acccessed 2022/12/02).

(157) Tamaki, M.; Akabori, S.; Muramatsu, I. Biomimetic synthesis of gramicidin S. Direct formation of the antibiotic from pentapeptide active esters having no

protecting group on the side chain of the Orn residue. *Journal of the American Chemical Society* **1993**, *115* (23), 10492-10496. DOI: 10.1021/ja00076a005.

(158) Liu, M.; Tang, Y. C.; Fan, K. Q.; Jiang, X.; Lai, L. H.; Ye, Y. H. Cyclization of several linear penta- and heptapeptides with different metal ions studied by CD spectroscopy*. *The Journal of Peptide Research* **2005**, *65* (1), 55-64, https://doi.org/10.1111/j.1399-3011.2004.00199.x. DOI: https://doi.org/10.1111/j.1399-3011.2004.00199.x (acccessed 2022/12/05).

(159) Wu, J.; Tang, J.; Chen, H.; He, Y.; Wang, H.; Yao, H. Recent developments in peptide macrocyclization. *Tetrahedron Letters* **2018**, *59* (4), 325-333. DOI: https://doi.org/10.1016/j.tetlet.2017.12.035.

(160) Eshelman, M. R.; Aldous, A. R.; Neupane, K. P.; Kritzer, J. A. Solution structure of a designed cyclic peptide ligand for nickel and copper ions. *Tetrahedron* **2014**, *70* (42), 7651-7654. DOI: https://doi.org/10.1016/j.tet.2014.07.083.

(161) Kotynia, A.; Pap, J. S.; Brasun, J. The binding abilities of homodetic cyclic His-peptides toward copper ions. *Inorganica Chimica Acta* **2018**, *472*, 3-11. DOI: https://doi.org/10.1016/j.ica.2017.07.028.

(162) Haas, K.; Ponikwar, W.; Nöth, H.; Beck, W. Facile Synthesis of Cyclic Tetrapeptides from Nonactivated Peptide Esters on Metal Centers. *Angewandte Chemie International Edition* **1998**, *37* (8), 1086-1089, https://doi.org/10.1002/(SICI)1521-3773(19980504)37:8<1086::AID-ANIE1086>3.0.CO;2-V. DOI: https://doi.org/10.1002/(SICI)1521-3773(19980504)37:8<1086::AID-ANIE1086>3.0.CO;2-V (acccessed 2022/12/08).

(163) Alfonso, I.; Bolte, M.; Bru, M.; Burguete, M. I.; Luis, S. V.; Rubio, J. Supramolecular Control for the Modular Synthesis of Pseudopeptidic Macrocycles through an Anion-Templated Reaction. *Journal of the American Chemical Society* **2008**, *130* (19), 6137-6144. DOI: 10.1021/ja710132c.

(164) Martí-Centelles, V.; Burguete, M. I.; Luis, S. V. Macrocycle Synthesis by Chloride-Templated Amide Bond Formation. *The Journal of Organic Chemistry* **2016**, *81* (5), 2143-2147. DOI: 10.1021/acs.joc.5b02676.

(165) Vidović, N.; Horvat, G.; Riva, D.; Rinkovec, T.; Cindro, N.; Tomišić, V.; Speranza, G. Chloride-Assisted Peptide Macrocyclization. *Organic Letters* **2020**, *22* (6), 2129-2134. DOI: 10.1021/acs.orglett.0c00036.

(166) Elmes, R. B. P.; Jolliffe, K. A. Anion recognition by cyclic peptides. *Chemical Communications* **2015**, *51* (24), 4951-4968, 10.1039/C4CC10095F. DOI: 10.1039/C4CC10095F.

(167) Young, P. G.; Clegg, J. K.; Bhadbhade, M.; Jolliffe, K. A. Hybrid cyclic peptide–thiourea cryptands for anion recognition. *Chemical Communications* **2011**, *47* (1), 463-465, 10.1039/C0CC02223C. DOI: 10.1039/C0CC02223C.

(168) Fischer, E. Ueber die Configuration des Traubenzuckers und seiner Isomeren. II. *Berichte der deutschen chemischen Gesellschaft* **1891**, *24* (2), 2683-2687, https://doi.org/10.1002/cber.18910240278. DOI: https://doi.org/10.1002/cber.18910240278 (acccessed 2022/12/21).

(169) Krebs, H. A. Metabolism of amino-acids: Deamination of amino-acids. *Biochemical Journal* **1935**, *29* (7), 1620-1644. DOI: 10.1042/bj0291620 (acccessed 12/21/2022).

(170) Seia, M.; Zisman, E. Different roles of D-amino acids in immune phenomena. *The FASEB Journal* **1997**, *11* (6), 449-456, https://doi.org/10.1096/fasebj.11.6.9194525. DOI: https://doi.org/10.1096/fasebj.11.6.9194525 (acccessed 2022/12/21).

(171) Tugyi, R.; Uray, K.; Iván, D.; Fellinger, E.; Perkins, A.; Hudecz, F. Partial d-amino acid substitution: Improved enzymatic stability and preserved Ab recognition of a MUC2 epitope peptide. *Proceedings of the National Academy of Sciences* **2005**, *102* (2), 413-418. DOI: 10.1073/pnas.0407677102 (acccessed 2022/12/22).

(172) Werner, H. M.; Cabalteja, C. C.; Horne, W. S. Peptide Backbone Composition and Protease Susceptibility: Impact of Modification Type, Position, and Tandem Substitution. *ChemBioChem* **2016**, *17* (8), 712-718, https://doi.org/10.1002/cbic.201500312. DOI: https://doi.org/10.1002/cbic.201500312 (acccessed 2022/12/22).

(173) Wada, S.-i.; Tsuda, H.; Okada, T.; Urata, H. Cellular uptake of Aib-containing amphipathic helix peptide. *Bioorganic & Medicinal Chemistry Letters* **2011**, *21* (19), 5688-5691. DOI: https://doi.org/10.1016/j.bmcl.2011.08.030.

(174) Ehrlich, P. The Relations existing between Chemical Constitution, Distribution, and Pharmacological Action**[Reprinted by permission of the publishers from Collected Studies on Immunity, New York: John Wiley & Sons, 1906, translated by C. BOLDUAN from Chapter XXXIV of Gesammelte Arbeiten zur Immunitätsforschung, edited by P. EHRLICH, Berlin: Hirschwald, 1904; (cf. Bibl. 158). The chapter was reprinted from the v. Leyden-Festschrift, 1902 (cf. pp. 570-595, this vol., and Bibl. 105) and is based on an Address given to the Verein für innere Medicin on December 12th, 1898. Revised by the editors of this Collection.]. In *The Collected Papers of Paul Ehrlich*, Himmelweit, F. Ed.; Pergamon, 2013; pp 596-618.

(175) Mathé, G.; Loc, T. B.; Bernard, J. Effet sur la leucemie 1210 de la souris dune combinaison par diazotation da-methopterine et de gamma-globulines de hamsters porteurs de cette leucemie par heterogreffe. *Comptes Rendus*

Hebdomadaires Des Seances De L Academie Des Sciences **1958**, *246* (10), 1626-1628.

(176) Ghose, T.; Cerini, M.; Carter, M.; Nairn, R. C. Immunoradioactive agent against cancer. *British Medical Journal* **1967**, *1* (5532), 90. DOI: 10.1136/bmj.1.5532.90.

(177) Ford, C. H.; Newman, C. E.; Johnson, J. R.; Woodhouse, C. S.; Reeder, T. A.; Rowland, G. F.; Simmonds, R. G. Localisation and toxicity study of a vindesine-anti-CEA conjugate in patients with advanced cancer. *British Journal of Cancer* **1983**, *47* (1), 35-42. DOI: 10.1038/bjc.1983.4.

(178) Bross, P. F.; Beitz J Fau - Chen, G.; Chen G Fau - Chen, X. H.; Chen Xh Fau - Duffy, E.; Duffy E Fau - Kieffer, L.; Kieffer L Fau - Roy, S.; Roy S Fau - Sridhara, R.; Sridhara R Fau - Rahman, A.; Rahman A Fau - Williams, G.; Williams G Fau - Pazdur, R.; et al. Approval summary: gemtuzumab ozogamicin in relapsed acute myeloid leukemia. (1078-0432 (Print)). From 2001 Jun.

(179) Kaspar, A. A.; Reichert, J. M. Future directions for peptide therapeutics development. *Drug Discovery Today* **2013**, *18* (17), 807-817. DOI: https://doi.org/10.1016/j.drudis.2013.05.011.

(180) Sun, X.; Ponte, J. F.; Yoder, N. C.; Laleau, R.; Coccia, J.; Lanieri, L.; Qiu, Q.; Wu, R.; Hong, E.; Bogalhas, M.; et al. Effects of Drug–Antibody Ratio on Pharmacokinetics, Biodistribution, Efficacy, and Tolerability of Antibody–Maytansinoid Conjugates. *Bioconjugate Chemistry* **2017**, *28* (5), 1371-1381. DOI: 10.1021/acs.bioconjchem.7b00062.

(181) Alas, M.; Saghaeidehkordi, A.; Kaur, K. Peptide–Drug Conjugates with Different Linkers for Cancer Therapy. *Journal of Medicinal Chemistry* **2021**, *64* (1), 216-232. DOI: 10.1021/acs.jmedchem.0c01530.

(182) Huang, T. L.; Székács, A.; Uematsu, T.; Kuwano, E.; Parkinson, A.; Hammock, B. D. Hydrolysis of Carbonates, Thiocarbonates, Carbamates, and Carboxylic Esters of α-Naphthol, β-Naphthol, and p-Nitrophenol by Human, Rat, and Mouse Liver Carboxylesterases. *Pharmaceutical Research* **1993**, *10* (5), 639-648. DOI: 10.1023/A:1018987111362.

(183) Shi, H.; Kwok, R. T. K.; Liu, J.; Xing, B.; Tang, B. Z.; Liu, B. Real-Time Monitoring of Cell Apoptosis and Drug Screening Using Fluorescent Light-Up Probe with Aggregation-Induced Emission Characteristics. *Journal of the American Chemical Society* **2012**, *134* (43), 17972-17981. DOI: 10.1021/ja3064588.

(184) Dubowchik, G. M.; Firestone, R. A.; Padilla, L.; Willner, D.; Hofstead, S. J.; Mosure, K.; Knipe, J. O.; Lasch, S. J.; Trail, P. A. Cathepsin B-Labile Dipeptide Linkers for Lysosomal Release of Doxorubicin from Internalizing Immunoconjugates: Model Studies of Enzymatic Drug Release and Antigen-

Specific In Vitro Anticancer Activity. *Bioconjugate Chemistry* **2002**, *13* (4), 855-869. DOI: 10.1021/bc025536j.

(185) Régina, A.; Demeule, M.; Ché, C.; Lavallée, I.; Poirier, J.; Gabathuler, R.; Béliveau, R.; Castaigne, J. P. Antitumour activity of ANG1005, a conjugate between paclitaxel and the new brain delivery vector Angiopep-2. *British Journal of Pharmacology* **2008**, *155* (2), 185-197, https://doi.org/10.1038/bjp.2008.260. DOI: https://doi.org/10.1038/bjp.2008.260 (acccessed 2023/06/10).

(186) Bushnell, D. L.; Bodeker, K. L. Overview and Current Status of Peptide Receptor Radionuclide Therapy. (1558-5042 (Electronic)). From 2020 Apr.

(187) Rogoza, O.; Megnis, K.; Kudrjavceva, M.; Gerina-Berzina, A.; Rovite, V. Role of Somatostatin Signalling in Neuroendocrine Tumours. In *International Journal of Molecular Sciences*, 2022; Vol. 23.

(188) Banerjee, S.; Pillai, M. R. A.; Knapp, F. F. Lutetium-177 Therapeutic Radiopharmaceuticals: Linking Chemistry, Radiochemistry, and Practical Applications. *Chemical Reviews* **2015**, *115* (8), 2934-2974. DOI: 10.1021/cr500171e.

(189) Vacondio, F.; Silva, C.; Mor, M.; Testa, B. Qualitative structure-metabolism relationships in the hydrolysis of carbamates. *Drug Metabolism Reviews* **2010**, *42* (4), 551-589. DOI: 10.3109/03602531003745960.

(190) Kumar, S. K.; Williams, S. A.; Isaacs, J. T.; Denmeade, S. R.; Khan, S. R. Modulating paclitaxel bioavailability for targeting prostate cancer. *Bioorganic & Medicinal Chemistry* **2007**, *15* (14), 4973-4984. DOI: https://doi.org/10.1016/j.bmc.2007.04.029.

(191) Ghosh, A. K.; Brindisi, M. Organic Carbamates in Drug Design and Medicinal Chemistry. *Journal of Medicinal Chemistry* **2015**, *58* (7), 2895-2940. DOI: 10.1021/jm501371s.

(192) Liang, Y.; Li, S.; Wang, X.; Zhang, Y.; Sun, Y.; Wang, Y.; Wang, X.; He, B.; Dai, W.; Zhang, H.; et al. A comparative study of the antitumor efficacy of peptide-doxorubicin conjugates with different linkers. *Journal of Controlled Release* **2018**, *275*, 129-141. DOI: https://doi.org/10.1016/j.jconrel.2018.01.033.

(193) Bajjuri, K. M.; Liu, Y.; Liu, C.; Sinha, S. C. The Legumain Protease-Activated Auristatin Prodrugs Suppress Tumor Growth and Metastasis without Toxicity. *ChemMedChem* **2011**, *6* (1), 54-59. DOI: https://doi.org/10.1002/cmdc.201000478 (acccessed 2023/08/28).

(194) Mai, C.-W.; Chung, F.-L. F.; Leong, C.-O. Targeting Legumain As a Novel Therapeutic Strategy in Cancers. *Current Drug Targets* **2017**, *18* (11), 1259-1268. DOI: http://dx.doi.org/10.2174/1389450117666161216125344.

(195) Chan, J.; Dodani, S. C.; Chang, C. J. Reaction-based small-molecule fluorescent probes for chemoselective bioimaging. *Nature Chemistry* **2012**, *4* (12), 973-984. DOI: 10.1038/nchem.1500.

(196) Nadler, A.; Schultz, C. The Power of Fluorogenic Probes. *Angewandte Chemie International Edition* **2013**, *52* (9), 2408-2410. DOI: https://doi.org/10.1002/anie.201209733 (acccessed 2023/08/31).

(197) Lakowicz, J. R. *Principles of fluorescence spectroscopy*; Springer, 2006.

(198) Grimm, J. B.; Heckman, L. M.; Lavis, L. D. Chapter One - The Chemistry of Small-Molecule Fluorogenic Probes. In *Progress in Molecular Biology and Translational Science*, Morris, M. C. Ed.; Vol. 113; Academic Press, 2013; pp 1-34.

(199) Zheng, Q.; Lavis, L. D. Development of photostable fluorophores for molecular imaging. *Current Opinion in Chemical Biology* **2017**, *39*, 32-38. DOI: https://doi.org/10.1016/j.cbpa.2017.04.017.

(200) Guilbault, G. G.; Kramer, D. N. Resorufin Butyrate and Indoxyl Acetate as Fluorogenic Substrates for Cholinesterase. *Analytical Chemistry* **1965**, *37* (1), 120-123. DOI: 10.1021/ac60220a031.

(201) Rotman, B. MEASUREMENT OF ACTIVITY OF SINGLE MOLECULES OF β-D-GALACTOSIDASE*. *Proceedings of the National Academy of Sciences* **1961**, *47* (12), 1981-1991. DOI: 10.1073/pnas.47.12.1981 (acccessed 2023/09/01).

(202) Kramer, D. N.; Guilbault, G. G. A Substrate for the Fluorometric Determination of Lipase Activity. *Analytical Chemistry* **1963**, *35* (4), 588-589. DOI: 10.1021/ac60197a027.

(203) Rotman, B.; Zderic, J. A.; Edelstein, M. FLUOROGENIC SUBSTRATES FOR β-D-GALACTOSIDASES AND PHOSPHATASES DERIVED FROM FLUORESCEIN (3, 6-DIHYDROXYFLUORAN) AND ITS MONOMETHYL ETHER*. *Proceedings of the National Academy of Sciences* **1963**, *50* (1), 1-6. DOI: 10.1073/pnas.50.1.1 (acccessed 2023/09/01).

(204) Rotman, B.; Papermaster, B. W. Membrane properties of living mammalian cells as studied by enzymatic hydrolysis of fluorogenic esters. *Proceedings of the National Academy of Sciences* **1966**, *55* (1), 134-141. DOI: 10.1073/pnas.55.1.134 (acccessed 2023/09/01).

(205) Coutlee, F.; Viscidi, R. P.; Yolken, R. H. Comparison of colorimetric, fluorescent, and enzymatic amplification substrate systems in an enzyme immunoassay for detection of DNA-RNA hybrids. *Journal of Clinical Microbiology* **1989**, *27* (5), 1002-1007. DOI: 10.1128/jcm.27.5.1002-1007.1989 (acccessed 2023/09/01).

(206) Xu, S.; Wang, Q.; Zhang, Q.; Zhang, L.; Zuo, L.; Jiang, J.-D.; Hu, H.-Y. Real time detection of ESKAPE pathogens by a nitroreductase-triggered fluorescence turn-on probe. *Chemical Communications* **2017**, *53* (81), 11177-11180, 10.1039/C7CC07050K. DOI: 10.1039/C7CC07050K.

(207) Jones, K. H.; Senft, J. A. An improved method to determine cell viability by simultaneous staining with fluorescein diacetate-propidium iodide. *Journal of Histochemistry & Cytochemistry* **1985**, *33* (1), 77-79. DOI: 10.1177/33.1.2578146 (acccessed 2023/09/01).

(208) Tan, Y.; Zhang, L.; Man, K. H.; Peltier, R.; Chen, G.; Zhang, H.; Zhou, L.; Wang, F.; Ho, D.; Yao, S. Q.; et al. Reaction-Based Off–On Near-infrared Fluorescent Probe for Imaging Alkaline Phosphatase Activity in Living Cells and Mice. *ACS Applied Materials & Interfaces* **2017**, *9* (8), 6796-6803. DOI: 10.1021/acsami.6b14176.

(209) Biswas, S.; McCullough, B. S.; Ma, E. S.; LaJoie, D.; Russell, C. W.; Garrett Brown, D.; Round, J. L.; Ullman, K. S.; Mulvey, M. A.; Barrios, A. M. Dual colorimetric and fluorogenic probes for visualizing tyrosine phosphatase activity. *Chemical Communications* **2017**, *53* (14), 2233-2236, 10.1039/C6CC09204G. DOI: 10.1039/C6CC09204G.

(210) Geraghty, C.; Wynne, C.; Elmes, R. B. P. 1,8-Naphthalimide based fluorescent sensors for enzymes. *Coordination Chemistry Reviews* **2021**, *437*, 213713. DOI: https://doi.org/10.1016/j.ccr.2020.213713.

(211) Gavriel, A. G.; Sambrook, M. R.; Russell, A. T.; Hayes, W. Recent advances in self-immolative linkers and their applications in polymeric reporting systems. *Polymer Chemistry* **2022**, *13* (22), 3188-3269, 10.1039/D2PY00414C. DOI: 10.1039/D2PY00414C.

(212) Dal Corso, A.; Arosio, S.; Arrighetti, N.; Perego, P.; Belvisi, L.; Pignataro, L.; Gennari, C. A trifunctional self-immolative spacer enables drug release with two non-sequential enzymatic cleavages. *Chemical Communications* **2021**, *57* (63), 7778-7781, 10.1039/D1CC02895B. DOI: 10.1039/D1CC02895B.

(213) Teale, F. W. J.; Weber, G. Ultraviolet fluorescence of the aromatic amino acids. *Biochemical Journal* **1957**, *65* (3), 476-482. DOI: 10.1042/bj0650476 (acccessed 9/5/2023).

(214) Pandit, G.; Roy, K.; Agarwal, U.; Chatterjee, S. Self-Assembly Mechanism of a Peptide-Based Drug Delivery Vehicle. *ACS Omega* **2018**, *3* (3), 3143-3155. DOI: 10.1021/acsomega.7b01871.

(215) Min, K.-I.; Yun, G.; Jang, Y.; Kim, K.-R.; Ko, Y. H.; Jang, H.-S.; Lee, Y.-S.; Kim, K.; Kim, D.-P. Covalent Self-Assembly and One-Step Photocrosslinking of Tyrosine-Rich Oligopeptides to Form Diverse Nanostructures. *Angewandte Chemie International Edition* **2016**, *55* (24), 6925-6928. DOI: https://doi.org/10.1002/anie.201601675 (acccessed 2023/09/05).

(216) Handelman, A.; Kuritz, N.; Natan, A.; Rosenman, G. Reconstructive Phase Transition in Ultrashort Peptide Nanostructures and Induced Visible Photoluminescence. *Langmuir* **2016**, *32* (12), 2847-2862. DOI: 10.1021/acs.langmuir.5b02784.

(217) Grigoryan, K. R.; Shilajyan, H. A. FLUORESCENCE 2D AND 3D SPECTRA ANALYSIS OF TRYPTOPHAN, TYROSINE AND PHENYLALANINE. *Proceedings of the YSU B: Chemical and Biological Sciences* **2017**, *51* (1 (242)), 3-7. DOI: 10.46991/PYSU:B/2017.51.1.003 (acccessed 2023/09/07).

(218) Ghisaidoobe, A. B. T.; Chung, S. J. Intrinsic Tryptophan Fluorescence in the Detection and Analysis of Proteins: A Focus on Förster Resonance Energy Transfer Techniques. In *International Journal of Molecular Sciences*, 2014; Vol. 15, pp 22518-22538.

(219) Adams, P. D.; Chen, Y.; Ma, K.; Zagorski, M. G.; Sönnichsen, F. D.; McLaughlin, M. L.; Barkley, M. D. Intramolecular Quenching of Tryptophan Fluorescence by the Peptide Bond in Cyclic Hexapeptides. *Journal of the American Chemical Society* **2002**, *124* (31), 9278-9286. DOI: 10.1021/ja0167710.

(220) Faggi, E.; Pérez, Y.; Luis, S. V.; Alfonso, I. Supramolecular protection from the enzymatic tyrosine phosphorylation in a polypeptide. *Chemical Communications* **2016**, *52* (52), 8142-8145, 10.1039/C6CC03875A. DOI: 10.1039/C6CC03875A.

(221) Biswas, S.; Samui, S.; Chakraborty, A.; Biswas, S.; De, D.; Ghosh, U.; Das, A. K.; Naskar, J. Insight into the binding of a non-toxic, self-assembling aromatic tripeptide with ct-DNA: Spectroscopic and viscositic studies. *Biochemistry and Biophysics Reports* **2017**, *11*, 112-118. DOI: https://doi.org/10.1016/j.bbrep.2017.07.001.

(222) Merkel, L.; Hoesl, M. G.; Albrecht, M.; Schmidt, A.; Budisa, N. Blue Fluorescent Amino Acids as In Vivo Building Blocks for Proteins. *ChemBioChem* **2010**, *11* (3), 305-314. DOI: https://doi.org/10.1002/cbic.200900651 (acccessed 2023/09/09).

(223) Talukder, P.; Chen, S.; Roy, B.; Yakovchuk, P.; Spiering, M. M.; Alam, M. P.; Madathil, M. M.; Bhattacharya, C.; Benkovic, S. J.; Hecht, S. M. Cyanotryptophans as Novel Fluorescent Probes for Studying Protein Conformational Changes and DNA–Protein Interaction. *Biochemistry* **2015**, *54* (51), 7457-7469. DOI: 10.1021/acs.biochem.5b01085.

(224) Fernandez, A.; Thompson, E. J.; Pollard, J. W.; Kitamura, T.; Vendrell, M. A Fluorescent Activatable AND-Gate Chemokine CCL2 Enables In Vivo Detection of Metastasis-Associated Macrophages. *Angewandte Chemie International Edition* **2019**, *58* (47), 16894-16898. DOI: https://doi.org/10.1002/anie.201910955 (acccessed 2023/09/10).

(225) Cheng, M. H. Y.; Savoie, H.; Bryden, F.; Boyle, R. W. A convenient method for multicolour labelling of proteins with BODIPY fluorophores via tyrosine residues. *Photochemical & Photobiological Sciences* **2017**, *16* (8), 1260-1267. DOI: 10.1039/c7pp00091j.

(226) Joshi, P. N.; Rai, V. Single-site labeling of histidine in proteins, on-demand reversibility, and traceless metal-free protein purification. *Chemical Communications* **2019**, *55* (8), 1100-1103, 10.1039/C8CC08733D. DOI: 10.1039/C8CC08733D.

(227) López-Abarrategui, C.; Alba, A.; Silva, O. N.; Reyes-Acosta, O.; Vasconcelos, I. M.; Oliveira, J. T. A.; Migliolo, L.; Costa, M. P.; Costa, C. R.; Silva, M. R. R.; et al. Functional characterization of a synthetic hydrophilic antifungal peptide derived from the marine snail Cenchritis muricatus. *Biochimie* **2012**, *94* (4), 968-974. DOI: https://doi.org/10.1016/j.biochi.2011.12.016.

(228) Mendive-Tapia, L.; Zhao, C.; Akram, A. R.; Preciado, S.; Albericio, F.; Lee, M.; Serrels, A.; Kielland, N.; Read, N. D.; Lavilla, R.; et al. Spacer-free BODIPY fluorogens in antimicrobial peptides for direct imaging of fungal infection in human tissue. *Nature Communications* **2016**, *7* (1), 10940. DOI: 10.1038/ncomms10940.

(229) Zhu, Y.; Mohapatra, S.; Weisshaar, J. C. Rigidification of the E. coli Cytoplasm by the Human Antimicrobial Peptide LI-37 Revealed by Superresolution Fluorescence Microscopy. *Biophysical Journal* **2019**, *116* (3, Supplement 1), 138a. DOI: https://doi.org/10.1016/j.bpj.2018.11.765.

(230) Gan, B.-H.; Siriwardena, T. N.; Javor, S.; Darbre, T.; Reymond, J.-L. Fluorescence Imaging of Bacterial Killing by Antimicrobial Peptide Dendrimer G3KL. *ACS Infectious Diseases* **2019**, *5* (12), 2164-2173. DOI: 10.1021/acsinfecdis.9b00299.

(231) Zhao, C.; Fernandez, A.; Avlonitis, N.; Vande Velde, G.; Bradley, M.; Read, N. D.; Vendrell, M. Searching for the Optimal Fluorophore to Label Antimicrobial Peptides. *ACS Combinatorial Science* **2016**, *18* (11), 689-696. DOI: 10.1021/acscombsci.6b00081.

(232) Fischer, R.; Waizenegger, T.; Köhler, K.; Brock, R. A quantitative validation of fluorophore-labelled cell-permeable peptide conjugates: fluorophore and cargo dependence of import. *Biochimica et Biophysica Acta (BBA) - Biomembranes* **2002**, *1564* (2), 365-374. DOI: https://doi.org/10.1016/S0005-2736(02)00471-6.

(233) Illien, F.; Rodriguez, N.; Amoura, M.; Joliot, A.; Pallerla, M.; Cribier, S.; Burlina, F.; Sagan, S. Quantitative fluorescence spectroscopy and flow cytometry analyses of cell-penetrating peptides internalization pathways: optimization, pitfalls, comparison with mass spectrometry quantification. *Scientific Reports* **2016**, *6* (1), 36938. DOI: 10.1038/srep36938.

(234) Birch, D.; Christensen, M. V.; Staerk, D.; Franzyk, H.; Nielsen, H. M. Fluorophore labeling of a cell-penetrating peptide induces differential effects on

its cellular distribution and affects cell viability. *Biochimica et Biophysica Acta (BBA) - Biomembranes* **2017**, *1859* (12), 2483-2494. DOI: https://doi.org/10.1016/j.bbamem.2017.09.015.

(235) Sainlos, M.; Iskenderian, W. S.; Imperiali, B. A General Screening Strategy for Peptide-Based Fluorogenic Ligands: Probes for Dynamic Studies of PDZ Domain-Mediated Interactions. *Journal of the American Chemical Society* **2009**, *131* (19), 6680-6682. DOI: 10.1021/ja900371q.

(236) Wang, W.; Uzawa, T.; Tochio, N.; Hamatsu, J.; Hirano, Y.; Tada, S.; Saneyoshi, H.; Kigawa, T.; Hayashi, N.; Ito, Y.; et al. A fluorogenic peptide probe developed by in vitro selection using tRNA carrying a fluorogenic amino acid. *Chemical Communications* **2014**, *50* (22), 2962-2964, 10.1039/C3CC47624C. DOI: 10.1039/C3CC47624C.

(237) Wang, W.; Zhu, L.; Hirano, Y.; Kariminavargani, M.; Tada, S.; Zhang, G.; Uzawa, T.; Zhang, D.; Hirose, T.; Taiji, M.; et al. Fluorogenic Enhancement of an in Vitro-Selected Peptide Ligand by Replacement of a Fluorescent Group. *Analytical Chemistry* **2016**, *88* (16), 7991-7997. DOI: 10.1021/acs.analchem.6b01032.

(238) Postupalenko, V. Y.; Zamotaiev, O. M.; Shvadchak, V. V.; Strizhak, A. V.; Pivovarenko, V. G.; Klymchenko, A. S.; Mely, Y. Dual-Fluorescence l-Amino Acid Reports Insertion and Orientation of Melittin Peptide in Cell Membranes. *Bioconjugate Chemistry* **2013**, *24* (12), 1998-2007. DOI: 10.1021/bc400325n.

(239) Chen, H.; Scherkenbeck, J.; Zdobinsky, T.; Antonicek, H. Fluorescent Analogues of the Insect Neuropeptide Helicokinin I: Synthesis,Photophysical Characterization and Biological Activity. *Protein & Peptide Letters* **2010**, *17* (4), 431-436. DOI: http://dx.doi.org/10.2174/092986610790963672.

(240) Akram, A. R.; Avlonitis, N.; Scholefield, E.; Vendrell, M.; McDonald, N.; Aslam, T.; Craven, T. H.; Gray, C.; Collie, D. S.; Fisher, A. J.; et al. Enhanced avidity from a multivalent fluorescent antimicrobial peptide enables pathogen detection in a human lung model. *Scientific Reports* **2019**, *9* (1), 8422. DOI: 10.1038/s41598-019-44804-0.

(241) Ge, J.; Li, L.; Yao, S. Q. A self-immobilizing and fluorogenic unnatural amino acid that mimics phosphotyrosine. *Chemical Communications* **2011**, *47* (39), 10939-10941, 10.1039/C1CC14653J. DOI: 10.1039/C1CC14653J.

(242) Heffern, M. C.; Matosziuk, L. M.; Meade, T. J. Lanthanide Probes for Bioresponsive Imaging. *Chemical Reviews* **2014**, *114* (8), 4496-4539. DOI: 10.1021/cr400477t.

(243) Bünzli, J.-C. G. Lanthanide light for biology and medical diagnosis. *Journal of Luminescence* **2016**, *170*, 866-878. DOI: https://doi.org/10.1016/j.jlumin.2015.07.033.

(244) Eliseeva, S. V.; Bünzli, J.-C. G. Lanthanide luminescence for functional materials and bio-sciences. *Chemical Society Reviews* **2010**, *39* (1), 189-227, 10.1039/B905604C. DOI: 10.1039/B905604C.

(245) Jia, Y.; Quinn, C. M.; Gagnon, A. I.; Talanian, R. Homogeneous time-resolved fluorescence and its applications for kinase assays in drug discovery. *Analytical Biochemistry* **2006**, *356* (2), 273-281. DOI: https://doi.org/10.1016/j.ab.2006.05.006.

(246) Hewitt, S. H.; Butler, S. J. Application of lanthanide luminescence in probing enzyme activity. *Chemical Communications* **2018**, *54* (50), 6635-6647, 10.1039/C8CC02824A. DOI: 10.1039/C8CC02824A.

(247) Moore, E. G.; Samuel, A. P. S.; Raymond, K. N. From Antenna to Assay: Lessons Learned in Lanthanide Luminescence. *Accounts of Chemical Research* **2009**, *42* (4), 542-552. DOI: 10.1021/ar800211j.

(248) Bünzli, J. C. G. On the design of highly luminescent lanthanide complexes. *Coordination Chemistry Reviews* **2015**, *293-294*, 19-47, Review. DOI: 10.1016/j.ccr.2014.10.013 Scopus.

(249) Bünzli, J.-C. G. Benefiting from the Unique Properties of Lanthanide Ions. *Accounts of Chemical Research* **2006**, *39* (1), 53-61. DOI: 10.1021/ar0400894.

(250) Junker, A. K. R.; Tropiano, M.; Faulkner, S.; Sørensen, T. J. Kinetically Inert Lanthanide Complexes as Reporter Groups for Binding of Potassium by 18-crown-6. *Inorganic Chemistry* **2016**, *55* (23), 12299-12308. DOI: 10.1021/acs.inorgchem.6b02063.

(251) Petoud, S.; Cohen, S. M.; Bünzli, J.-C. G.; Raymond, K. N. Stable Lanthanide Luminescence Agents Highly Emissive in Aqueous Solution: Multidentate 2-Hydroxyisophthalamide Complexes of Sm3+, Eu3+, Tb3+, Dy3+. *Journal of the American Chemical Society* **2003**, *125* (44), 13324-13325. DOI: 10.1021/ja0379363.

(252) Beeby, A.; M. Clarkson, I.; S. Dickins, R.; Faulkner, S.; Parker, D.; Royle, L.; S. de Sousa, A.; A. Gareth Williams, J.; Woods, M. Non-radiative deactivation of the excited states of europium, terbium and ytterbium complexes by proximate energy-matched OH, NH and CH oscillators: an improved luminescence method for establishing solution hydration states. *Journal of the Chemical Society, Perkin Transactions 2* **1999**, (3), 493-504, 10.1039/A808692C. DOI: 10.1039/A808692C.

(253) Peuralahti, J.; Hakala, H.; Mukkala, V.-M.; Loman, K.; Hurskainen, P.; Mulari, O.; Hovinen, J. Introduction of Lanthanide(III) Chelates to Oligopeptides on Solid Phase. *Bioconjugate Chemistry* **2002**, *13* (4), 870-875. DOI: 10.1021/bc025521l.

(254) Pazos, E.; Vázquez, M. E. Advances in lanthanide-based luminescent peptide probes for monitoring the activity of kinase and phosphatase. *Biotechnology Journal* **2014**, *9* (2), 241-252. DOI: https://doi.org/10.1002/biot.201300203 (acccessed 2023/09/14).

(255) Tremblay, M. S.; Zhu, Q.; Martí, A. A.; Dyer, J.; Halim, M.; Jockusch, S.; Turro, N. J.; Sames, D. Phosphorylation State-Responsive Lanthanide Peptide Conjugates: A Luminescence Switch Based on Reversible Complex Reorganization. *Organic Letters* **2006**, *8* (13), 2723-2726. DOI: 10.1021/ol060614u.

(256) Tremblay, M. S.; Lee, M.; Sames, D. A Luminescent Sensor for Tyrosine Phosphorylation. *Organic Letters* **2008**, *10* (1), 5-8. DOI: 10.1021/ol701920x.

(257) Pazos, E.; Goličnik, M.; Mascareñas, J. L.; Eugenio Vázquez, M. Detection of phosphorylation states by intermolecular sensitization of lanthanide–peptide conjugates. *Chemical Communications* **2012**, *48* (76), 9534-9536, 10.1039/C2CC34958B. DOI: 10.1039/C2CC34958B.

(258) Kerr, J. F. R.; Wyllie, A. H.; Currie, A. R. Apoptosis: A Basic Biological Phenomenon with Wideranging Implications in Tissue Kinetics. *British Journal of Cancer* **1972**, *26* (4), 239-257. DOI: 10.1038/bjc.1972.33.

(259) Mehić, B. Apoptosis – is it good or bad? *Bosnian Journal of Basic Medical Sciences* **2012**, *12* (3), 143. DOI: 10.17305/bjbms.2012.2458 (acccessed 2022/01/11).

(260) Hanahan, D.; Weinberg, Robert A. Hallmarks of Cancer: The Next Generation. *Cell* **2011**, *144* (5), 646-674. DOI: https://doi.org/10.1016/j.cell.2011.02.013.

(261) Thompson Craig, B. Apoptosis in the Pathogenesis and Treatment of Disease. *Science* **1995**, *267* (5203), 1456-1462. DOI: 10.1126/science.7878464 (acccessed 2022/01/11).

(262) Chun, H. J.; Zheng, L.; Ahmad, M.; Wang, J.; Speirs, C. K.; Siegel, R. M.; Dale, J. K.; Puck, J.; Davis, J.; Hall, C. G.; et al. Pleiotropic defects in lymphocyte activation caused by caspase-8 mutations lead to human immunodeficiency. *Nature* **2002**, *419* (6905), 395-399. DOI: 10.1038/nature01063.

(263) Valko, M.; Leibfritz, D.; Moncol, J.; Cronin, M. T. D.; Mazur, M.; Telser, J. Free radicals and antioxidants in normal physiological functions and human disease. *The International Journal of Biochemistry & Cell Biology* **2007**, *39* (1), 44-84. DOI: https://doi.org/10.1016/j.biocel.2006.07.001.

(264) Lin, M. T.; Beal, M. F. Mitochondrial dysfunction and oxidative stress in neurodegenerative diseases. *Nature* **2006**, *443* (7113), 787-795. DOI: 10.1038/nature05292.

(265) Fischer, U.; Schulze-Osthoff, K. New Approaches and Therapeutics Targeting Apoptosis in Disease. *Pharmacological Reviews* **2005**, *57* (2), 187. DOI: 10.1124/pr.57.2.6.

(266) Shaulov-Rotem, Y.; Merquiol, E.; Weiss-Sadan, T.; Moshel, O.; Salpeter, S.; Shabat, D.; Kaschani, F.; Kaiser, M.; Blum, G. A novel quenched fluorescent activity-based probe reveals caspase-3 activity in the endoplasmic reticulum during apoptosis. *Chemical Science* **2016**, *7* (2), 1322-1337, 10.1039/C5SC03207E. DOI: 10.1039/C5SC03207E.

(267) Alnemri, E. S.; Livingston, D. J.; Nicholson, D. W.; Salvesen, G.; Thornberry, N. A.; Wong, W. W.; Yuan, J. Human ICE/CED-3 Protease Nomenclature. *Cell* **1996**, *87* (2), 171. DOI: https://doi.org/10.1016/S0092-8674(00)81334-3.

(268) Denault, J.-B.; Salvesen, G. S. Apoptotic Caspase Activation and Activity. In *Apoptosis and Cancer: Methods and Protocols*, Mor, G., Alvero, A. B. Eds.; Humana Press, 2008; pp 191-220.

(269) Poręba, M.; Stróżyk, A.; Salvesen, G. S.; Drąg, M. Caspase Substrates and Inhibitors. *Cold Spring Harbor Perspectives in Biology* **2013**, *5* (8). DOI: 10.1101/cshperspect.a008680.

(270) Vickers, C. J.; González-Páez, G. E.; Wolan, D. W. Selective Detection of Caspase-3 versus Caspase-7 Using Activity-Based Probes with Key Unnatural Amino Acids. *ACS Chemical Biology* **2013**, *8* (7), 1558-1566. DOI: 10.1021/cb400209w.

(271) Nicholls, S. B.; Hyman, B. T. Chapter Ten - Measuring Caspase Activity In Vivo. In *Methods in Enzymology*, Ashkenazi, A., Yuan, J., Wells, J. A. Eds.; Vol. 544; Academic Press, 2014; pp 251-269.

(272) Kim, T.-I.; Jin, H.; Bae, J.; Kim, Y. Excimer Emission-Based Fluorescent Probe Targeting Caspase-3. *Analytical Chemistry* **2017**, *89* (19), 10565-10569. DOI: 10.1021/acs.analchem.7b02790.

(273) Gurtu, V.; Kain, S. R.; Zhang, G. Fluorometric and Colorimetric Detection of Caspase Activity Associated with Apoptosis. *Analytical Biochemistry* **1997**, *251* (1), 98-102. DOI: https://doi.org/10.1006/abio.1997.2220.

(274) Wang, Z.-Q.; Liao, J.; Diwu, Z. N-DEVD-N′-morpholinecarbonyl-rhodamine 110: novel caspase-3 fluorogenic substrates for cell-based apoptosis assay. *Bioorganic & Medicinal Chemistry Letters* **2005**, *15* (9), 2335-2338. DOI: https://doi.org/10.1016/j.bmcl.2005.02.081.

(275) Vuojola, J.; Riuttamäki, T.; Kulta, E.; Arppe, R.; Soukka, T. Fluorescence-quenching-based homogeneous caspase-3 activity assay using photon upconversion. *Analytica Chimica Acta* **2012**, *725*, 67-73. DOI: https://doi.org/10.1016/j.aca.2012.03.010.

(276) Wu, Q.; Zhang, K. Y.; Dai, P.; Zhu, H.; Wang, Y.; Song, L.; Wang, L.; Liu, S.; Zhao, Q.; Huang, W. Bioorthogonal "Labeling after Recognition" Affording an FRET-Based Luminescent Probe for Detecting and Imaging Caspase-3 via Photoluminescence Lifetime Imaging. *Journal of the American Chemical Society* **2020**, *142* (2), 1057-1064. DOI: 10.1021/jacs.9b12191.

(277) Dunn, K. W.; Mayor, S.; Myers, J. N.; Maxfield, F. R. Applications of ratio fluorescence microscopy in the study of cell physiology. *The FASEB Journal* **1994**, *8* (9), 573-582, https://doi.org/10.1096/fasebj.8.9.8005385. DOI: https://doi.org/10.1096/fasebj.8.9.8005385 (acccessed 2022/01/13).

(278) Chen, Y.; Zhu, C.; Yang, Z.; Chen, J.; He, Y.; Jiao, Y.; He, W.; Qiu, L.; Cen, J.; Guo, Z. A Ratiometric Fluorescent Probe for Rapid Detection of Hydrogen Sulfide in Mitochondria. *Angewandte Chemie International Edition* **2013**, *52* (6), 1688-1691, https://doi.org/10.1002/anie.201207701. DOI: https://doi.org/10.1002/anie.201207701 (acccessed 2022/01/13).

(279) He, X.; Xu, Y.; Shi, W.; Ma, H. Ultrasensitive Detection of Aminopeptidase N Activity in Urine and Cells with a Ratiometric Fluorescence Probe. *Analytical Chemistry* **2017**, *89* (5), 3217-3221. DOI: 10.1021/acs.analchem.7b00021.

(280) Madhu, M.; Santhoshkumar, S.; Tseng, W.-B.; Tseng, W.-L. Maximizing analytical precision: exploring the advantages of ratiometric strategy in fluorescence, Raman, electrochemical, and mass spectrometry detection. *Frontiers in Analytical Science* **2023**, *3*, Review.

(281) Duke, R. M.; Veale, E. B.; Pfeffer, F. M.; Kruger, P. E.; Gunnlaugsson, T. Colorimetric and fluorescent anion sensors: an overview of recent developments in the use of 1,8-naphthalimide-based chemosensors. *Chem Soc Rev* **2010**, *39* (10), 3936-3953. DOI: 10.1039/b910560n.

(282) Banerjee, S.; Veale, E. B.; Phelan, C. M.; Murphy, S. A.; Tocci, G. M.; Gillespie, L. J.; Frimannsson, D. O.; Kelly, J. M.; Gunnlaugsson, T. Recent advances in the development of 1,8-naphthalimide based DNA targeting binders, anticancer and fluorescent cellular imaging agents. *Chemical Society Reviews* **2013**, *42* (4), 1601-1618, 10.1039/C2CS35467E. DOI: 10.1039/C2CS35467E.

(283) Middleton, R. W.; Parrick, J.; Clarke, E. D.; Wardman, P. Synthesis and fluorescence of N-substituted-1,8-naphthalimides. *Journal of Heterocyclic Chemistry* **1986**, *23* (3), 849-855. DOI: 10.1002/jhet.5570230337 (acccessed 2020/06/14).

(284) Fu, Y.; Finney, N. S. Small-molecule fluorescent probes and their design. *RSC Advances* **2018**, *8* (51), 29051-29061, 10.1039/C8RA02297F. DOI: 10.1039/C8RA02297F.

(285) Ao, X.; Bright, S. A.; Taylor, N. C.; Elmes, R. B. P. 2-Nitroimidazole based fluorescent probes for nitroreductase; monitoring reductive stress in cellulo. *Org Biomol Chem* **2017**, *15* (29), 6104-6108. DOI: 10.1039/c7ob01406f.

(286) Jin, Y.; Xu, K.; Huang, Y.; Zhong, H.; Zhao, R. Activity-Based Probe for Ratiometric Fluorescence Imaging of Caspase-3 in Living Cells. *Analytical Chemistry* **2021**, *93* (4), 2045-2052. DOI: 10.1021/acs.analchem.0c03762.

(287) Belleau, B.; Malek, G. New convenient reagent for peptide syntheses. *Journal of the American Chemical Society* **1968**, *90* (6), 1651-1652. DOI: 10.1021/ja01008a045.

(288) Zacharie, B.; Connolly, T. P.; Penney, C. L. A Simple One-Step Conversion of Carboxylic Acids to Esters Using EEDQ. *The Journal of Organic Chemistry* **1995**, *60* (21), 7072-7074. DOI: 10.1021/jo00126a080.

(289) Valeur, E.; Bradley, M. Amide bond formation: beyond the myth of coupling reagents. *Chemical Society Reviews* **2009**, *38* (2), 606-631, 10.1039/B701677H. DOI: 10.1039/B701677H.

(290) Chiriac, C. I.; Nechifor, M.; Tanasa, F.; Marioara, N. Formamide, a novel challenging reagent for the direct synthesis of non-N-substituted cyclic imides. *Rev. Roum. Chim* **2007**, *52*, 883-886.

(291) Duke, R. M.; Veale, E. B.; Pfeffer, F. M.; Kruger, P. E.; Gunnlaugsson, T. Colorimetric and fluorescent anion sensors: an overview of recent developments in the use of 1,8-naphthalimide-based chemosensors. *Chemical Society Reviews* **2010**, *39* (10), 3936-3953, 10.1039/B910560N. DOI: 10.1039/B910560N.

(292) Gunnlaugsson, T.; Glynn, M.; Tocci, G. M.; Kruger, P. E.; Pfeffer, F. M. Anion recognition and sensing in organic and aqueous media using luminescent and colorimetric sensors. *Coordination Chemistry Reviews* **2006**, *250* (23), 3094-3117. DOI: https://doi.org/10.1016/j.ccr.2006.08.017.

(293) Peris-Vicente, J.; Esteve-Romero, J.; Carda-Broch, S. Validation of Analytical Methods Based on Chromatographic Techniques: An Overview. In *Analytical Separation Science*, 2015; pp 1757-1808.

(294) Lehninger, A. L.; Nelson, D. L.; Cox, M. M. *Lehninger principles of biochemistry*; W.H. Freeman New York, 2005.

(295) Li, H.; Kim, Y.; Jung, H.; Hyun, J. Y.; Shin, I. Near-infrared (NIR) fluorescence-emitting small organic molecules for cancer imaging and therapy. *Chemical Society Reviews* **2022**, *51* (21), 8957-9008, 10.1039/D2CS00722C. DOI: 10.1039/D2CS00722C.

(296) Homan, K.; Min-Woong, K.; Satoshi, K.; Hak Soo, C. NIR fluorescence imaging and treatment for cancer immunotherapy. *Journal for ImmunoTherapy of Cancer* **2022**, *10* (7), e004936. DOI: 10.1136/jitc-2022-004936.

(297) Jia, X.; Yang, Y.; Xu, Y.; Qian, X. Naphthalimides for labeling and sensing applications. **2014**, *86* (7), 1237-1246. DOI: doi:10.1515/pac-2013-1025 (acccessed 2023-10-03).

(298) Kagatikar, S.; Sunil, D. A systematic review on 1,8-naphthalimide derivatives as emissive materials in organic light-emitting diodes. *Journal of Materials Science* **2022**, *57* (1), 105-139. DOI: 10.1007/s10853-021-06602-w.

(299) Lee, J.; Yoon, S. A.; Chun, J.; Kang, C.; Lee, M. H. A red-emitting styrylnaphthalimide-based fluorescent probe providing a ratiometric signal change for the precise and quantitative detection of H2O2. *Anal Chim Acta* **2019**, *1080*, 153-161. DOI: 10.1016/j.aca.2019.07.008.

(300) Watts, V. S.; Goldstein, J. H. Nuclear Magnetic Resonance Spectra of Alkenes. In *The Alkenes (1970)*, PATAI'S Chemistry of Functional Groups, 1970; pp 1-38.

(301) Blencowe, C. A.; Russell, A. T.; Greco, F.; Hayes, W.; Thornthwaite, D. W. Self-immolative linkers in polymeric delivery systems. *Polymer Chemistry* **2011**, *2* (4), 773-790, 10.1039/C0PY00324G. DOI: 10.1039/C0PY00324G.

(302) Baskerville, C. The Elements: Verified and Unverified. *Science* **1904**, *19* (472), 88-100. DOI: 10.1126/science.19.472.88 (acccessed 2023/10/11).

(303) Jørgensen, C. B. The inner mechanism of rare earths elucidated by photo-electron spectra. In *Rare Earths*, Berlin, Heidelberg, 1973//, 1973; Springer Berlin Heidelberg: pp 199-253.

(304) Weeks, M. E. The discovery of the elements. XVI. The rare earth elements. *Journal of Chemical Education* **1932**, *9* (10), 1751. DOI: 10.1021/ed009p1751.

(305) Bünzli, J.-C. G.; Piguet, C. Taking advantage of luminescent lanthanide ions. *Chemical Society Reviews* **2005**, *34* (12), 1048-1077, 10.1039/B406082M. DOI: 10.1039/B406082M.

(306) Moeller, T. Periodicity and the lanthanides and actinides. *Journal of Chemical Education* **1970**, *47* (6), 417. DOI: 10.1021/ed047p417.

(307) Rizkalla, E. N. Systematics of Lanthanide Coordination. **1993**, *61* (3-4), 181-190. DOI: doi:10.1524/ract.1993.61.34.181 (acccessed 2023-10-12).

(308) Armelao, L.; Quici, S.; Barigelletti, F.; Accorsi, G.; Bottaro, G.; Cavazzini, M.; Tondello, E. Design of luminescent lanthanide complexes: From molecules to highly efficient photo-emitting materials. *Coordination Chemistry Reviews* **2010**, *254* (5), 487-505. DOI: https://doi.org/10.1016/j.ccr.2009.07.025.

(309) Vögtle, F.; Weber, E. Multidentate Acyclic Neutral Ligands and Their Complexation. *Angewandte Chemie International Edition in English* **1979**, *18* (10), 753-776, Review. DOI: 10.1002/anie.197907531 Scopus.

(310) Chan, K. W.-Y.; Wong, W.-T. Small molecular gadolinium(III) complexes as MRI contrast agents for diagnostic imaging. *Coordination Chemistry Reviews* **2007**, *251* (17), 2428-2451. DOI: https://doi.org/10.1016/j.ccr.2007.04.018.

(311) Reichert, D. E.; Lewis, J. S.; Anderson, C. J. Metal complexes as diagnostic tools. *Coordination Chemistry Reviews* **1999**, *184* (1), 3-66. DOI: https://doi.org/10.1016/S0010-8545(98)00207-0.

(312) Aime, S.; Batsanov, A. S.; Botta, M.; Howard, J. A. K.; Parker, D.; Senanayake, K.; Williams, G. Solution and Solid-State Characterization of Highly Rigid, Eight-Coordinate Lanthanide(III) Complexes of a Macrocyclic Tetrabenzylphosphinate. *Inorganic Chemistry* **1994**, *33* (21), 4696-4706. DOI: 10.1021/ic00099a020.

(313) Latva, M.; Takalo, H.; Mukkala, V.-M.; Matachescu, C.; Rodríguez-Ubis, J. C.; Kankare, J. Correlation between the lowest triplet state energy level of the ligand and lanthanide(III) luminescence quantum yield. *Journal of Luminescence* **1997**, *75* (2), 149-169. DOI: https://doi.org/10.1016/S0022-2313(97)00113-0.

(314) Wurm, F. R.; Klok, H.-A. Be squared: expanding the horizon of squaric acid-mediated conjugations. *Chemical Society Reviews* **2013**, *42* (21), 8220-8236, 10.1039/C3CS60153F. DOI: 10.1039/C3CS60153F.

(315) Cai, X.-J.; Li, Z.; Chen, W.-H. Synthesis, Anion Recognition and Transmembrane Anion-Transport Properties of Squaramides and Their Derivatives. *Mini-Reviews in Organic Chemistry* **2018**, *15* (2), 148-156. DOI: http://dx.doi.org/10.2174/1570193X14666171114115629.

(316) Ian Storer, R.; Aciro, C.; Jones, L. H. Squaramides: physical properties, synthesis and applications. *Chemical Society Reviews* **2011**, *40* (5), 2330-2346, 10.1039/C0CS00200C. DOI: 10.1039/C0CS00200C.

(317) Agnew-Francis, K. A.; Williams, C. M. Squaramides as Bioisosteres in Contemporary Drug Design. *Chemical Reviews* **2020**, *120* (20), 11616-11650. DOI: 10.1021/acs.chemrev.0c00416.

(318) Lane, J. D. E.; Jolliffe, K. A. Squaramides for colorimetric and fluorescent anion sensing. *Organic & Biomolecular Chemistry* **2023**, *21* (15), 3226-3234, 10.1039/D3OB00069A. DOI: 10.1039/D3OB00069A.

(319) Ronchetti, R.; Moroni, G.; Carotti, A.; Gioiello, A.; Camaioni, E. Recent advances in urea- and thiourea-containing compounds: focus on innovative approaches in medicinal chemistry and organic synthesis. *RSC Medicinal Chemistry* **2021**, *12* (7), 1046-1064, 10.1039/D1MD00058F. DOI: 10.1039/D1MD00058F.

(320) Jiang, W.; Zheng, H.; Wu, Y.; Wu, P.; Jing, L.; Yuan, X.; Wang, X.; Wang, J. A squaramide-based anionic hydrogen-bonded organic framework: enhancing sensing performance for pesticides by post-metallization with in situ imaging. *Inorganic Chemistry Frontiers* **2023**, *10* (18), 5430-5438, 10.1039/D3QI01054F. DOI: 10.1039/D3QI01054F.

(321) Aime, S.; Geninatti Crich, S.; Botta, M.; Giovenzana, G.; Palmisano, G.; Sisti, M. A macromolecular Gd(III) complex as pH-responsive relaxometric probe for MRI applications. *Chemical Communications* **1999**, (16), 1577-1578, 10.1039/A900499H. DOI: 10.1039/A900499H.

(322) Marchetti, L. A.; Kumawat, L. K.; Mao, N.; Stephens, J. C.; Elmes, R. B. P. The Versatility of Squaramides: From Supramolecular Chemistry to Chemical Biology. *Chem* **2019**, *5* (6), 1398-1485. DOI: https://doi.org/10.1016/j.chempr.2019.02.027.

(323) Abogunrin, A. A.; Healy, S. A.; Fenelon, O.; Elmes, R. B. P. Head vs. Tail Squaramide–Naphthalimide Conjugates: Self-Assembly and Anion Binding Behaviour. In *Chemistry*, 2022; Vol. 4, pp 1288-1299.

(324) Kumawat, L. K.; Abogunrin, A. A.; Kickham, M.; Pardeshi, J.; Fenelon, O.; Schroeder, M.; Elmes, R. B. P. Squaramide-Naphthalimide Conjugates as "Turn-On" Fluorescent Sensors for Bromide Through an Aggregation-Disaggregation Approach. *Front Chem* **2019**, *7*, 354. DOI: 10.3389/fchem.2019.00354.

(325) Liu, H.; Tomooka, C. S.; Moore, H. W. An Efficient General Synthesis of Squarate Esters. *Synthetic Communications* **1997**, *27* (12), 2177-2180. DOI: 10.1080/00397919708006826.

(326) Corsi, D. M.; Vander Elst, L.; Muller, R. N.; van Bekkum, H.; Peters, J. A. Inulin as a Carrier for Contrast Agents in Magnetic Resonance Imaging. *Chemistry – A European Journal* **2001**, *7* (1), 64-71. DOI: https://doi.org/10.1002/1521-3765(20010105)7:1<64::AID-CHEM64>3.0.CO;2-S (acccessed 2023/10/15).

(327) Budzelaar, P. H. M.; Dietrich, H.; Macheleid, J.; Weiss, R.; von Ragué Schleyer, P. The molecular and electronic structure of dipiperidinosquaraine. *Chemische Berichte* **1985**, *118* (5), 2118-2126. DOI: https://doi.org/10.1002/cber.19851180531 (acccessed 2023/10/18).

(328) Englman, R.; Jortner, J. The energy gap law for radiationless transitions in large molecules. *Molecular Physics* **1970**, *18* (2), 145-164. DOI: 10.1080/00268977000100171.

(329) Hänninen, P.; Härmä, H. *Lanthanide Luminescence: Photophysical, Analytical and Biological Aspects*; Springer Berlin Heidelberg, 2011.

(330) Yip, Y.-W.; Wen, H.; Wong, W.-T.; Tanner, P. A.; Wong, K.-L. Increased Antenna Effect of the Lanthanide Complexes by Control of a Number of

Terdentate N-Donor Pyridine Ligands. *Inorganic Chemistry* **2012**, *51* (13), 7013-7015. DOI: 10.1021/ic300916e.

(331) Ranganathan, R. S.; Raju, N.; Fan, H.; Zhang, X.; Tweedle, M. F.; Desreux, J. F.; Jacques, V. Polymethylated DOTA Ligands. 2. Synthesis of Rigidified Lanthanide Chelates and Studies on the Effect of Alkyl Substitution on Conformational Mobility and Relaxivity. *Inorganic Chemistry* **2002**, *41* (25), 6856-6866. DOI: 10.1021/ic025695e.

(332) Venkataramana, G.; Sankararaman, S. Synthesis and Spectroscopic Investigation of Aggregation through Cooperative π−π and C−H···O Interactions in a Novel Pyrene Octaaldehyde Derivative. *Organic Letters* **2006**, *8* (13), 2739-2742. DOI: 10.1021/ol060767h.

(333) Brotzel, F.; Chu, Y. C.; Mayr, H. Nucleophilicities of Primary and Secondary Amines in Water. *The Journal of Organic Chemistry* **2007**, *72* (10), 3679-3688. DOI: 10.1021/jo062586z.

(334) Nain, S.; Singh, R.; Ravichandran, S. Importance of Microwave Heating In Organic Synthesis. *Advanced Journal of Chemistry, Section A* **2019**, *2* (2), 94-104. DOI: 10.29088/SAMI/AJCA.2019.2.94104.

(335) Corporation, C. *Microwave Synthesis*. 2023. https://cem.com/en/microwave-synthesis (accessed.

(336) Brockerman, J. A. Characterizing labile protons by NMR spectroscopy. Text, 2019. https://open.library.ubc.ca/collections/24/items/1.0376560.

(337) Nishioka, T.; Yuan, J.; Yamamoto, Y.; Sumitomo, K.; Wang, Z.; Hashino, K.; Hosoya, C.; Ikawa, K.; Wang, G.; Matsumoto, K. New Luminescent Europium(III) Chelates for DNA Labeling. *Inorganic Chemistry* **2006**, *45* (10), 4088-4096. DOI: 10.1021/ic051276g. Xu, J.; Corneillie, T. M.; Moore, E. G.; Law, G.-L.; Butlin, N. G.; Raymond, K. N. Octadentate Cages of Tb(III) 2-Hydroxyisophthalamides: A New Standard for Luminescent Lanthanide Labels. *Journal of the American Chemical Society* **2011**, *133* (49), 19900-19910. DOI: 10.1021/ja2079898.

(338) Cho, U.; Chen, J. K. Lanthanide-Based Optical Probes of Biological Systems. *Cell Chemical Biology* **2020**, *27* (8), 921-936. DOI: 10.1016/j.chembiol.2020.07.009 (acccessed 2023/11/04).

(339) Morley, J. O. Theoretical studies on the electronic structure and nonlinear properties of dicyanomethylene substituted squaramides, croconamides and rhodizonamides. *Journal of Molecular Structure: THEOCHEM* **1995**, *357* (1), 49-57. DOI: https://doi.org/10.1016/0166-1280(95)04279-F. Quiñonero, D.; Frontera, A.; Ballester, P.; Deyà, P. M. A theoretical study of aromaticity in squaramide and oxocarbons. *Tetrahedron Letters* **2000**, *41* (12), 2001-2005. DOI: https://doi.org/10.1016/S0040-4039(00)00084-8.

(340) Hegarty, I. N.; Hawes, C. S.; Gunnlaugsson, T. Synthesis of α-amino acid derived (1,2,3-triazol-4-yl)-picolinamide (tzpa) ligands and their corresponding luminescent Tb(iii) complexes. *Organic Chemistry Frontiers* **2023**, *10* (8), 1915-1926, 10.1039/D3QO00232B. DOI: 10.1039/D3QO00232B.

(341) Langmuir, I. ISOMORPHISM, ISOSTERISM AND COVALENCE. *Journal of the American Chemical Society* **1919**, *41* (10), 1543-1559. DOI: 10.1021/ja02231a009.

(342) Grimm, H. G. Über Bau und Grösse der Nichtmetallhydride. *Zeitschrift für Elektrochemie und angewandte physikalische Chemie* **1925**, *31* (9), 474-480. DOI: https://doi.org/10.1002/bbpc.19250310906 (acccessed 2023/11/07). Grimm, H. G. Zur Systematik der chemischen Verbindungen vom Standpunkt der Atomforschung, zugleich über einige Aufgaben der Experimentalchemie. *Naturwissenschaften* **1929**, *17* (28), 557-564. DOI: 10.1007/BF01505929.

(343) Erlenmeyer, H.; Leo, M. Über Pseudoatome. *Helvetica Chimica Acta* **1932**, *15* (1), 1171-1186. DOI: https://doi.org/10.1002/hlca.193201501132 (acccessed 2023/11/07).

(344) National Research, C. *First Symposium on Chemical-Biological Correlation, May 26-27, 1950*; The National Academies Press, 1951. DOI: 10.17226/18474.

(345) Thornber, C. W. Isosterism and molecular modification in drug design. *Chemical Society Reviews* **1979**, *8* (4), 563-580, 10.1039/CS9790800563. DOI: 10.1039/CS9790800563.

(346) Burger, A. *Medicinal chemistry*; Wiley-Interscience New York, 1970.

(347) Nicholls, A.; McGaughey, G. B.; Sheridan, R. P.; Good, A. C.; Warren, G.; Mathieu, M.; Muchmore, S. W.; Brown, S. P.; Grant, J. A.; Haigh, J. A.; et al. Molecular Shape and Medicinal Chemistry: A Perspective. *Journal of Medicinal Chemistry* **2010**, *53* (10), 3862-3886. DOI: 10.1021/jm900818s.

(348) Wassermann, A. M.; Bajorath, J. Large-scale exploration of bioisosteric replacements on the basis of matched molecular pairs. *Future Medicinal Chemistry* **2011**, *3* (4), 425-436. DOI: 10.4155/fmc.10.293 (acccessed 2023/11/07).

(349) Patani, G. A.; LaVoie, E. J. Bioisosterism: A Rational Approach in Drug Design. *Chemical Reviews* **1996**, *96* (8), 3147-3176. DOI: 10.1021/cr950066q.

(350) Ballatore, C.; Huryn, D. M.; Smith Iii, A. B. Carboxylic Acid (Bio)Isosteres in Drug Design. *ChemMedChem* **2013**, *8* (3), 385-395. DOI: https://doi.org/10.1002/cmdc.201200585 (acccessed 2023/11/13).

(351) Brück, A.; McCoy, L. L.; Kilway, K. V. Hydrogen Bonds in Carboxylic Acid−Carboxylate Systems in Solution. 1. In Anhydrous, Aprotic Media. *Organic Letters* **2000**, *2* (14), 2007-2009. DOI: 10.1021/ol005776j.

(352) Huggins, D. J.; Sherman, W.; Tidor, B. Rational Approaches to Improving Selectivity in Drug Design. *Journal of Medicinal Chemistry* **2012**, *55* (4), 1424-1444. DOI: 10.1021/jm2010332.

(353) Lee, A. C.; Harris, J. L.; Khanna, K. K.; Hong, J.-H. A Comprehensive Review on Current Advances in Peptide Drug Development and Design. In *International Journal of Molecular Sciences*, 2019; Vol. 20.

(354) Gopalakrishnan, R.; Frolov, A. I.; Knerr, L.; Drury, W. J., III; Valeur, E. Therapeutic Potential of Foldamers: From Chemical Biology Tools To Drug Candidates? *Journal of Medicinal Chemistry* **2016**, *59* (21), 9599-9621. DOI: 10.1021/acs.jmedchem.6b00376.

(355) Martinek, T. A.; Fülöp, F. Peptidic foldamers: ramping up diversity. *Chemical Society Reviews* **2012**, *41* (2), 687-702, 10.1039/C1CS15097A. DOI: 10.1039/C1CS15097A.

(356) Cheng, R. P.; Gellman, S. H.; DeGrado, W. F. β-Peptides: From Structure to Function. *Chemical Reviews* **2001**, *101* (10), 3219-3232. DOI: 10.1021/cr000045i.

(357) Cabrele, C.; Martinek, T. A.; Reiser, O.; Berlicki, Ł. Peptides Containing β-Amino Acid Patterns: Challenges and Successes in Medicinal Chemistry. *Journal of Medicinal Chemistry* **2014**, *57* (23), 9718-9739. DOI: 10.1021/jm5010896.

(358) Appella, D. H.; Christianson, L. A.; Karle, I. L.; Powell, D. R.; Gellman, S. H. β-Peptide Foldamers: Robust Helix Formation in a New Family of β-Amino Acid Oligomers. *Journal of the American Chemical Society* **1996**, *118* (51), 13071-13072. DOI: 10.1021/ja963290l. Appella, D. H.; Christianson, L. A.; Klein, D. A.; Powell, D. R.; Huang, X.; Barchi, J. J.; Gellman, S. H. Residue-based control of helix shape in β-peptide oligomers. *Nature* **1997**, *387* (6631), 381-384. DOI: 10.1038/387381a0.

(359) Semetey, V.; Rognan, D.; Hemmerlin, C.; Graff, R.; Briand, J.-P.; Marraud, M.; Guichard, G. Stable Helical Secondary Structure in Short-Chain N,N′-Linked Oligoureas Bearing Proteinogenic Side Chains. *Angewandte Chemie International Edition* **2002**, *41* (11), 1893-1895. DOI: https://doi.org/10.1002/1521-3773(20020603)41:11<1893::AID-ANIE1893>3.0.CO;2-F (acccessed 2023/11/13).

(360) Fremaux, J.; Mauran, L.; Pulka-Ziach, K.; Kauffmann, B.; Odaert, B.; Guichard, G. α-Peptide–Oligourea Chimeras: Stabilization of Short α-Helices by Non-Peptide Helical Foldamers. *Angewandte Chemie International Edition* **2015**, *54* (34), 9816-9820. DOI: https://doi.org/10.1002/anie.201500901 (acccessed 2023/11/13). Pendem, N.; Douat, C.; Claudon, P.; Laguerre, M.; Castano, S.;

Desbat, B.; Cavagnat, D.; Ennifar, E.; Kauffmann, B.; Guichard, G. Helix-Forming Propensity of Aliphatic Urea Oligomers Incorporating Noncanonical Residue Substitution Patterns. *Journal of the American Chemical Society* **2013**, *135* (12), 4884-4892. DOI: 10.1021/ja401151v.

(361) Douat-Casassus, C.; Pulka, K.; Claudon, P.; Guichard, G. Microwave-Enhanced Solid-Phase Synthesis of N,N′-Linked Aliphatic Oligoureas and Related Hybrids. *Organic Letters* **2012**, *14* (12), 3130-3133. DOI: 10.1021/ol3012106.

(362) Teyssières, E.; Corre, J.-P.; Antunes, S.; Rougeot, C.; Dugave, C.; Jouvion, G.; Claudon, P.; Mikaty, G.; Douat, C.; Goossens, P. L.; et al. Proteolytically Stable Foldamer Mimics of Host-Defense Peptides with Protective Activities in a Murine Model of Bacterial Infection. *Journal of Medicinal Chemistry* **2016**, *59* (18), 8221-8232. DOI: 10.1021/acs.jmedchem.6b00144.

(363) Maury, J.; Le Bailly, B. A. F.; Raftery, J.; Clayden, J. Conformational cooperativity between helical domains of differing geometry in oligoamide–oligourea foldamer chimeras. *Chemical Communications* **2015**, *51* (59), 11802-11805, 10.1039/C5CC02995C. DOI: 10.1039/C5CC02995C.

(364) Fremaux, J.; Venin, C.; Mauran, L.; Zimmer, R. H.; Guichard, G.; Goudreau, S. R. Peptide-oligourea hybrids analogue of GLP-1 with improved action in vivo. *Nature Communications* **2019**, *10* (1), 924. DOI: 10.1038/s41467-019-08793-y.

(365) Drucker, Daniel J. The Cardiovascular Biology of Glucagon-like Peptide-1. *Cell Metabolism* **2016**, *24* (1), 15-30. DOI: 10.1016/j.cmet.2016.06.009 (acccessed 2023/11/13).

(366) Drucker, D. J. Mechanisms of Action and Therapeutic Application of Glucagon-like Peptide-1. *Cell Metabolism* **2018**, *27* (4), 740-756. DOI: 10.1016/j.cmet.2018.03.001 (acccessed 2023/11/13).

(367) Xiao, Q.; Giguere, J.; Parisien, M.; Jeng, W.; St-Pierre, S. A.; Brubaker, P. L.; Wheeler, M. B. Biological Activities of Glucagon-Like Peptide-1 Analogues in Vitro and in Vivo. *Biochemistry* **2001**, *40* (9), 2860-2869. DOI: 10.1021/bi0014498.

(368) Cheang, J. Y.; Moyle, P. M. Glucagon-Like Peptide-1 (GLP-1)-Based Therapeutics: Current Status and Future Opportunities beyond Type 2 Diabetes. *ChemMedChem* **2018**, *13* (7), 662-671. DOI: https://doi.org/10.1002/cmdc.201700781 (acccessed 2023/11/13).

(369) Madsbad, S. Review of head-to-head comparisons of glucagon-like peptide-1 receptor agonists. *Diabetes, Obesity and Metabolism* **2016**, *18* (4), 317-332. DOI: https://doi.org/10.1111/dom.12596 (acccessed 2023/11/13).

(370) Johnson, L. M.; Barrick, S.; Hager, M. V.; McFedries, A.; Homan, E. A.; Rabaglia, M. E.; Keller, M. P.; Attie, A. D.; Saghatelian, A.; Bisello, A.; et al. A

Potent α/β-Peptide Analogue of GLP-1 with Prolonged Action in Vivo. *Journal of the American Chemical Society* **2014**, *136* (37), 12848-12851. DOI: 10.1021/ja507168t.

(371) Murage, E. N.; Gao, G.; Bisello, A.; Ahn, J.-M. Development of Potent Glucagon-like Peptide-1 Agonists with High Enzyme Stability via Introduction of Multiple Lactam Bridges. *Journal of Medicinal Chemistry* **2010**, *53* (17), 6412-6420. DOI: 10.1021/jm100602m.

(372) Fletcher, M. D.; Campbell, M. M. Partially Modified Retro-Inverso Peptides: Development, Synthesis, and Conformational Behavior. *Chemical Reviews* **1998**, *98* (2), 763-796. DOI: 10.1021/cr970468t.

(373) Li, C.; Zhan, C.; Zhao, L.; Chen, X.; Lu, W.-Y.; Lu, W. Functional consequences of retro-inverso isomerization of a miniature protein inhibitor of the p53–MDM2 interaction. *Bioorganic & Medicinal Chemistry* **2013**, *21* (14), 4045-4050. DOI: https://doi.org/10.1016/j.bmc.2013.04.039.

(374) Xi, W.; Hansmann, U. H. E. The effect of retro-inverse D-amino acid Aβ-peptides on Aβ-fibril formation. *The Journal of Chemical Physics* **2019**, *150* (9), 095101. DOI: 10.1063/1.5082194 (acccessed 5/8/2024).

(375) Stupp, R.; Mason, W. P.; van den Bent, M. J.; Weller, M.; Fisher, B.; Taphoorn, M. J. B.; Belanger, K.; Brandes, A. A.; Marosi, C.; Bogdahn, U.; et al. Radiotherapy plus Concomitant and Adjuvant Temozolomide for Glioblastoma. *New England Journal of Medicine* **2005**, *352* (10), 987-996. DOI: 10.1056/NEJMoa043330 (acccessed 2023/11/14).

(376) Guyon, J.; Chapouly, C.; Andrique, L.; Bikfalvi, A.; Daubon, T. The Normal and Brain Tumor Vasculature: Morphological and Functional Characteristics and Therapeutic Targeting. *Frontiers in Physiology* **2021**, *12*, Review.

(377) Tucker, G. C. Integrins: Molecular targets in cancer therapy. *Current Oncology Reports* **2006**, *8* (2), 96-103. DOI: 10.1007/s11912-006-0043-3.

(378) Bello, L.; Francolini, M.; Marthyn, P.; Zhang, J.; Carroll, R. S.; Nikas, D. C.; Strasser, J. F.; Villani, R.; Cheresh, D. A.; McL. Black, P. αvβ3 and αvβ5 Integrin Expression in Glioma Periphery. *Neurosurgery* **2001**, *49* (2).

(379) Smith, J. W. Cilengitide Merck. (1472-4472 (Print)). From 2003 Jun.

(380) Yamada, S.; Bu, X.-Y.; Khankaldyyan, V.; Gonzales-Gomez, I.; McComb, J. G.; Laug, W. E. EFFECT OF THE ANGIOGENESIS INHIBITOR CILENGITIDE (EMD 121974) ON GLIOBLASTOMA GROWTH IN NUDE MICE. *Neurosurgery* **2006**, *59* (6).

(381) Stupp, R.; Hegi, M. E.; Gorlia, T.; Erridge, S. C.; Perry, J.; Hong, Y.-K.; Aldape, K. D.; Lhermitte, B.; Pietsch, T.; Grujicic, D.; et al. Cilengitide combined

with standard treatment for patients with newly diagnosed glioblastoma with methylated MGMT promoter (CENTRIC EORTC 26071-22072 study): a multicentre, randomised, open-label, phase 3 trial. *The Lancet Oncology* **2014**, *15* (10), 1100-1108. DOI: https://doi.org/10.1016/S1470-2045(14)70379-1.

(382) Stupp, R.; Picard, M.; Weller, M. Does cilengitide deserve another chance?–Authors' reply. *The Lancet Oncology* **2014**, *15* (13), e585-e586. DOI: 10.1016/S1470-2045(14)71121-0 (acccessed 2023/11/15).

(383) Lassalas, P.; Gay, B.; Lasfargeas, C.; James, M. J.; Tran, V.; Vijayendran, K. G.; Brunden, K. R.; Kozlowski, M. C.; Thomas, C. J.; Smith, A. B., III; et al. Structure Property Relationships of Carboxylic Acid Isosteres. *Journal of Medicinal Chemistry* **2016**, *59* (7), 3183-3203. DOI: 10.1021/acs.jmedchem.5b01963.

(384) Ishida, T.; Shinada, T.; Ohfune, Y. Synthesis of novel amino squaric acids via addition of dianion enolates derived from N-Boc amino acid esters. *Tetrahedron Letters* **2005**, *46* (2), 311-314. DOI: https://doi.org/10.1016/j.tetlet.2004.11.044.

(385) Onaran, M. B.; Comeau, A. B.; Seto, C. T. Squaric Acid-Based Peptidic Inhibitors of Matrix Metalloprotease-1. *The Journal of Organic Chemistry* **2005**, *70* (26), 10792-10802. DOI: 10.1021/jo0517848.

(386) Del Gatto, A.; Cobb, S. L.; Zhang, J.; Zaccaro, L. Editorial: Peptidomimetics: Synthetic Tools for Drug Discovery and Development. *Frontiers in Chemistry* **2021**, *9*, Editorial.

(387) Delouvrié, B.; Al-Kadhimi, K.; Arnould, J.-C.; Barry, S. T.; Cross, D. A. E.; Didelot, M.; Gavine, P. R.; Germain, H.; Harris, C. S.; Hughes, A. M.; et al. Structure–activity relationship of a series of non peptidic RGD integrin antagonists targeting α5β1: Part 1. *Bioorganic & Medicinal Chemistry Letters* **2012**, *22* (12), 4111-4116. DOI: https://doi.org/10.1016/j.bmcl.2012.04.063.

(388) Carpino, L. A.; Imazumi, H.; Foxman, B. M.; Vela, M. J.; Henklein, P.; El-Faham, A.; Klose, J.; Bienert, M. Comparison of the Effects of 5- and 6-HOAt on Model Peptide Coupling Reactions Relative to the Cases for the 4- and 7-Isomers. *Organic Letters* **2000**, *2* (15), 2253-2256. DOI: 10.1021/ol006013z.

(389) Roth, H. J.; Sporleder, H. Zur Darstellung gemischt-substituierter Cyclobutendione. *Archiv der Pharmazie* **1970**, *303* (11), 886-895. DOI: https://doi.org/10.1002/ardp.19703031105 (acccessed 2023/11/20).

(390) Taylor, K. I.; Ho, J. S.; Trial, H. O.; Carter, A. W.; Kiessling, L. L. Assessing Squarates as Amine-Reactive Probes. *Journal of the American Chemical Society* **2023**. DOI: 10.1021/jacs.2c05691.

(391) Boeijen, A.; van Ameijde, J.; Liskamp, R. M. J. Solid-Phase Synthesis of Oligourea Peptidomimetics Employing the Fmoc Protection Strategy. *The Journal of Organic Chemistry* **2001**, *66* (25), 8454-8462. DOI: 10.1021/jo010656q.

(392) Rodriguez, M.; Llinares, M.; Doulut, S.; Heitz, A.; Martinez, J. A facile synthesis of chiral N-protected β-amino alcohols. *Tetrahedron Letters* **1991**, *32* (7), 923-926. DOI: https://doi.org/10.1016/S0040-4039(00)92121-X.

(393) Hamlin, T. A.; Swart, M.; Bickelhaupt, F. M. Nucleophilic Substitution (SN2): Dependence on Nucleophile, Leaving Group, Central Atom, Substituents, and Solvent. *ChemPhysChem* **2018**, *19* (11), 1315-1330. DOI: https://doi.org/10.1002/cphc.201701363 (acccessed 2023/11/22). Garegg, P. J.; Samuelsson, B. Novel reagent system for converting a hydroxy-group into an iodo-group in carbohydrates with inversion of configuration. *Journal of the Chemical Society, Chemical Communications* **1979**, (22), 978-980, 10.1039/C39790000978. DOI: 10.1039/C39790000978.

(394) Bräse, S.; Gil, C.; Knepper, K.; Zimmermann, V. Organic Azides: An Exploding Diversity of a Unique Class of Compounds. *Angewandte Chemie International Edition* **2005**, *44* (33), 5188-5240. DOI: https://doi.org/10.1002/anie.200400657 (acccessed 2023/11/22).

(395) Fundamentals of NMR Spectroscopy in Liquids. In *NMR Spectroscopy Explained*, 2007; pp 1-38.

(396) Vícha, J.; Novotný, J.; Komorovsky, S.; Straka, M.; Kaupp, M.; Marek, R. Relativistic Heavy-Neighbor-Atom Effects on NMR Shifts: Concepts and Trends Across the Periodic Table. *Chemical Reviews* **2020**, *120* (15), 7065-7103. DOI: 10.1021/acs.chemrev.9b00785.

(397) Melo, J. I.; Ruiz de Azua, M. C.; Giribet, C. G.; Aucar, G. A.; Provasi, P. F. Relativistic effects on nuclear magnetic shielding constants in HX and CH3X(X=Br,I) based on the linear response within the elimination of small component approach. *The Journal of Chemical Physics* **2004**, *121* (14), 6798-6808. DOI: 10.1063/1.1787495 (acccessed 11/24/2023).

(398) Kaupp, M.; Malkina, O. L.; Malkin, V. G.; Pyykkö, P. How Do Spin–Orbit-Induced Heavy-Atom Effects on NMR Chemical Shifts Function? Validation of a Simple Analogy to Spin–Spin Coupling by Density Functional Theory (DFT) Calculations on Some Iodo Compounds. *Chemistry – A European Journal* **1998**, *4* (1), 118-126. DOI: https://doi.org/10.1002/(SICI)1521-3765(199801)4:1<118::AID-CHEM118>3.0.CO;2-6 (acccessed 2023/11/24).

(399) Vícha, J.; Straka, M.; Munzarová, M. L.; Marek, R. Mechanism of Spin–Orbit Effects on the Ligand NMR Chemical Shift in Transition-Metal Complexes: Linking NMR to EPR. *Journal of Chemical Theory and Computation* **2014**, *10* (4), 1489-1499. DOI: 10.1021/ct400726y.

(400) Rugutt, J. K.; Yarabe, H. H.; Shamsi, S. A.; Billodeaux, D. R.; Fronczek, F. R.; Warner, I. M. GR 24 Enantiomers: Synthesis, NMR Spectroscopy, X-ray Crystallography, and Separation by Chiral Electrokinetic Capillary Chromatography. *Analytical Chemistry* **2000**, *72* (16), 3887-3895. DOI: 10.1021/ac991438o.

(401) Parker, D. NMR determination of enantiomeric purity. *Chemical Reviews* **1991**, *91* (7), 1441-1457. DOI: 10.1021/cr00007a009.

(402) Ward, T. J.; Hamburg, D.-M. Chiral Separations. *Analytical Chemistry* **2004**, *76* (16), 4635-4644. DOI: 10.1021/ac040093t.

Appendix

Appendix

Chapter 2 – Supplementary Characterisation Data
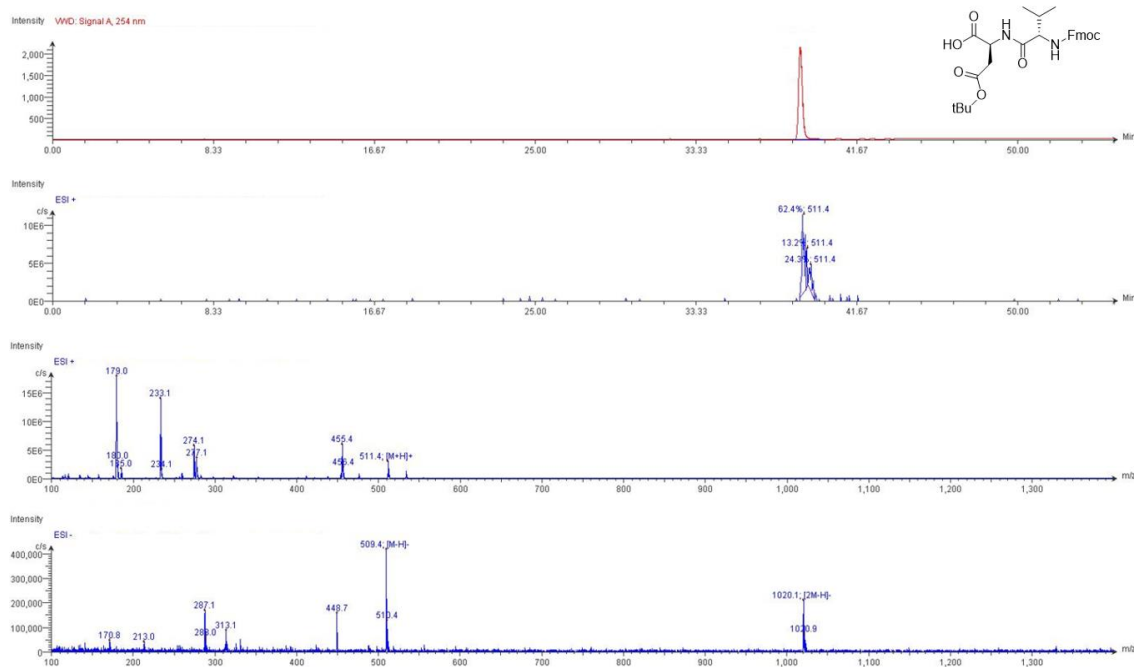
Figure S2.1: LC-MS data for **Fmoc-VD(O*t*Bu)-OH**.
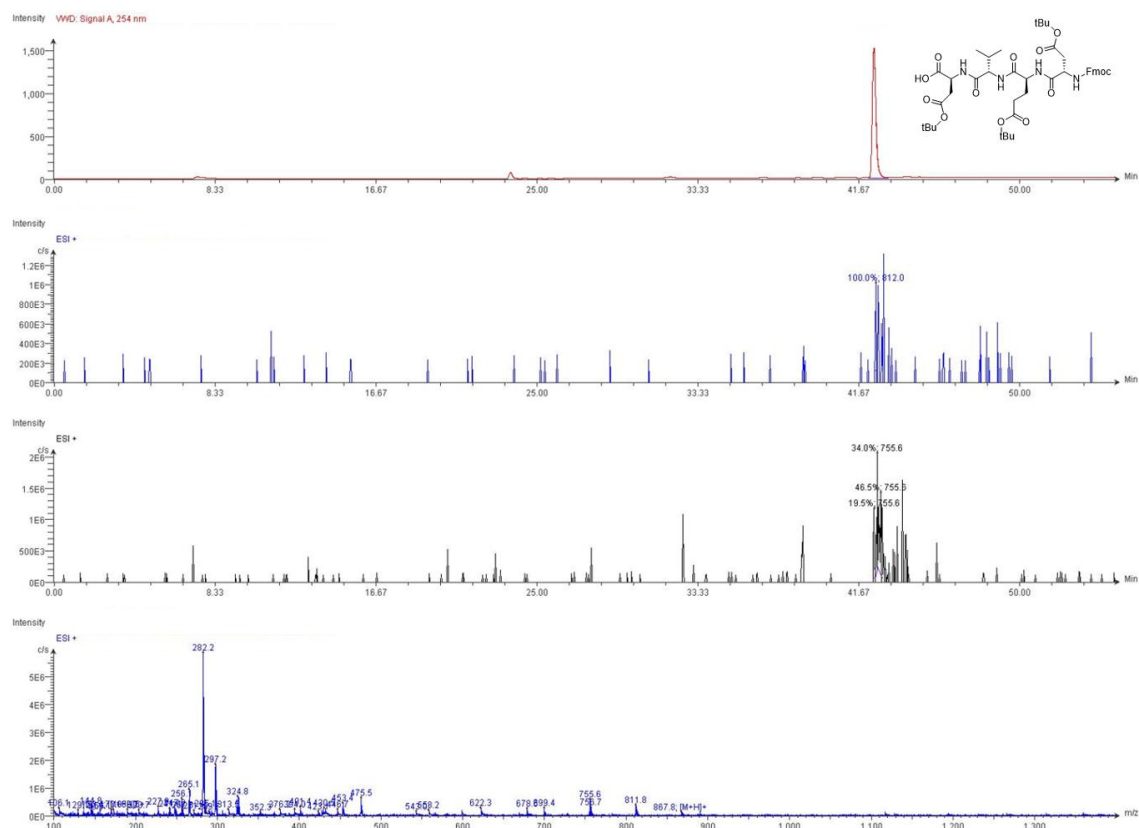
Figure S2.2: LC-MS data for **Fmoc-DEVD(O*t*Bu)-OH**.
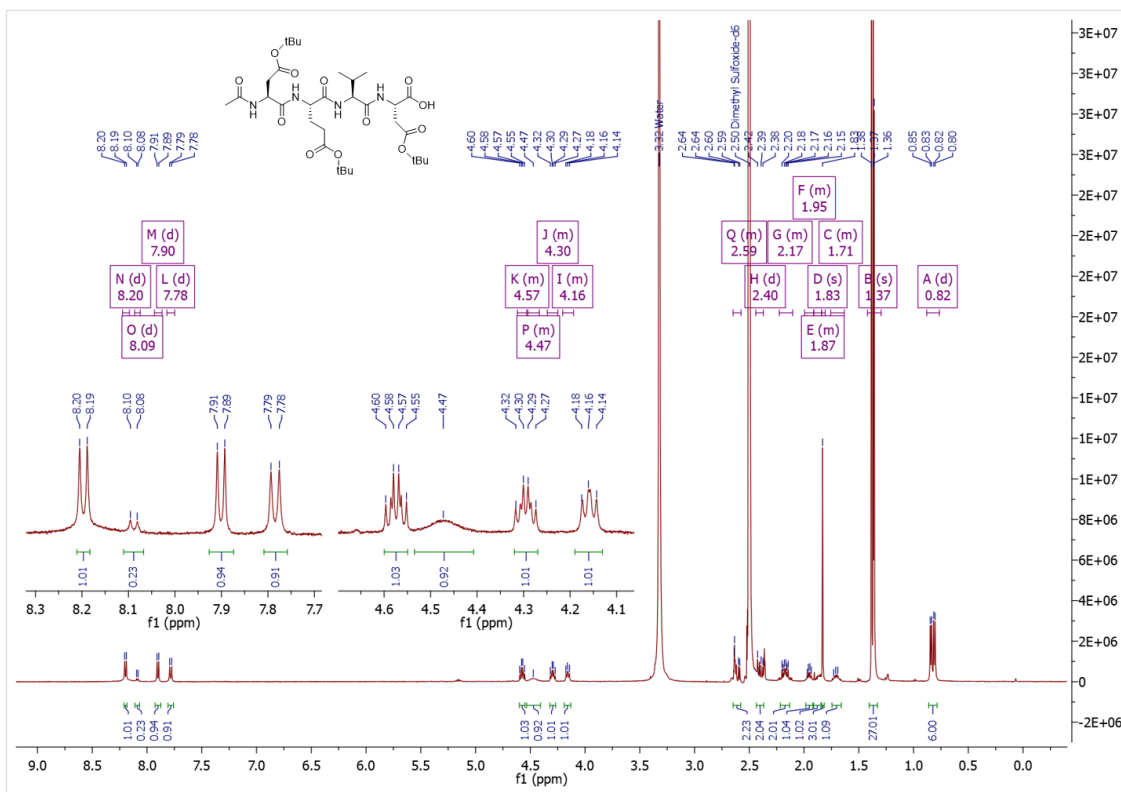
Figure S2.3: ^{1}H NMR spectrum of **Ac-DEVD(O*t*Bu)-OH (2.1)** in DMSO-*d*$_{6}$.
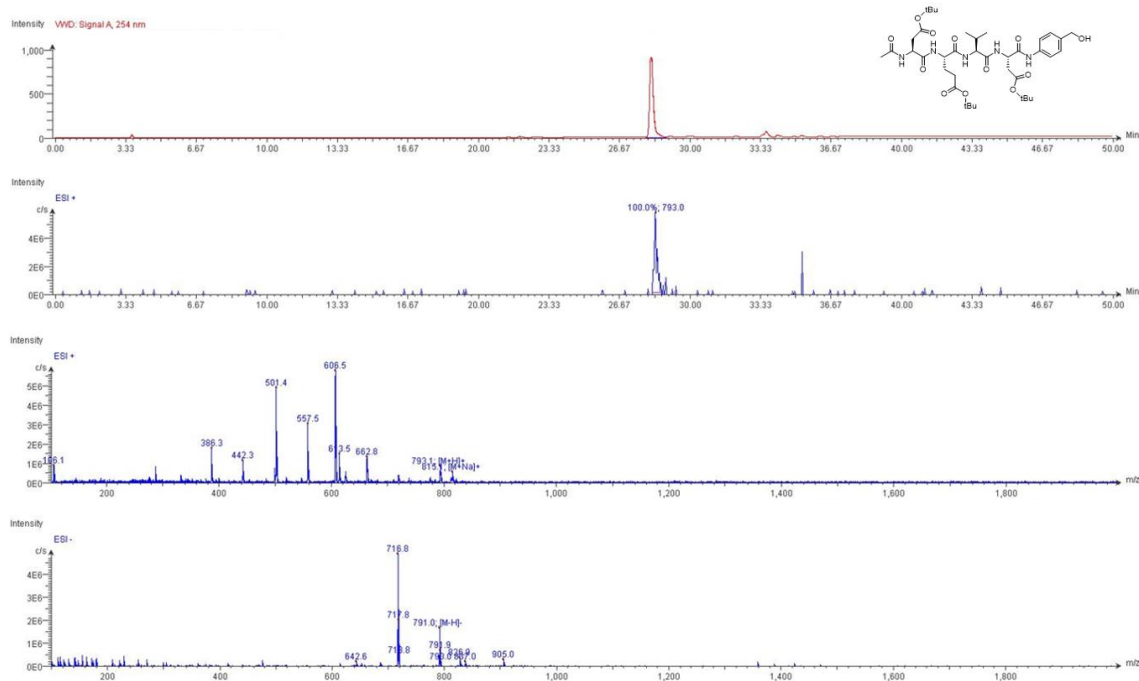
Figure S2.4: LC-MS data for **Ac-DEVD(O*t*Bu)-PABA-OH (2.2)**.

270
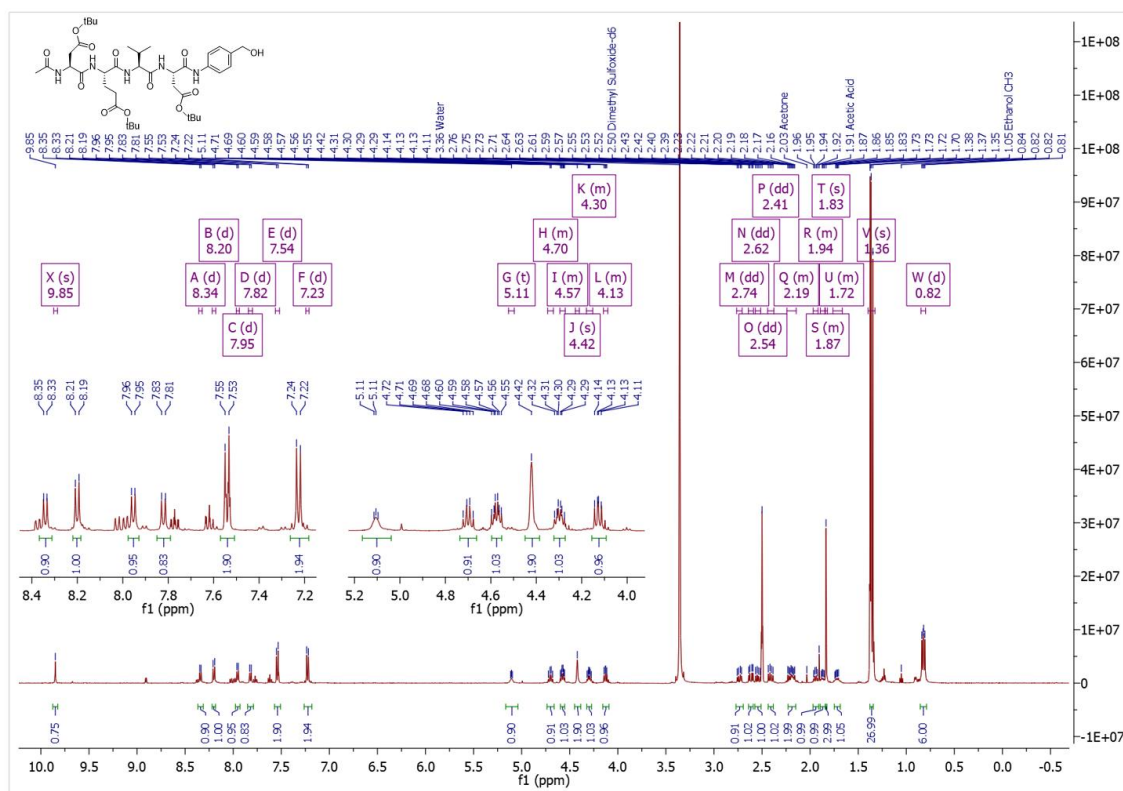
Figure S2.5: ^{1}H NMR spectrum of **Ac-DEVD(O*t*Bu)-PABA-OH (2.2)** in DMSO-d_6.
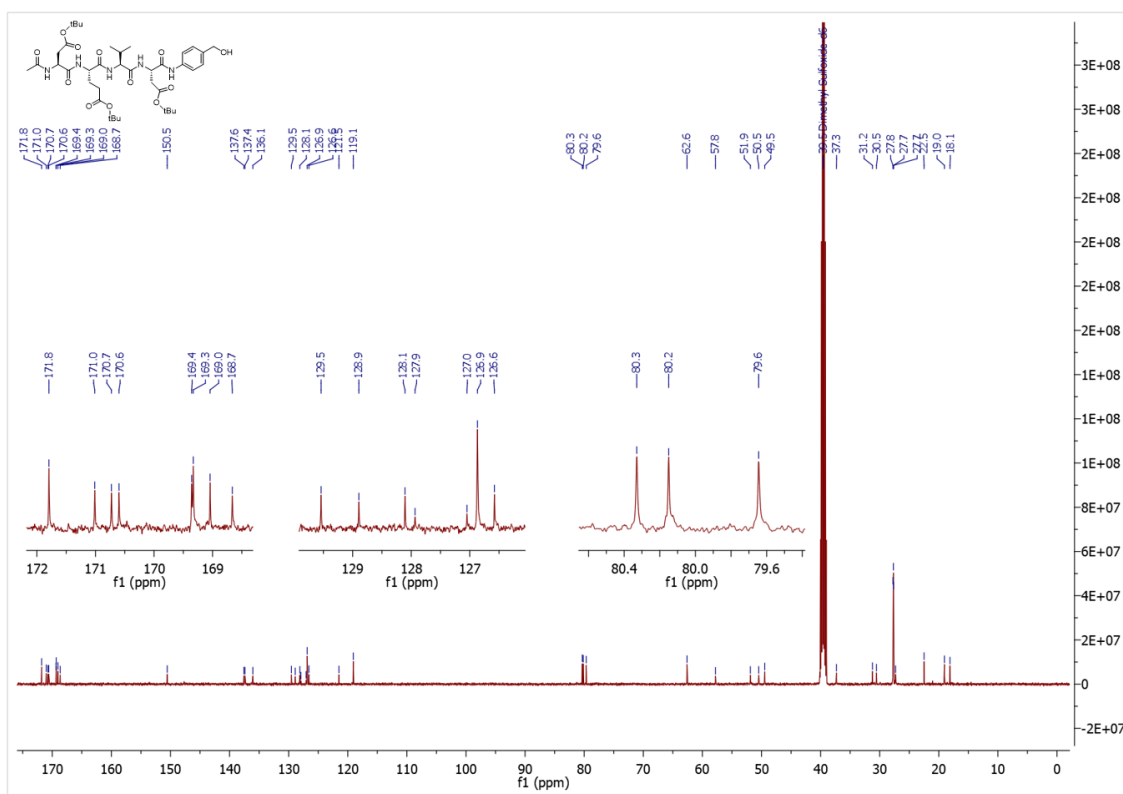
Figure S2.6: ^{13}C NMR spectrum of **Ac-DEVD(O*t*Bu)-PABA-OH (2.2)** in DMSO-d_6.
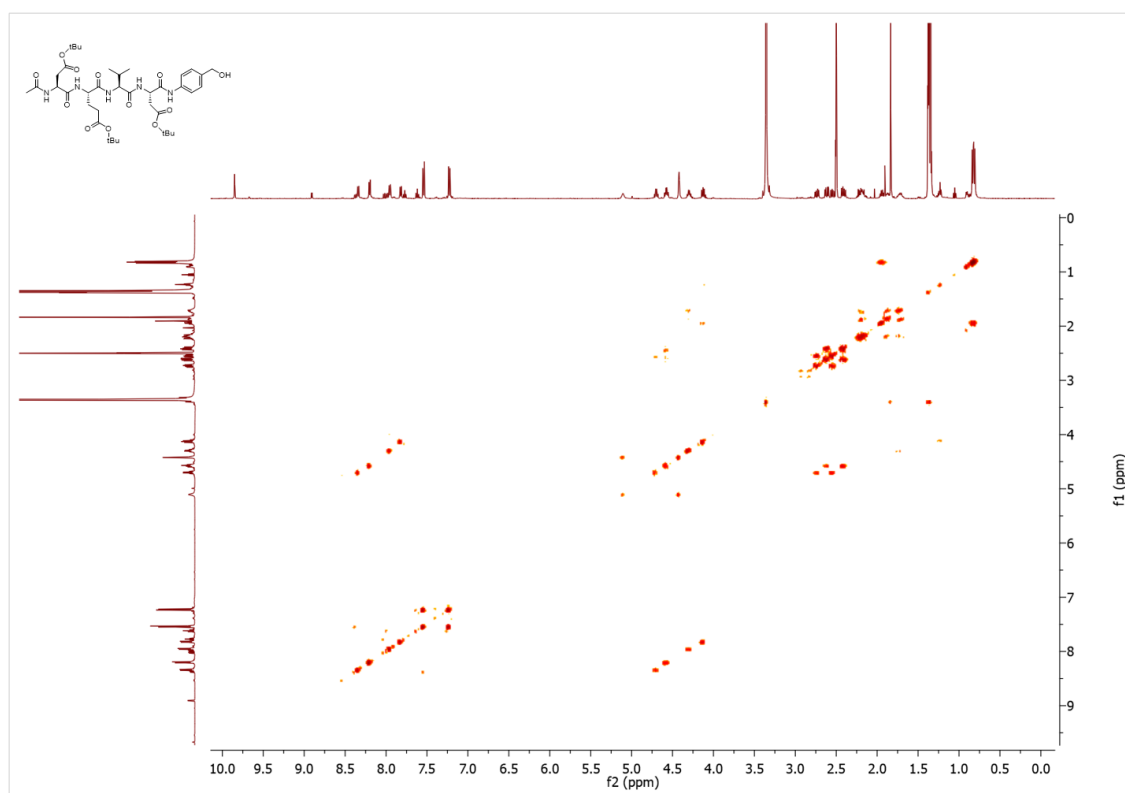
Figure S2.7: COSY spectrum of **Ac-DEVD(O*t*Bu)-PABA-OH (2.2)** in DMSO-*d*₆.
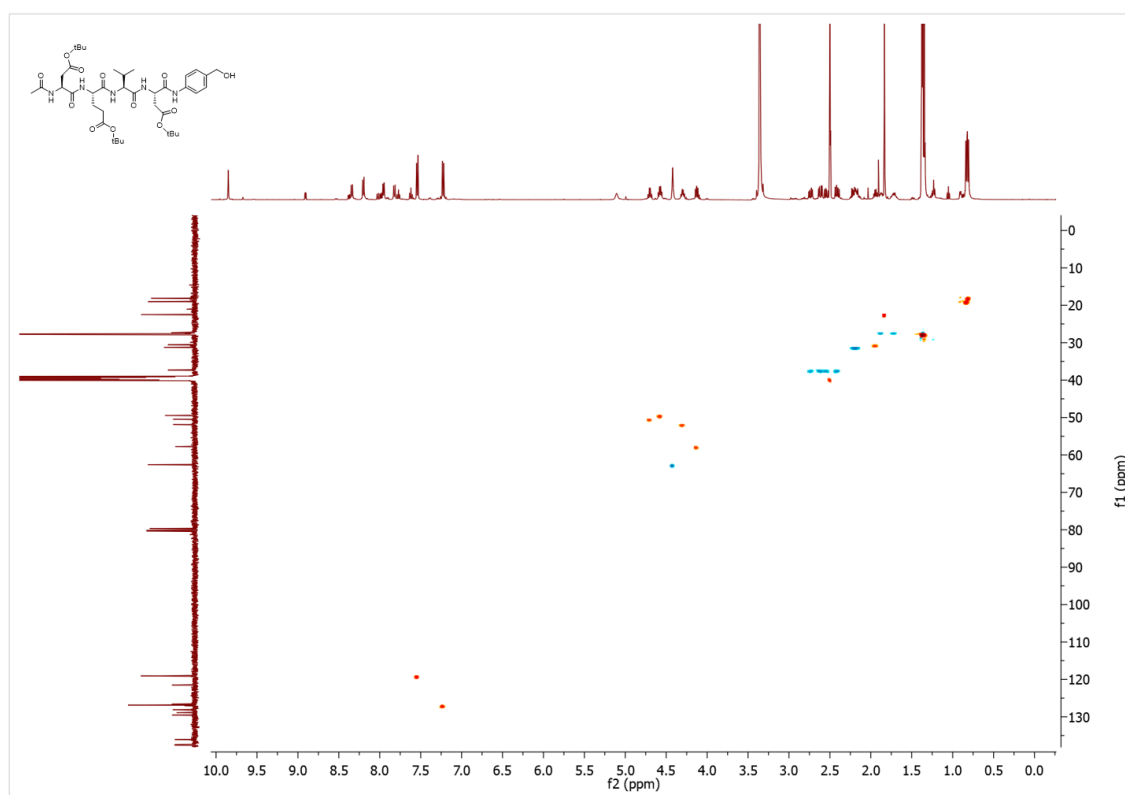
Figure S2.8: HSQC spectrum of **Ac-DEVD(O*t*Bu)-PABA-OH (2.2)** in DMSO-*d*₆.
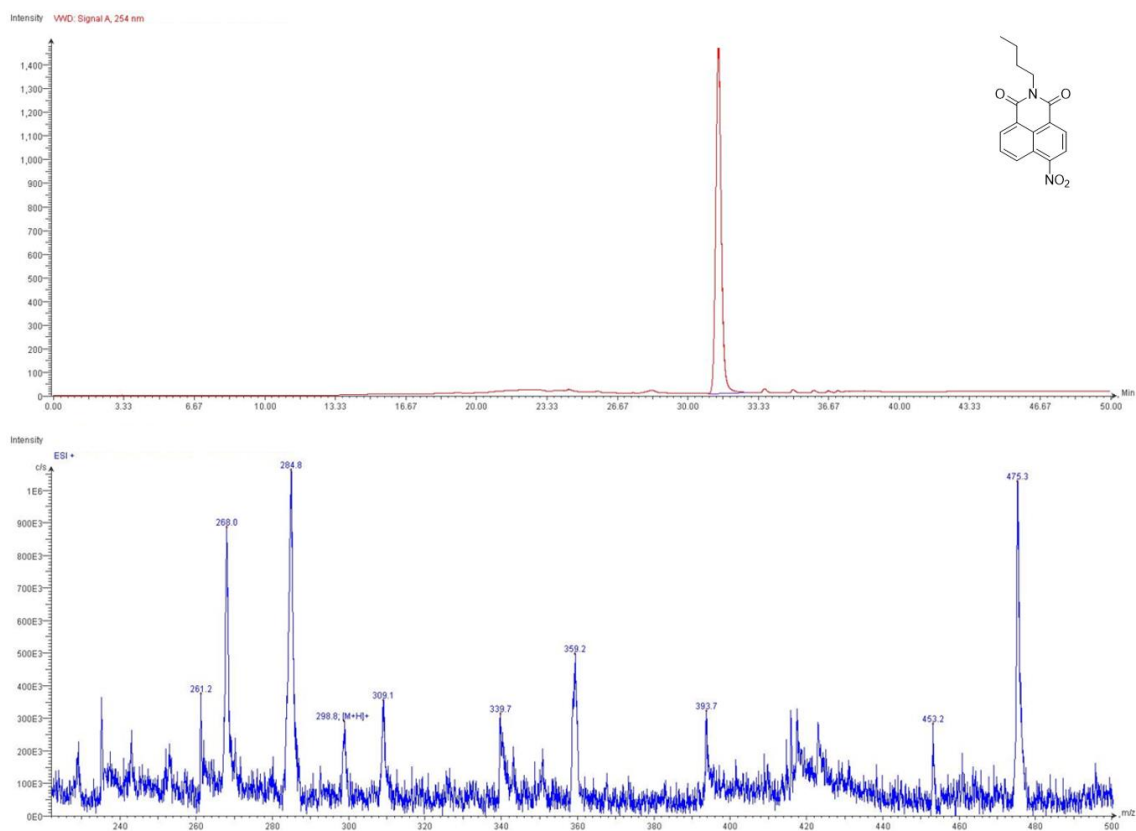
Figure S2.9: LC-MS data for **4-nitro-*N*-butyl-1,8-naphthalimide (2.3)**.
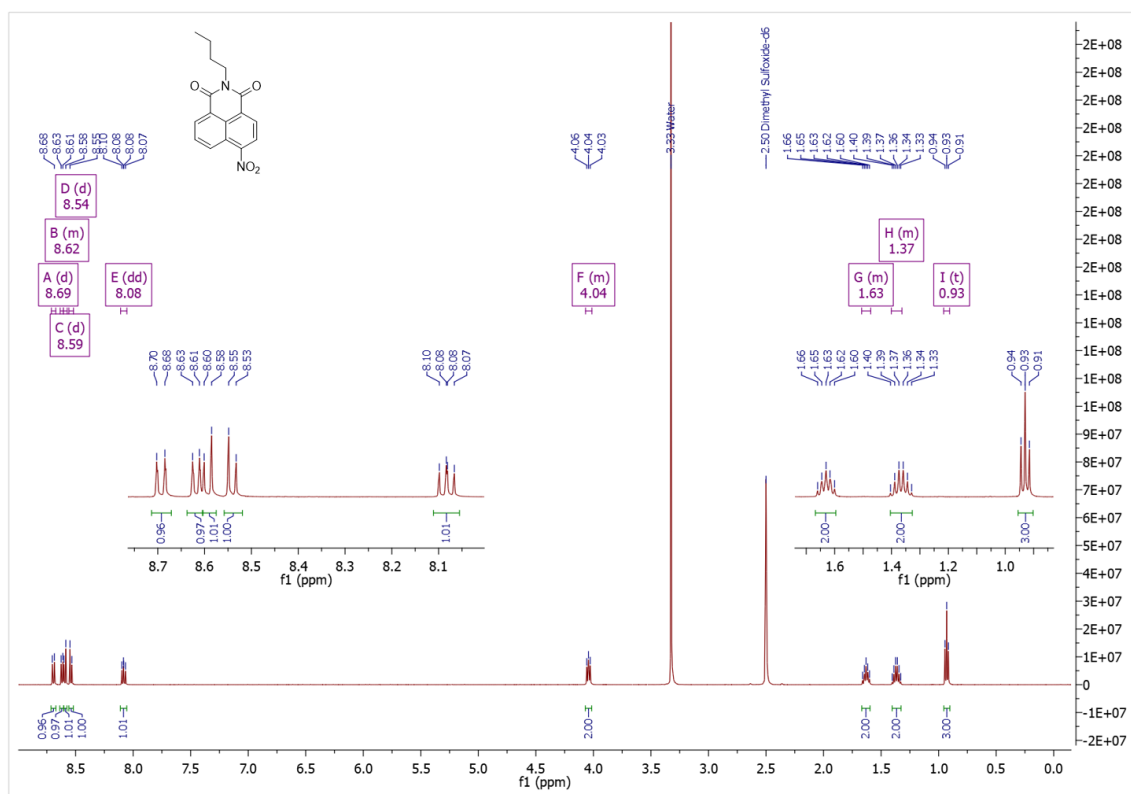
Figure S2.10: ^{1}H NMR Spectrum of **4-nitro-*N*-butyl-1,8-naphthalimide (2.3)** in DMSO-d_6.
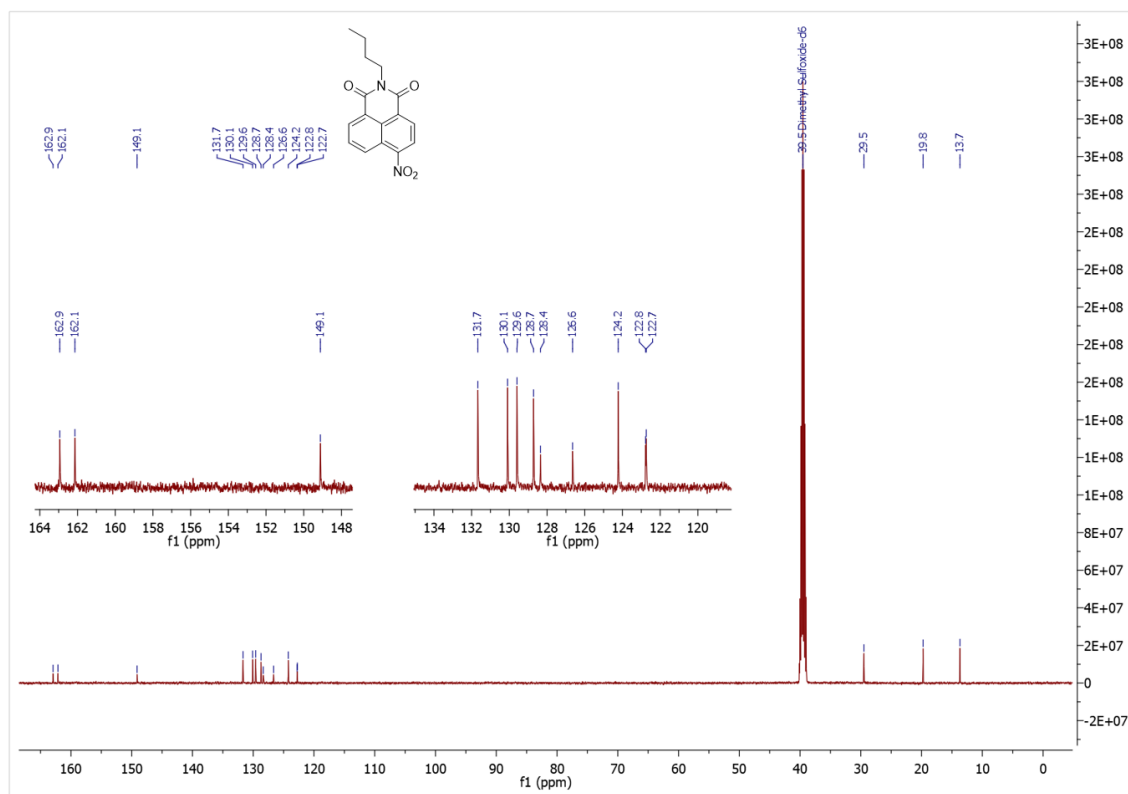
Figure S2.11: ^{13}C NMR Spectrum of **4-nitro-*N*-butyl-1,8-naphthalimide (2.3)** in DMSO-d_6.
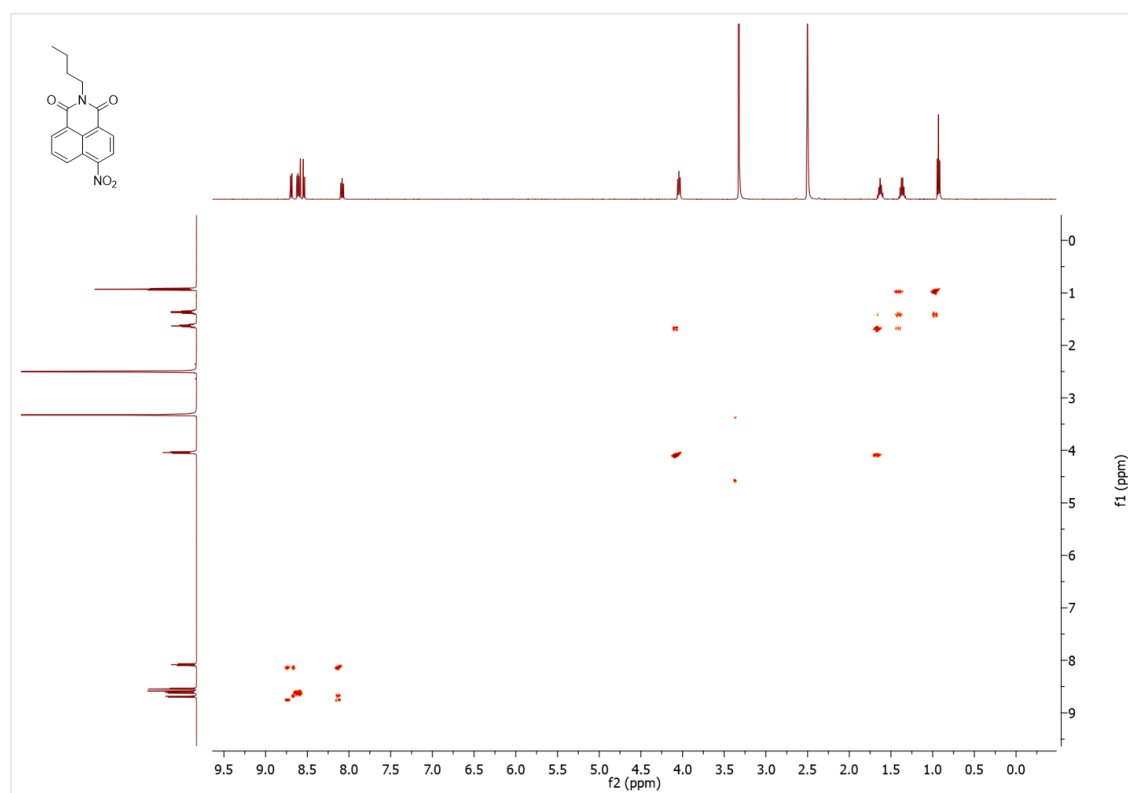
Figure S2.12: COSY Spectrum of **4-nitro-*N*-butyl-1,8-naphthalimide (2.3)** in DMSO-d_6.
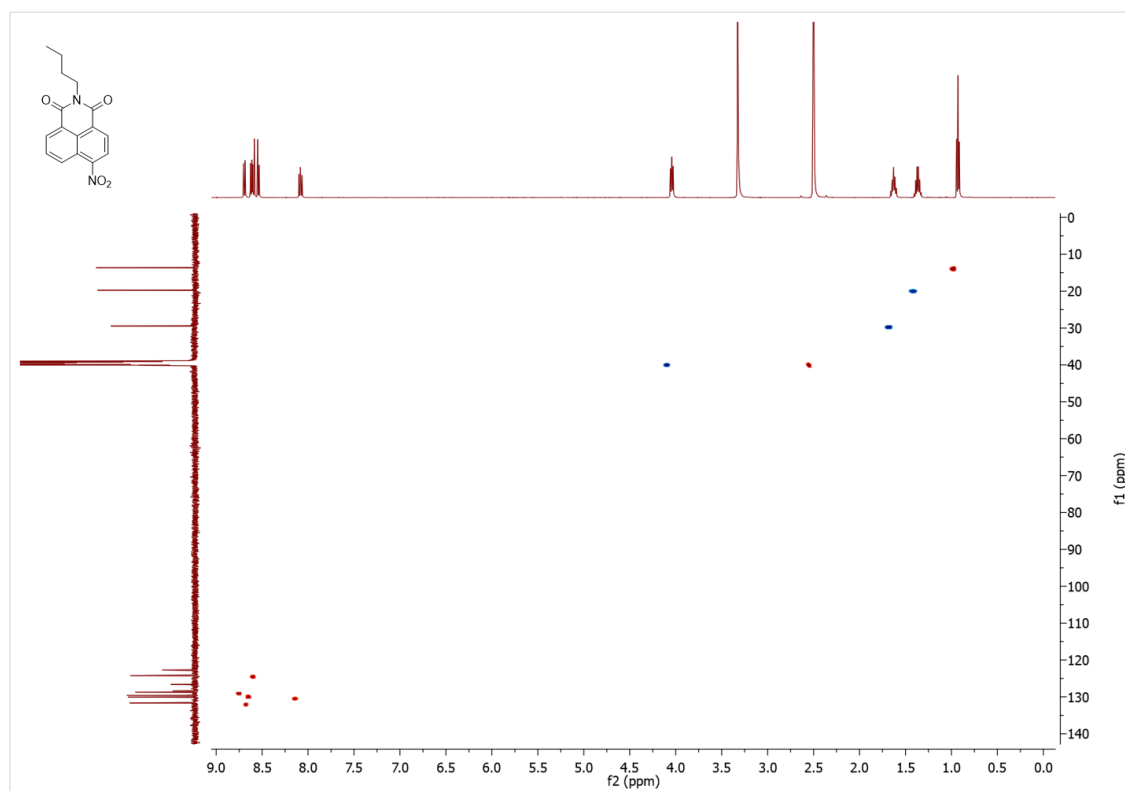
Figure S2.13: HSQC Spectrum of **4-nitro-*N*-butyl-1,8-naphthalimide (2.3)** in DMSO-*d*₆.
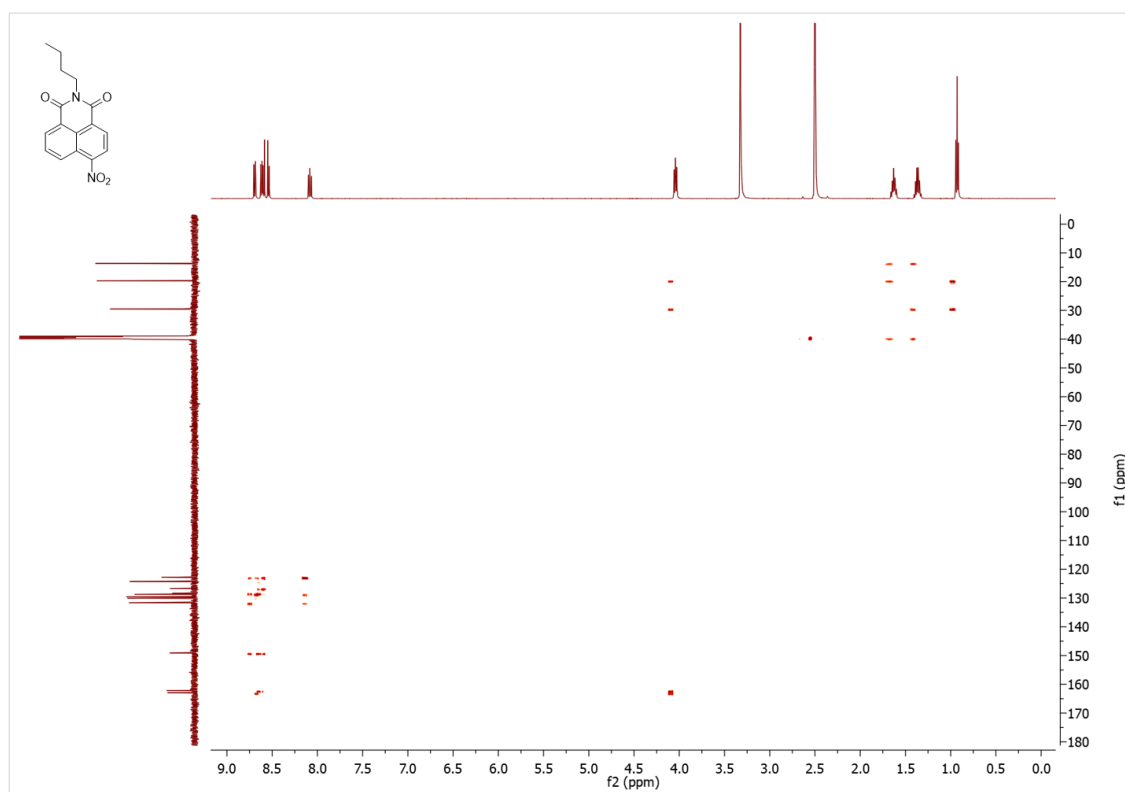
Figure S2.14: HMBC Spectrum of **4-nitro-*N*-butyl-1,8-naphthalimide (2.3)** in DMSO-*d*₆.
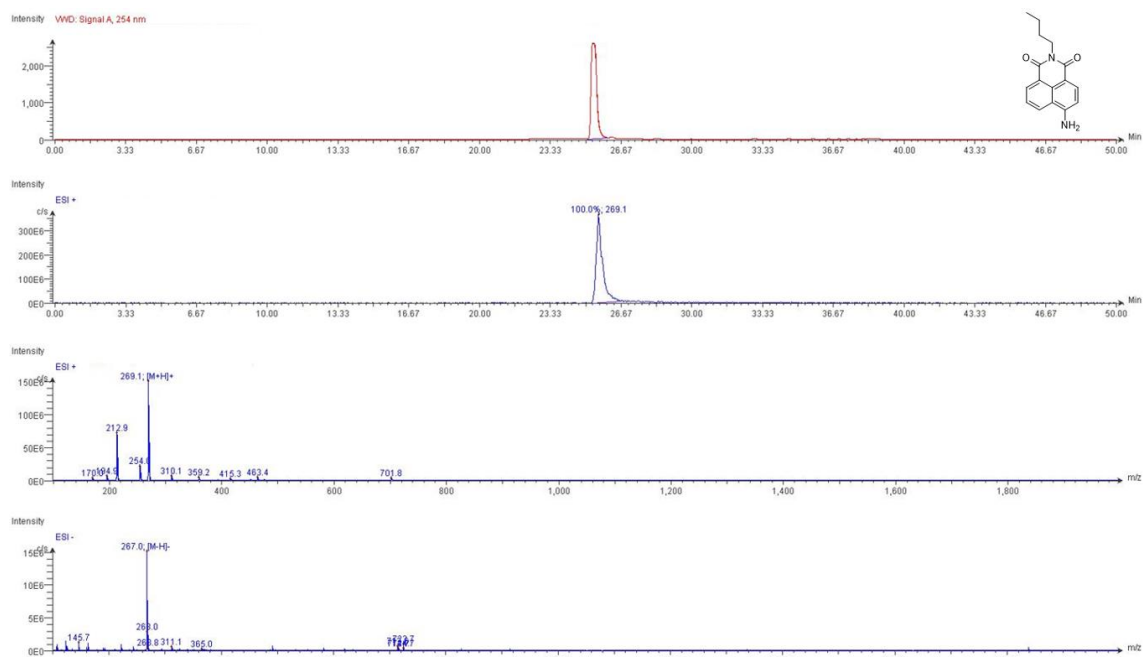
Figure S2.15: LC-MS data for **4-amino-*N*-butyl-1,8-naphthalimide (2.4)**.
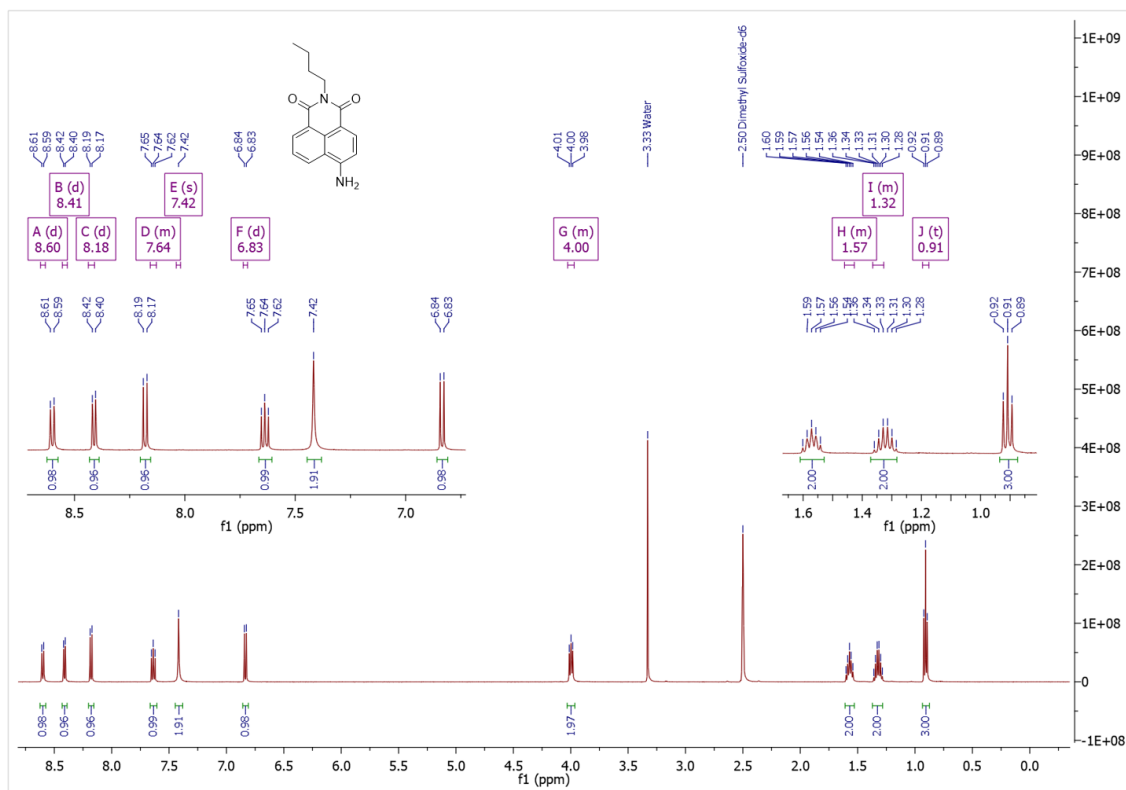
Figure S2.16: ¹H NMR spectrum of **4-amino-*N*-butyl-1,8-naphthalimide (2.4)** in DMSO-*d*₆.
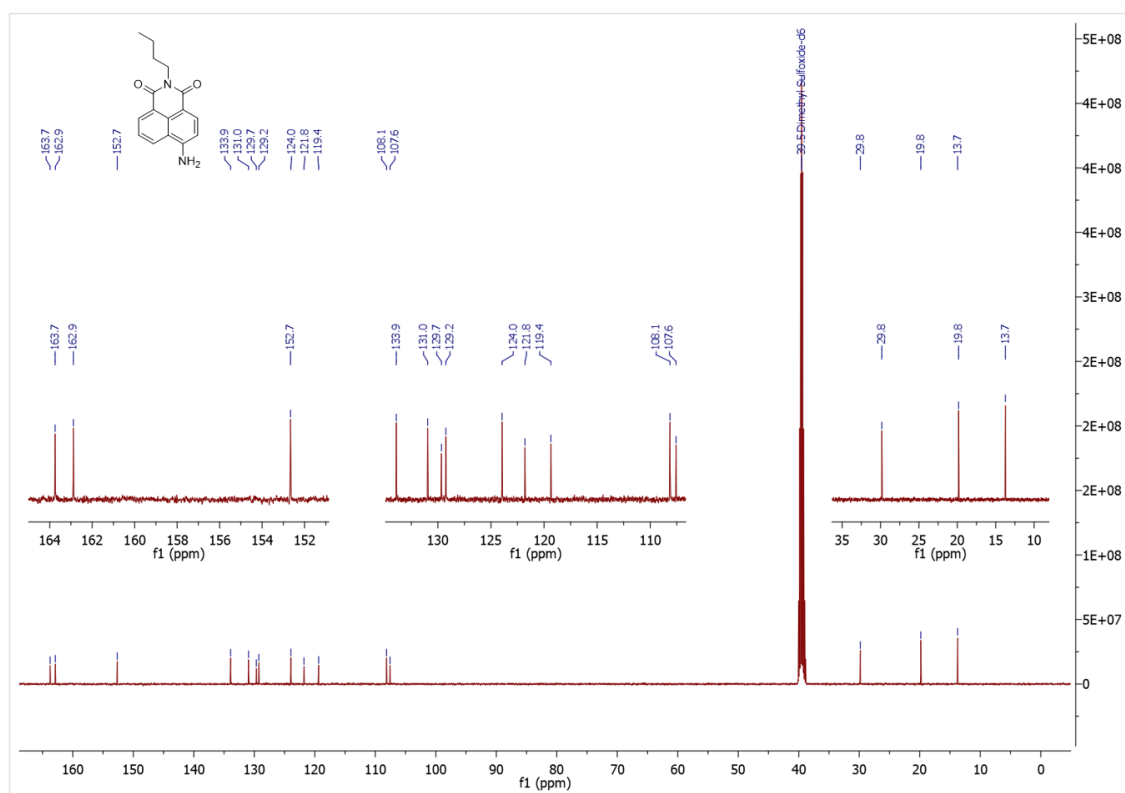
Figure S2.17: ^{13}C NMR spectrum of **4-amino-*N*-butyl-1,8-naphthalimide (2.4)** in DMSO-d_6.
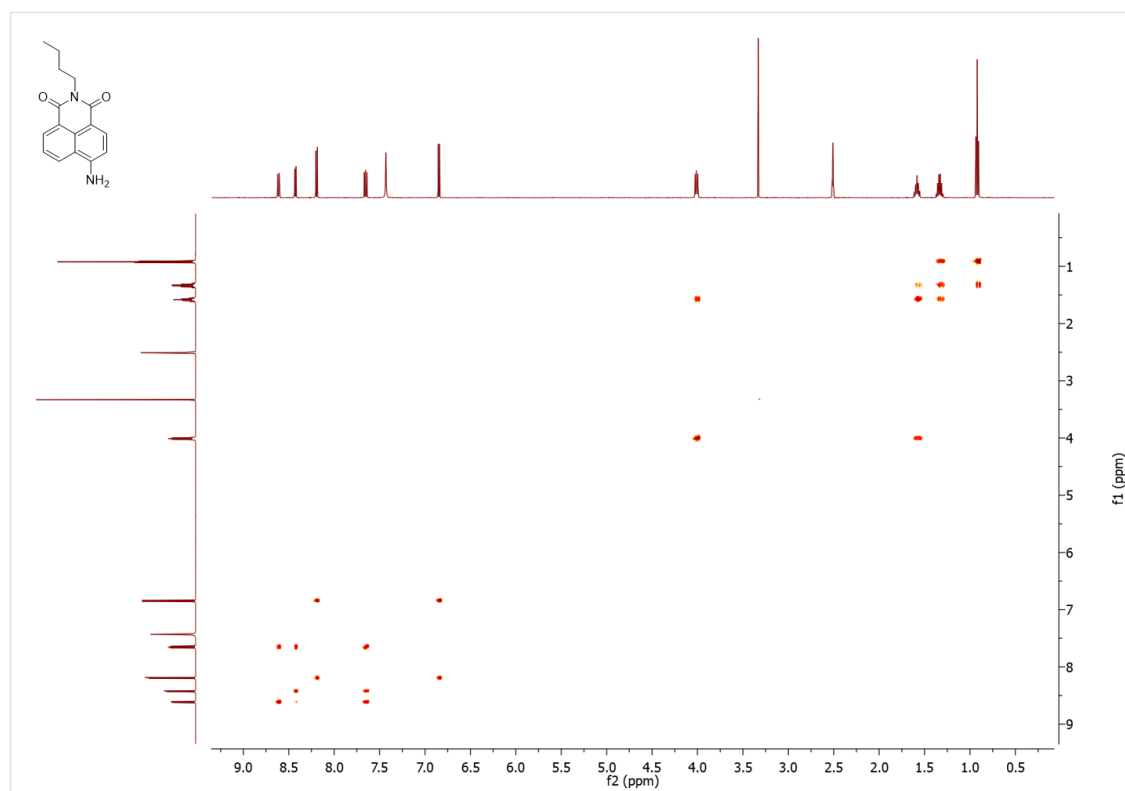
Figure S2.18: COSY spectrum of **4-amino-*N*-butyl-1,8-naphthalimide (2.4)** in DMSO-d_6.

277
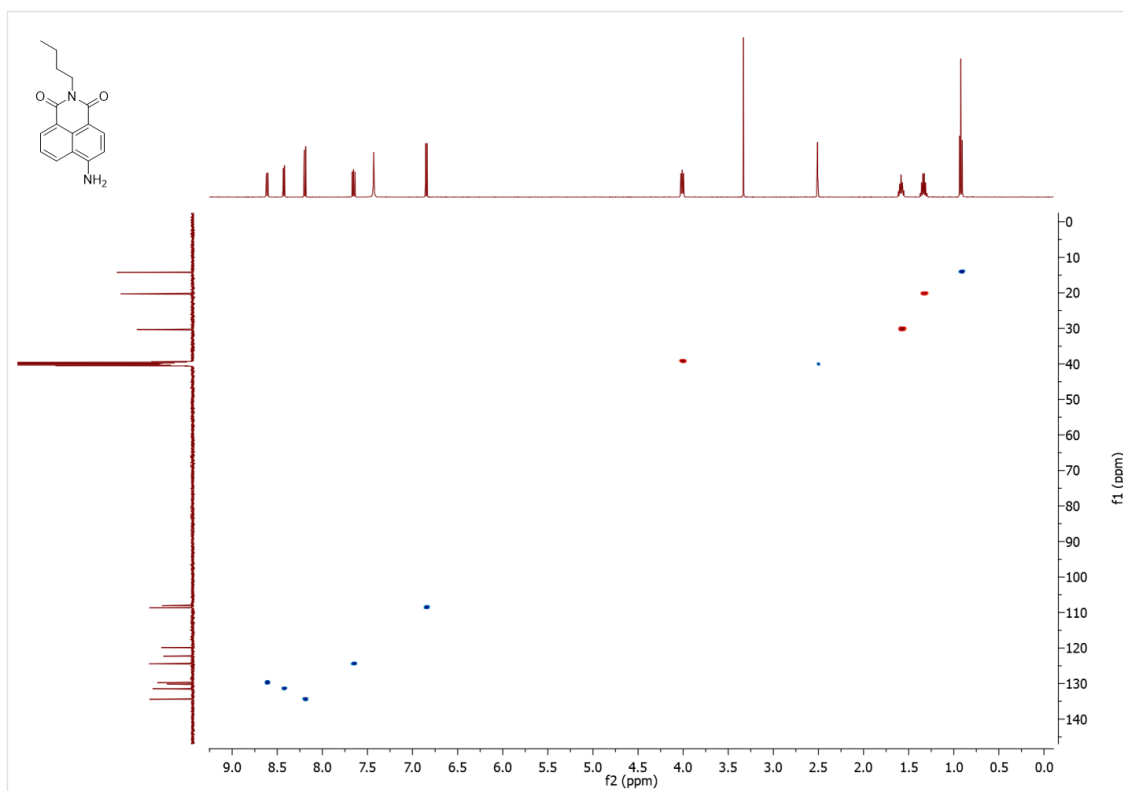
Figure S2.19: HSQC spectrum of **4-amino-*N*-butyl-1,8-naphthalimide (2.4)** in DMSO-*d*₆.
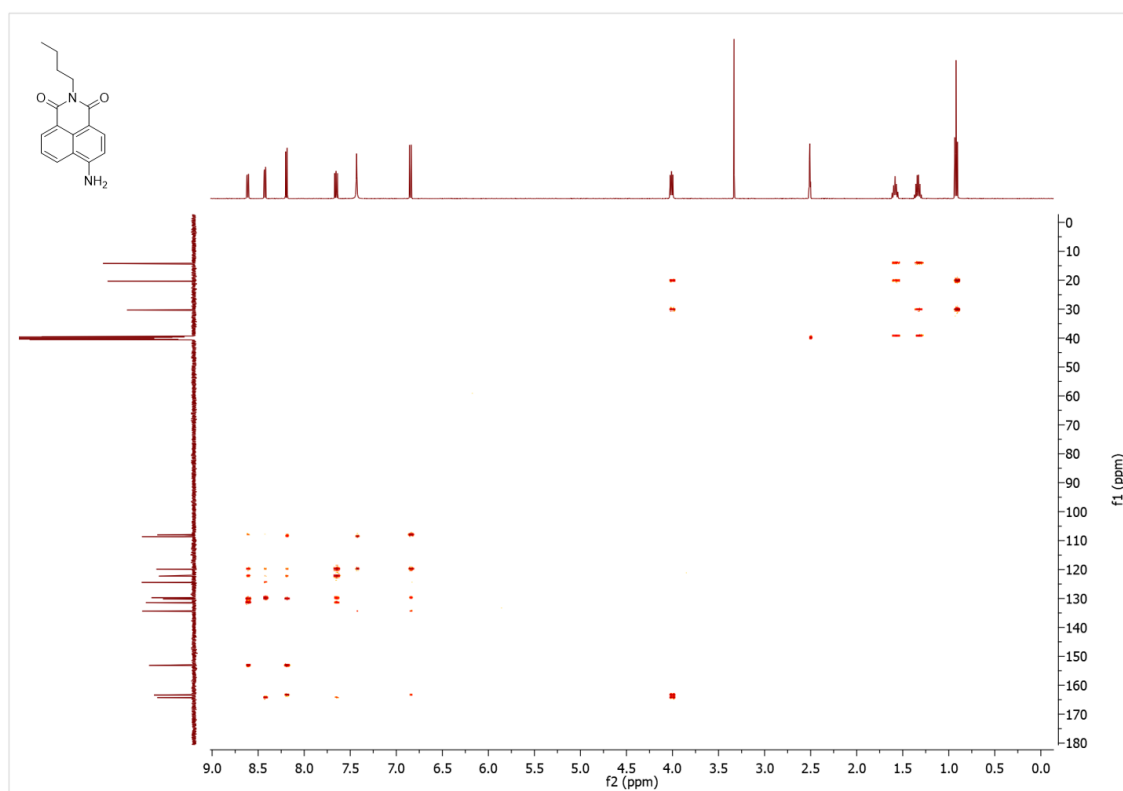
Figure S2.20: HMBC spectrum of **4-amino-*N*-butyl-1,8-naphthalimide (2.4)** in DMSO-*d*₆.
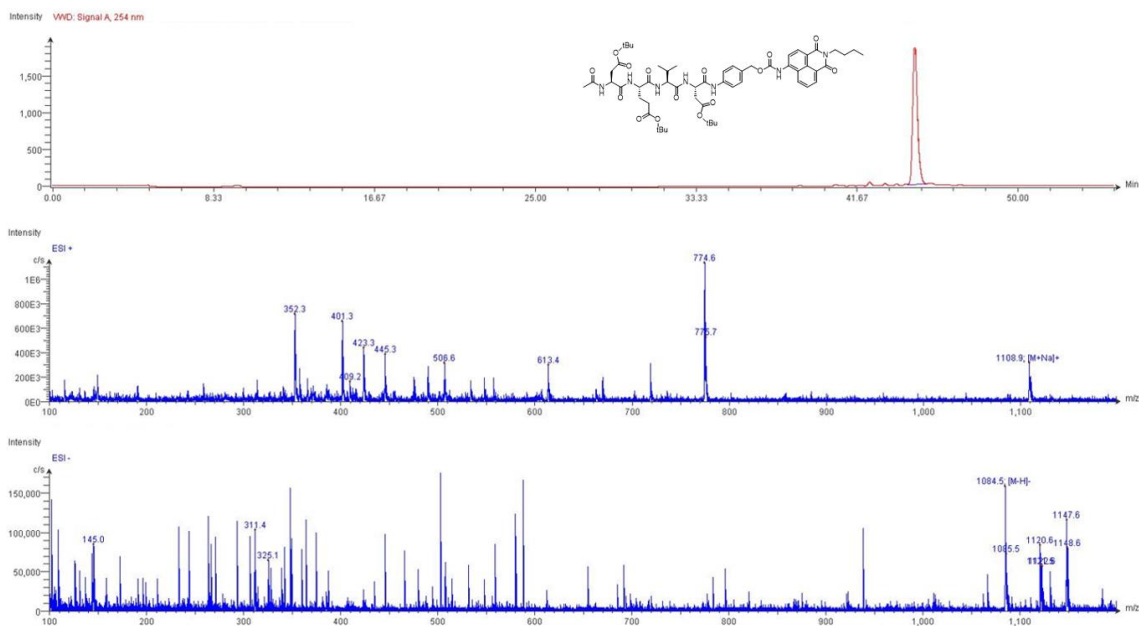
Figure S2.21: LC-MS data for **Ac-DEVD(O*t*Bu)-PABC-Naph (2.5)**.

Compound Table

Compound Label	RT (min)	Observed mass (m/z)	Neutral observed mass (Da)	Theoretical mass (Da)	Mass error (ppm)	Isotope match score (%)
Cpd 1: C56 H75 N7 O15	0.97	1108.5187	1085.5292	1085.5321	-2.67	99.69

Mass errors of between -5.00 and 5.00 ppm with isotope match scores above 60% are considered confirmation of molecular formulae
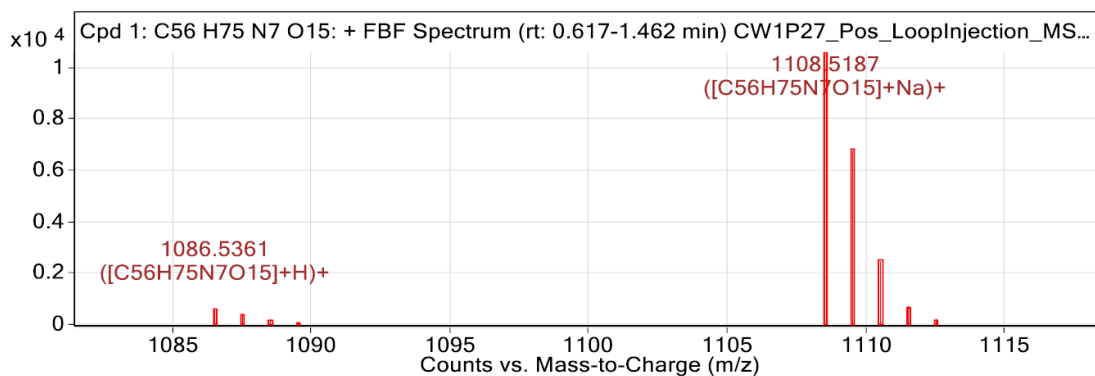
Figure: Zoomed Compound spectra view
(red boxes indicating expected theoretical isotope spacing and abundance)

Compound isotope peak List

m/z	z	Abund	Formula	Ion
1086.5361	1	552.5	C56H75N7O15	(M+H)+
1087.5397	1	365.0	C56H75N7O15	(M+H)+
1088.5408	1	204.6	C56H75N7O15	(M+H)+
1089.5189	1	89.5	C56H75N7O15	(M+H)+
1108.5187	1	10592.9	C56H75N7O15	(M+Na)+
1109.5217	1	6771.3	C56H75N7O15	(M+Na)+
1110.5247	1	2454.9	C56H75N7O15	(M+Na)+
1111.5269	1	711.9	C56H75N7O15	(M+Na)+
1112.5265	1	218.2	C56H75N7O15	(M+Na)+

Figure S2.22: HRMS data for **Ac-DEVD(O*t*Bu)-PABC-Naph (2.5)**.

279
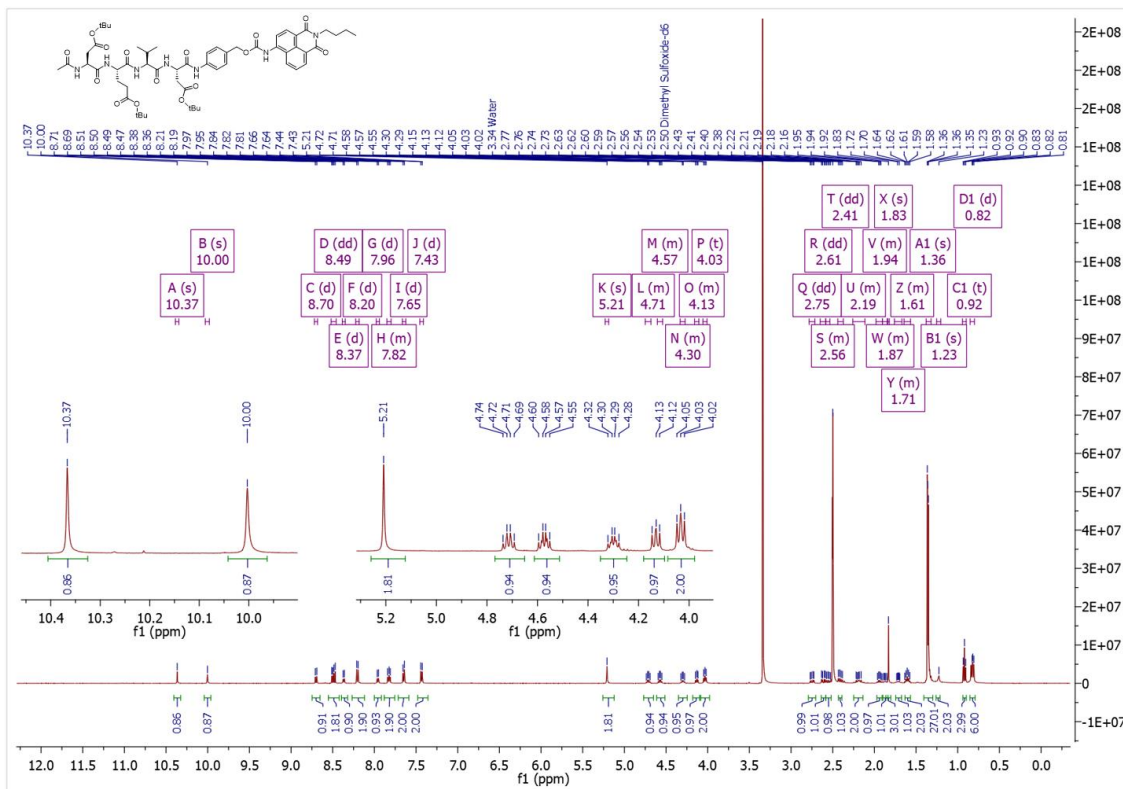
Figure S2.23: ^{1}H NMR spectrum of **Ac-DEVD(OtBu)-PABC-Naph (2.5)** in DMSO-d_6.
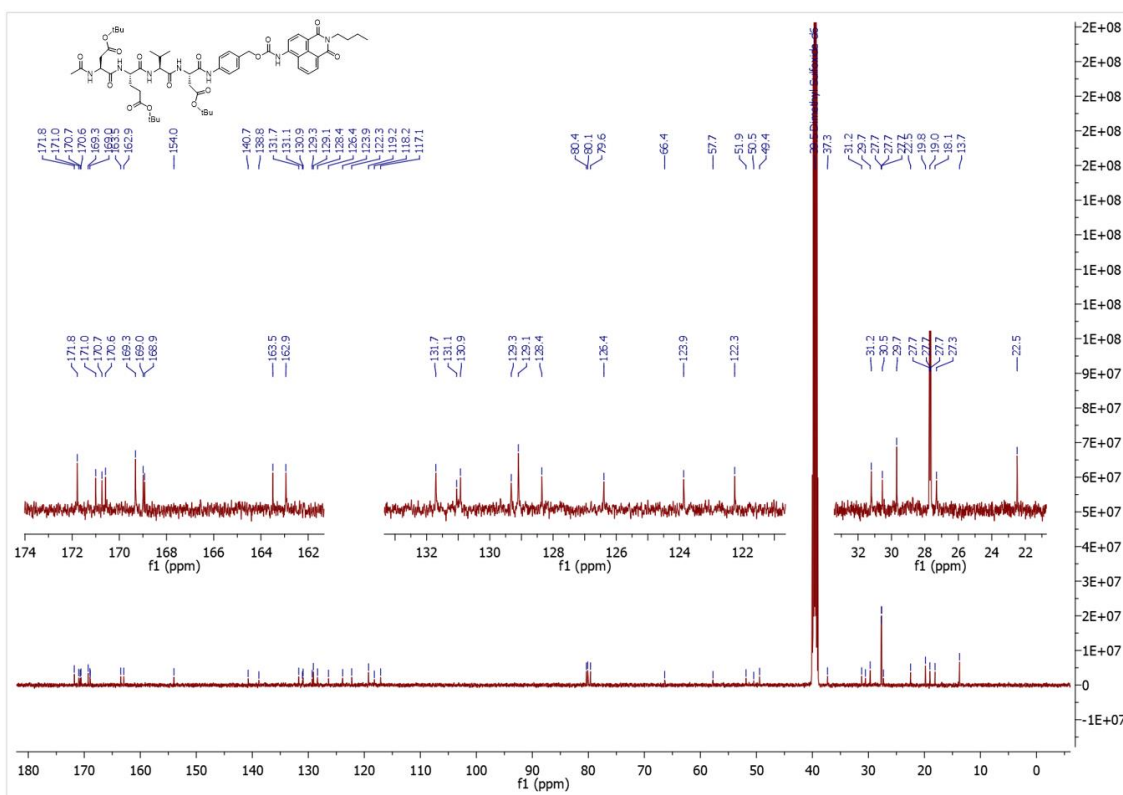
Figure S2.24: ^{13}C NMR spectrum of **Ac-DEVD(OtBu)-PABC-Naph (2.5)** in DMSO-d_6.
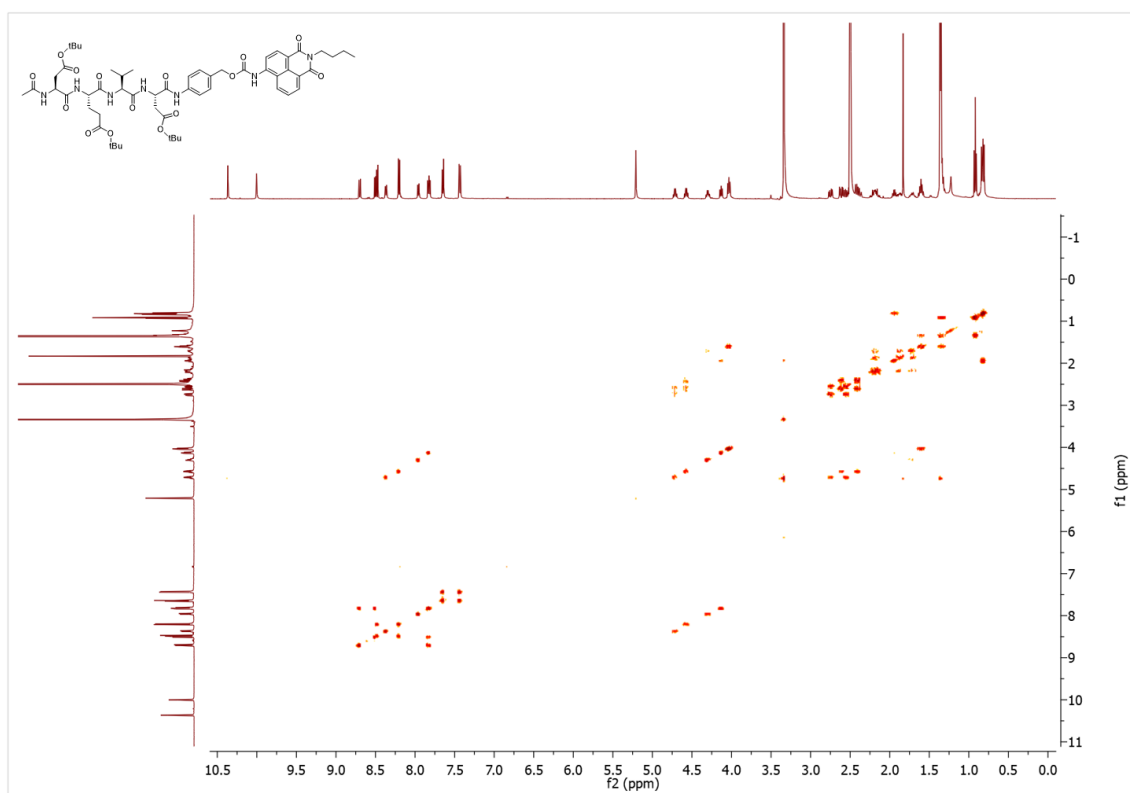
Figure S2.25: COSY spectrum of **Ac-DEVD(O*t*Bu)-PABC-Naph (2.5)** in DMSO-*d*₆.
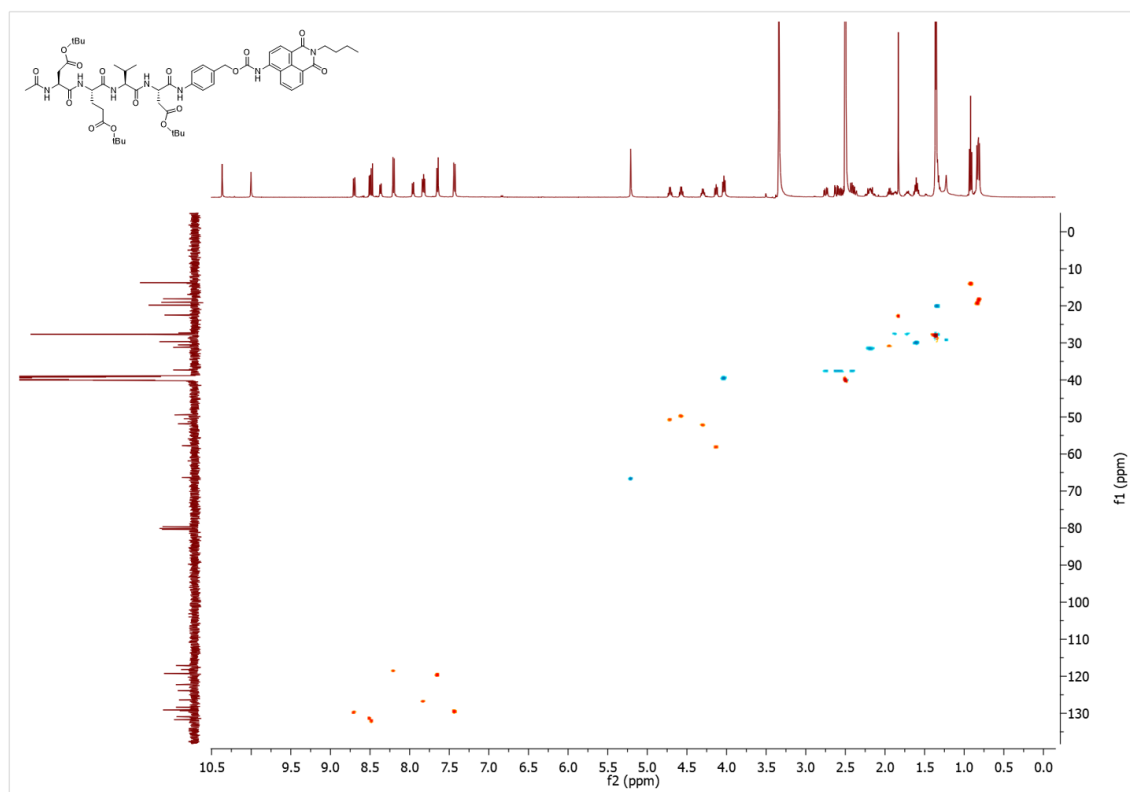
Figure S2.26: HSQC spectrum of **Ac-DEVD(O*t*Bu)-PABC-Naph (2.5)** in DMSO-*d*₆.
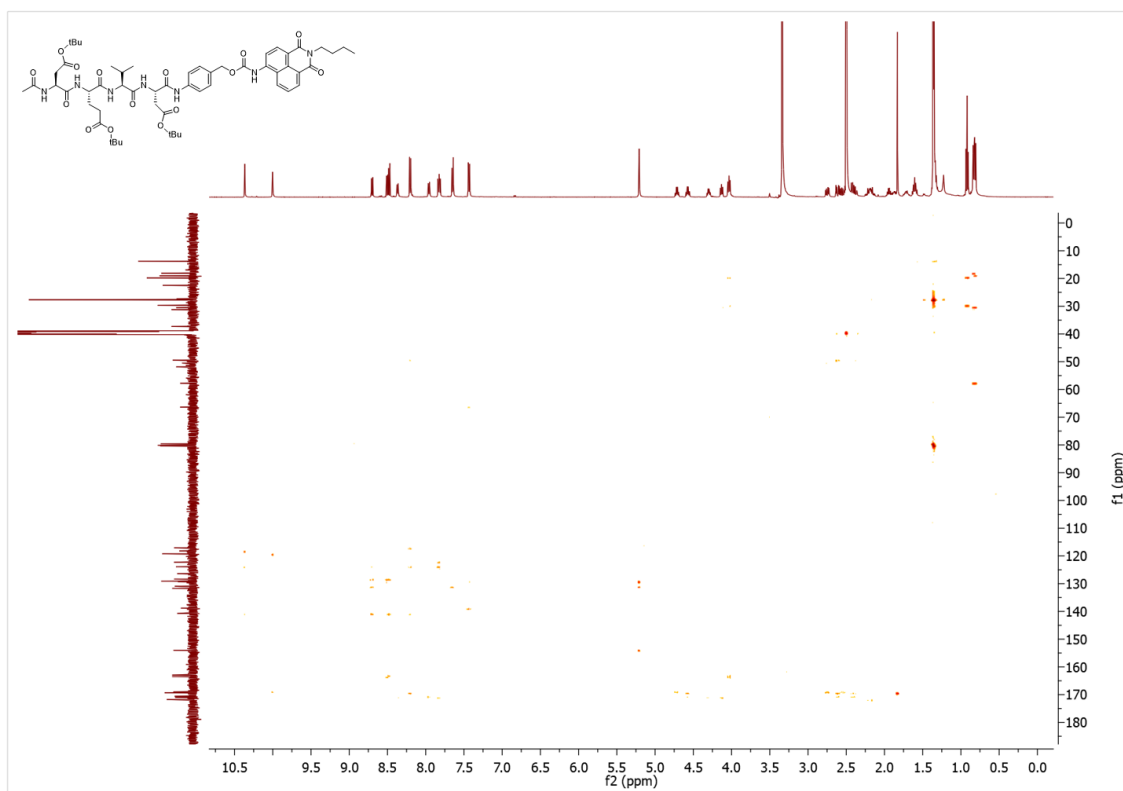
Figure S2.27: HMBC spectrum of **Ac-DEVD(O*t*Bu)-PABC-Naph (2.5)** in DMSO-*d*₆.
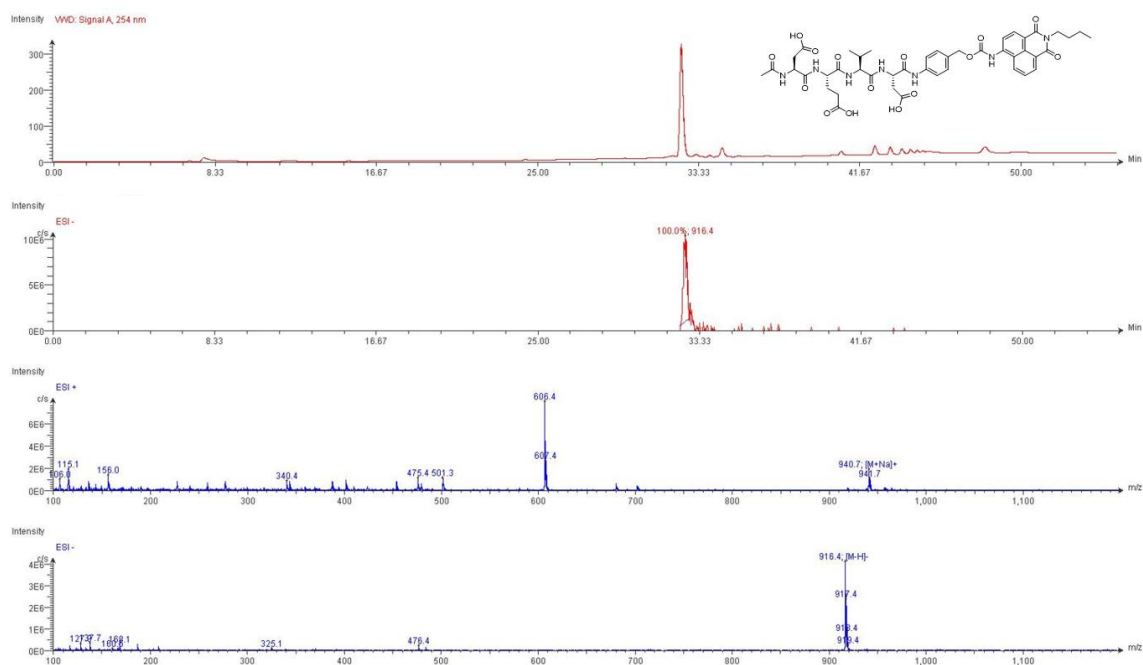
Figure S2.28: LC-MS data for **Ac-DEVD-PABC-Naph (2.6)**.

Compound Table

| Compound Label	RT (min)	Observed mass (m/z)	Neutral observed mass (Da)	Theoretical mass (Da)	Mass error (ppm)	Isotope match score (%)
Cpd 1: C44 H51 N7 O15	0.73	918.3502	917.3395	917.3443	-5.29	86.82
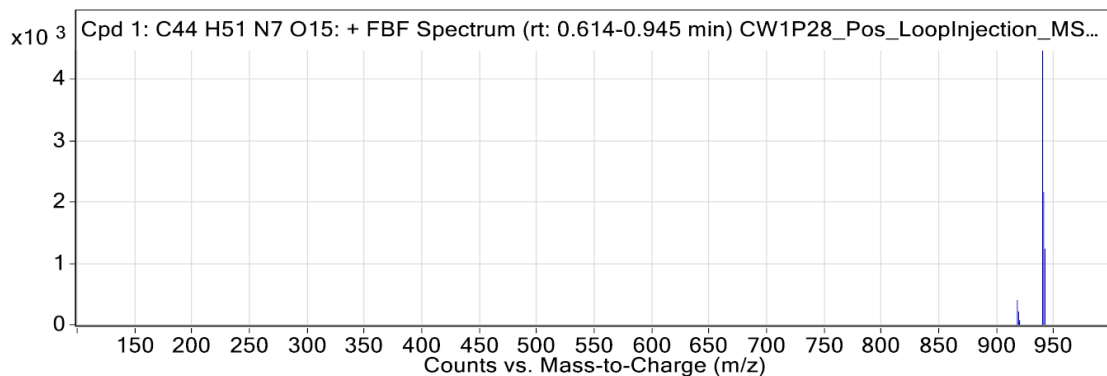
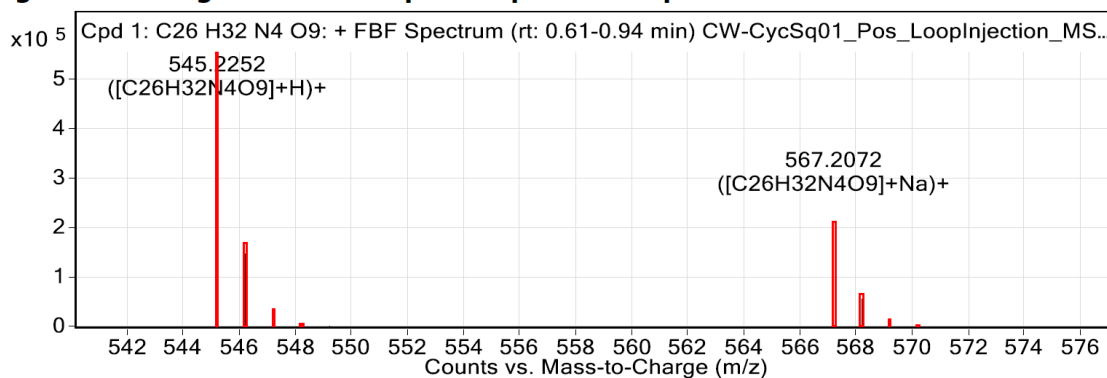**Figure: Full range view of Compound spectra and potential adducts.**
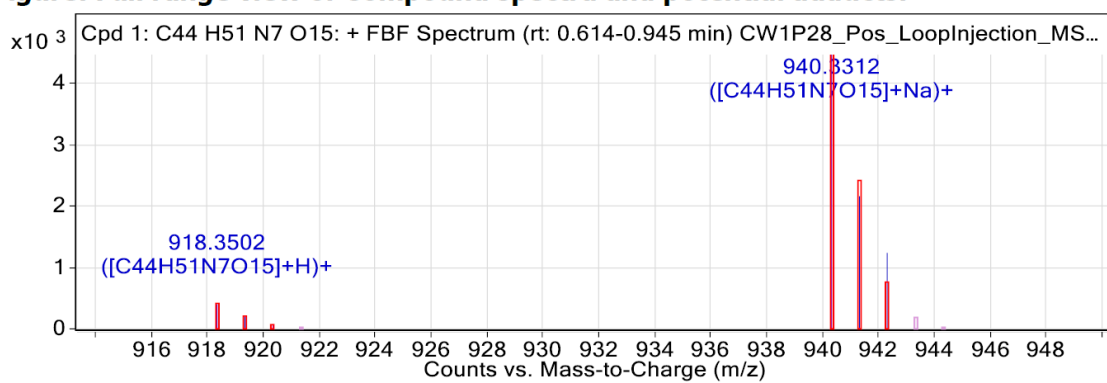

Figure: Zoomed Compound spectra view
(red boxes indicating expected theoretical isotope spacing and abundance)

Compound isotope peak List

m/z	z	Abund	Formula	Ion
918.3502	1	402.8	C44H51N7O15	(M+H)+
919.3562	1	213.4	C44H51N7O15	(M+H)+
920.3581	1	72.6	C44H51N7O15	(M+H)+
940.3312	1	4471.5	C44H51N7O15	(M+Na)+
941.3342	1	2163.0	C44H51N7O15	(M+Na)+
942.3185	1	1238.4	C44H51N7O15	(M+Na)+

Figure S2.29: HRMS data for **Ac-DEVD-PABC-Naph (2.6)**.
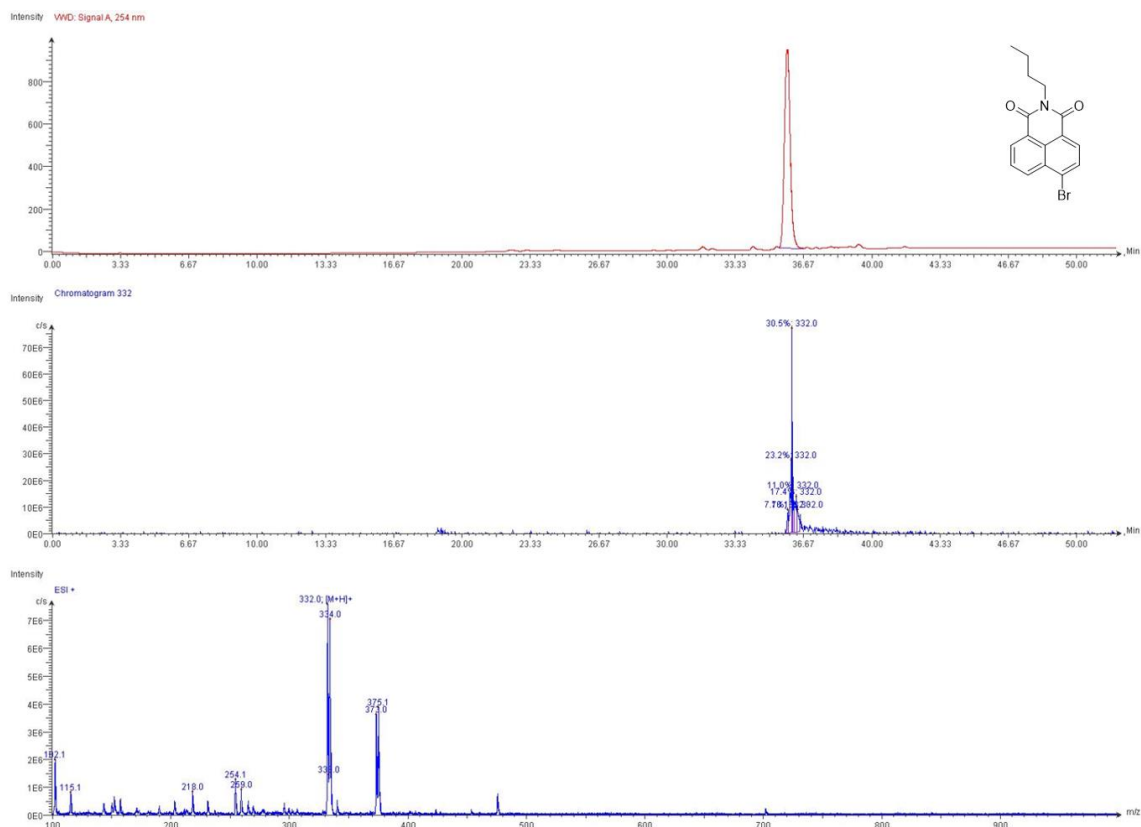
Figure S2.30: LC-MS data for **4-bromo-*N*-butyl-1,8-naphthalimide (2.7)**.
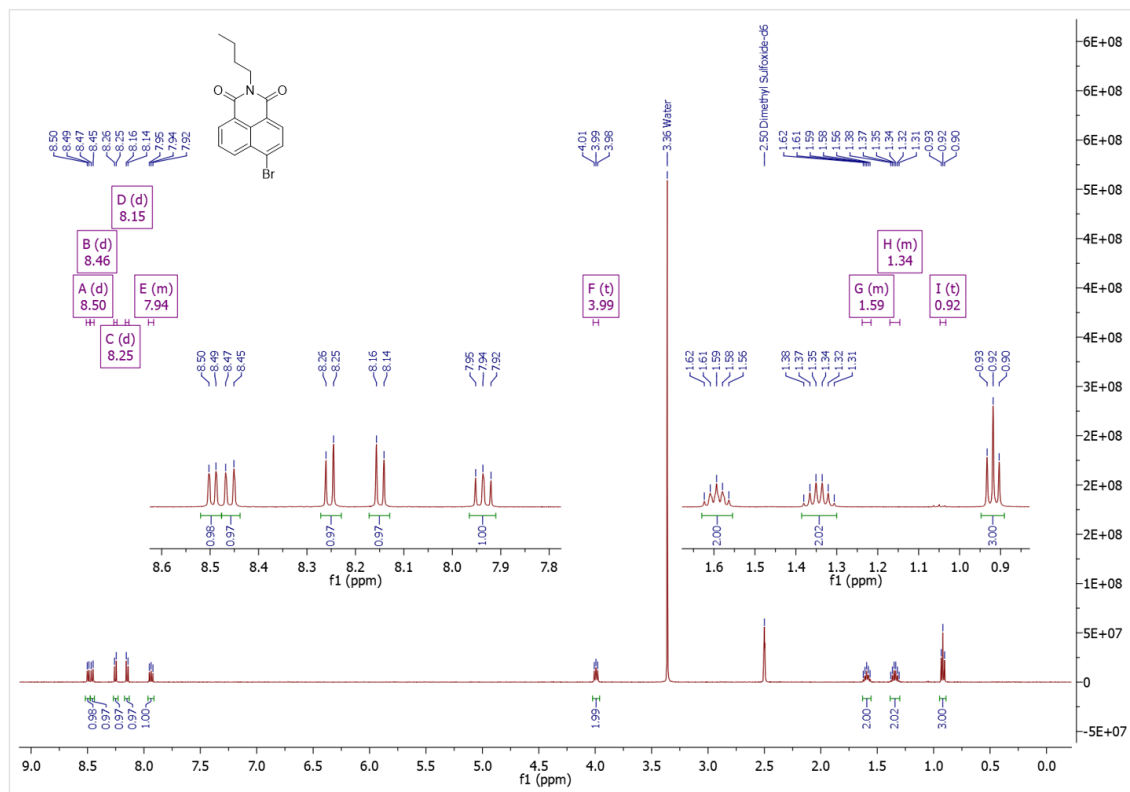
Figure S2.31: ¹H NMR spectrum of **4-bromo-*N*-butyl-1,8-naphthalimide (2.7)** in DMSO-*d*₆.
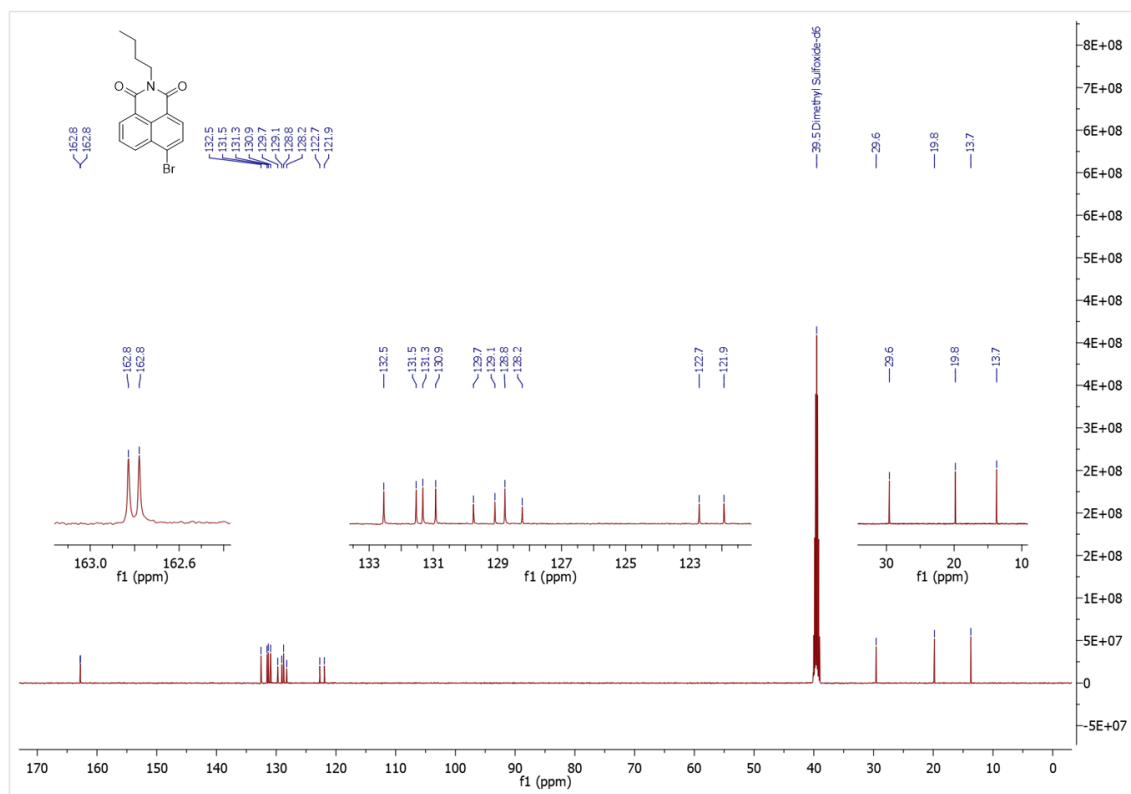
Figure S2.32: ^{13}C NMR spectrum of **4-bromo-*N*-butyl-1,8-naphthalimide (2.7)** in DMSO-*d*$_6$.
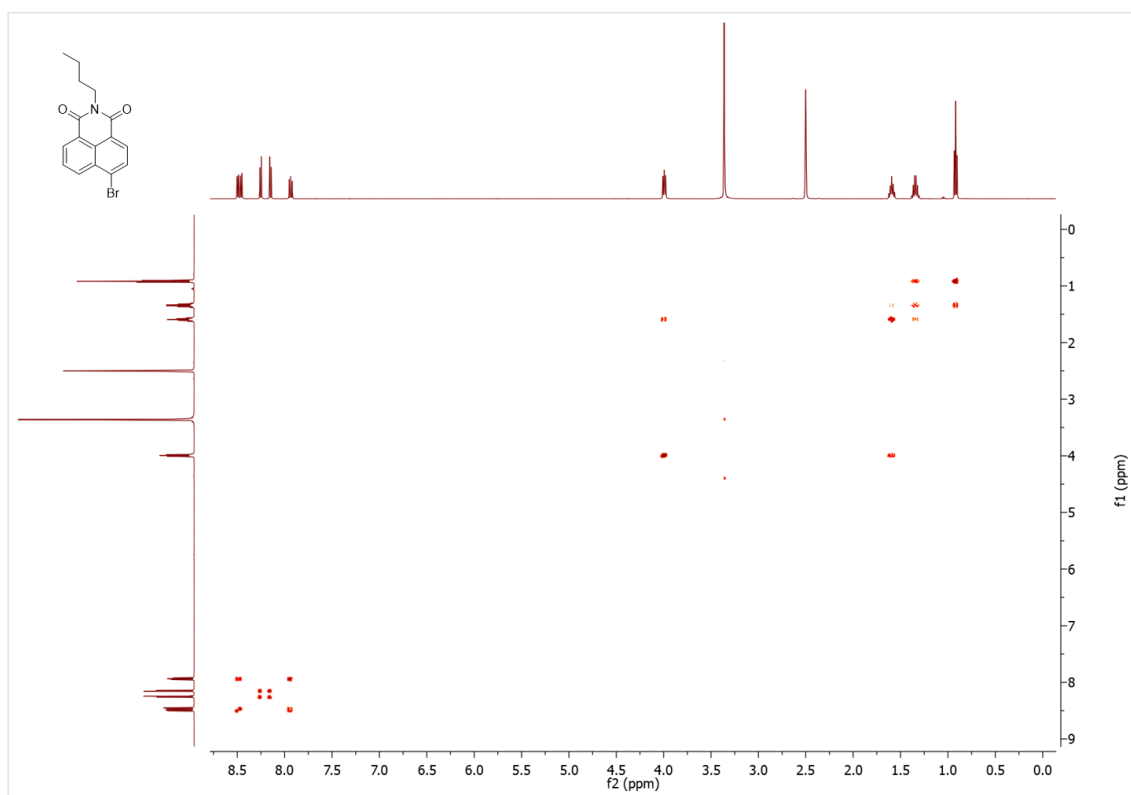
Figure S2.33: COSY spectrum of **4-bromo-*N*-butyl-1,8-naphthalimide (2.7)** in DMSO-*d*$_6$.
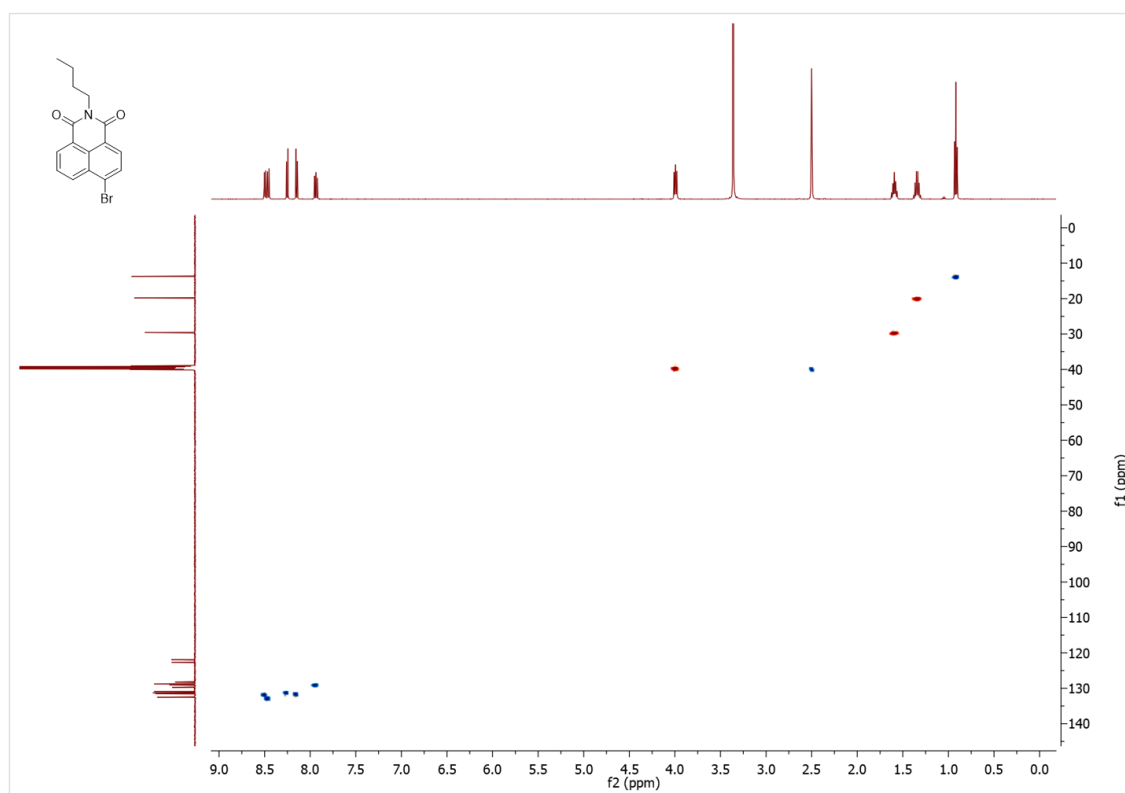
Figure S2.34: HSQC spectrum of **4-bromo-*N*-butyl-1,8-naphthalimide (2.7)** in DMSO-d_6.
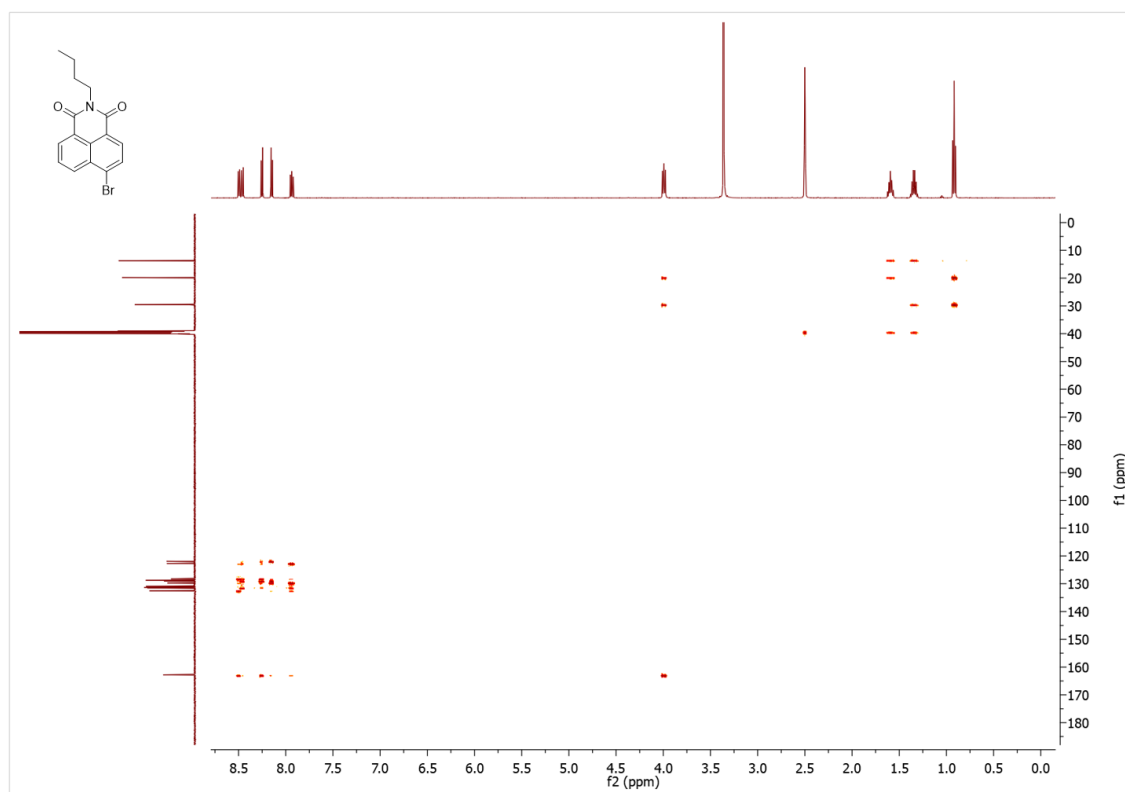
Figure S2.35: HMBC spectrum of **4-bromo-*N*-butyl-1,8-naphthalimide (2.7)** in DMSO-d_6.
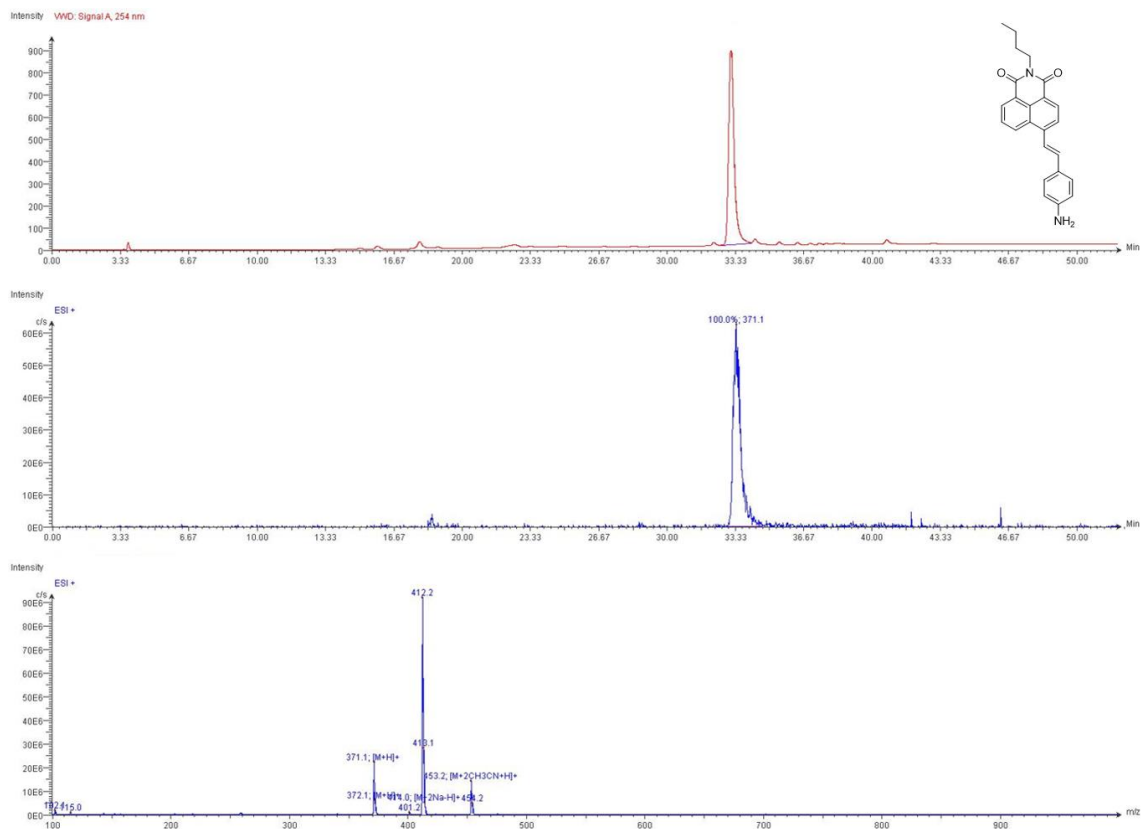
Figure S2.36: LC-MS data for **4-aminostyryl-*N*-butyl-1,8-naphthalimide (2.8)**.
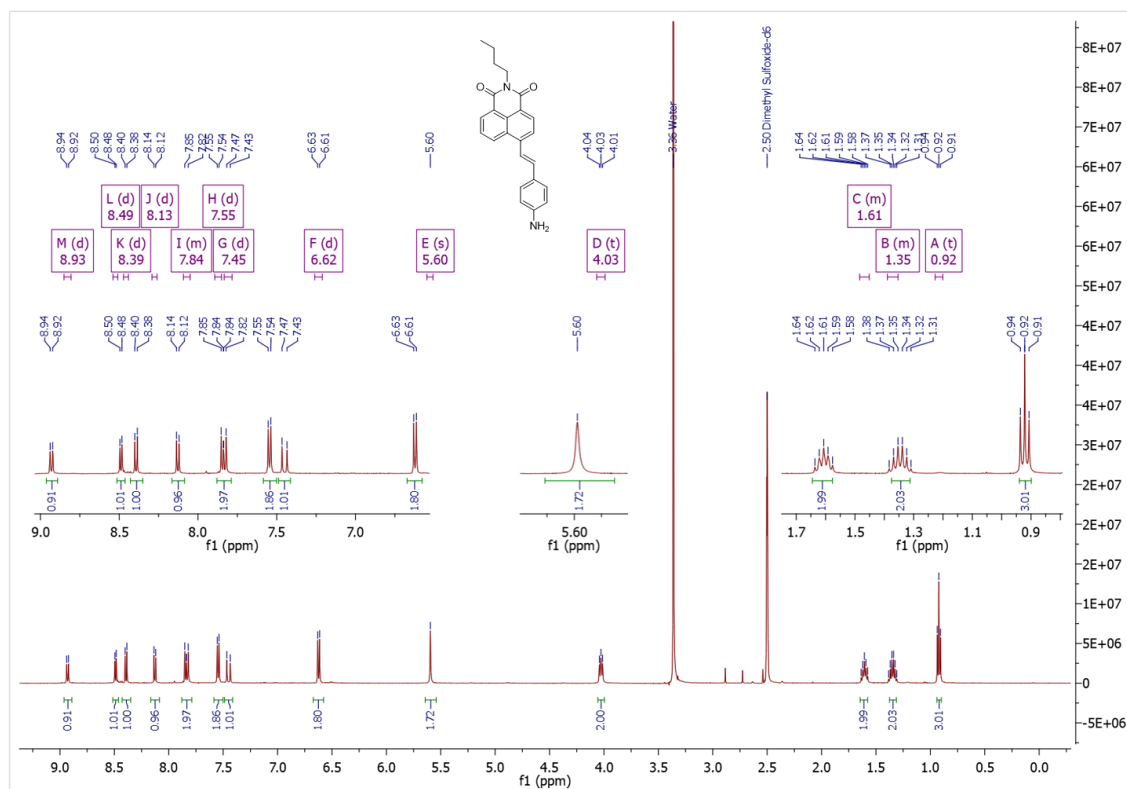
Figure S2.37: ¹H NMR spectrum of **4-aminostyryl-*N*-butyl-1,8-naphthalimide (2.8)** in DMSO-

*d*₆.
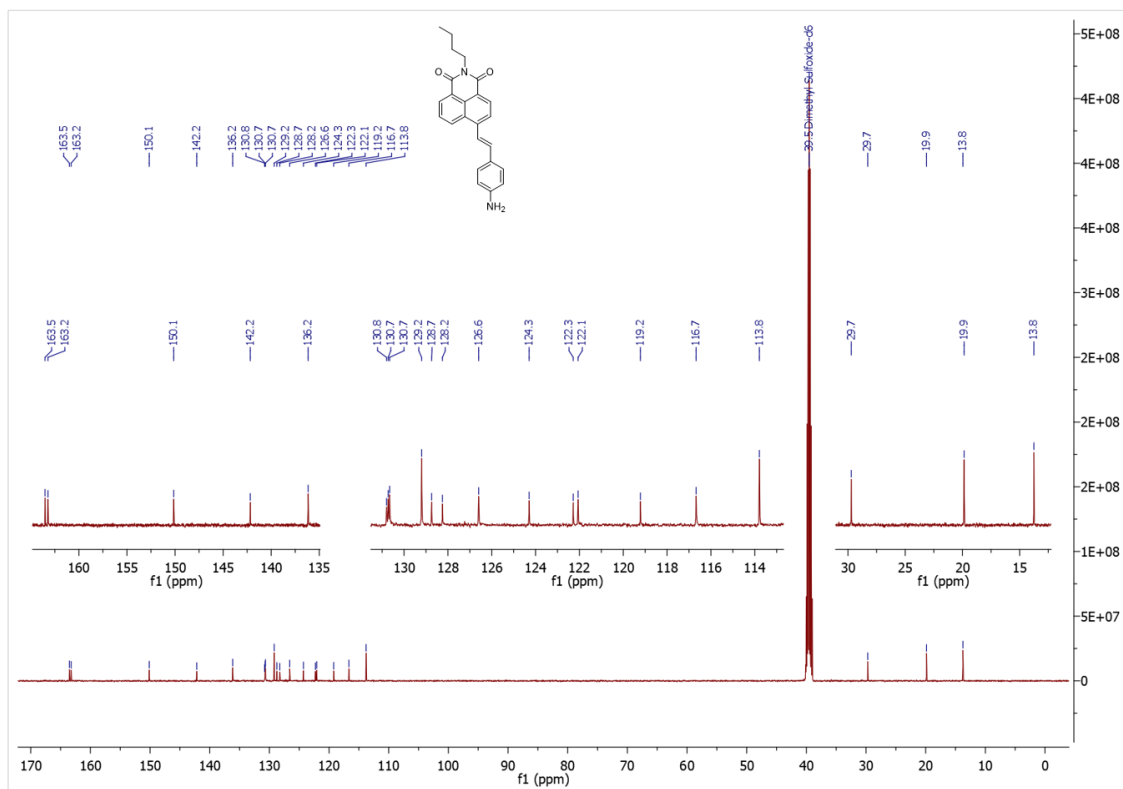
Figure S2.38: ^{13}C NMR spectrum of **4-aminostyryl-*N*-butyl-1,8-naphthalimide (2.8)** in DMSO-d_6.
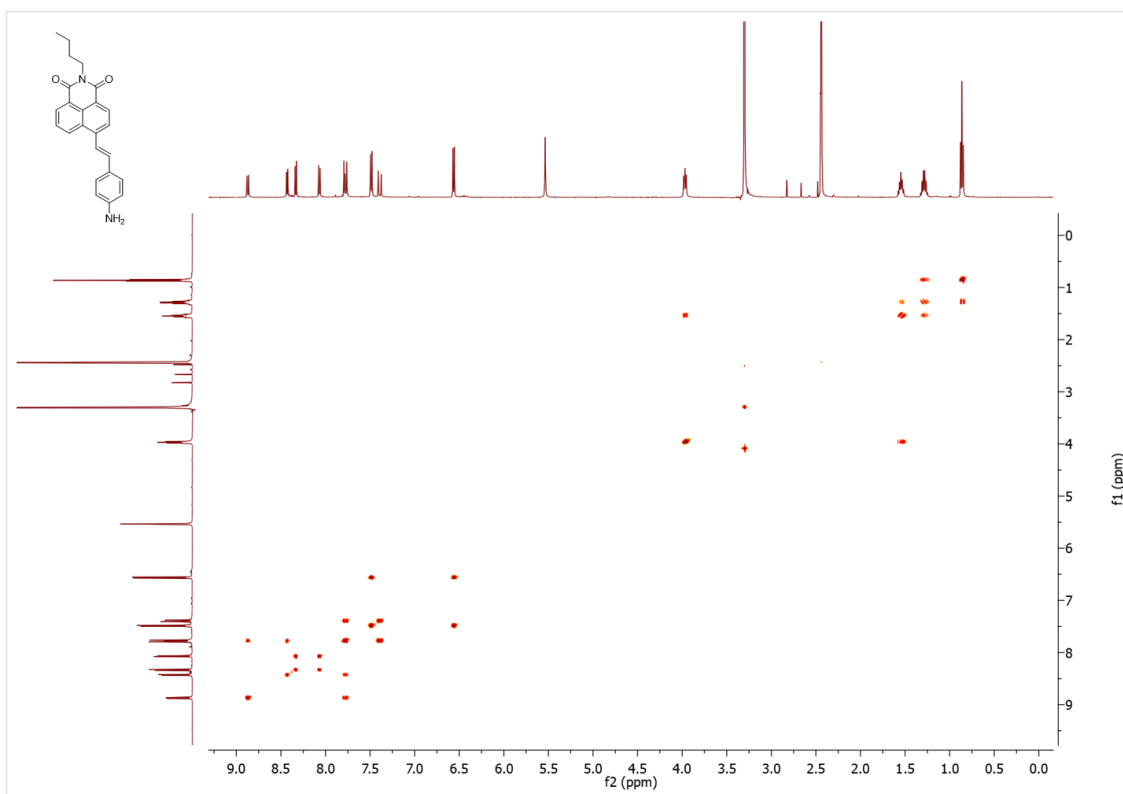
Figure S2.39: COSY spectrum of **4-aminostyryl-*N*-butyl-1,8-naphthalimide (2.8)** in DMSO-d_6.
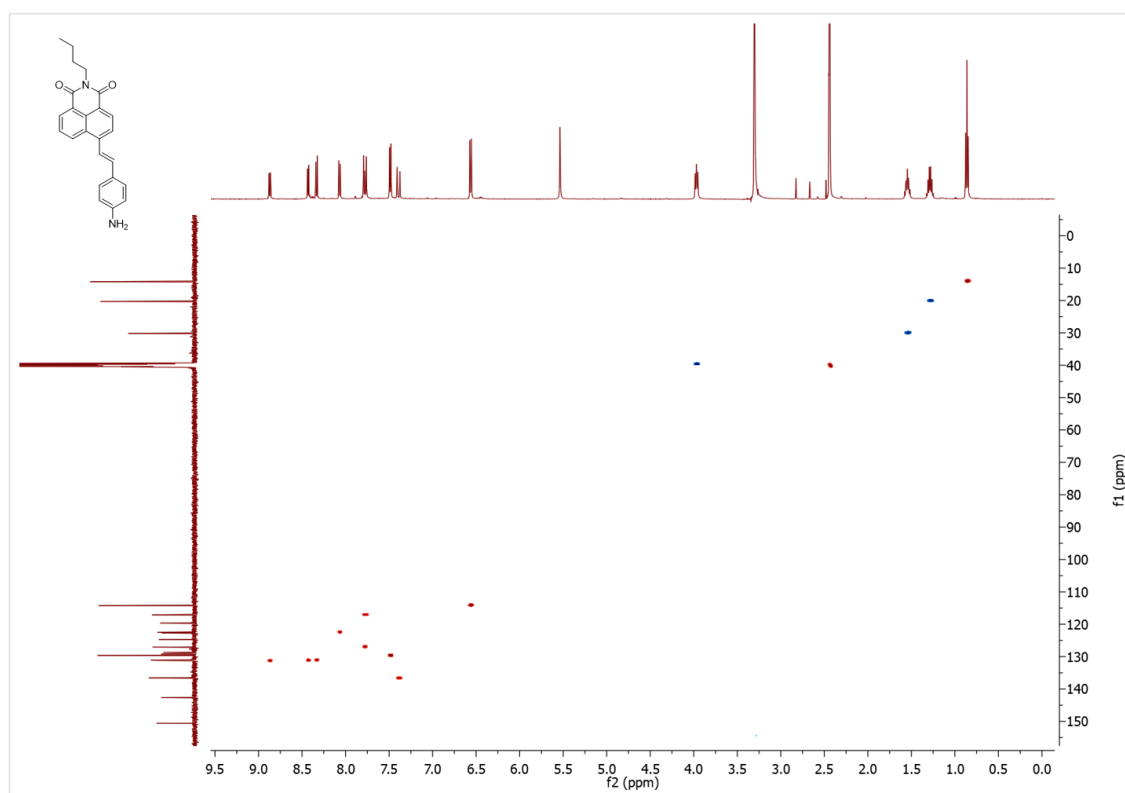
Figure S2.40: HSQC spectrum of **4-aminostyryl-*N*-butyl-1,8-naphthalimide (2.8)** in DMSO-*d*₆.
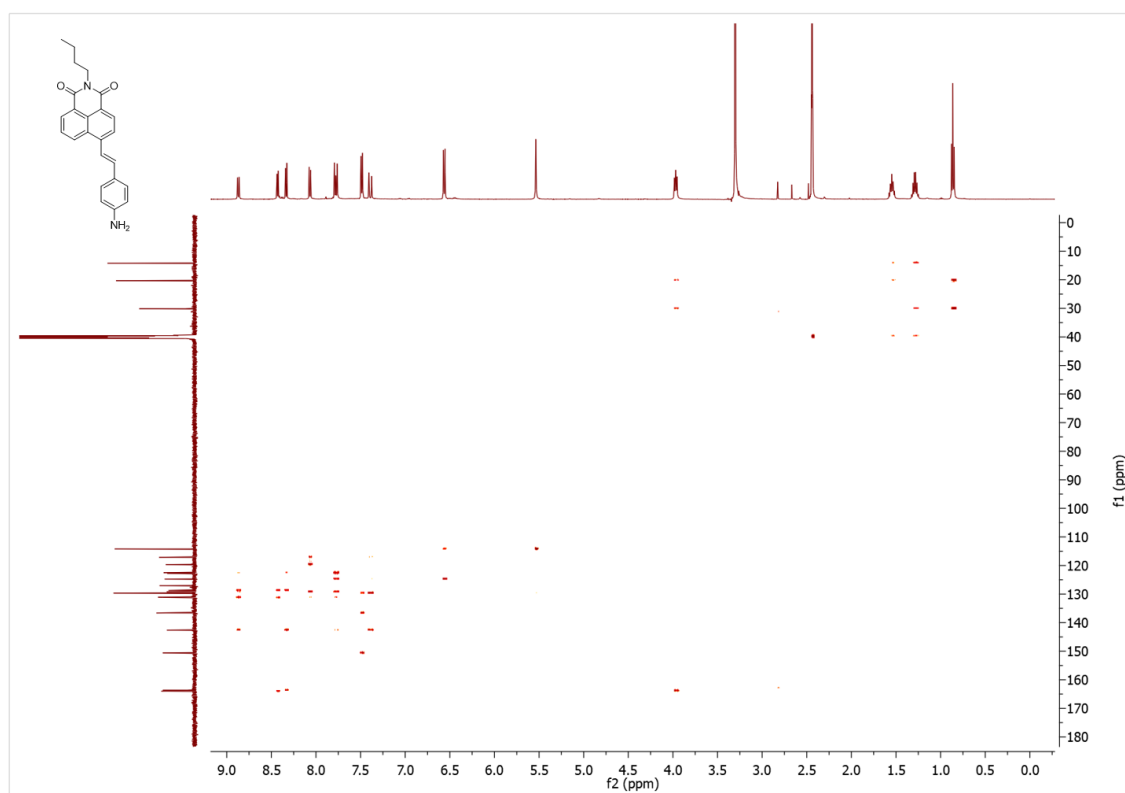
Figure S2.41: HMBC spectrum of **4-aminostyryl-*N*-butyl-1,8-naphthalimide (2.8)** in DMSO-*d*₆.

Chapter 3 – Supplementary Characterisation Data
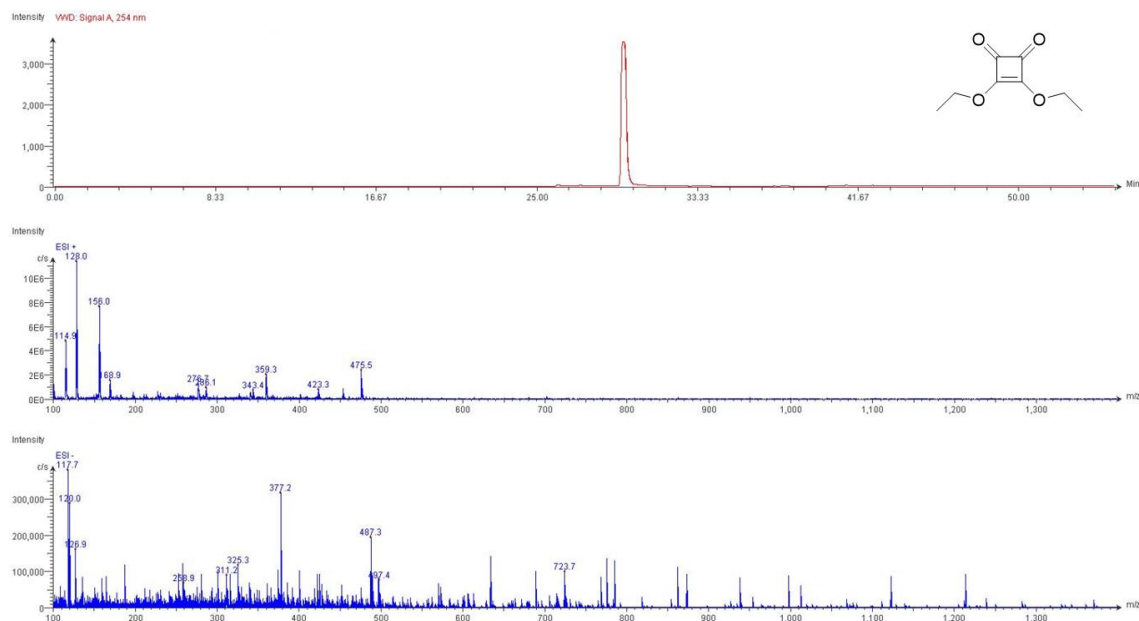
Figure S3.1: LC-MS data for diethyl squarate (**DESq, 3.1**).
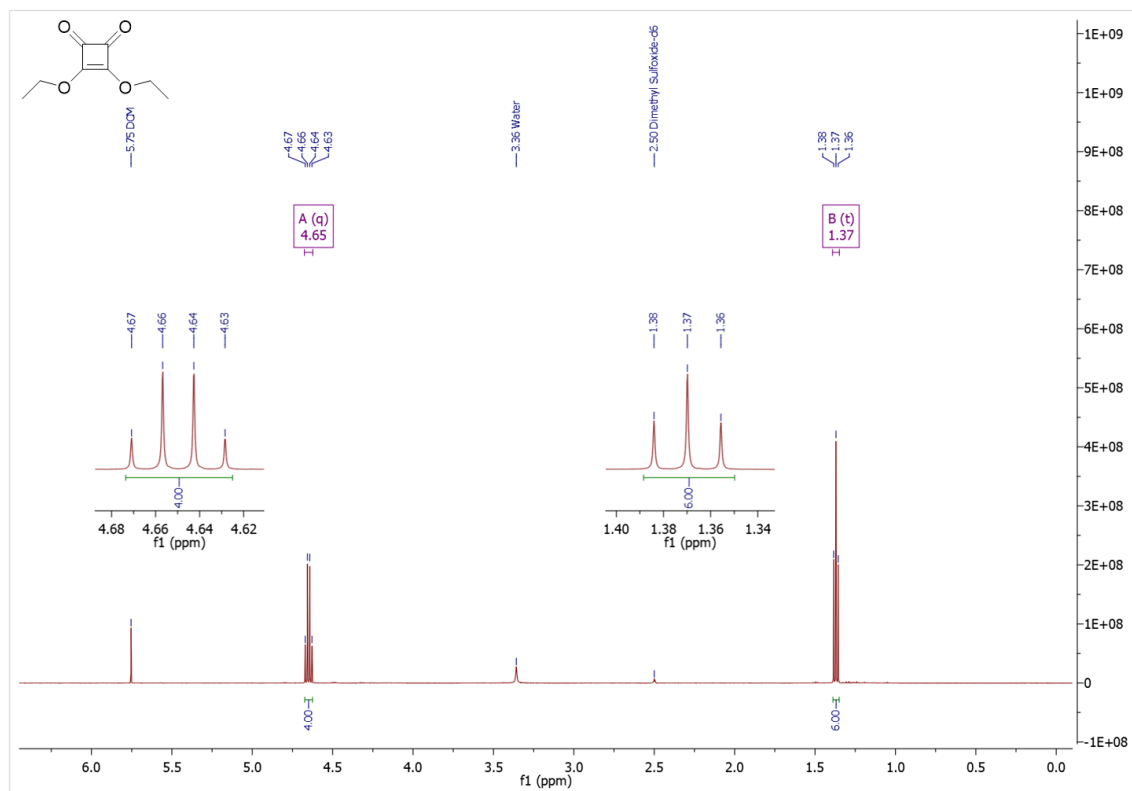
Figure S3.2: ^{1}H NMR spectrum of diethyl squarate (**DESq, 3.1**) in DMSO-d_6.

296
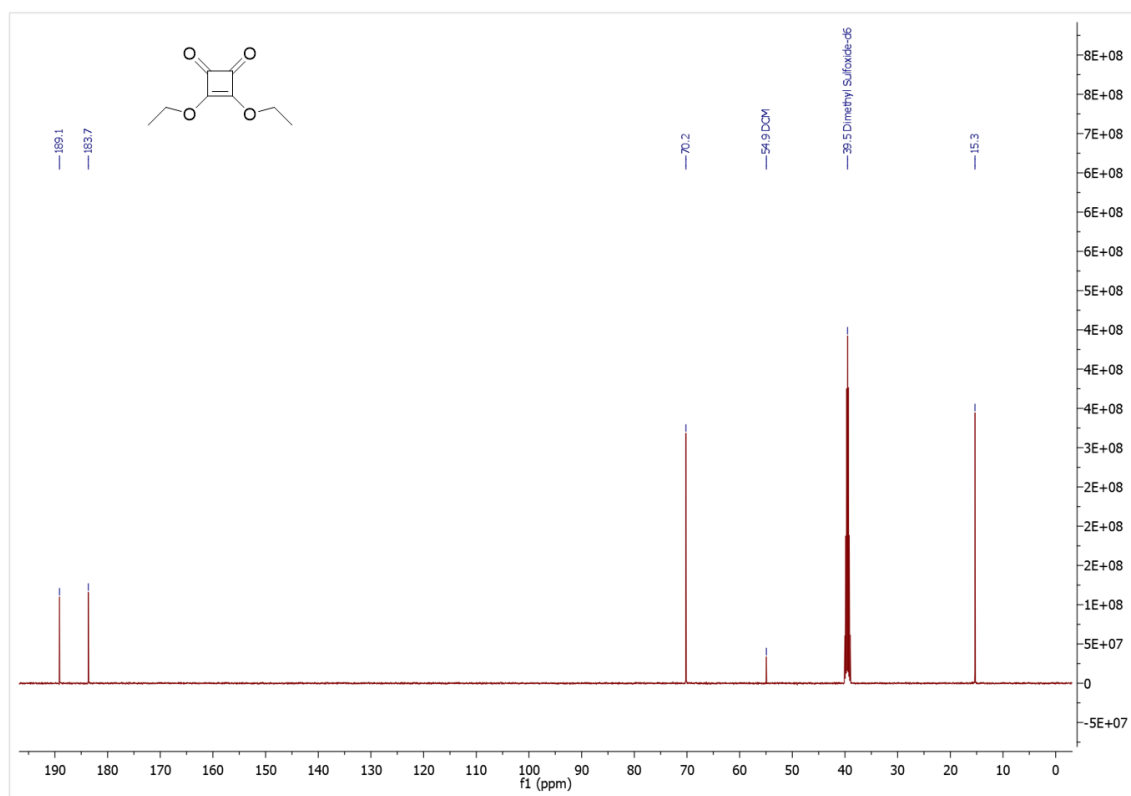
Figure S3.3: ^{13}C NMR spectrum of diethyl squarate (**DESq, 3.1**) in DMSO-d_6.
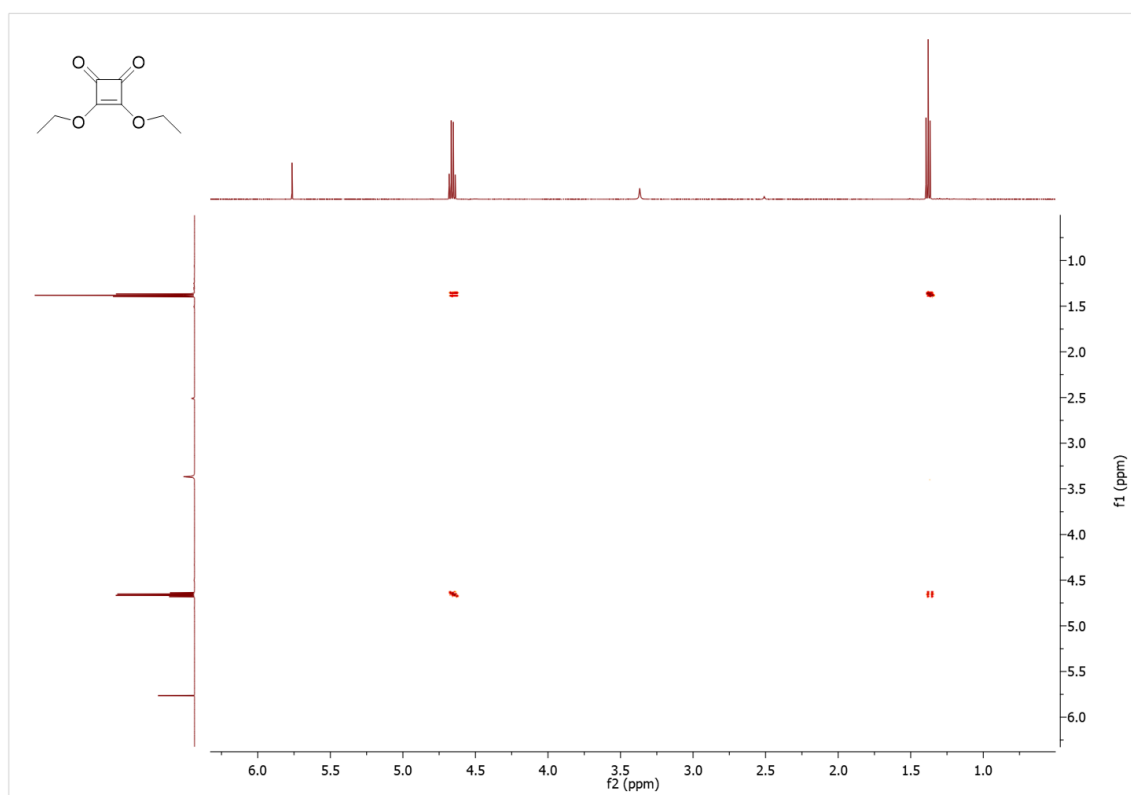
Figure S3.4: COSY spectrum of diethyl squarate (**DESq, 3.1**) in DMSO-d_6.
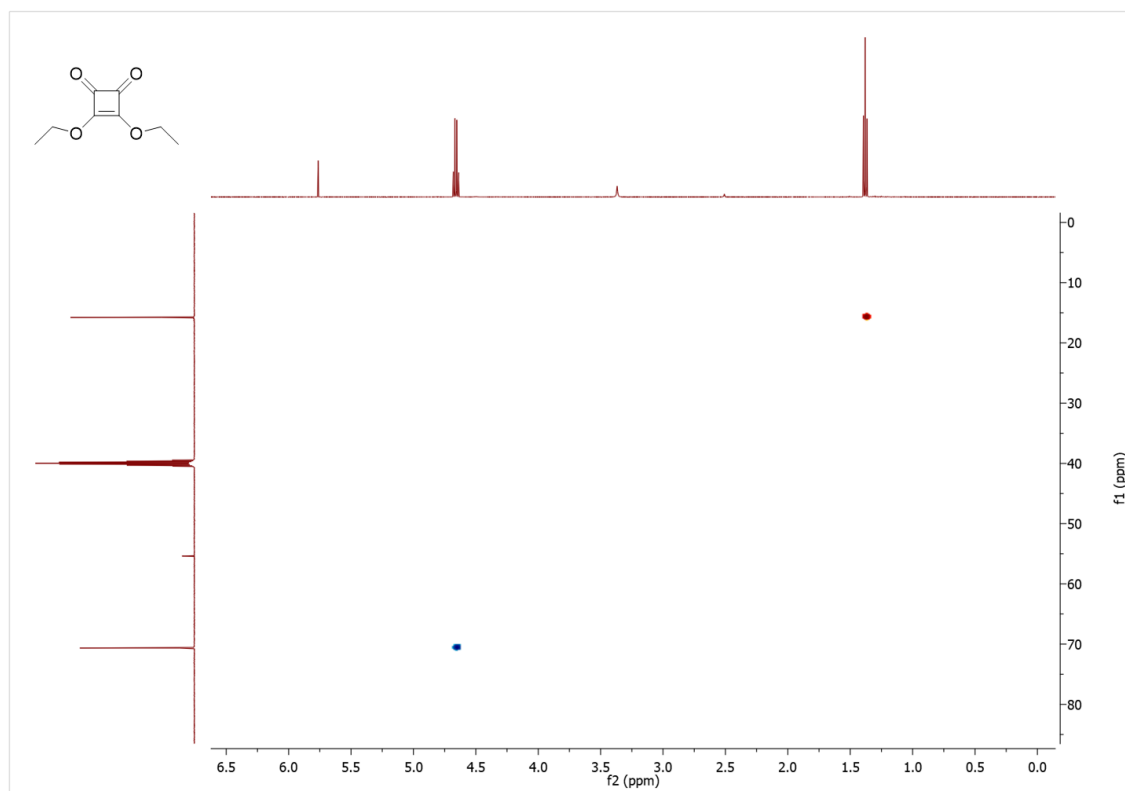
Figure S3.5: HSQC spectrum of diethyl squarate (**DESq, 3.1**) in DMSO-d_6.
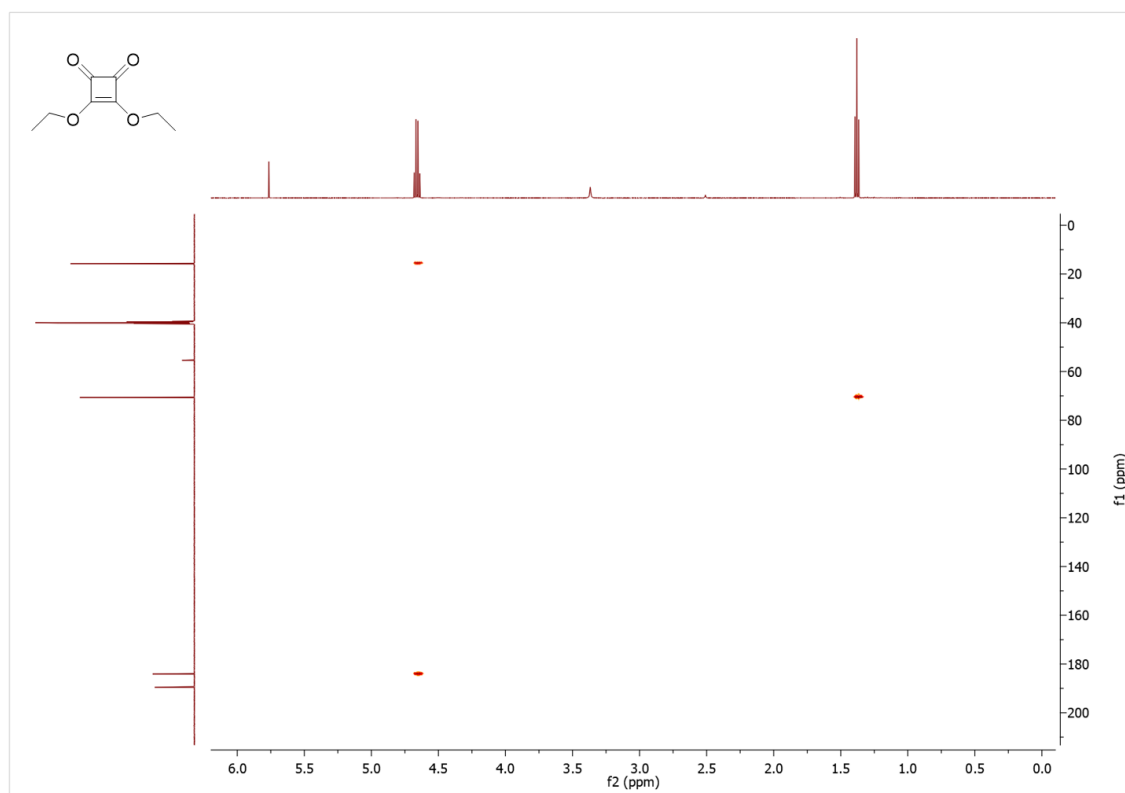
Figure S3.6: HMBC spectrum of diethyl squarate (**DESq, 3.1**) in DMSO-d_6.
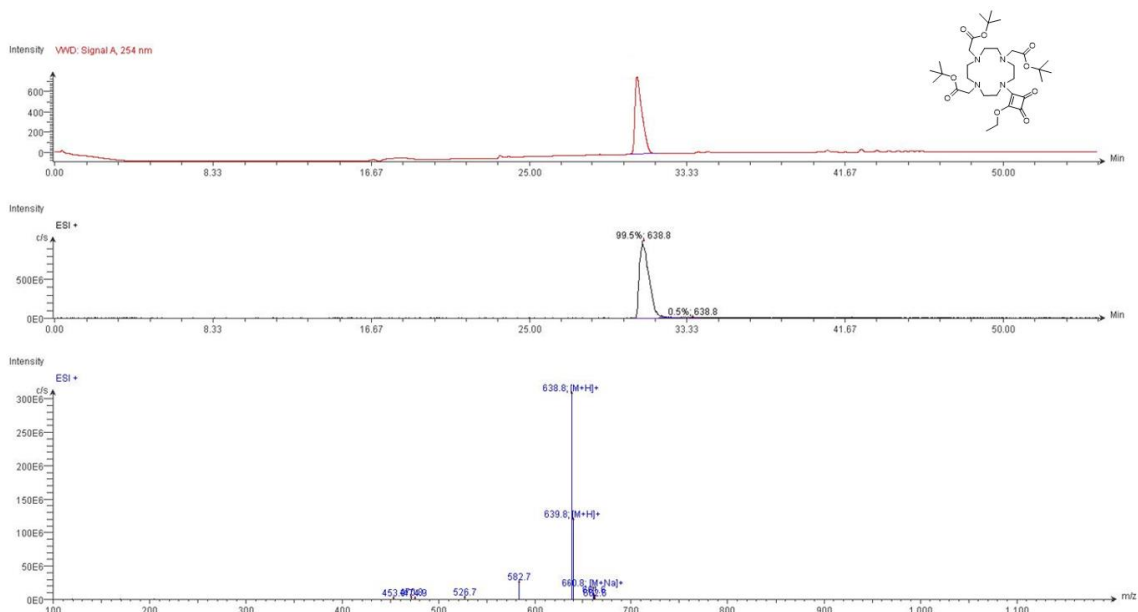
Figure S3.7: LC-MS data for **DO3A*t*Bu-ESq (3.2)**.
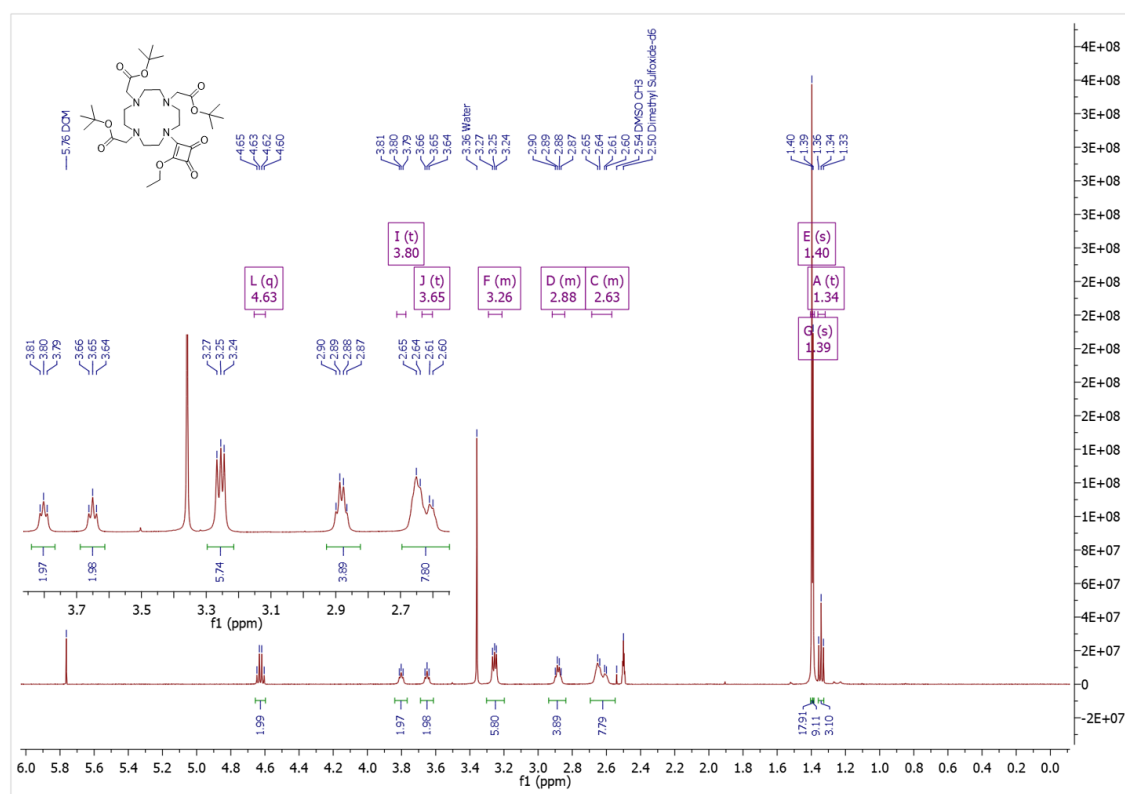
Figure S3.8: ¹H NMR spectrum of **DO3A*t*Bu-ESq (3.2)** in DMSO-*d*₆.
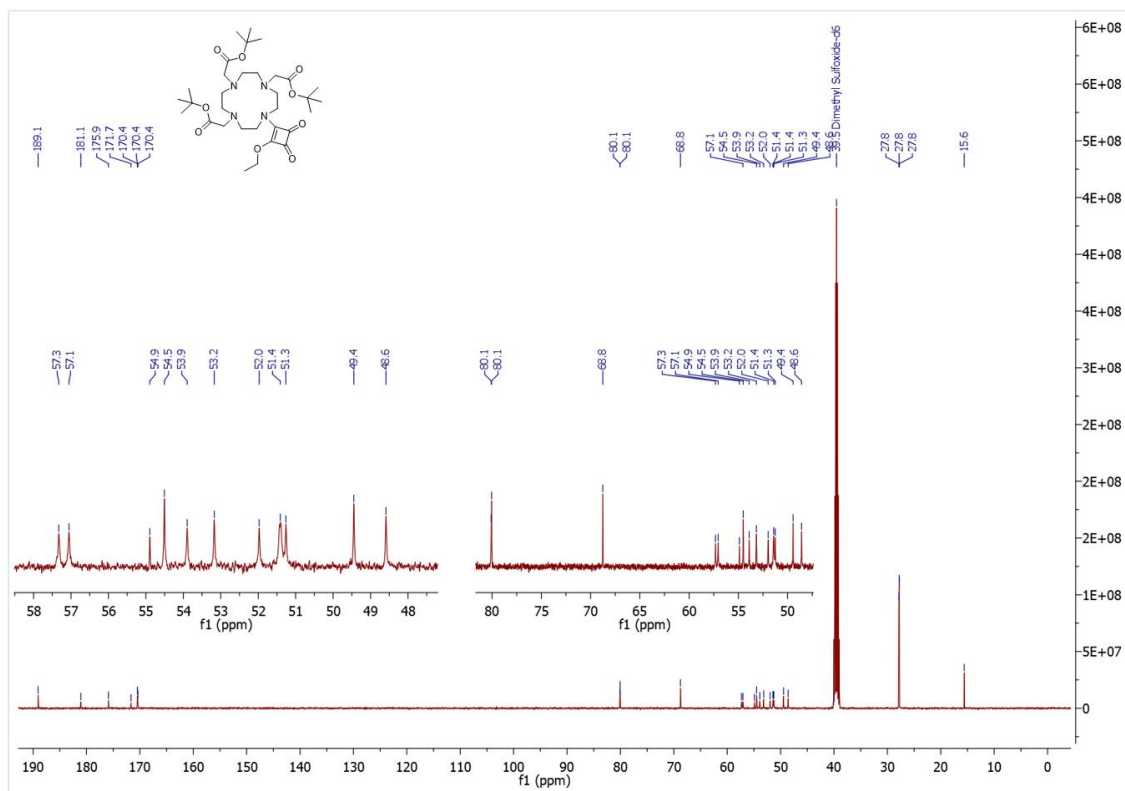
Figure S3.9: ^{13}C NMR spectrum of **DO3A*t*Bu-ESq (3.2)** in DMSO-d_6.
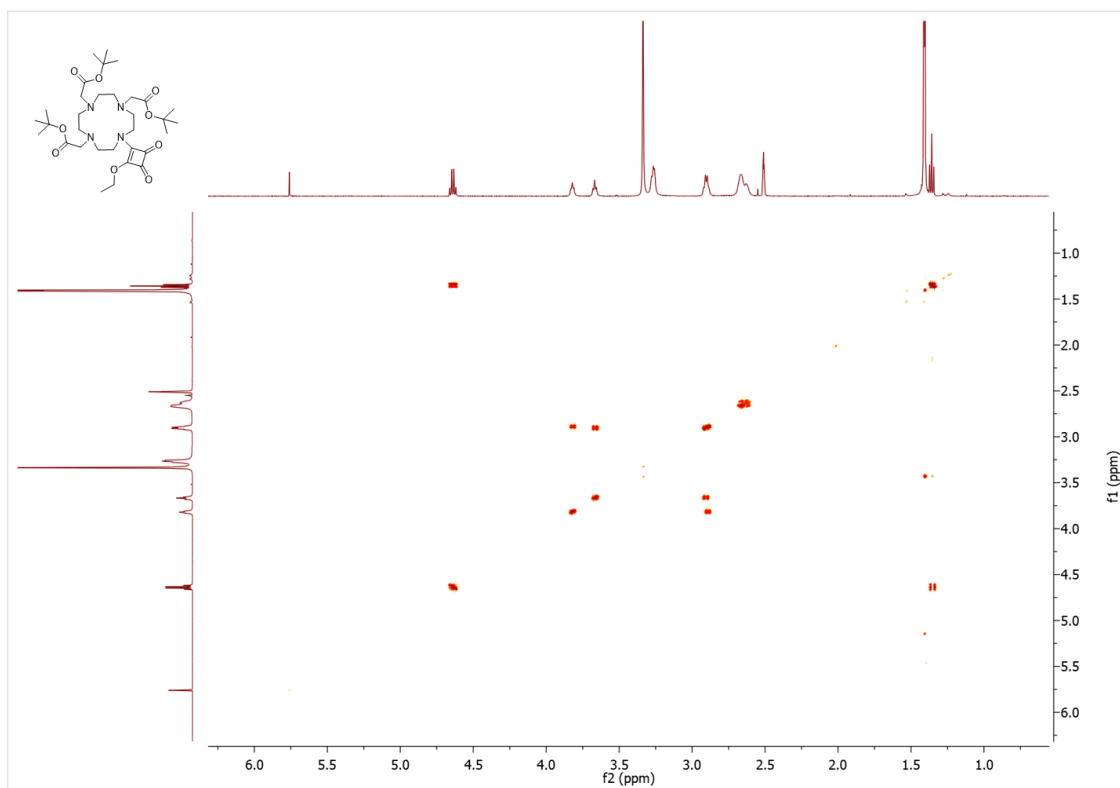
Figure S3.10: COSY spectrum of **DO3A*t*Bu-ESq (3.2)** in DMSO-d_6.
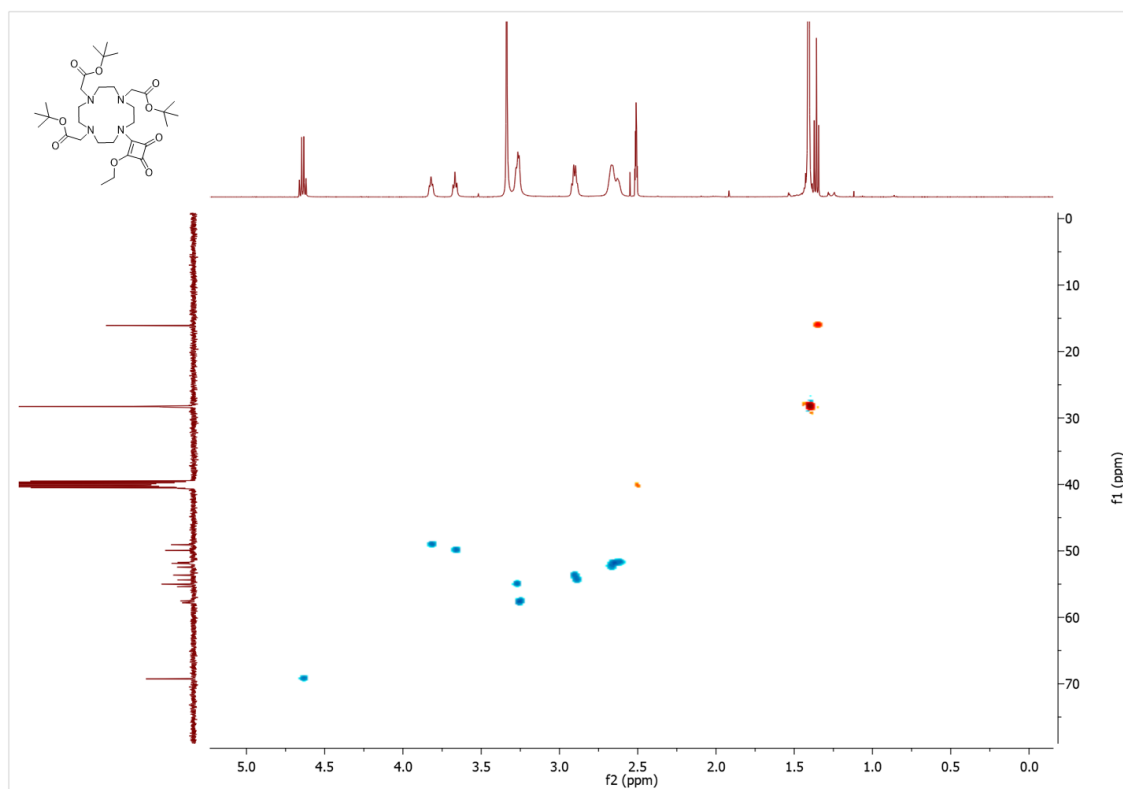
Figure S3.11: HSQC spectrum of **DO3A*t*Bu-ESq (3.2)** in DMSO-d_6.
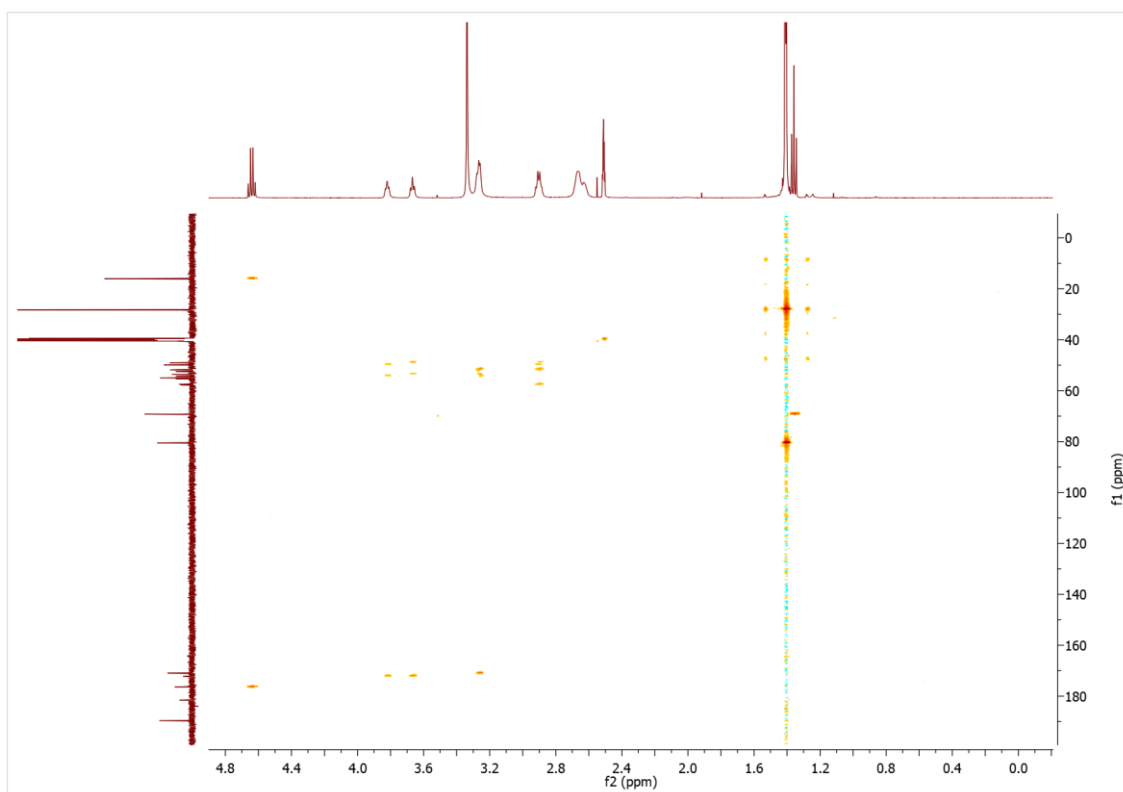
Figure S3.12: HMBC spectrum of **DO3A*t*Bu-ESq (3.2)** in DMSO-d_6.

Compound Table

Compound Label	RT (min)	Observed mass (m/z)	Neutral observed mass (Da)	Theoretical mass (Da)	Mass error (ppm)	Isotope match score (%)
Cpd 1: C32 H54 N4 O9	0.68	639.3968	638.3894	638.3891	0.53	99.60

Mass errors of between -5.00 and 5.00 ppm with isotope match scores above 60% are considered confirmation of molecular formulae
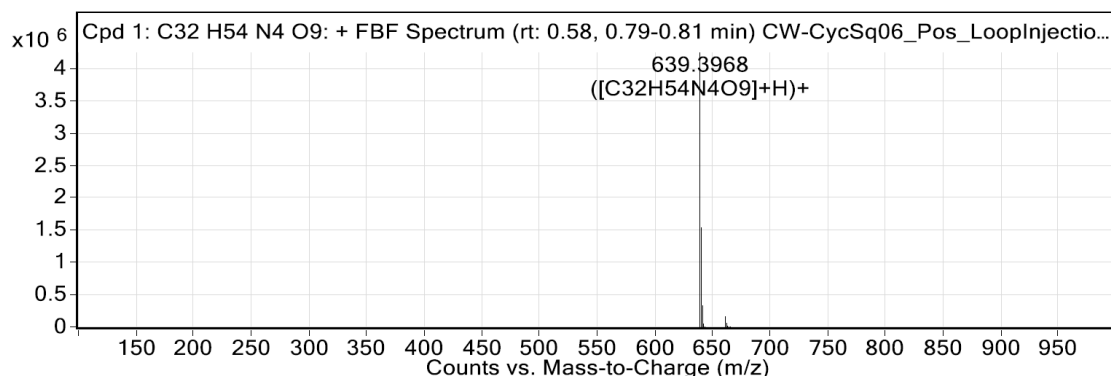
Figure: Full range view of Compound spectra and potential adducts.
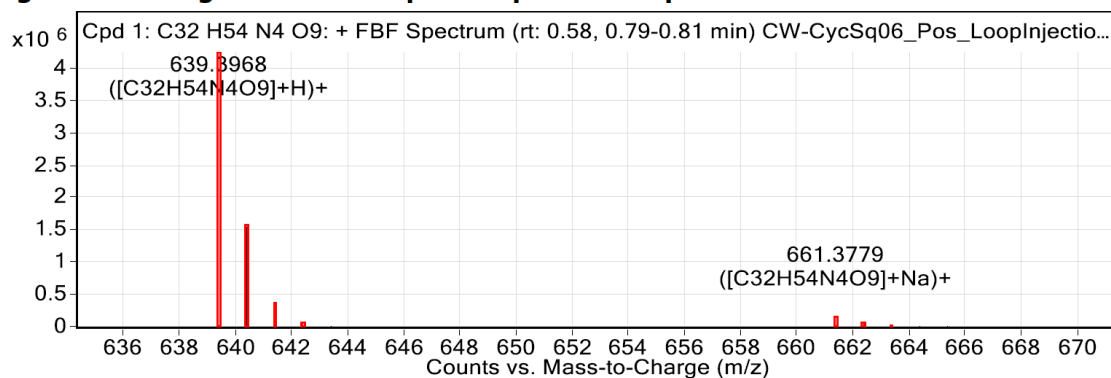
Figure: Zoomed Compound spectra view
(red boxes indicating expected theoretical isotope spacing and abundance)

Compound isotope peak List

m/z	z	Abund	Formula	Ion
639.3968	1	4237712.5	C32H54N4O9	(M+H)+
640.3997	1	1540792.8	C32H54N4O9	(M+H)+
641.4025	1	326114.5	C32H54N4O9	(M+H)+
642.4045	1	49457.7	C32H54N4O9	(M+H)+
643.4063	1	6663.7	C32H54N4O9	(M+H)+
661.3779	1	161228.8	C32H54N4O9	(M+Na)+
662.3810	1	55869.9	C32H54N4O9	(M+Na)+
663.3836	1	12030.7	C32H54N4O9	(M+Na)+
664.3850	1	2327.2	C32H54N4O9	(M+Na)+
665.3877	1	316.5	C32H54N4O9	(M+Na)+

Figure S3.13: HRMS data for **DO3A*t*Bu-ESq (3.2)**.
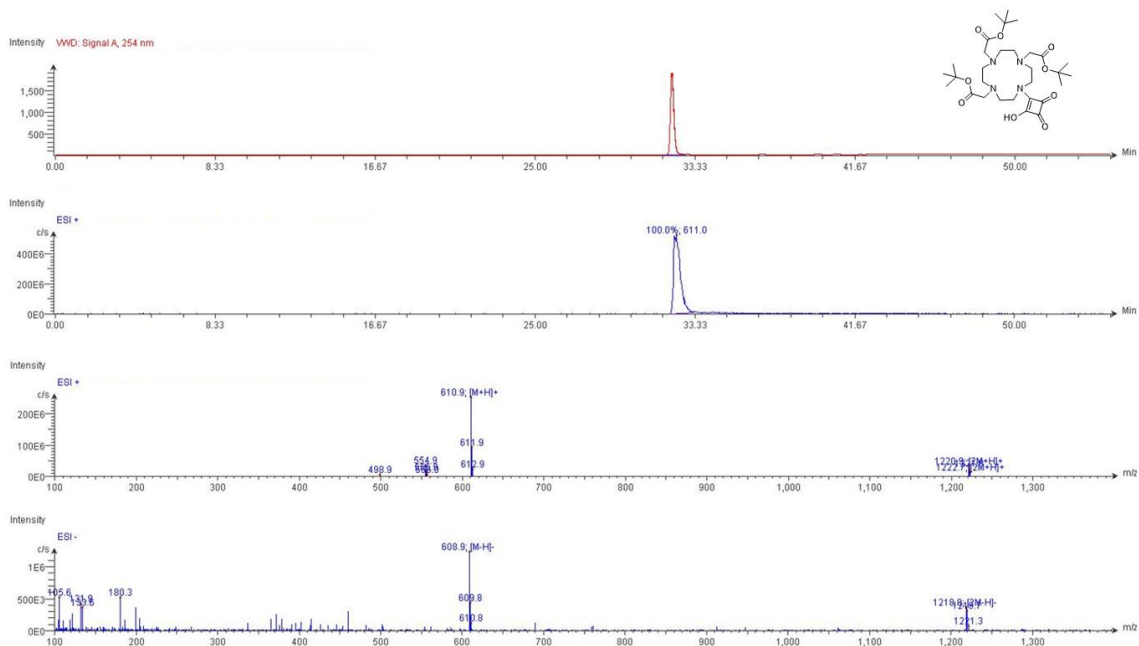
Figure S3.14: LC-MS data for **DO3A*t*Bu-Sq-OH (3.3)**.
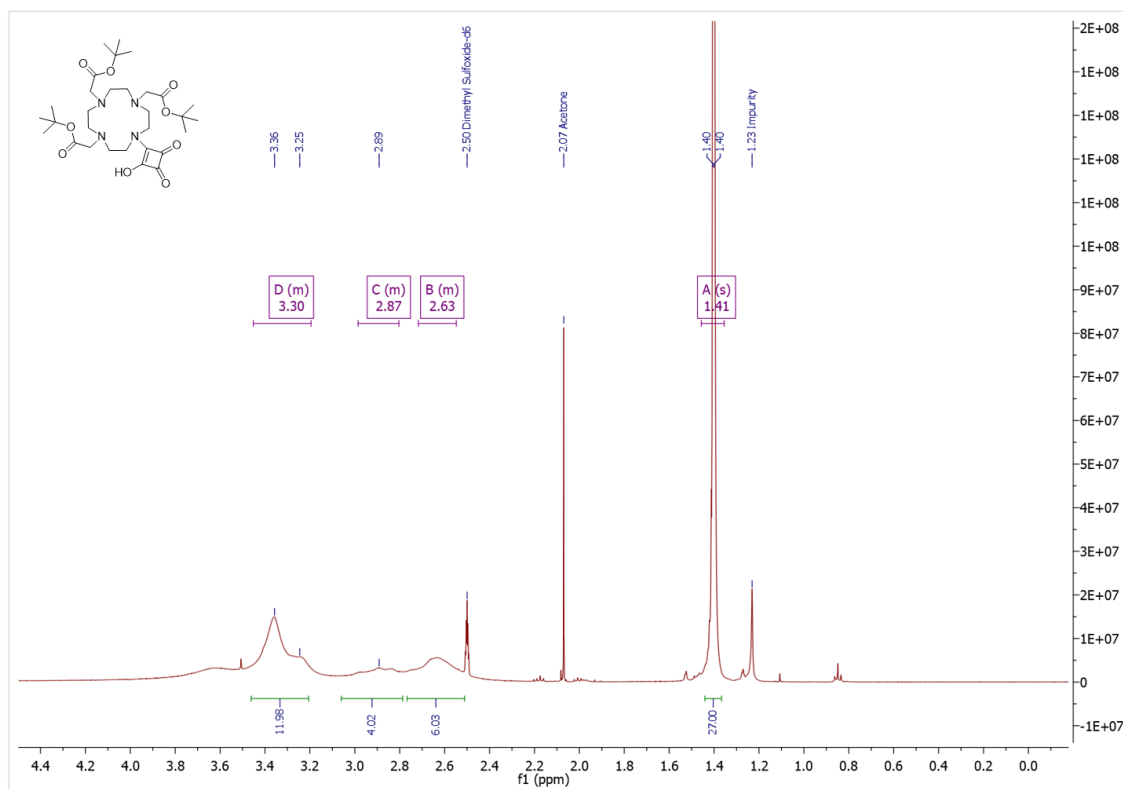
Figure S3.15: ¹H NMR spectrum of **DO3A*t*Bu-Sq-OH (3.3)** in DMSO-*d*₆.
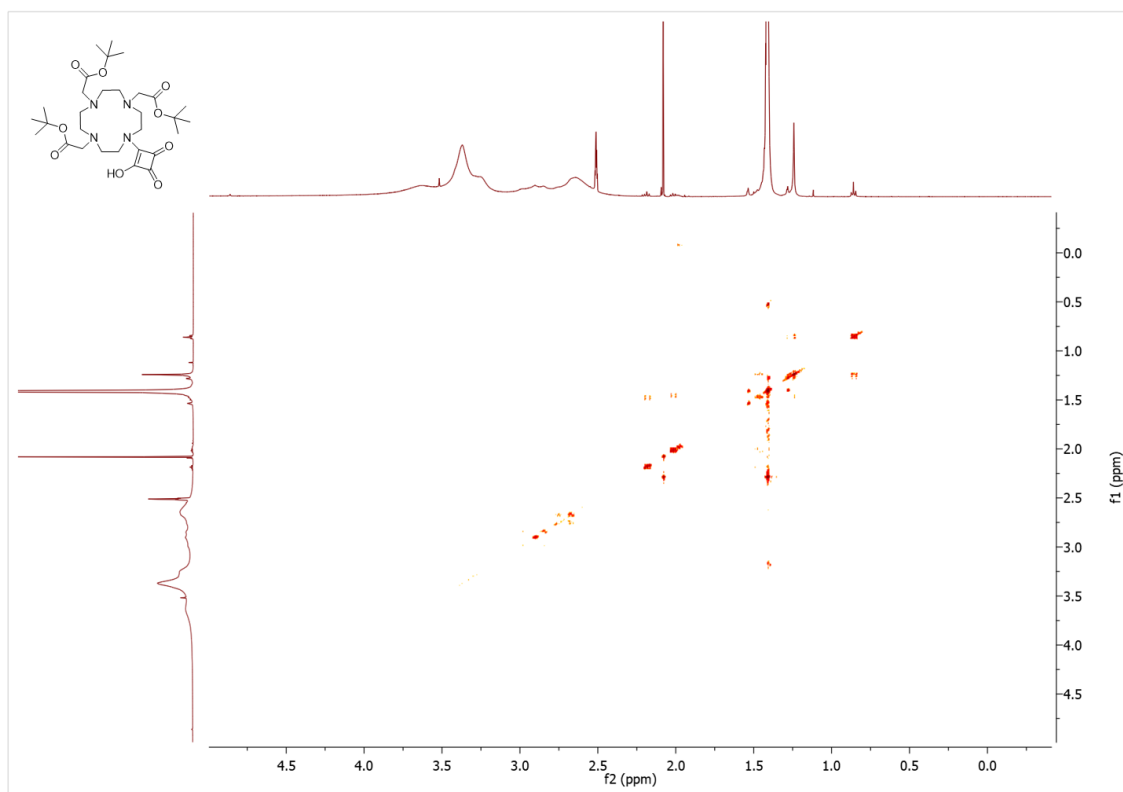
Figure S3.16: COSY spectrum of **DO3A*t*Bu-Sq-OH (3.3)** in DMSO-*d*₆.

Compound Table

Compound Label	RT (min)	Observed mass (m/z)	Neutral observed mass (Da)	Theoretical mass (Da)	Mass error (ppm)	Isotope match score (%)
Cpd 1: C30 H50 N4 O9	0.74	633.3453	610.3568	610.3578	-1.63	98.07

Mass errors of between -5.00 and 5.00 ppm with isotope match scores above 60% are considered confirmation of molecular formulae
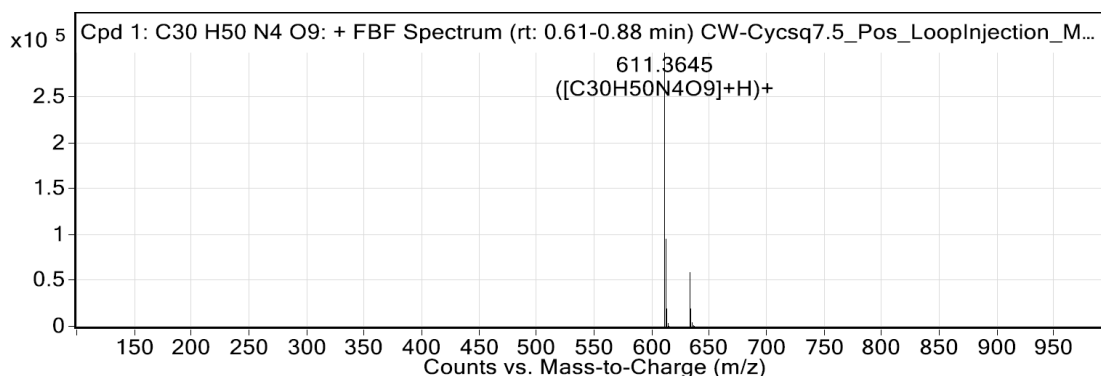
Figure: Full range view of Compound spectra and potential adducts.
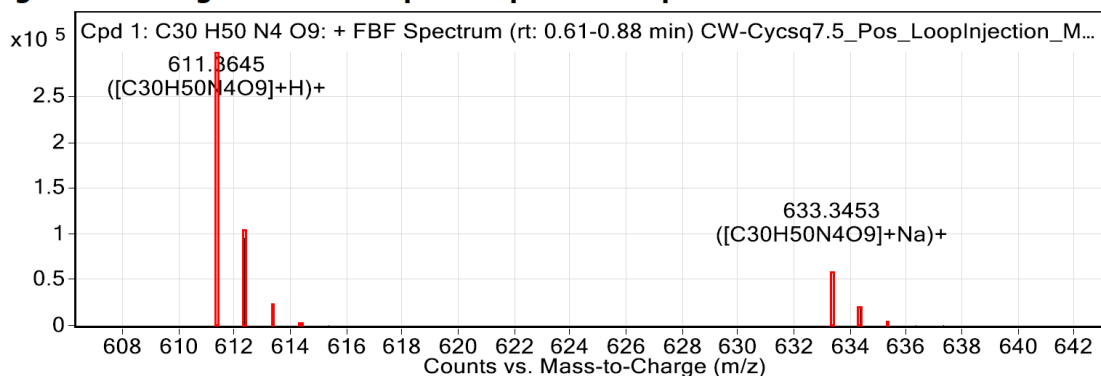
Figure: Zoomed Compound spectra view
(red boxes indicating expected theoretical isotope spacing and abundance)

Compound isotope peak List

m/z	z	Abund	Formula	Ion
611.3645	1	297829.2	C30H50N4O9	(M+H)+
612.3671	1	95124.7	C30H50N4O9	(M+H)+
613.3685	1	18933.7	C30H50N4O9	(M+H)+
614.3698	1	3104.2	C30H50N4O9	(M+H)+
615.3742	1	410.2	C30H50N4O9	(M+H)+
633.3453	1	58549.1	C30H50N4O9	(M+Na)+
634.3479	1	19101.3	C30H50N4O9	(M+Na)+
635.3498	1	3988.1	C30H50N4O9	(M+Na)+
636.3518	1	701.0	C30H50N4O9	(M+Na)+
637.3461	1	130.1	C30H50N4O9	(M+Na)+

Figure S3.17: HRMS data for **DO3A*t*Bu-Sq-OH (3.3)**.
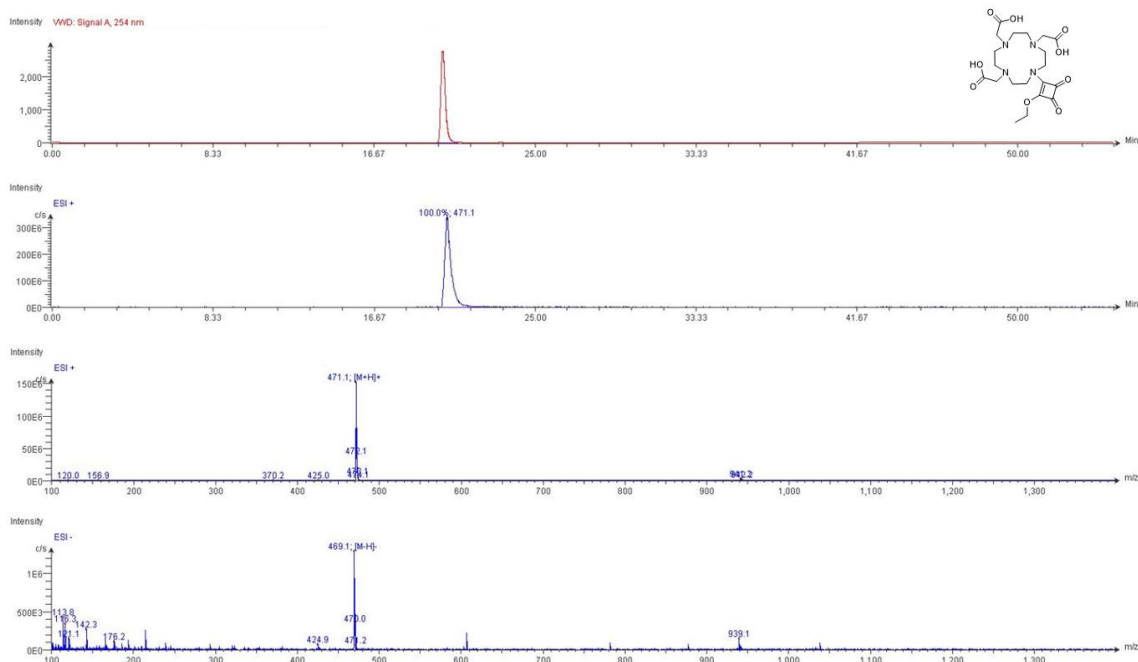
Figure S3.18: LC-MS data for **DO3A-ESq (3.4)**.
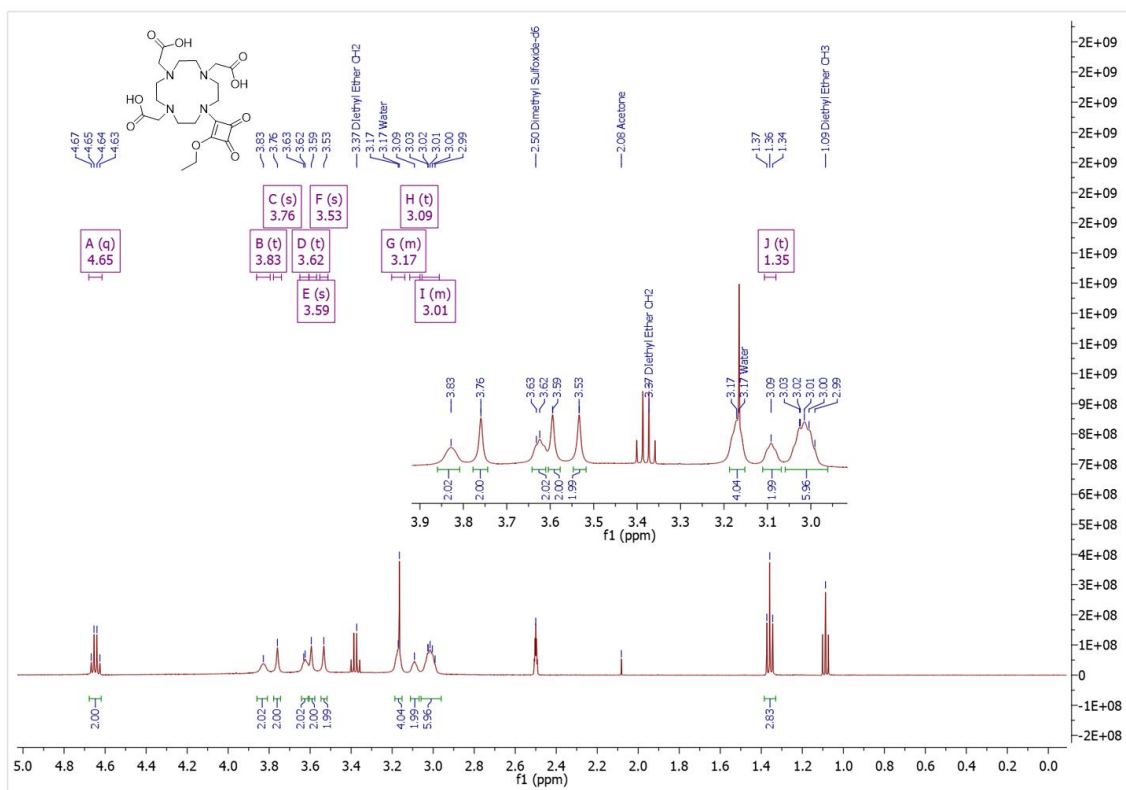
Figure S3.19: ^{1}H NMR spectrum of **DO3A-ESq (3.4)** in DMSO-d_6.
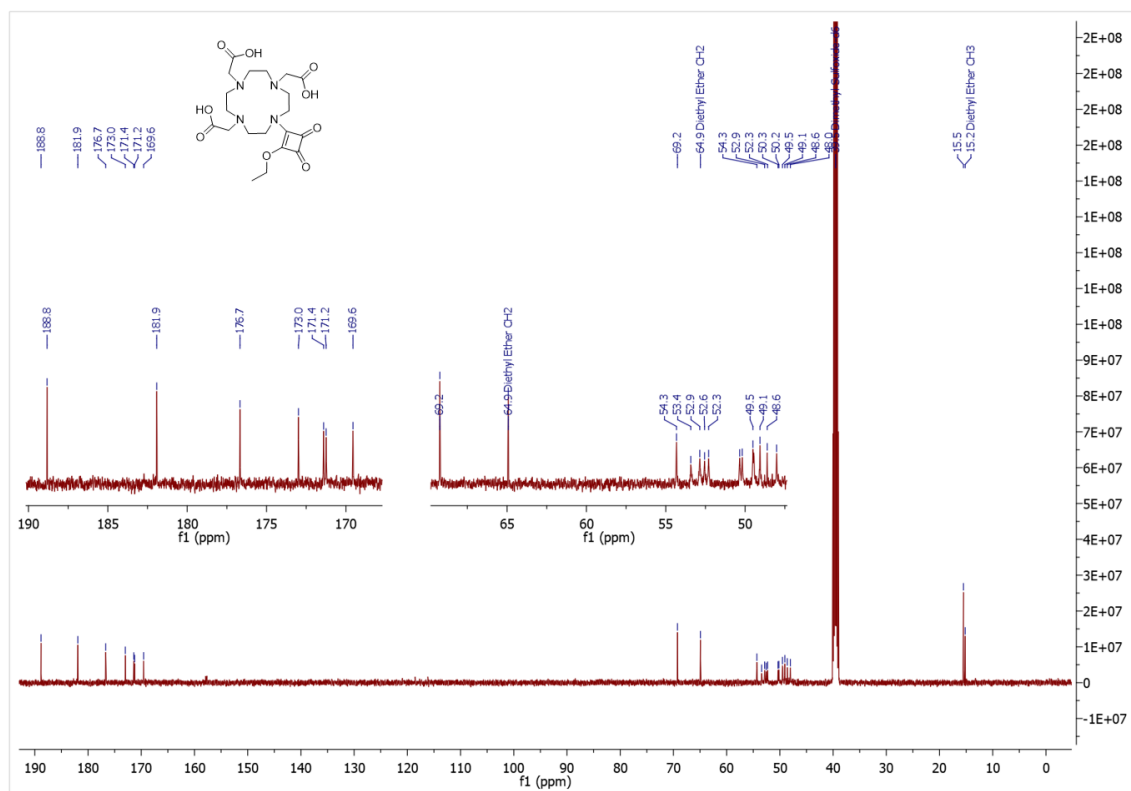
Figure S3.20: ^{13}C NMR spectrum of **DO3A-ESq (3.4)** in DMSO-d_6.
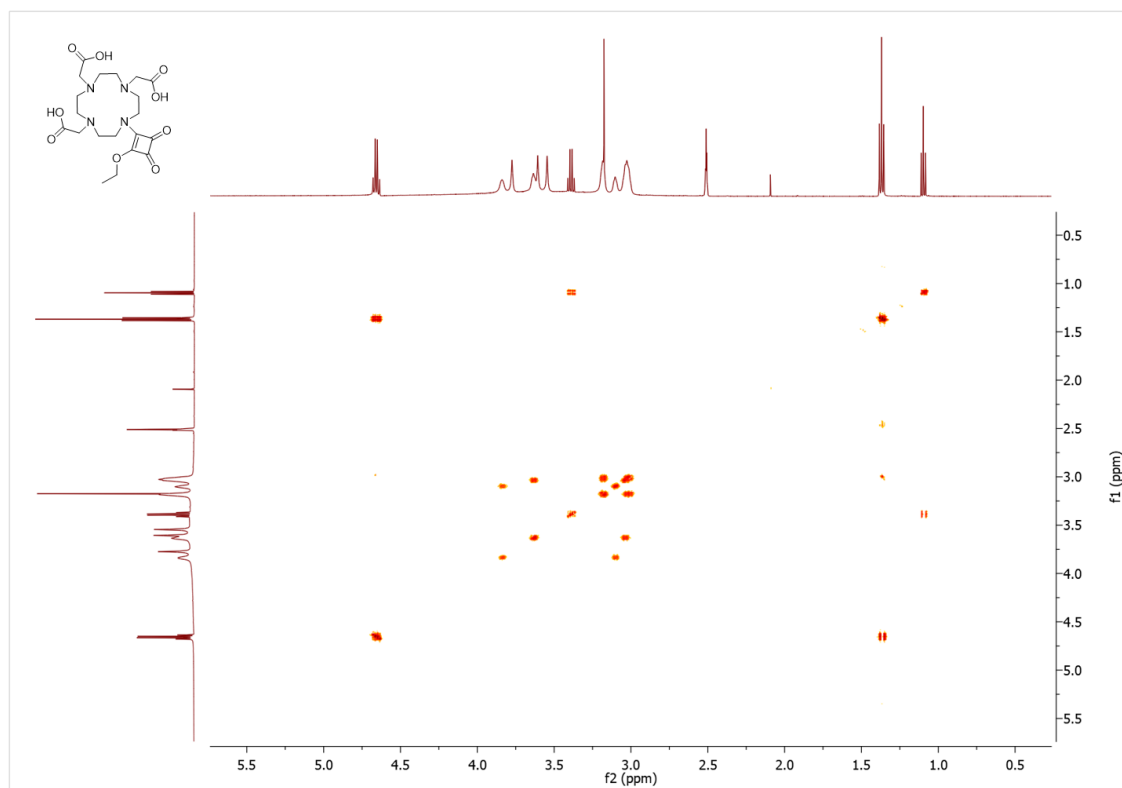
Figure S3.21: COSY spectrum of **DO3A-ESq (3.4)** in DMSO-d_6.
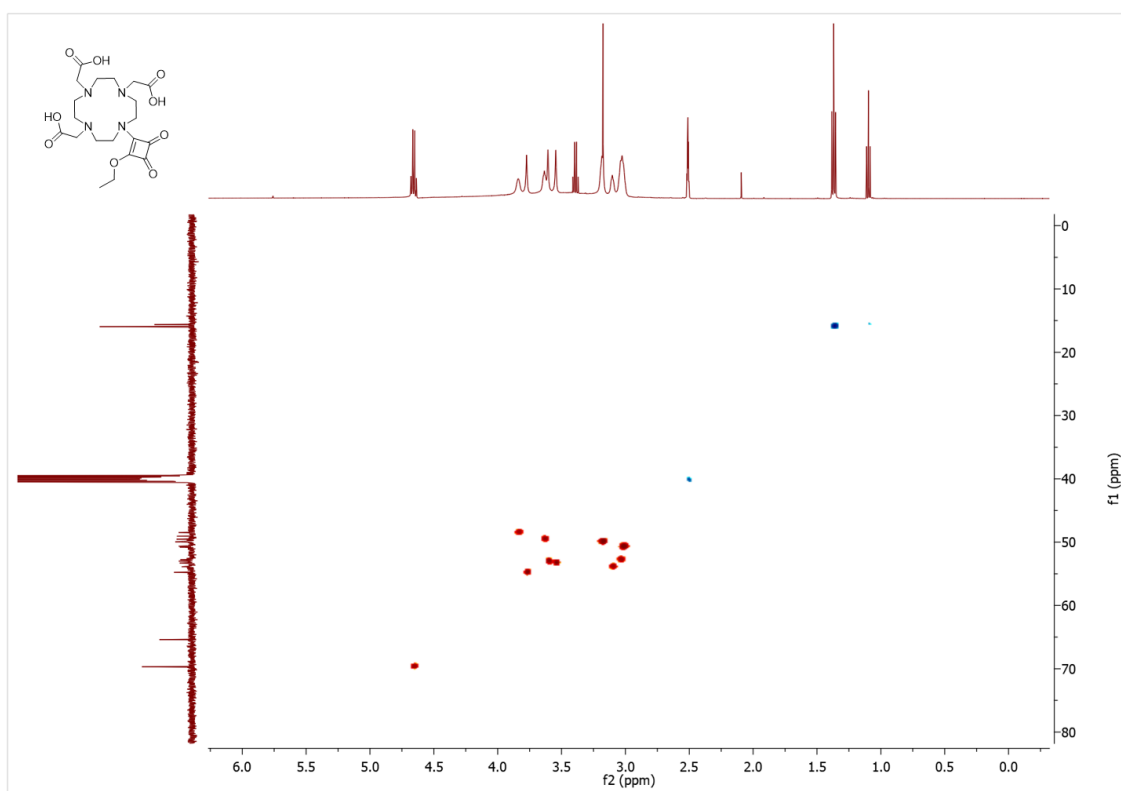
Figure S3.22: HSQC spectrum of **DO3A-ESq (3.4)** in DMSO-d_6.
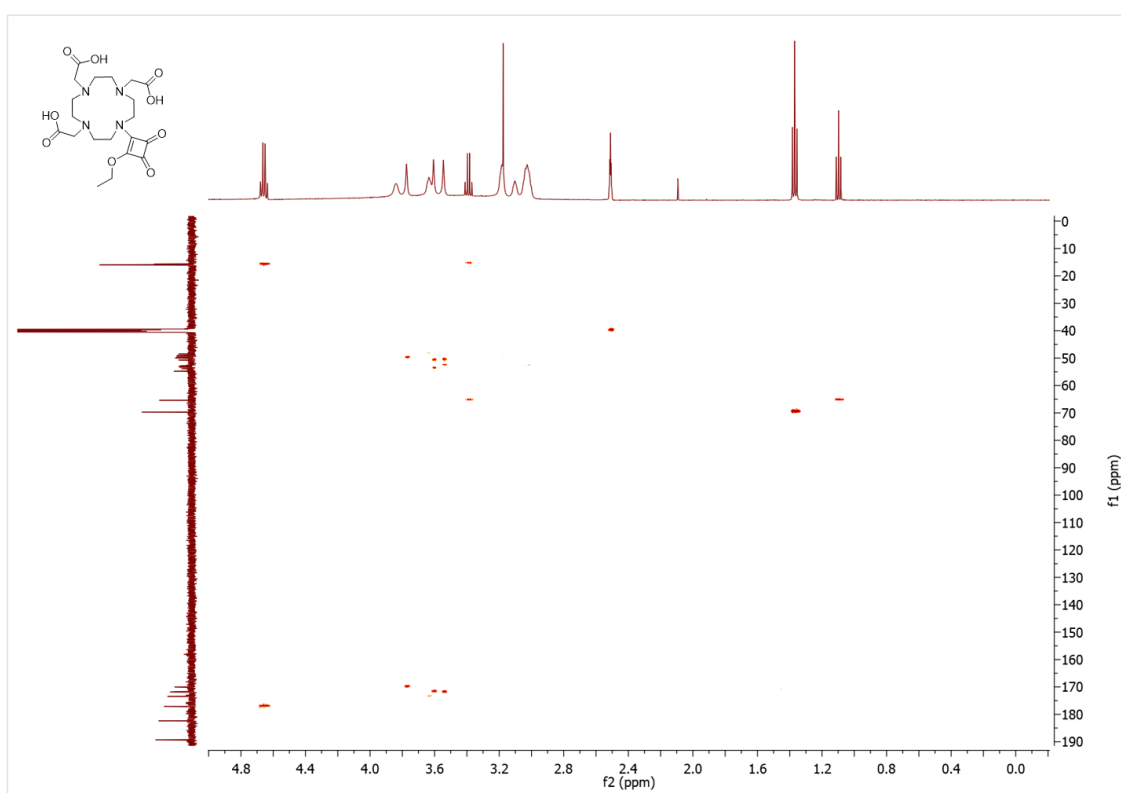
Figure S3.23: HMBC spectrum of **DO3A-ESq (3.4)** in DMSO-d_6.

Compound Table

Compound Label	RT (min)	Observed mass (m/z)	Neutral observed mass (Da)	Theoretical mass (Da)	Mass error (ppm)	Isotope match score (%)
Cpd 1: C20 H30 N4 O9	0.72	471.2088	470.2016	470.2013	0.62	98.63

Mass errors of between -5.00 and 5.00 ppm with isotope match scores above 60% are considered confirmation of molecular formulae
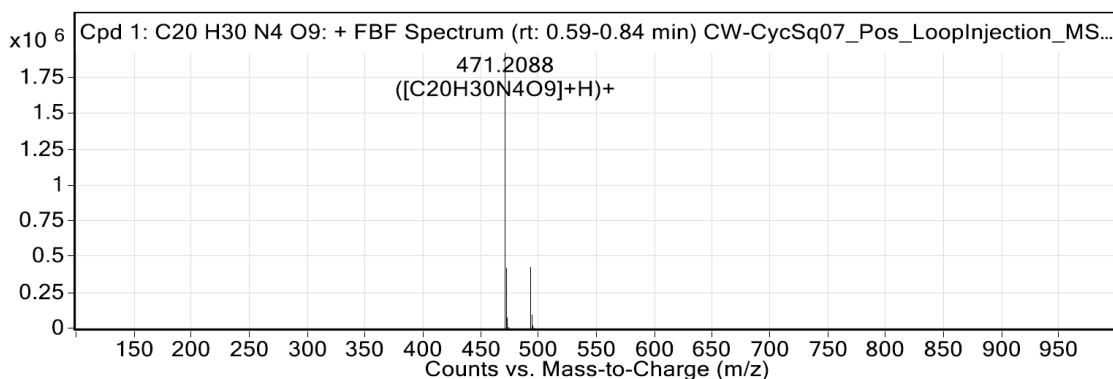
Figure: Full range view of Compound spectra and potential adducts.
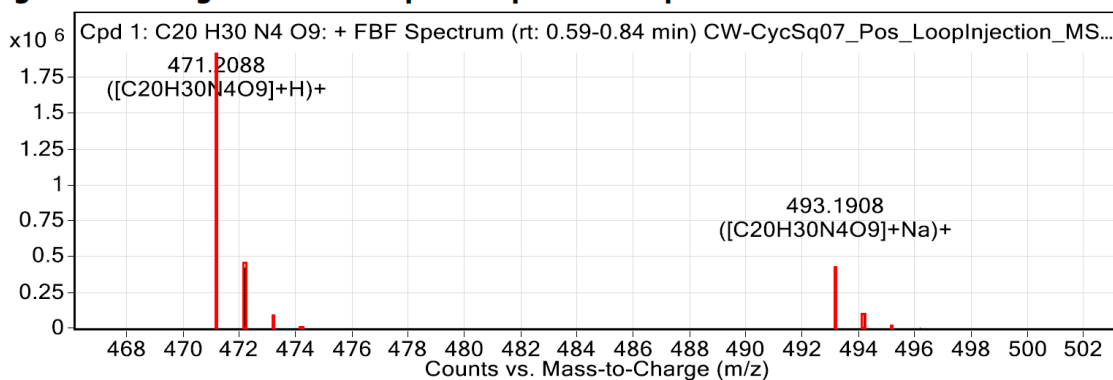
Figure: Zoomed Compound spectra view
(red boxes indicating expected theoretical isotope spacing and abundance)

Compound isotope peak List

m/z	z	Abund	Formula	Ion
471.2088	1	1919071.6	C20H30N4O9	(M+H)+
472.2121	1	421241.0	C20H30N4O9	(M+H)+
473.2139	1	73595.4	C20H30N4O9	(M+H)+
474.2163	1	9191.7	C20H30N4O9	(M+H)+
493.1908	1	423145.7	C20H30N4O9	(M+Na)+
494.1936	1	90989.6	C20H30N4O9	(M+Na)+
495.1947	1	16981.1	C20H30N4O9	(M+Na)+
496.1953	1	2484.6	C20H30N4O9	(M+Na)+

Figure S3.24: HRMS data for **DO3A-ESq (3.4)**.
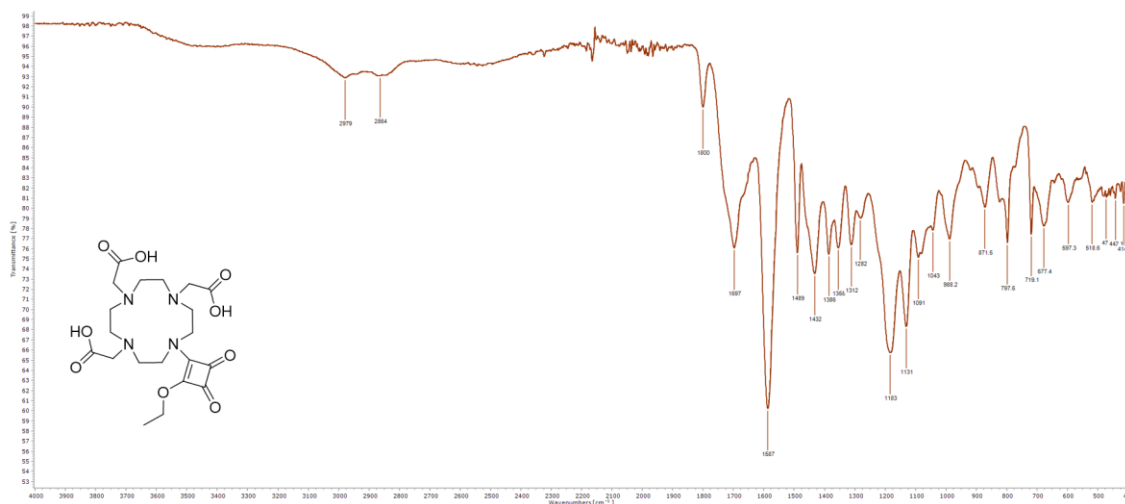
Figure S3.25: FTIR-ATR spectrum of **DO3A-ESq (3.4)**.
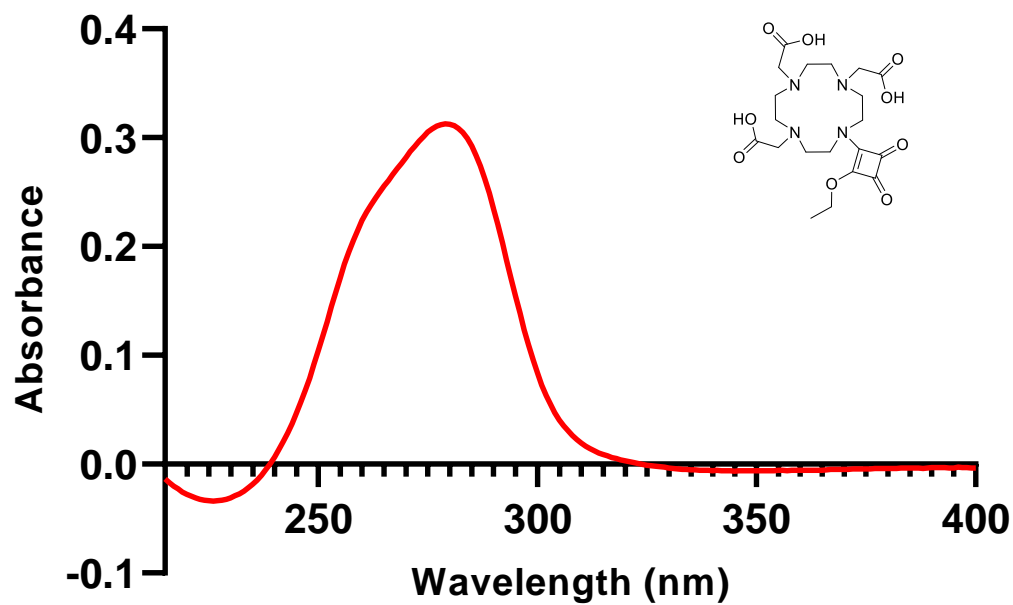
Figure S3.26: Absorbance spectrum of **DO3A-ESq (3.4)** (20 μM) in H$_2$O.
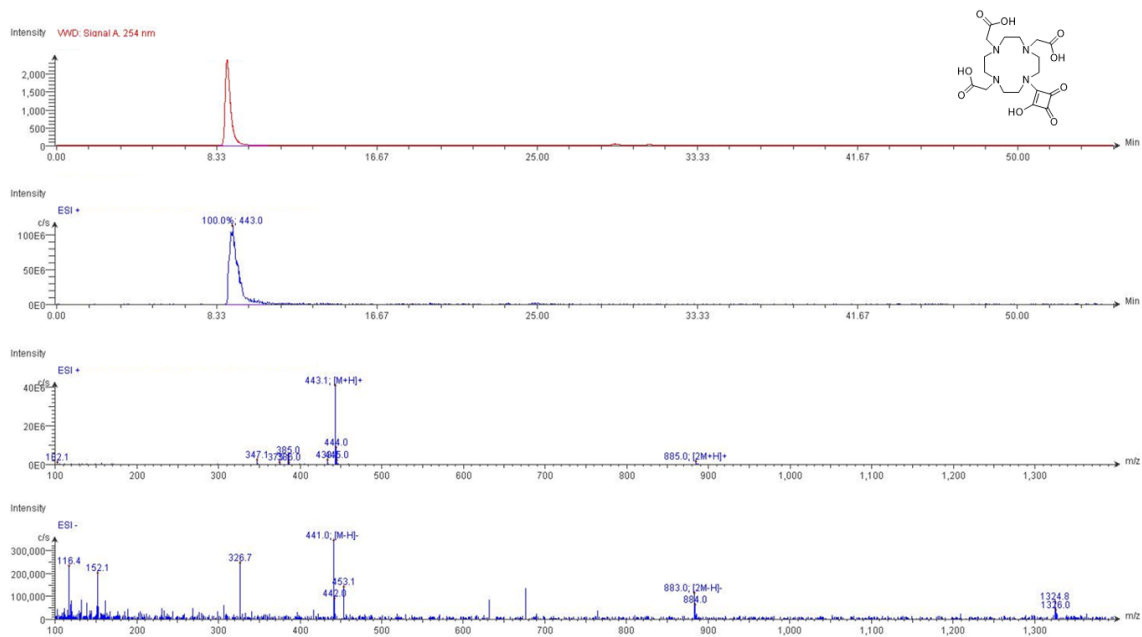
Figure S3.27: LC-MS data for **DO3A-Sq-OH (3.5)**.
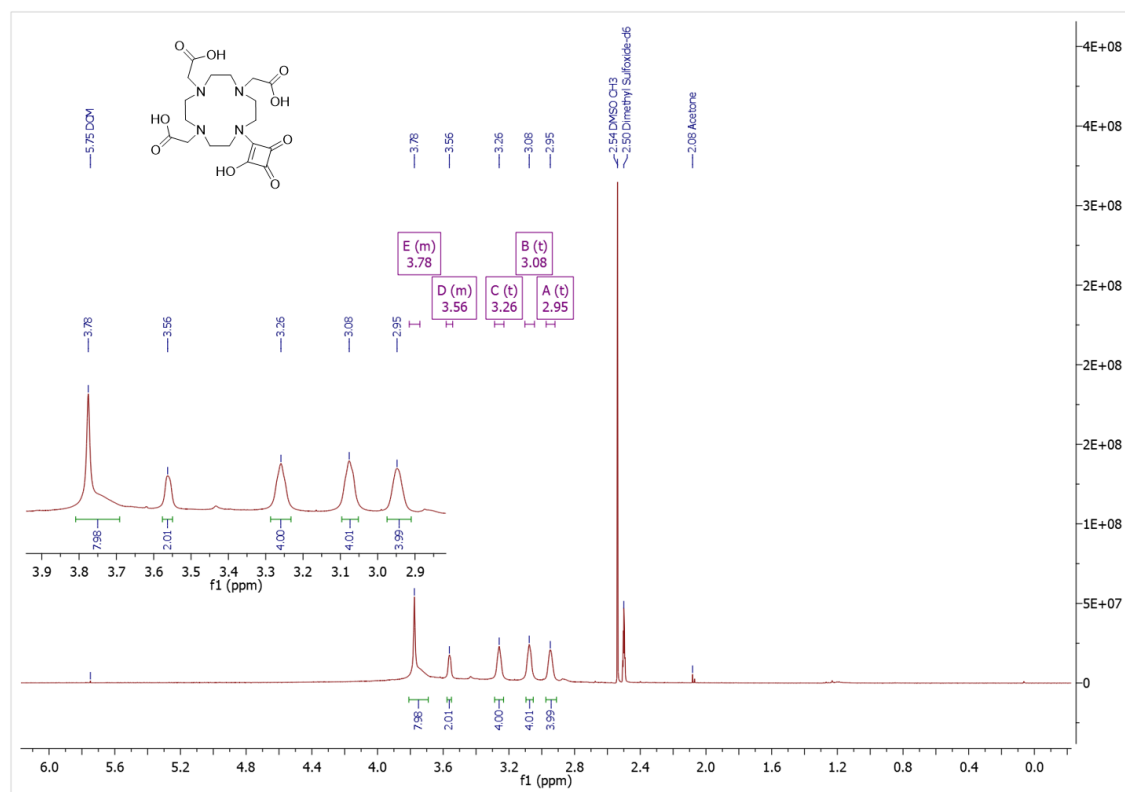
Figure S3.28: ^{1}H NMR spectrum of **DO3A-Sq-OH (3.5)** in DMSO-*d*6.
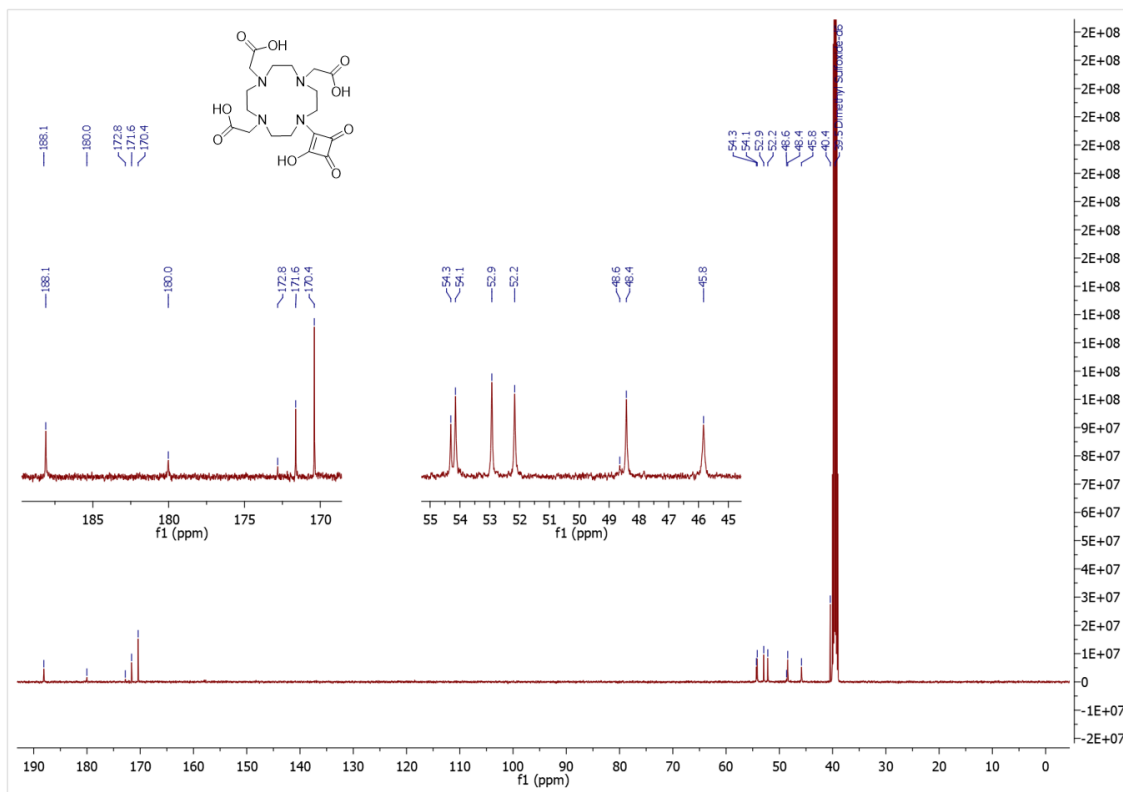
Figure S3.29: ^{13}C NMR spectrum of **DO3A-Sq-OH (3.5)** in DMSO-d_6.
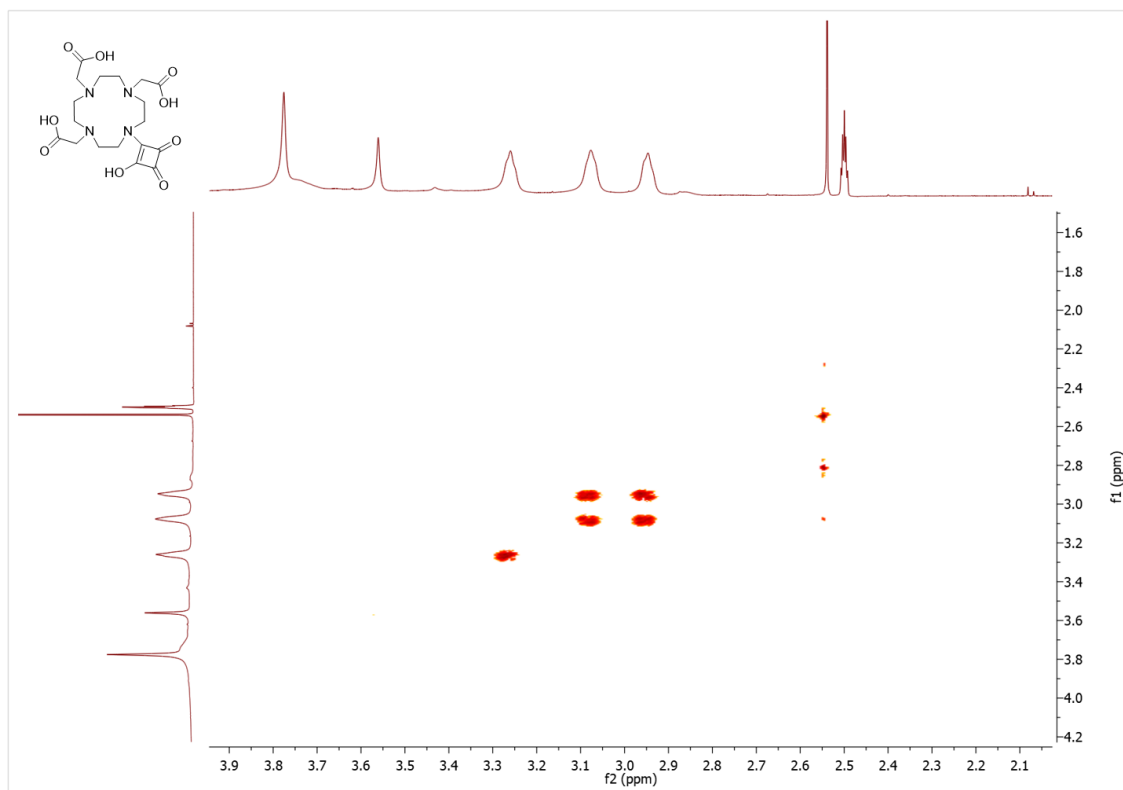
Figure S3.30: COSY spectrum of **DO3A-Sq-OH (3.5)** in DMSO-d_6.
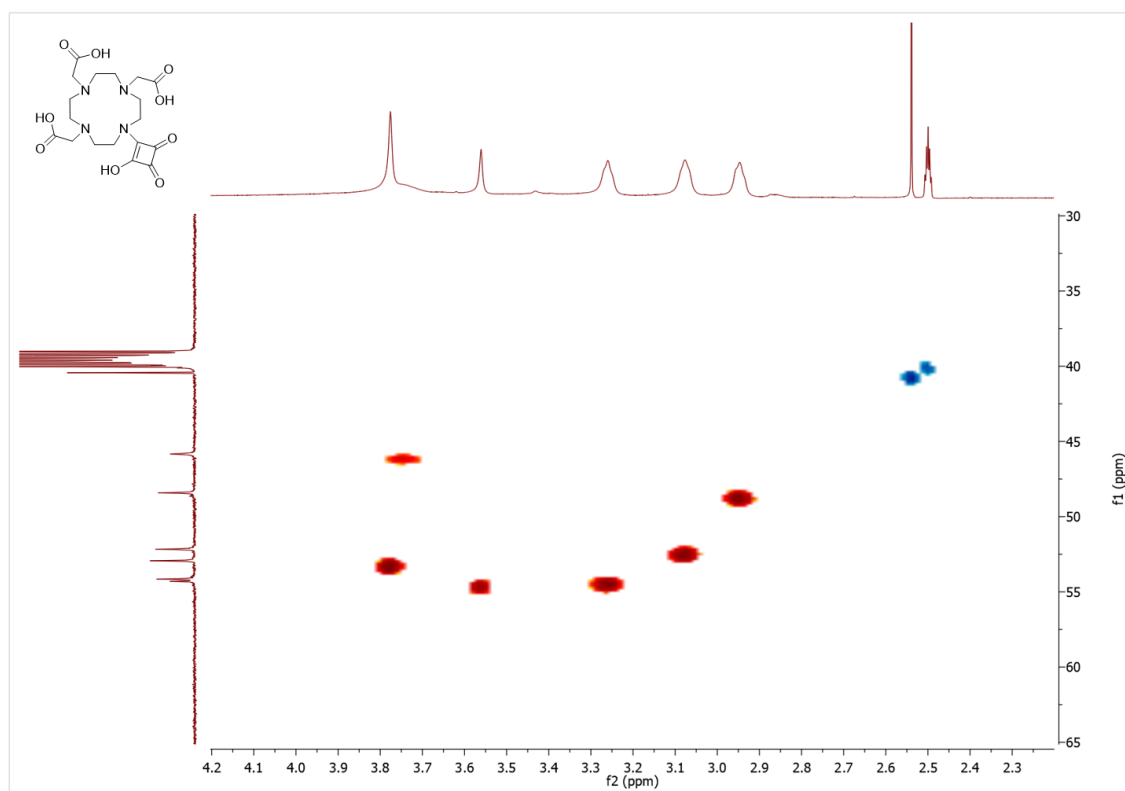
Figure S3.31: HSQC spectrum of **DO3A-Sq-OH (3.5)** in DMSO-d_6.
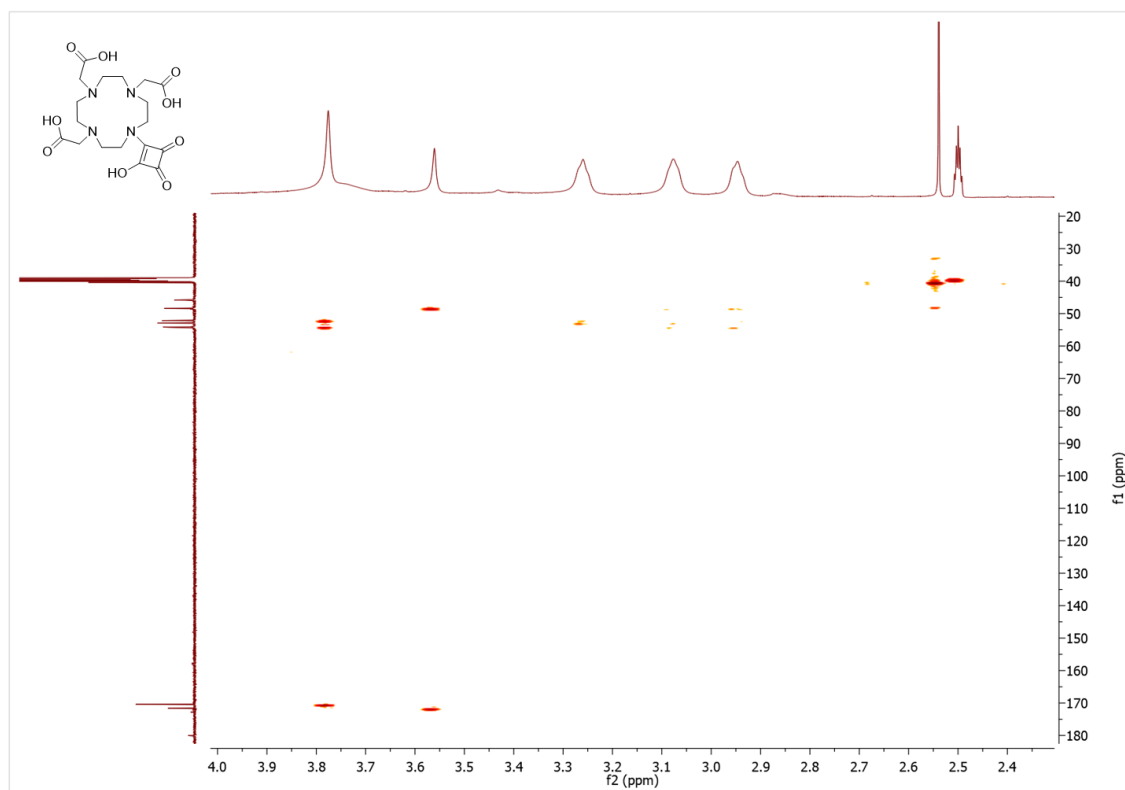
Figure S3.32: HMBC spectrum of **DO3A-Sq-OH (3.5)** in DMSO-d_6.

Compound Table

Compound Label	RT (min)	Observed mass (m/z)	Neutral observed mass (Da)	Theoretical mass (Da)	Mass error (ppm)	Isotope match score (%)
Cpd 1: C18 H26 N4 O9	0.84	443.1780	442.1707	442.1700	1.59	99.51

Mass errors of between -5.00 and 5.00 ppm with isotope match scores above 60% are considered confirmation of molecular formulae
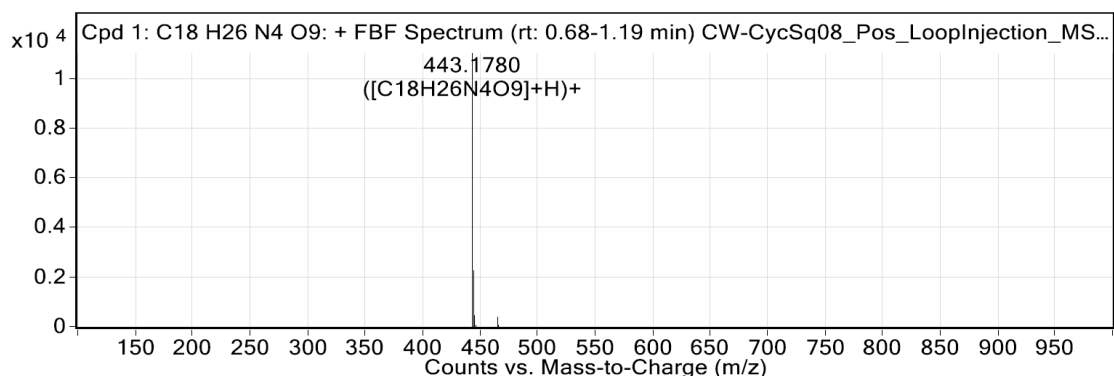
Figure: Full range view of Compound spectra and potential adducts.
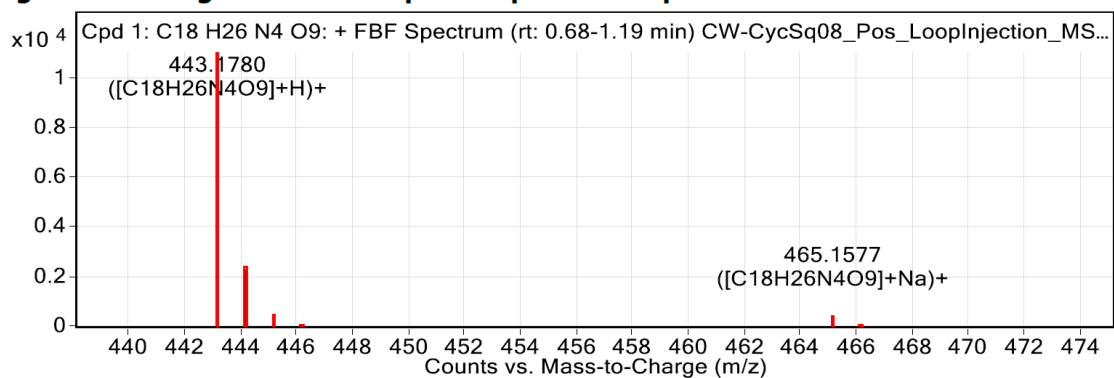
Figure: Zoomed Compound spectra view
(red boxes indicating expected theoretical isotope spacing and abundance)

Compound isotope peak List

m/z	z	Abund	Formula	Ion
443.1780	1	10995.4	C18H26N4O9	(M+H)+
444.1813	1	2274.8	C18H26N4O9	(M+H)+
445.1833	1	442.4	C18H26N4O9	(M+H)+
446.1834	1	65.7	C18H26N4O9	(M+H)+
465.1577	1	393.4	C18H26N4O9	(M+Na)+
466.1598	1	77.1	C18H26N4O9	(M+Na)+

Figure S3.33: HRMS data for **DO3A-Sq-OH (3.5)**.
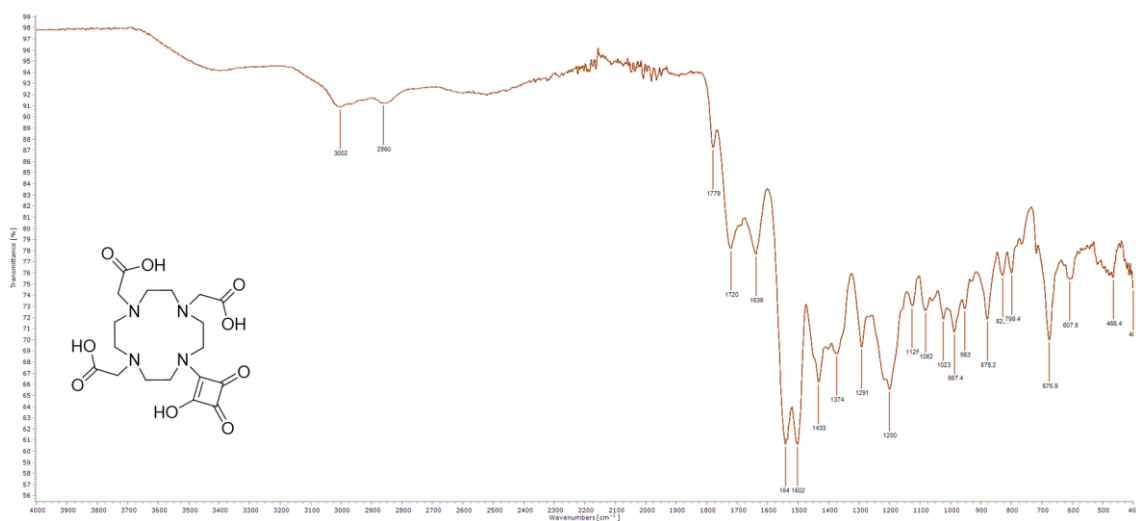
Figure S3.34: FTIR-ATR spectrum of **DO3A-Sq-OH (3.5)**.
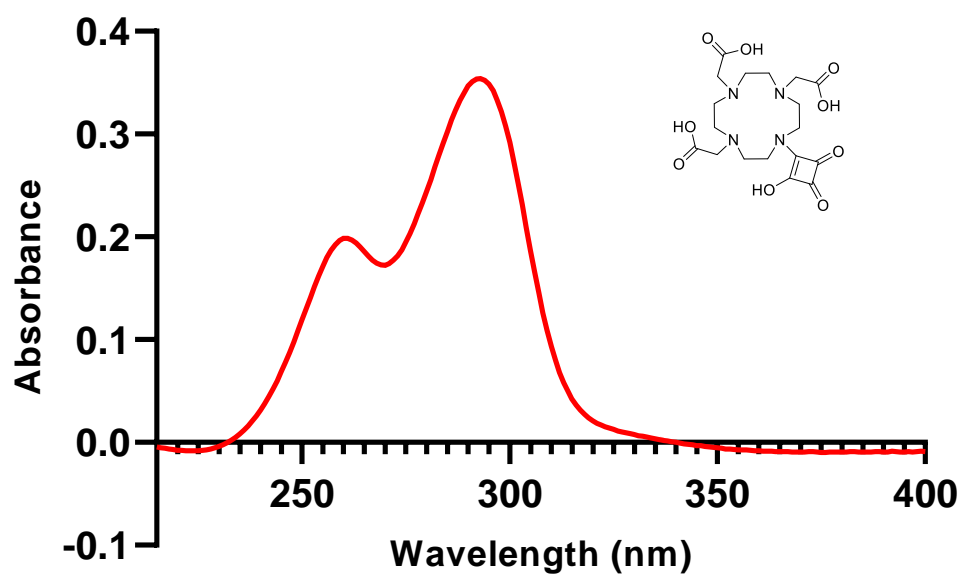
Figure S3.35: Absorbance spectrum of **DO3A-Sq-OH (3.5)** (20 µM) in H$_2$O.
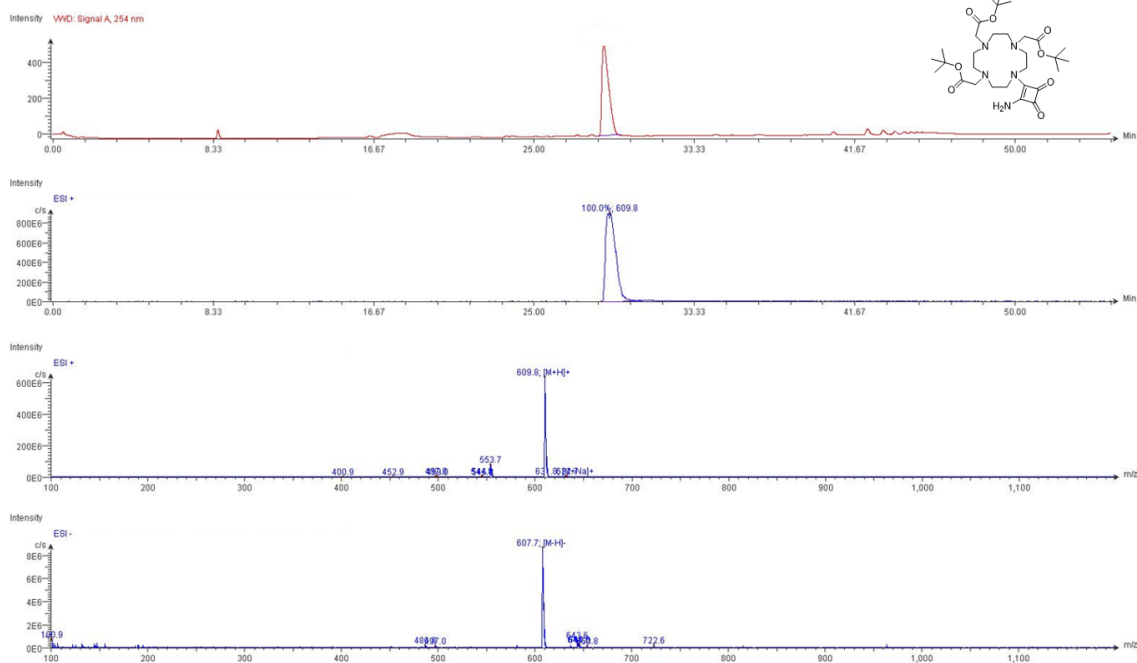
Figure S3.36: LC-MS data for **DO3A*t*Bu-Sq-NH₂ (3.6*)**.
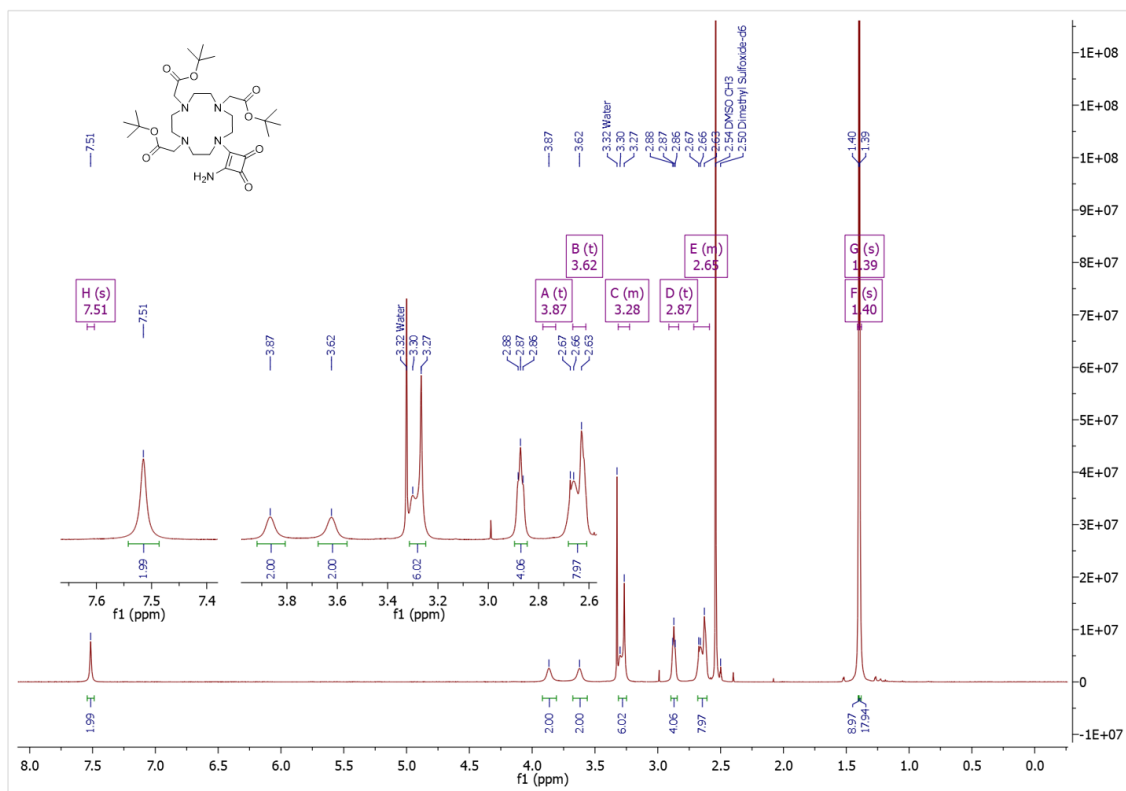
Figure S3.37: ¹H NMR spectrum of **DO3A*t*Bu-Sq-NH₂ (3.6*)** in DMSO-*d₆*.
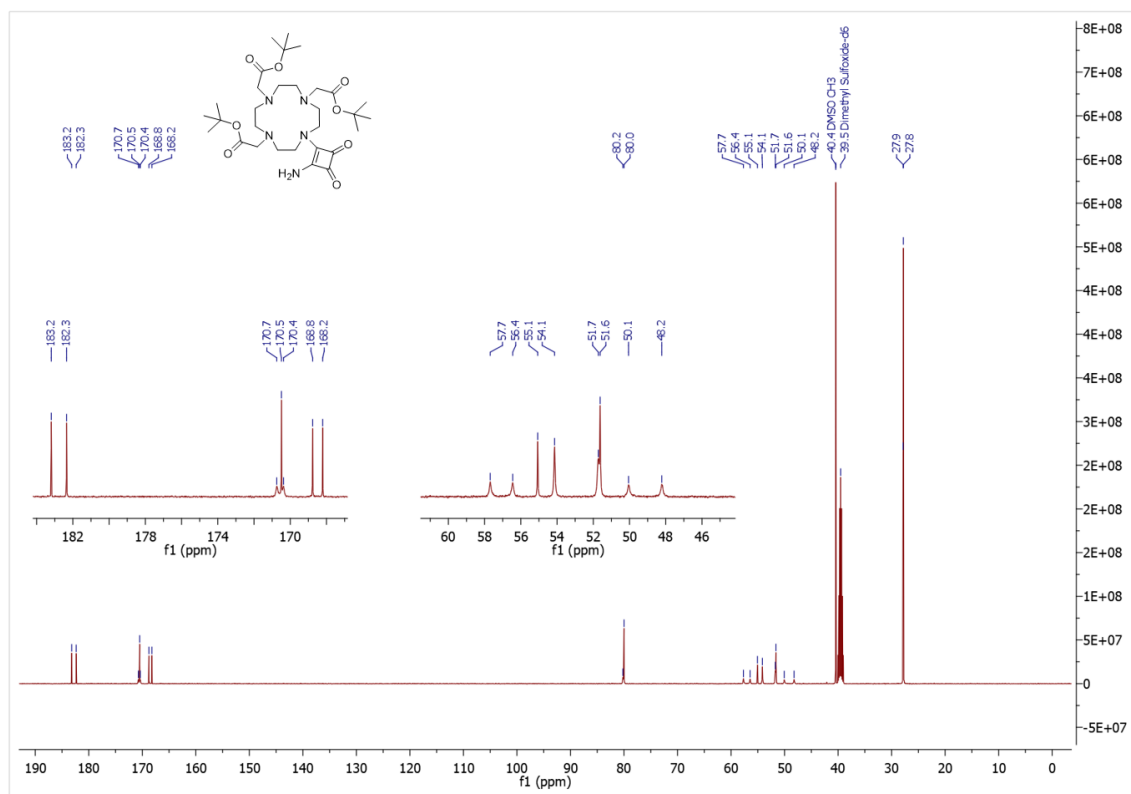
Figure S3.38: ^{13}C NMR spectrum of **DO3A*t*Bu-Sq-NH$_2$ (3.6*)** in DMSO-d_6.
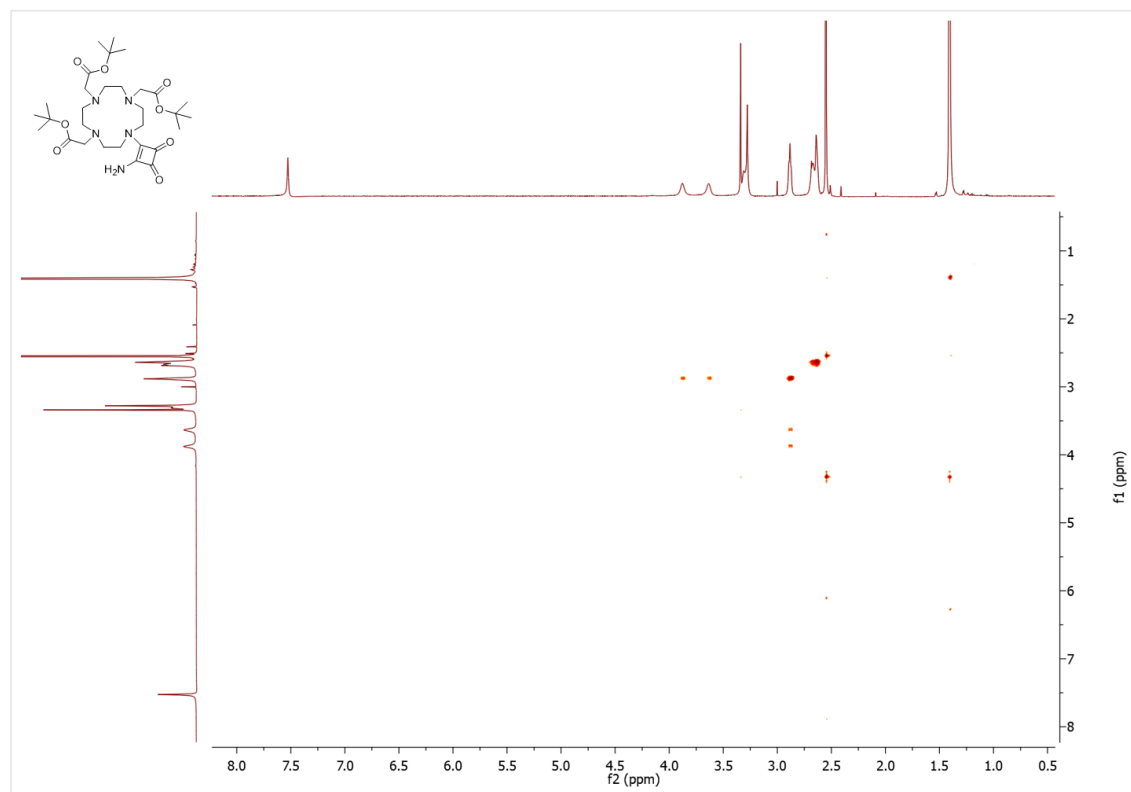
Figure S3.39: COSY spectrum of **DO3A*t*Bu-Sq-NH$_2$ (3.6*)** in DMSO-d_6.

317
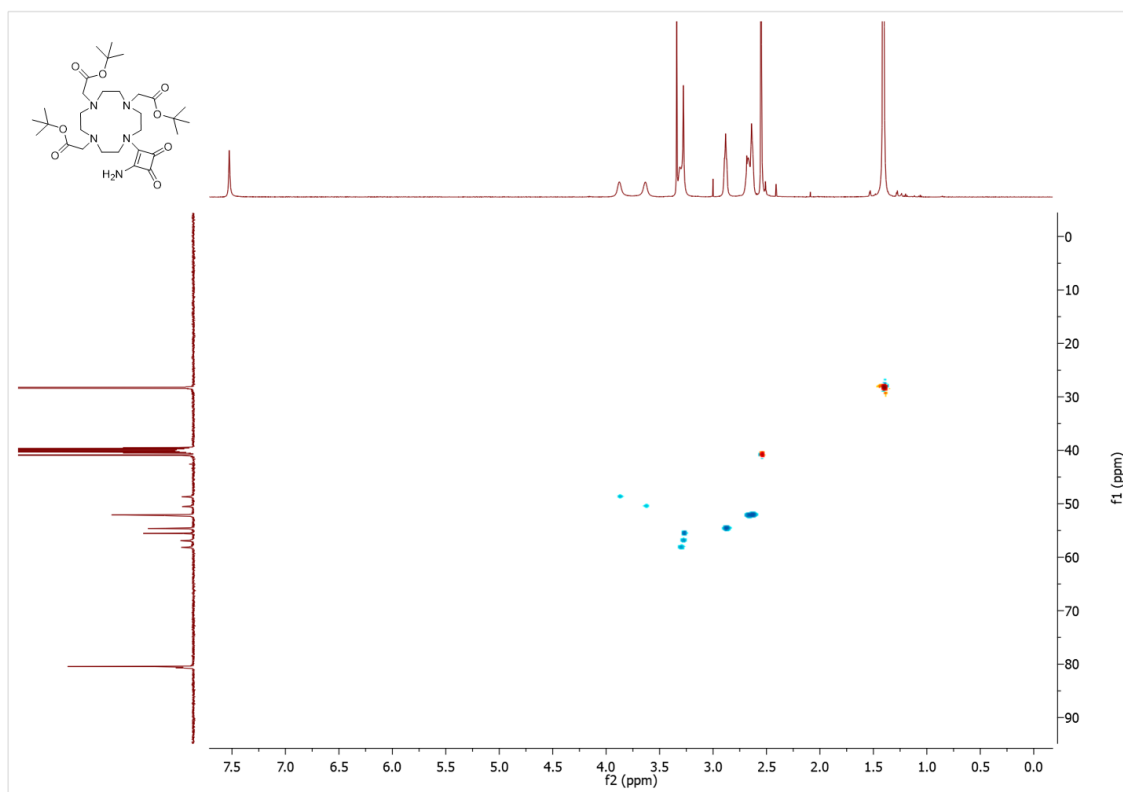
Figure S3.40: HSQC spectrum of **DO3A*t*Bu-Sq-NH₂ (3.6*)** in DMSO-*d*₆.
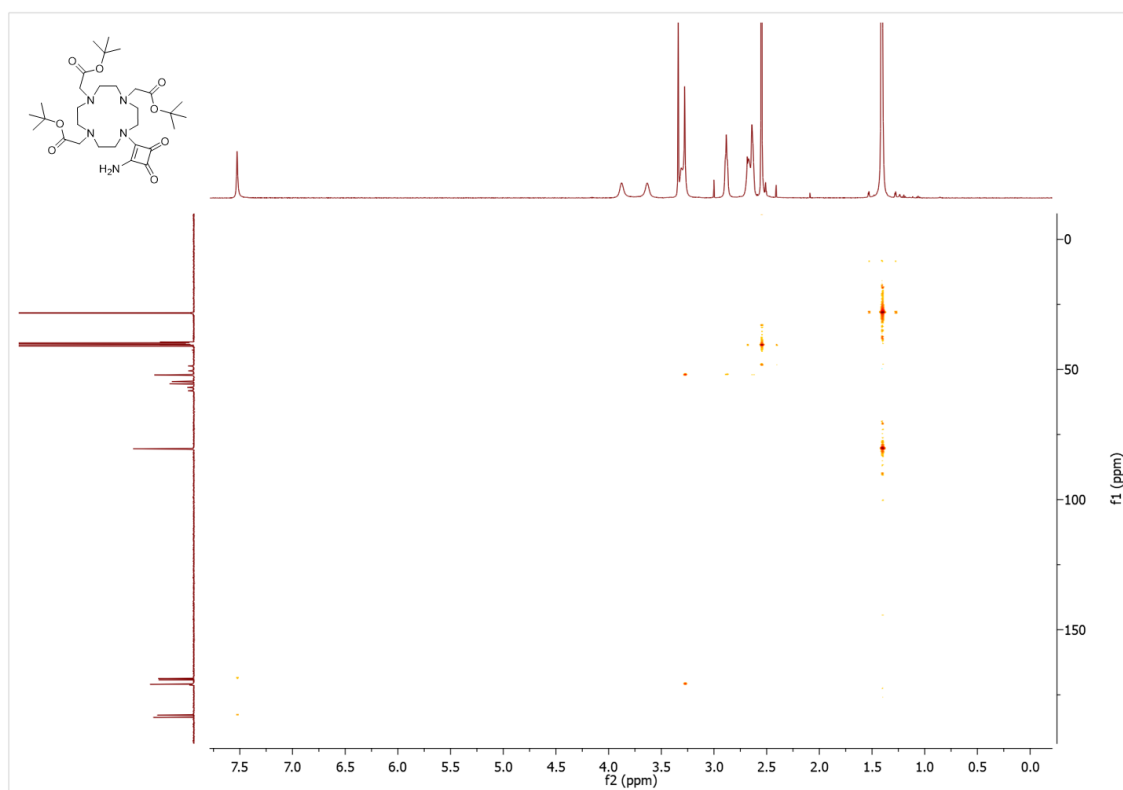
Figure S3.41: HMBC spectrum of **DO3A*t*Bu-Sq-NH₂ (3.6*)** in DMSO-*d*₆.
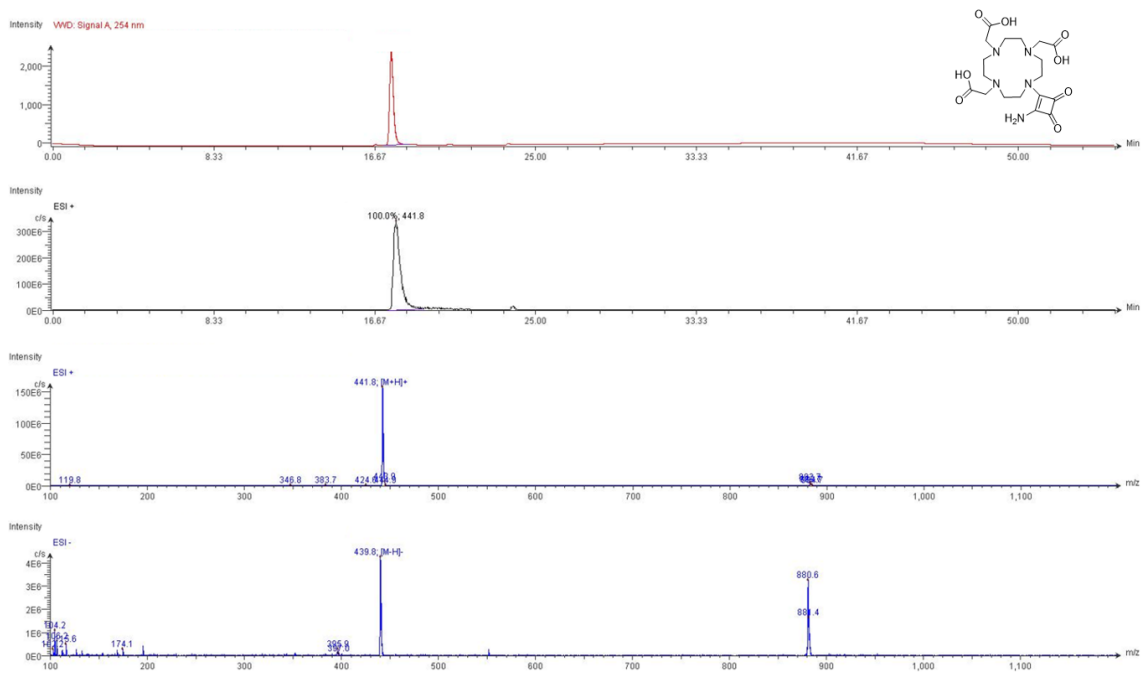
Figure S3.42: LC-MS data for **DO3A-Sq-NH₂ (3.6)**.
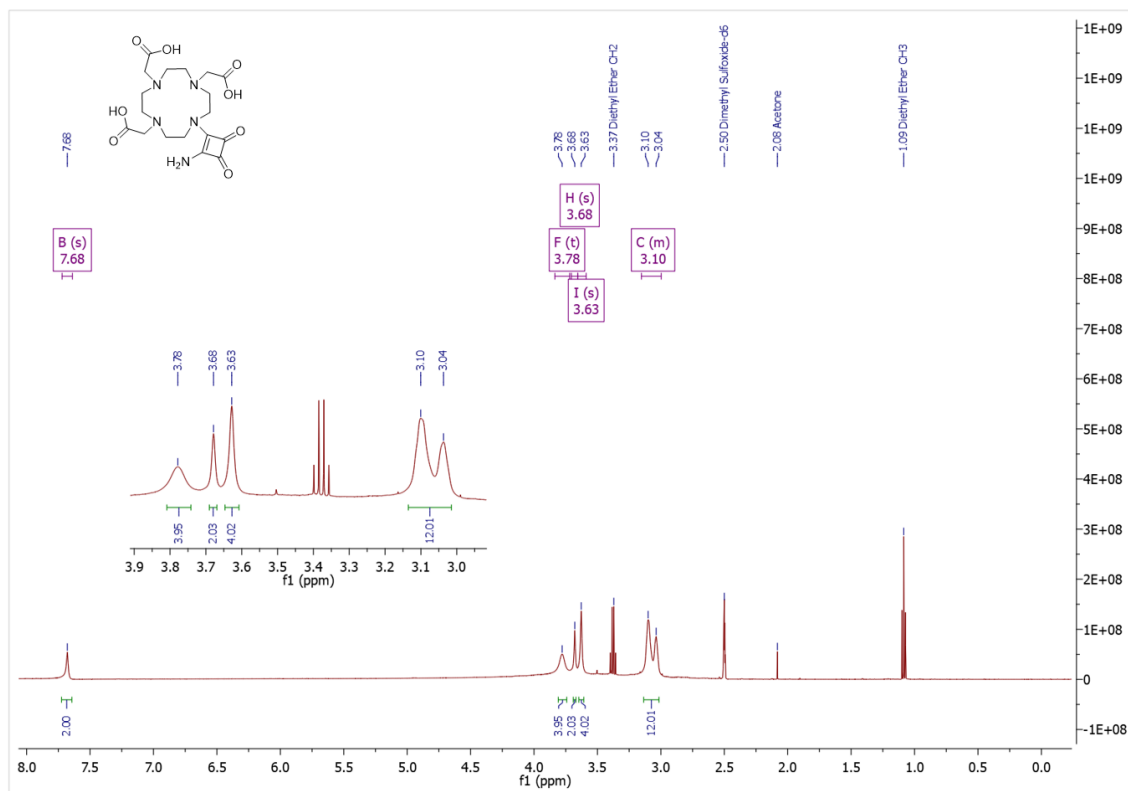
Figure S3.43: ¹H NMR spectrum of **DO3A-Sq-NH₂ (3.6)** in DMSO-*d*₆.
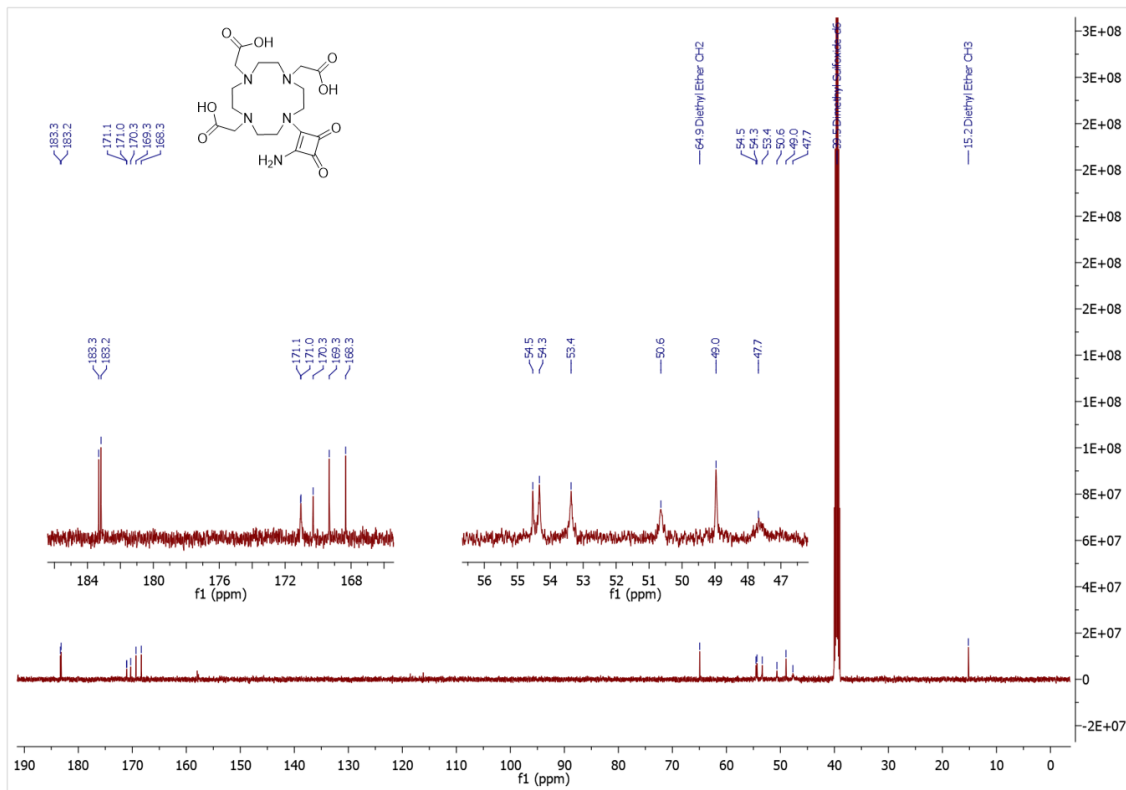
Figure S3.44: ^{13}C NMR spectrum of **DO3A-Sq-NH₂ (3.6)** in DMSO-d_6.
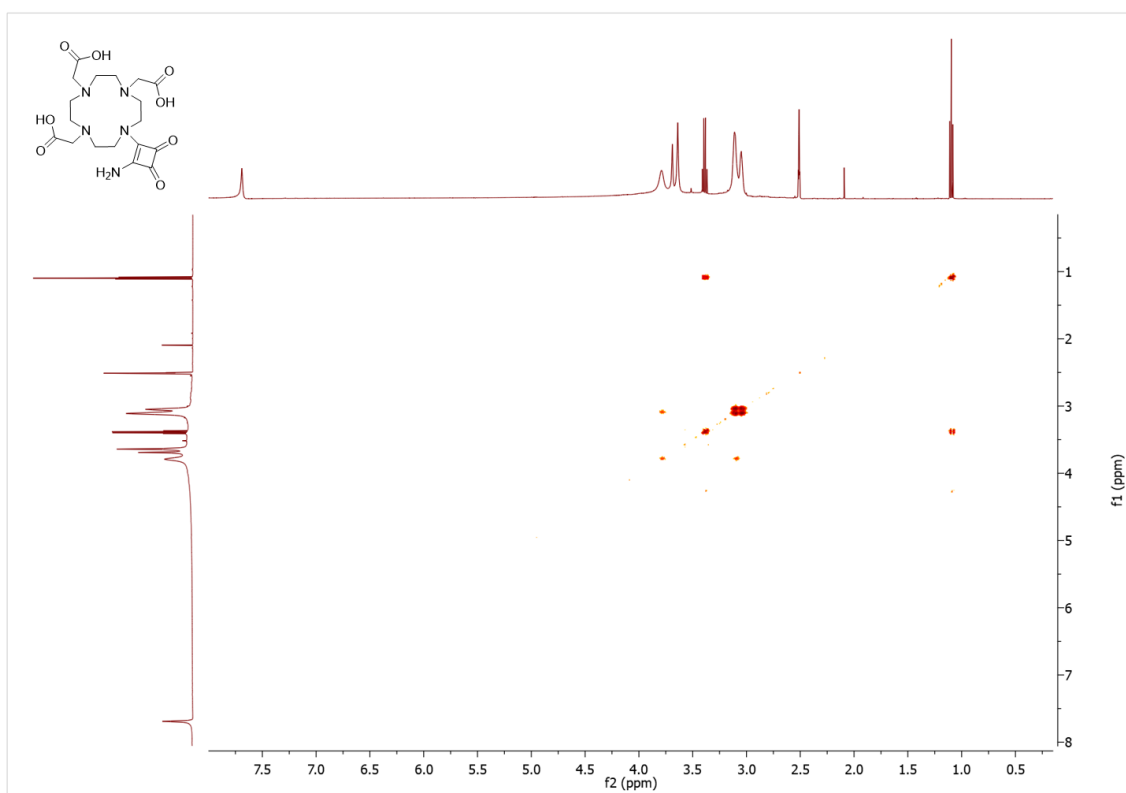
Figure S3.45: COSY spectrum of **DO3A-Sq-NH₂ (3.6)** in DMSO-d_6.
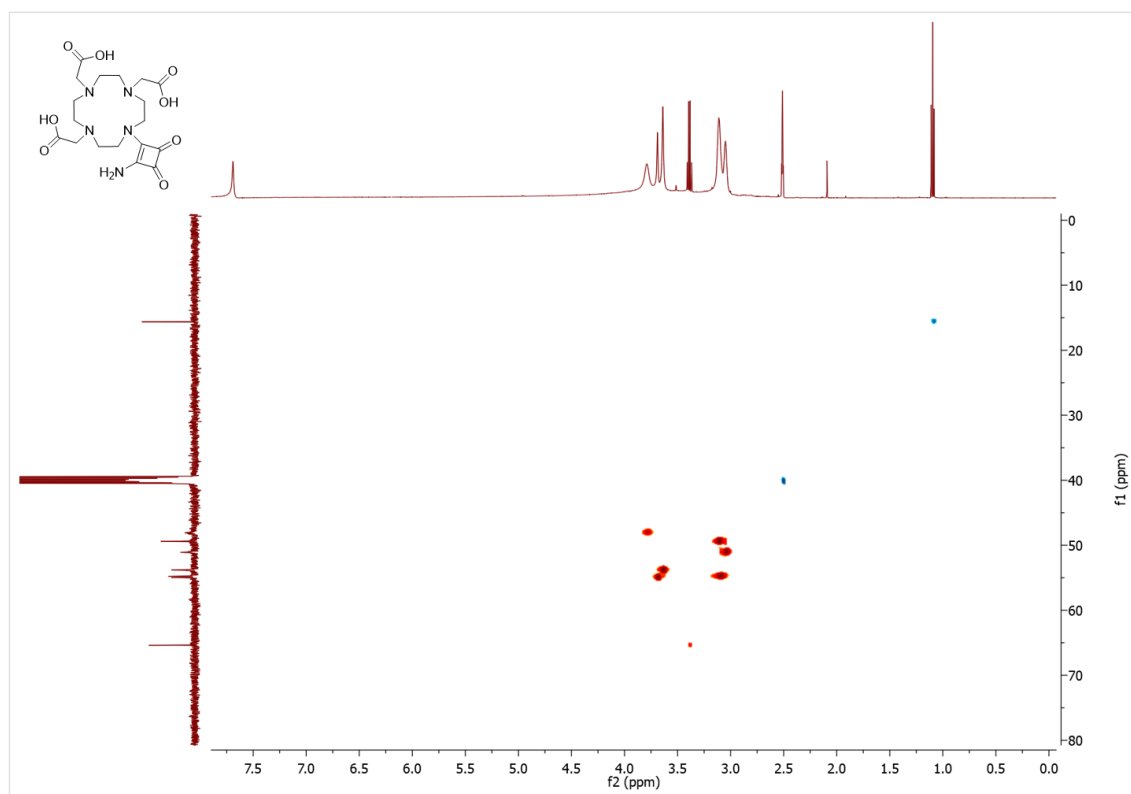
Figure S3.46: HSQC spectrum of **DO3A-Sq-NH₂ (3.6)** in DMSO-d_6.
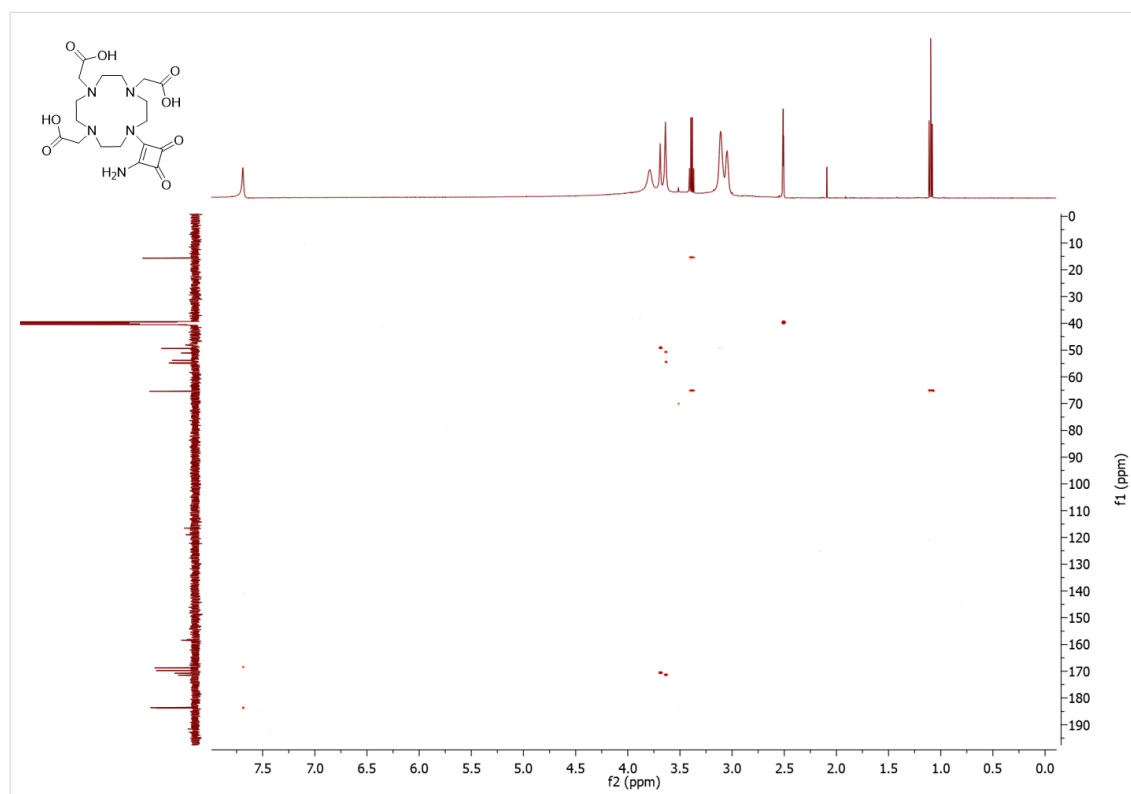
Figure S3.47: HMBC spectrum of **DO3A-Sq-NH₂ (3.6)** in DMSO-d_6.

Compound Table

Compound Label	RT (min)	Observed mass (m/z)	Neutral observed mass (Da)	Theoretical mass (Da)	Mass error (ppm)	Isotope match score (%)
Cpd 1: C18 H27 N5 O8	0.73	442.1935	441.1861	441.1860	0.39	97.58

Mass errors of between -5.00 and 5.00 ppm with isotope match scores above 60% are considered confirmation of molecular formulae

x10 5   Cpd 1: C18 H27 N5 O8: + FBF Spectrum (rt: 0.61-0.86 min) CW-CycSq09_Pos_LoopInjection_MS...
442.1935
([C18H27N5O8]+H)+

Figure: Full range view of Compound spectra and potential adducts.

x10 5   Cpd 1: C18 H27 N5 O8: + FBF Spectrum (rt: 0.61-0.86 min) CW-CycSq09_Pos_LoopInjection_MS...
442.1935
([C18H27N5O8]+H)+
464.1750
([C18H27N5O8]+Na)+
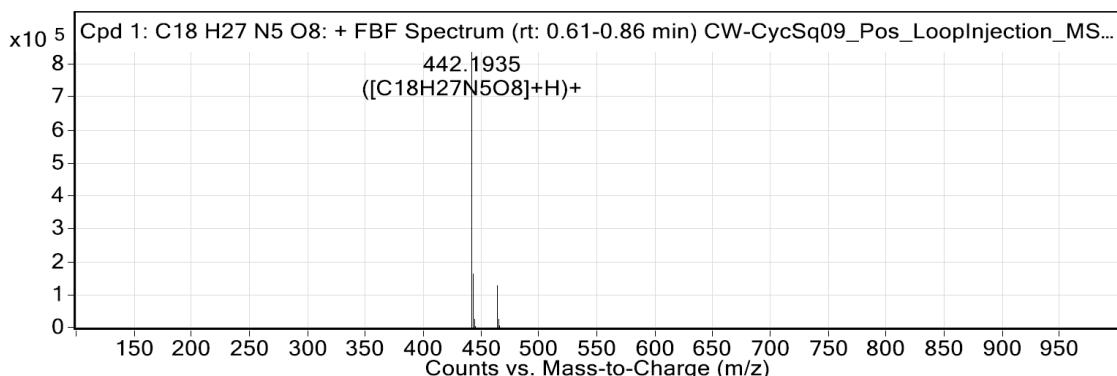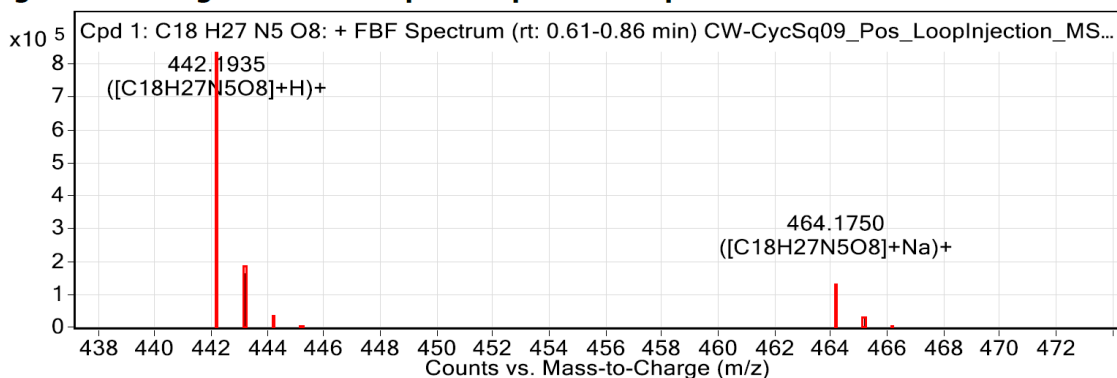
Figure: Zoomed Compound spectra view
(red boxes indicating expected theoretical isotope spacing and abundance)

Compound isotope peak List

m/z	z	Abund	Formula	Ion
442.1935	1	835137.6	C18H27N5O8	(M+H)+
443.1964	1	162025.8	C18H27N5O8	(M+H)+
444.1983	1	26033.3	C18H27N5O8	(M+H)+
445.2011	1	3587.4	C18H27N5O8	(M+H)+
464.1750	1	128079.0	C18H27N5O8	(M+Na)+
465.1778	1	24792.0	C18H27N5O8	(M+Na)+
466.1717	1	5203.3	C18H27N5O8	(M+Na)+

Figure S3.48: HRMS data for **DO3A-Sq-NH$_2$ (3.6)**.

322
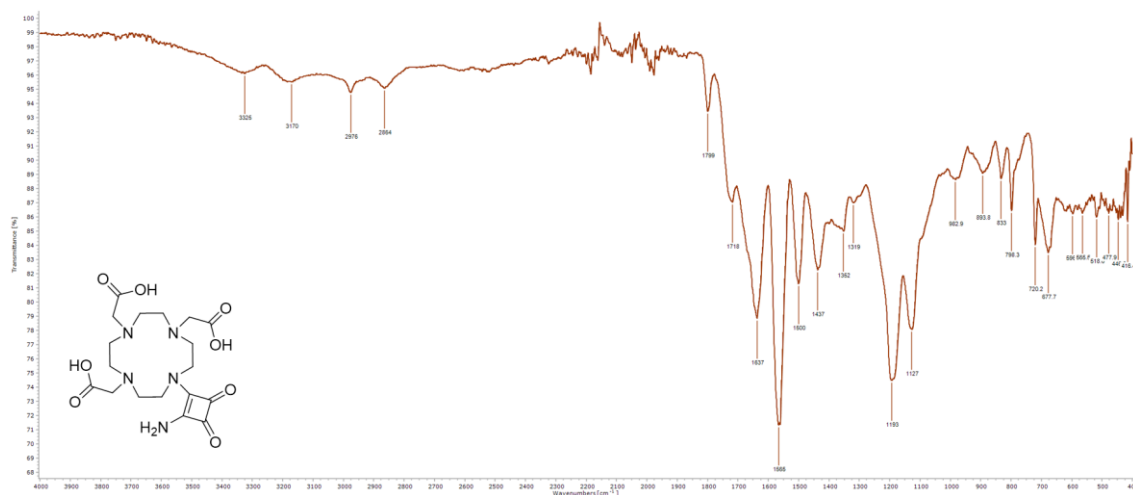
Figure S3.49: FTIR-ATR spectrum of **DO3A-Sq-NH₂ (3.6)**.
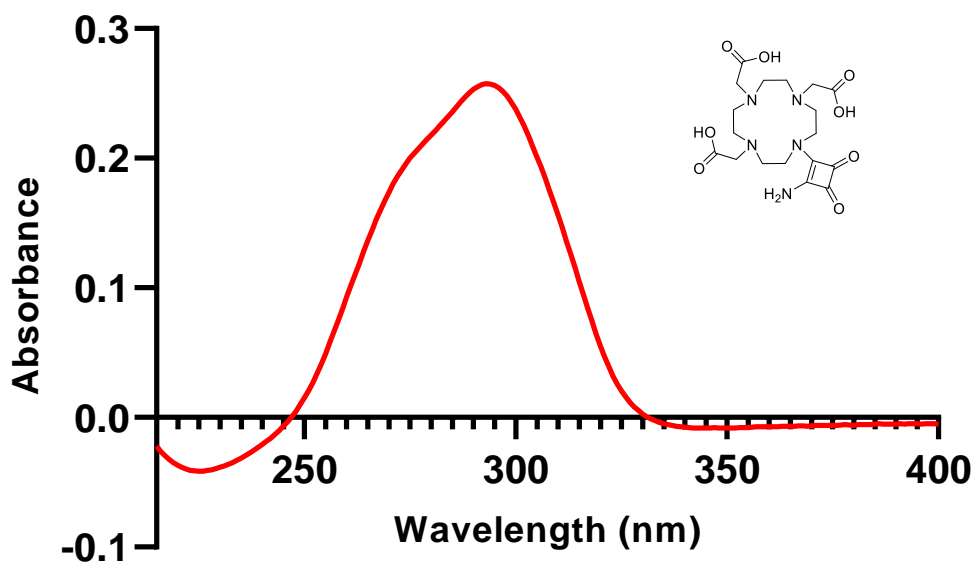
Figure S3.50: Absorbance spectrum of **DO3A-Sq-NH₂ (3.6)** (20 μM) in H₂O.

Figure S3.51: LC-MS data for **DO3A*t*Bu-Sq-EDA (3.7*)**.

Figure S3.52: ¹H NMR spectrum of **DO3A*t*Bu-Sq-EDA (3.7*)** in DMSO-*d*₆.

Figure S3.53: ^{13}C NMR spectrum of **DO3A*t*Bu-Sq-EDA (3.7*)** in DMSO-*d*₆.

Figure S3.54: COSY spectrum of **DO3A*t*Bu-Sq-EDA (3.7*)** in DMSO-*d*₆.
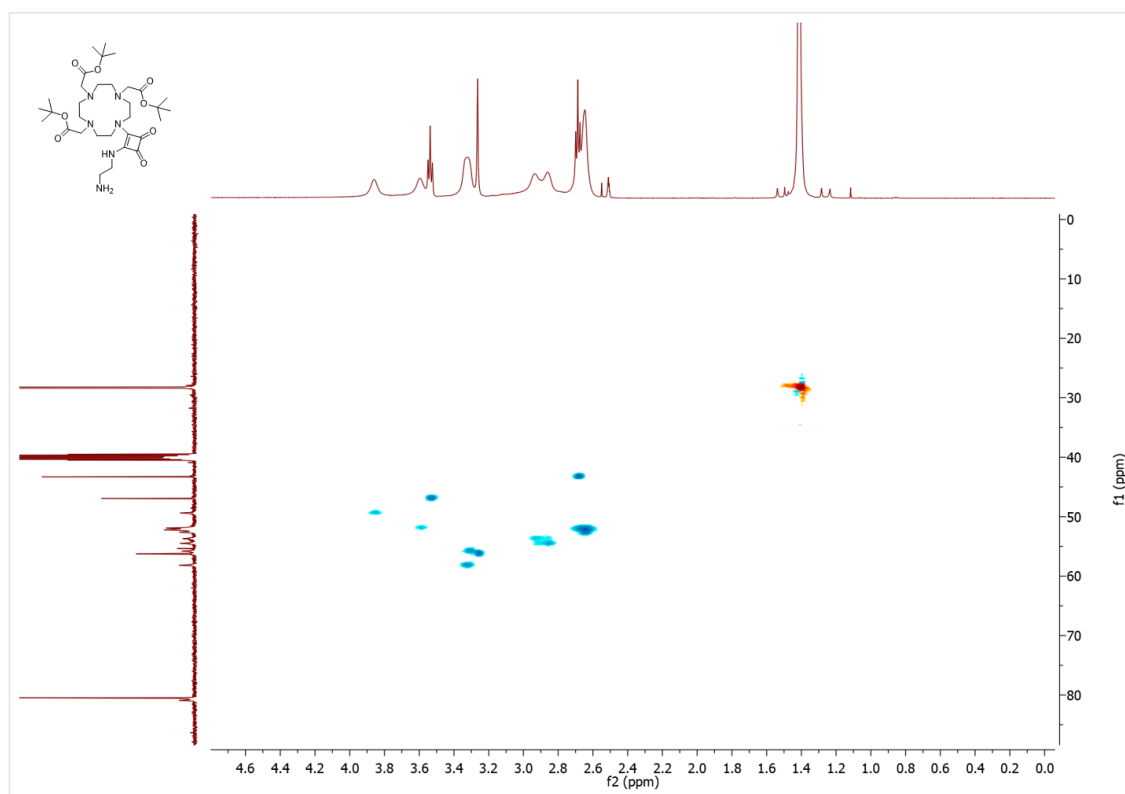
Figure S3.55: HSQC spectrum of **DO3A*t*Bu-Sq-EDA (3.7*)** in DMSO-d_6.
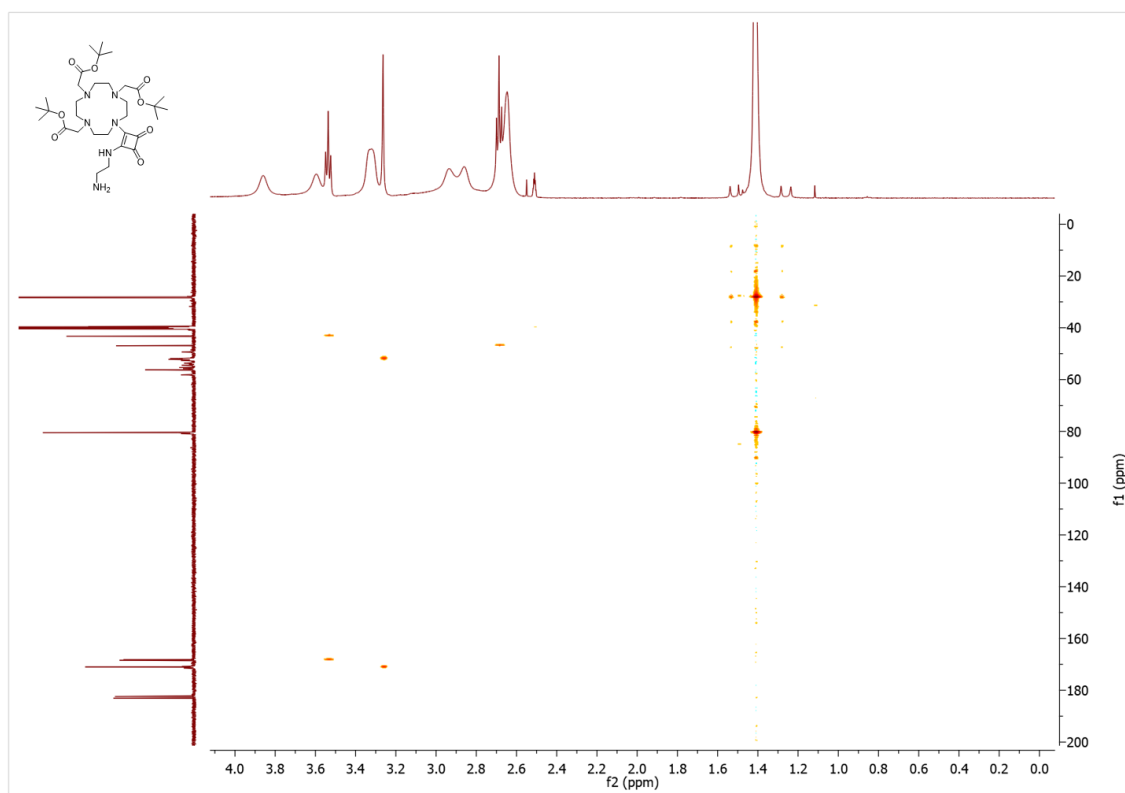
Figure S3.56: HNBC spectrum of **DO3A*t*Bu-Sq-EDA (3.7*)** in DMSO-d_6.

Compound Table

Compound Label	RT (min)	Observed mass (m/z)	Neutral observed mass (Da)	Theoretical mass (Da)	Mass error (ppm)	Isotope match score (%)
Cpd 1: C32 H56 N6 O8	0.72	653.4237	652.4163	652.4160	0.54	99.81

Mass errors of between -5.00 and 5.00 ppm with isotope match scores above 60% are considered confirmation of molecular formulae
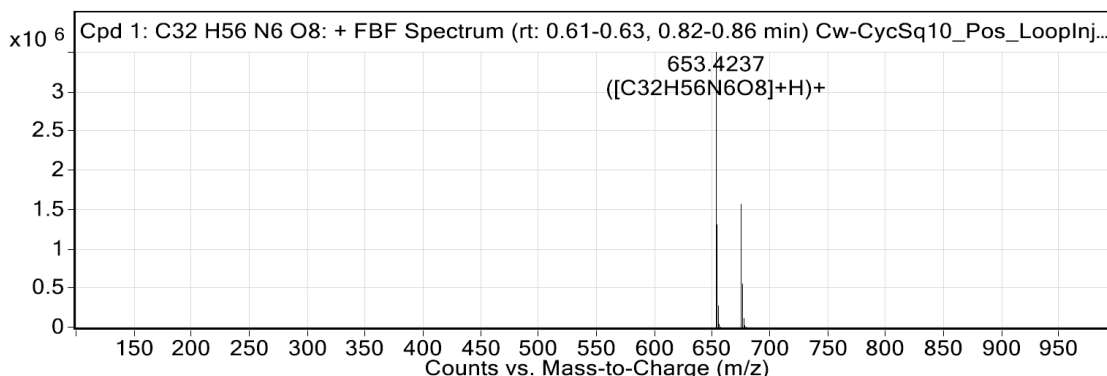
Figure: Full range view of Compound spectra and potential adducts.
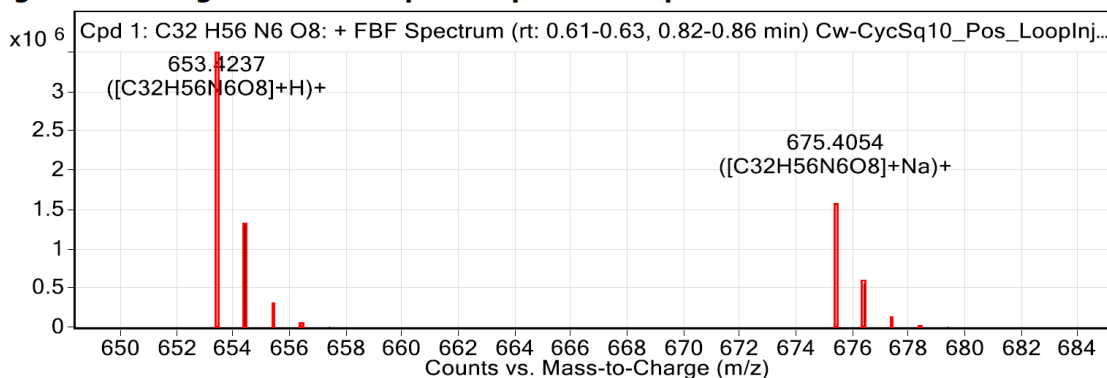
Figure: Zoomed Compound spectra view
(red boxes indicating expected theoretical isotope spacing and abundance)

Compound isotope peak List

m/z	z	Abund	Formula	Ion
653.4237	1	3501042.3	C32H56N6O8	(M+H)+
654.4266	1	1310049.4	C32H56N6O8	(M+H)+
655.4293	1	277183.3	C32H56N6O8	(M+H)+
656.4311	1	40306.7	C32H56N6O8	(M+H)+
657.4328	1	5462.9	C32H56N6O8	(M+H)+
675.4054	1	1567033.3	C32H56N6O8	(M+Na)+
676.4087	1	551677.6	C32H56N6O8	(M+Na)+
677.4108	1	113709.0	C32H56N6O8	(M+Na)+
678.4128	1	17917.1	C32H56N6O8	(M+Na)+
679.4144	1	3690.4	C32H56N6O8	(M+Na)+

Figure S3.57: HRMS data for **DO3A*t*Bu-Sq-EDA (3.7*)**.
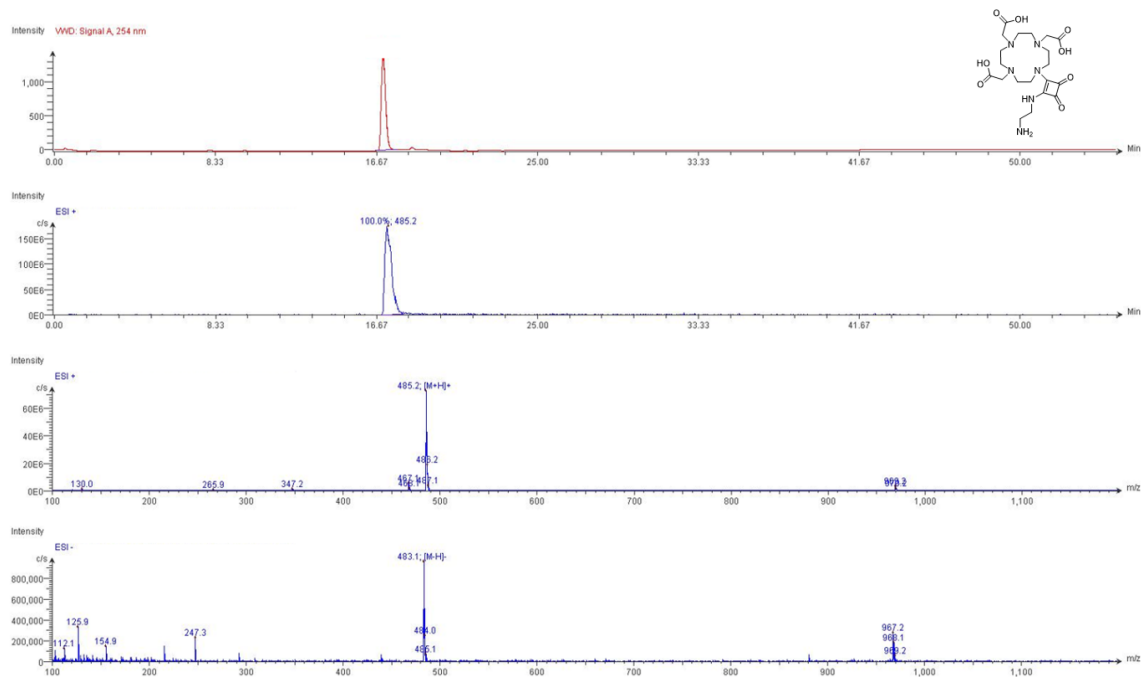
Figure S3.58: LC-MS data for **DO3A-Sq-EDA (3.7)**.
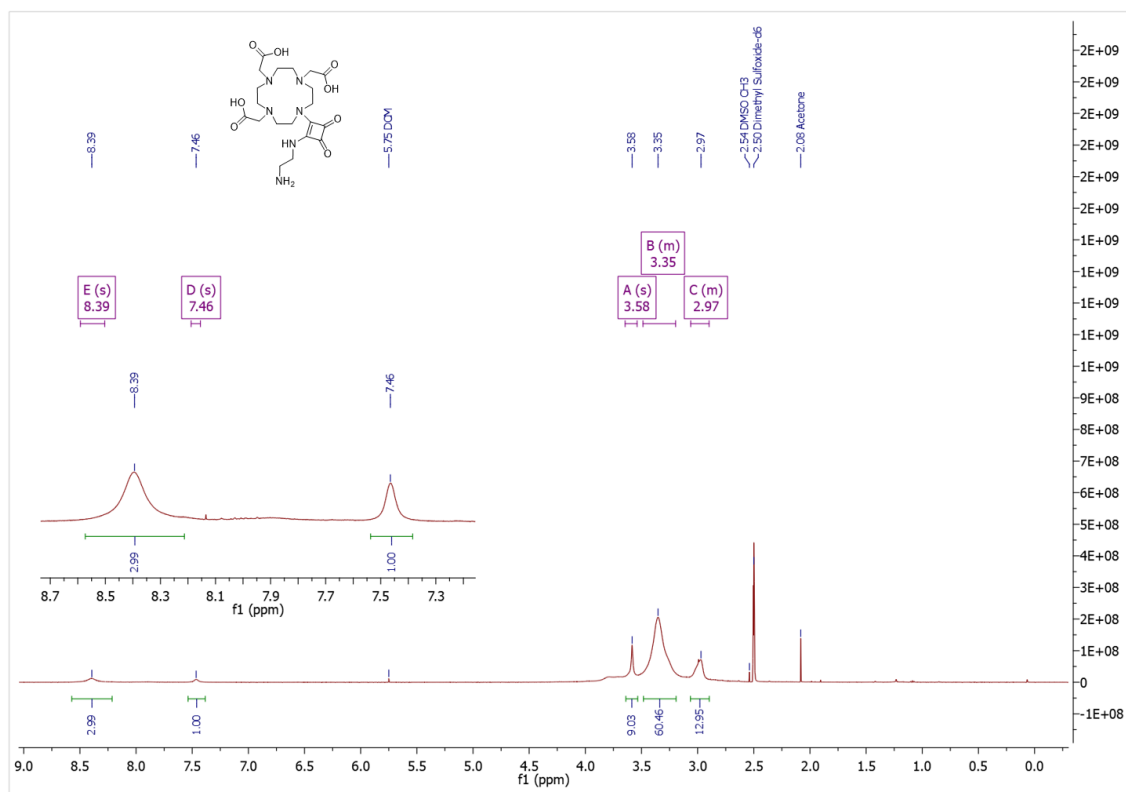
Figure S3.59: ^{1}H NMR spectrum of **DO3A-Sq-EDA (3.7)** in DMSO-d_6.
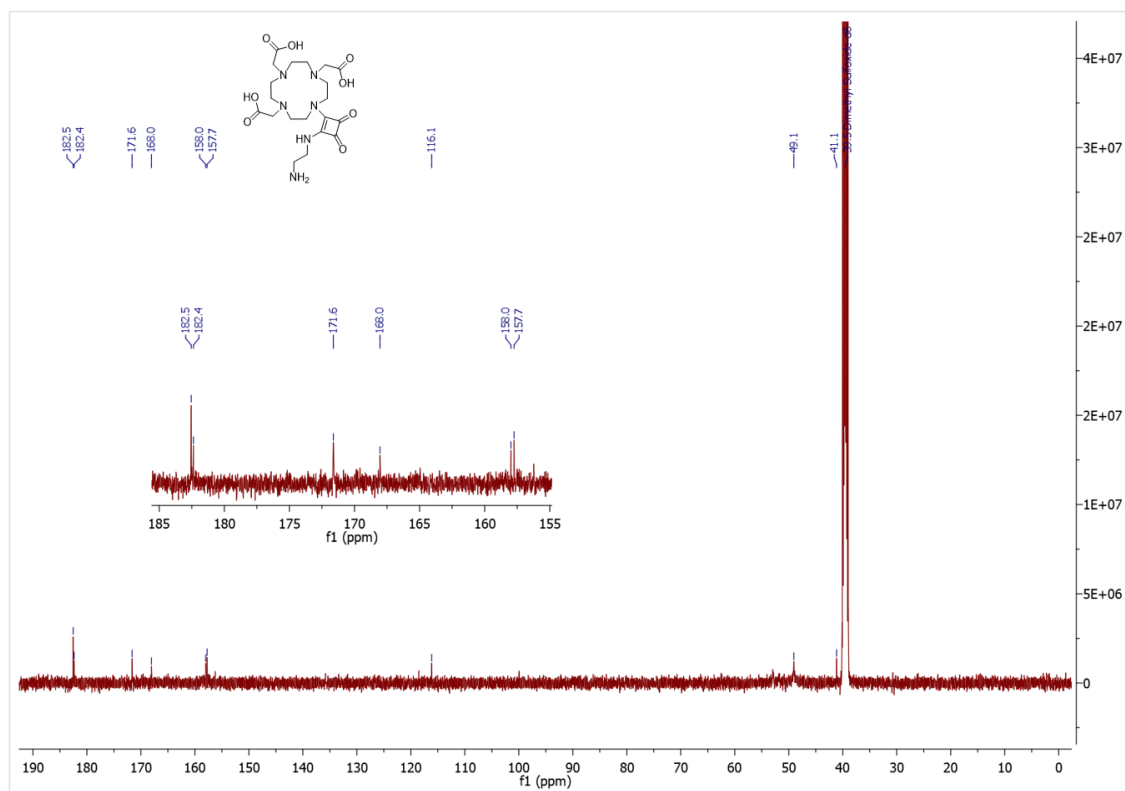
Figure S3.60: ^{13}C NMR spectrum of **DO3A-Sq-EDA (3.7)** in DMSO-d_6.

Compound Table

Compound Label	RT (min)	Observed mass (m/z)	Neutral observed mass (Da)	Theoretical mass (Da)	Mass error (ppm)	Isotope match score (%)
Cpd 1: C20 H32 N6 O8	0.72	485.2357	484.2285	484.2282	0.62	99.26

Mass errors of between -5.00 and 5.00 ppm with isotope match scores above 60% are considered confirmation of molecular formulae

Cpd 1: C20 H32 N6 O8: + FBF Spectrum (rt: 0.61-0.84 min) CW-CycSq11_Pos_LoopInjection_MS...

485.2357
([C20H32N6O8]+H)+

Figure: Full range view of Compound spectra and potential adducts.

Cpd 1: C20 H32 N6 O8: + FBF Spectrum (rt: 0.61-0.84 min) CW-CycSq11_Pos_LoopInjection_MS...

485.2357
([C20H32N6O8]+H)+

507.2176
([C20H32N6O8]+Na)+
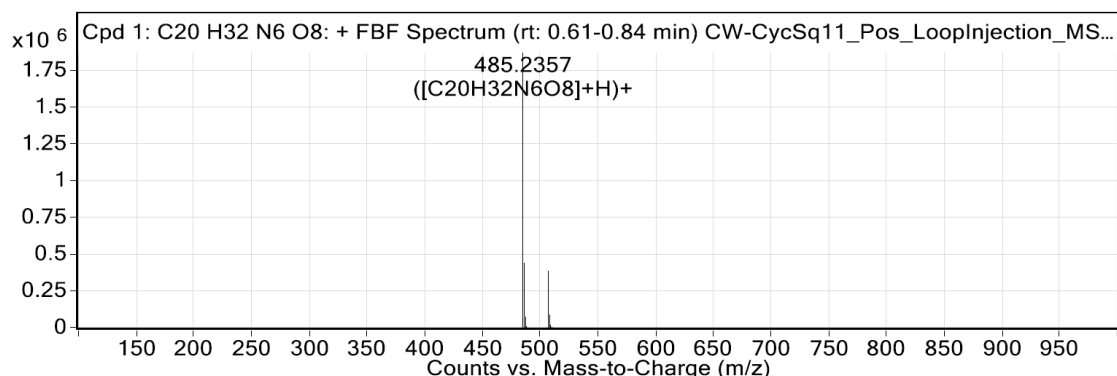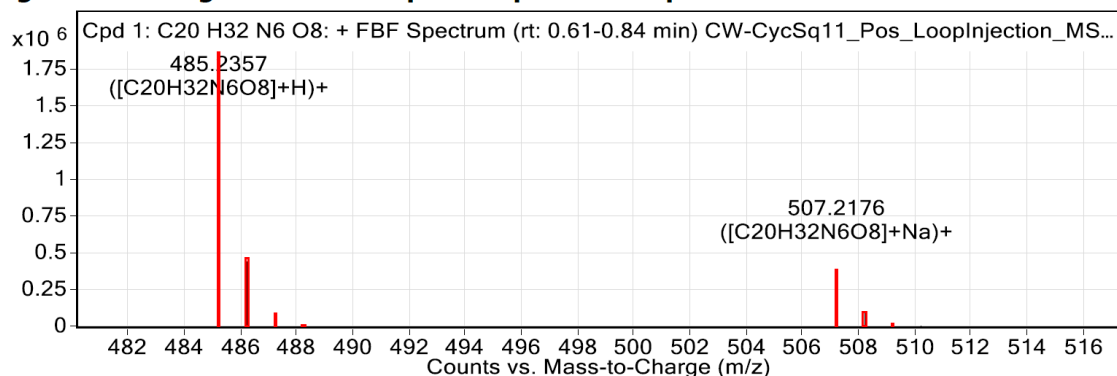
Figure: Zoomed Compound spectra view
(red boxes indicating expected theoretical isotope spacing and abundance)

Compound isotope peak List

m/z	z	Abund	Formula	Ion
485.2357	1	1869529.5	C20H32N6O8	(M+H)+
486.2389	1	437387.3	C20H32N6O8	(M+H)+
487.2407	1	69952.4	C20H32N6O8	(M+H)+
488.2430	1	8747.3	C20H32N6O8	(M+H)+
507.2176	1	386149.2	C20H32N6O8	(M+Na)+
508.2202	1	86187.6	C20H32N6O8	(M+Na)+
509.2224	1	14955.4	C20H32N6O8	(M+Na)+
510.2236	1	2149.0	C20H32N6O8	(M+Na)+

Figure S3.61: HRMS data for **DO3A-Sq-EDA (3.7)**.
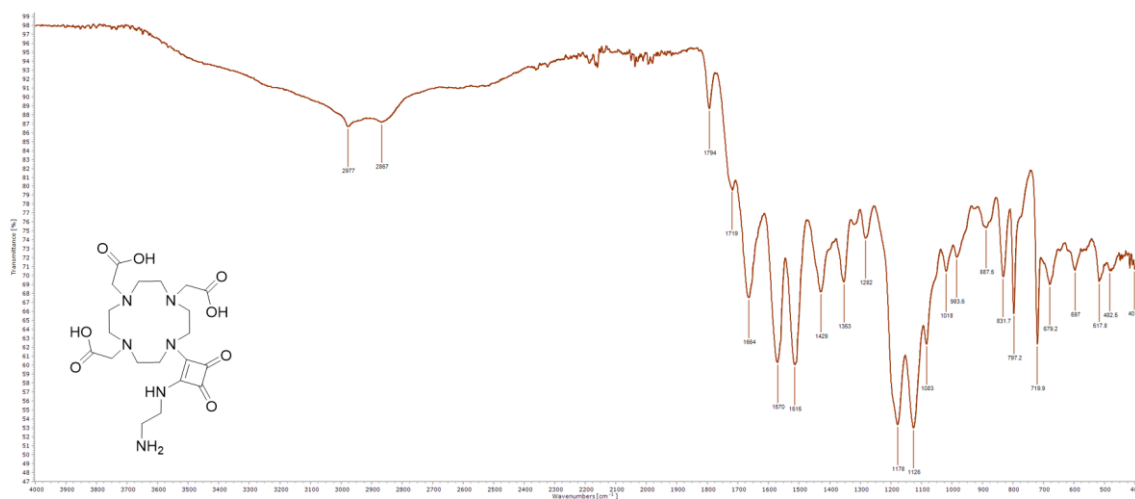
Figure S3.62: FTIR-ATR spectrum of **DO3A-Sq-EDA (3.7)**.
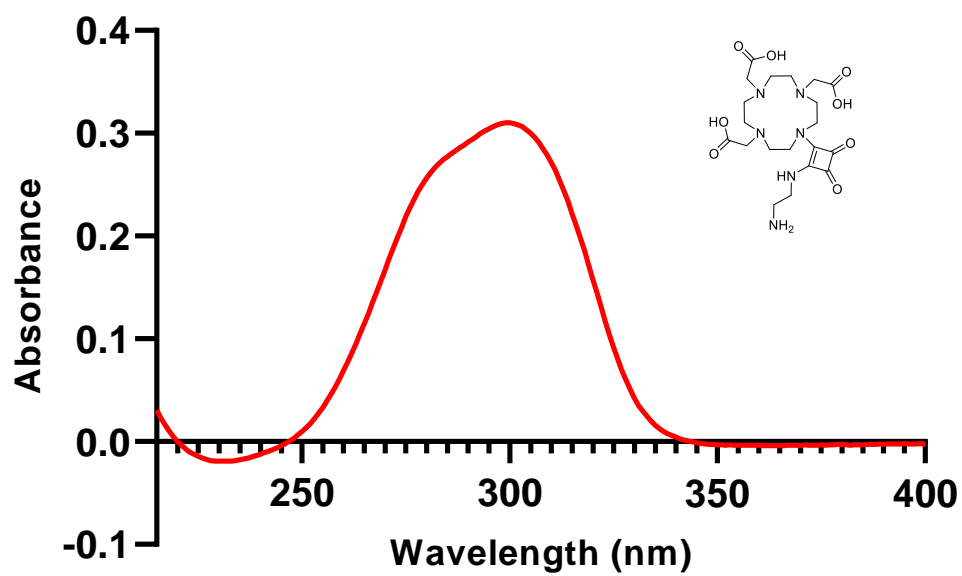
Figure S3.63: Absorbance spectrum of **DO3A-Sq-EDA (3.7)** (20 µM) in H$_2$O.

Figure S3.64: LC-MS data for **DO2A*t*Bu-2ESq (3.8)**.

Figure S3.65: ¹H NMR spectrum of **DO2A*t*Bu-2ESq (3.8)** in DMSO-*d₆*.
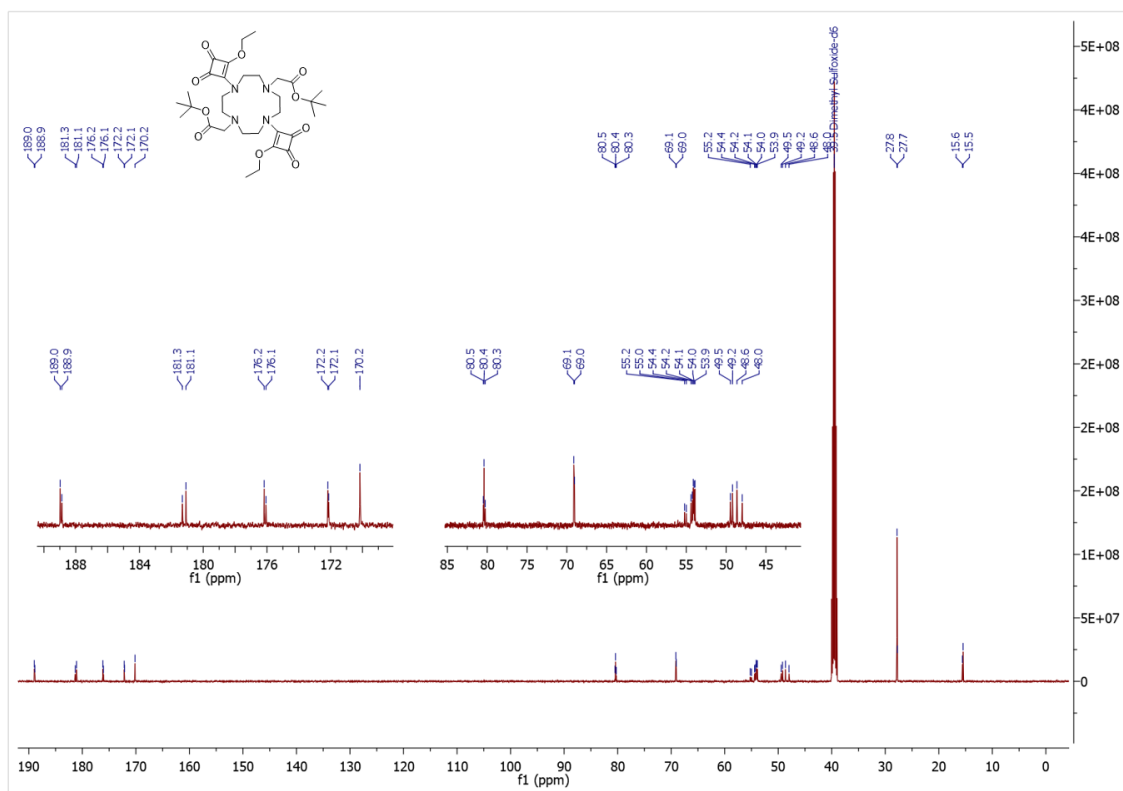
Figure S3.66: ^{13}C NMR spectrum of **DO2A*t*Bu-2ESq (3.8)** in DMSO-d_6.
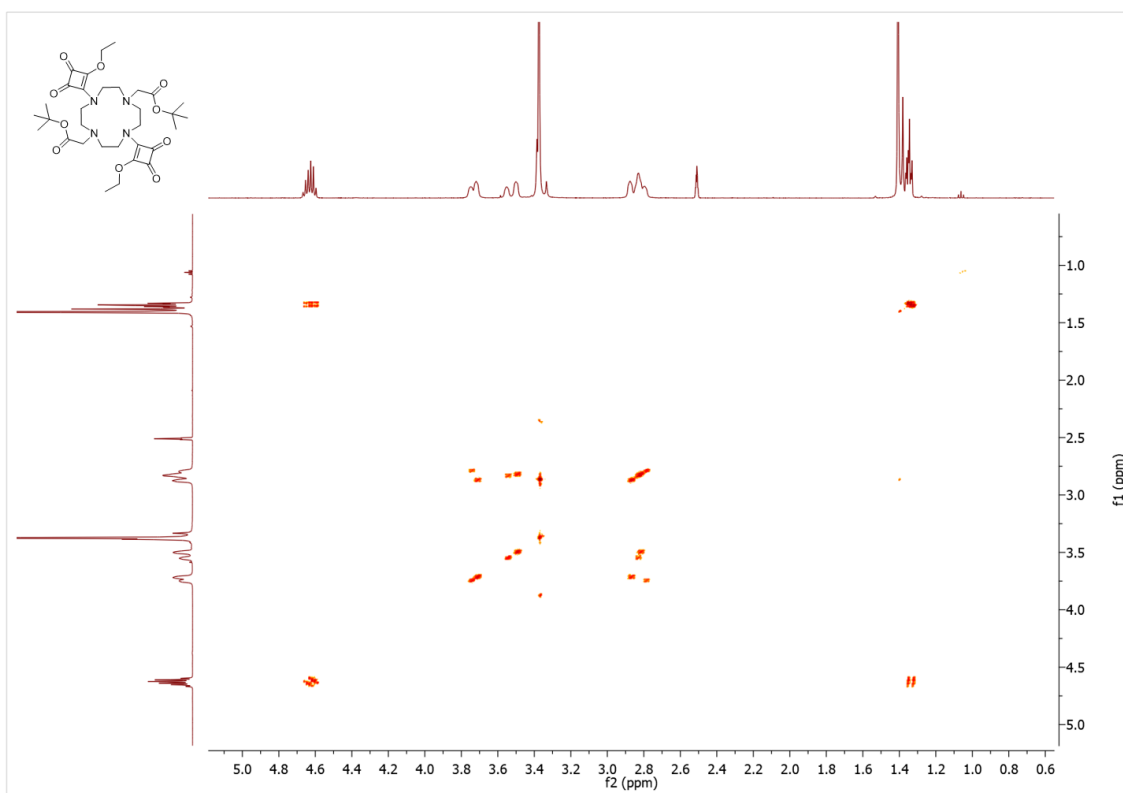
Figure S3.67: COSY spectrum of **DO2A*t*Bu-2ESq (3.8)** in DMSO-d_6.
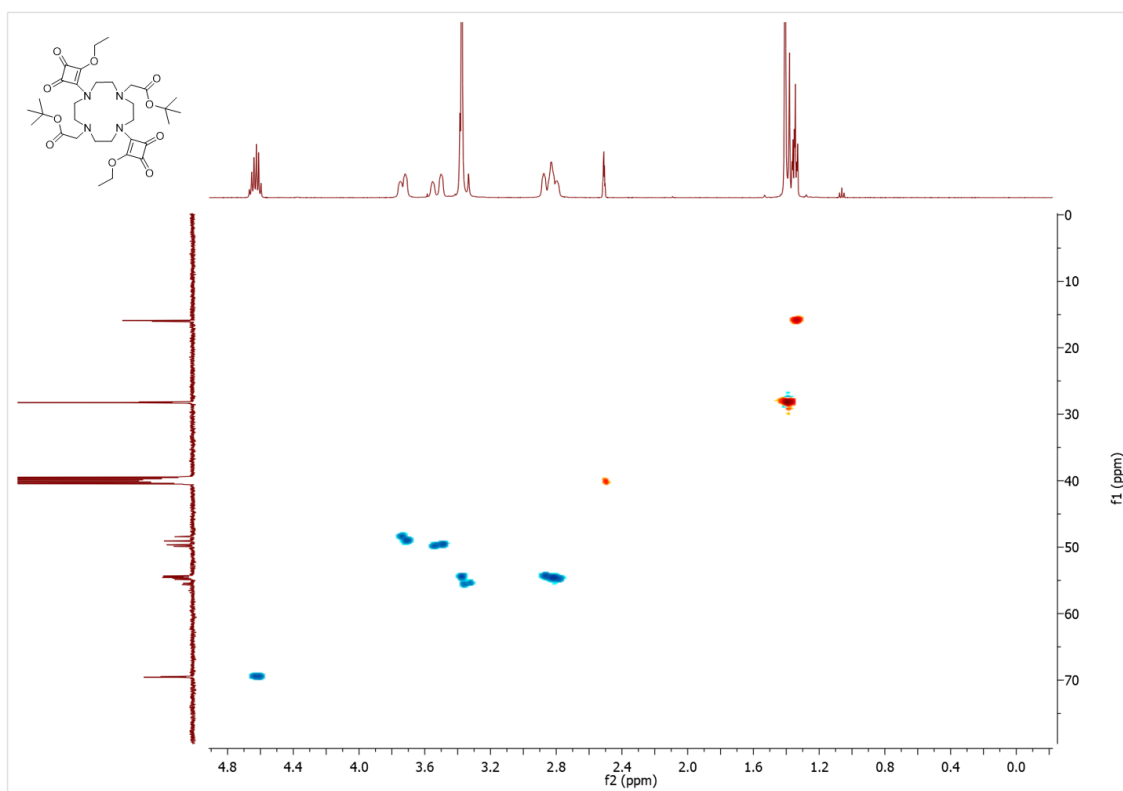
Figure S3.68: HSQC spectrum of **DO2A*t*Bu-2ESq (3.8)** in DMSO-*d*₆.
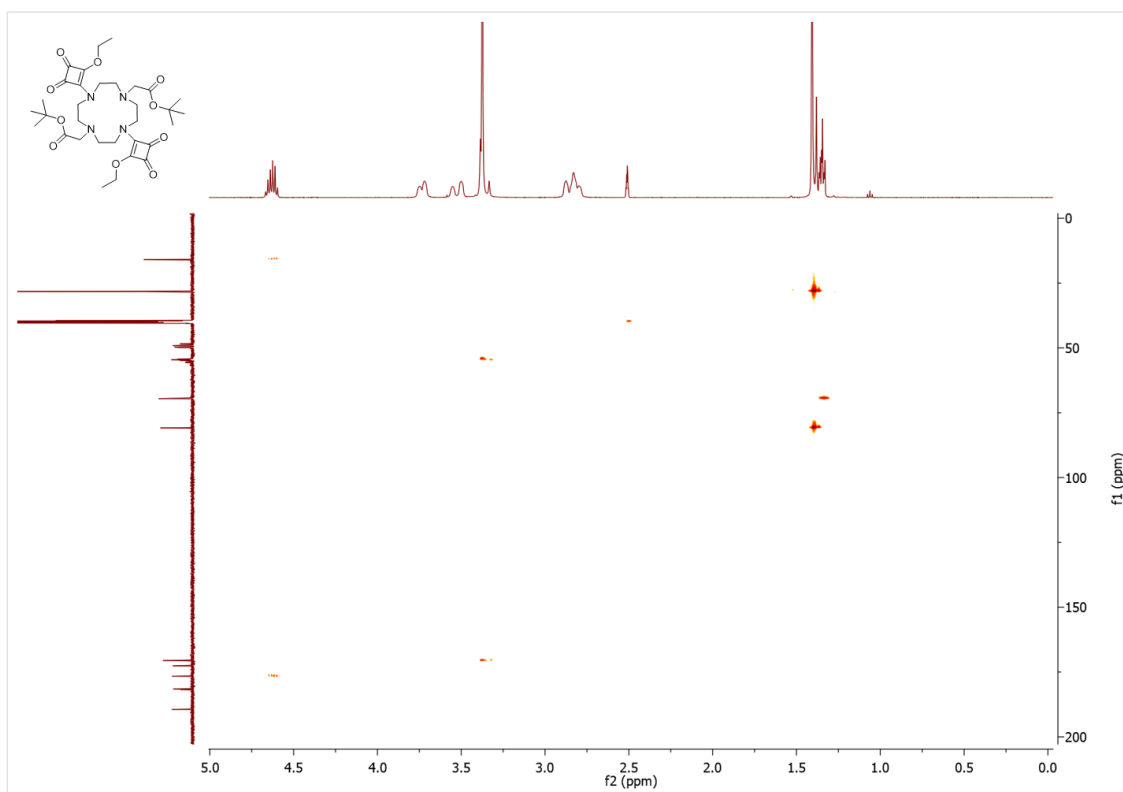
Figure S3.69: HMBC spectrum of **DO2A*t*Bu-2ESq (3.8)** in DMSO-*d*₆.

Compound Table

Compound Label	RT (min)	Observed mass (m/z)	Neutral observed mass (Da)	Theoretical mass (Da)	Mass error (ppm)	Isotope match score (%)
Cpd 1: C32 H48 N4 O10	0.73	649.3439	648.3367	648.3370	-0.48	99.76

Mass errors of between -5.00 and 5.00 ppm with isotope match scores above 60% are considered confirmation of molecular formulae
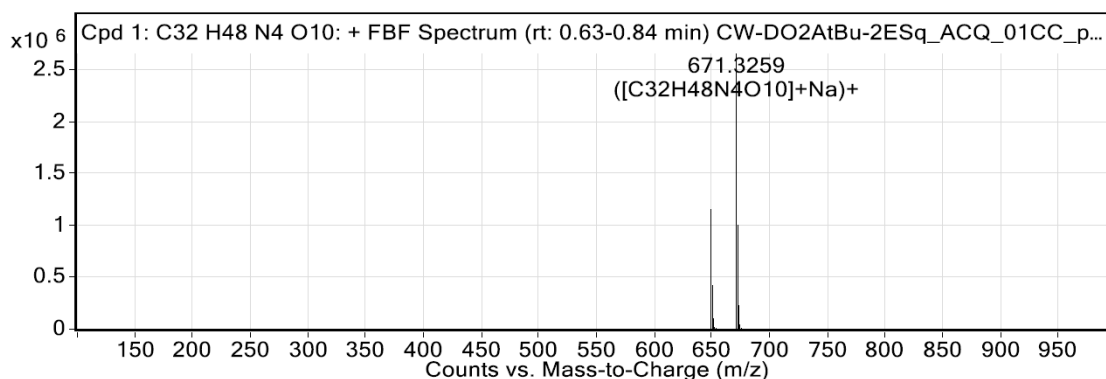
Figure: Full range view of Compound spectra and potential adducts.
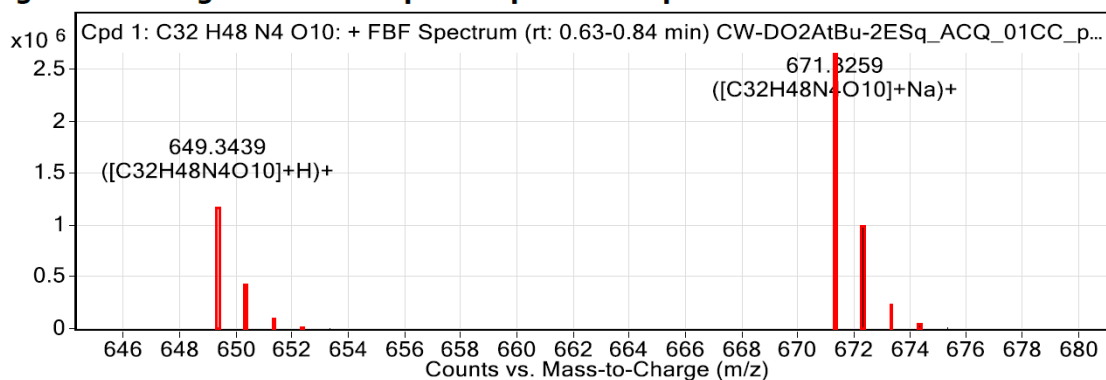
Figure: Zoomed Compound spectra view
(red boxes indicating expected theoretical isotope spacing and abundance)

Compound isotope peak List

m/z	z	Abund	Formula	Ion
649.3439	1	1154071.3	C32H48N4O10	(M+H)+
650.3474	1	418830.5	C32H48N4O10	(M+H)+
651.3499	1	96005.6	C32H48N4O10	(M+H)+
652.3524	1	15785.4	C32H48N4O10	(M+H)+
653.3542	1	2695.6	C32H48N4O10	(M+H)+
671.3259	1	2649577.8	C32H48N4O10	(M+Na)+
672.3291	1	997999.3	C32H48N4O10	(M+Na)+
673.3322	1	223490.6	C32H48N4O10	(M+Na)+
674.3345	1	37623.0	C32H48N4O10	(M+Na)+
675.3364	1	5773.9	C32H48N4O10	(M+Na)+

Figure S3.70: HRMS data for **DO2A*t*Bu-2ESq (3.8)**.
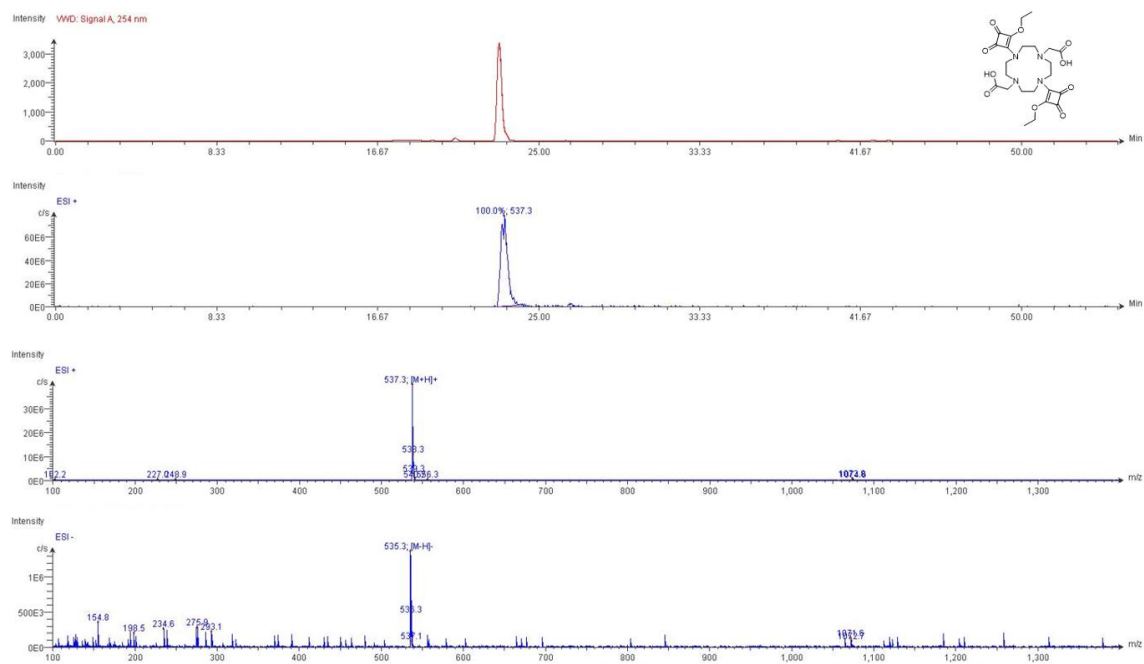
Figure S3.71: LC-MS data for **DO2A-2ESq (3.9)**.
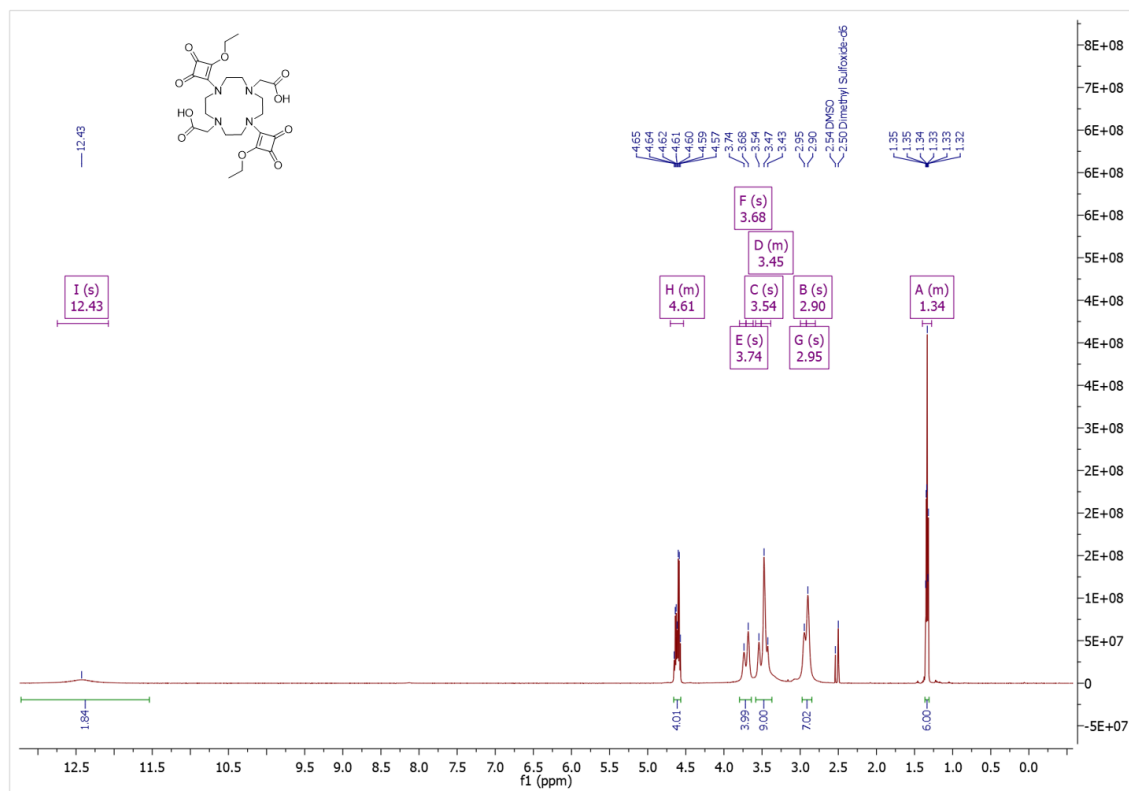
Figure S3.72: ¹H NMR spectrum of **DO2A-2ESq (3.9)** in DMSO-d_6.
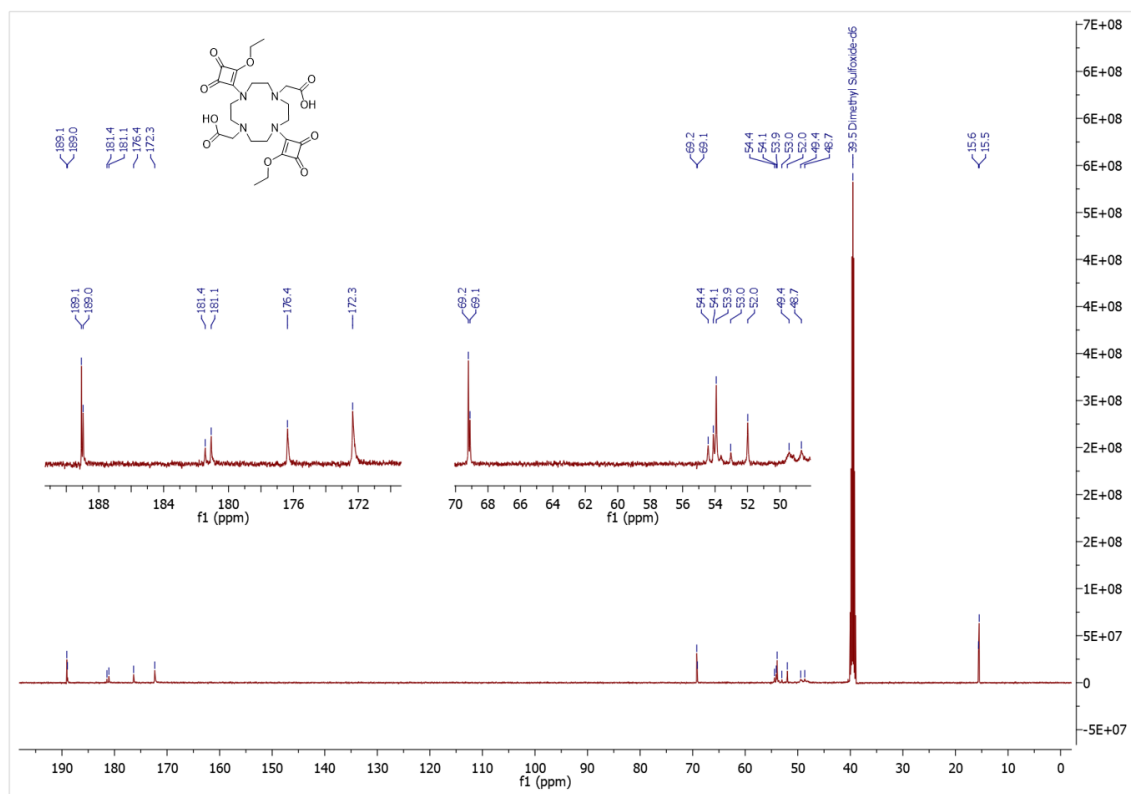
Figure S3.73: ^{13}C NMR spectrum of **DO2A-2ESq (3.9)** in DMSO-d_6.
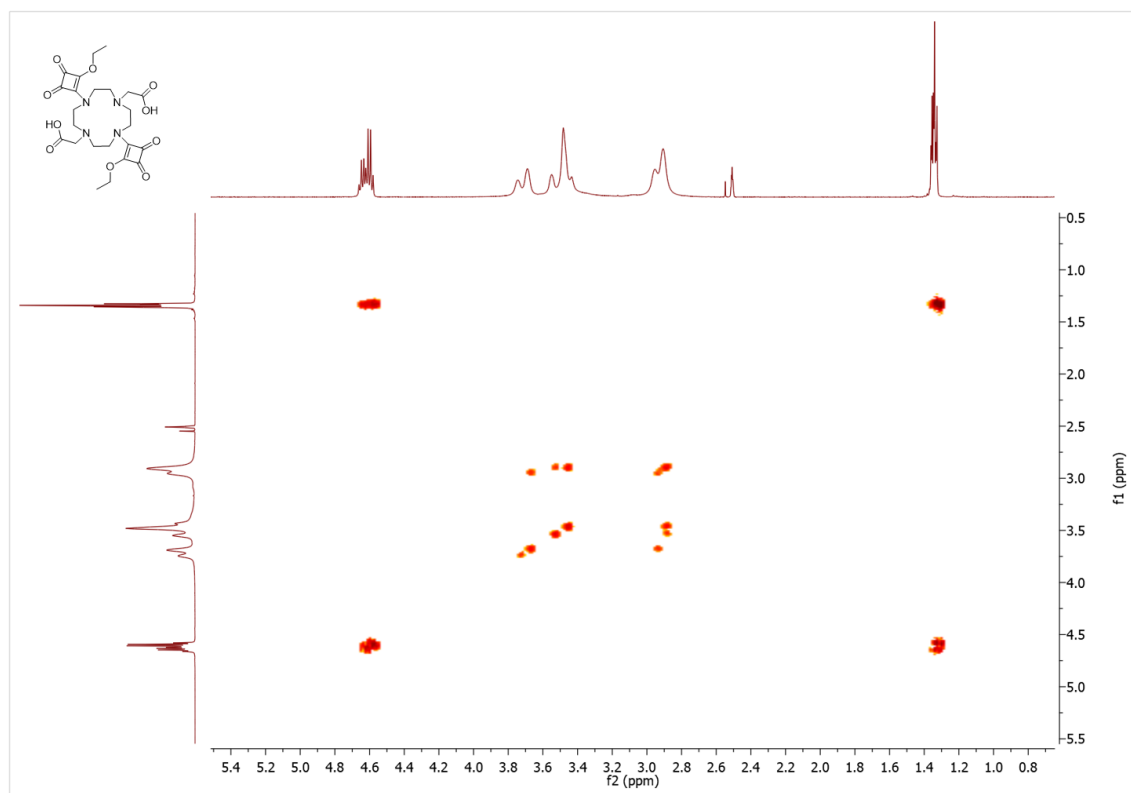
Figure S3.74: COSY spectrum of **DO2A-2ESq (3.9)** in DMSO-d_6.
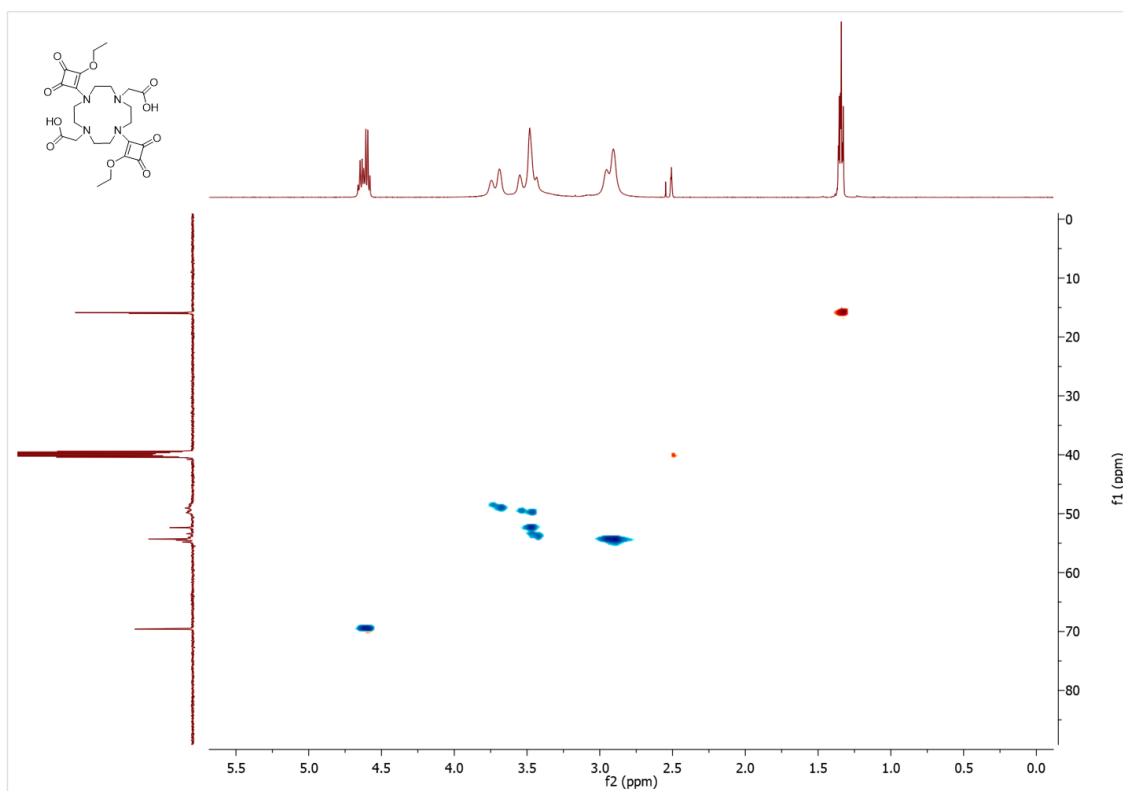
Figure S3.75: HSQC spectrum of **DO2A-2ESq (3.9)** in DMSO-d_6.
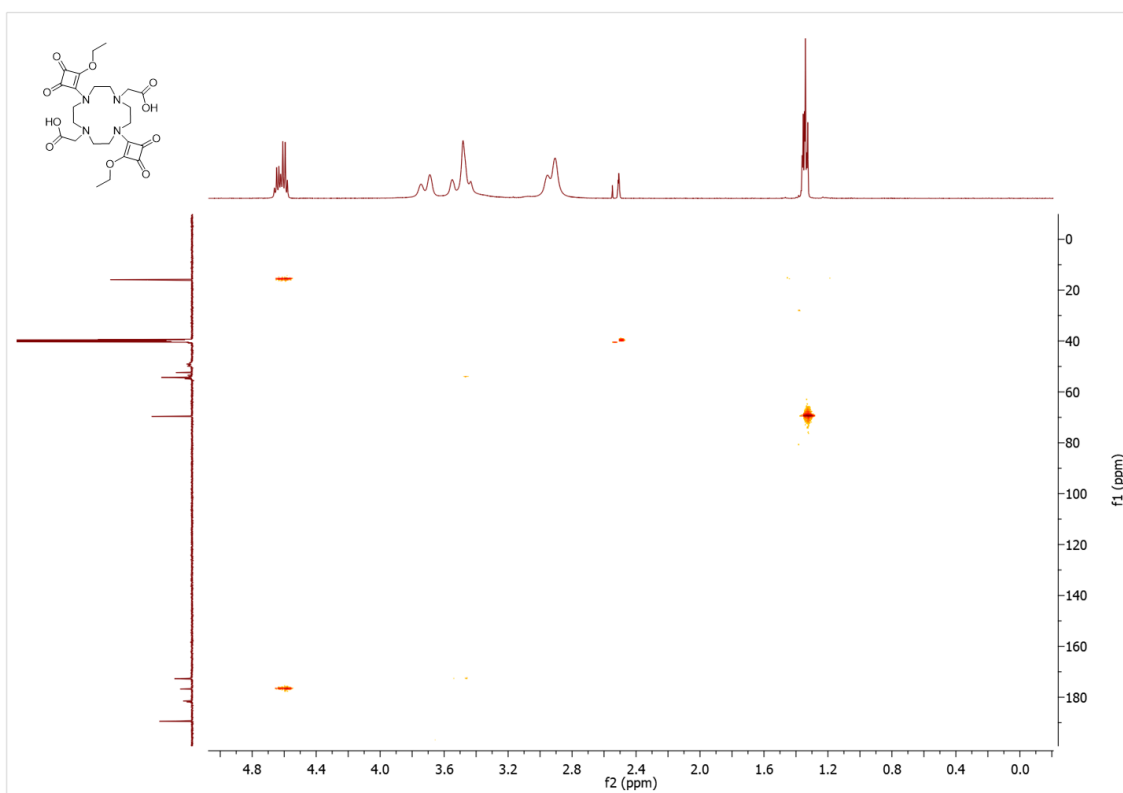
Figure S3.76: HMBC spectrum of **DO2A-2ESq (3.9)** in DMSO-d_6.

Compound Table

Compound Label	RT (min)	Observed mass (m/z)	Neutral observed mass (Da)	Theoretical mass (Da)	Mass error (ppm)	Isotope match score (%)
Cpd 1: C24 H32 N4 O10	0.74	537.2187	536.2113	536.2118	-0.98	99.85

Mass errors of between -5.00 and 5.00 ppm with isotope match scores above 60% are considered confirmation of molecular formulae
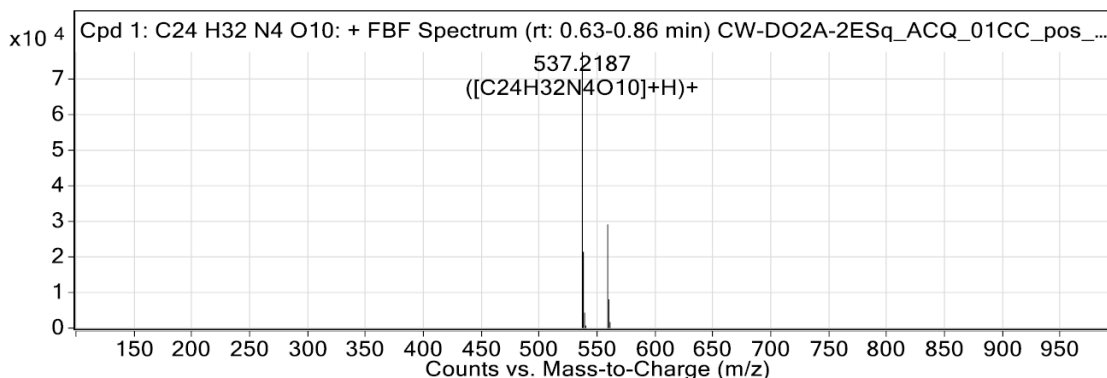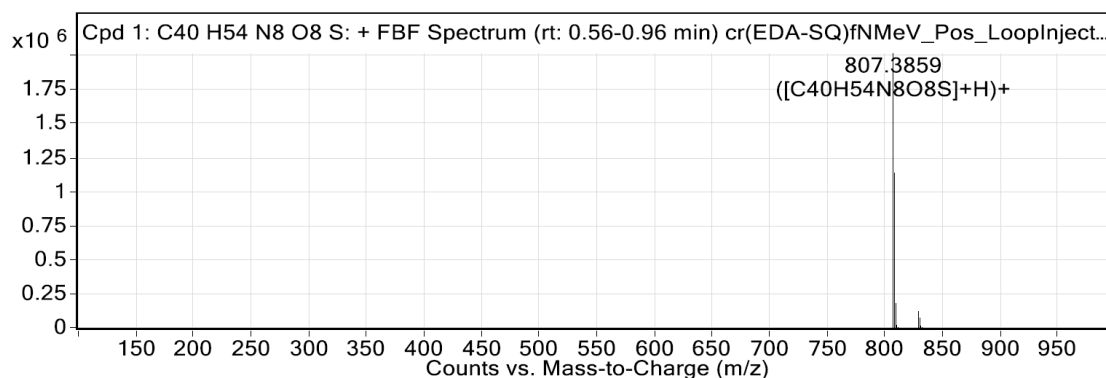

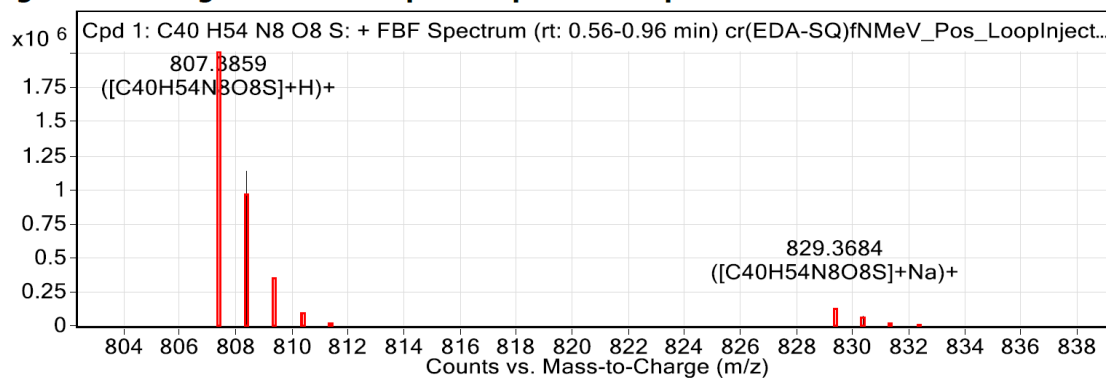**Figure: Full range view of Compound spectra and potential adducts.**
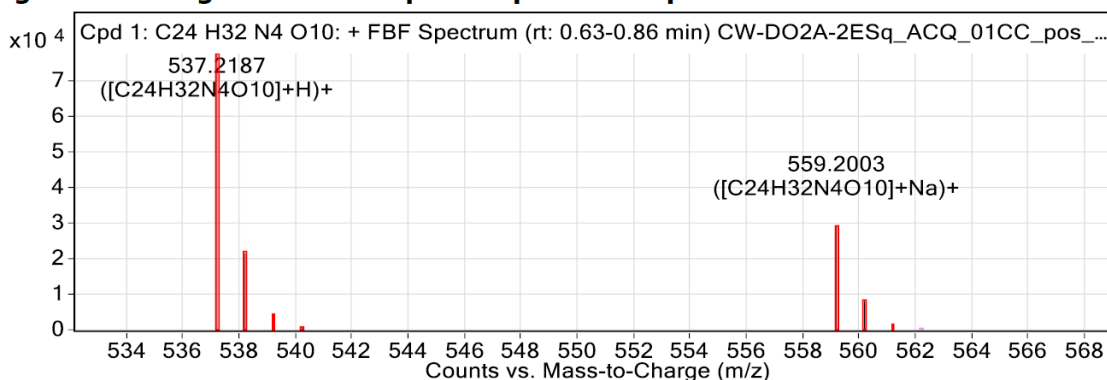

Figure: Zoomed Compound spectra view
(red boxes indicating expected theoretical isotope spacing and abundance)

Compound isotope peak List

m/z	z	Abund	Formula	Ion
537.2187	1	77595.2	C24H32N4O10	(M+H)+
538.2219	1	21462.7	C24H32N4O10	(M+H)+
539.2245	1	4332.3	C24H32N4O10	(M+H)+
540.2282	1	713.2	C24H32N4O10	(M+H)+
559.2003	1	29118.7	C24H32N4O10	(M+Na)+
560.2033	1	8078.8	C24H32N4O10	(M+Na)+
561.2051	1	1675.6	C24H32N4O10	(M+Na)+

Figure S3.77: HRMS data for **DO2A-2ESq (3.9)**.
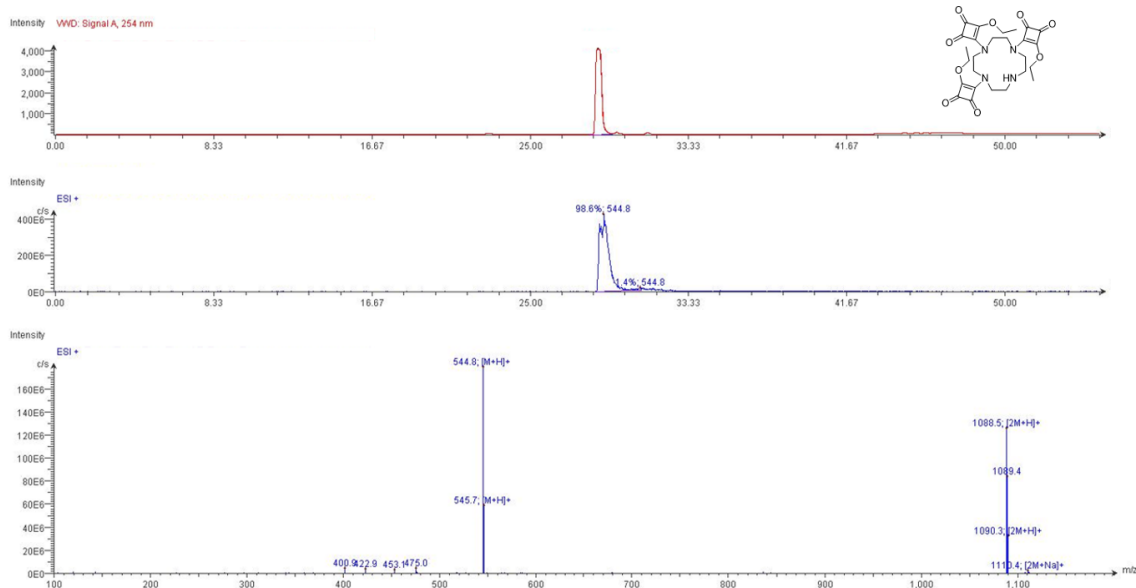
Figure S3.78: LC-MS data for **ESqO3A-NH (3.12)**.
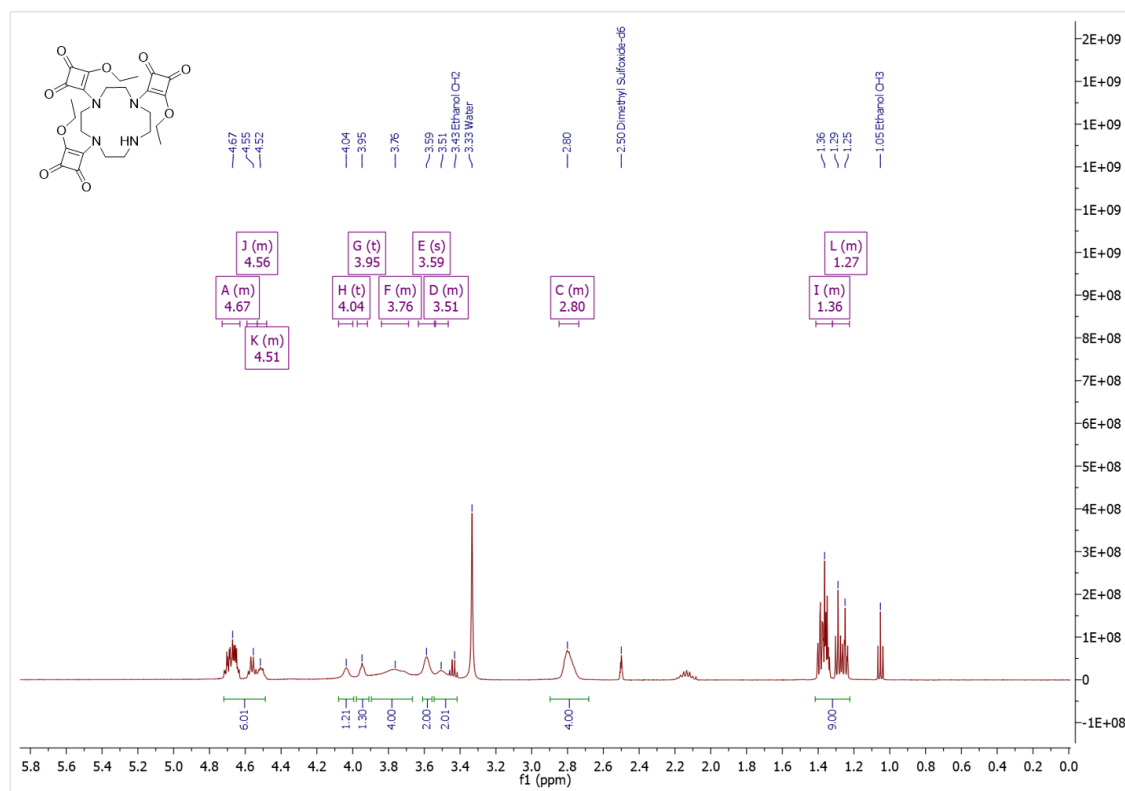
Figure S3.79: ¹H NMR spectrum of **ESqO3A-NH (3.12)** in DMSO-d_6.

340
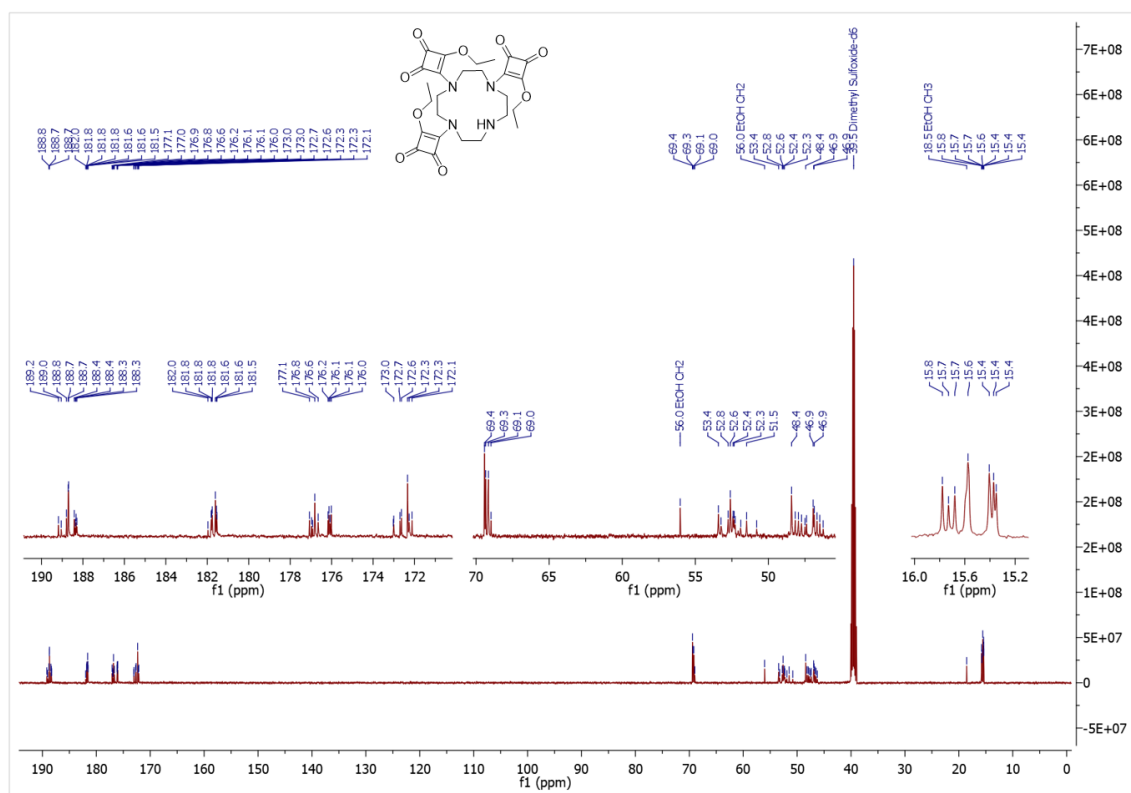
Figure S3.80: ^{13}C NMR spectrum of **ESqO3A-NH (3.12)** in DMSO-d_6.
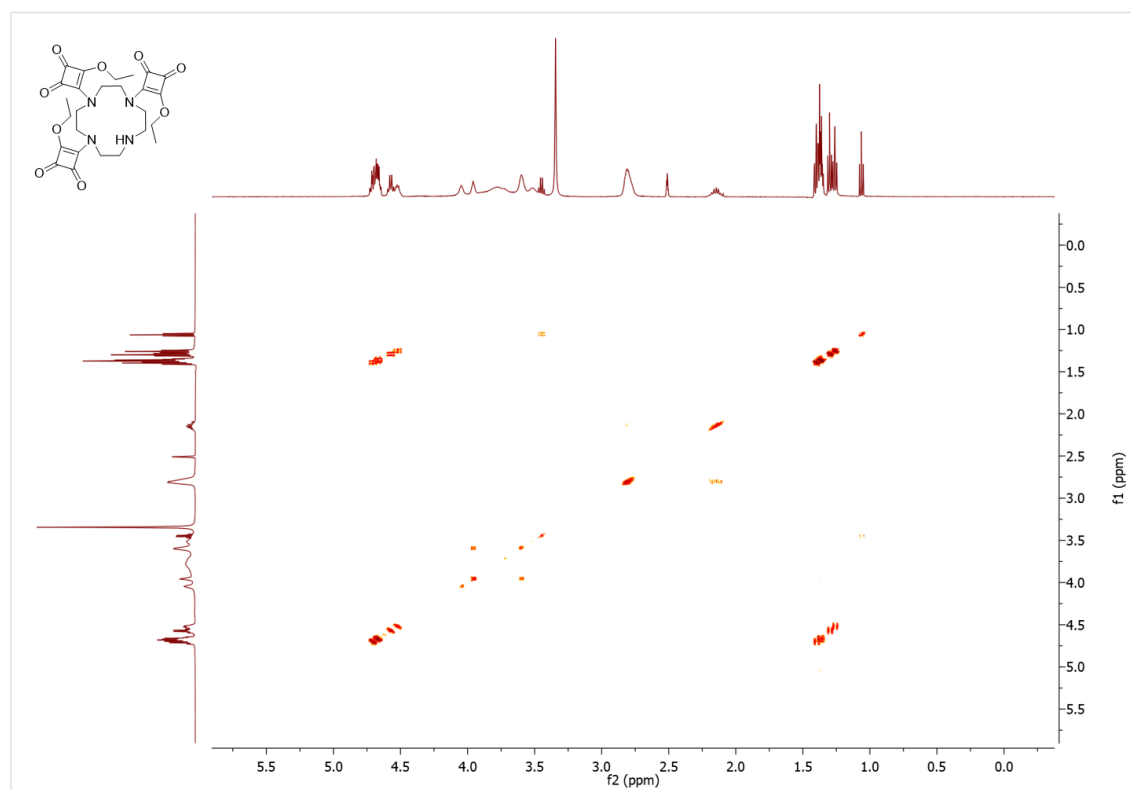
Figure S3.81: COSY spectrum of **ESqO3A-NH (3.12)** in DMSO-d_6.
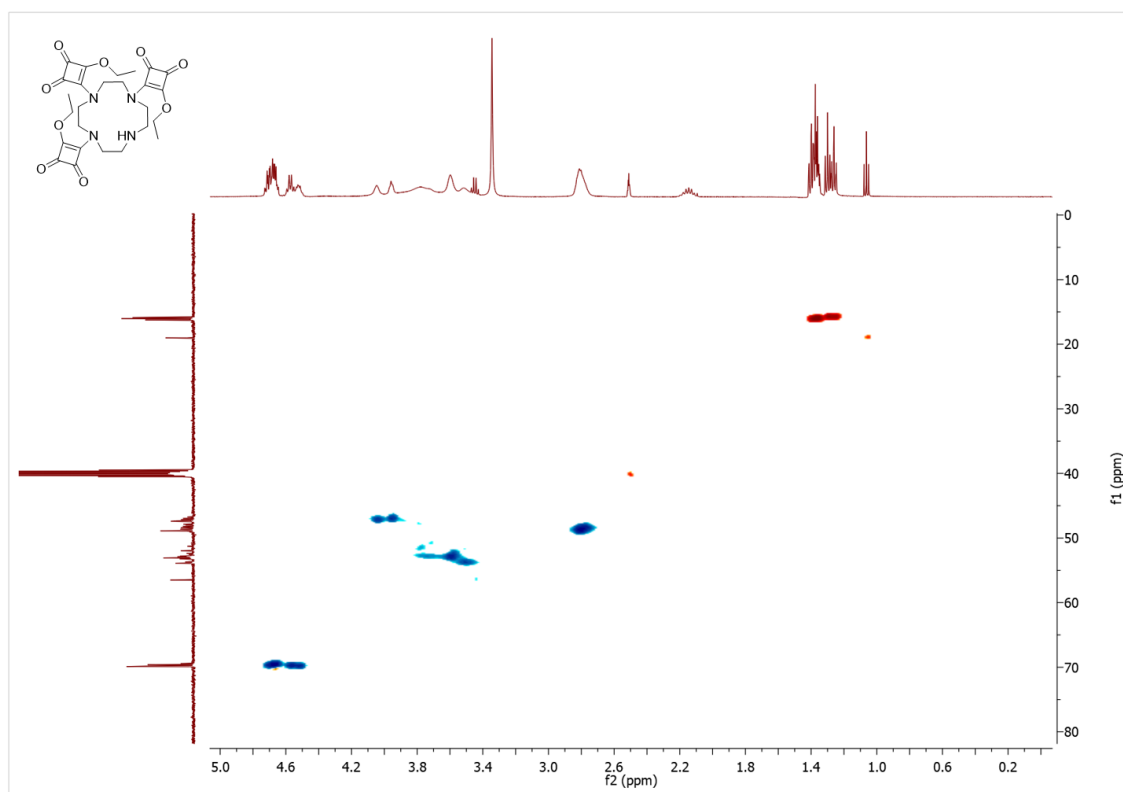
Figure S3.82: HSQC spectrum of **ESqO3A-NH (3.12)** in DMSO-d_6.
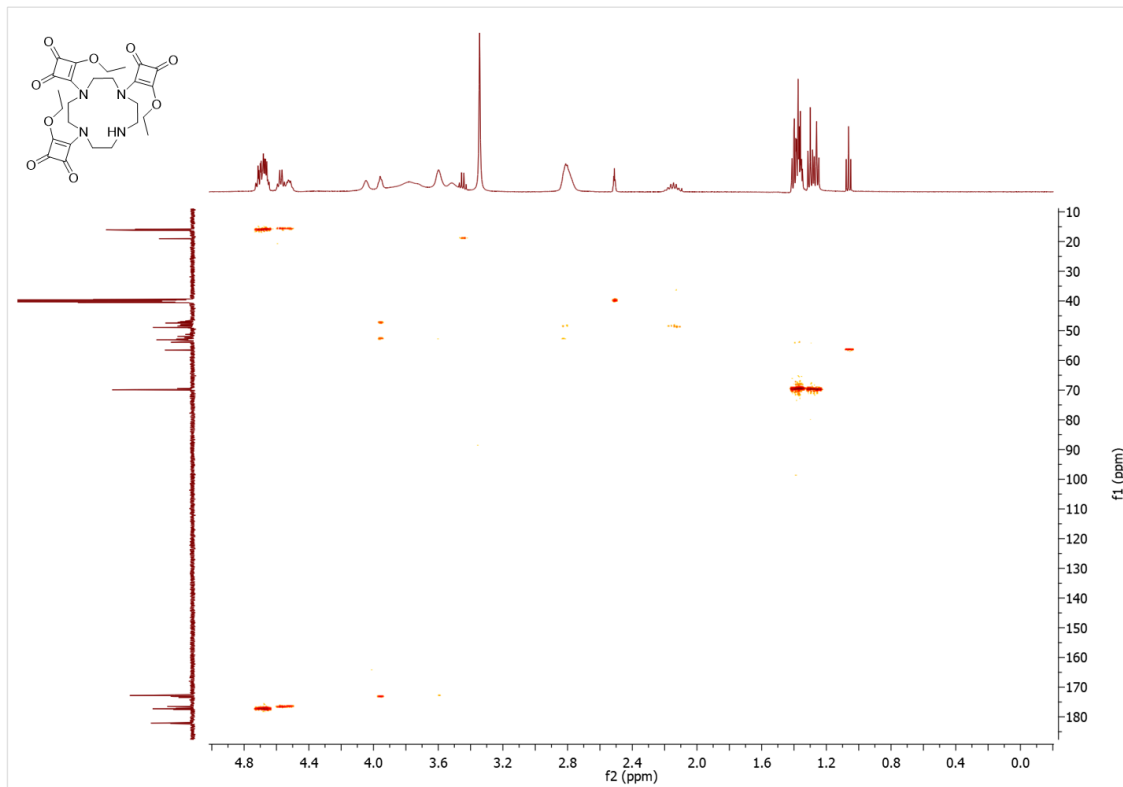
Figure S3.83: HMBC spectrum of **ESqO3A-NH (3.12)** in DMSO-d_6.

Compound Table

| Compound Label	RT (min)	Observed mass (m/z)	Neutral observed mass (Da)	Theoretical mass (Da)	Mass error (ppm)	Isotope match score (%)
Cpd 1: C26 H32 N4 O9	0.79	545.2252	544.2179	544.2169	1.74	95.79

Mass errors of between -5.00 and 5.00 ppm with isotope match scores above 60% are considered confirmation of molecular formulae
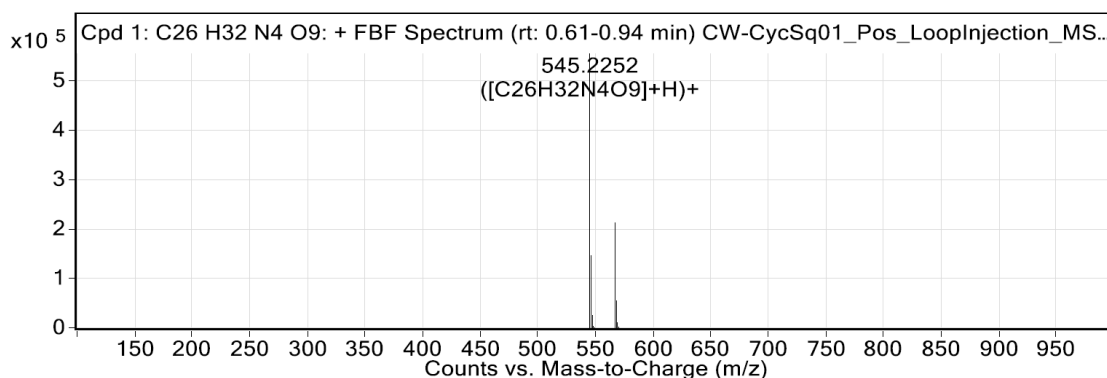
Figure: Full range view of Compound spectra and potential adducts.

Figure: Zoomed Compound spectra view
(red boxes indicating expected theoretical isotope spacing and abundance)

Compound isotope peak List

m/z	z	Abund	Formula	Ion
545.2252	1	555273.5	C26H32N4O9	(M+H)+
546.2282	1	147383.0	C26H32N4O9	(M+H)+
547.2301	1	25638.9	C26H32N4O9	(M+H)+
548.2319	1	4024.6	C26H32N4O9	(M+H)+
549.2349	1	532.7	C26H32N4O9	(M+H)+
567.2072	1	212616.1	C26H32N4O9	(M+Na)+
568.2097	1	55375.8	C26H32N4O9	(M+Na)+
569.2117	1	10526.0	C26H32N4O9	(M+Na)+
570.2142	1	1552.9	C26H32N4O9	(M+Na)+

Figure S3.84: HRMS data for **ESqO3A-NH (3.12)**.
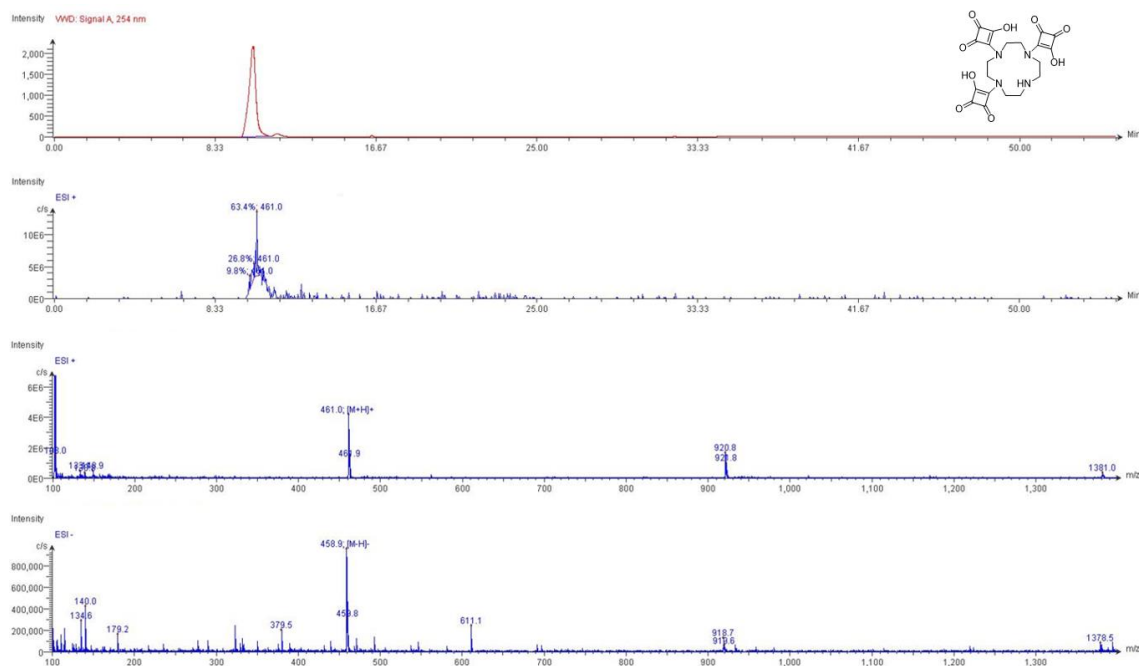
Figure S3.85: LC-MS data for **SqO3A-NH (3.13)**.
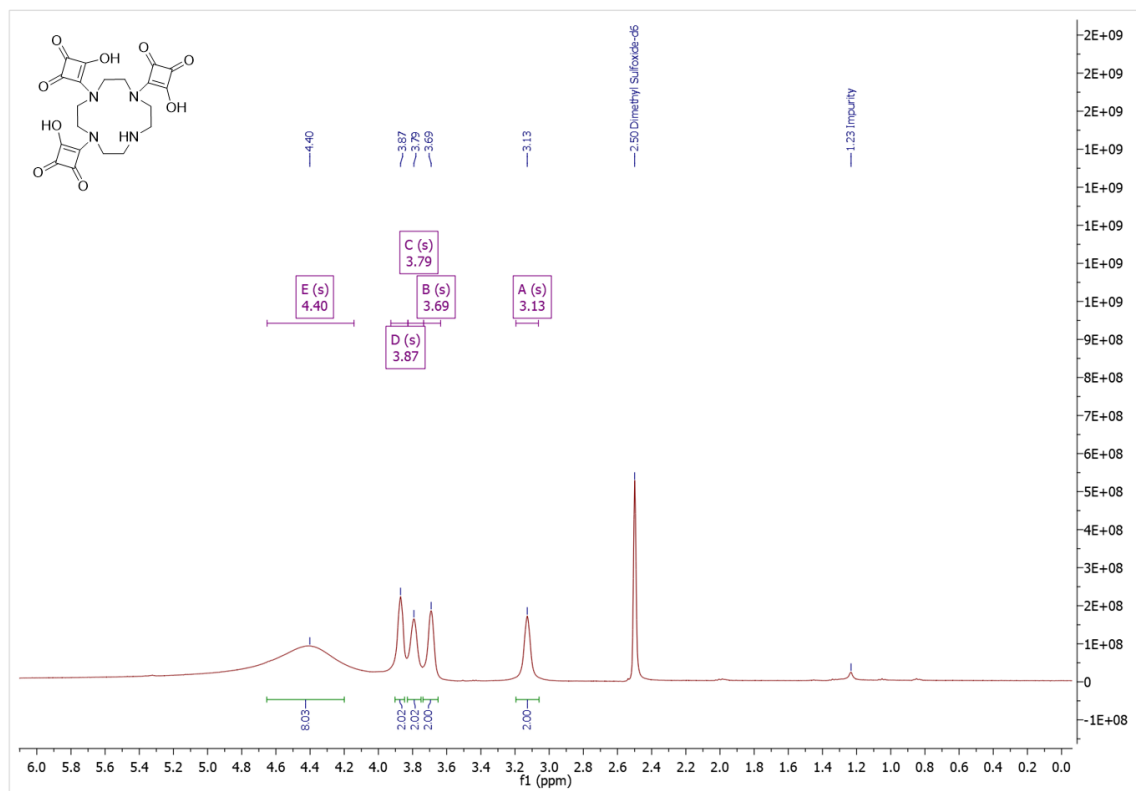
Figure S3.86: ¹H NMR spectrum of **SqO3A-NH (3.13)** in DMSO-d_6.
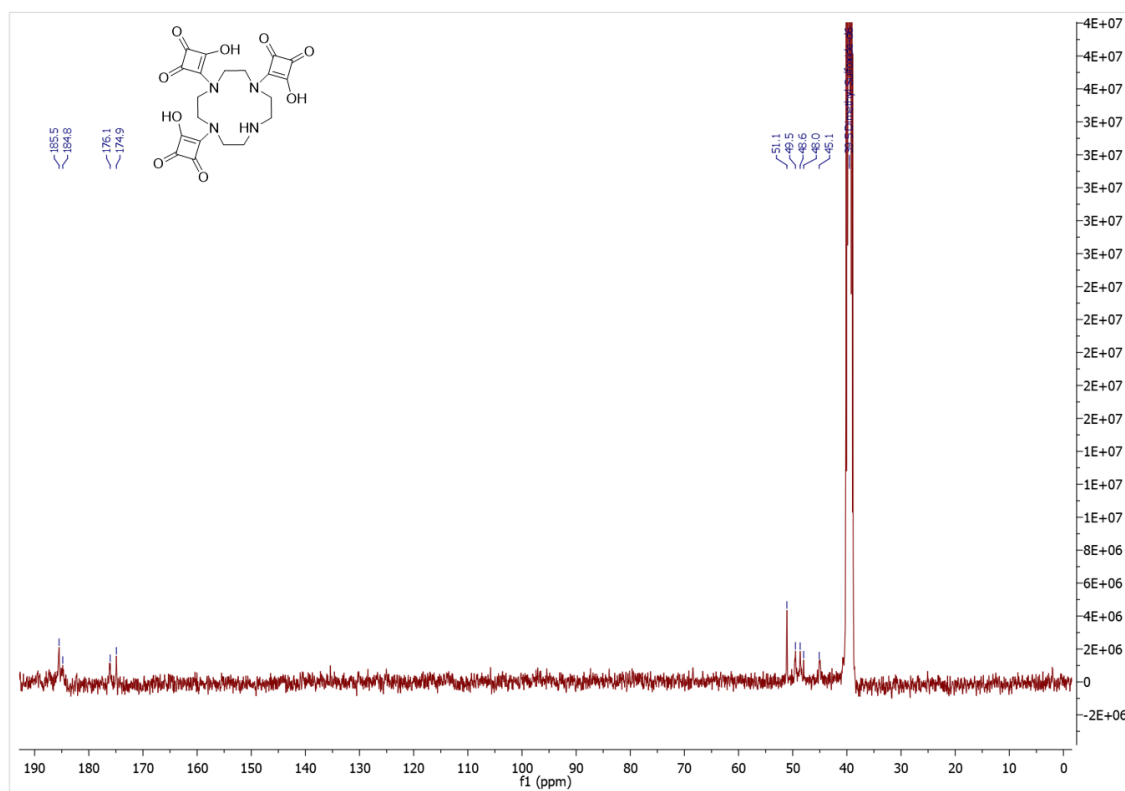
Figure S3.87: ^{13}C NMR spectrum of **SqO3A-NH (3.13)** in DMSO-d_6.
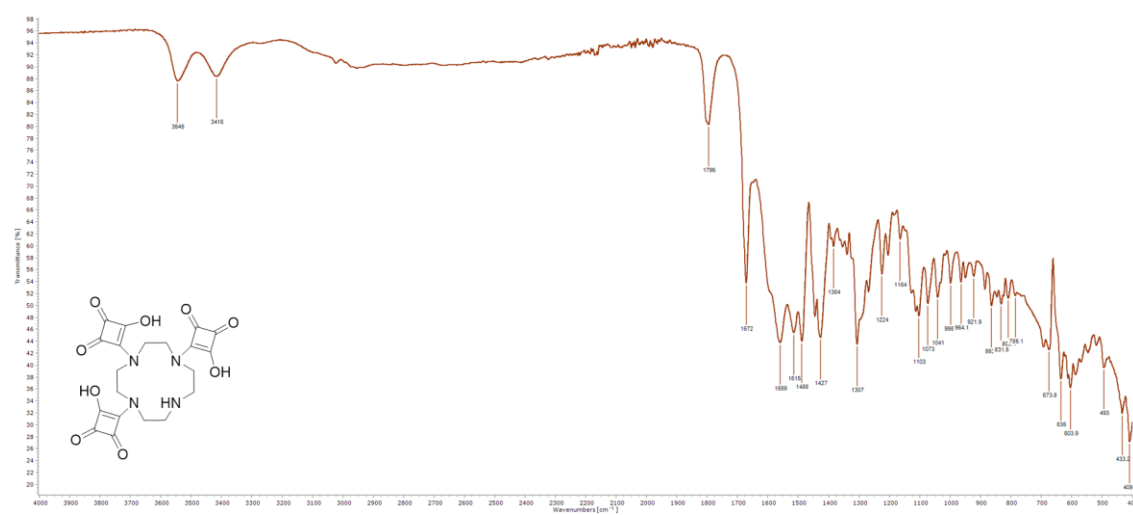
Figure S3.88: FTIR-ATR spectrum of **SqO3A-NH (3.13)**.
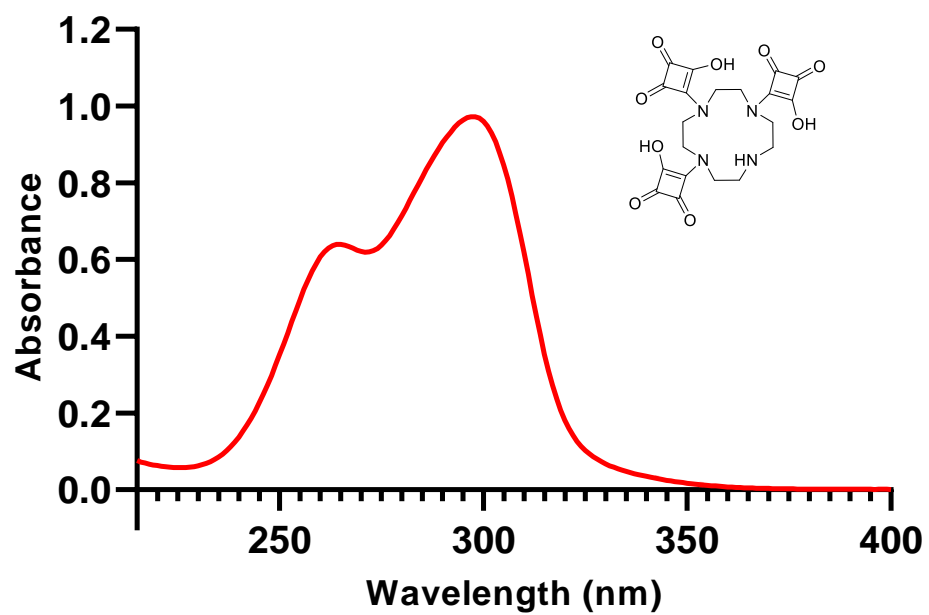
Figure S3.89: Absorbance spectrum of **SqO3A-NH (3.13)** (20 μM) in H₂O.

Compound Table

Compound Label	RT (min)	Observed mass (m/z)	Neutral observed mass (Da)	Theoretical mass (Da)	Mass error (ppm)	Isotope match score (%)
Cpd 1: C20 H20 N4 O9	1.23	459.1151	460.1221	460.1230	-2.05	88.53

Mass errors of between -5.00 and 5.00 ppm with isotope match scores above 60% are considered confirmation of molecular formulae
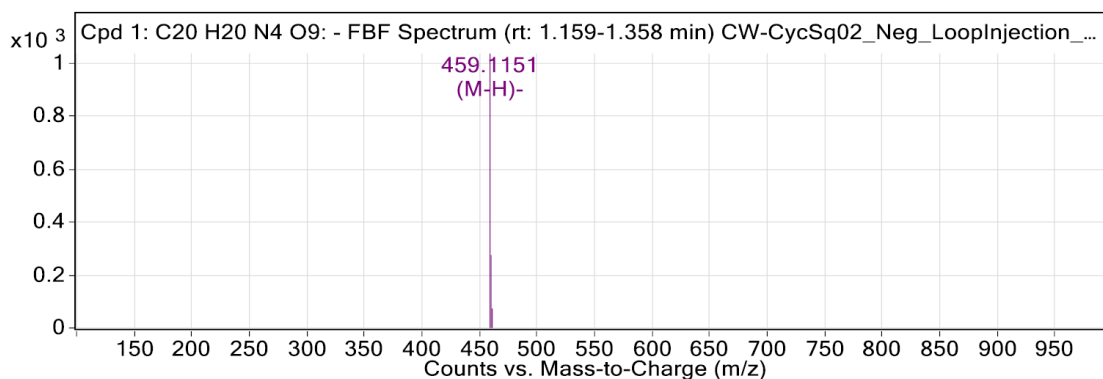
Figure: Full range view of Compound spectra and potential adducts.
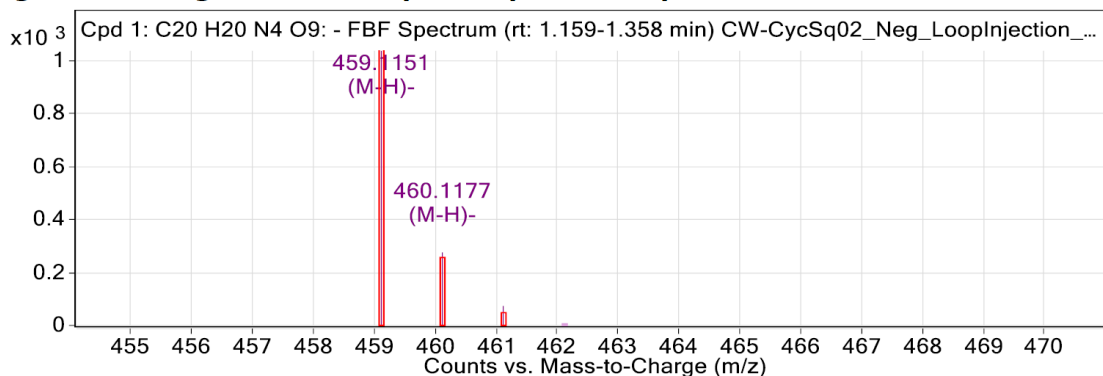
Figure: Zoomed Compound spectra view
(red boxes indicating expected theoretical isotope spacing and abundance)

Compound isotope peak List

m/z	z	Abund	Ion
459.1151	1	1035.0	(M-H)-
460.1177	1	275.1	(M-H)-
461.1163	1	73.6	(M-H)-

Figure S3.90: HRMS data for **SqO3A-NH (3.13)**.
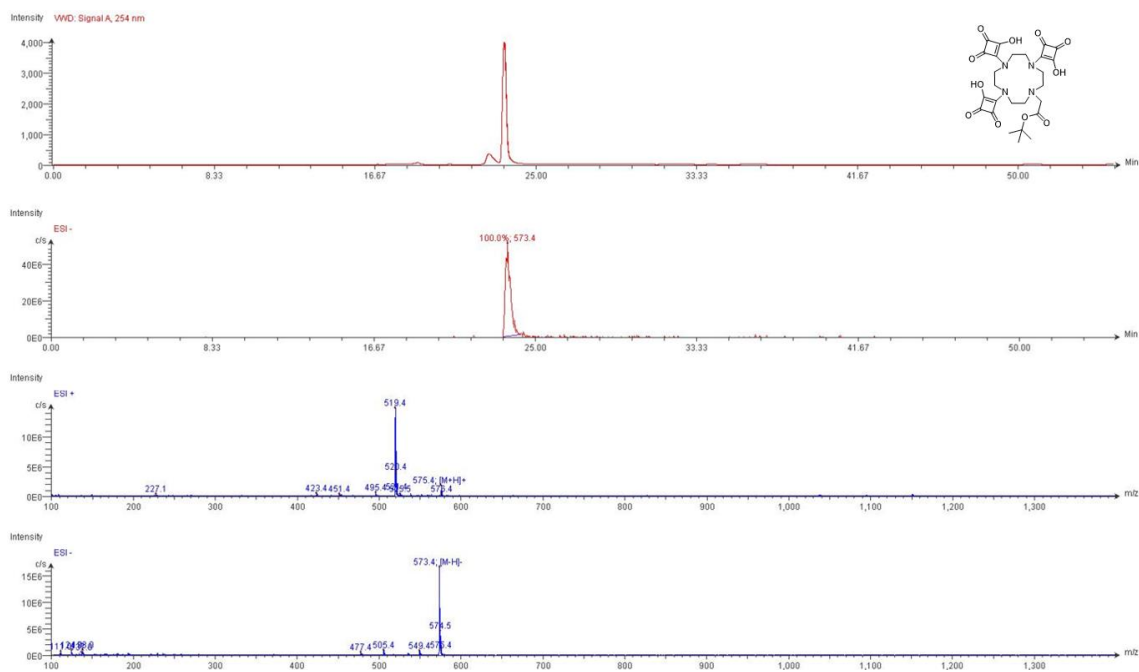
Figure S3.91: LC-MS data for **SqO3A-O*t*Bu (3.14)**.
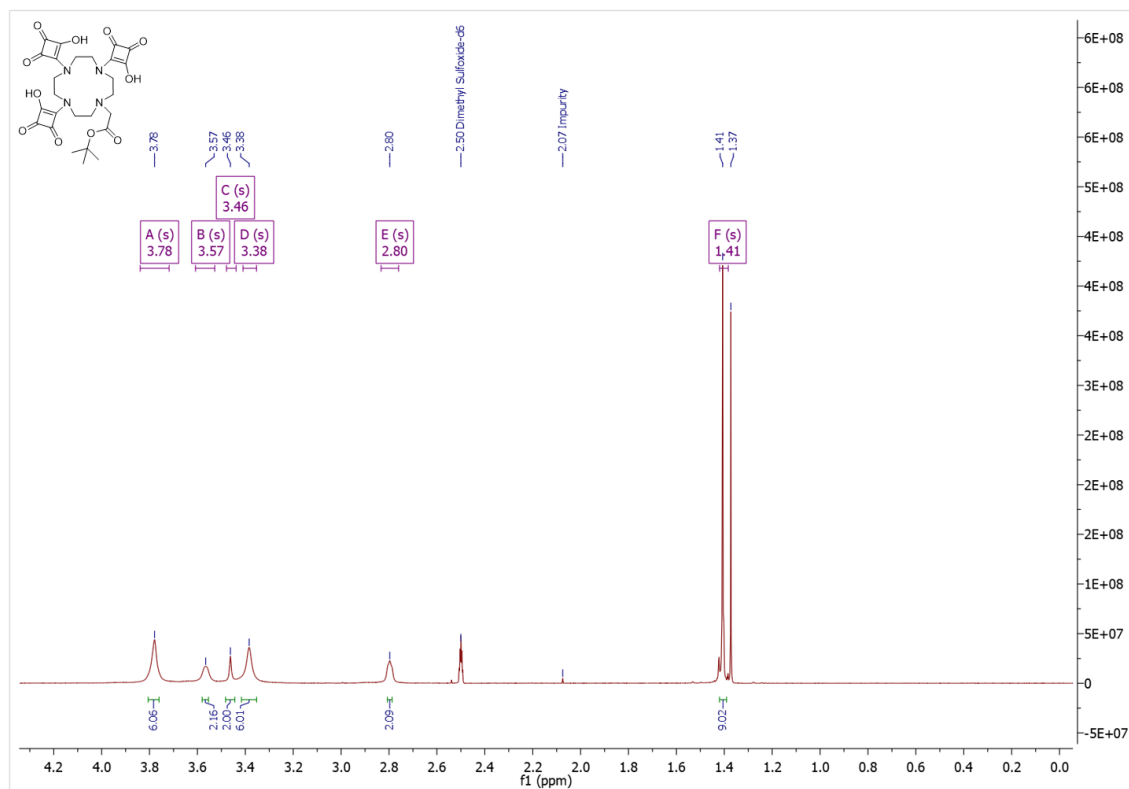
Figure S3.92: ¹H NMR spectrum of **SqO3A-O*t*Bu (3.14)** in DMSO-*d*₆.
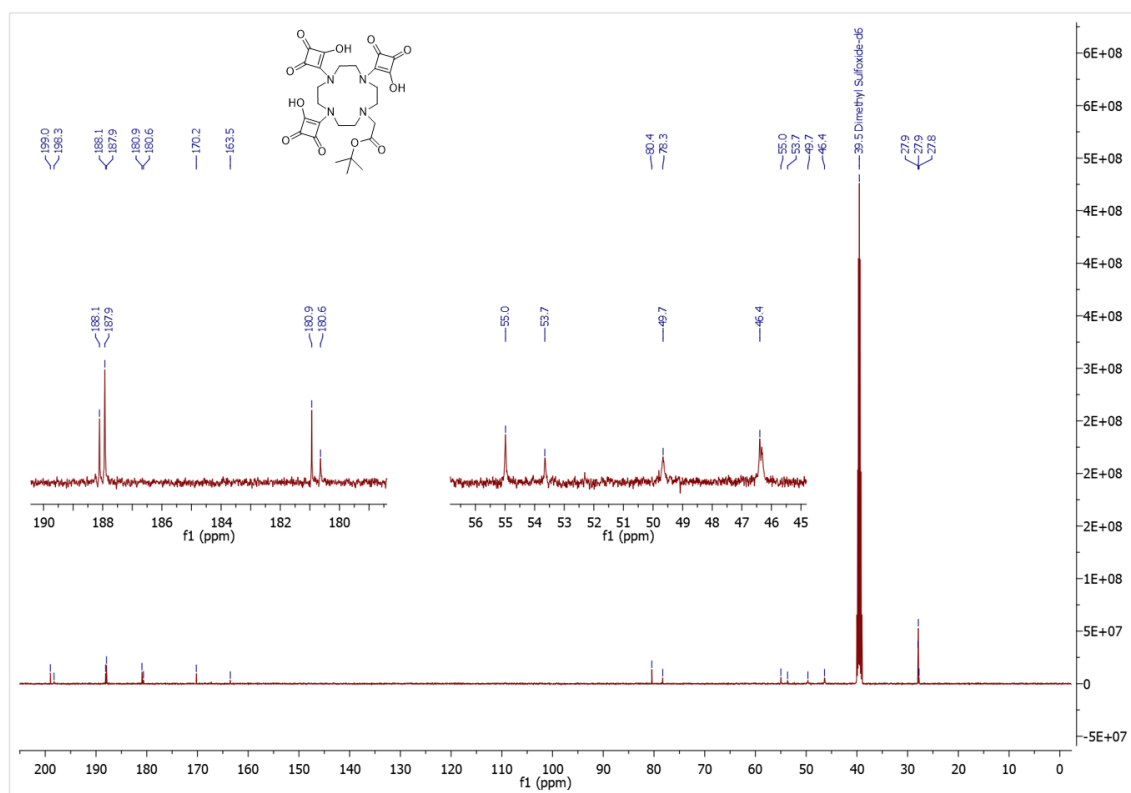
Figure S3.93: ^{13}C NMR spectrum of **SqO3A-O***t***Bu (3.14)** in DMSO-d_6.
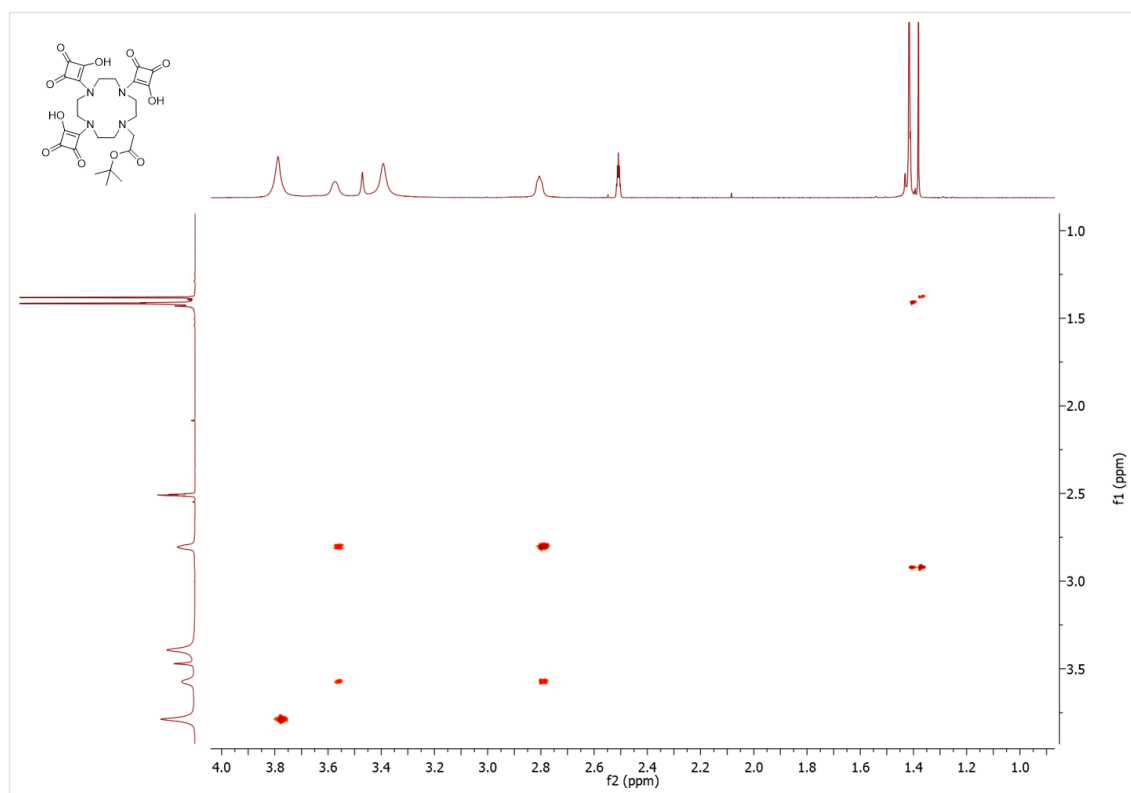
Figure S3.94: COSY spectrum of **SqO3A-O***t***Bu (3.14)** in DMSO-d_6.

349
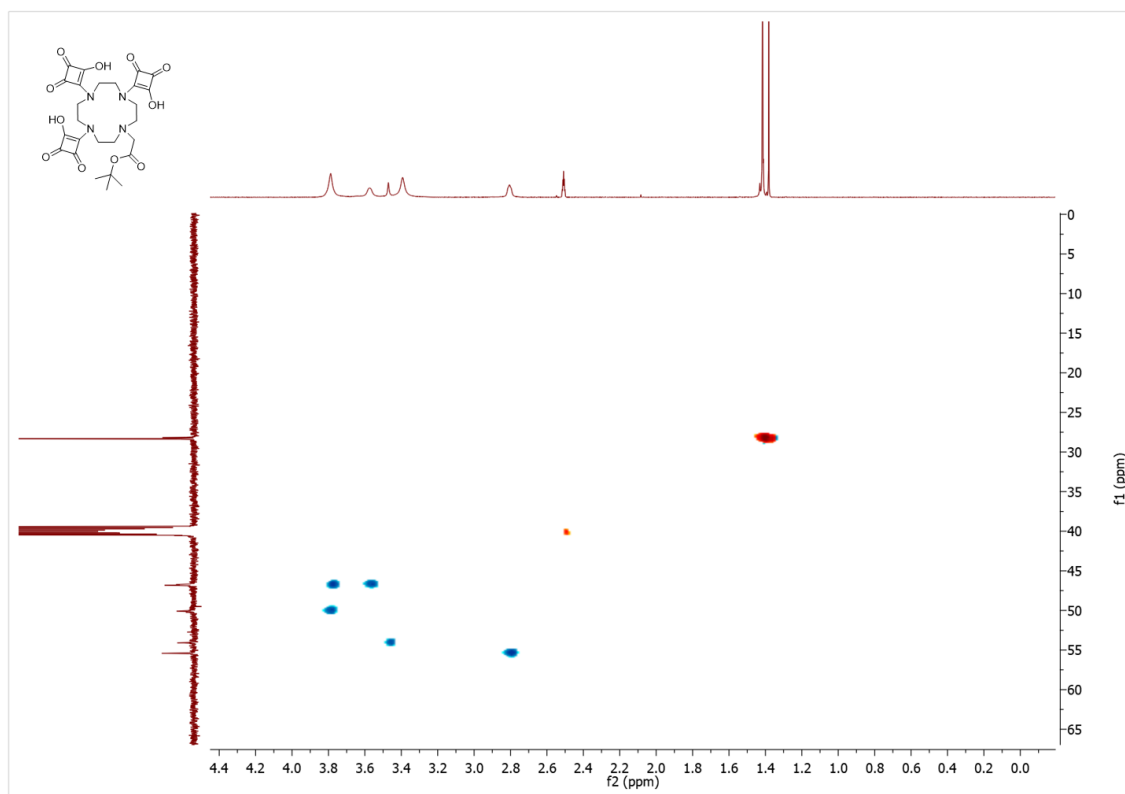
Figure S3.95: HSQC spectrum of **SqO3A-O*t*Bu (3.14)** in DMSO-*d*₆.
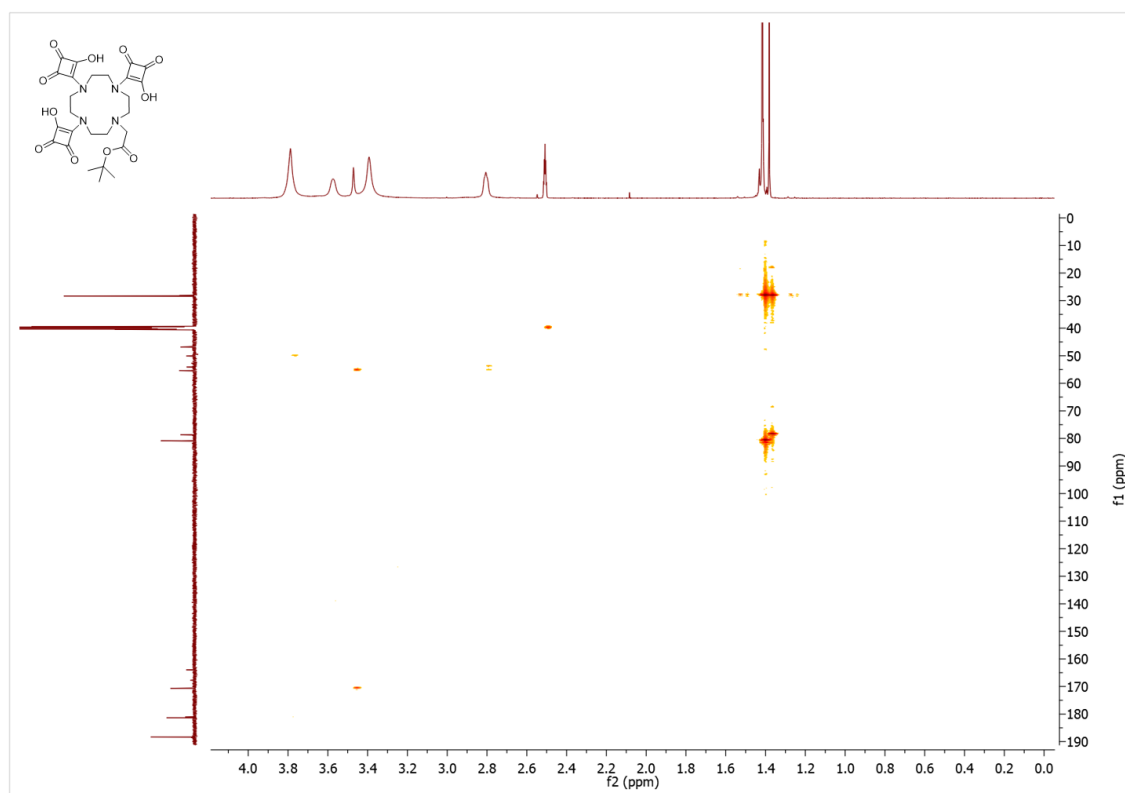
Figure S3.96: HMBC spectrum of **SqO3A-O*t*Bu (3.14)** in DMSO-*d*₆.
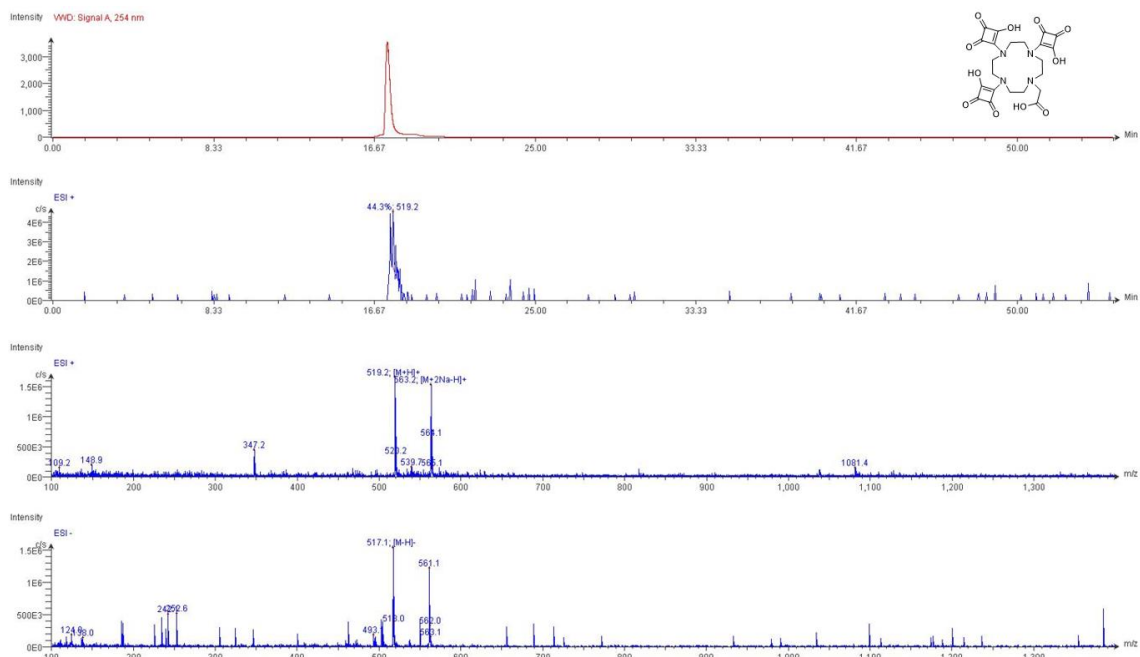
Figure S3.97: LC-MS data for **SqO3A-COOH (3.15)**.
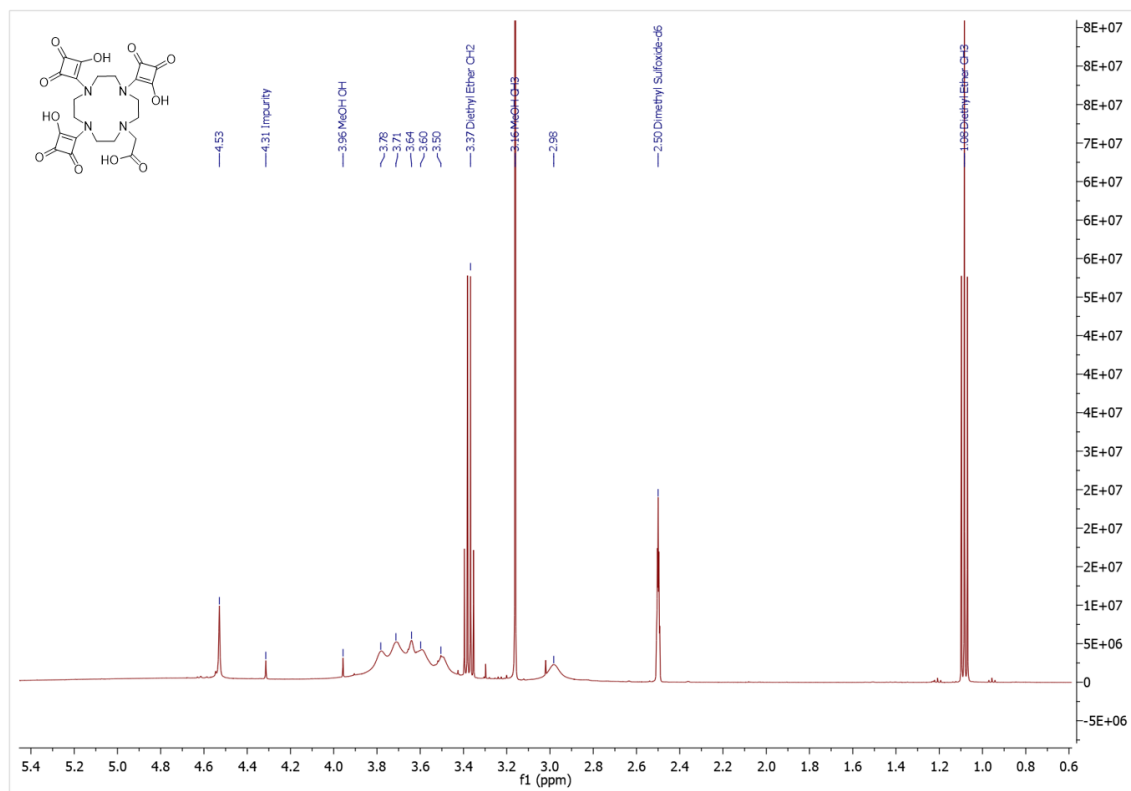
Figure S3.98: ^{1}H NMR spectrum of **SqO3A-COOH (3.15)** in DMSO-d_6.
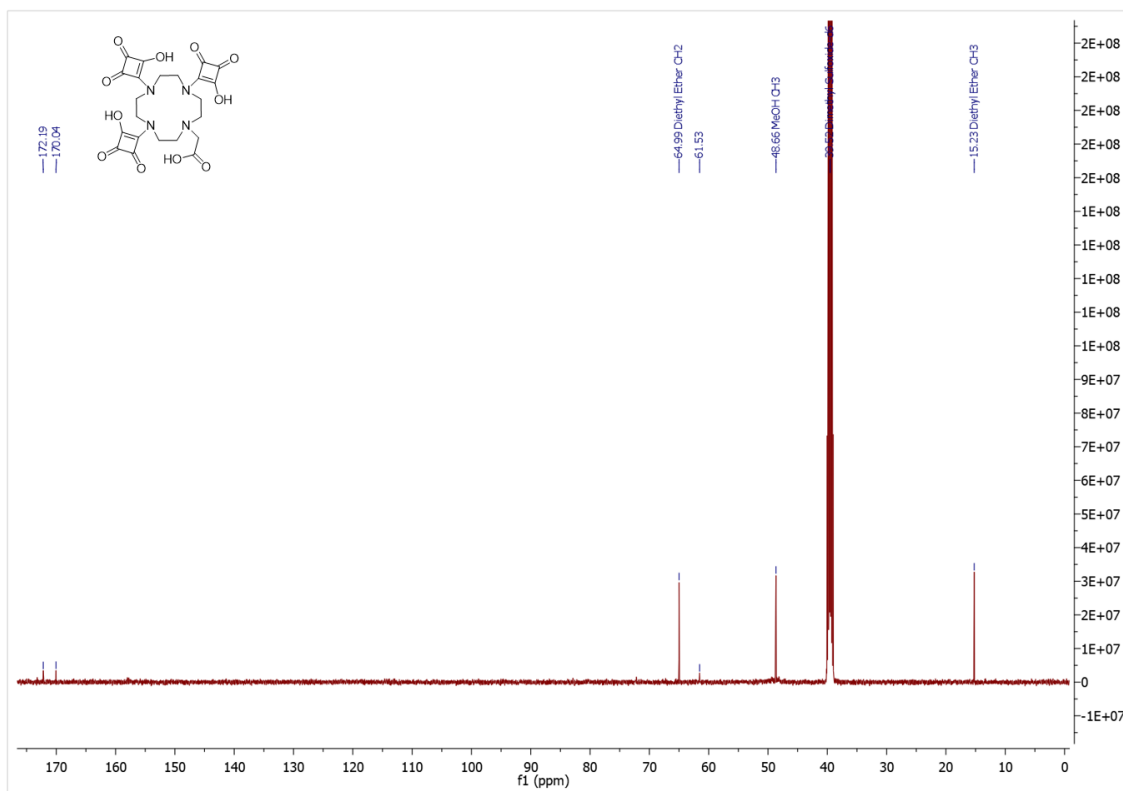
Figure S3.99: ^{13}C NMR spectrum of **SqO3A-COOH (3.15)** in DMSO-d_6.
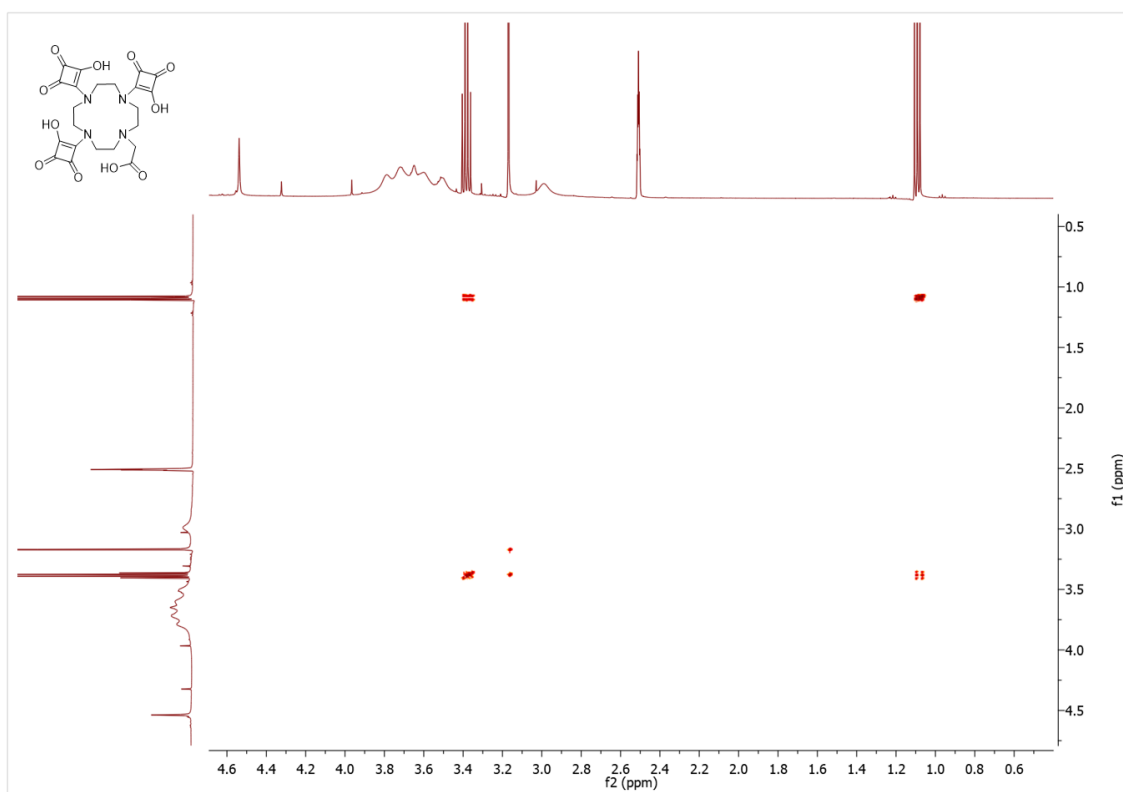
Figure S3.100: COSY spectrum of **SqO3A-COOH (3.15)** in DMSO-d_6.
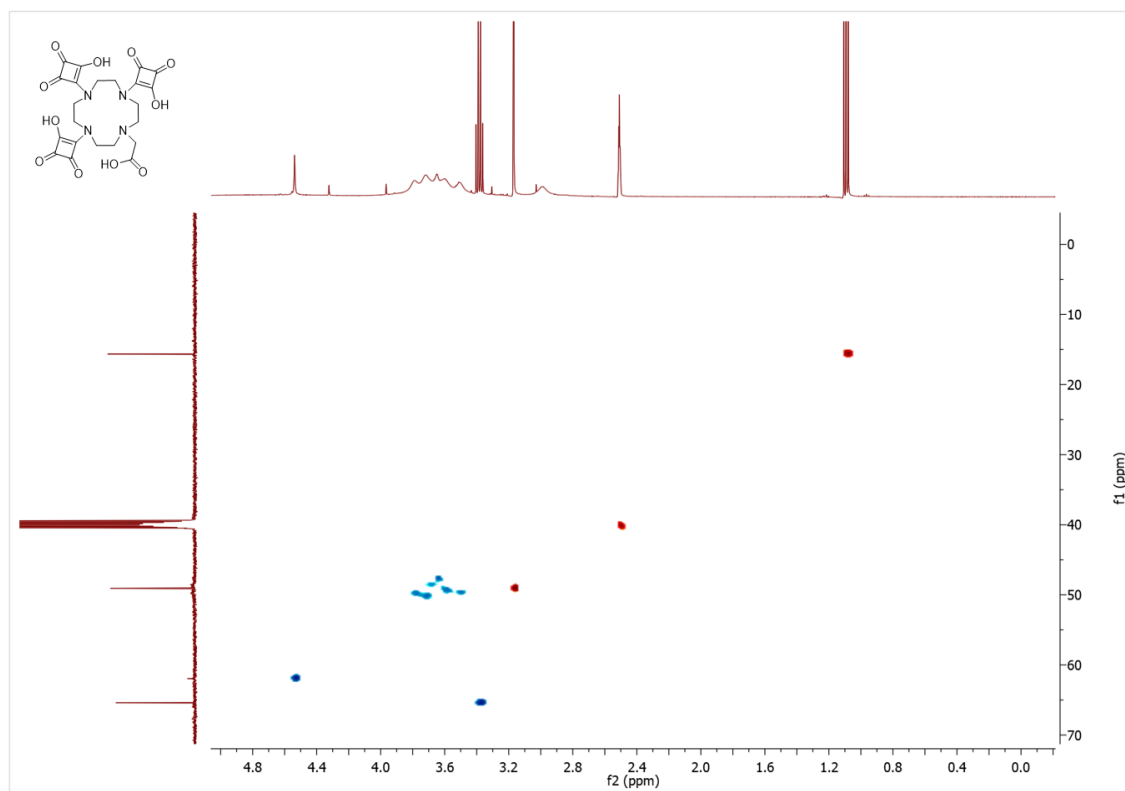
Figure S3.101: HSQC spectrum of **SqO3A-COOH (3.15)** in DMSO-d_6.
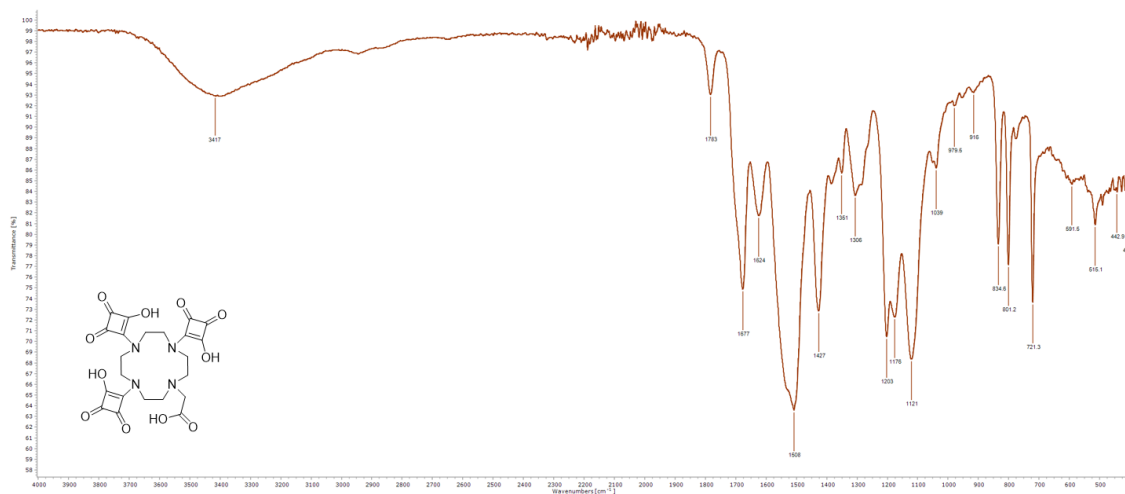
Figure S3.102: FTIR-ATR spectrum of **SqO3A-COOH (3.15)**.
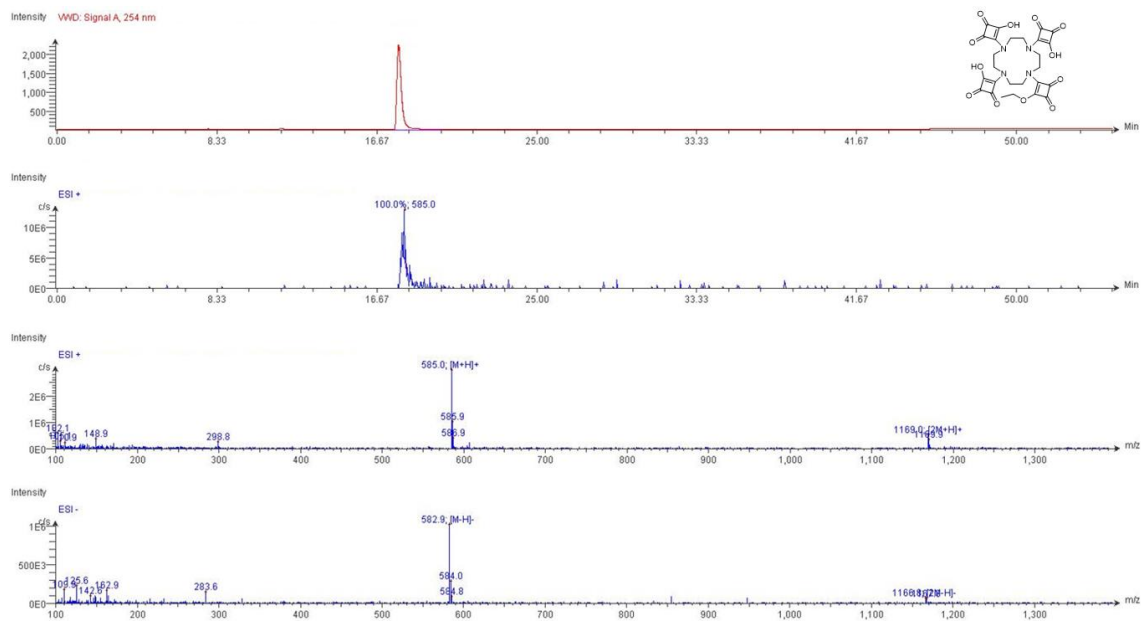
Figure S3.103: LC-MS data for **SqO3A-ESq (3.16)**.
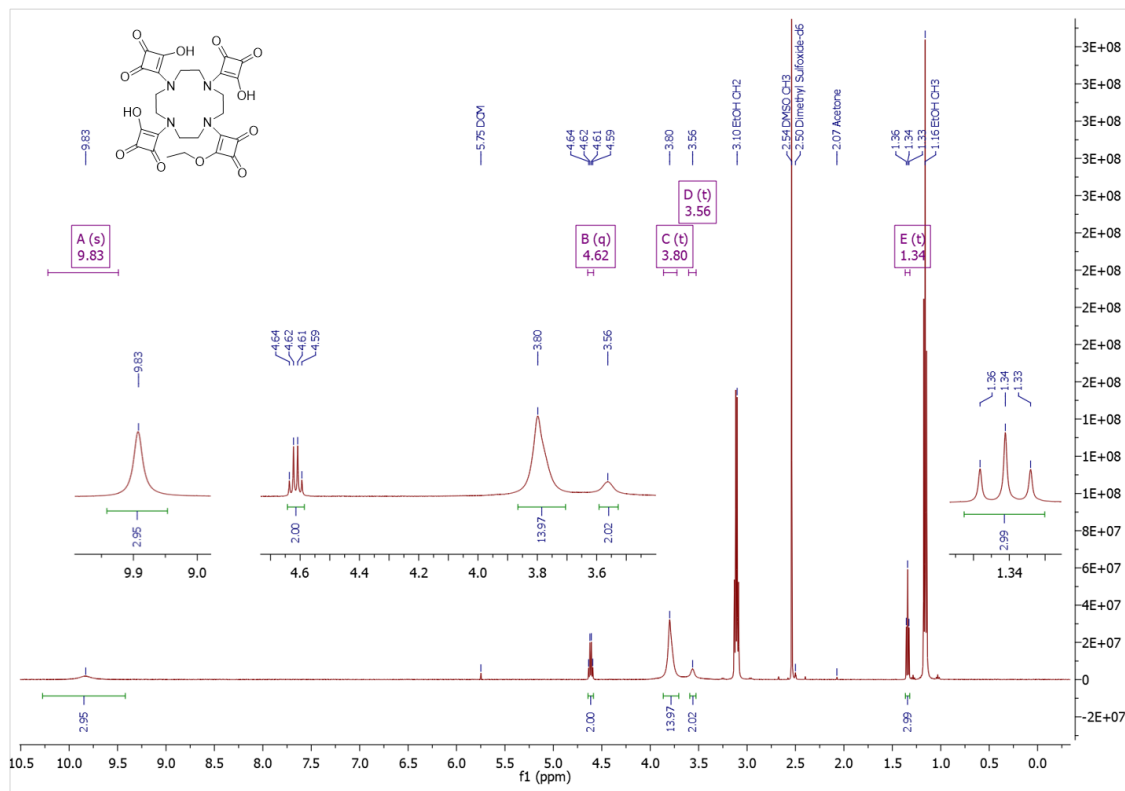
Figure S3.104: ¹H NMR spectrum of **SqO3A-ESq (3.16)** in DMSO-*d*₆.
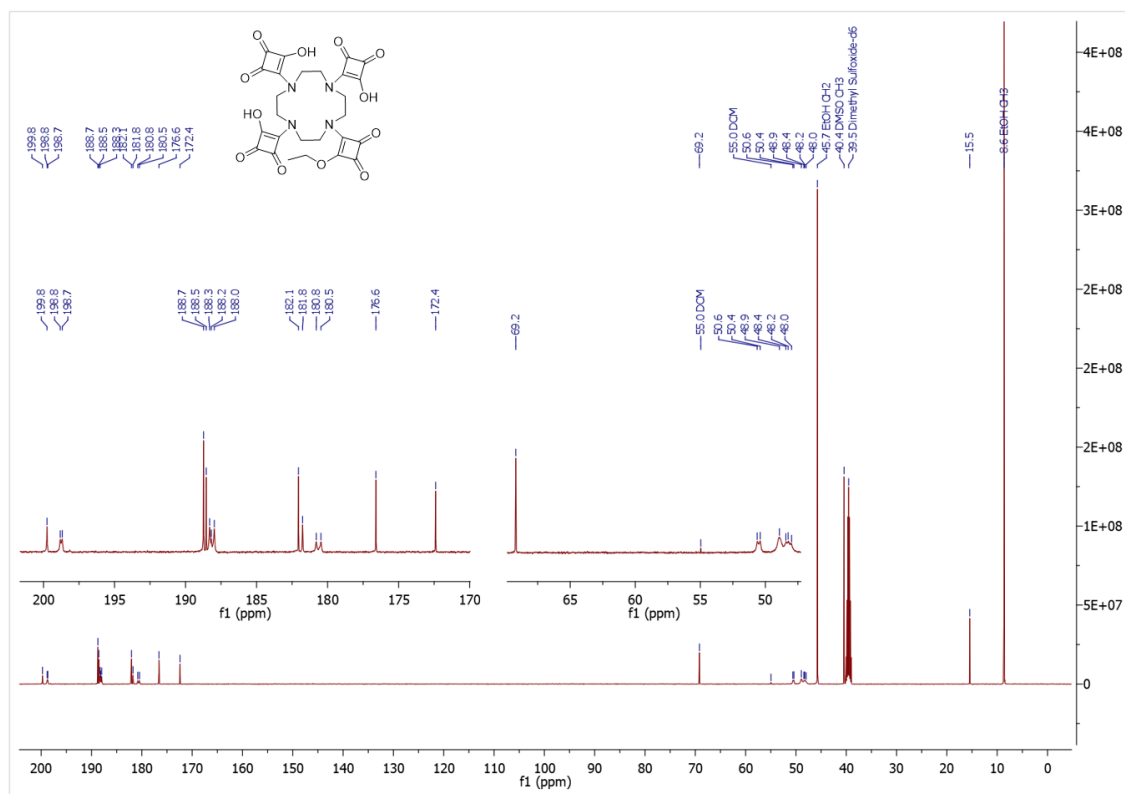
Figure S3.105: ^{13}C NMR spectrum of **SqO3A-ESq (3.16)** in DMSO-d_6.
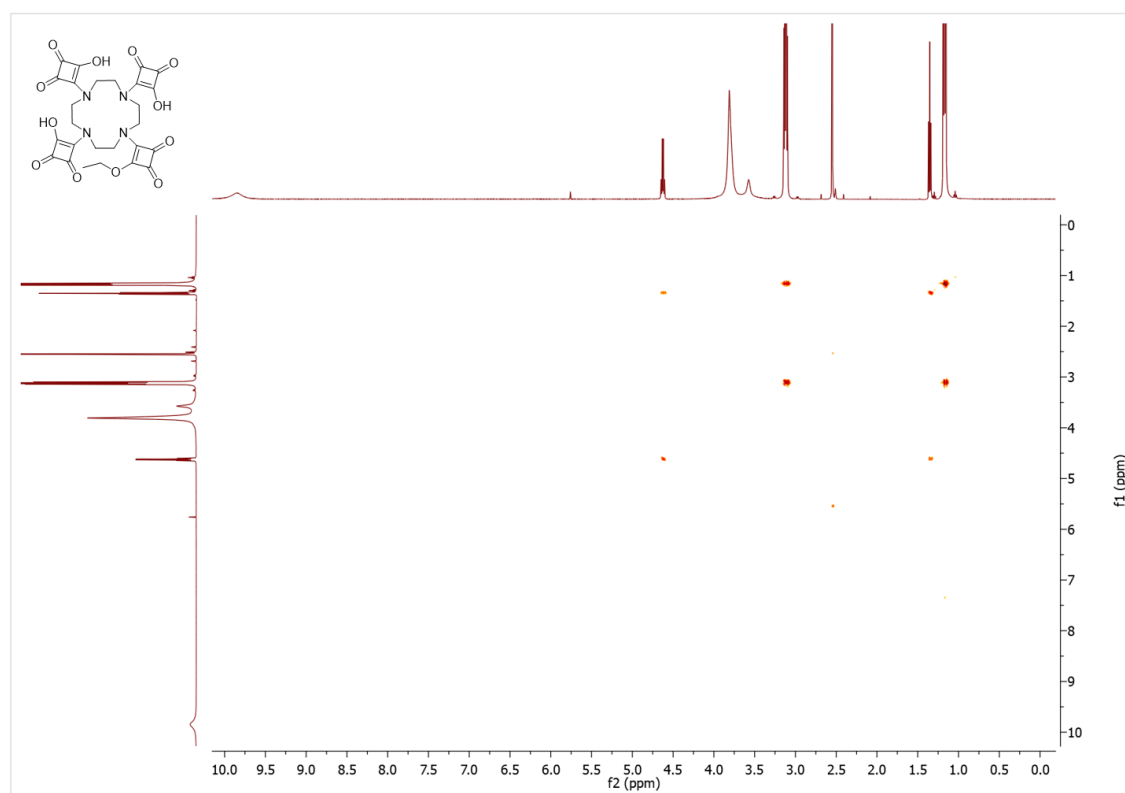
Figure S3.106: COSY spectrum of **SqO3A-ESq (3.16)** in DMSO-d_6.
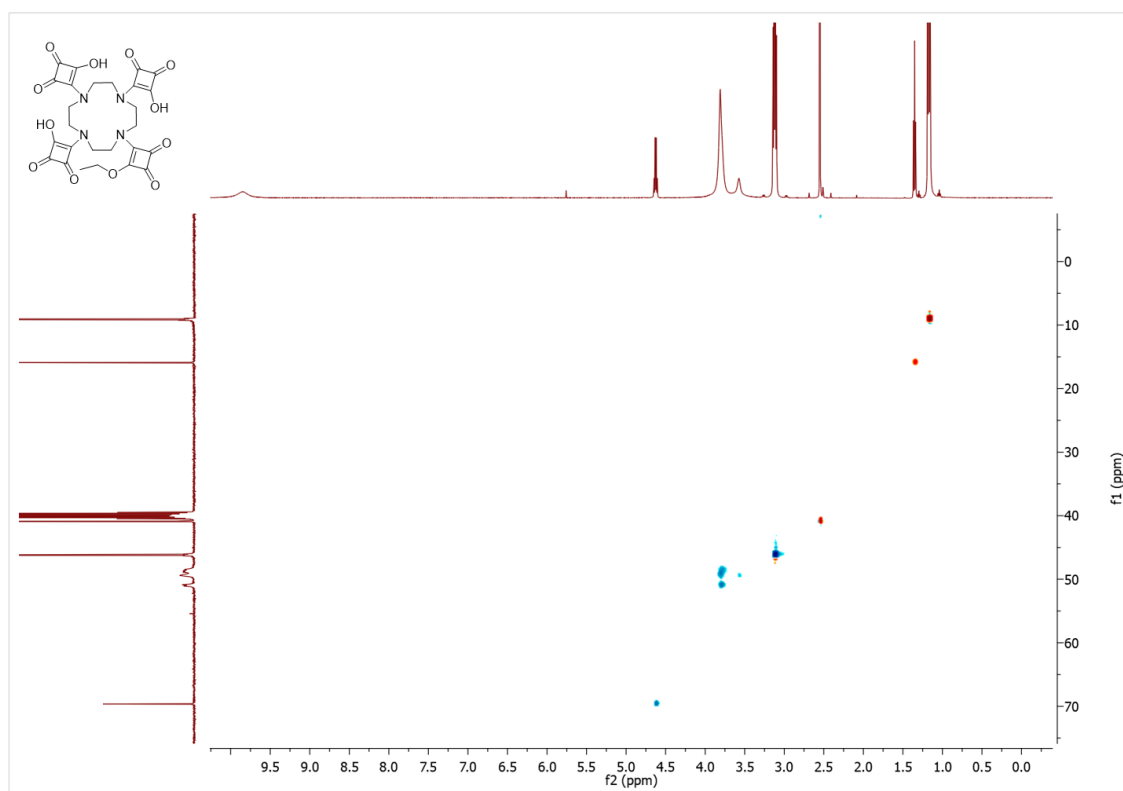
Figure S3.107: HSQC spectrum of **SqO3A-ESq (3.16)** in DMSO-d_6.
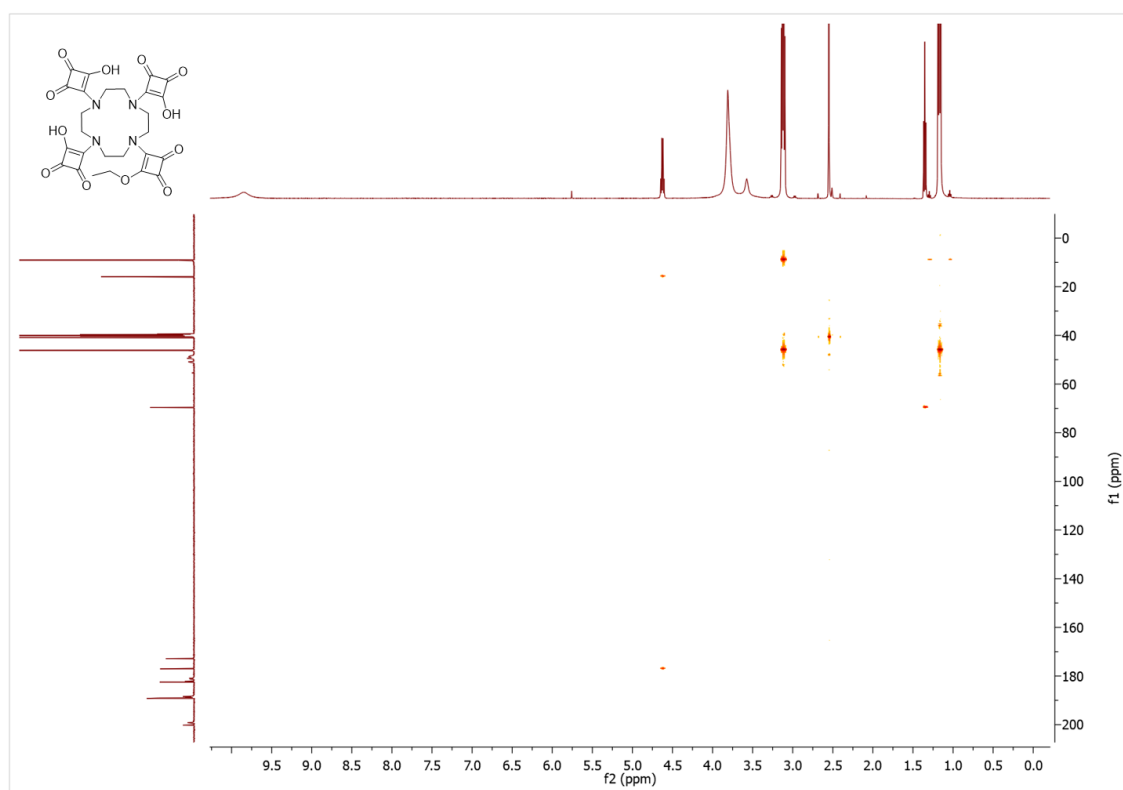
Figure S3.108: HMBC spectrum of **SqO3A-ESq (3.16)** in DMSO-d_6.

Acquisition Parameter

Source Type	ESI	Ion Polarity	Negative	Set Nebulizer	2.0 Bar
Focus	Active	Set Capillary	3000 V	Set Dry Heater	220 °C
Scan Begin	50 m/z	Set End Plate Offset	-500 V	Set Dry Gas	11.0 l/min
Scan End	1000 m/z	Set Charging Voltage	2000 V	Set Divert Valve	Source
		Set Corona	4000 nA	Set APCI Heater	200 °C
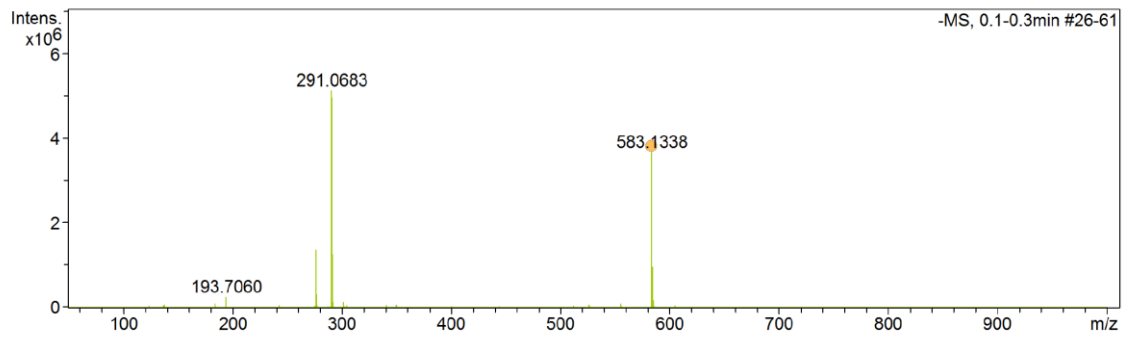
Meas. m/z	#	Ion Formula	m/z	err [ppm]	mSigma	# mSigma	Score	rdb	e⁻ Conf	N-Rule
583.1338	1	C26H23N4O12	583.1318	-3.5	23.3	1	100.00	17.5	even	ok
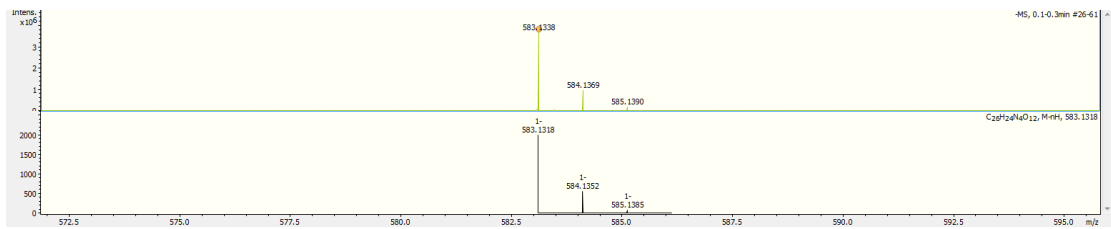
Figure S3.109: HRMS data for **SqO3A-ESq (3.16)**.
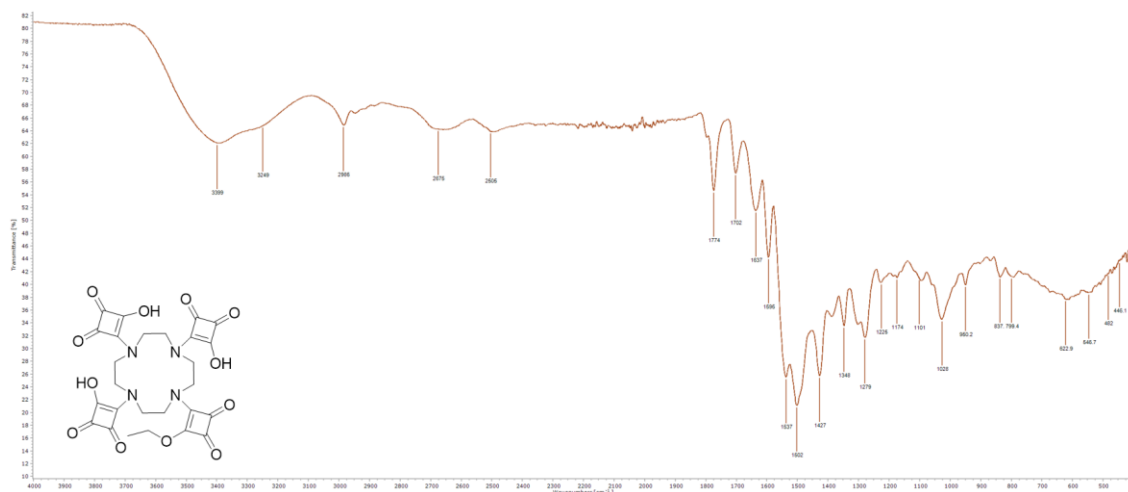
Figure S3.110: FTIR-ATR spectrum of **SqO3A-ESq (3.16)**.
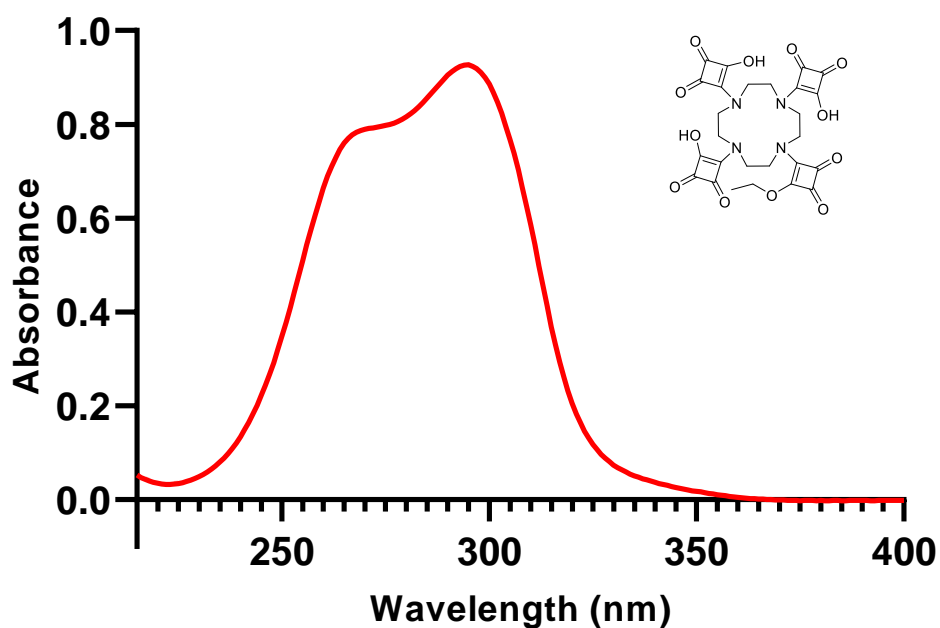
Figure S3.111: Absorbance spectrum of **SqO3A-ESq (3.16)** (20 µM) in H$_2$O.
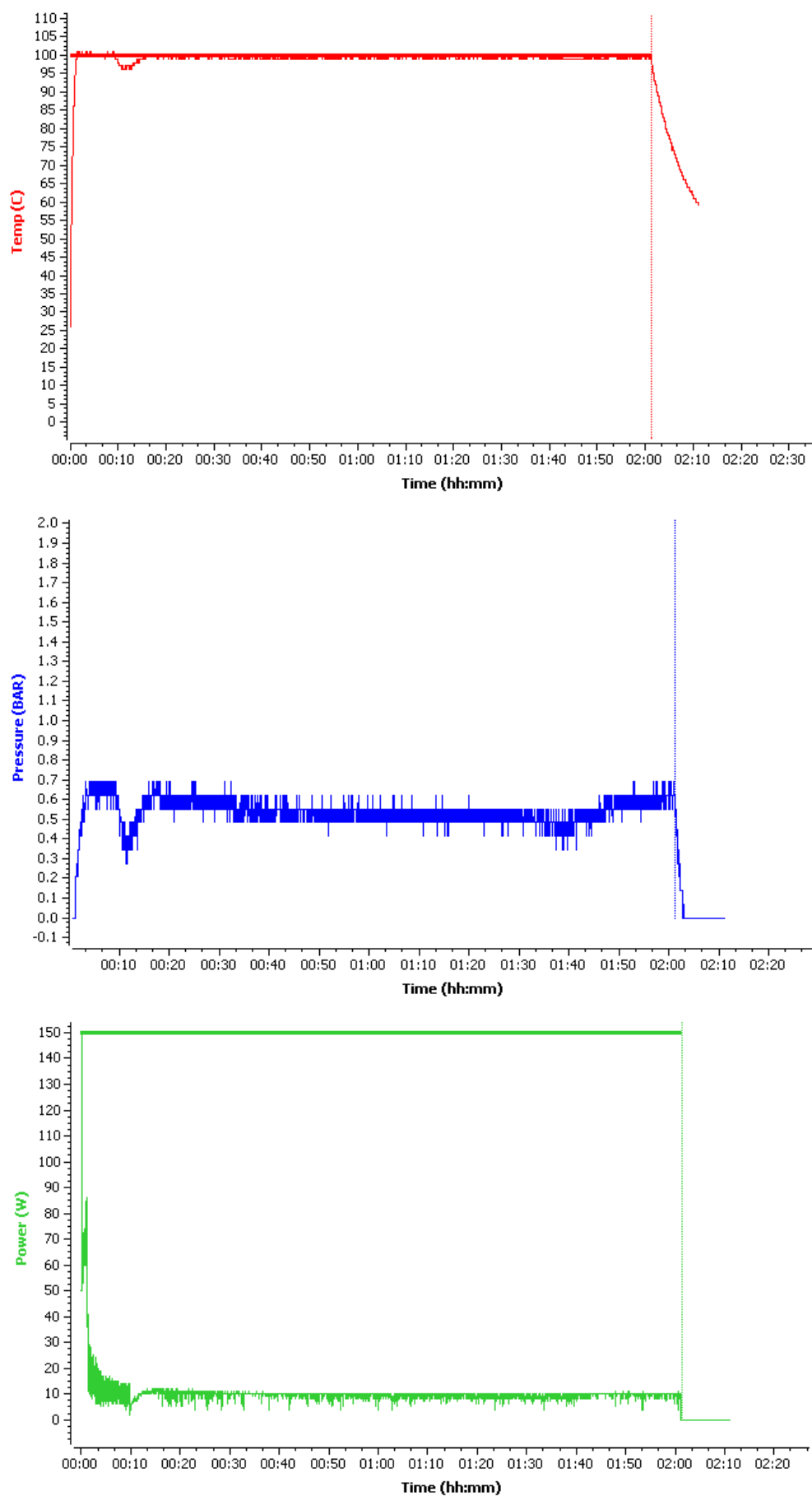
Figure S3.112: Microwave reaction conditions for the synthesis of **SqO3A-ESq (3.16)**.
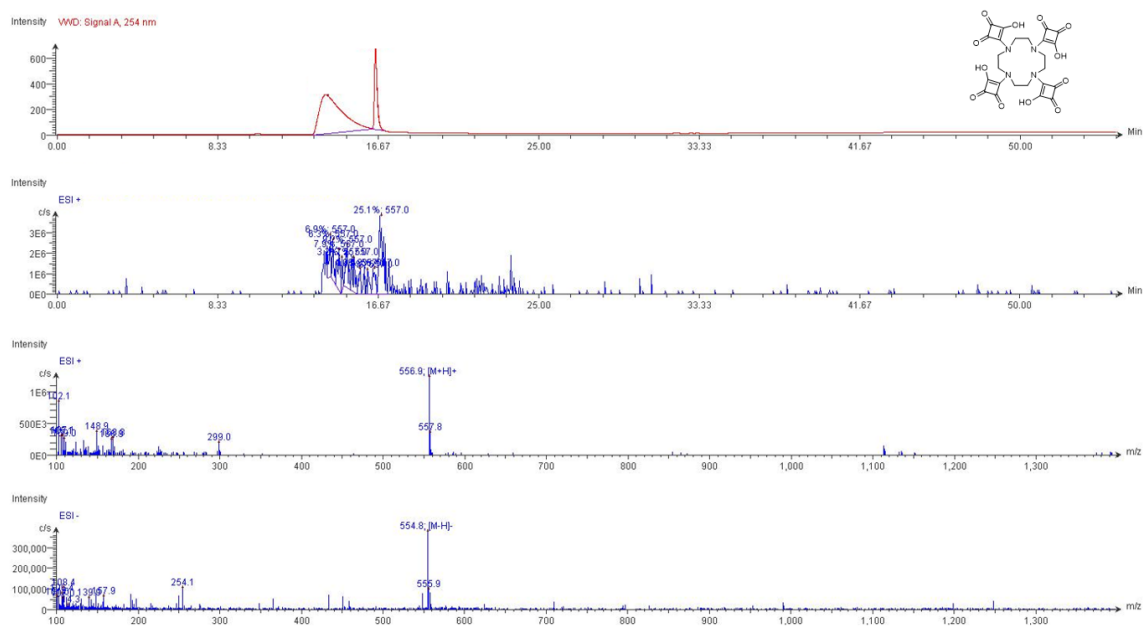
Figure S3.113: LC-MS data for **SqOTA (3.17)**.
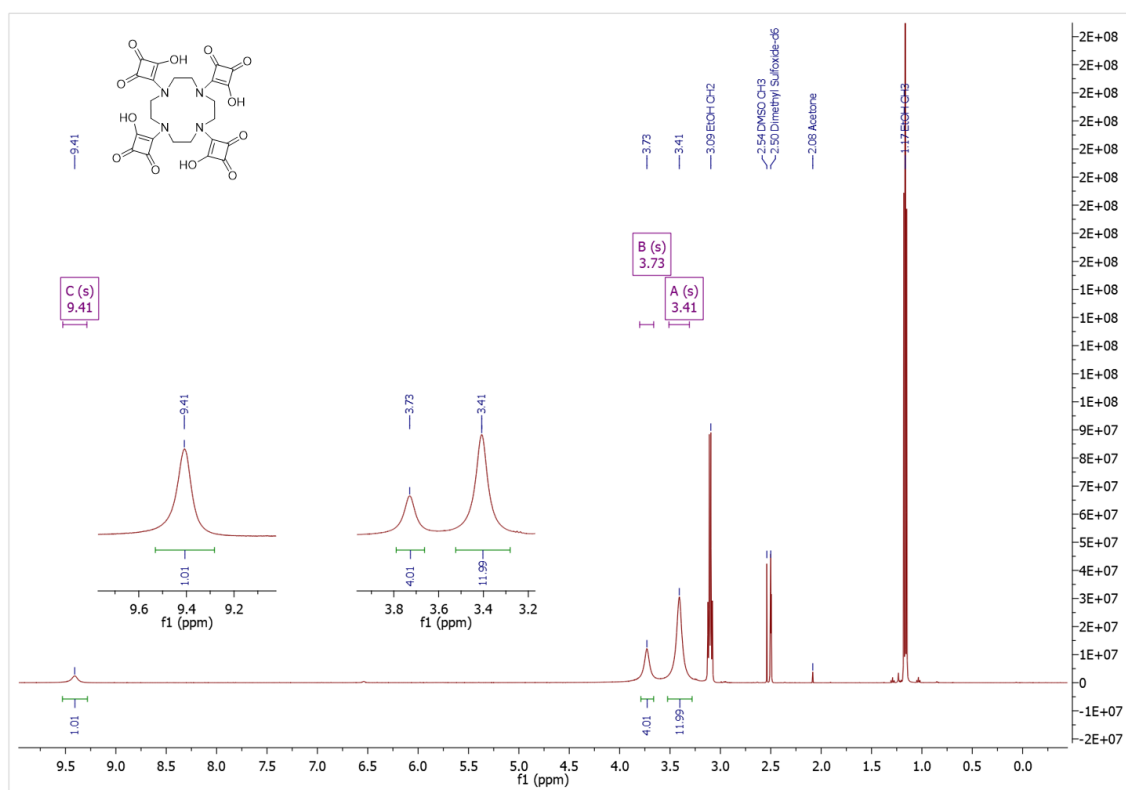
Figure S3.114: ¹H NMR spectrum of **SqOTA (3.17)** in DMSO-*d*₆.

Acquisition Parameter

Source Type	ESI	Ion Polarity	Positive	Set Nebulizer	0.8 Bar
Focus	Active	Set Capillary	6000 V	Set Dry Heater	180 °C
Scan Begin	50 m/z	Set End Plate Offset	-500 V	Set Dry Gas	2.0 l/min
Scan End	1000 m/z	Set Charging Voltage	2000 V	Set Divert Valve	Source
		Set Corona	4000 nA	Set APCI Heater	200 °C
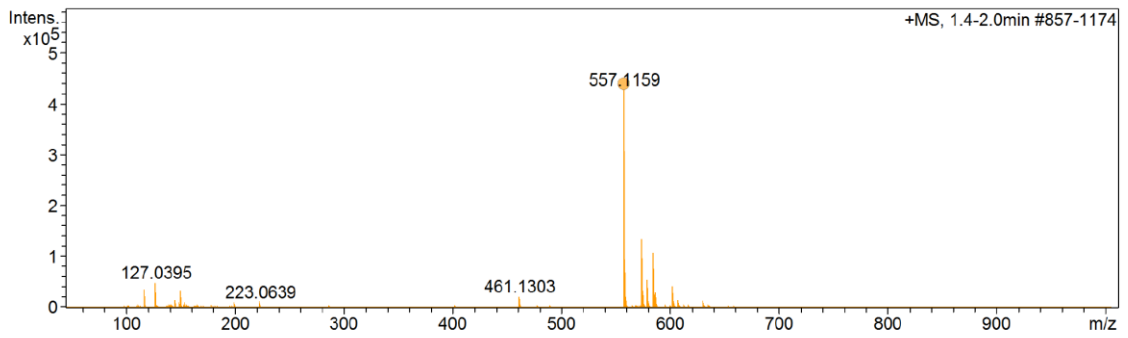
Meas. m/z	#	Ion Formula	m/z	err [ppm]	mSigma	# mSigma	Score	rdb	e⁻ Conf	N-Rule
557.1159	1	C24H21N4O12	557.1150	-1.6	29.8	1	100.00	16.5	even	ok
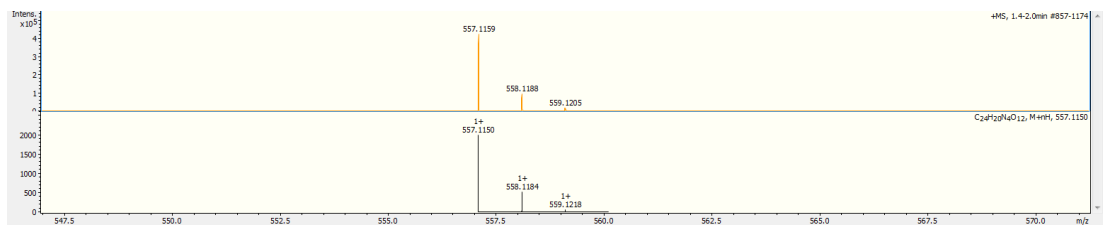
Figure S3.115: HRMS data for **SqOTA (3.17)**.

Figure S3.116: LC-MS data for **Ac-DEVD(O*t*Bu)-EDA-Sq-DO3A*t*Bu (3.18)**.

Figure S3.117: ^{1}H NMR spectrum of **Ac-DEVD(O*t*Bu)-EDA-Sq-DO3A*t*Bu (3.18)** in DMSO-*d*₆.
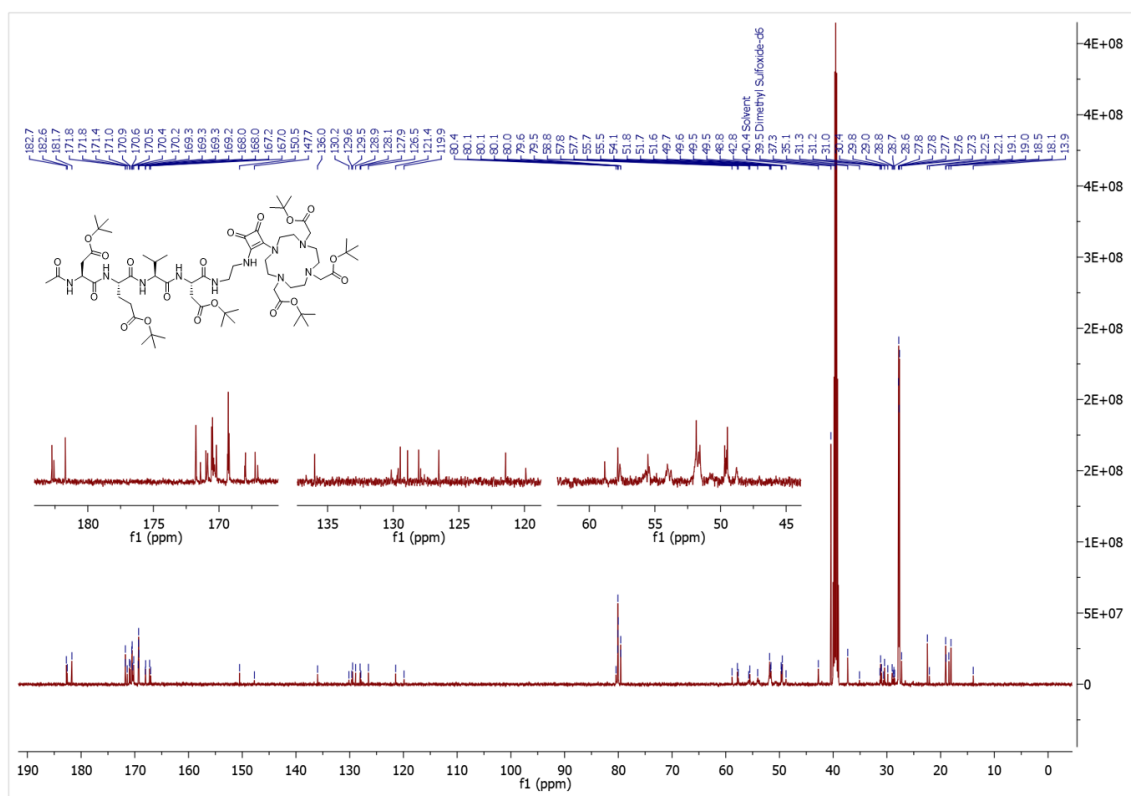
Figure S3.118: ^{13}C NMR spectrum of **Ac-DEVD(O*t*Bu)-EDA-Sq-DO3A*t*Bu (3.18)** in DMSO-d_6.
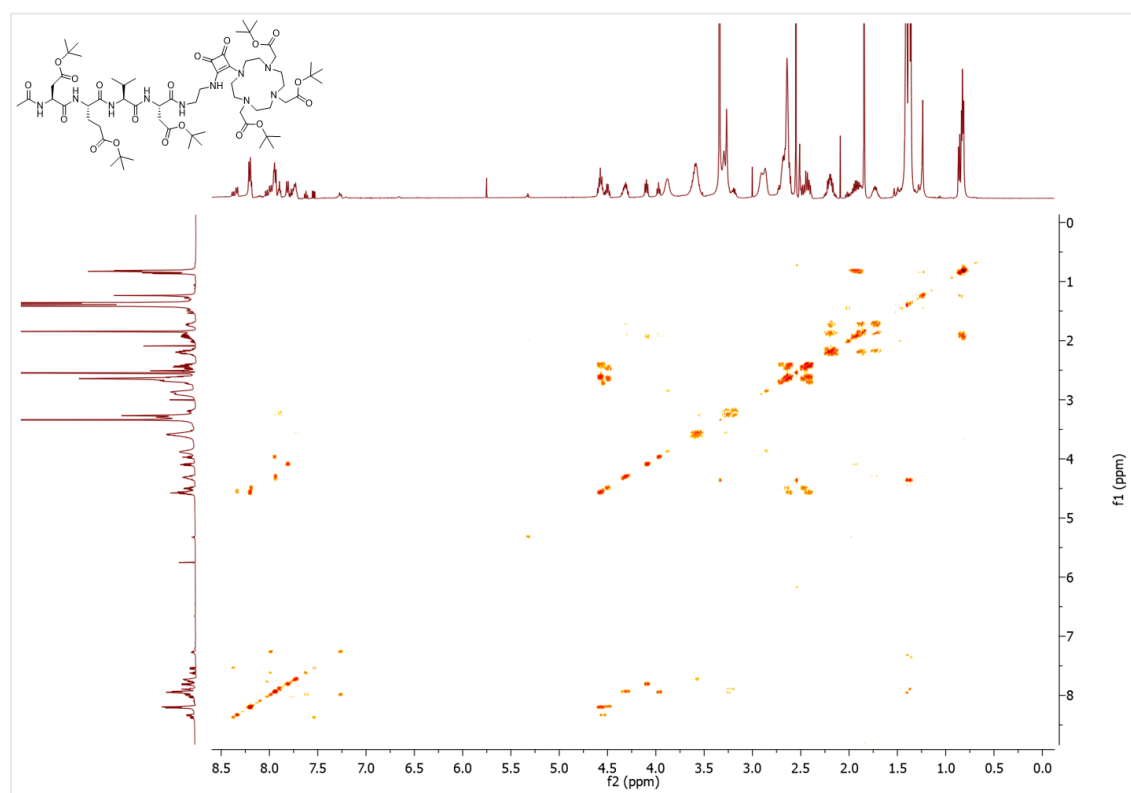
Figure S3.119: COSY spectrum of **Ac-DEVD(O*t*Bu)-EDA-Sq-DO3A*t*Bu (3.18)** in DMSO-d_6.
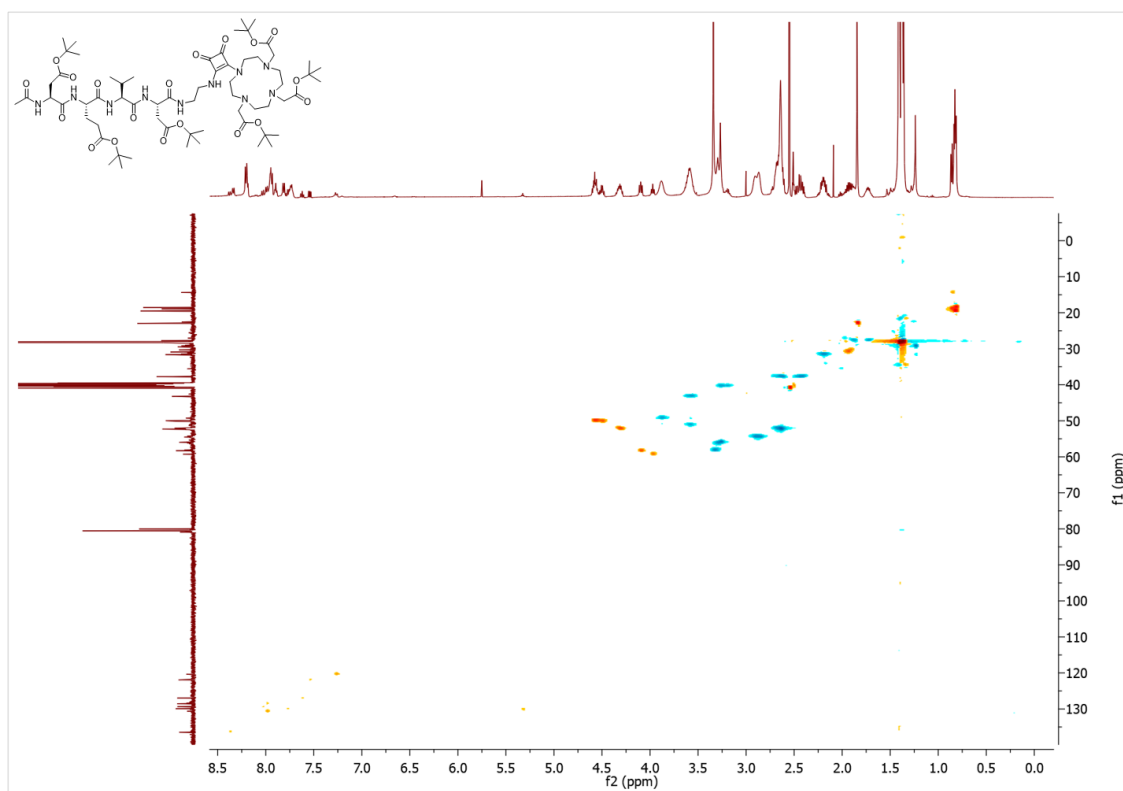
Figure S3.120: HSQC spectrum of **Ac-DEVD(O*t*Bu)-EDA-Sq-DO3A*t*Bu (3.18)** in DMSO-*d*₆.
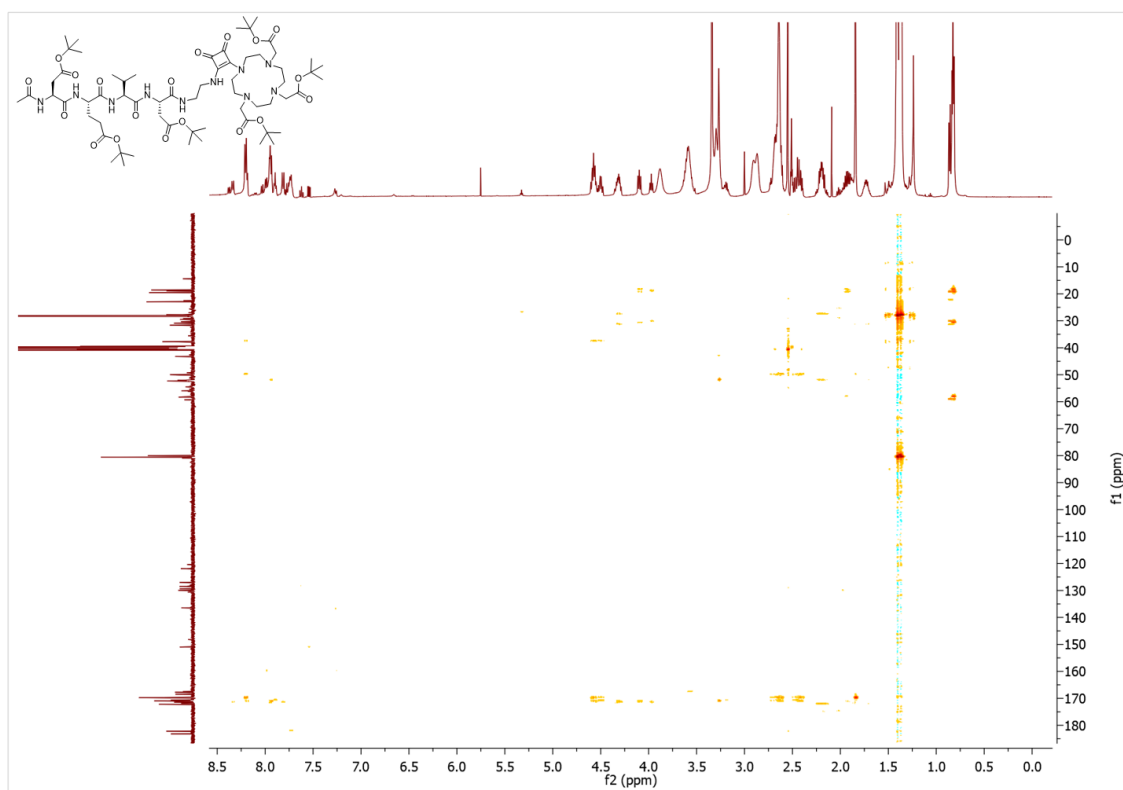
Figure S3.121: HMBC spectrum of **Ac-DEVD(O*t*Bu)-EDA-Sq-DO3A*t*Bu (3.18)** in DMSO-*d*₆.

Compound Table

Compound Label	RT (min)	Observed mass (m/z)	Neutral observed mass (Da)	Theoretical mass (Da)	Mass error (ppm)	Isotope match score (%)
Cpd 1: C64 H108 N10 O19	0.67	1321.7888	1320.7811	1320.7792	1.44	98.58

Mass errors of between -5.00 and 5.00 ppm with isotope match scores above 60% are considered confirmation of molecular formulae
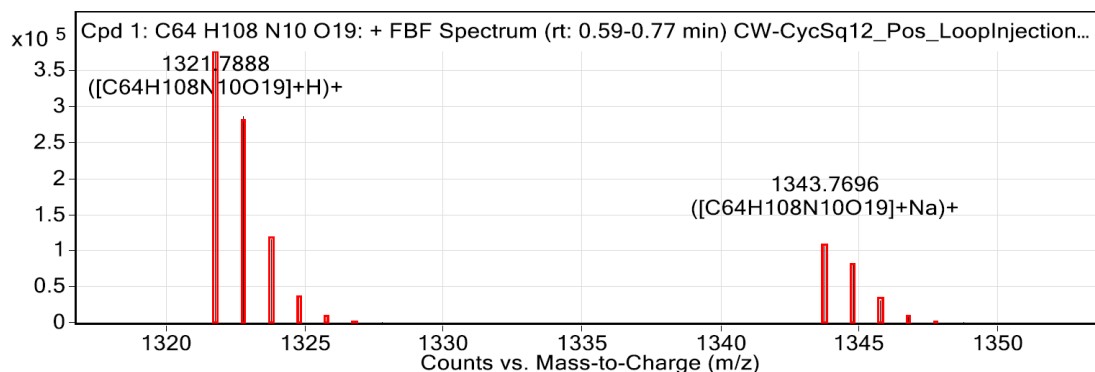
Figure: Zoomed Compound spectra view
(red boxes indicating expected theoretical isotope spacing and abundance)

Compound isotope peak List

m/z	z	Abund	Formula	Ion
1321.7888	1	375484.6	C64H108N10O19	(M+H)+
1322.7922	1	285854.8	C64H108N10O19	(M+H)+
1323.7942	1	115114.7	C64H108N10O19	(M+H)+
1324.7954	1	29964.7	C64H108N10O19	(M+H)+
1325.7966	1	6466.3	C64H108N10O19	(M+H)+
1343.7696	1	107641.2	C64H108N10O19	(M+Na)+
1344.7725	1	80616.2	C64H108N10O19	(M+Na)+
1345.7742	1	30165.6	C64H108N10O19	(M+Na)+
1346.7757	1	8371.5	C64H108N10O19	(M+Na)+
1347.7773	1	2055.8	C64H108N10O19	(M+Na)+

Figure S3.122: HRMS data for **Ac-DEVD(O*t*Bu)-EDA-Sq-DO3A*t*Bu (3.18)**.
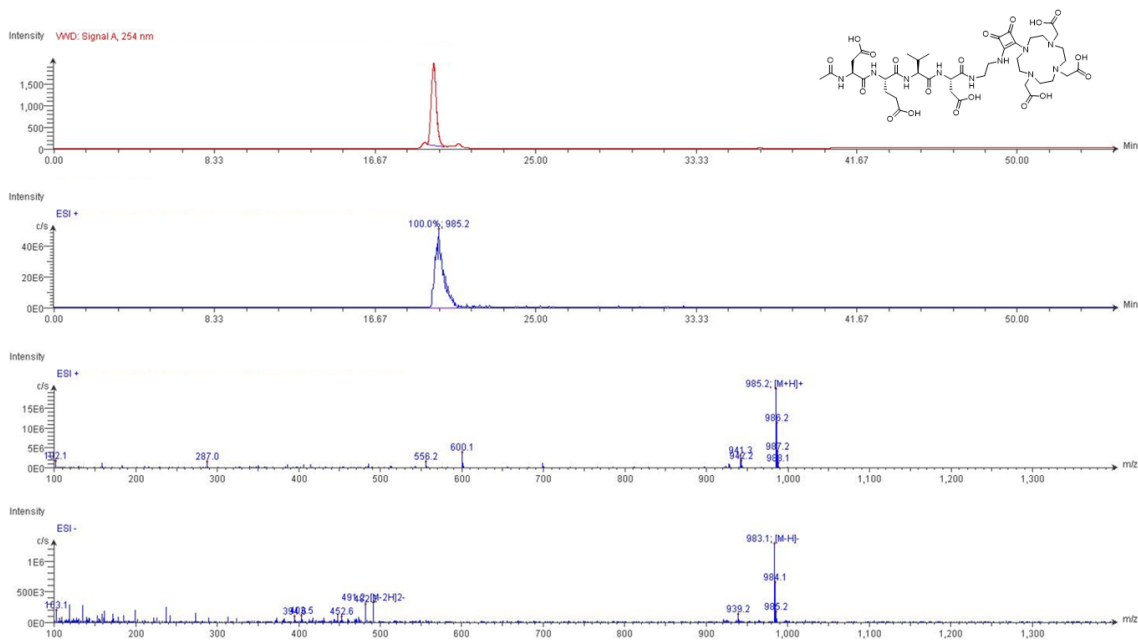
Figure S3.123: LC-MS data for **Ac-DEVD-EDA-Sq-DO3A (3.19)**.
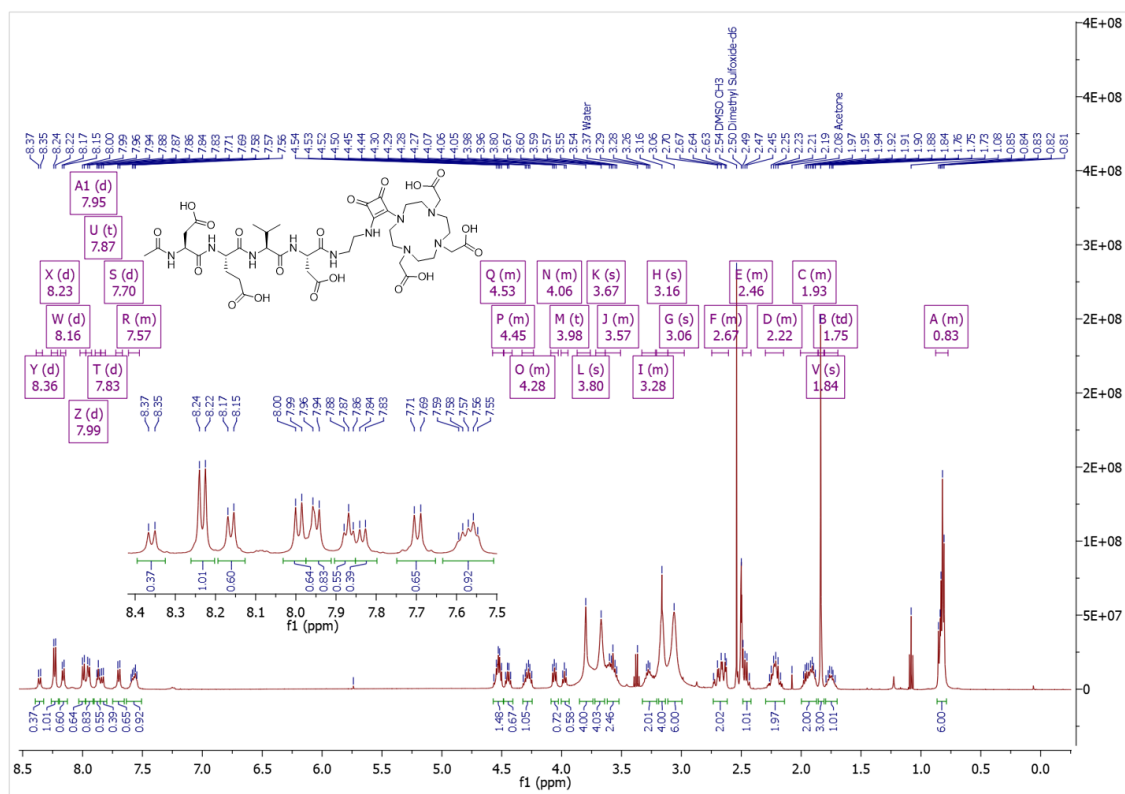
Figure S3.124: ¹H NMR spectrum of **Ac-DEVD-EDA-Sq-DO3A (3.19)** in DMSO-*d*₆.
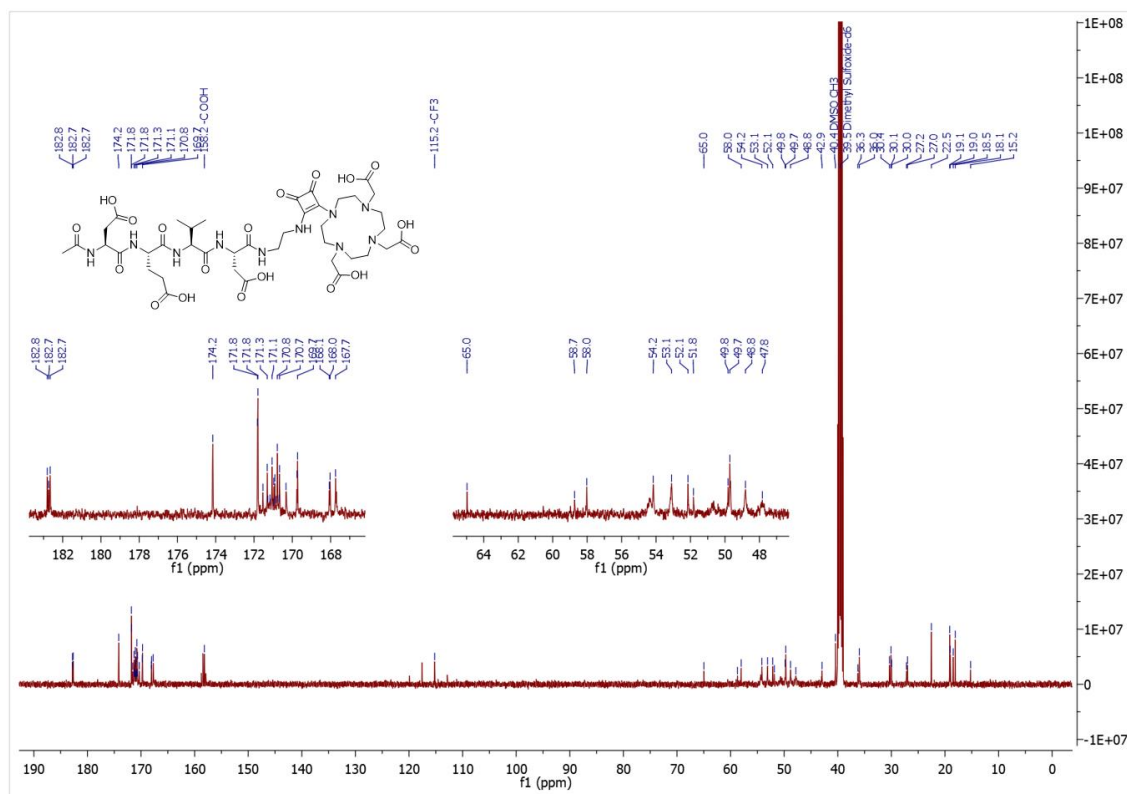
Figure S3.125: ^{13}C NMR spectrum of **Ac-DEVD-EDA-Sq-DO3A (3.19)** in DMSO-d_6.
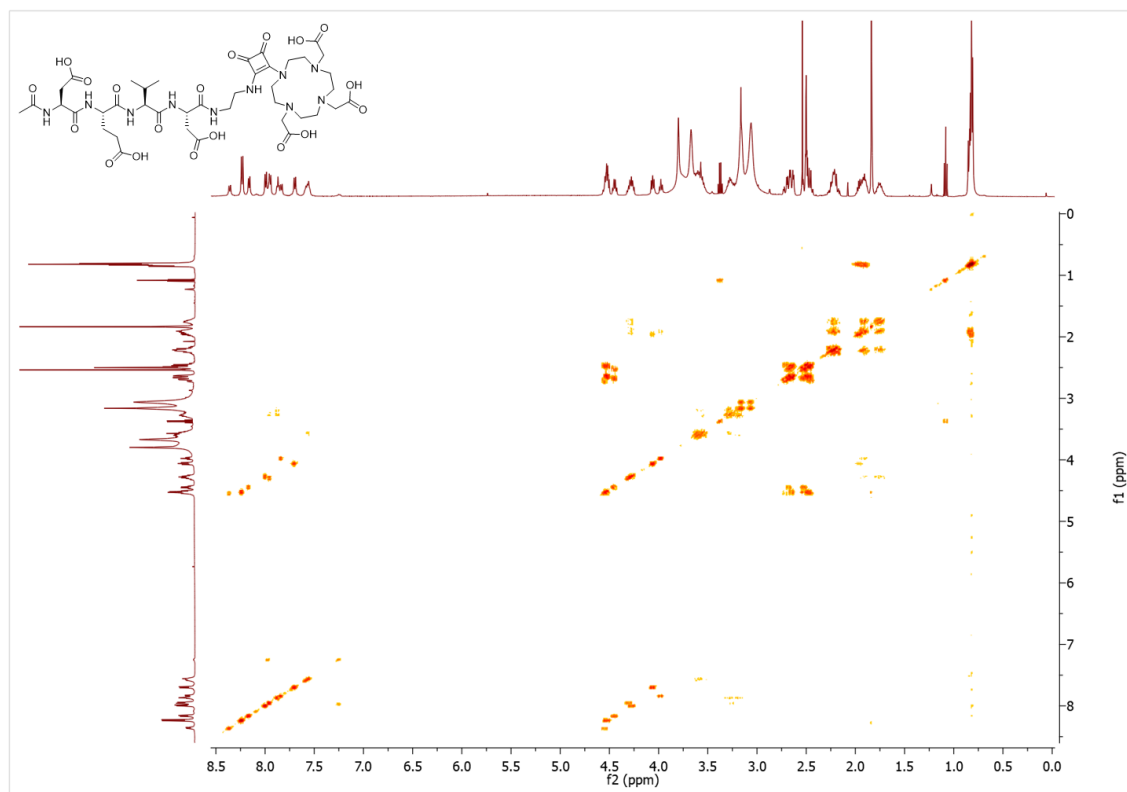
Figure S3.126: COSY spectrum of **Ac-DEVD-EDA-Sq-DO3A (3.19)** in DMSO-d_6.
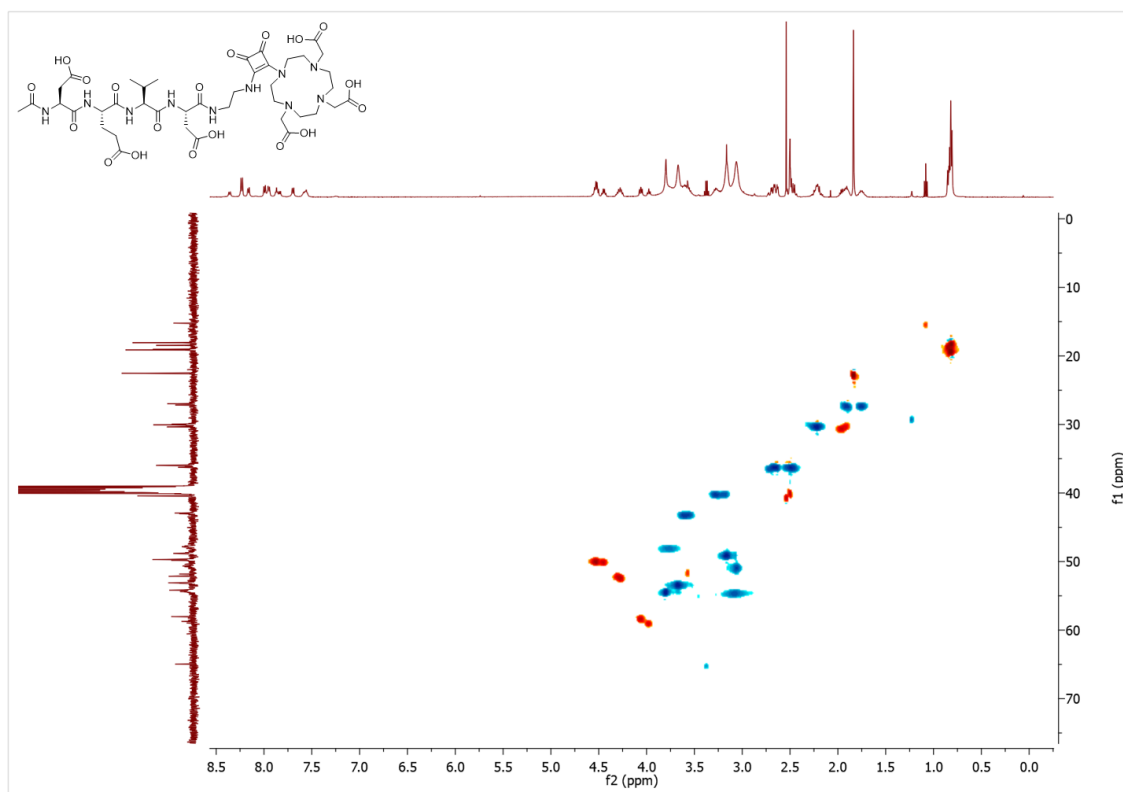
Figure S3.127: HSQC spectrum of **Ac-DEVD-EDA-Sq-DO3A (3.19)** in DMSO-d_6.
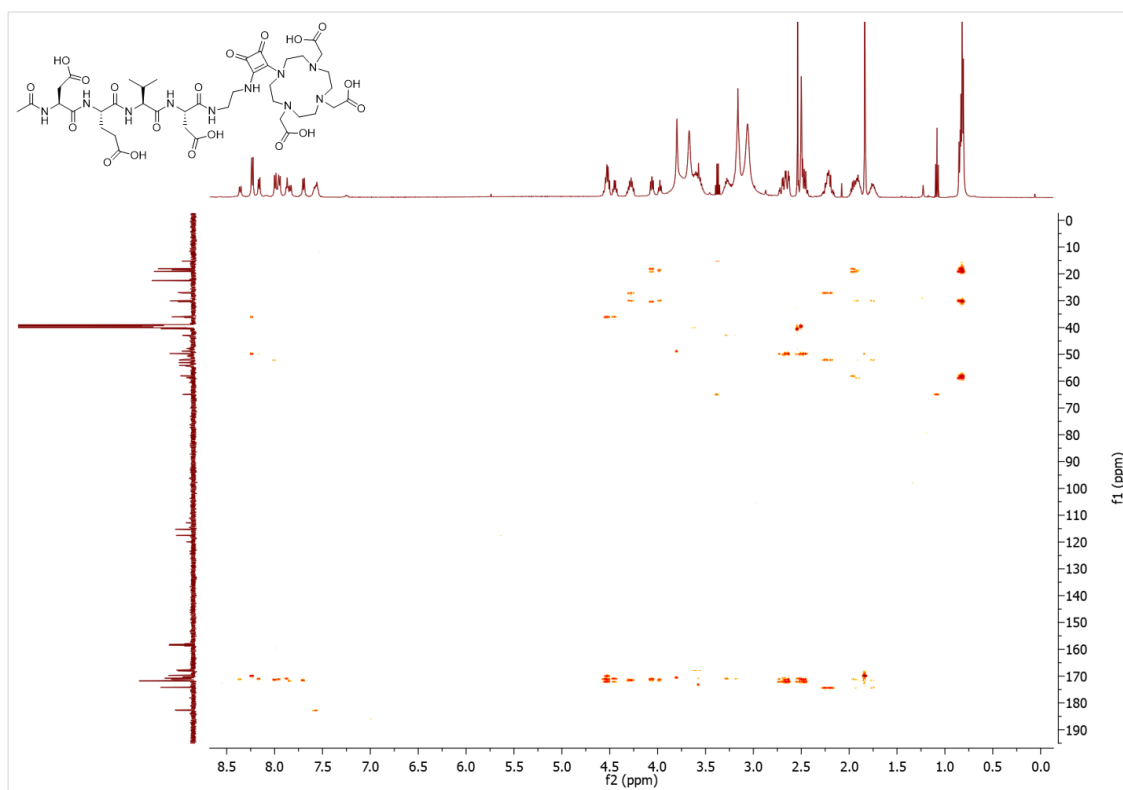
Figure S3.128: HMBC spectrum of **Ac-DEVD-EDA-Sq-DO3A (3.19)** in DMSO-d_6.

Compound Table

Compound Label	RT (min)	Observed mass (m/z)	Neutral observed mass (Da)	Theoretical mass (Da)	Mass error (ppm)	Isotope match score (%)
Cpd 1: C40 H60 N10 O19	0.73	985.4115	984.4037	984.4036	0.11	97.27

Mass errors of between -5.00 and 5.00 ppm with isotope match scores above 60% are considered confirmation of molecular formulae
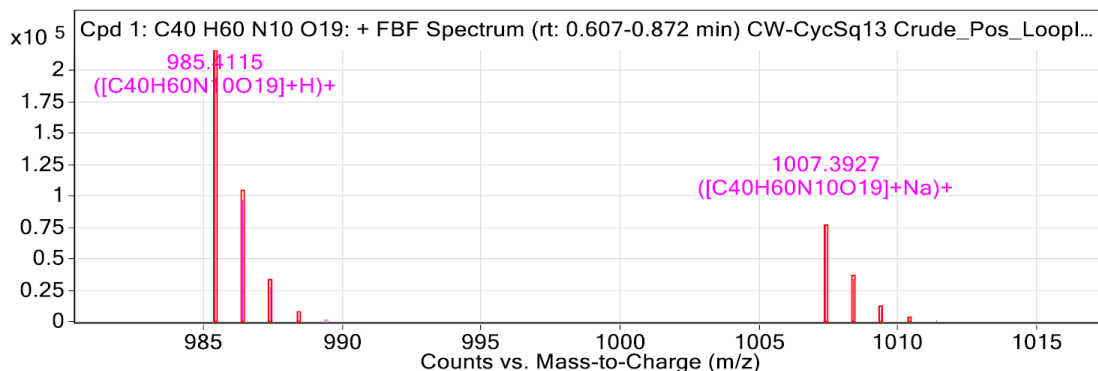
Figure: Zoomed Compound spectra view
(red boxes indicating expected theoretical isotope spacing and abundance)

Compound isotope peak List

m/z	z	Abund	Formula	Ion
985.4115	1	215607.8	C40H60N10O19	(M+H)+
986.4139	1	96553.8	C40H60N10O19	(M+H)+
987.4159	1	27352.0	C40H60N10O19	(M+H)+
988.4177	1	6491.3	C40H60N10O19	(M+H)+
1007.3927	1	76637.5	C40H60N10O19	(M+Na)+
1008.3951	1	33786.1	C40H60N10O19	(M+Na)+
1009.3968	1	10465.7	C40H60N10O19	(M+Na)+
1010.3983	1	2662.9	C40H60N10O19	(M+Na)+
1011.3908	1	768.5	C40H60N10O19	(M+Na)+

Figure S3.129: HRMS data for **Ac-DEVD-EDA-Sq-DO3A (3.19)**.
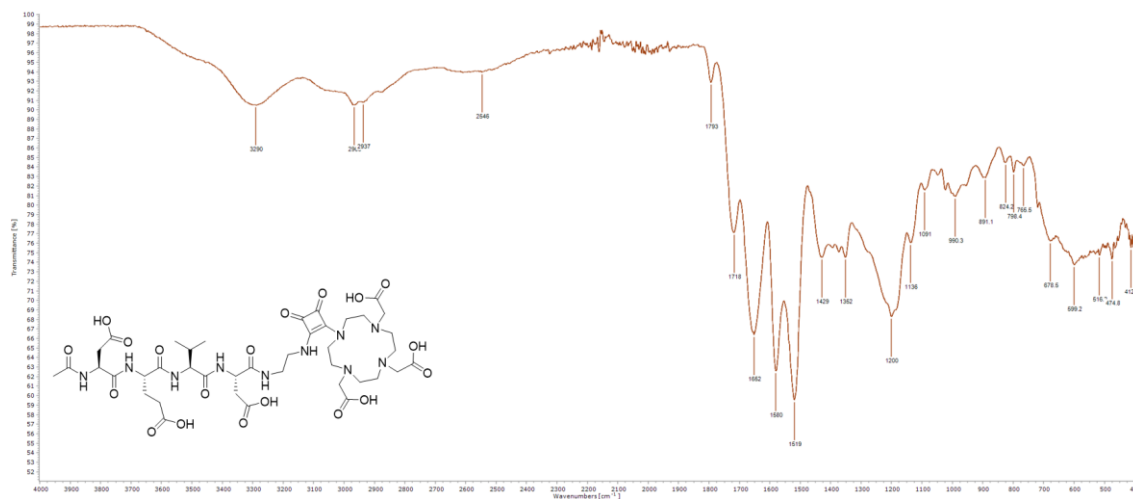
Figure S3.130: FTIR-ATR spectrum of **Ac-DEVD-EDA-Sq-DO3A (3.19)**.
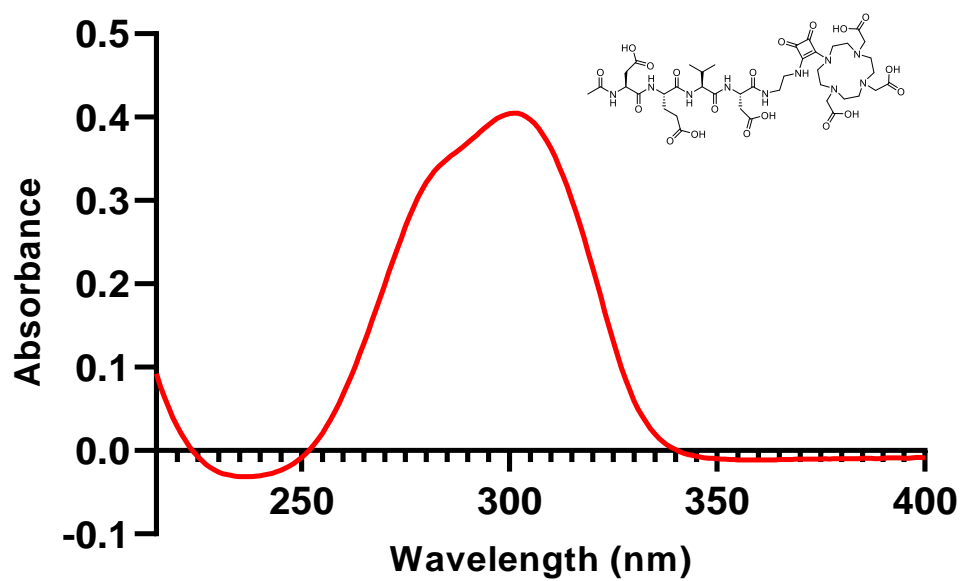
Figure S3.131: Absorbance spectrum of **Ac-DEVD-EDA-Sq-DO3A (3.19)** (20 µM) in H$_2$O.

Chapter 4 – Supplementary Characterisation Data

Figure S4.1: LC-MS data for **Fmoc-NMeV-R(Pbf)-OH**.

Figure S4.2: LC-MS data for **Fmoc-f-NMeV-R(Pbf)-OH**.

Figure S4.3: LC-MS data for **Fmoc-D(O*t*Bu)-f-*N*MeV-R(Pbf)-OH**.

Figure S4.4: LC-MS data for **ESq-D(O*t*Bu)-f-*N*MeV-R(Pbf)-OH (4.1)**.

Figure S4.5: LC-MS data for **ASq-D(O*t*Bu)-f-*N*MeV-R(Pbf)-OH (4.2)**.

Figure S4.6: LC-MS data for **ESq-f-*N*MeV-R(Pbf)-OH (4.5)**.
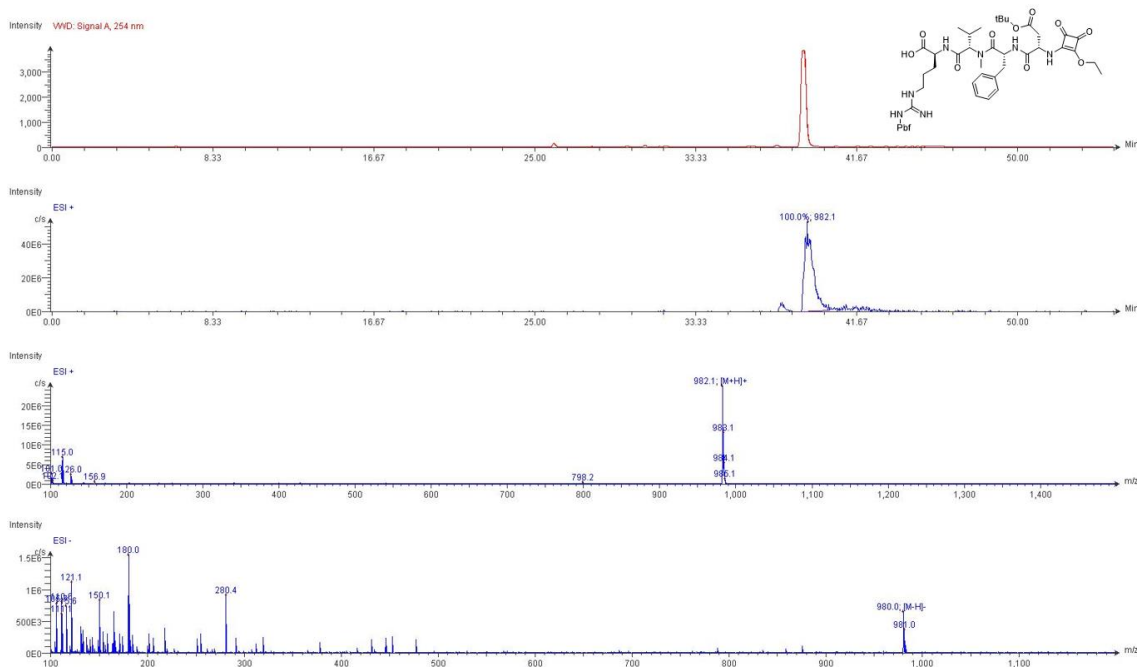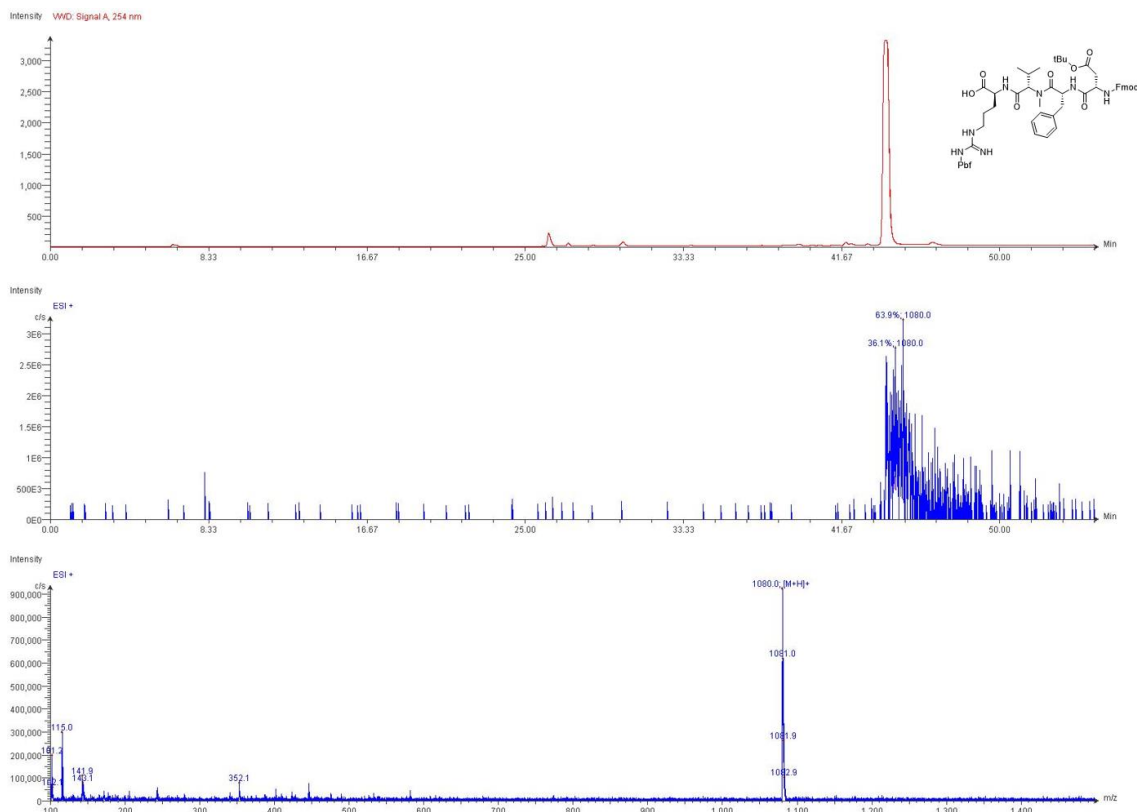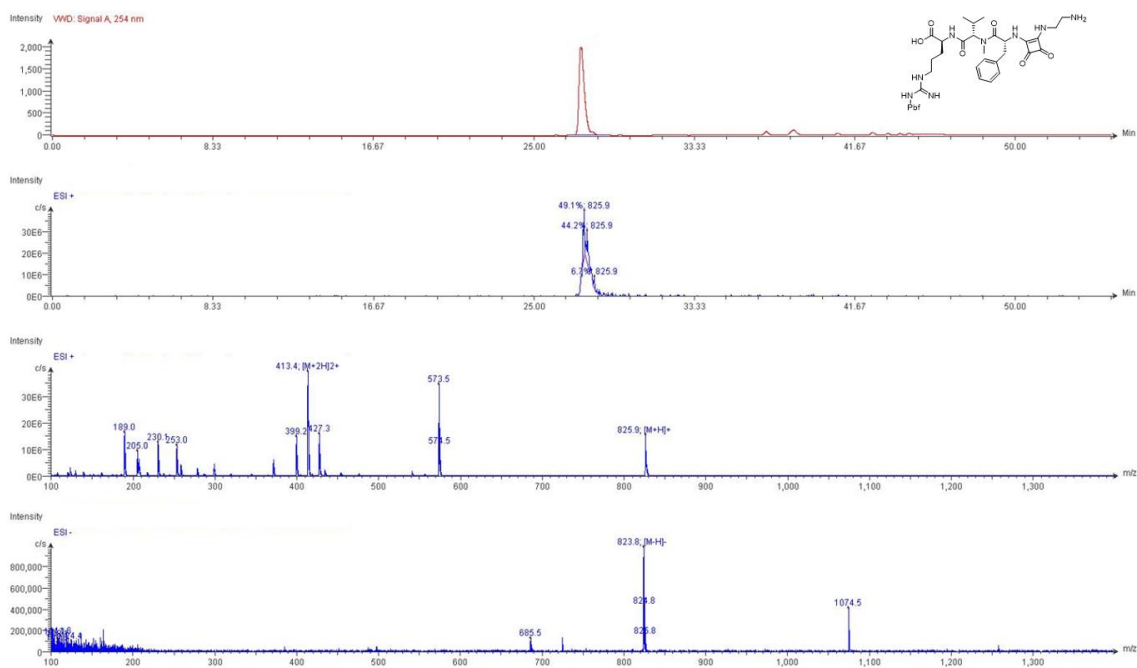
Figure S4.7: LC-MS data for **NH₂-G(*ψ*)-Sq-f-*N*MeV-R(Pbf)-OH (4.6)**.
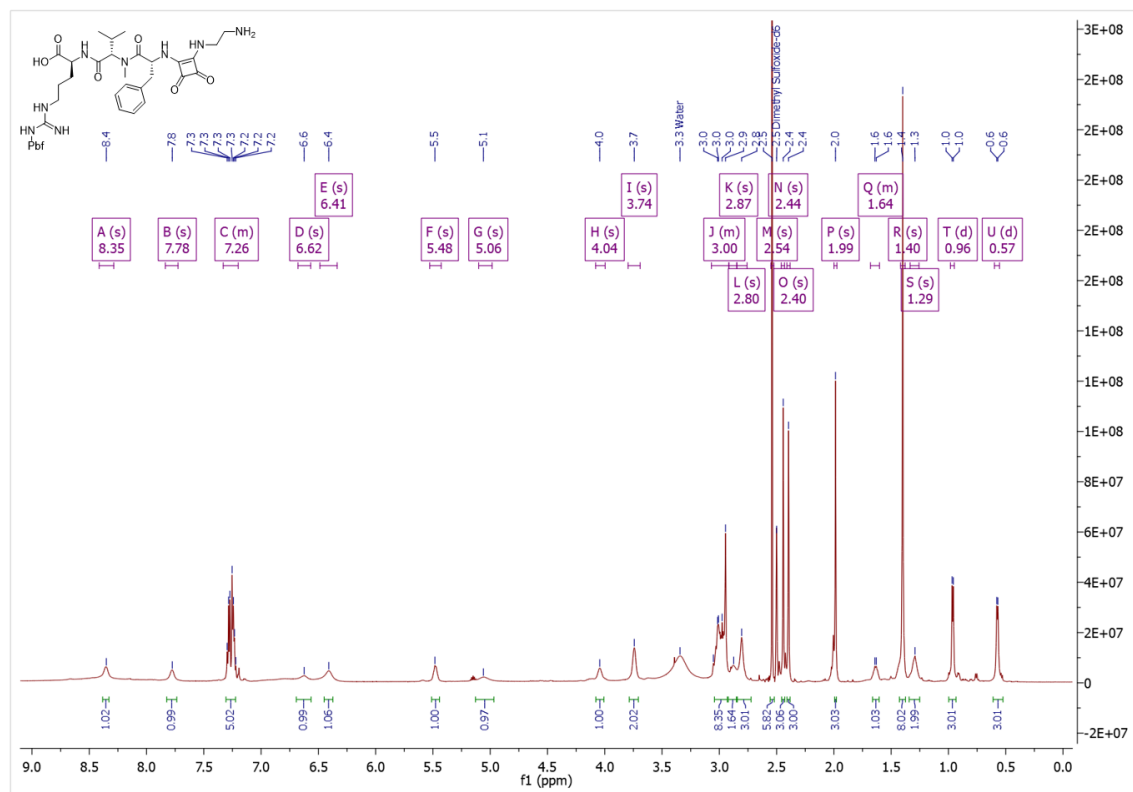
Figure S4.8: ¹H NMR spectrum of **NH₂-G(*ψ*)-Sq-f-*N*MeV-R(Pbf)-OH (4.6)** in DMSO-*d₆*.
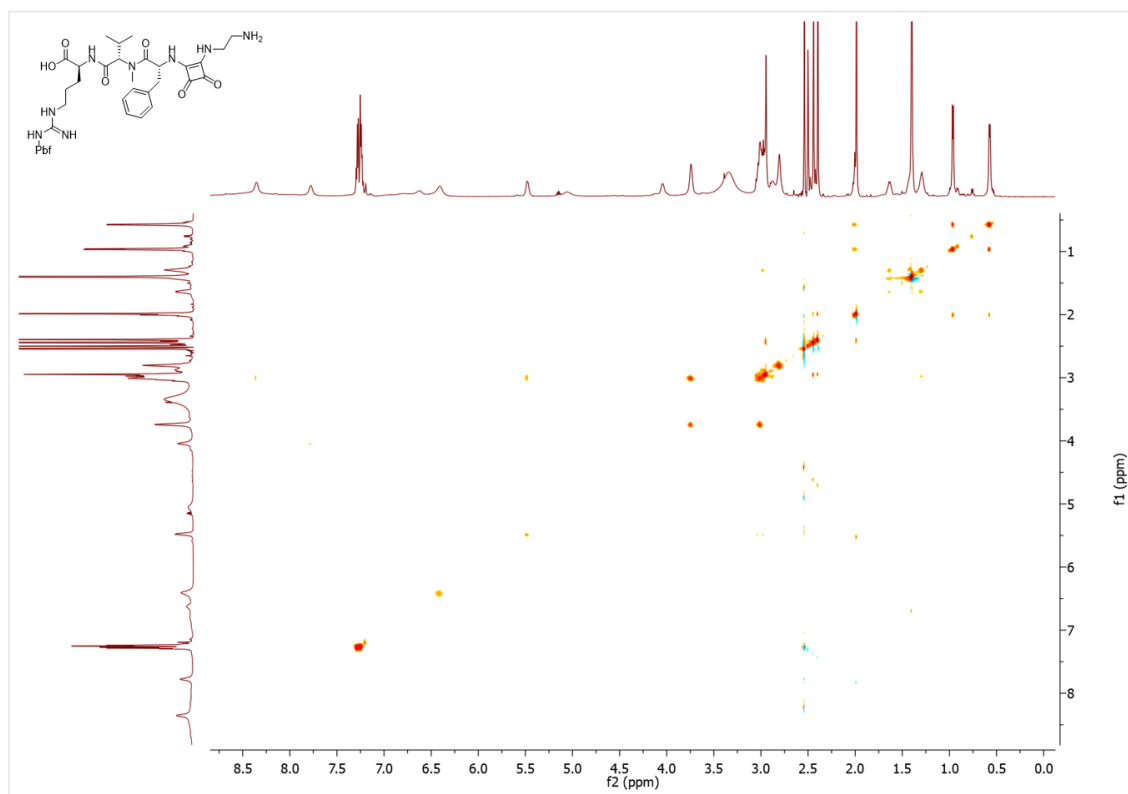
Figure S4.9: COSY spectrum of **NH$_2$-G(ψ)-Sq-f-*N*MeV-R(Pbf)-OH (4.6)** in DMSO-*d$_6$*.
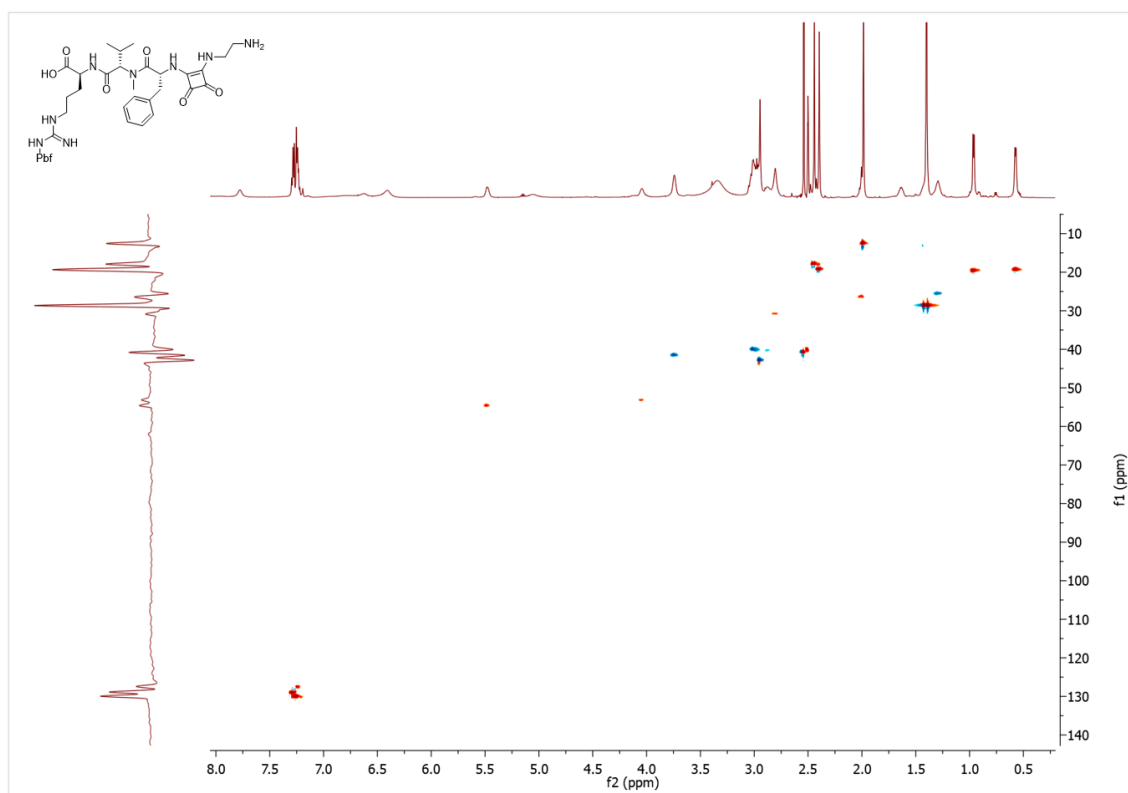
Figure S4.10: HSQC spectrum of **NH$_2$-G(ψ)-Sq-f-*N*MeV-R(Pbf)-OH (4.6)** in DMSO-*d$_6$*.

Compound Table

Compound Label	RT (min)	Observed mass (m/z)	Neutral observed mass (Da)	Theoretical mass (Da)	Mass error (ppm)	Isotope match score (%)
Cpd 1: C40 H56 N8 O9 S	0.73	847.3779	824.3889	824.3891	-0.22	98.33

Mass errors of between -5.00 and 5.00 ppm with isotope match scores above 60% are considered confirmation of molecular formulae
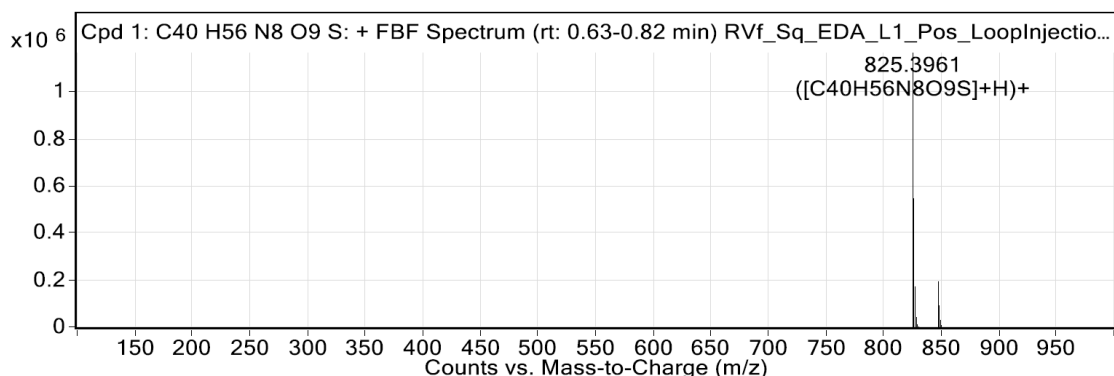
Figure: Full range view of Compound spectra and potential adducts.
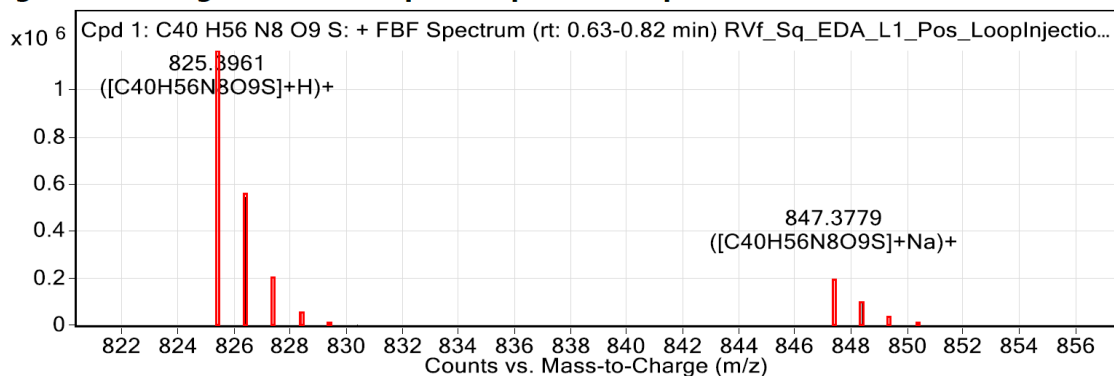
Figure: Zoomed Compound spectra view
(red boxes indicating expected theoretical isotope spacing and abundance)

Compound isotope peak List

m/z	z	Abund	Formula	Ion
825.3961	1	1162702.1	C40H56N8O9S	(M+H)+
826.3993	1	543844.7	C40H56N8O9S	(M+H)+
827.4000	1	171841.8	C40H56N8O9S	(M+H)+
828.4003	1	41933.5	C40H56N8O9S	(M+H)+
829.4009	1	8812.0	C40H56N8O9S	(M+H)+
830.4012	1	1629.3	C40H56N8O9S	(M+H)+
847.3779	1	193847.2	C40H56N8O9S	(M+Na)+
848.3805	1	91164.3	C40H56N8O9S	(M+Na)+
849.3806	1	29635.3	C40H56N8O9S	(M+Na)+
850.3845	1	7653.4	C40H56N8O9S	(M+Na)+

Figure S4.11: HRMS data for **NH₂-G(ψ)-Sq-f-NMeV-R(Pbf)-OH (4.6)**.
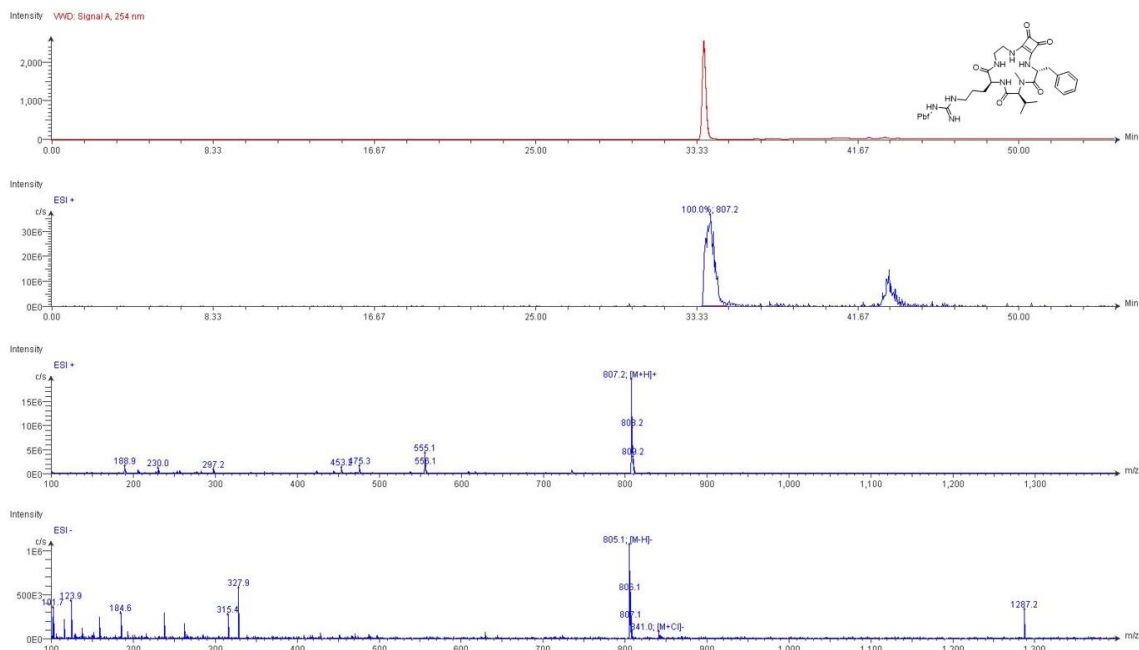
Figure S4.12: LC-MS data for the protected cyclic squaratide – *c*(RG(*ψ*)-Sq-f*N*MeV) (4.7).
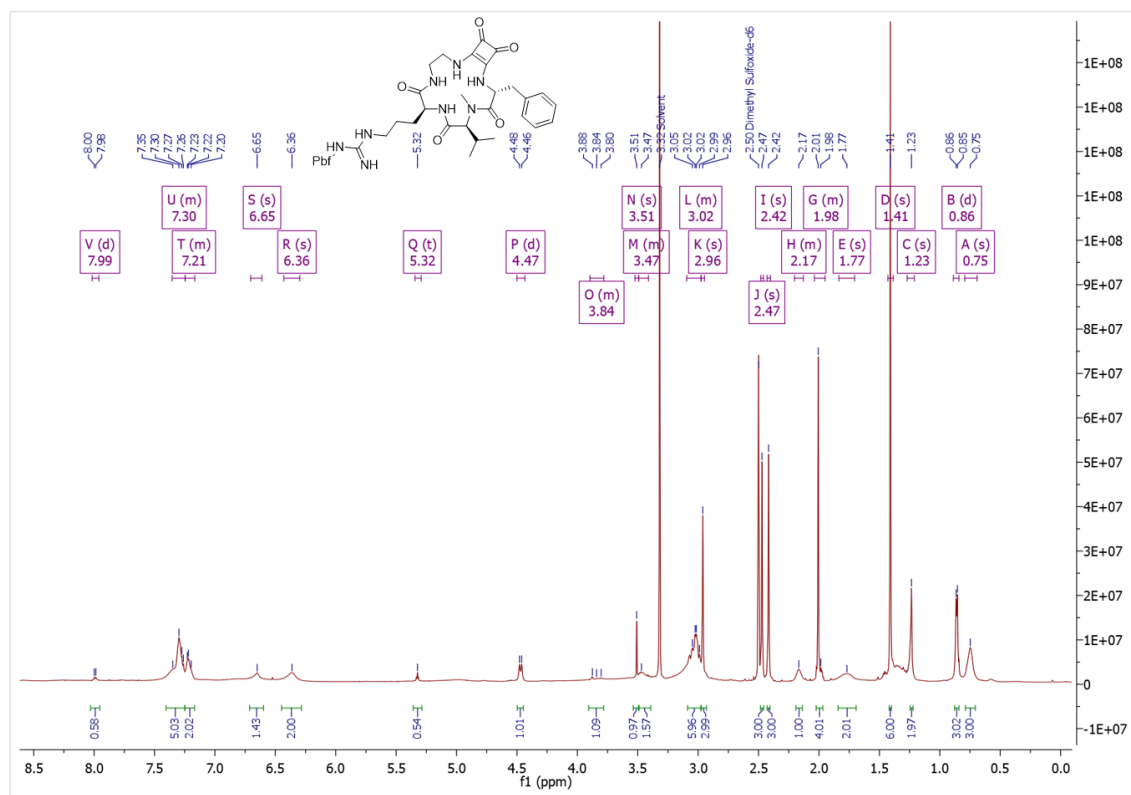
Figure S4.13: ¹H NMR spectrum of *c*(RG(*ψ*)-Sq-f*N*MeV) (4.7) in DMSO-*d*₆.

377

Figure S4.14: ^{13}C NMR spectrum of **c(RG(ψ)-Sq-fNMeV) (4.7)** in DMSO-d_6.

Figure S4.15: HSQC spectrum of **c(RG(ψ)-Sq-fNMeV) (4.7)** in DMSO-d_6.

Compound Table

Compound Label	RT (min)	Observed mass (m/z)	Neutral observed mass (Da)	Theoretical mass (Da)	Mass error (ppm)	Isotope match score (%)
Cpd 1: C40 H54 N8 O8 S	0.84	829.3684	806.3785	806.3785	-0.05	68.08

Mass errors of between -5.00 and 5.00 ppm with isotope match scores above 60% are considered confirmation of molecular formulae

Figure: Full range view of Compound spectra and potential adducts.

Figure: Zoomed Compound spectra view
(red boxes indicating expected theoretical isotope spacing and abundance)

Compound isotope peak List

m/z	z	Abund	Formula	Ion
807.3859	1	2012663.4	C40H54N8O8S	(M+H)+
808.3882	1	1139063.3	C40H54N8O8S	(M+H)+
809.3900	1	178261.8	C40H54N8O8S	(M+H)+
810.3908	1	15754.6	C40H54N8O8S	(M+H)+
811.3924	1	1791.8	C40H54N8O8S	(M+H)+
829.3684	1	117823.0	C40H54N8O8S	(M+Na)+
830.3705	1	70477.5	C40H54N8O8S	(M+Na)+
831.3731	1	14097.9	C40H54N8O8S	(M+Na)+
832.3791	1	2954.1	C40H54N8O8S	(M+Na)+

Figure S4.16: HRMS data for the protected cyclic squaratide – *c*(RG(ψ)-Sq-f*N*MeV) (4.7).
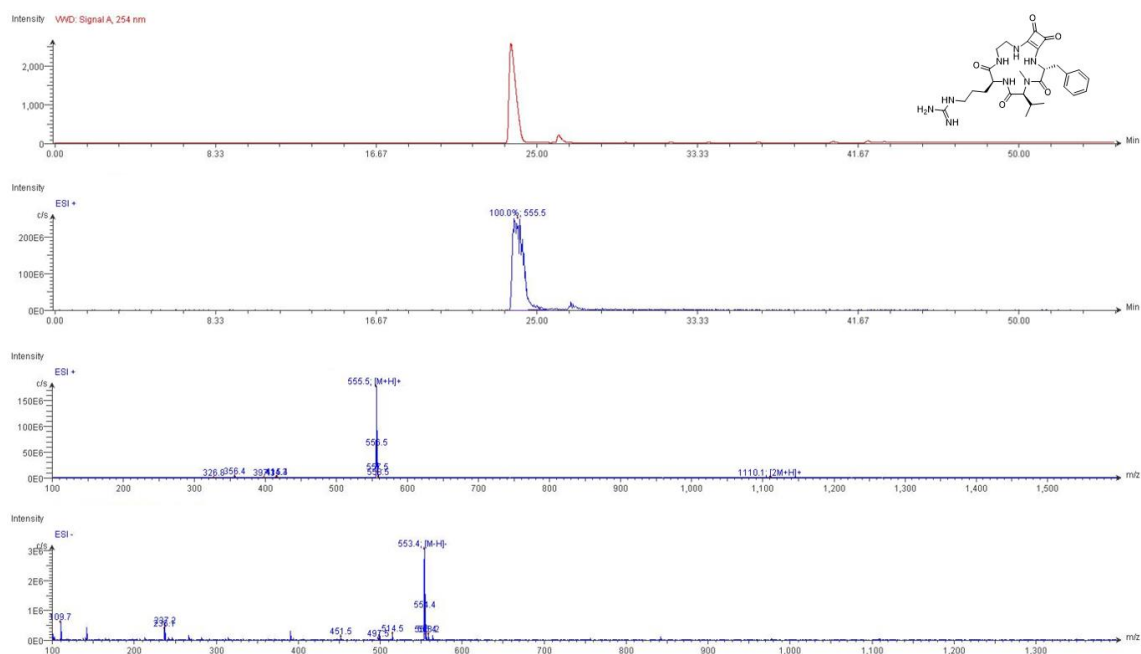
Figure S4.17: LC-MS data for the *deprotected* final cyclic squaratide – *c***(RG(**ψ**)-Sq-f***N***MeV) (4.8)**.

Compound Table

Compound Label	RT (min)	Observed mass (m/z)	Neutral observed mass (Da)	Theoretical mass (Da)	Mass error (ppm)	Isotope match score (%)
Cpd 1: C27 H38 N8 O5	0.74	555.3038	554.2966	554.2965	0.18	94.68

Mass errors of between -5.00 and 5.00 ppm with isotope match scores above 60% are considered confirmation of molecular formulae
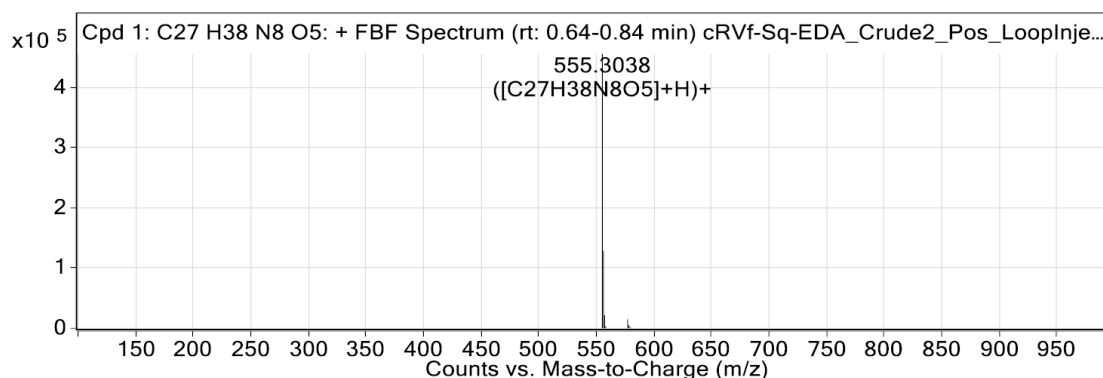
Figure: Full range view of Compound spectra and potential adducts.
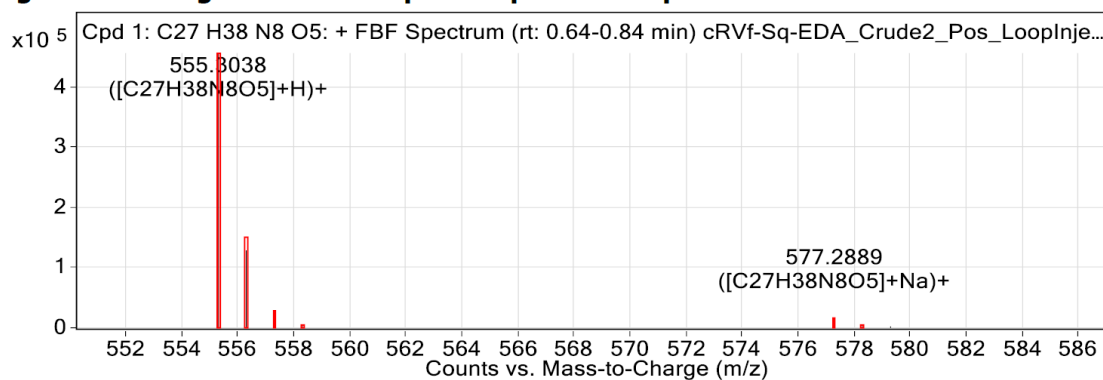
Figure: Zoomed Compound spectra view
(red boxes indicating expected theoretical isotope spacing and abundance)

Figure S4.18: HRMS data for the deprotected final cyclic squaratide – *c*(RG(ψ)-Sq-f*N*MeV) (4.8).
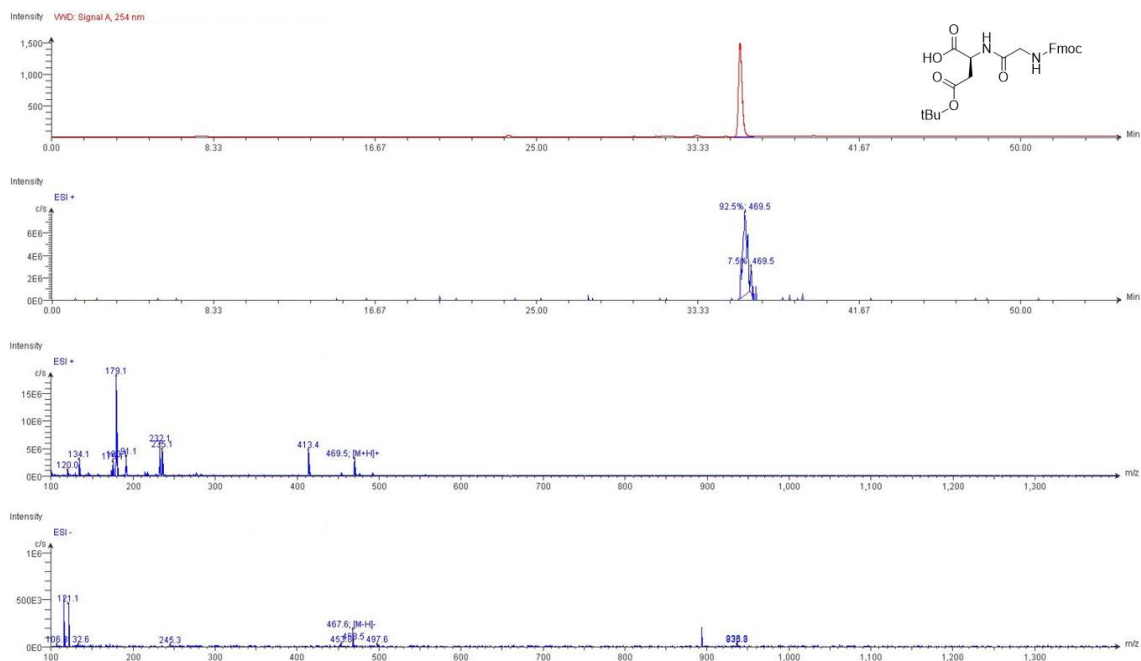
Figure S4.19: LC-MS data for **Fmoc-G-D(O*t*Bu)**.
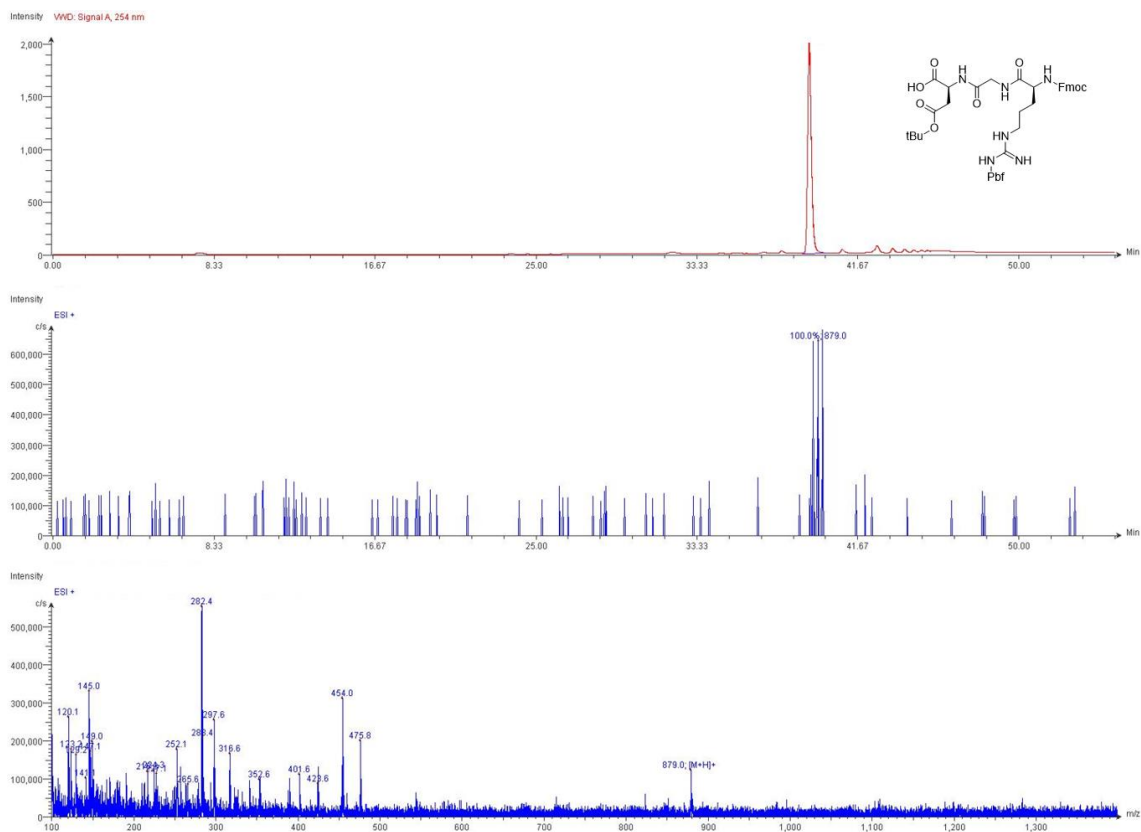
Figure S4.20: LC-MS data for **Fmoc-R(Pbf)-G-D(O*t*Bu)**.
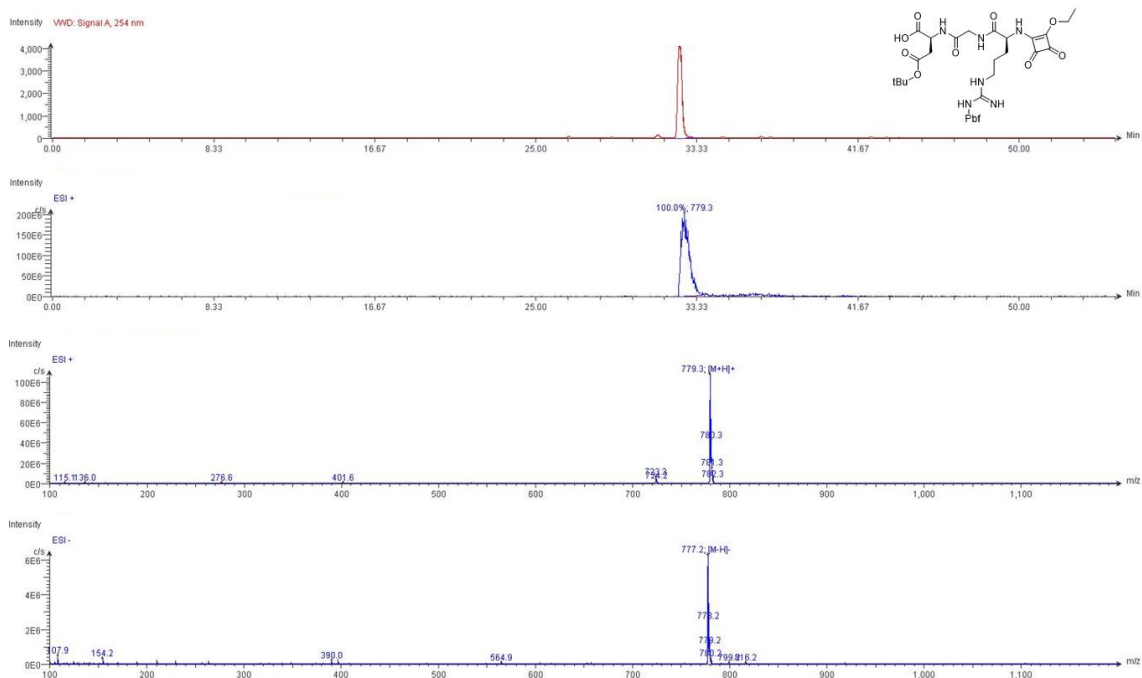
Figure S4.21: LC-MS data for **ESq-R(Pbf)-G-D(O*t*Bu)**.
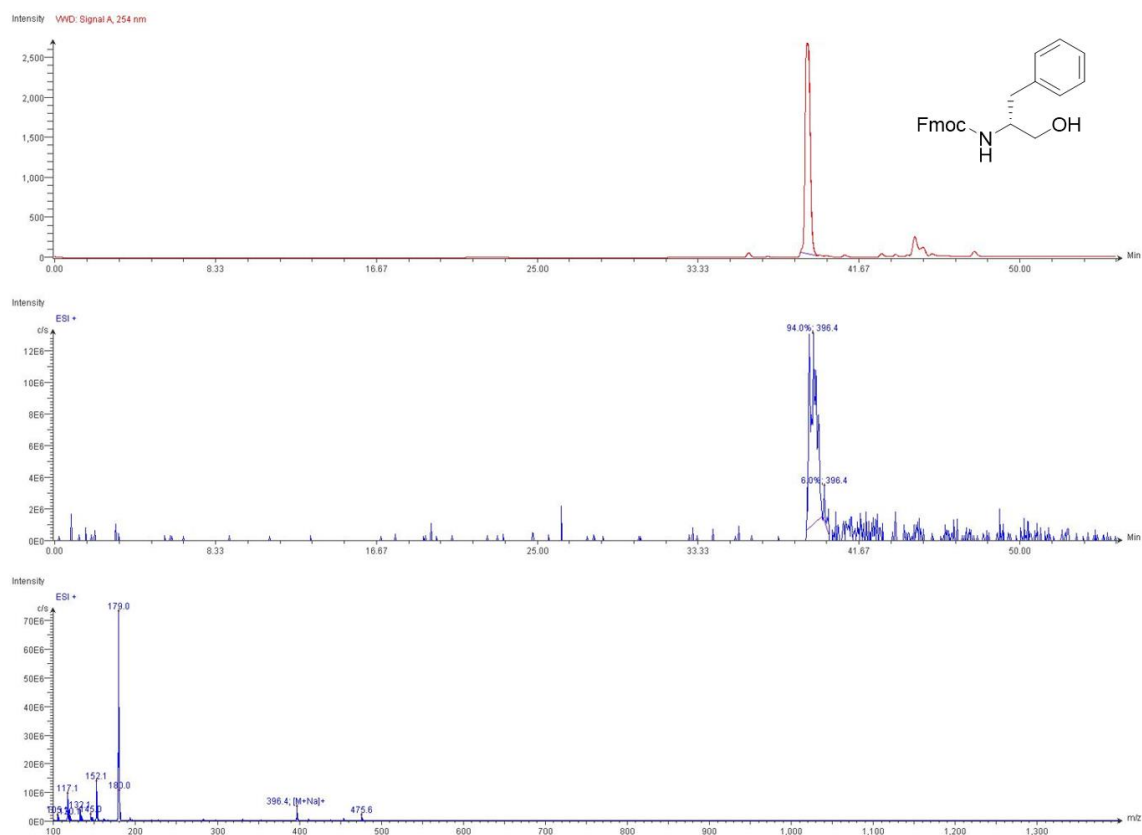
Figure S4.22: LC-MS data for **Fmoc-*D*-Phe-ψ[CH₂OH] (4.9b)**.
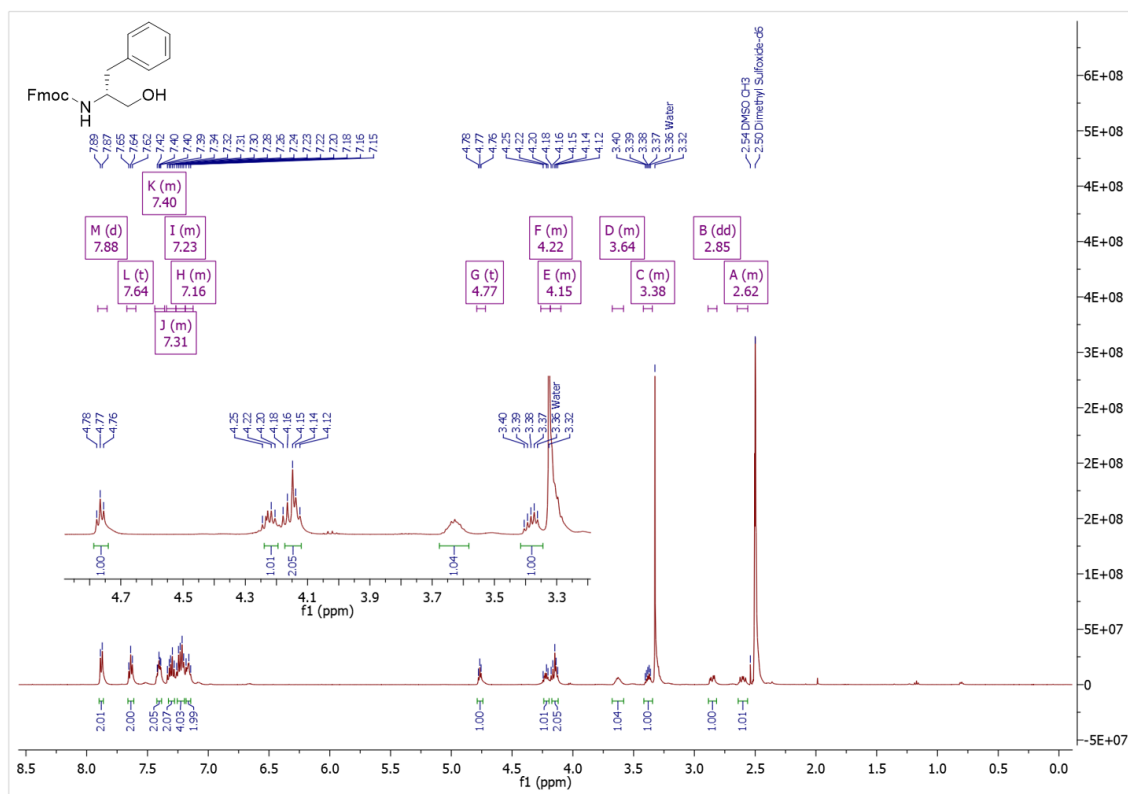
Figure S4.23: ^{1}H NMR spectrum of **Fmoc-*D*-Phe-ψ[CH₂OH] (4.9b)** in DMSO-d_6.
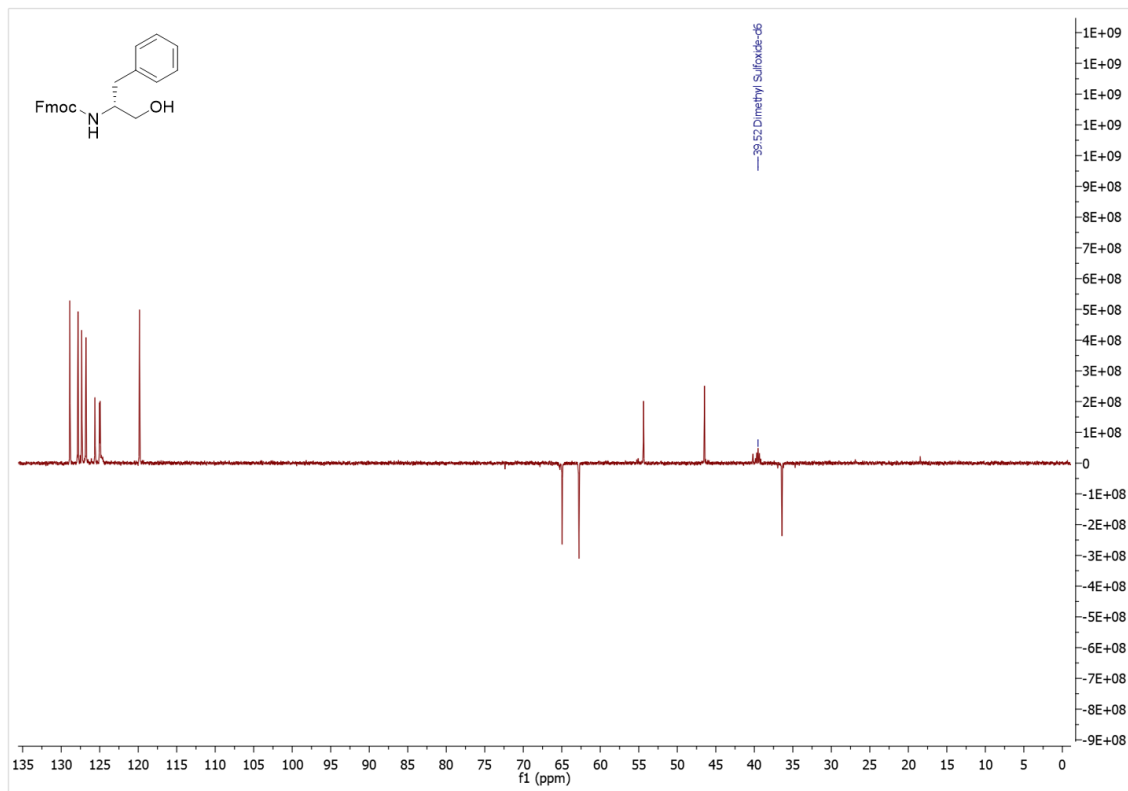
Figure S4.24: DEPT 135 spectrum of **Fmoc-*D*-Phe-ψ[CH₂OH] (4.9b)** in DMSO-d_6.
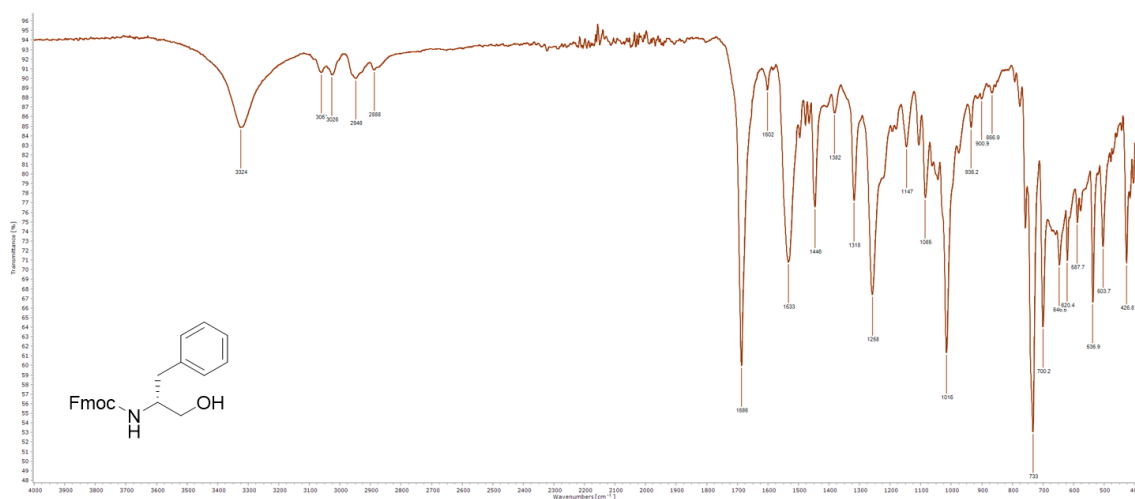
Figure S4.25: FTIR-ATR spectrum of **Fmoc-*D*-Phe-ψ[CH$_2$OH] (4.9b)**.
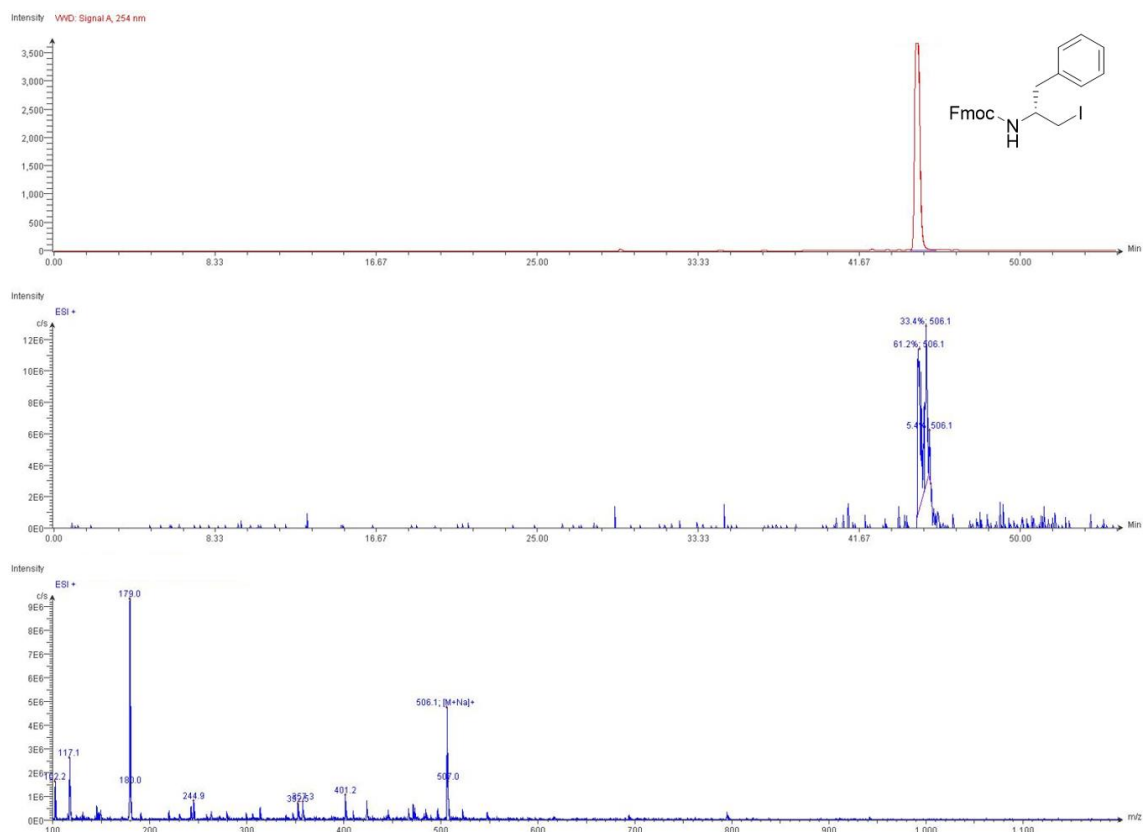
Figure S4.26: LC-MS data for **Fmoc-*D*-Phe-ψ[CH$_2$I] (4.9c)**.
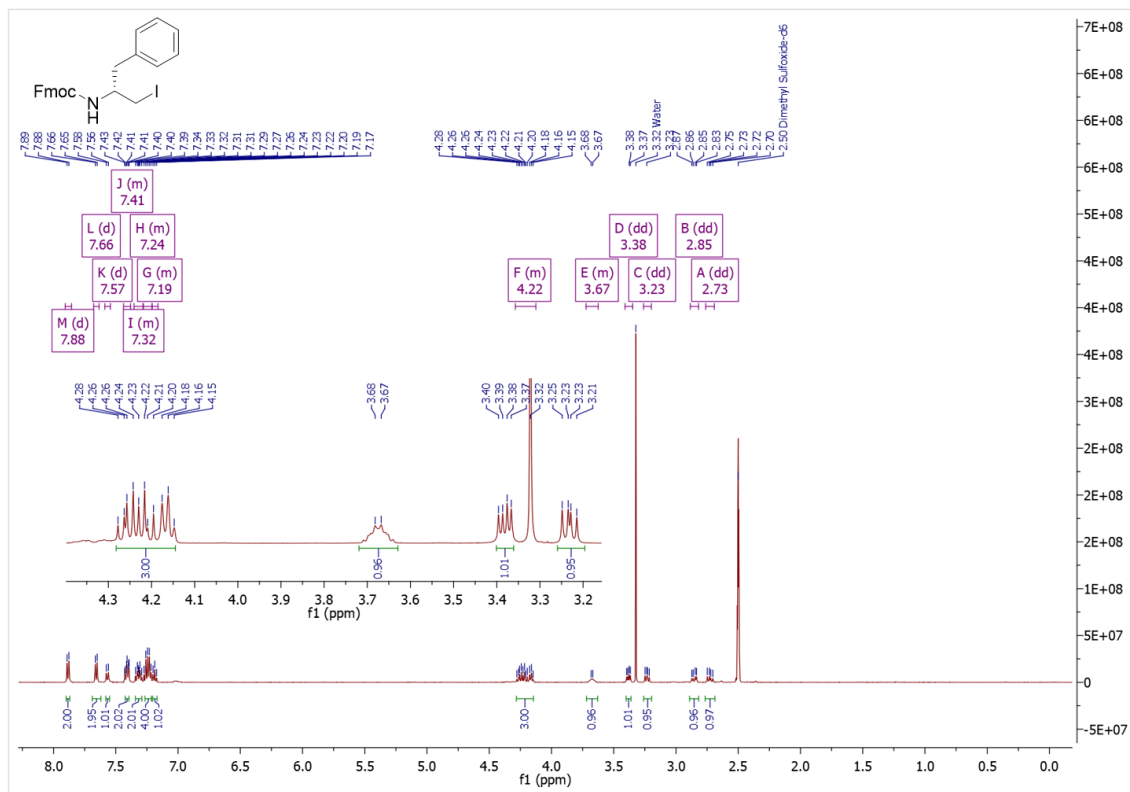
Figure S4.27: ^{1}H NMR spectrum of **Fmoc-_D_-Phe-_ψ_[CH$_2$I] (4.9c)** in DMSO-d_6.
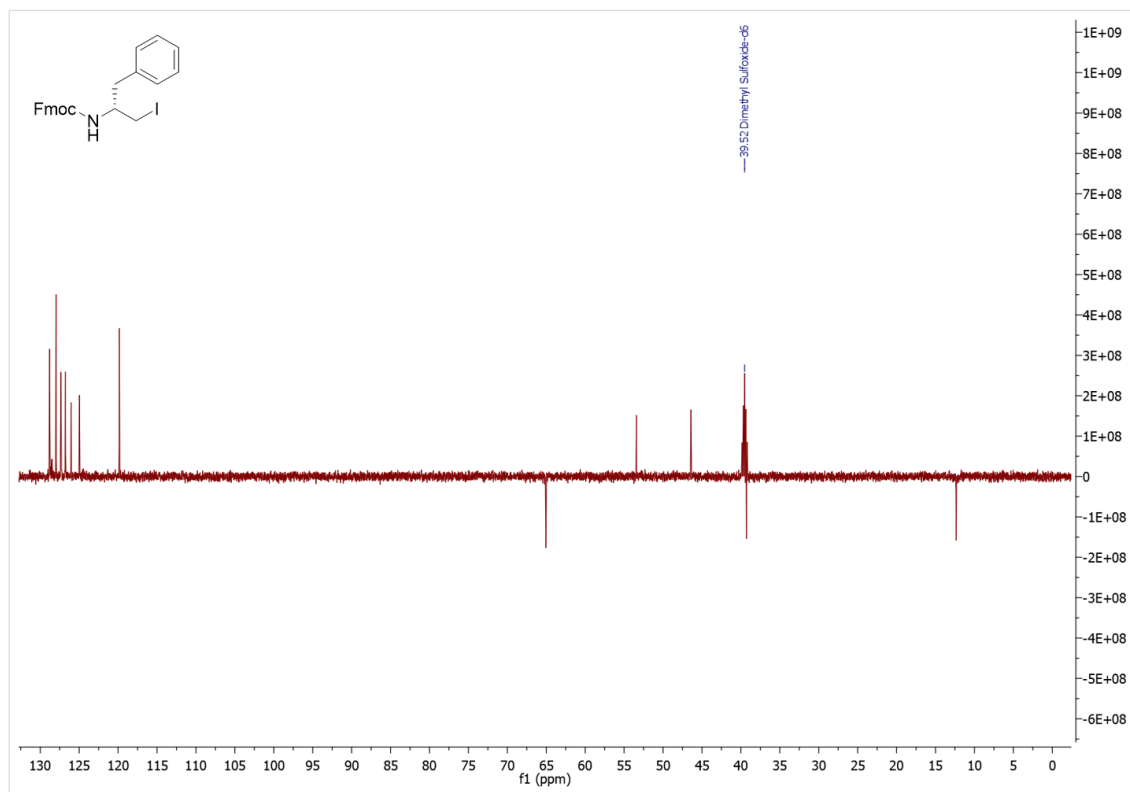
Figure S4.28: DEPT 135 spectrum of **Fmoc-_D_-Phe-_ψ_[CH$_2$I] (4.9c)** in DMSO-d_6.
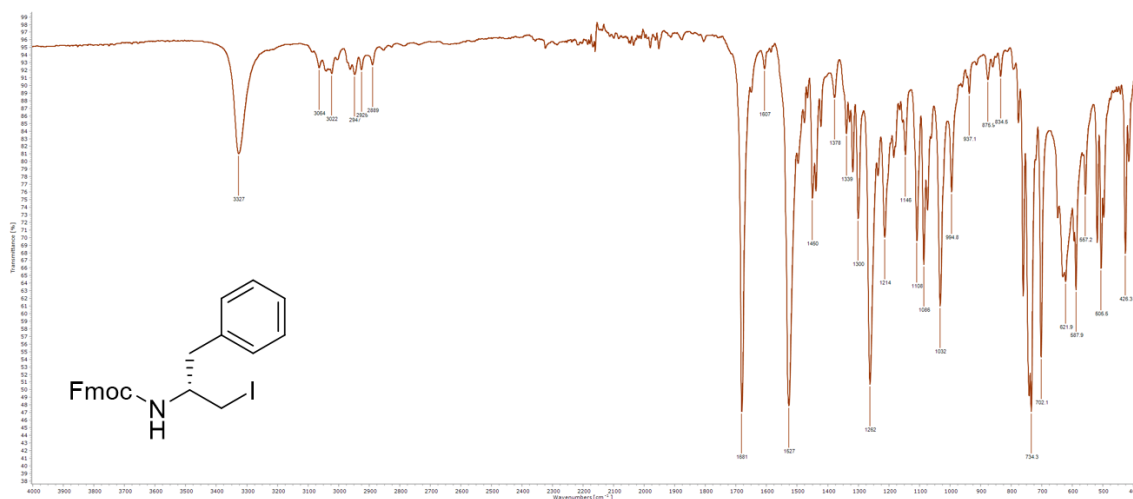
Figure S4.29: FTIR-ATR spectrum of **Fmoc-*D*-Phe-ψ[CH₂I] (4.9c)**.
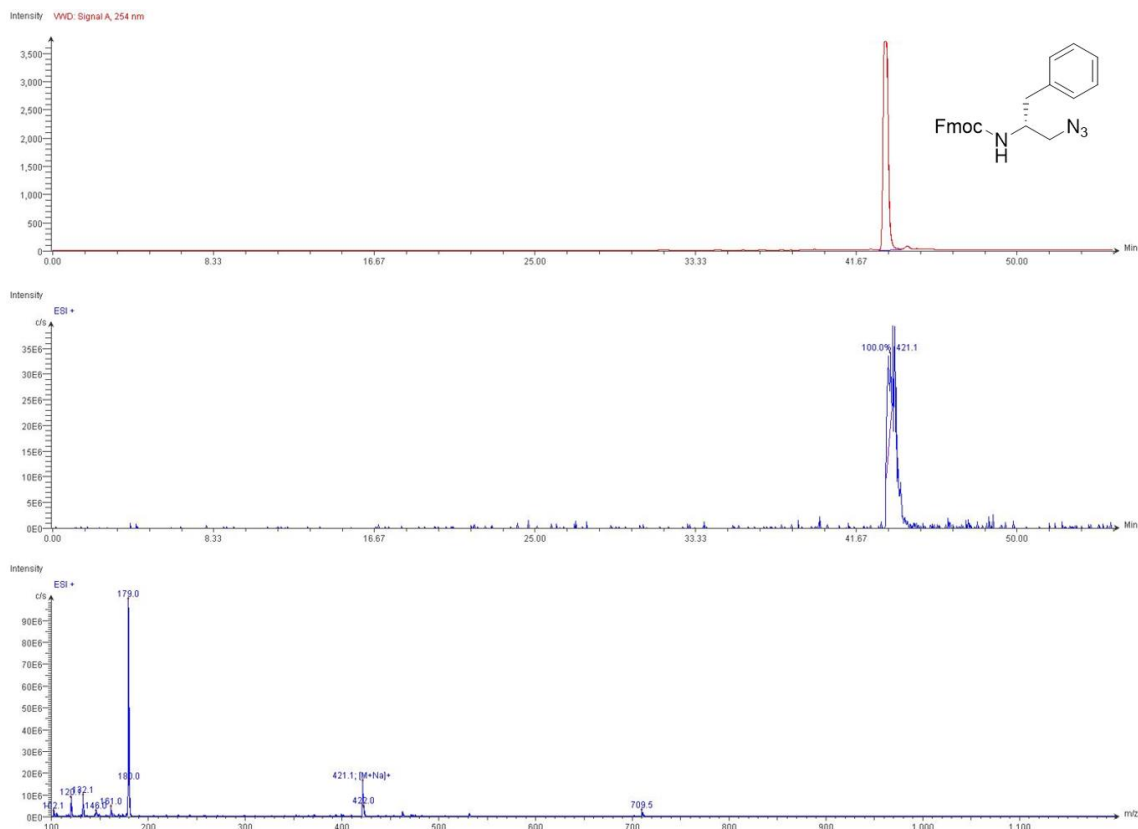
Figure S4.30: LC-MS data for **Fmoc-*D*-Phe-ψ[CH₂N₃] (4.9d)**.
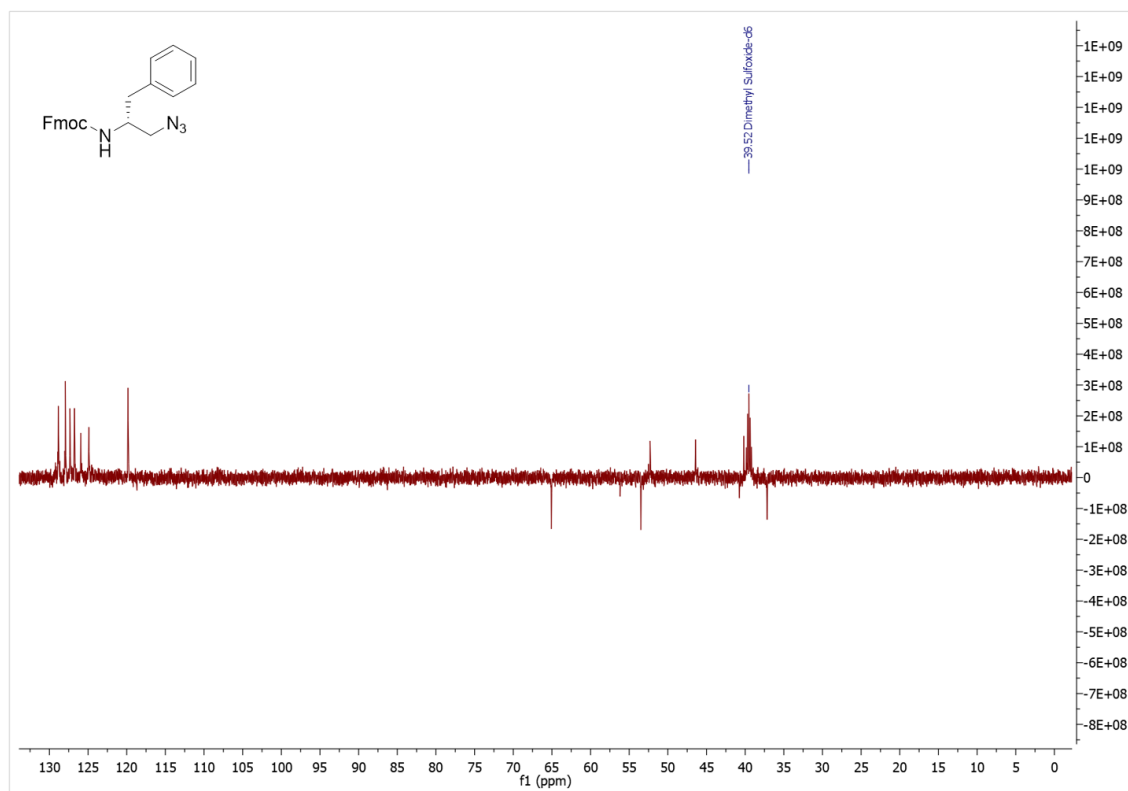
Figure S4.31: DEPT 135 spectrum of **Fmoc-*D*-Phe-*ψ*[CH₂N₃] (4.9d)** in DMSO-*d*₆.
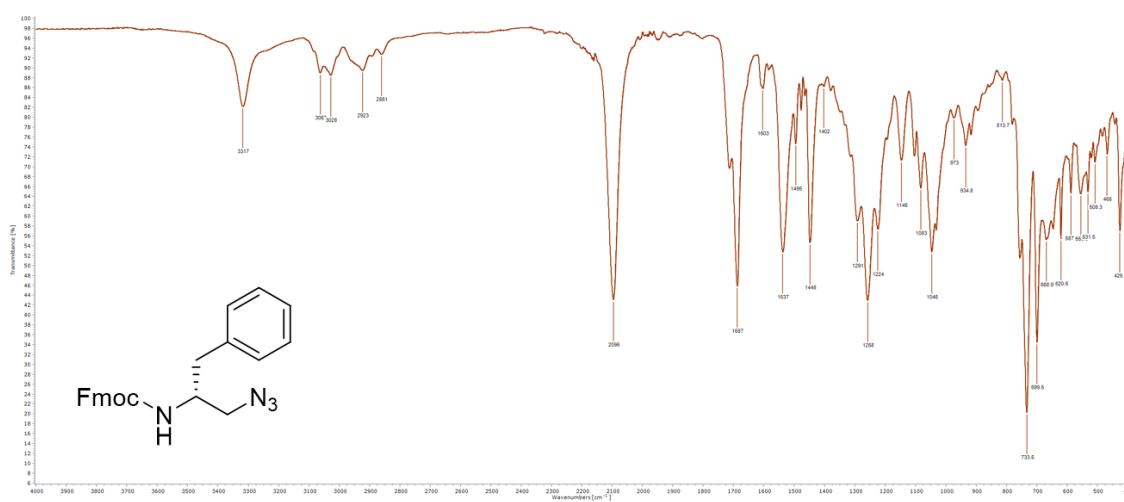
Figure S4.32: FTIR-ATR spectrum of **Fmoc-*D*-Phe-*ψ*[CH₂N₃] (4.9d)**.

Figure S4.33: LC-MS data for **Fmoc-*D*-Phe-*ψ*[CH₂NH₂] (4.9e)**.

Figure S4.34: ¹H NMR spectrum of **Fmoc-*D*-Phe-*ψ*[CH₂NH₂] (4.9e)** in DMSO-*d*₆.
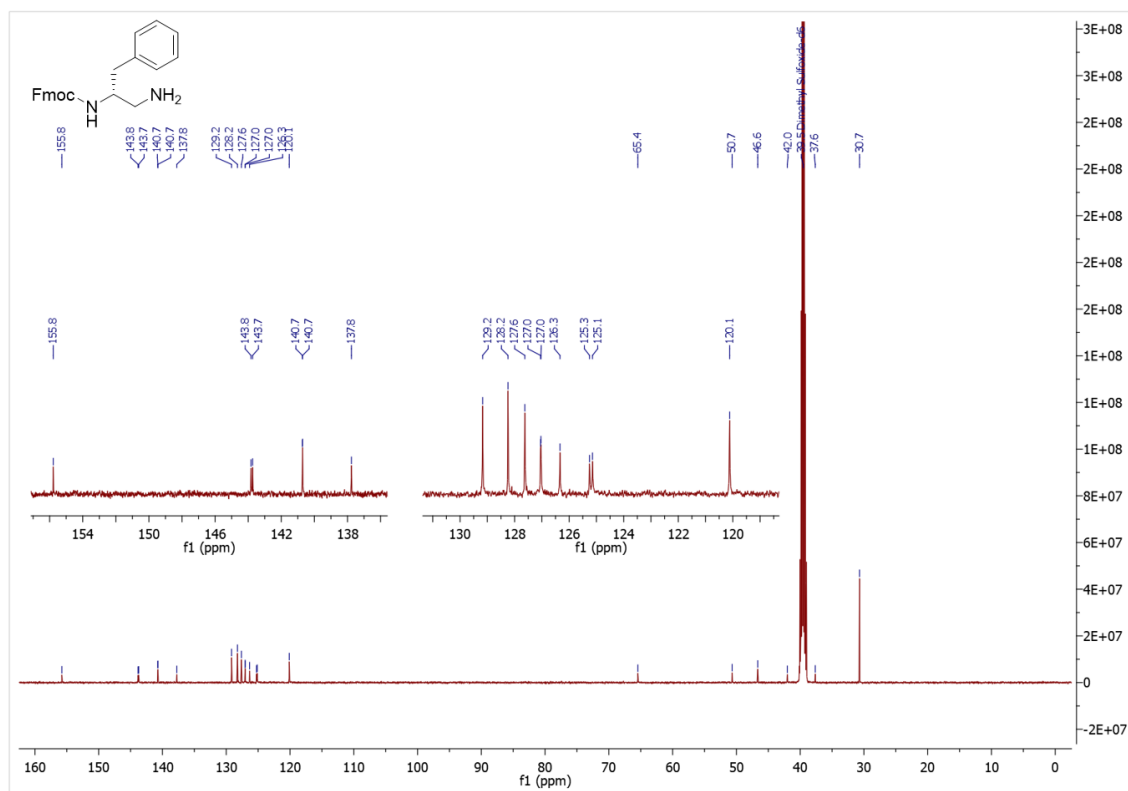
Figure S4.35: ^{13}C NMR spectrum of **Fmoc-*D*-Phe-*ψ*[CH₂NH₂] (4.9e)** in DMSO-d_6.
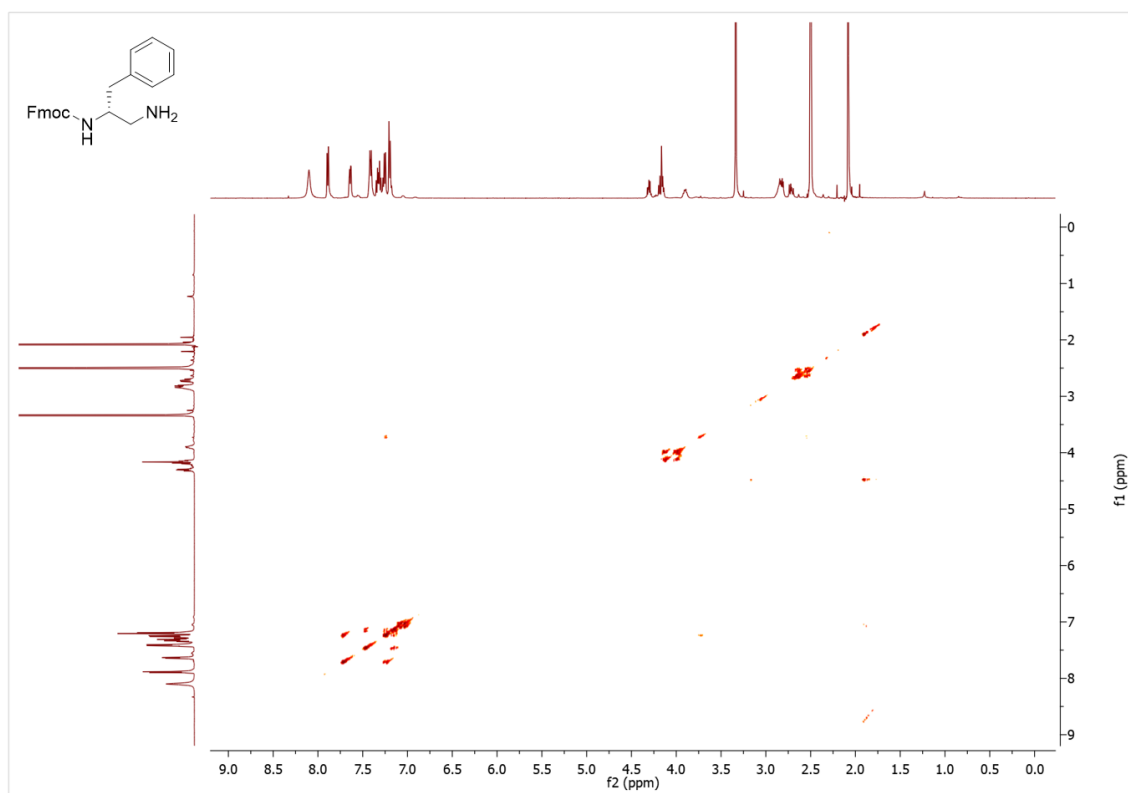
Figure S4.36: COSY spectrum of **Fmoc-*D*-Phe-*ψ*[CH₂NH₂] (4.9e)** in DMSO-d_6.
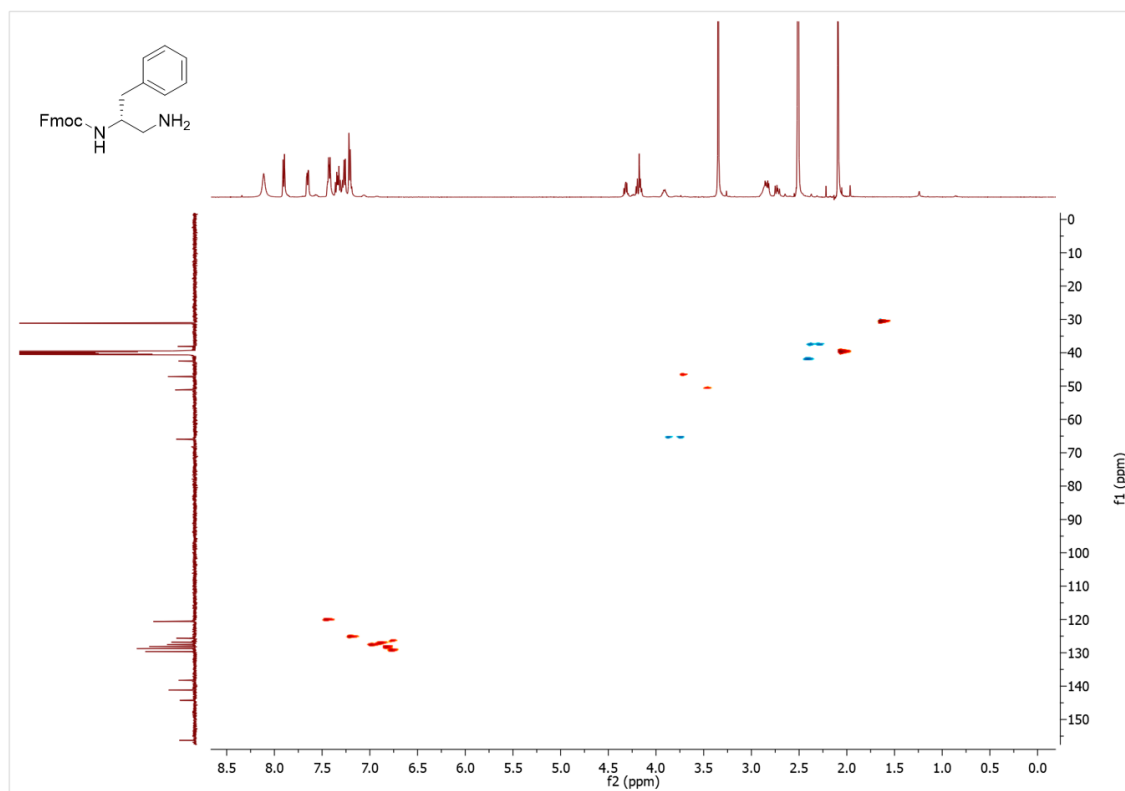
Figure S4.37: HSQC spectrum of **Fmoc-*D*-Phe-*ψ*[CH₂NH₂] (4.9e)** in DMSO-*d*₆.
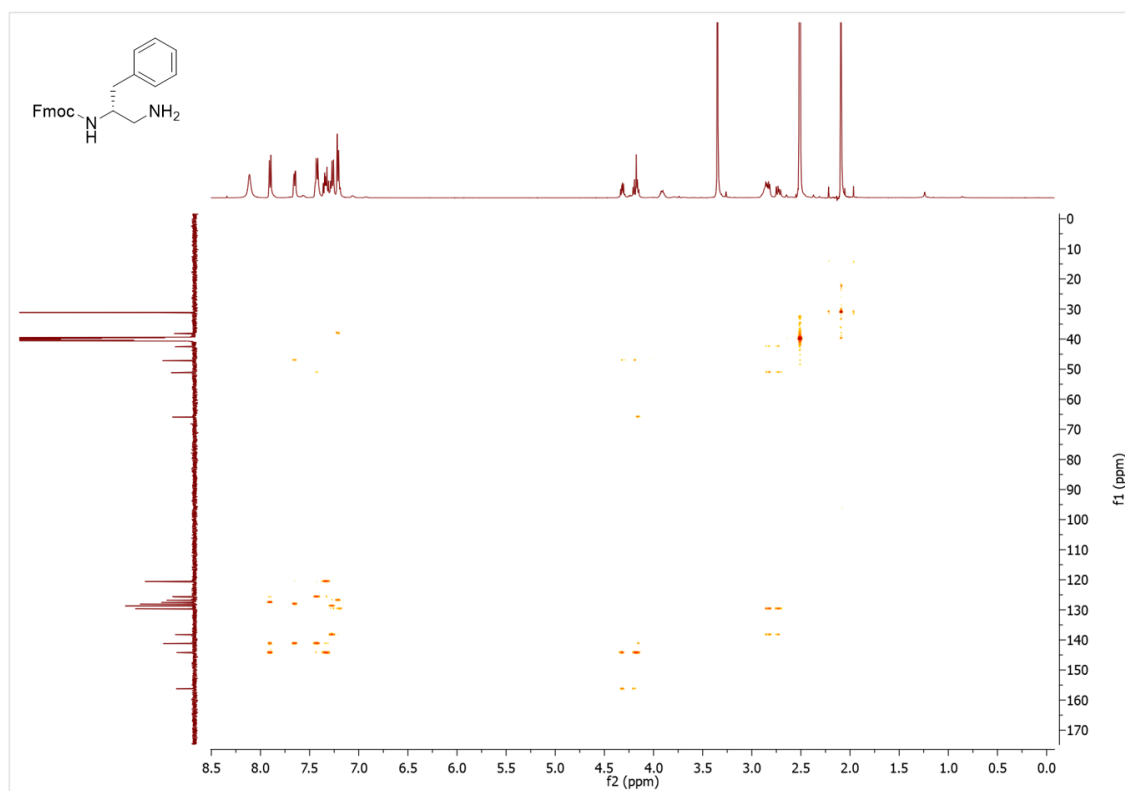
Figure S4.38: HMBC spectrum of **Fmoc-*D*-Phe-*ψ*[CH₂NH₂] (4.9e)** in DMSO-*d*₆.
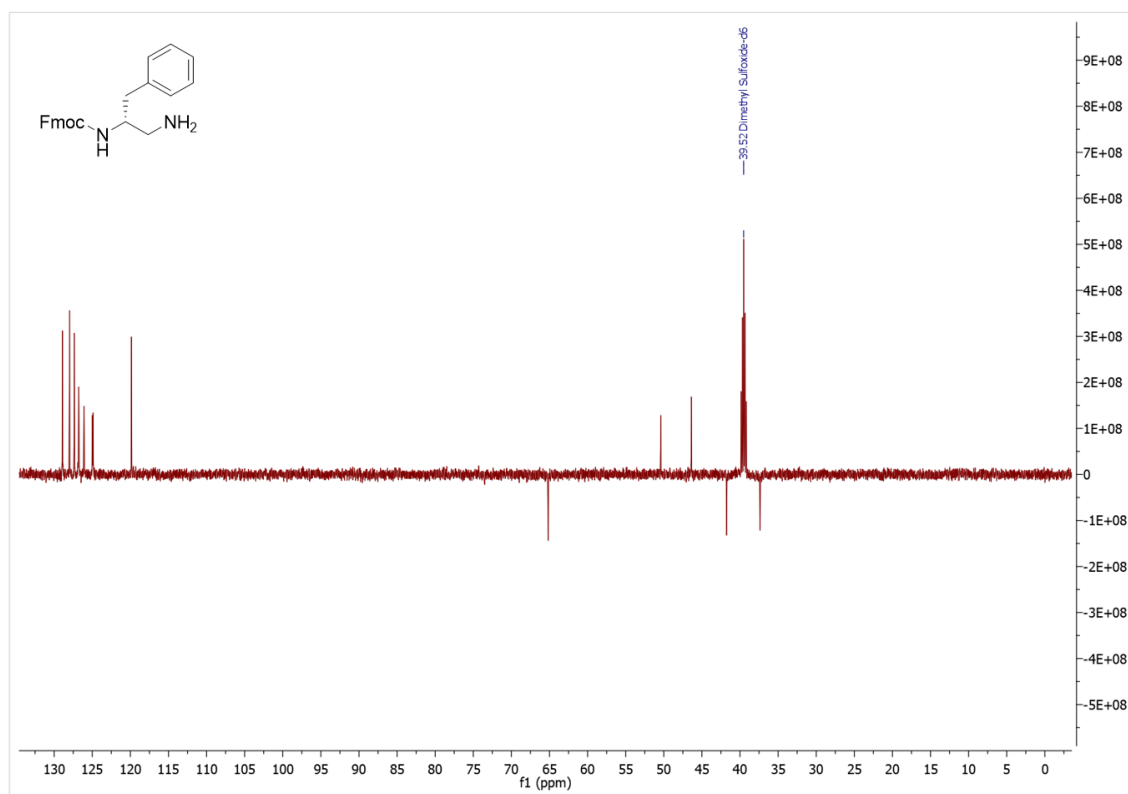
Figure S4.39: DEPT 135 spectrum of **Fmoc-*D*-Phe-*ψ*[CH₂NH₂] (4.9e)** in DMSO-*d*₆.
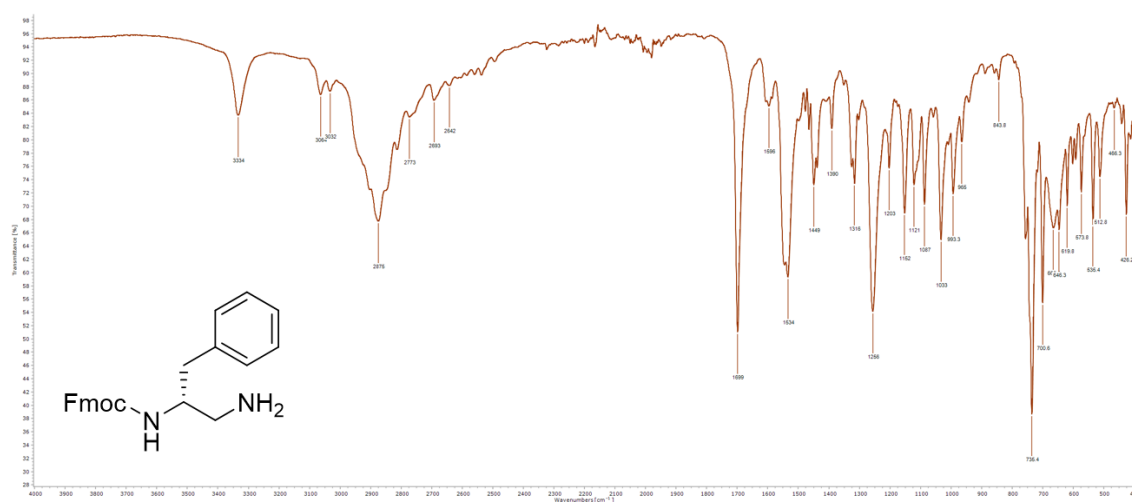
Figure S4.40: FTIR-ATR spectrum of **Fmoc-*D*-Phe-*ψ*[CH₂NH₂] (4.9e)**.
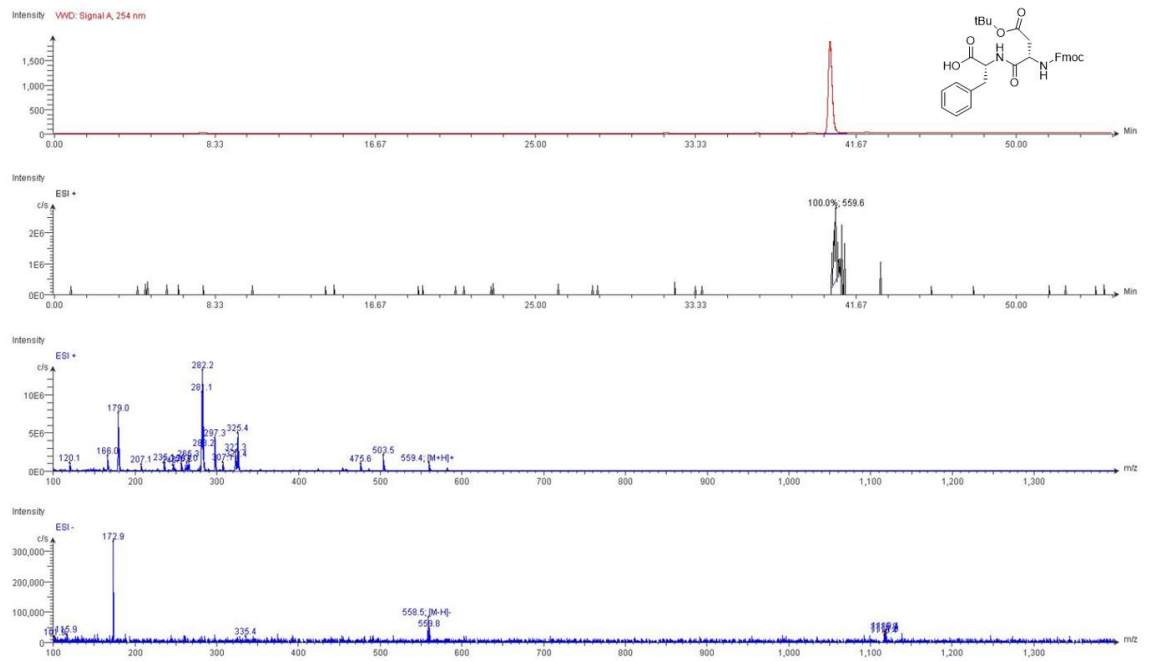
Figure S4.41: LC-MS data for **Fmoc-D(O*t*Bu)-f-OH**.
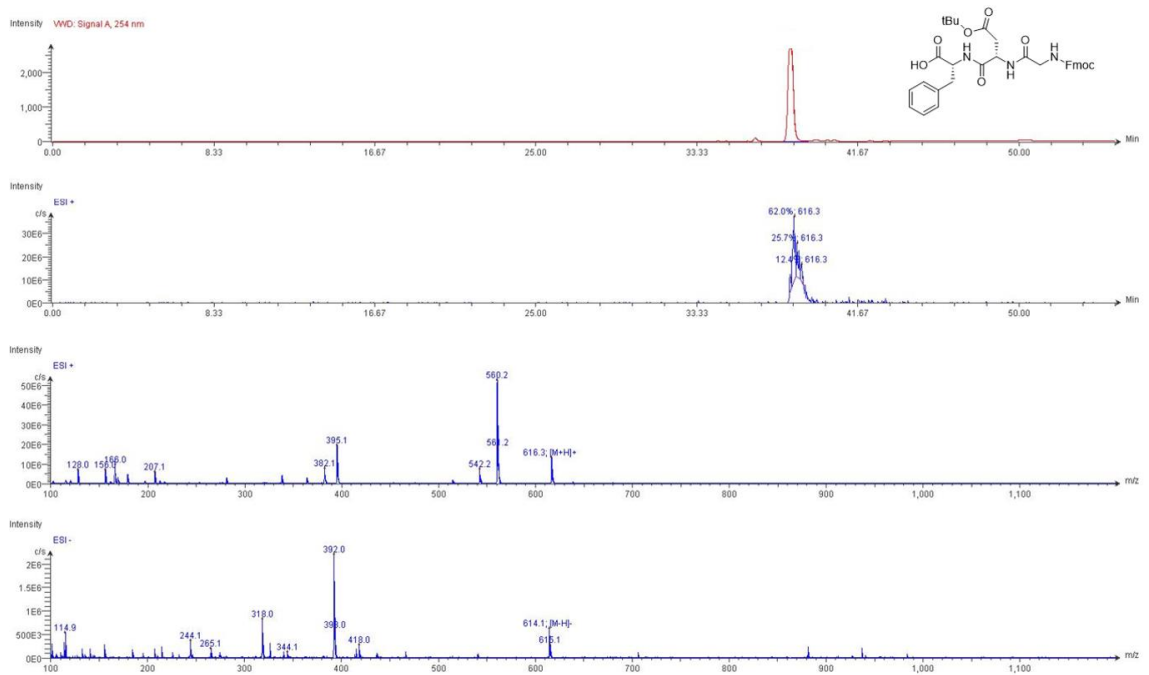
Figure S4.42: LC-MS data for **Fmoc-G-D(O*t*Bu)-f-OH**.
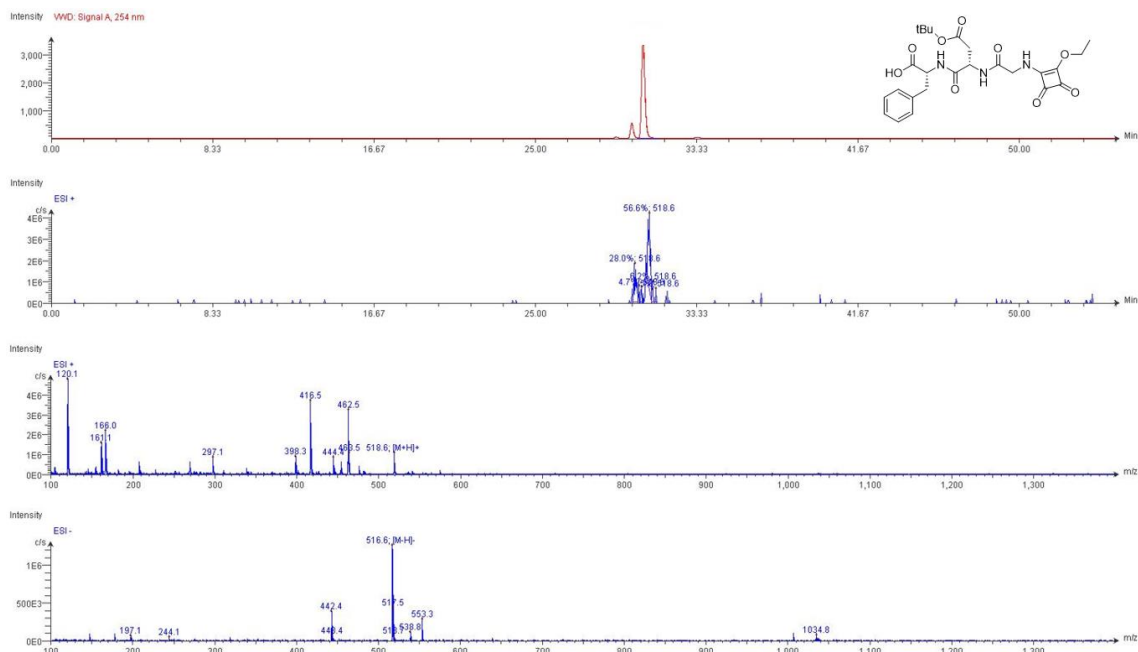
Figure S4.43: LC-MS data for **ESq-G-D(O*t*Bu)-f-OH**.
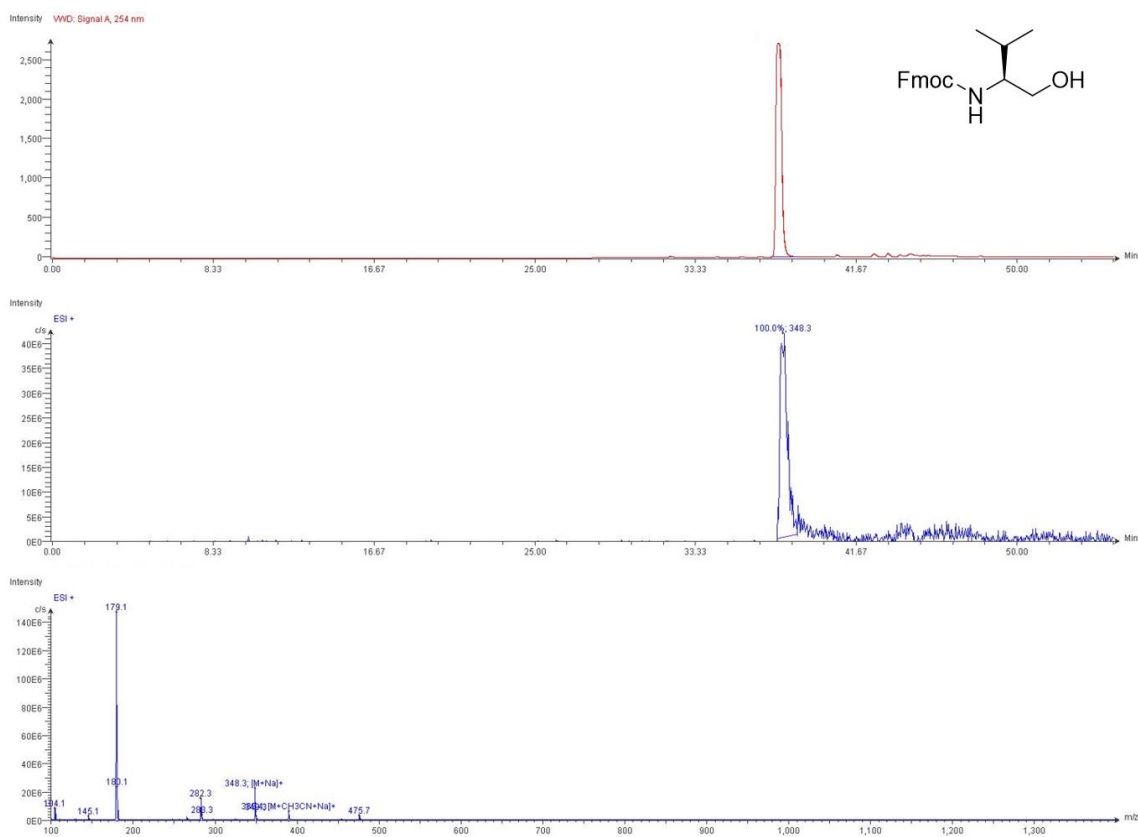
Figure S4.44: LC-MS data for **Fmoc-Val-ψ[CH₂OH] (4.10b)**.
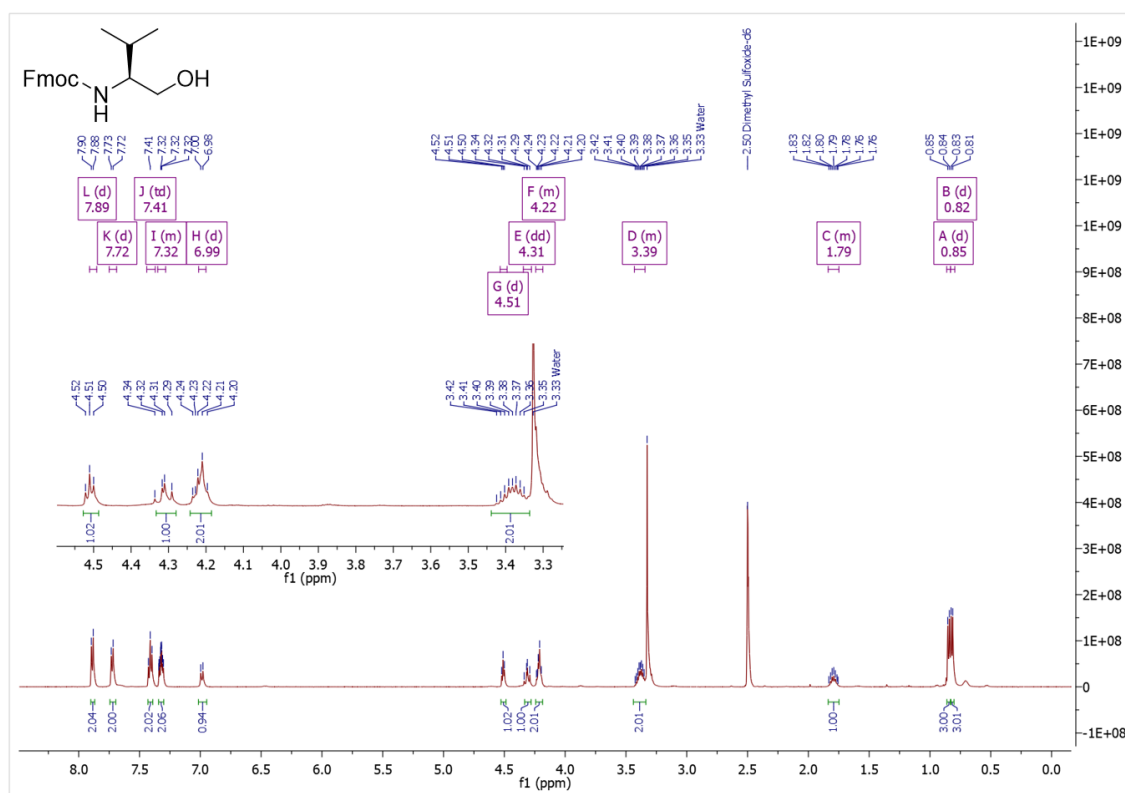
Figure S4.45: ¹H NMR spectrum of **Fmoc-Val-ψ[CH₂OH] (4.10b)** in DMSO-*d*₆.
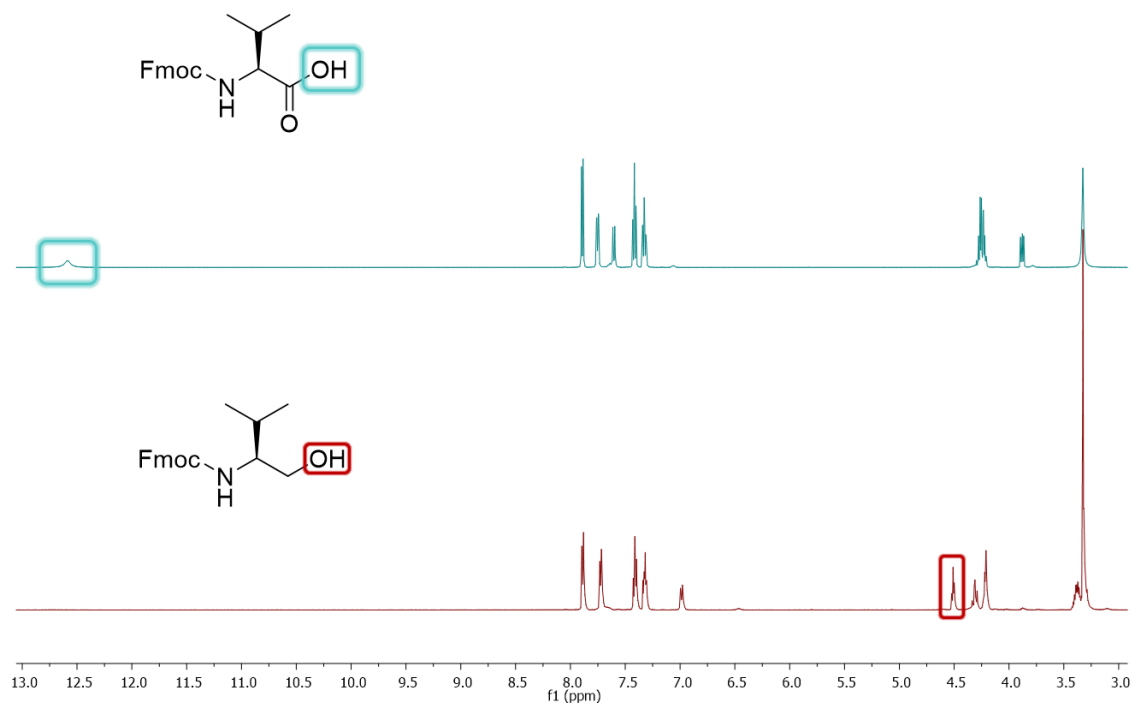
Figure S4.46: ¹H NMR spectra of (Top) Fmoc-Val-OH starting material (**4.10a**), and (Bottom) *β*-amino alcohol **Fmoc-Val-ψ[CH₂OH] (4.10b)** in DMSO-*d*₆.
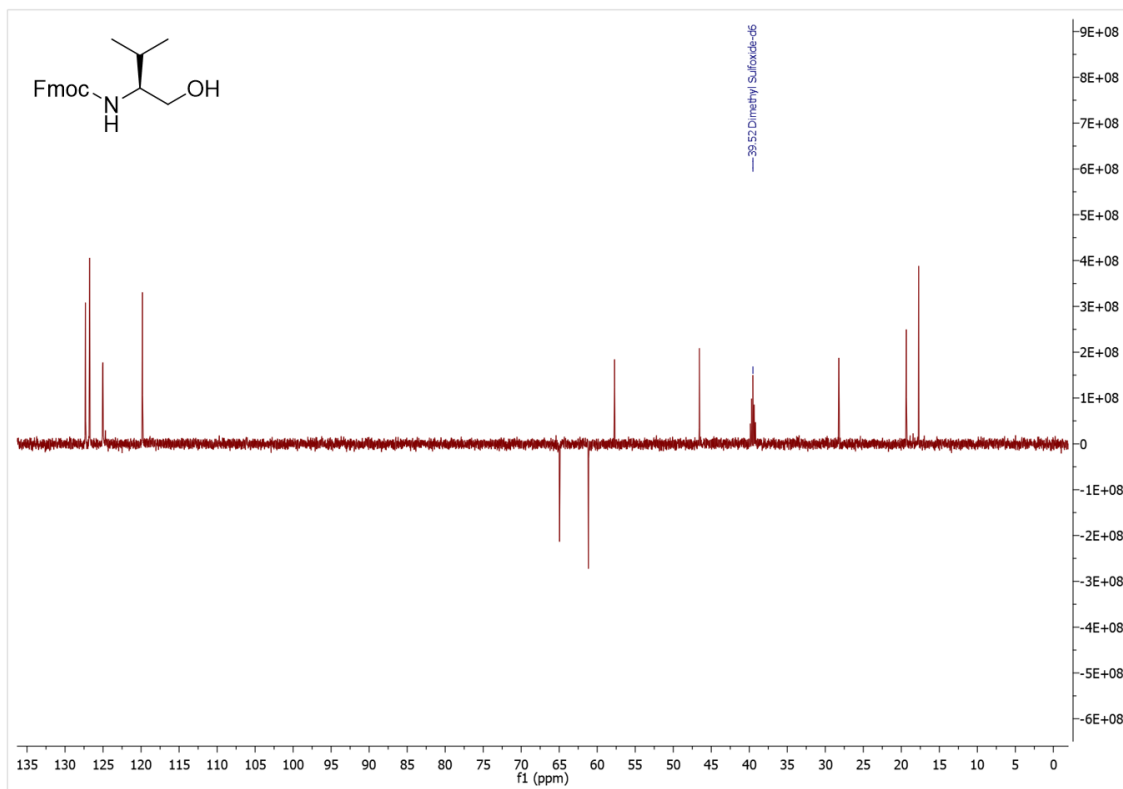
Figure S4.47: DEPT 135 spectrum of **Fmoc-Val-ψ[CH₂OH] (4.10b)** in DMSO-d_6.
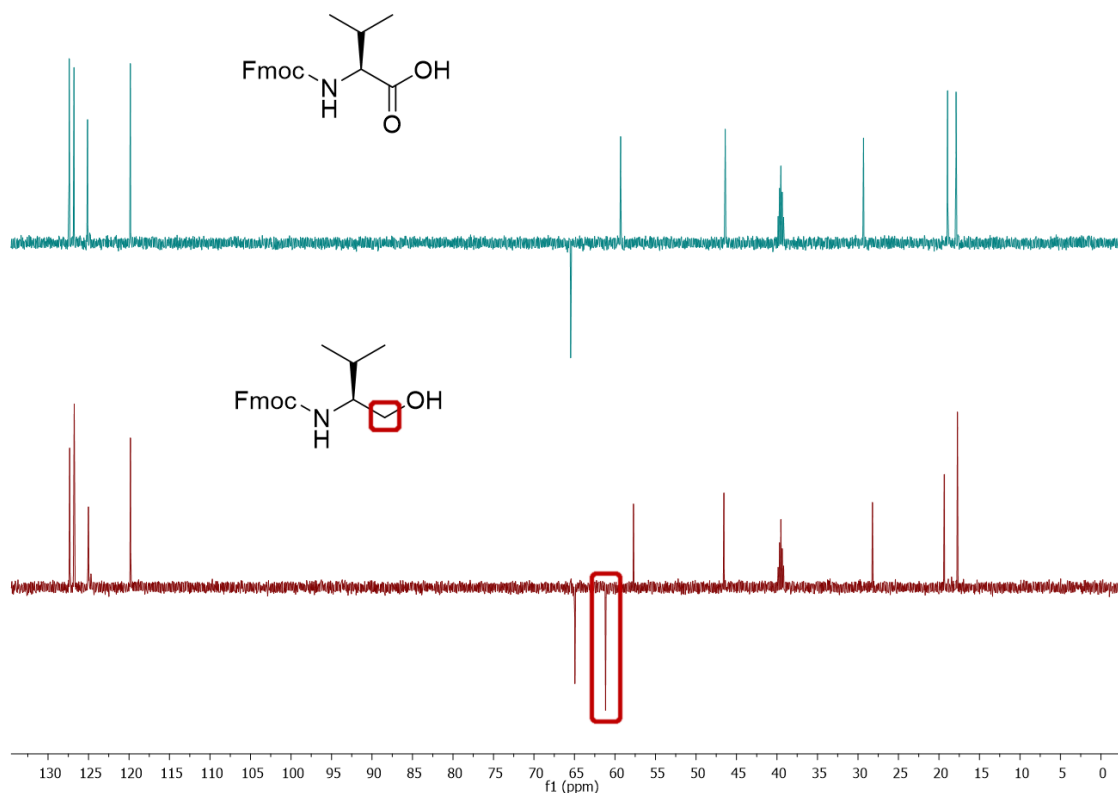
Figure S4.48: DEPT 135 spectra of (Top) Fmoc-Val-OH starting material (**4.10a**), and (Bottom) β-amino alcohol **Fmoc-Val-ψ[CH₂OH] (4.10b)** in DMSO-d_6.
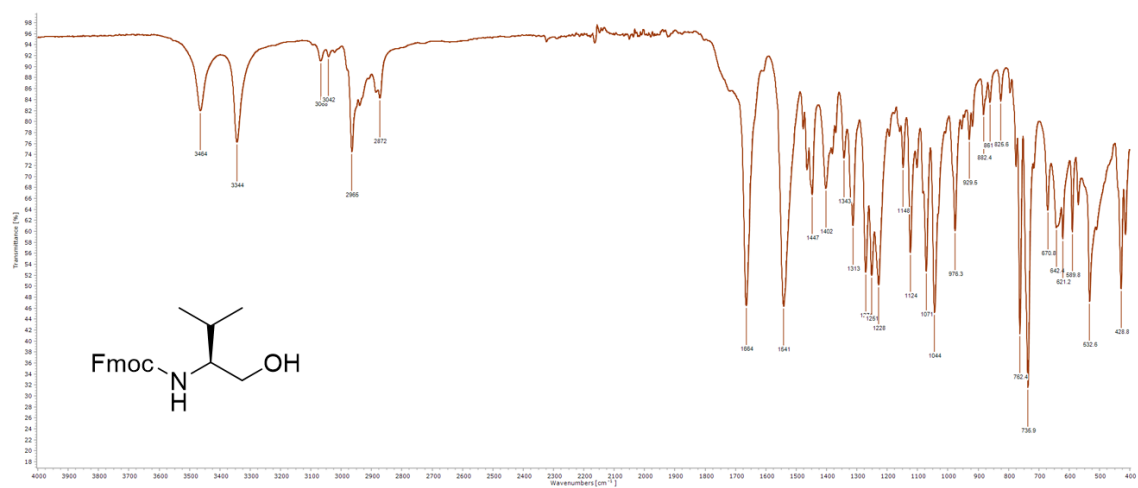
Figure S4.49: FTIR-ATR spectrum of **Fmoc-Val-ψ[CH₂OH] (4.10b)**.
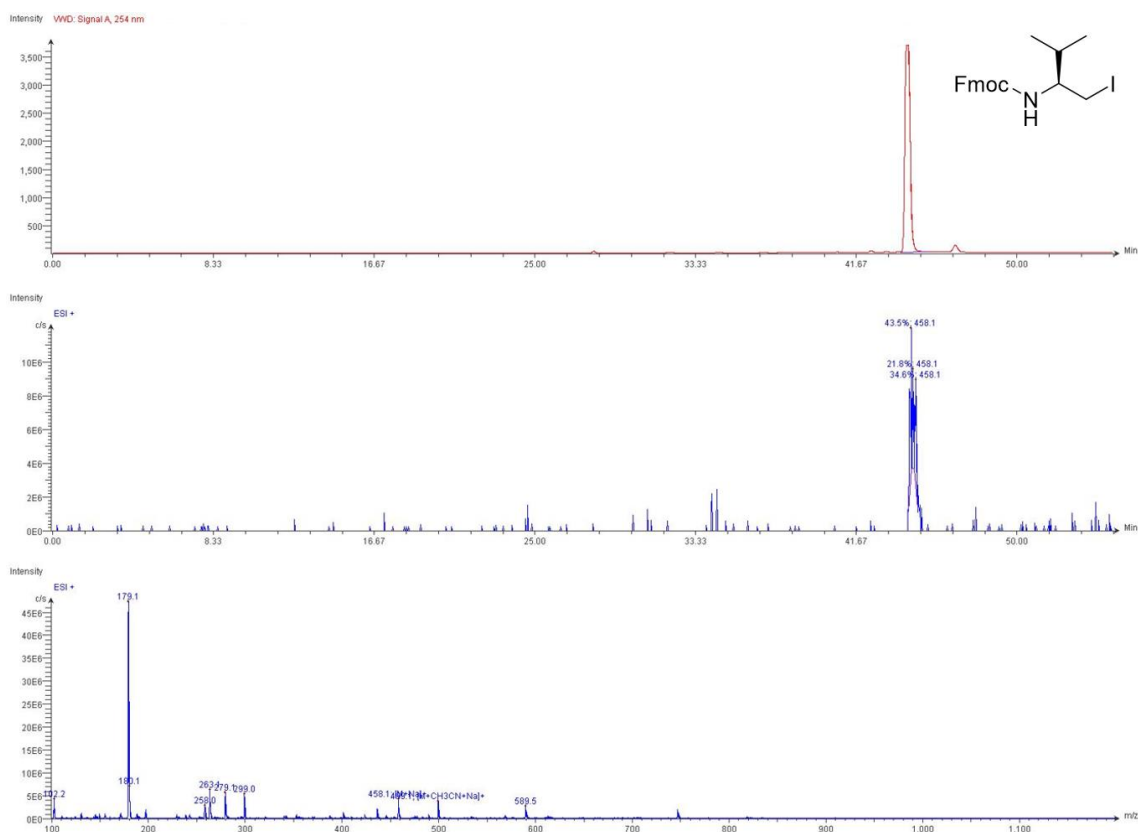
Figure S4.50: LC-MS data for **Fmoc-Val-ψ[CH₂I] (4.10c)**.
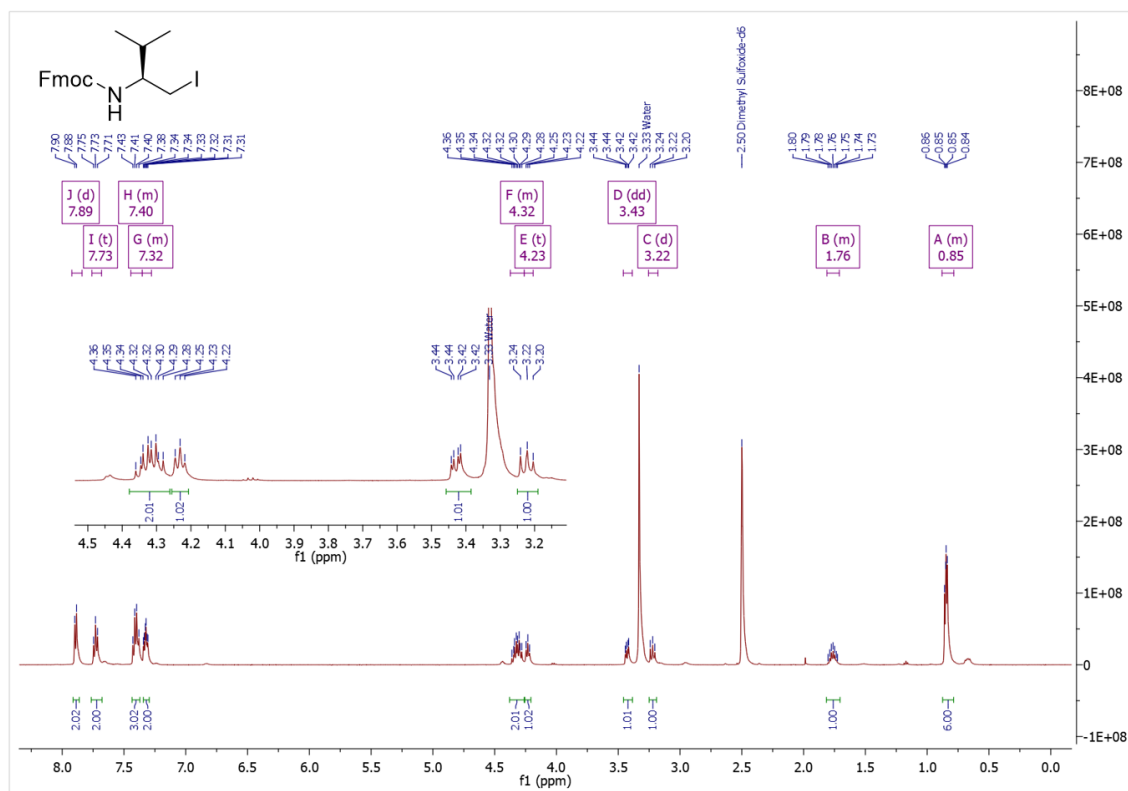
Figure S4.51: ^{1}H NMR spectrum of **Fmoc-Val-ψ[CH$_2$I] (4.10c)** in DMSO-d_6.
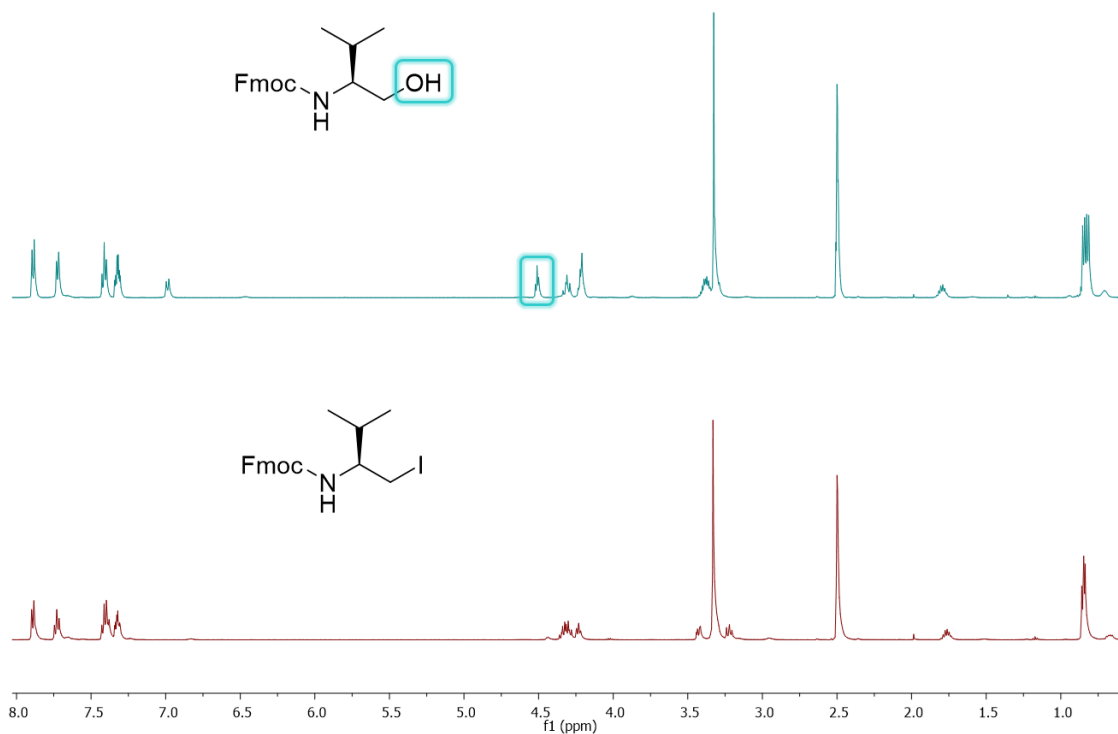
Figure S4.52: ^{1}H NMR spectra of (Top) Fmoc-Val-ψ[CH$_2$OH] starting material (**4.10b**), and (Bottom) β-amino iodide **Fmoc-Val-ψ[CH$_2$I] (4.10c)** in DMSO-d_6.
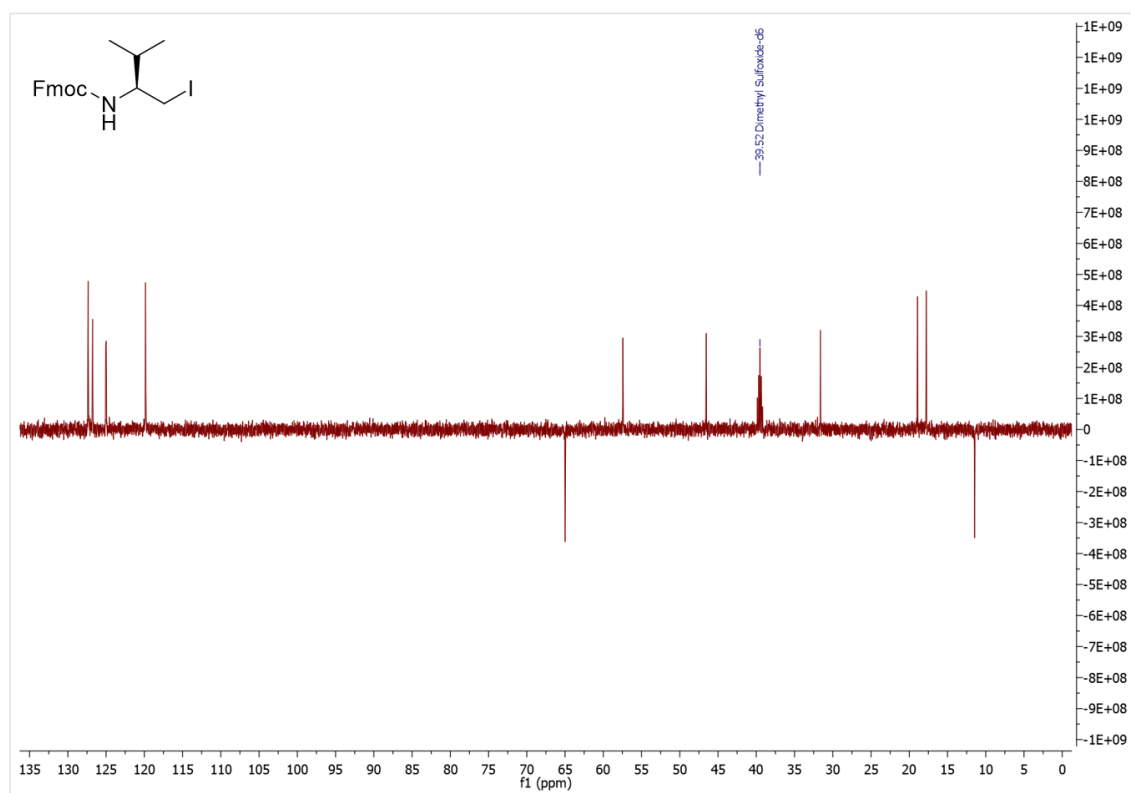
Figure S4.53: DEPT 135 spectrum of **Fmoc-Val-ψ[CH₂I] (4.10c)** in DMSO-d_6.
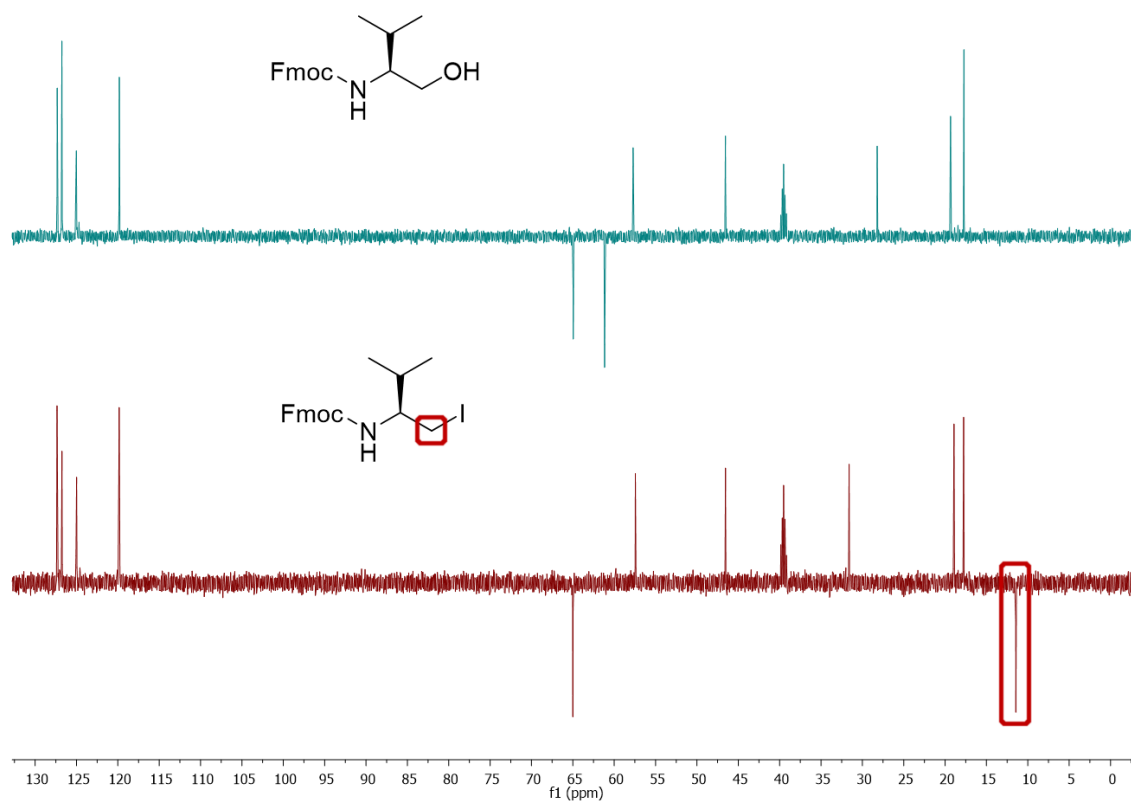
Figure S4.54: DEPT 135 spectra of (Top) Fmoc-Val-ψ[CH₂OH] starting material (**4.10b**), and (Bottom) β-amino iodide **Fmoc-Val-ψ[CH₂I] (4.10c)** in DMSO-d_6.
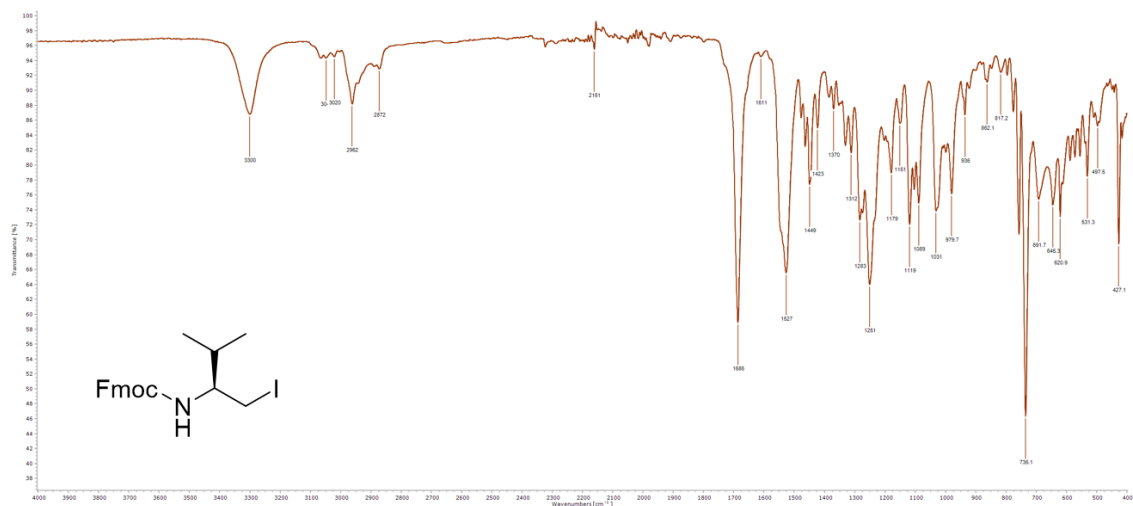
Figure S4.55: FTIR-ATR spectrum of **Fmoc-Val-ψ[CH$_2$I] (4.10c)**.
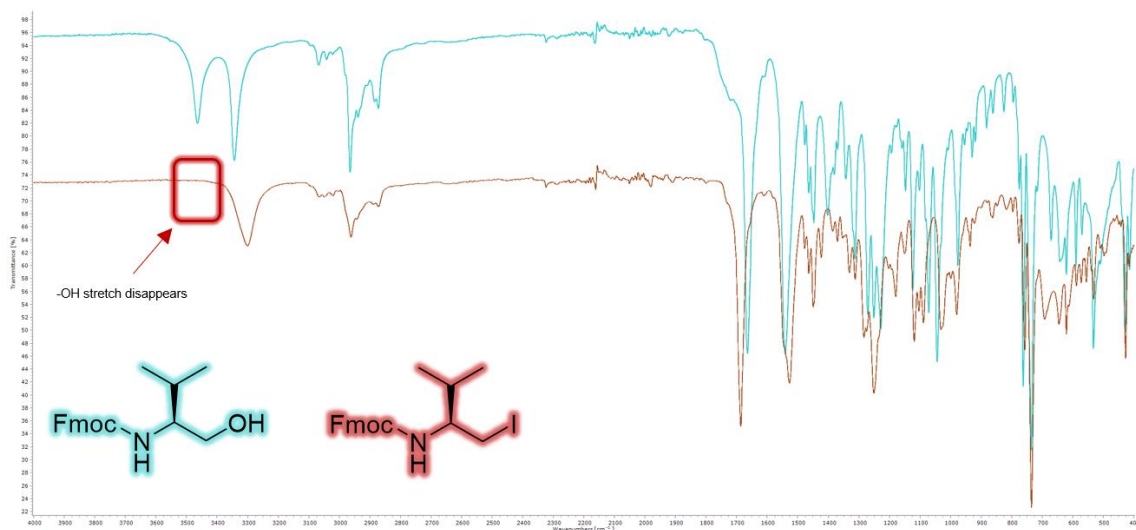
Figure S4.56: FTIR-ATR spectra of (Top) Fmoc-Val-ψ[CH$_2$OH] starting material (**4.10b**), and (Bottom) β-amino iodide **Fmoc-Val-ψ[CH$_2$I] (4.10c)**.

Figure S4.57: LC-MS data for **Fmoc-Val-*ψ*[CH₂N₃] (4.10d)**.

Figure S4.58: DEPT 135 spectrum of **Fmoc-Val-*ψ*[CH₂N₃] (4.10d)** in DMSO-*d₆*.
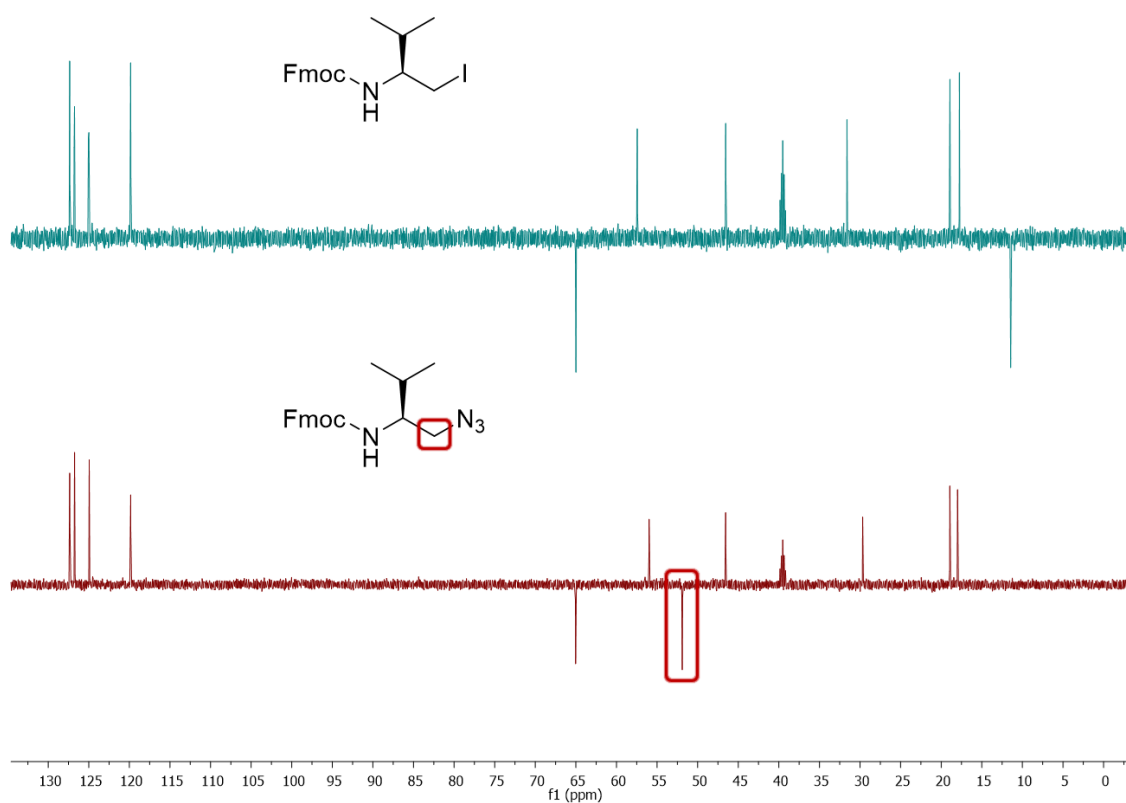
Figure S4.59: DEPT 135 spectra of (Top) Fmoc-Val-ψ[CH$_2$I] starting material (**4.10c**), and (Bottom) alkyl-azide **Fmoc-Val-ψ[CH$_2$N$_3$] (4.10d)** in DMSO-d_6.
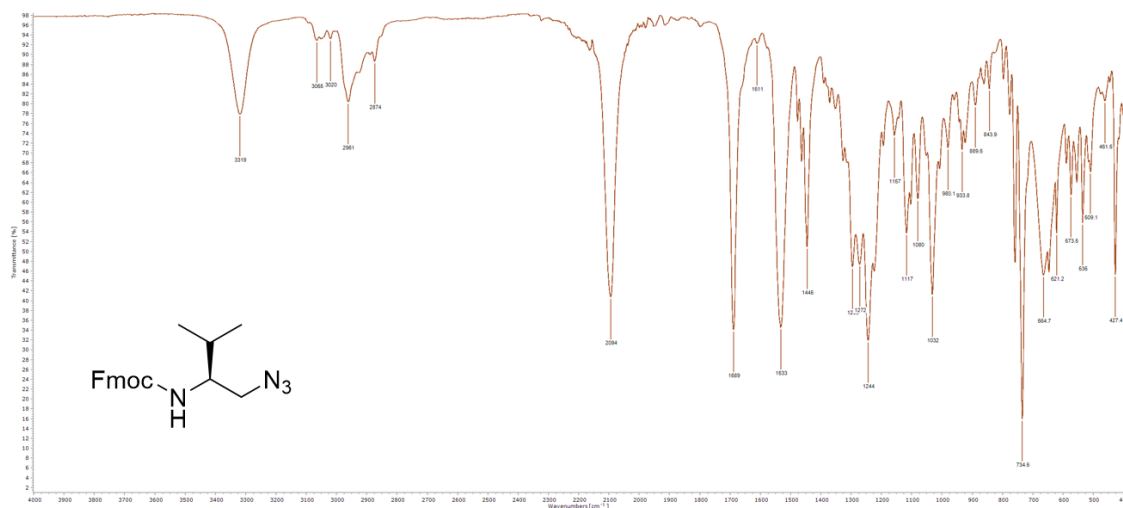
Figure S4.60: FTIR-ATR spectrum of **Fmoc-Val-ψ[CH$_2$N$_3$] (4.10d)**.
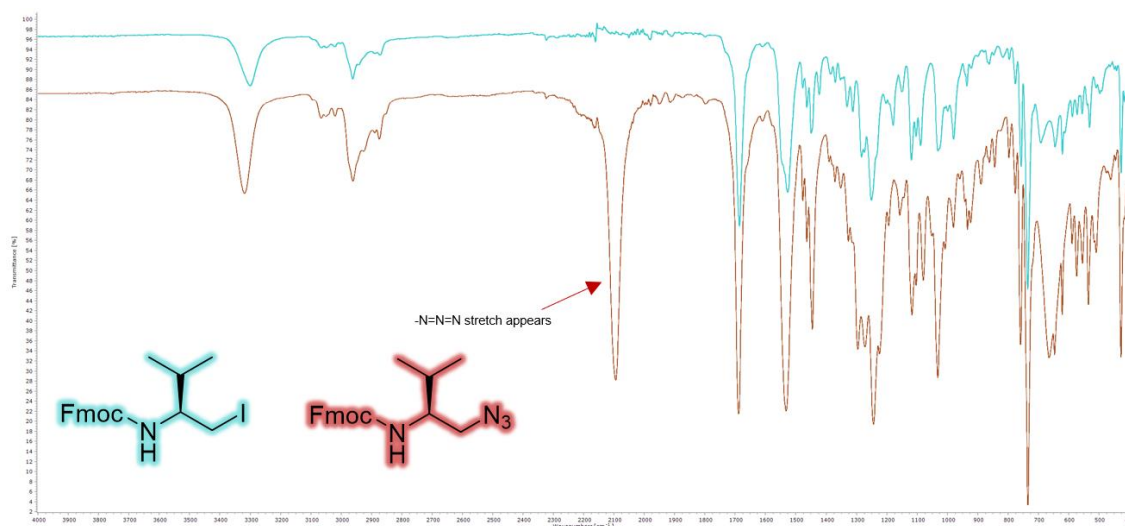
Figure S4.61: FTIR-ATR spectra of (Top) Fmoc-Val-ψ[CH$_2$I] starting material (**4.10c**), and (Bottom) alkyl-azide **Fmoc-Val-ψ[CH$_2$N$_3$] (4.10d)**.
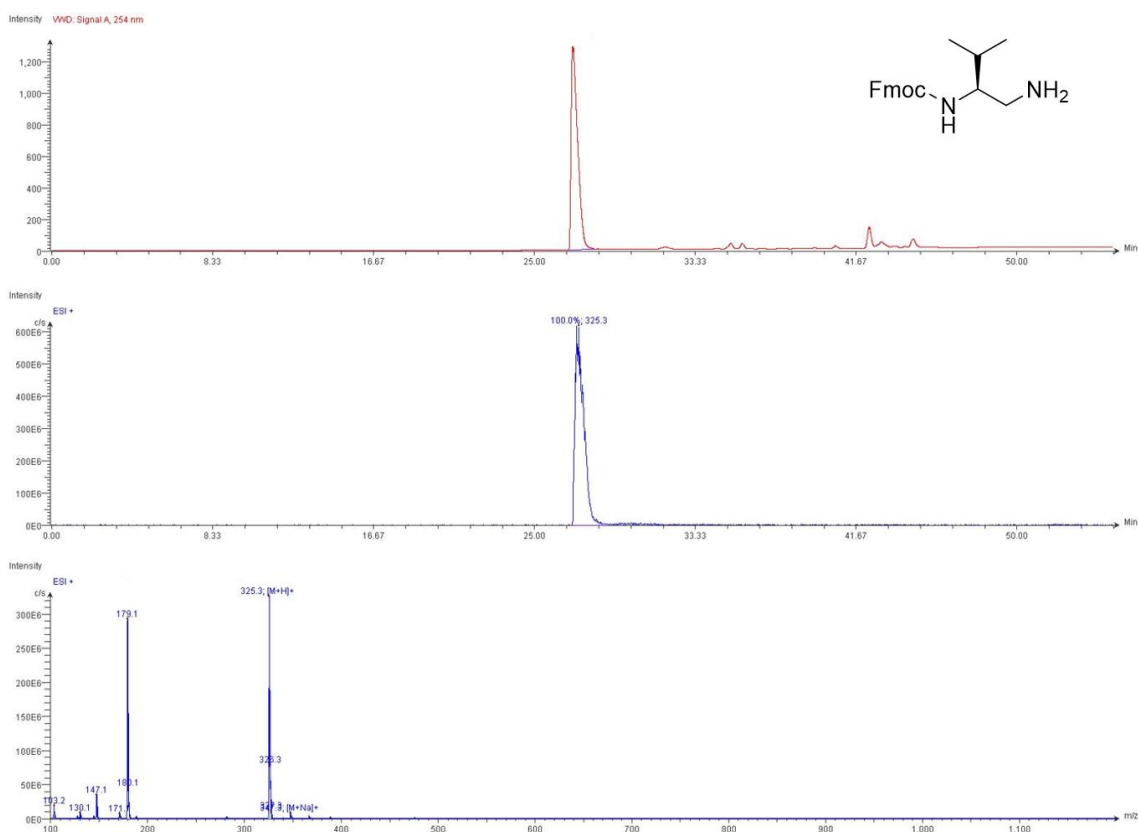
Figure S4.62: LC-MS data for **Fmoc-Val-ψ[CH$_2$NH$_2$] (4.10e)**.

403
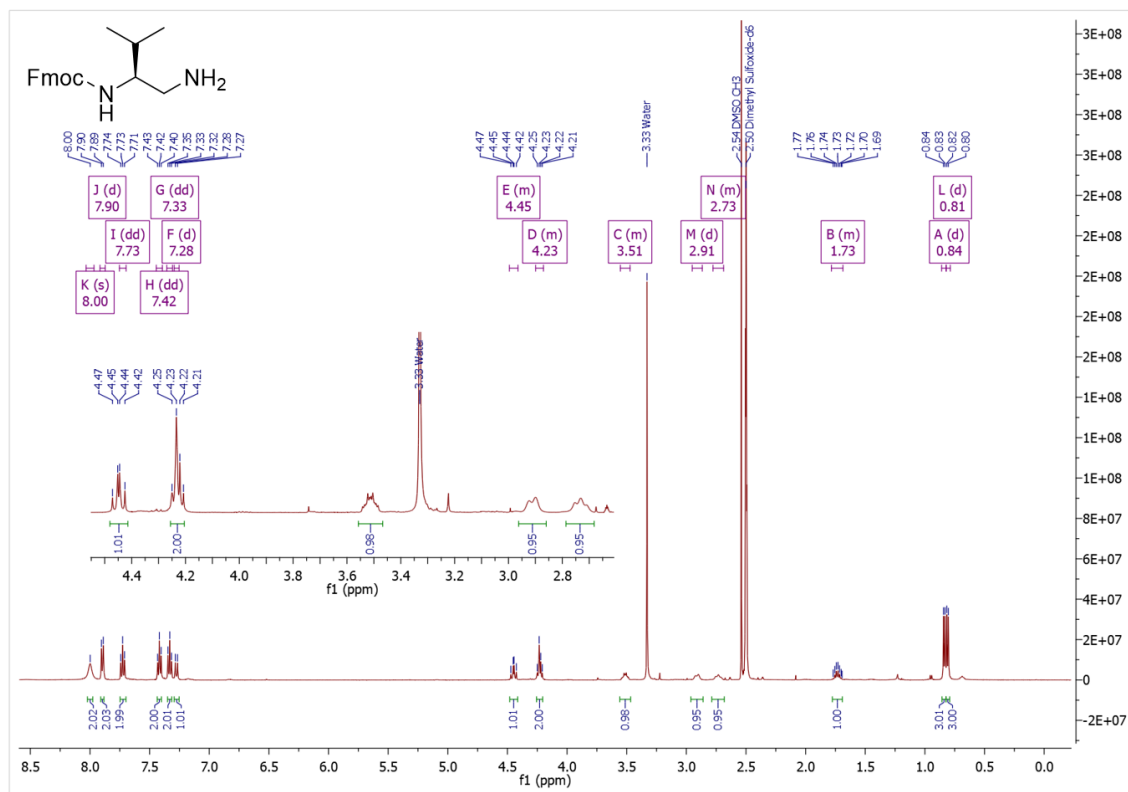
Figure S4.63: ^{1}H NMR spectrum of **Fmoc-Val-ψ[CH$_2$NH$_2$] (4.10e)** in DMSO-d_6.
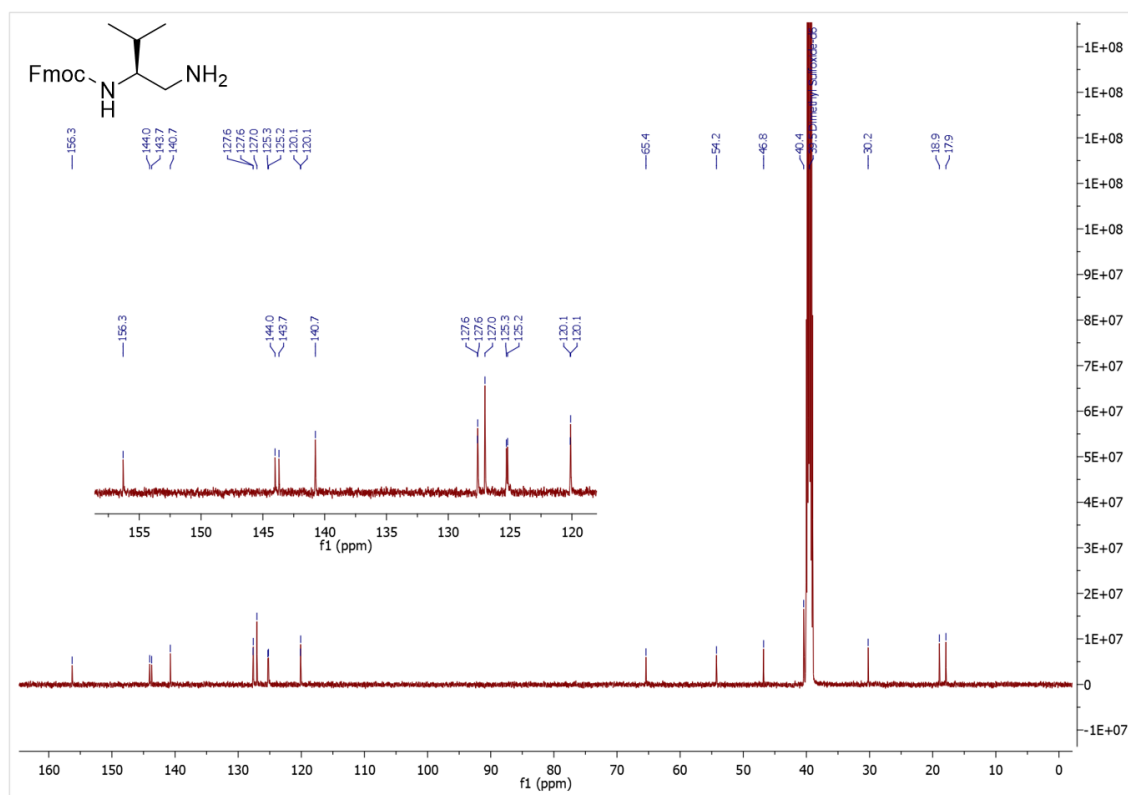
Figure S4.64: ^{13}C NMR spectrum of **Fmoc-Val-ψ[CH$_2$NH$_2$] (4.10e)** in DMSO-d_6.
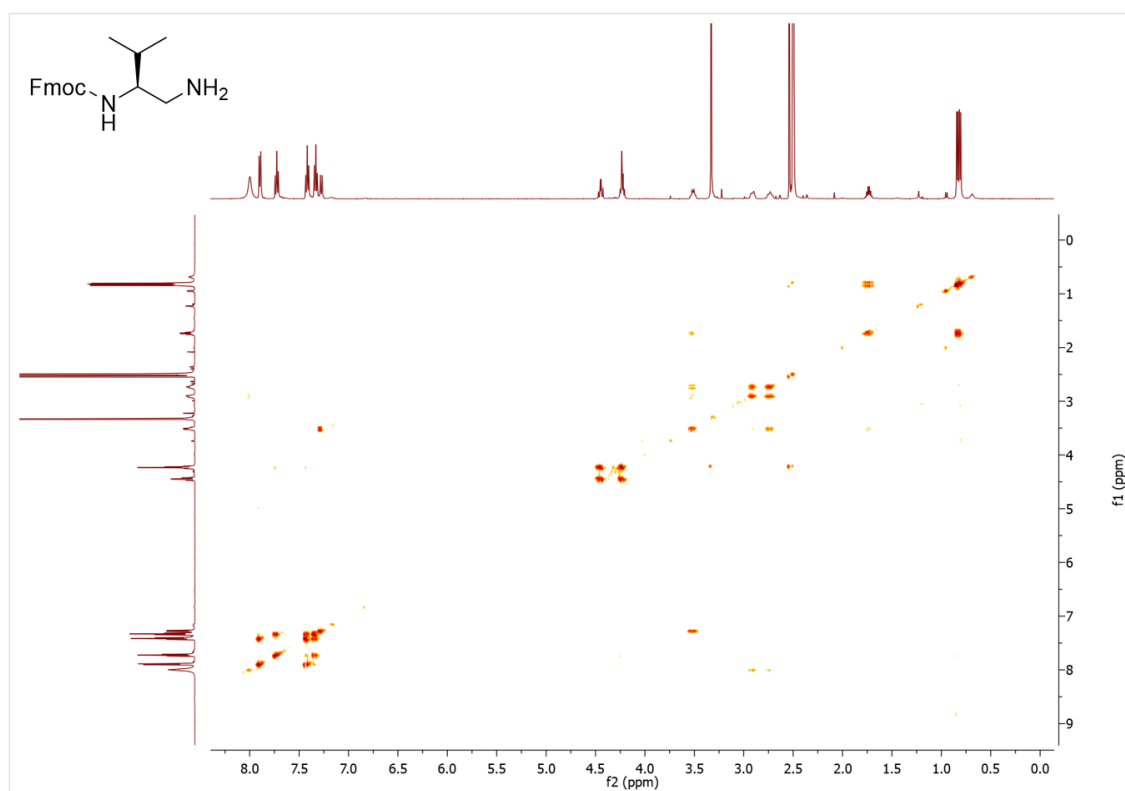
Figure S4.65: COSY spectrum of **Fmoc-Val-ψ[CH₂NH₂] (4.10e)** in DMSO-*d*₆.
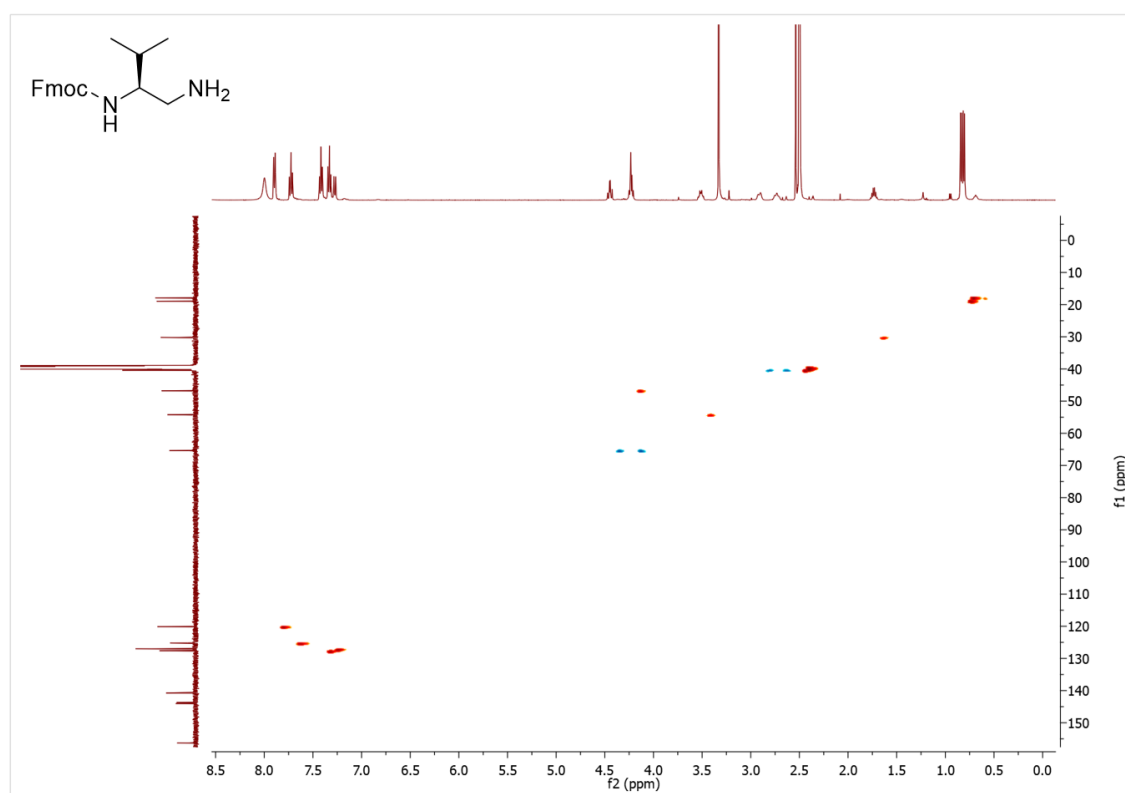
Figure S4.66: HSQC spectrum of **Fmoc-Val-ψ[CH₂NH₂] (4.10e)** in DMSO-*d*₆.
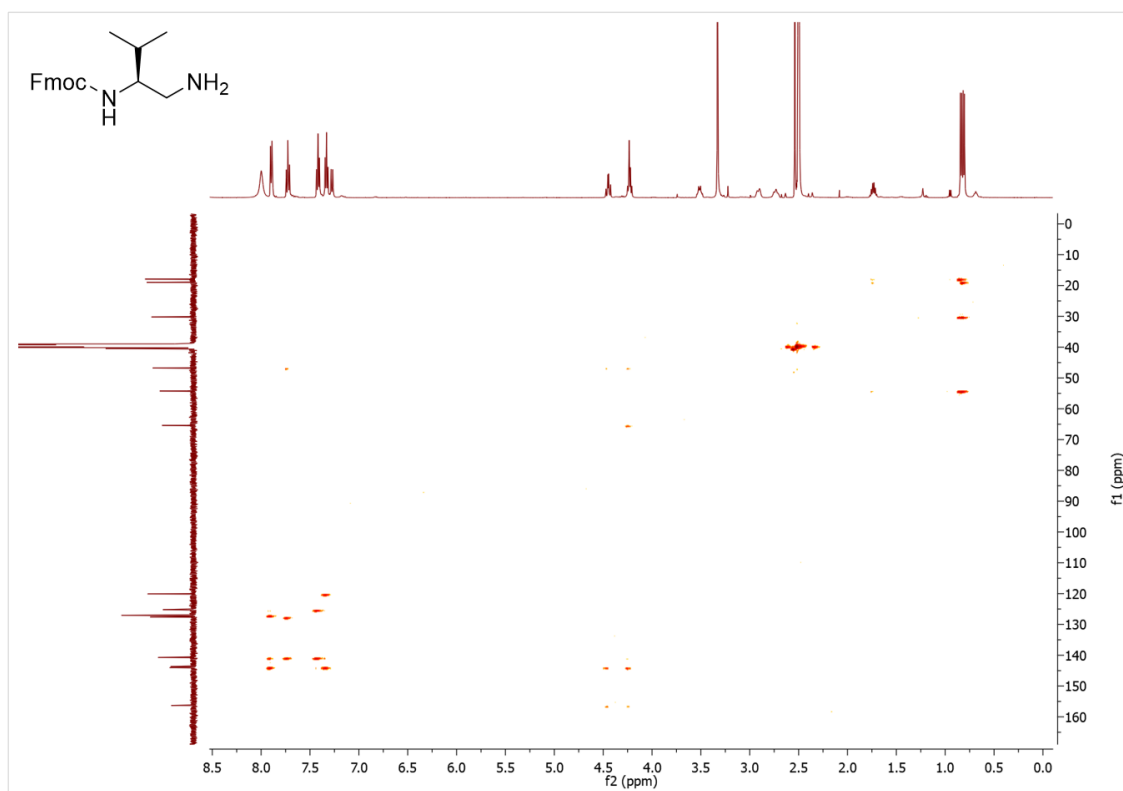
Figure S4.67: HMBC spectrum of **Fmoc-Val-ψ[CH₂NH₂] (4.10e)** in DMSO-d_6.
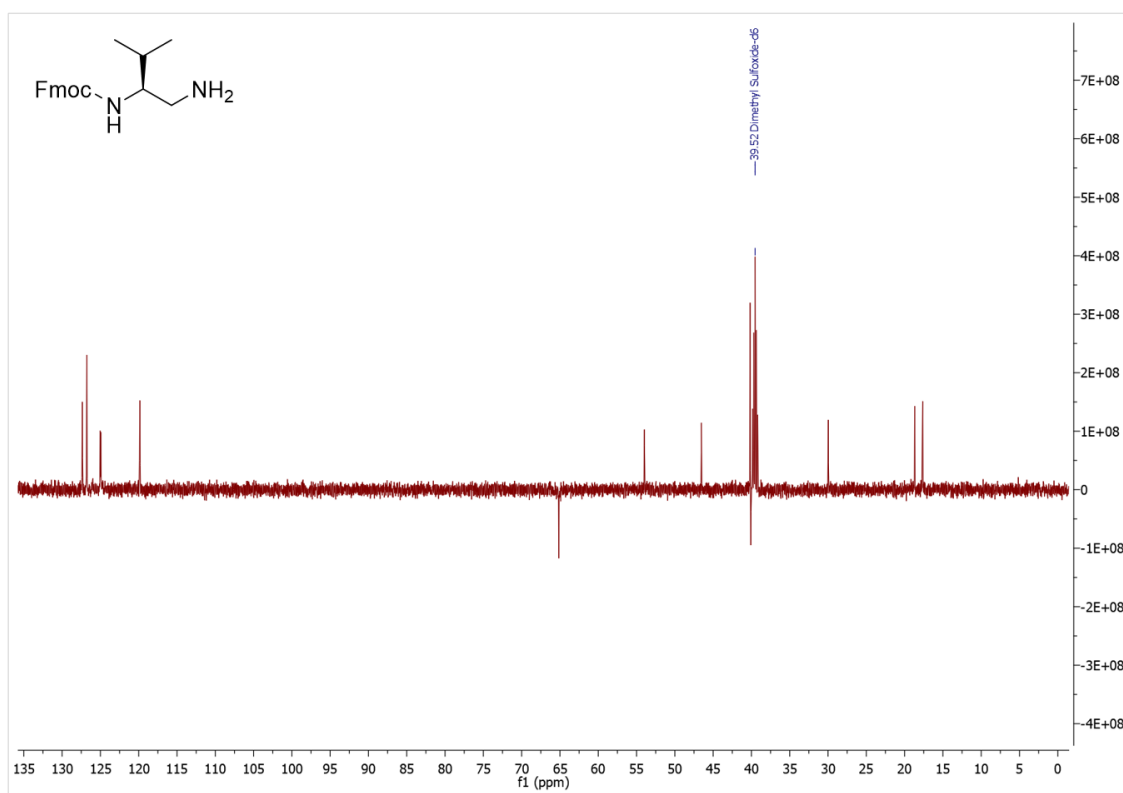
Figure S4.68: DEPT 135 spectrum of **Fmoc-Val-ψ[CH₂NH₂] (4.10e)** in DMSO-d_6.
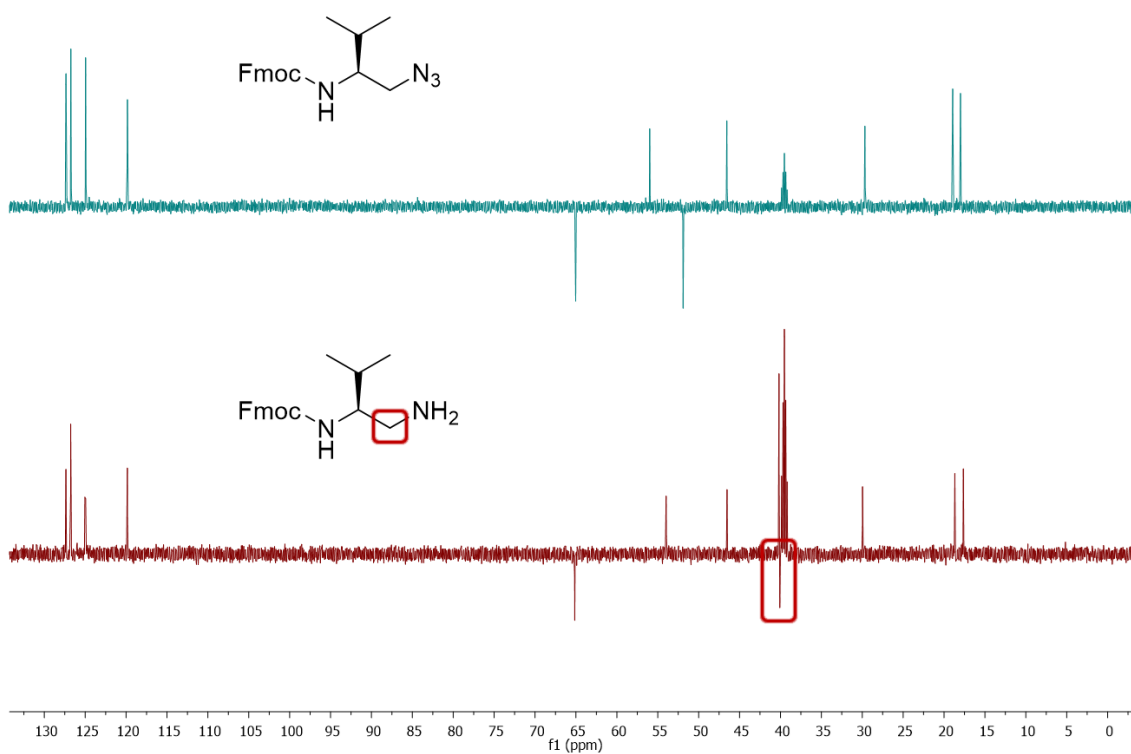
Figure S4.69: DEPT 135 spectra of (Top) Fmoc-Val-ψ[CH$_2$N$_3$] starting material (**4.10d**), and (Bottom) N^β-Fmoc alkyl-amine **Fmoc-Val-ψ[CH$_2$NH$_2$] (4.10e)** in DMSO-d_6.
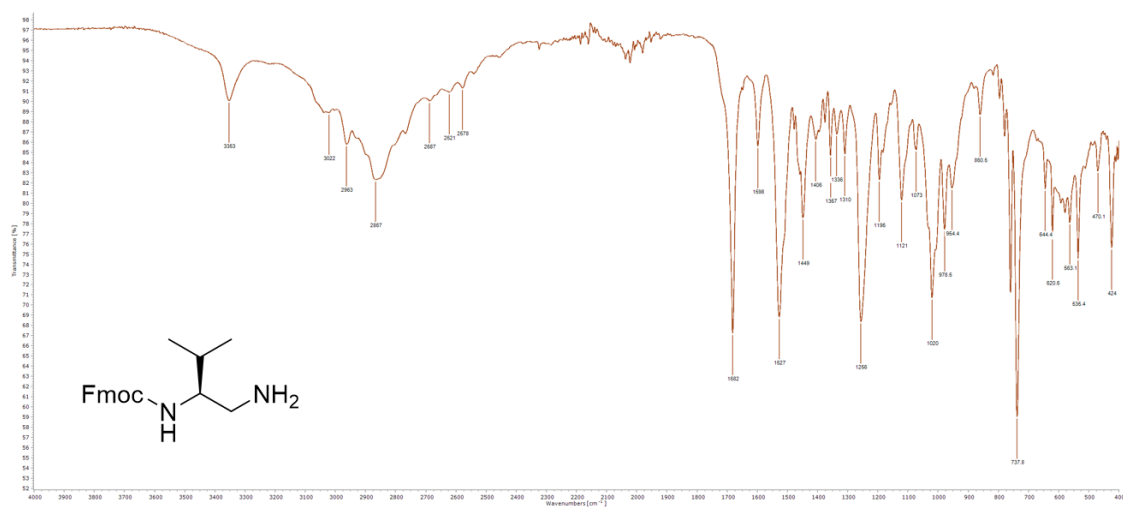
Figure S4.70: FTIR-ATR spectrum of **Fmoc-Val-ψ[CH$_2$NH$_2$] (4.10e)**.
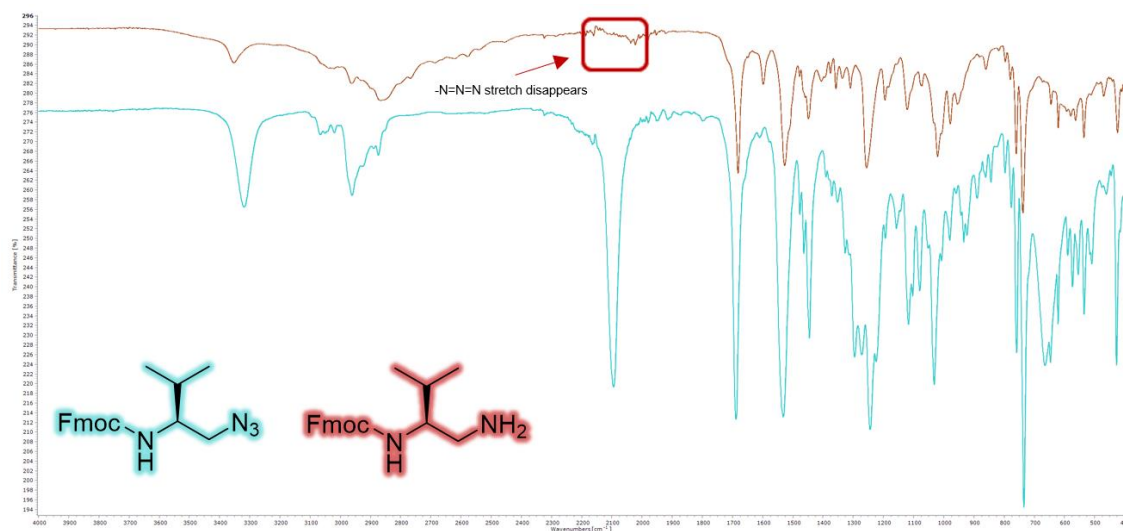
Figure S4.71: FTIR-ATR spectra of (Top) N^β-Fmoc alkyl-amine (**Fmoc-Val-ψ[CH$_2$NH$_2$], 4.10e**), and (Bottom) Fmoc-Val-ψ[CH$_2$N$_3$] starting material (**4.10d**).
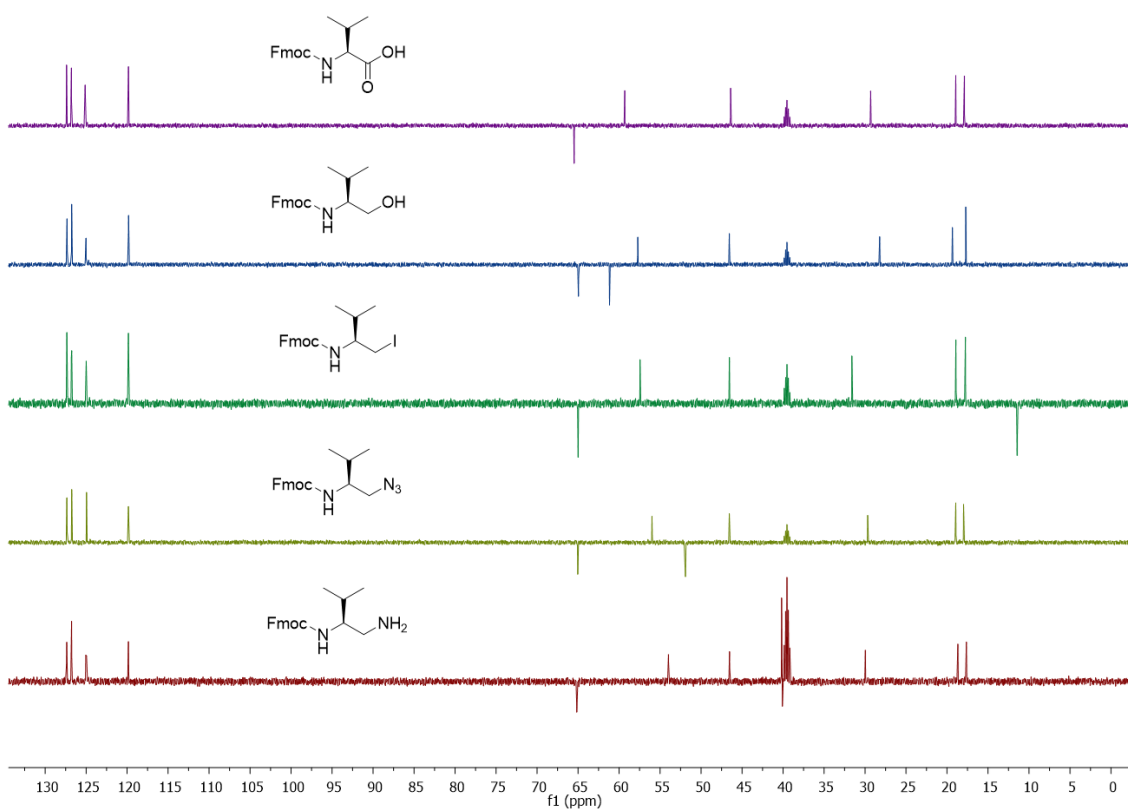
Figure S4.72: DEPT 135 comparison of the different β*-CH$_2$ chemical shifts, from the Fmoc-Val-OH starting material (purple) to the N^β-Fmoc alkyl-amine product (red).
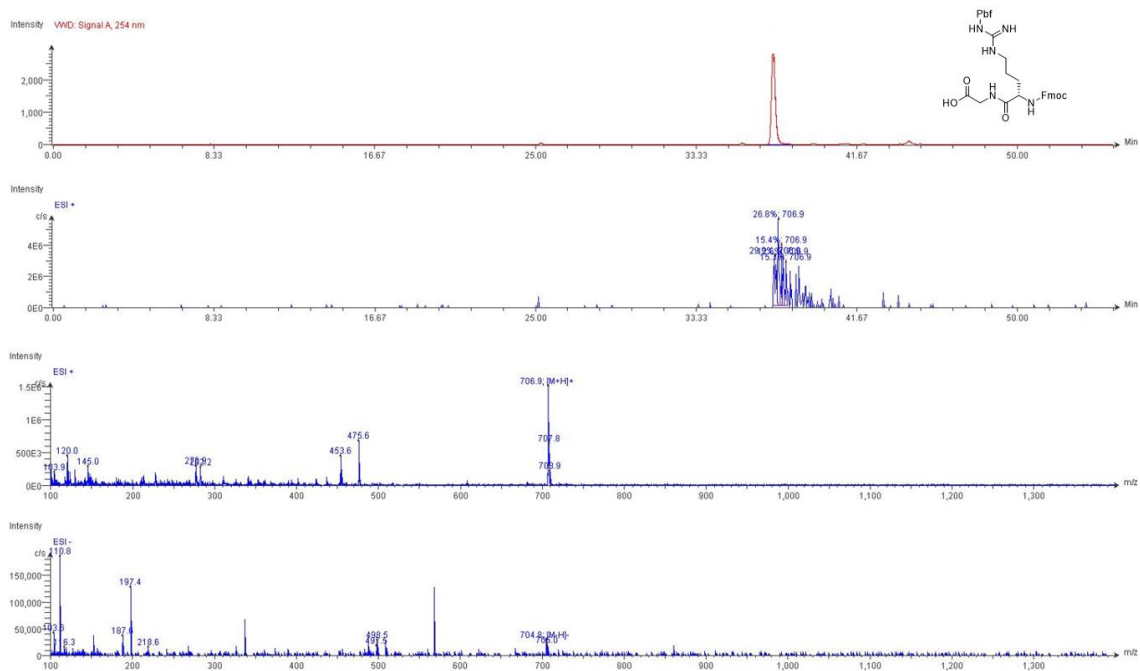
Figure S4.73: LC-MS data for **Fmoc-R(Pbf)-G-OH**.
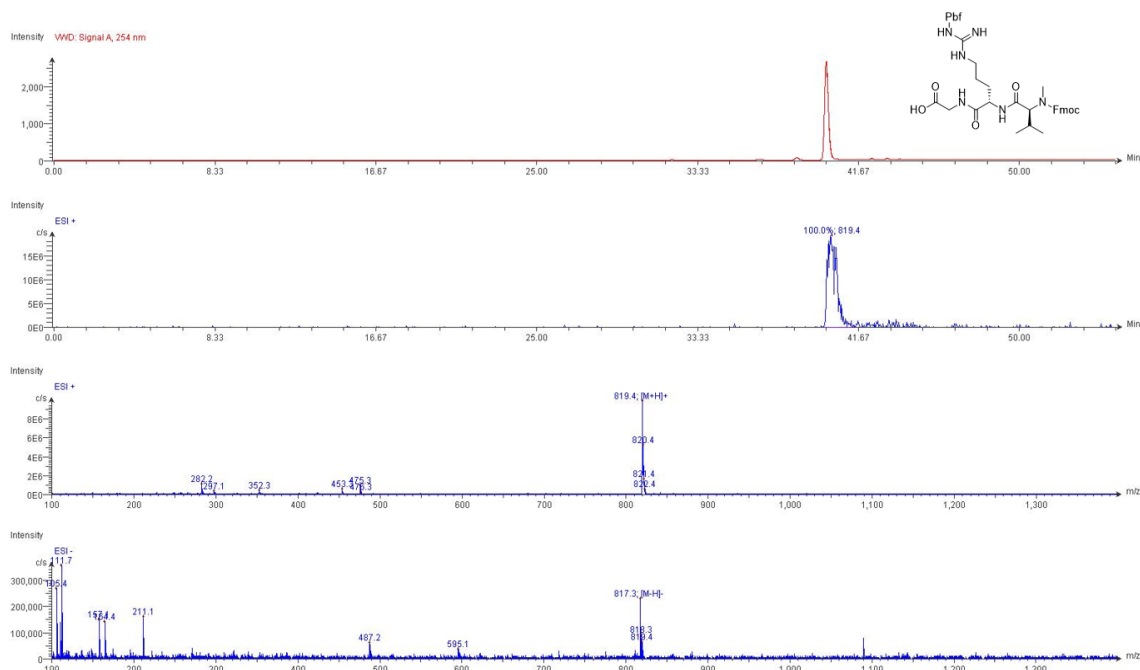
Figure S4.74: LC-MS data for **Fmoc-*N*Me-V-R(Pbf)-G-OH**.
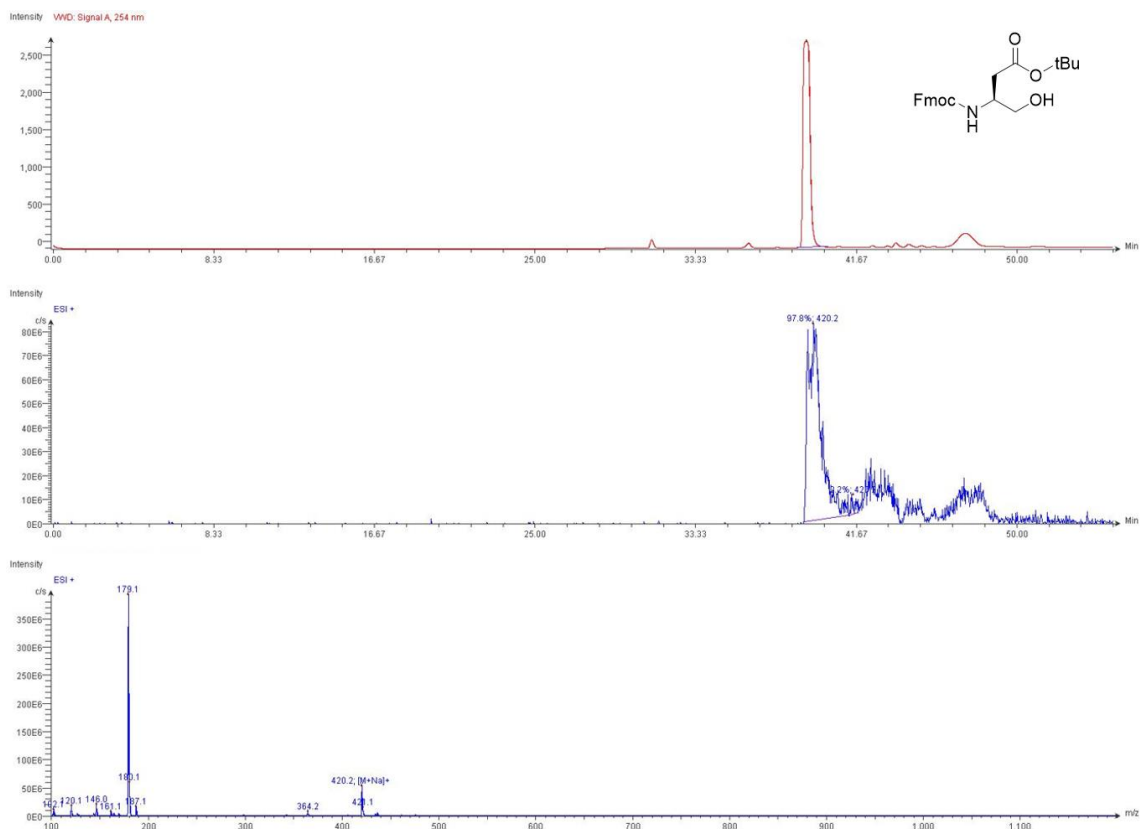
Figure S4.75: LC-MS data for **Fmoc-Asp(O*t*Bu)-ψ[CH$_2$OH] (4.11b)**.
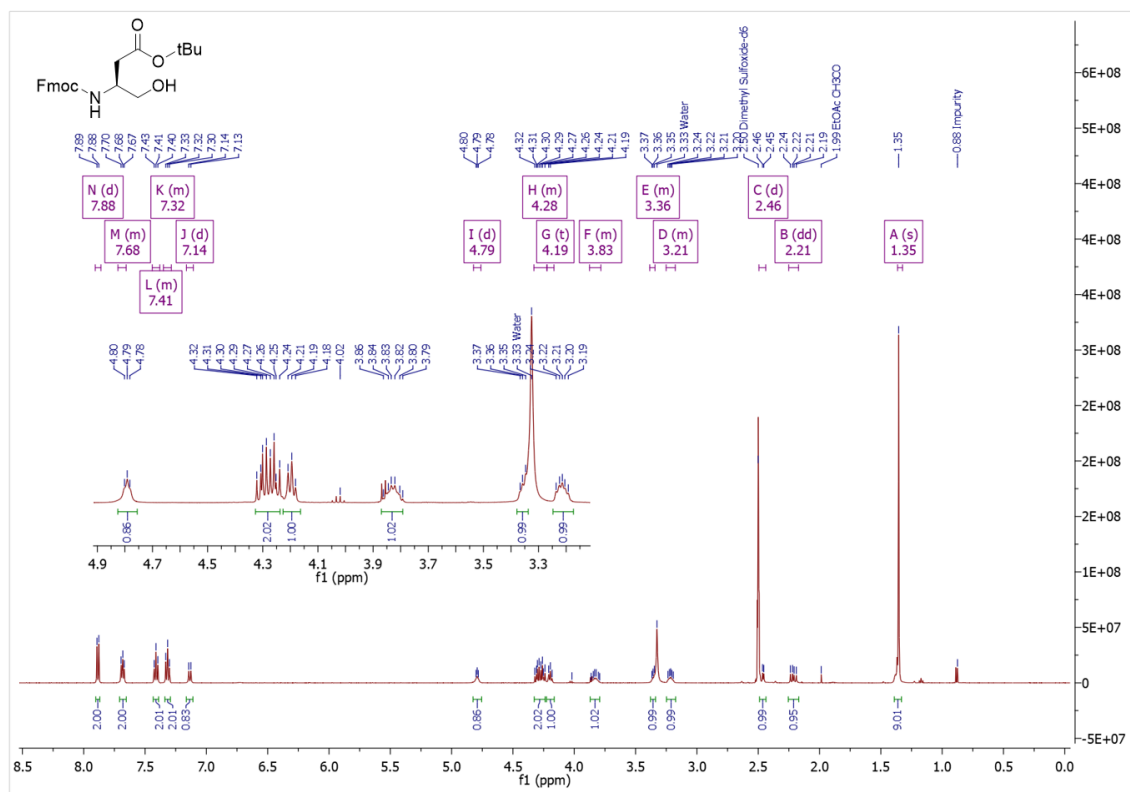
Figure S4.76: ^{1}H NMR spectrum of **Fmoc-Asp(O*t*Bu)-ψ[CH$_2$OH] (4.11b)** in DMSO-*d*$_6$.
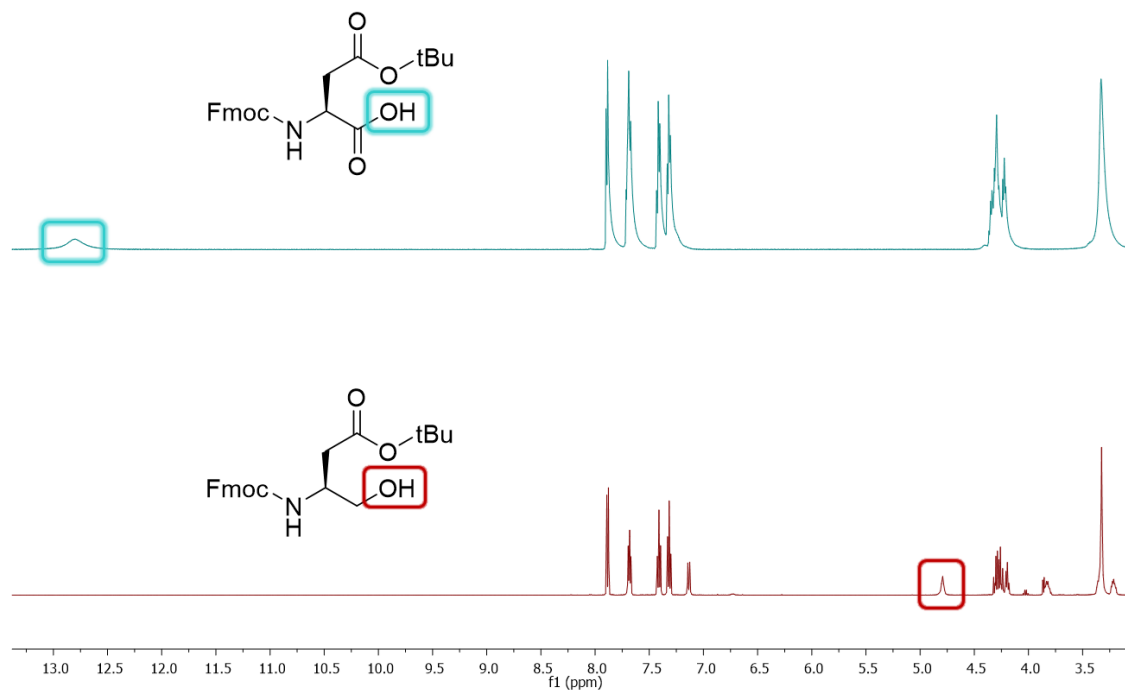
Figure S4.77: ^{1}H NMR spectra of (Top) Fmoc-Asp(O*t*Bu)-OH starting material (**4.11a**), and (Bottom) β-amino alcohol **Fmoc-Asp(O*t*Bu)-ψ[CH$_2$OH] (4.11b)** in DMSO-d_6.
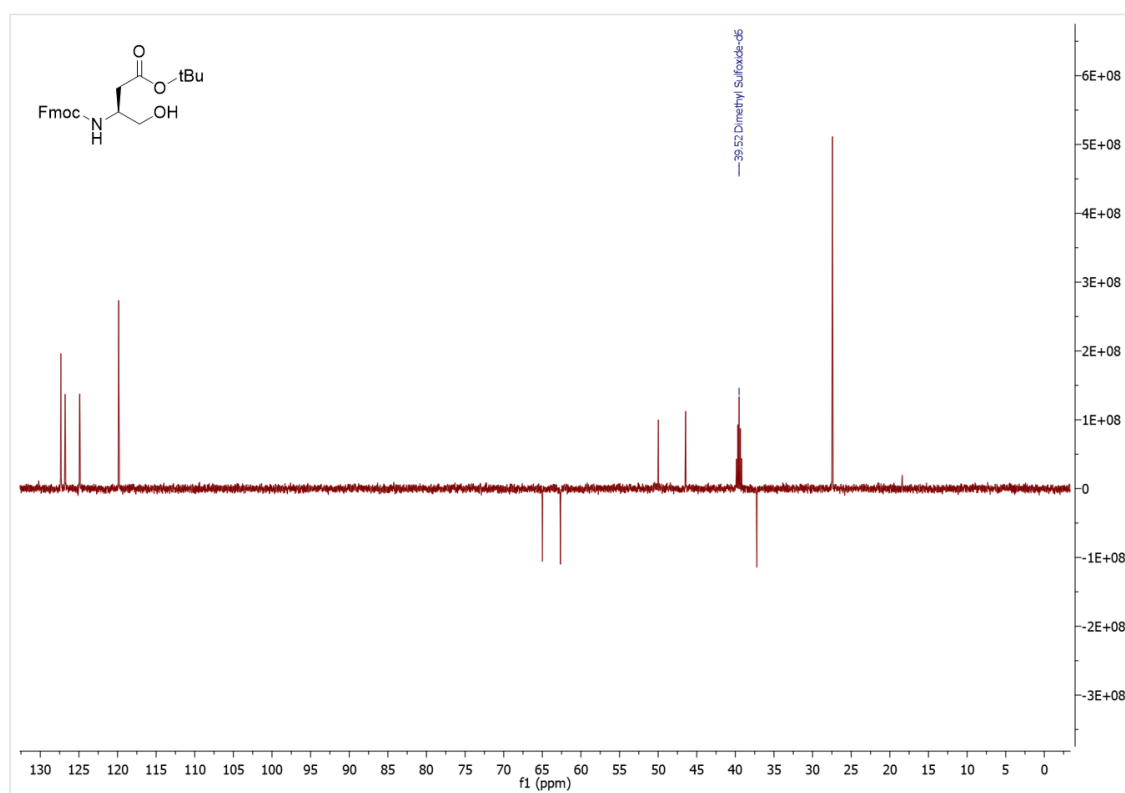
Figure S4.78: DEPT 135 spectrum of **Fmoc-Asp(O*t*Bu)-ψ[CH$_2$OH] (4.11b)** in DMSO-d_6.

411
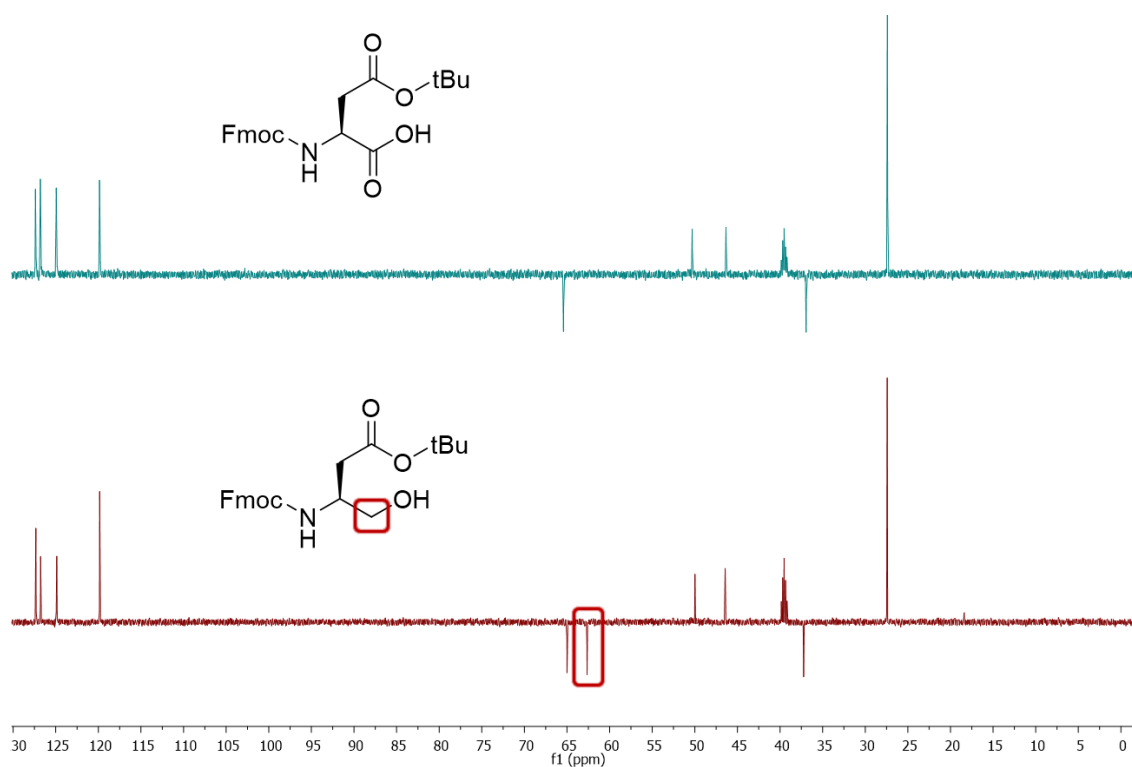
Figure S4.79: DEPT 135 spectra of (Top) Fmoc-Asp(O*t*Bu)-OH starting material (**4.11a**), and (Bottom) β-amino alcohol **Fmoc-Asp(O*t*Bu)-ψ[CH$_2$OH] (4.11b)** in DMSO-d_6.
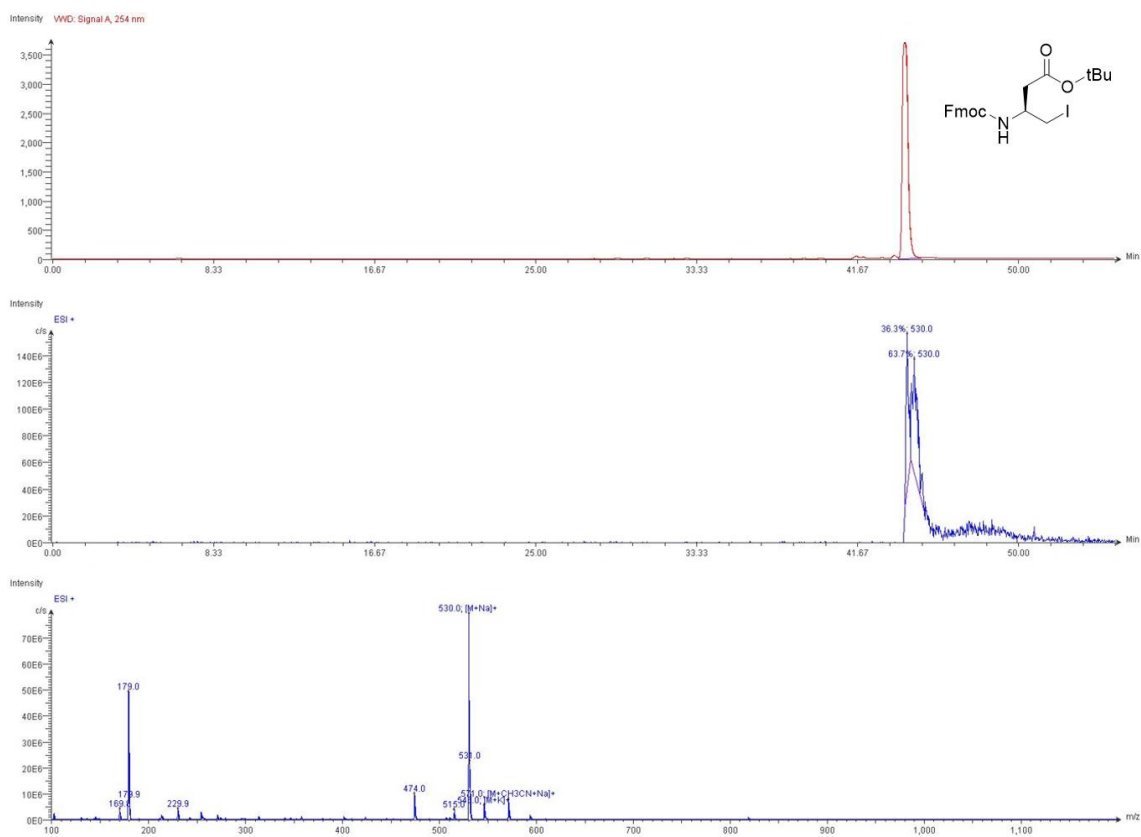
Figure S4.80: LC-MS data for **Fmoc-Asp(O*t*Bu)-ψ[CH$_2$I] (4.11c)**.

412
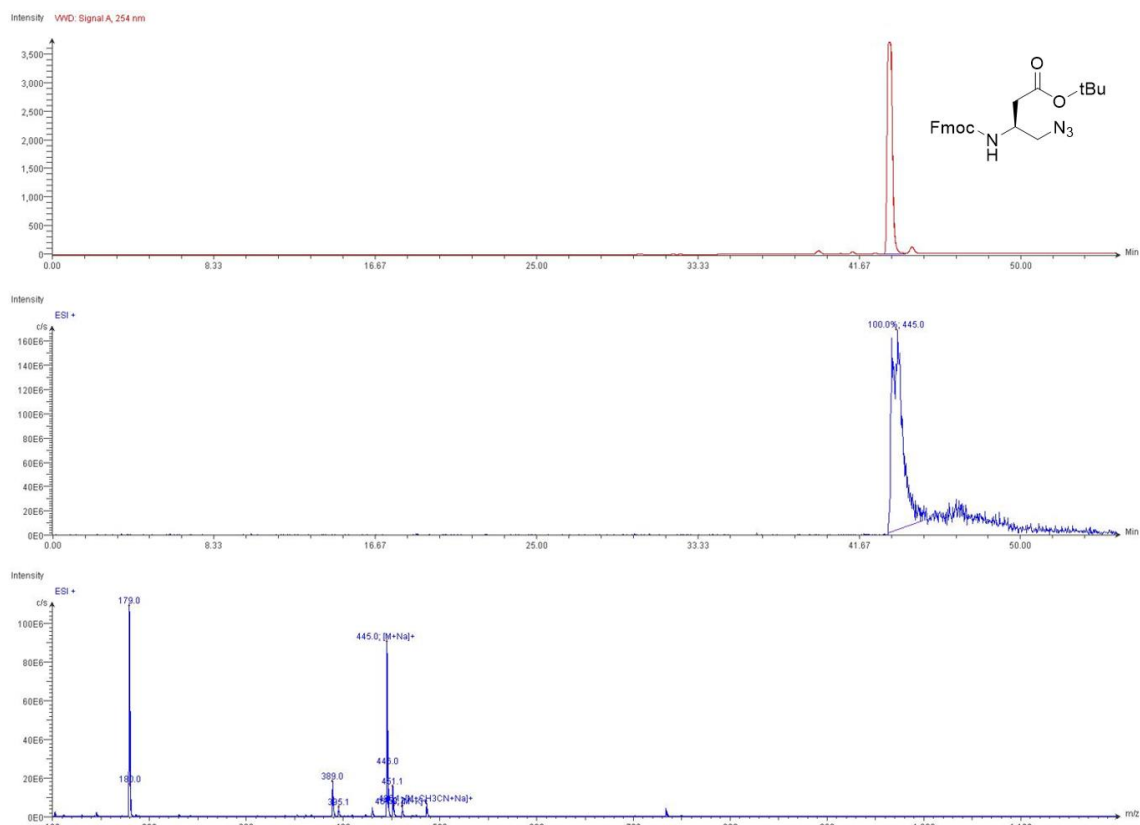
Figure S4.81: LC-MS data for **Fmoc-Asp(O*t*Bu)-ψ[CH₂N₃] (4.11d)**.
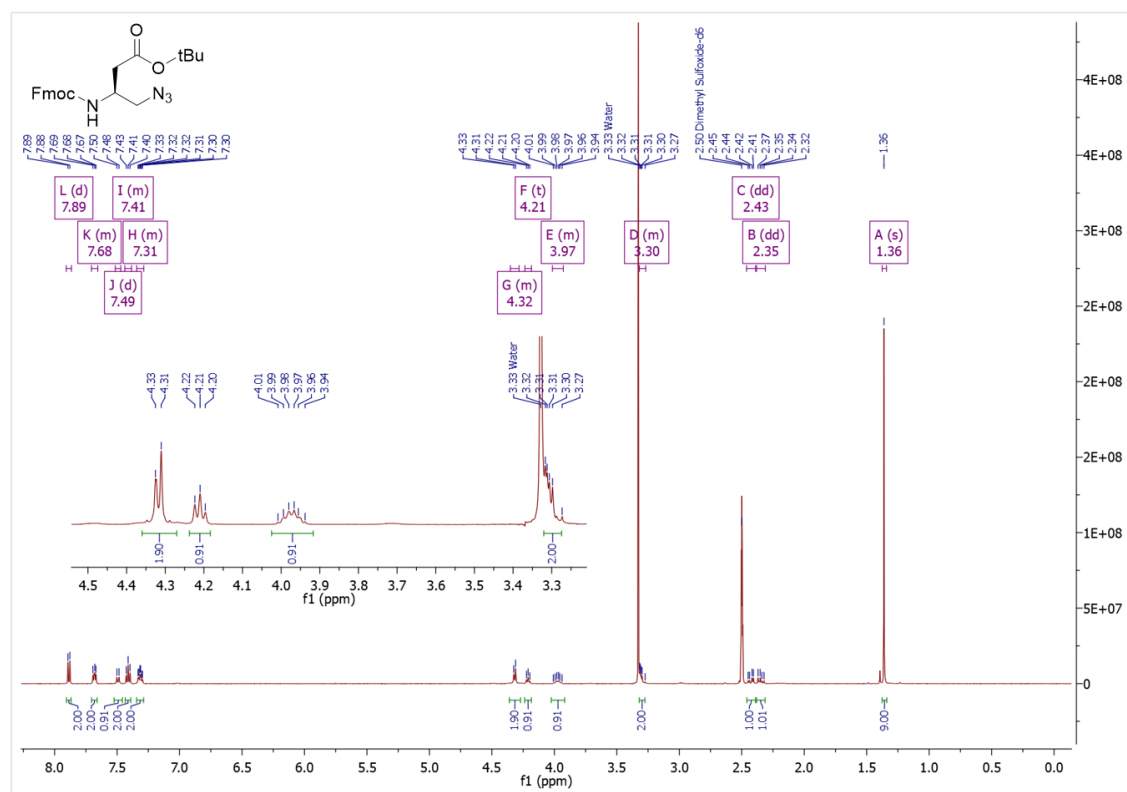
Figure S4.82: ¹H NMR spectrum of **Fmoc-Asp(O*t*Bu)-ψ[CH₂N₃] (4.11d)** in DMSO-*d*₆.
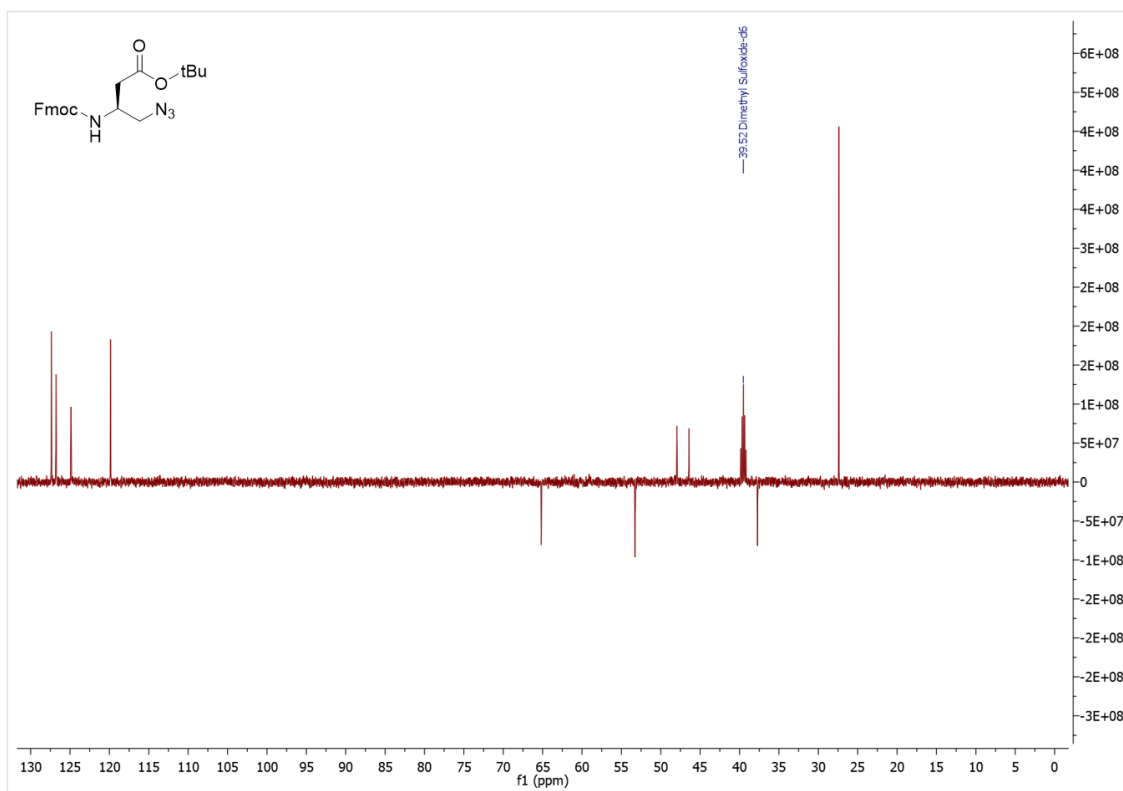
Figure S4.83: DEPT 135 spectrum of **Fmoc-Asp(OtBu)-ψ[CH₂N₃] (4.11d)** in DMSO-d₆.
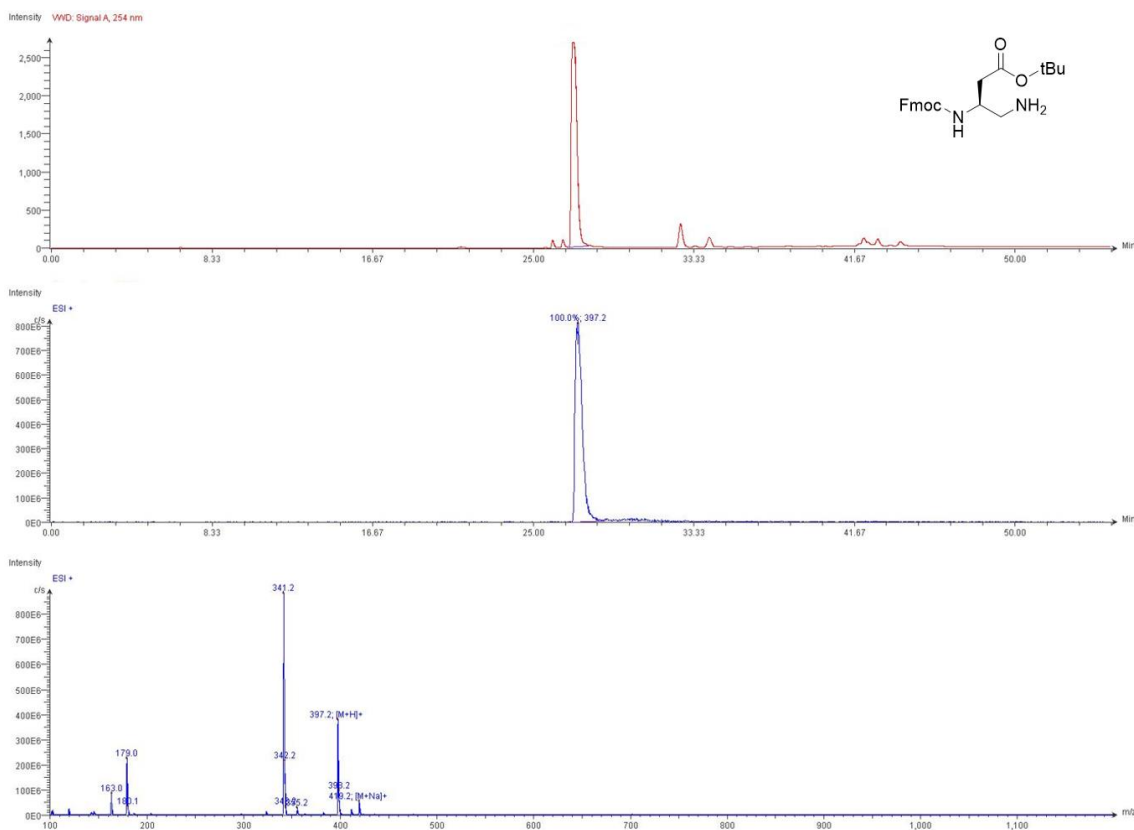
Figure S4.84: LC-MS data for **Fmoc-Asp(OtBu)-ψ[CH₂NH₂] (4.11e)**.

414
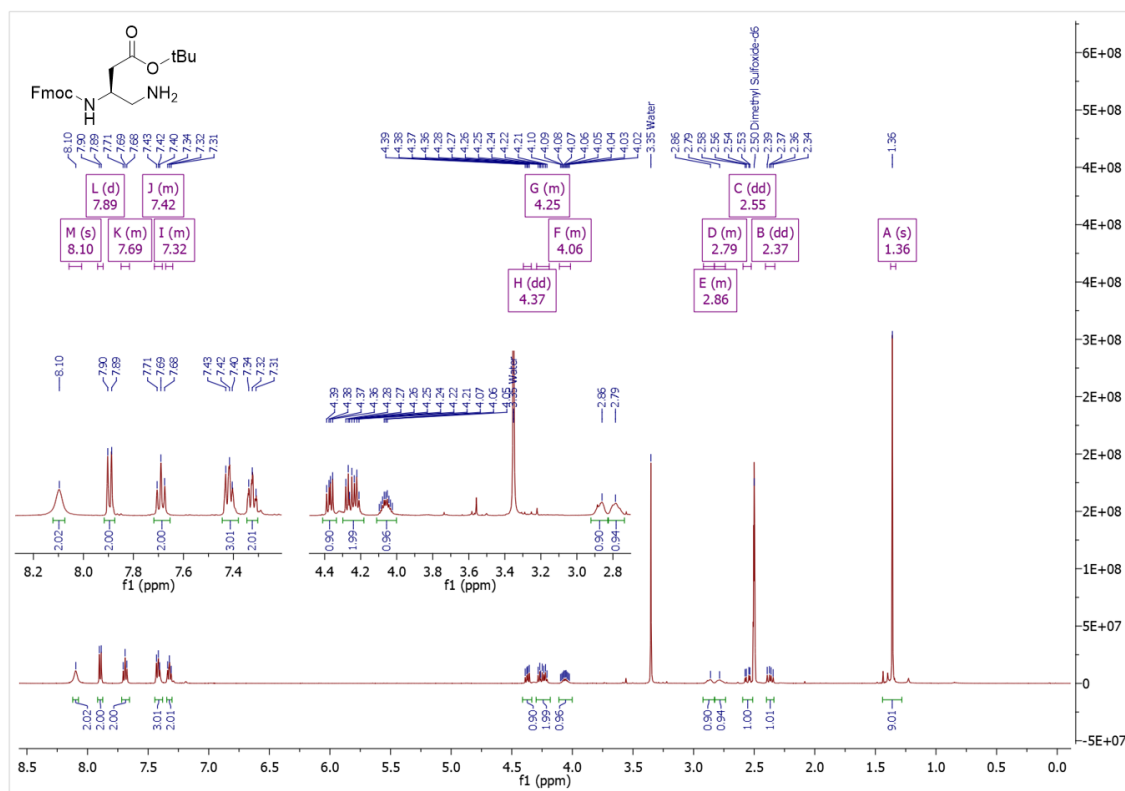
Figure S4.85: ^{1}H NMR spectrum of **Fmoc-Asp(O*t*Bu)-ψ[CH$_2$NH$_2$] (4.11e)** in DMSO-*d*$_6$.
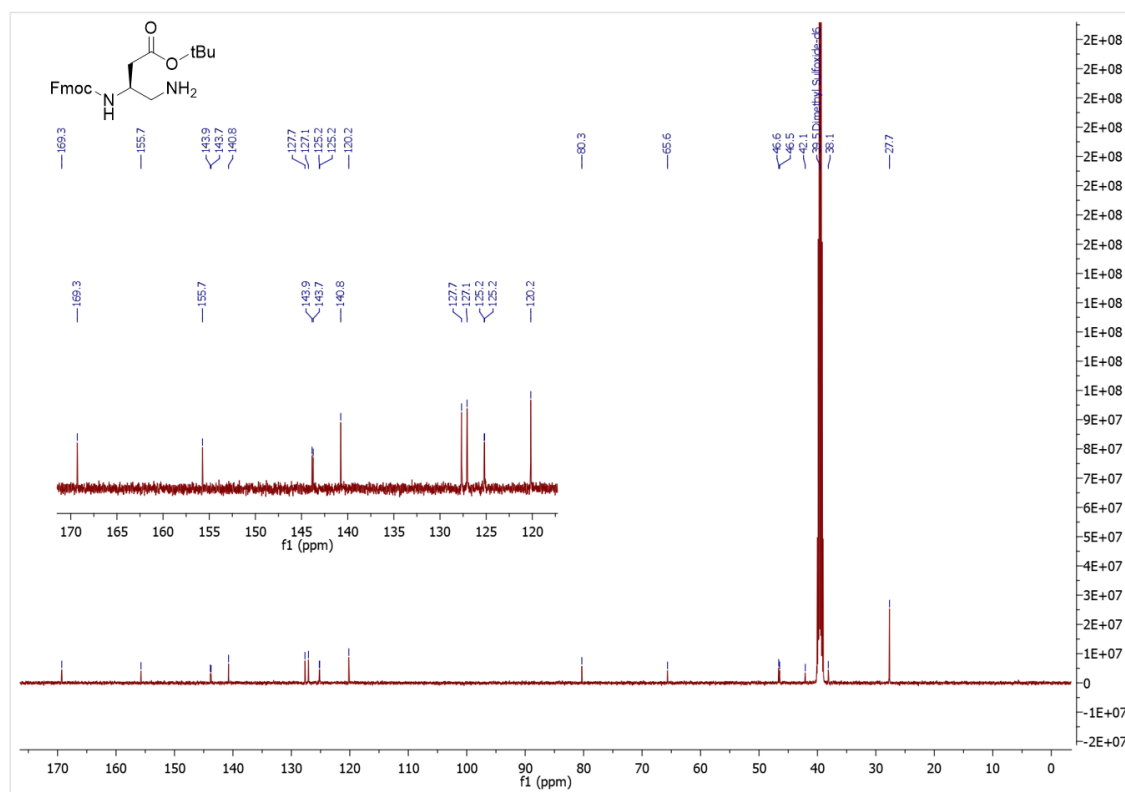
Figure S4.86: ^{13}C NMR spectrum of **Fmoc-Asp(O*t*Bu)-ψ[CH$_2$NH$_2$] (4.11e)** in DMSO-*d*$_6$.
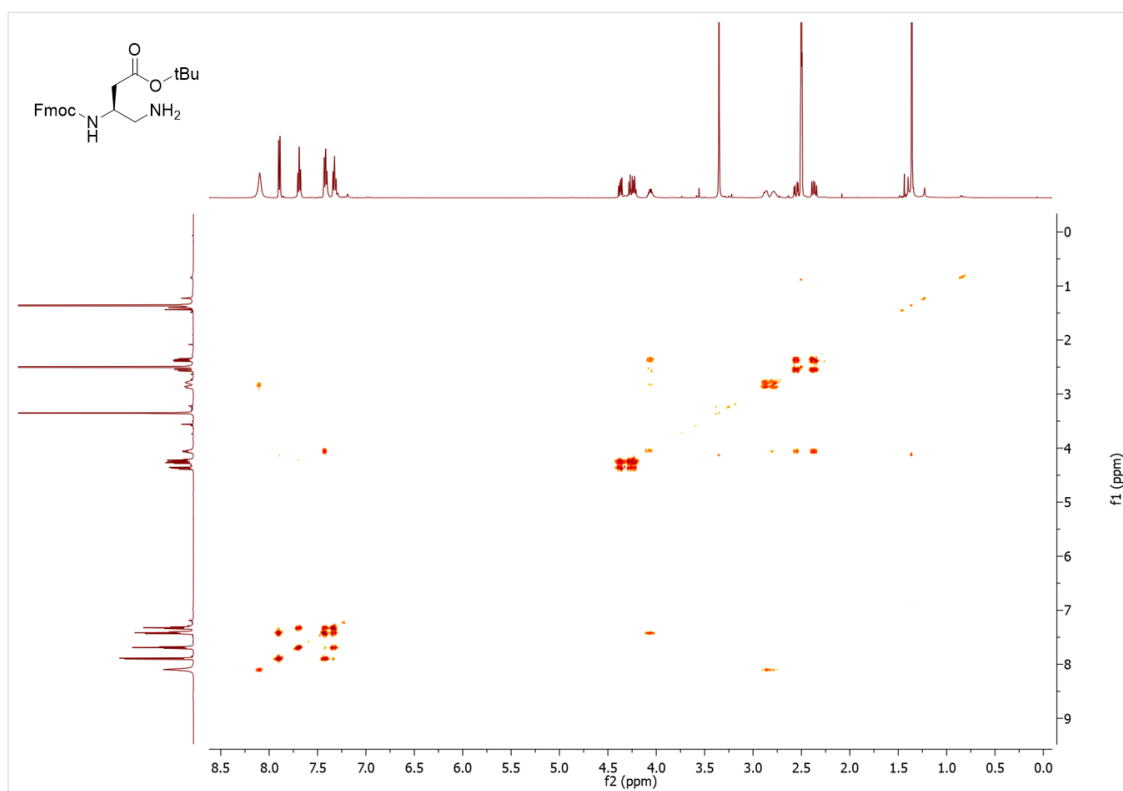
Figure S4.87: COSY spectrum of **Fmoc-Asp(O*t*Bu)-ψ[CH₂NH₂] (4.11e)** in DMSO-*d₆*.
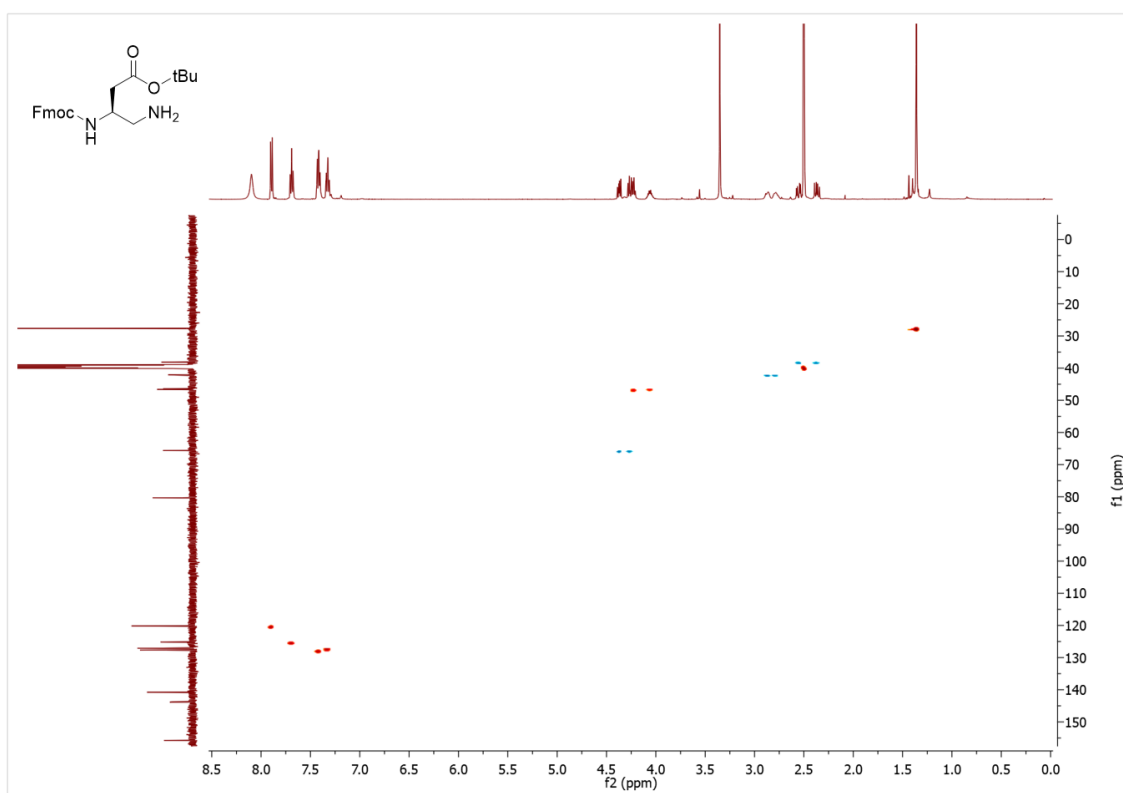
Figure S4.88: HSQC spectrum of **Fmoc-Asp(O*t*Bu)-ψ[CH₂NH₂] (4.11e)** in DMSO-*d₆*.
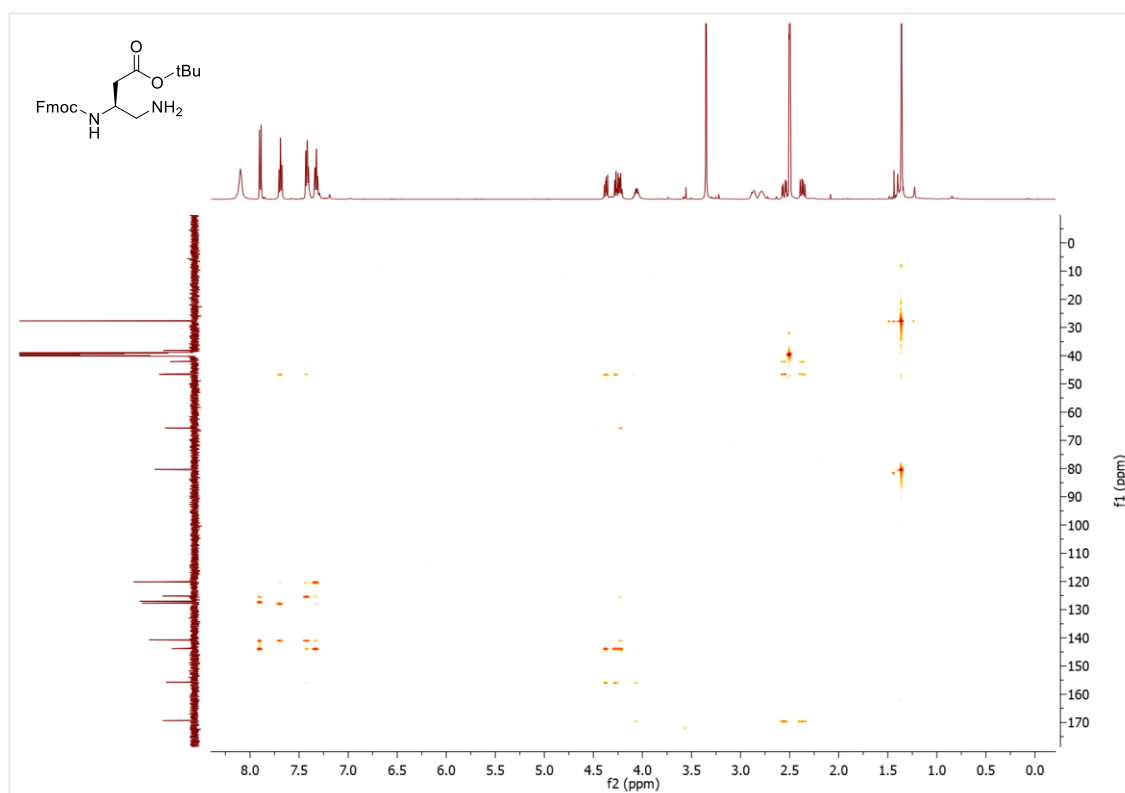
Figure S4.89: HMBC spectrum of **Fmoc-Asp(O*t*Bu)-ψ[CH₂NH₂] (4.11e)** in DMSO-*d*₆.
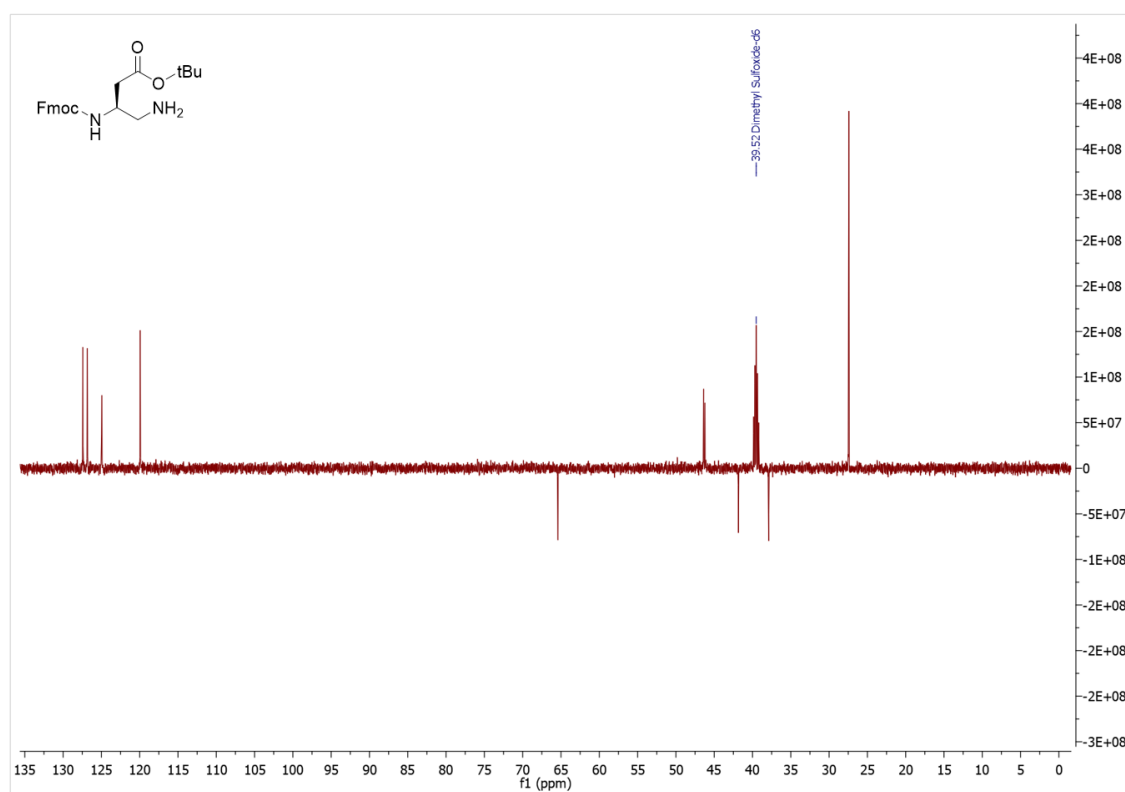
Figure S4.90: DEPT 135 spectrum of **Fmoc-Asp(O*t*Bu)-ψ[CH₂NH₂] (4.11e)** in DMSO-*d*₆.

417
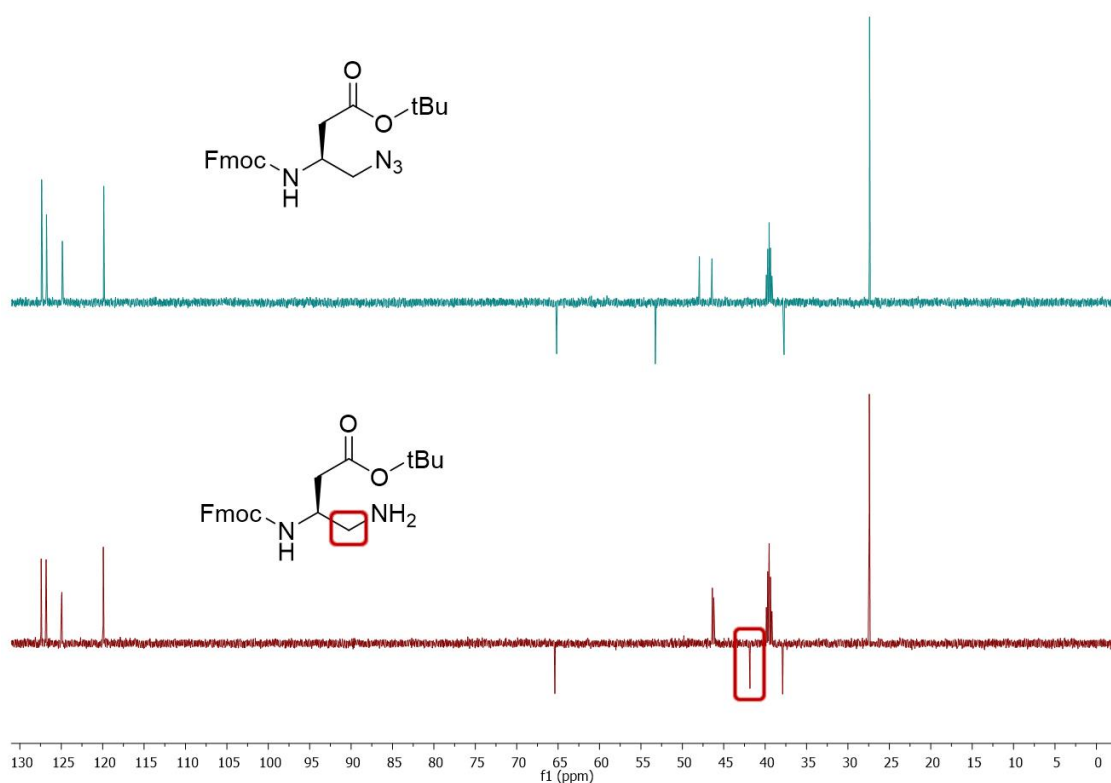
Figure S4.91: DEPT 135 spectra of (Top) Fmoc-Asp(O*t*Bu)-ψ[CH$_2$N$_3$] starting material (**4.11d**), and (Bottom) N^β-Fmoc alkyl-amine **Fmoc-Asp(O*t*Bu)-ψ[CH$_2$NH$_2$] (4.11e)** in DMSO-d_6.
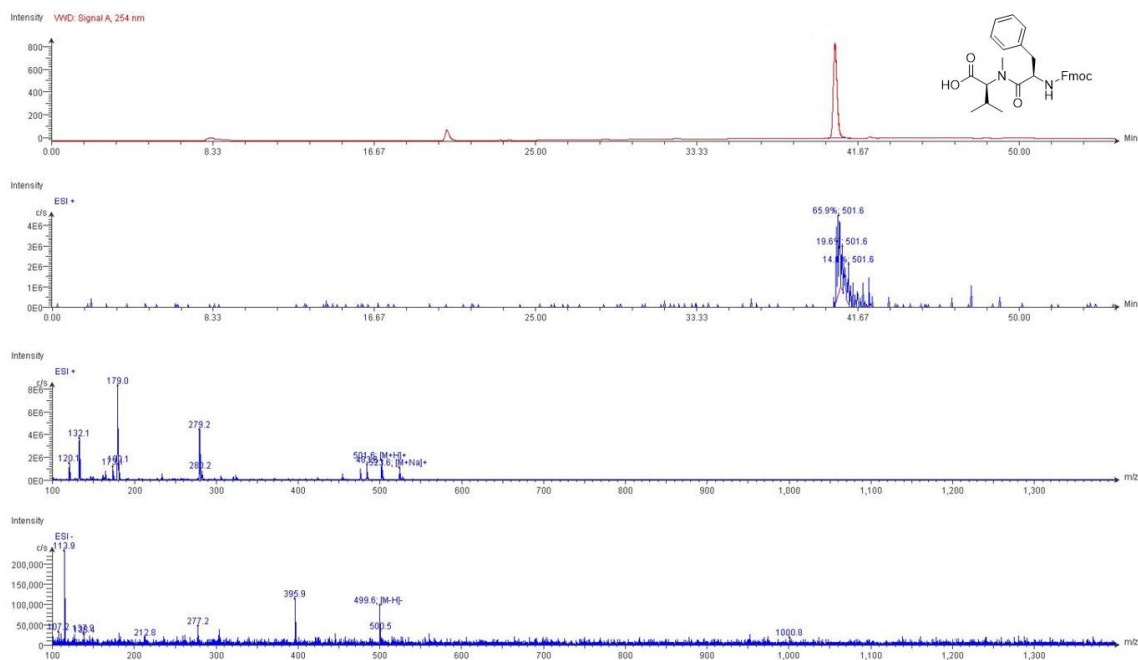
Figure S4.92: LC-MS data for **Fmoc-f-*N*MeV-OH**.
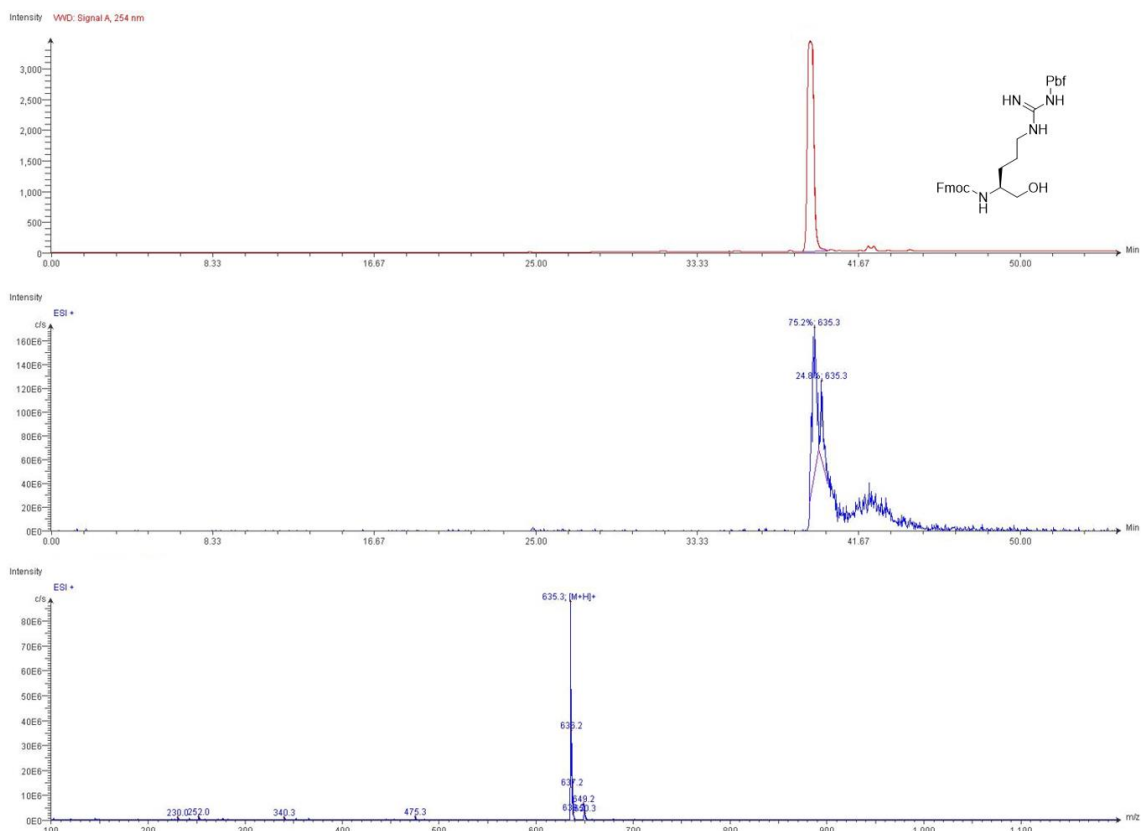
Figure S4.93: LC-MS data for **Fmoc-Arg(Pbf)-ψ[CH₂OH] (4.12b)**.
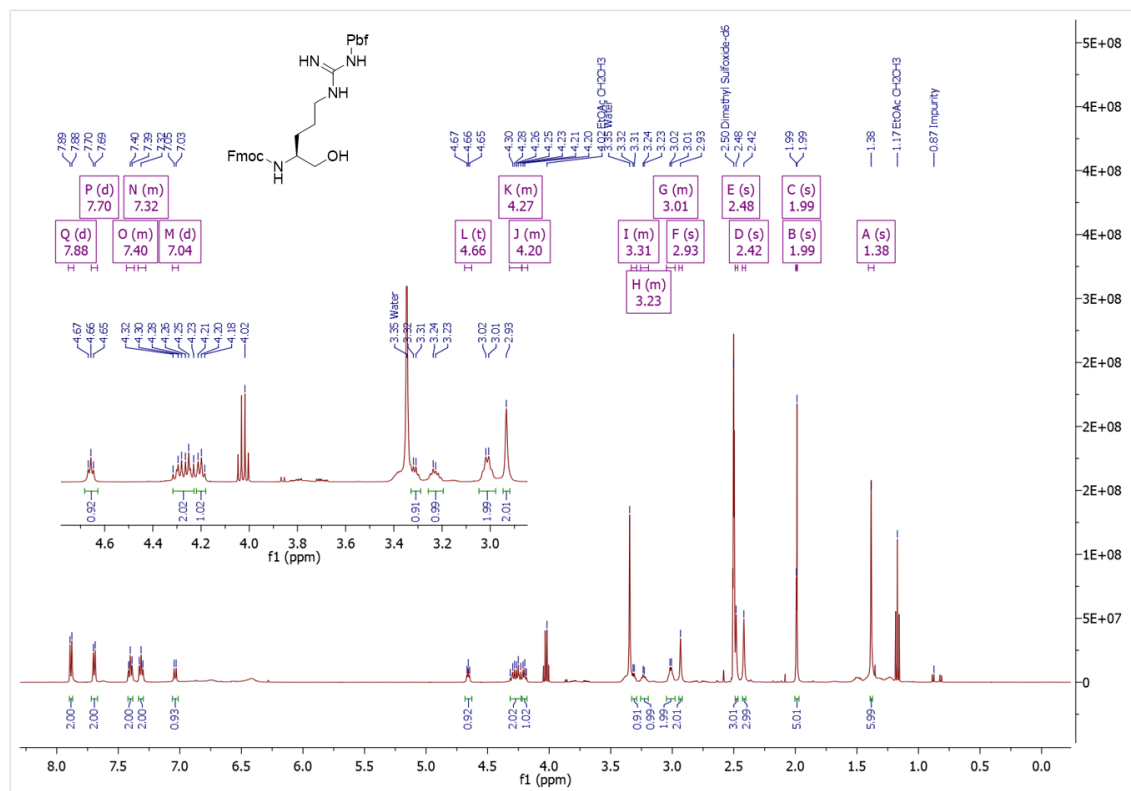
Figure S4.94: ¹H NMR spectrum of **Fmoc-Arg(Pbf)-ψ[CH₂OH] (4.12b)** in DMSO-d₆.
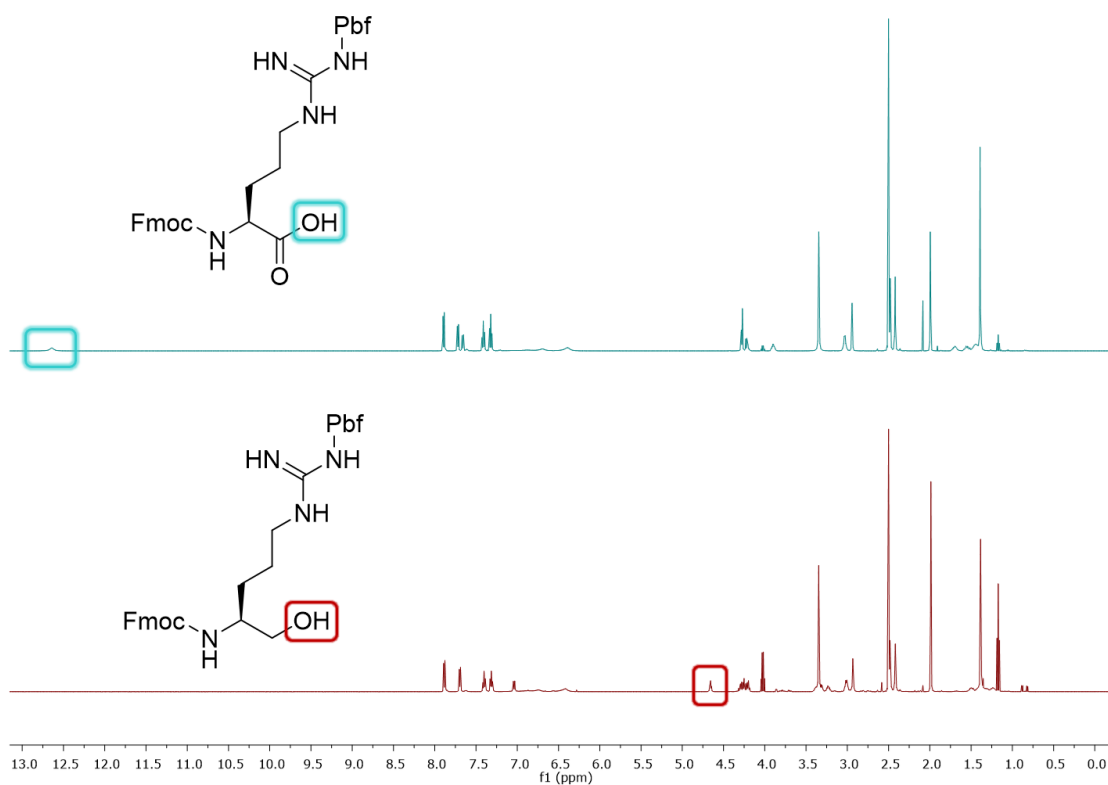
Figure S4.95: ^{1}H NMR spectra of (Top) Fmoc-Arg(Pbf)-OH starting material (**4.12a**), and (Bottom) β-amnio alcohol **Fmoc-Arg(Pbf)-ψ[CH$_2$OH] (4.12b)** in DMSO-d_6.
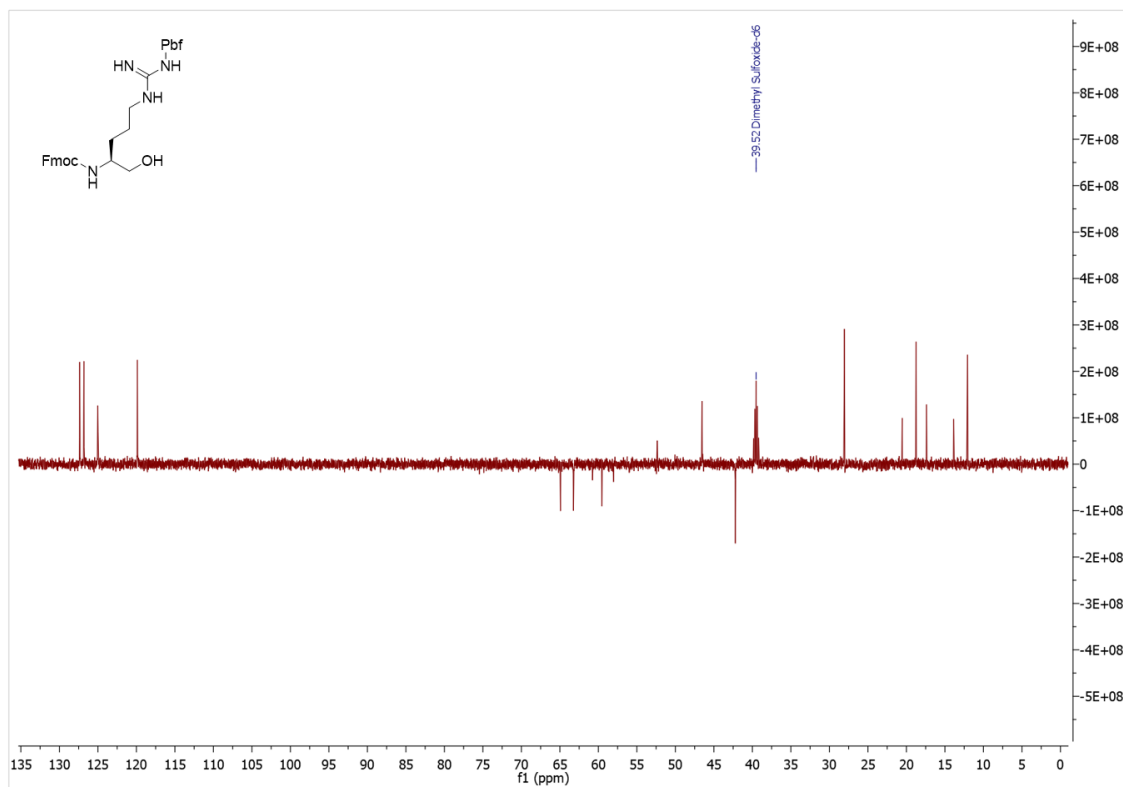
Figure S4.96: DEPT 135 spectrum of **Fmoc-Arg(Pbf)-ψ[CH$_2$OH] (4.12b)** in DMSO-d_6.
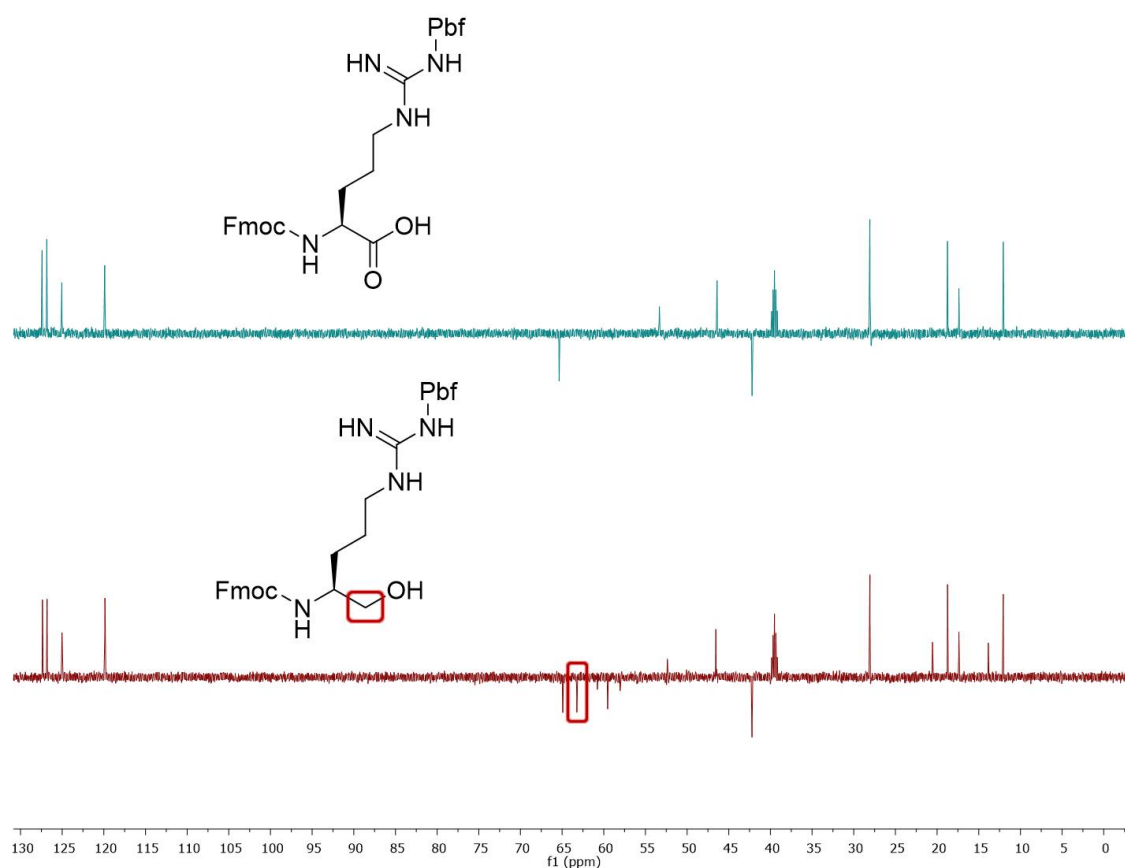
Figure S4.97: DEPT 135 spectra of (Top) Fmoc-Arg(Pbf)-OH starting material (**4.12a**), and (Bottom) β-amnio alcohol **Fmoc-Arg(Pbf)-ψ[CH$_2$OH] (4.12b)** in DMSO-d_6.
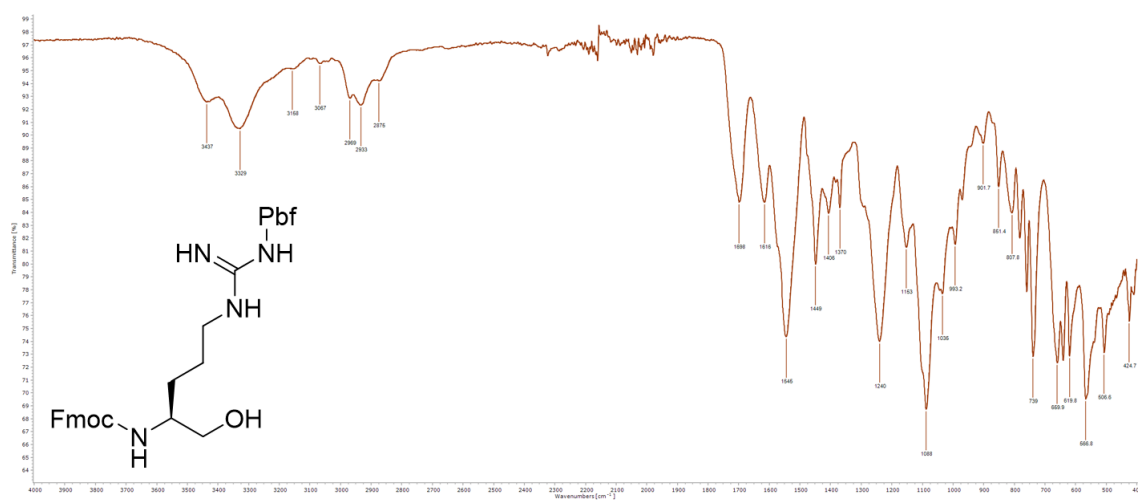
Figure S4.98: FTIR-ATR spectrum of **Fmoc-Arg(Pbf)-ψ[CH$_2$OH] (4.12b)**.
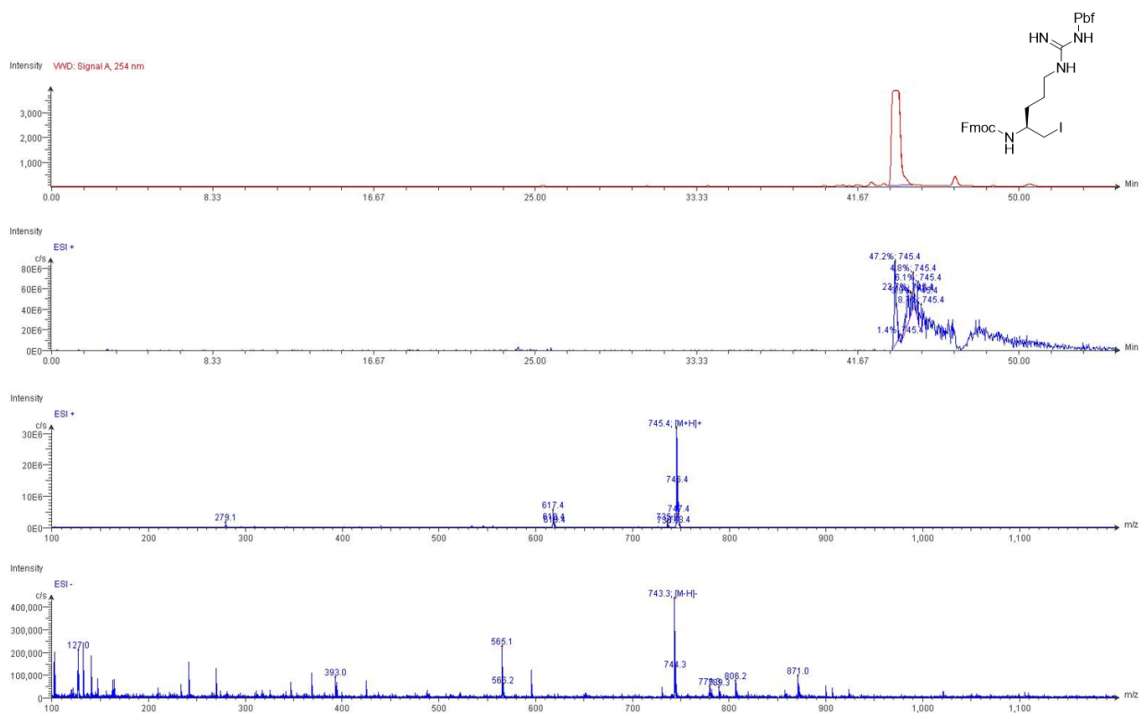
Figure S4.99: LC-MS data for **Fmoc-Arg(Pbf)-*ψ*[CH₂I] (4.12c)**.
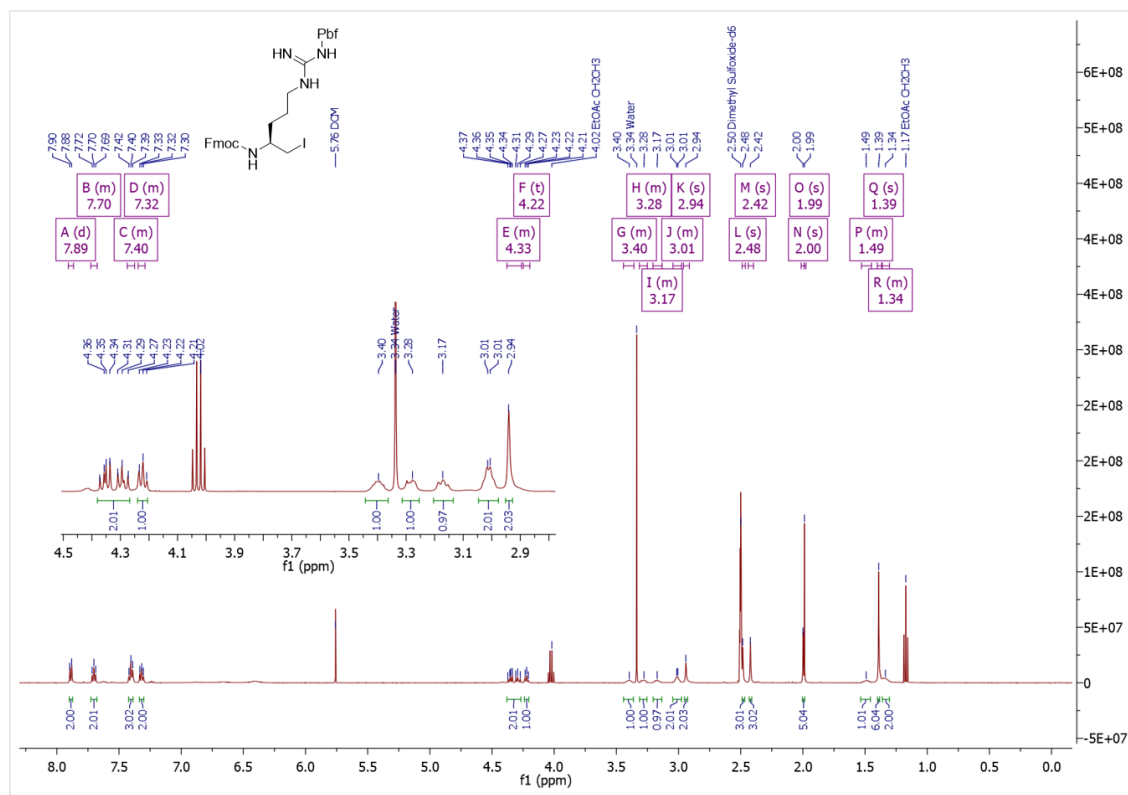
Figure S4.100: ^{1}H NMR spectrum of **Fmoc-Arg(Pbf)-*ψ*[CH₂I] (4.12c)** in DMSO-d_6.
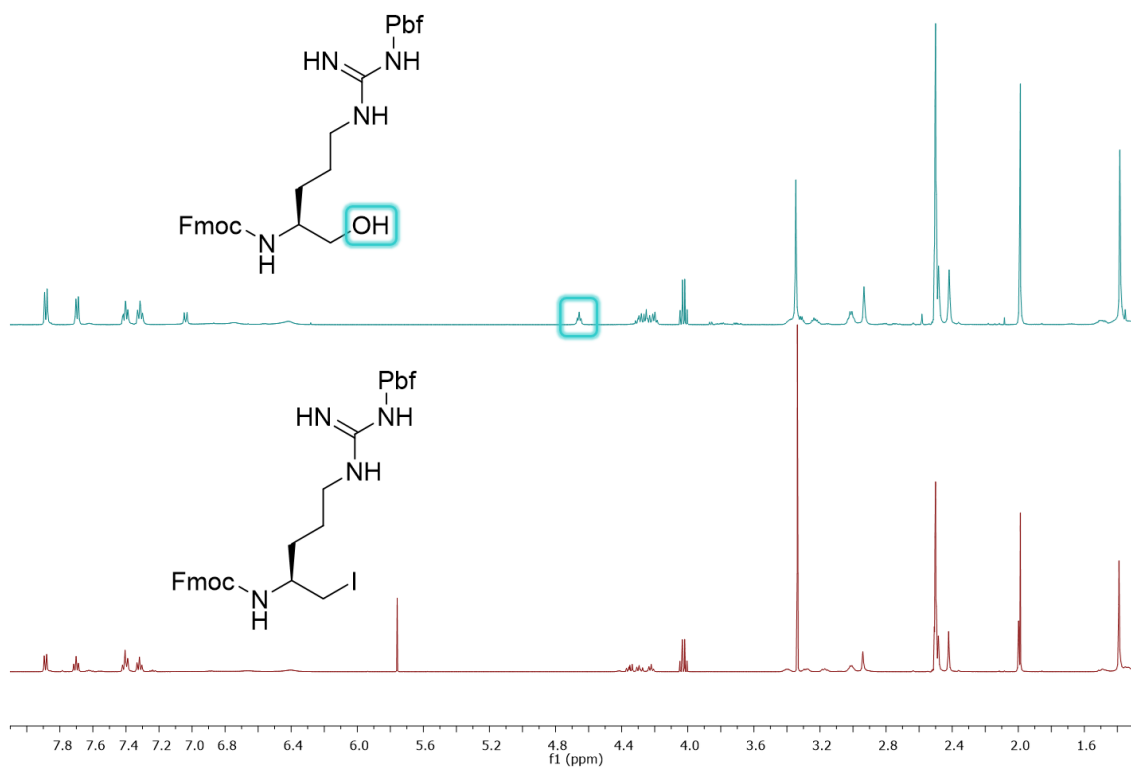
Figure S4.101: ¹H NMR spectra of (Top) Fmoc-Arg(Pbf)-ψ[CH₂OH] starting material (**4.12b**), and (Bottom) β-amnio iodide **Fmoc-Arg(Pbf)-ψ[CH₂I] (4.12c)** in DMSO-d₆.
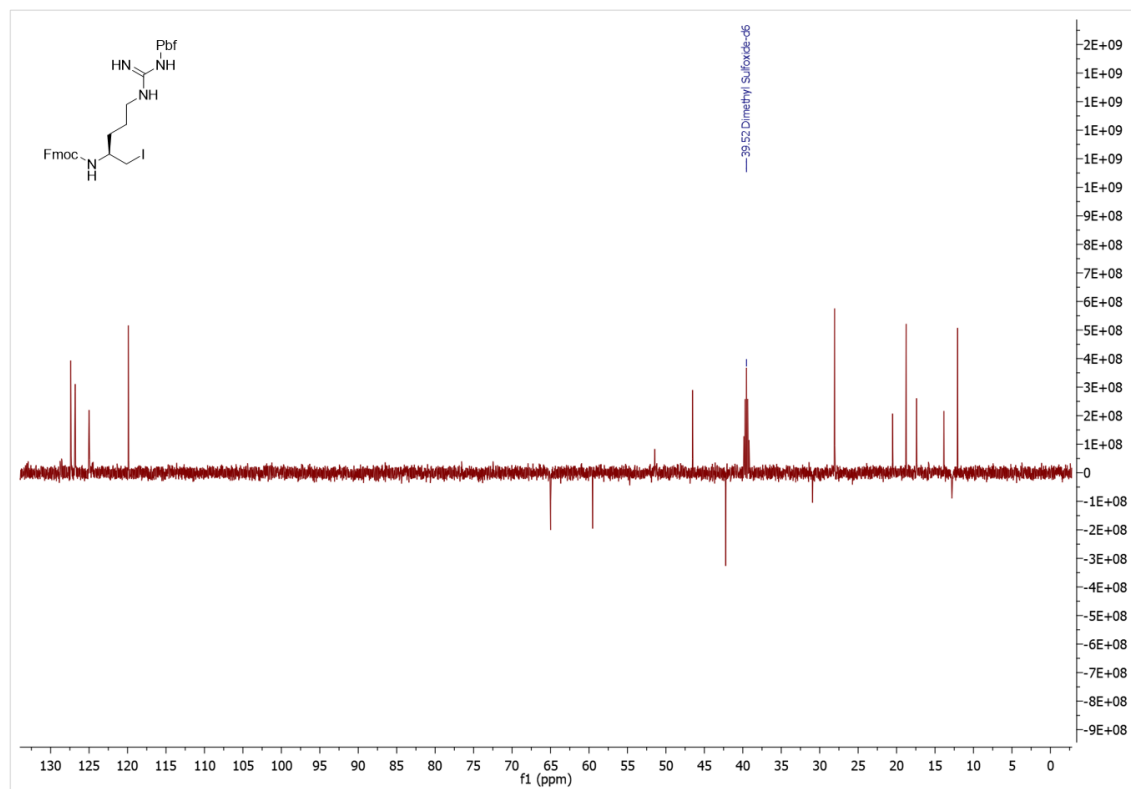
Figure S4.102: DEPT 135 spectrum of **Fmoc-Arg(Pbf)-ψ[CH₂I] (4.12c)** in DMSO-d₆.
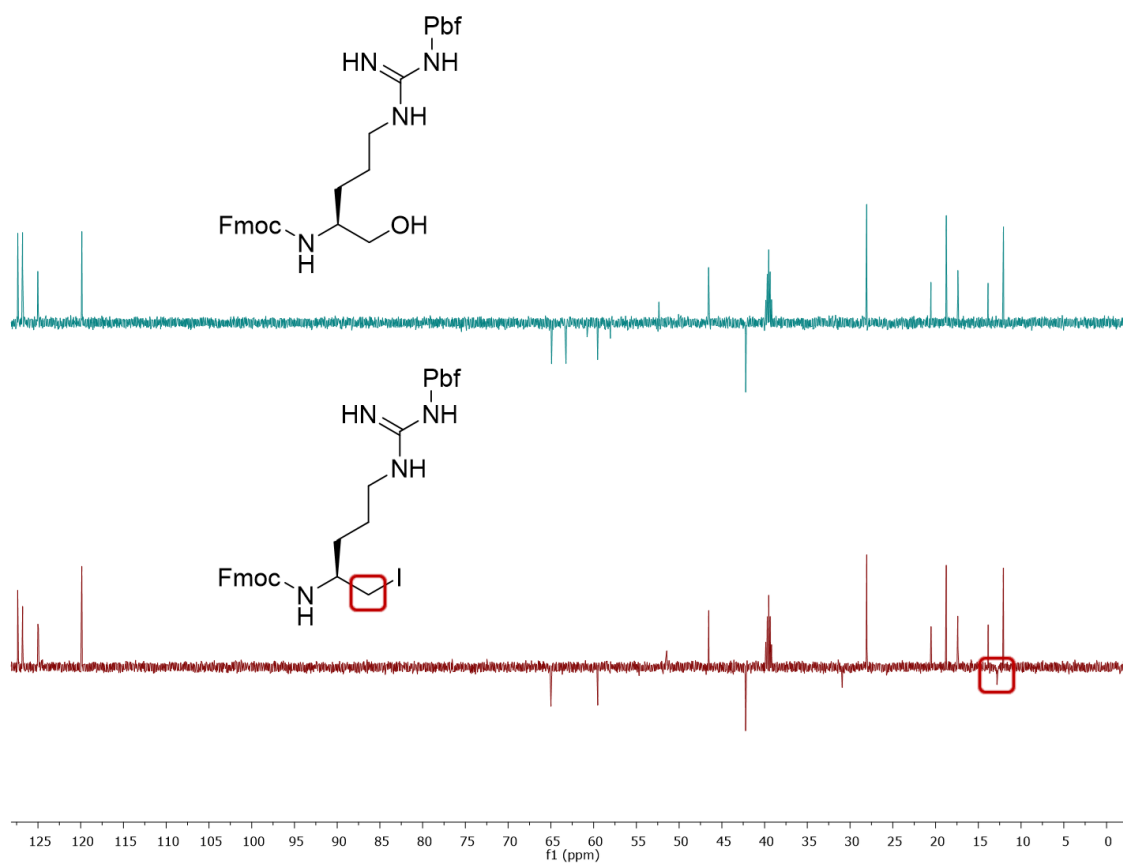
Figure S4.103: DEPT 135 spectra of (Top) Fmoc-Arg(Pbf)-ψ[CH$_2$OH] starting material (**4.12b**), and (Bottom) β-amnio iodide **Fmoc-Arg(Pbf)-ψ[CH$_2$I] (4.12c)** in DMSO-d_6.
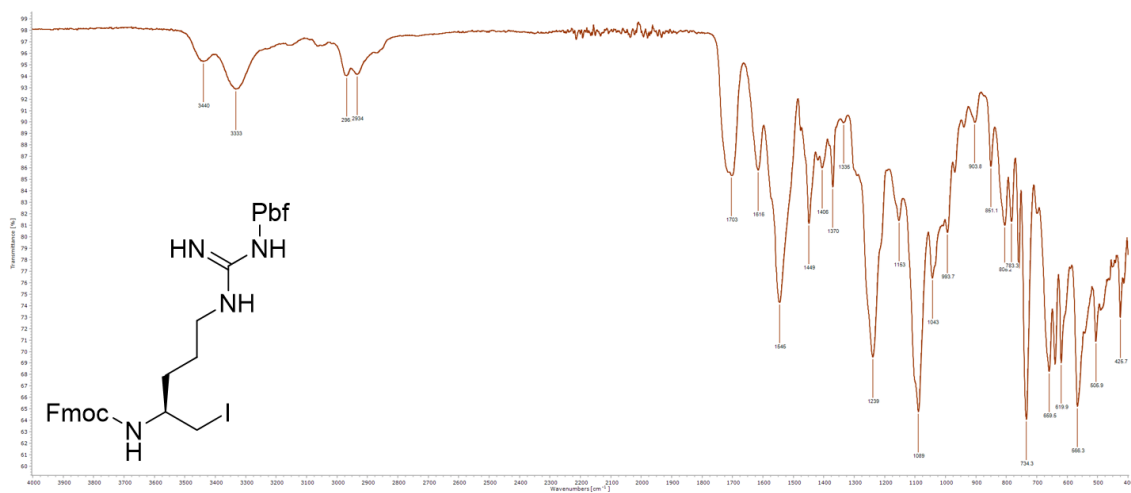
Figure S4.104: FTIR-ATR spectrum of **Fmoc-Arg(Pbf)-ψ[CH$_2$I] (4.12c)**.
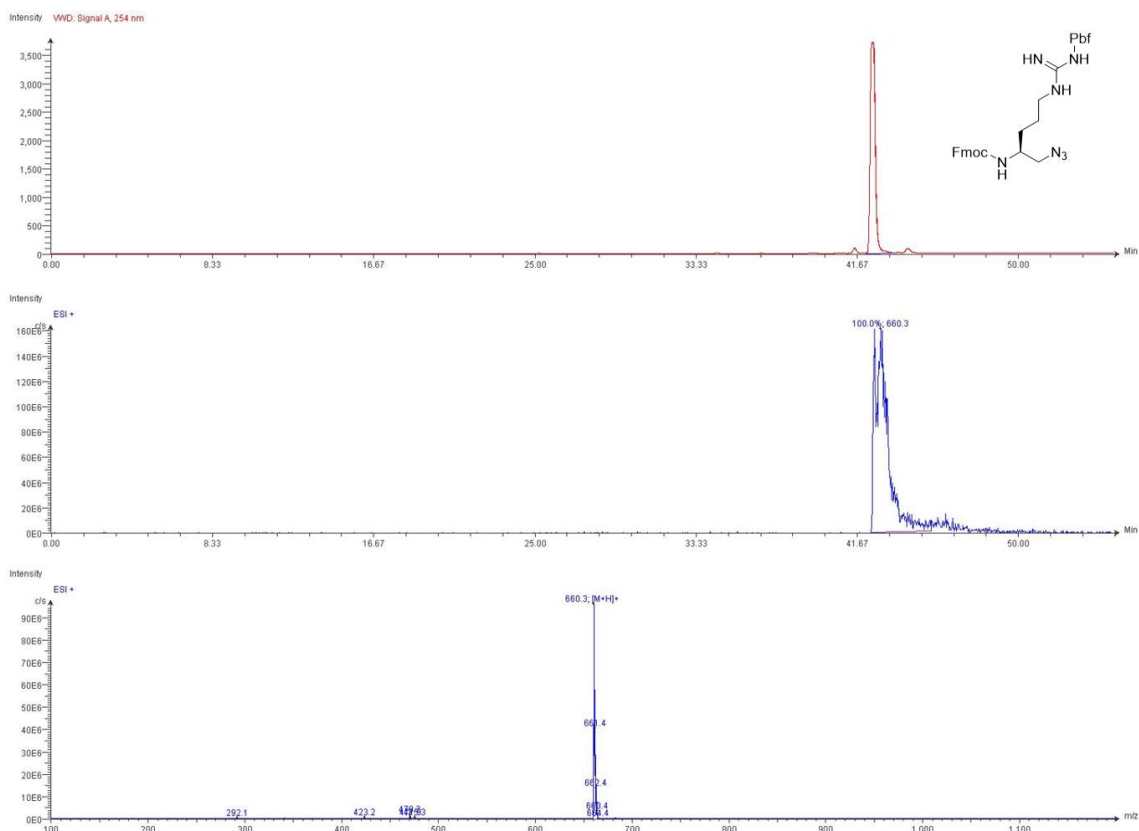
Figure S4.105: LC-MS data for **Fmoc-Arg(Pbf)-ψ[CH₂N₃] (4.12d)**.
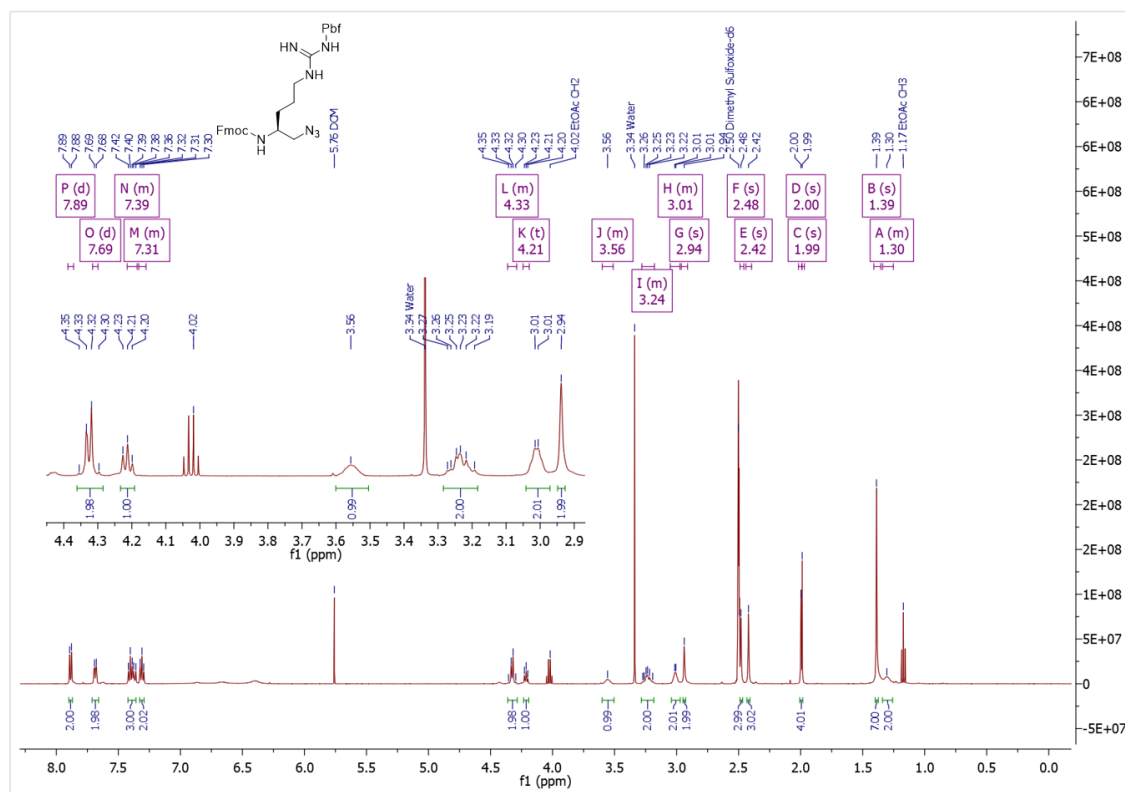
Figure S4.106: ¹H NMR spectrum of **Fmoc-Arg(Pbf)-ψ[CH₂N₃] (4.12d)** in DMSO-d_6.
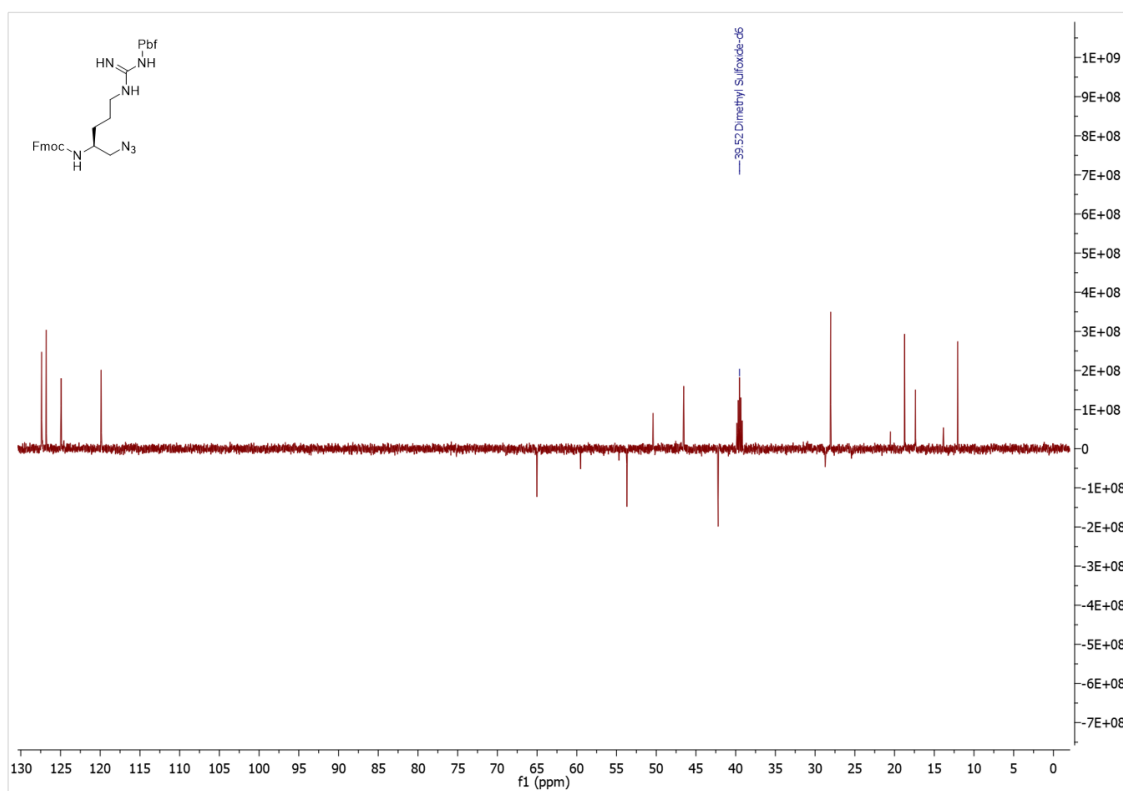
**Figure S4.107:** DEPT 135 spectrum of **Fmoc-Arg(Pbf)-ψ[CH₂N₃] (4.12d)** in DMSO-d_6.
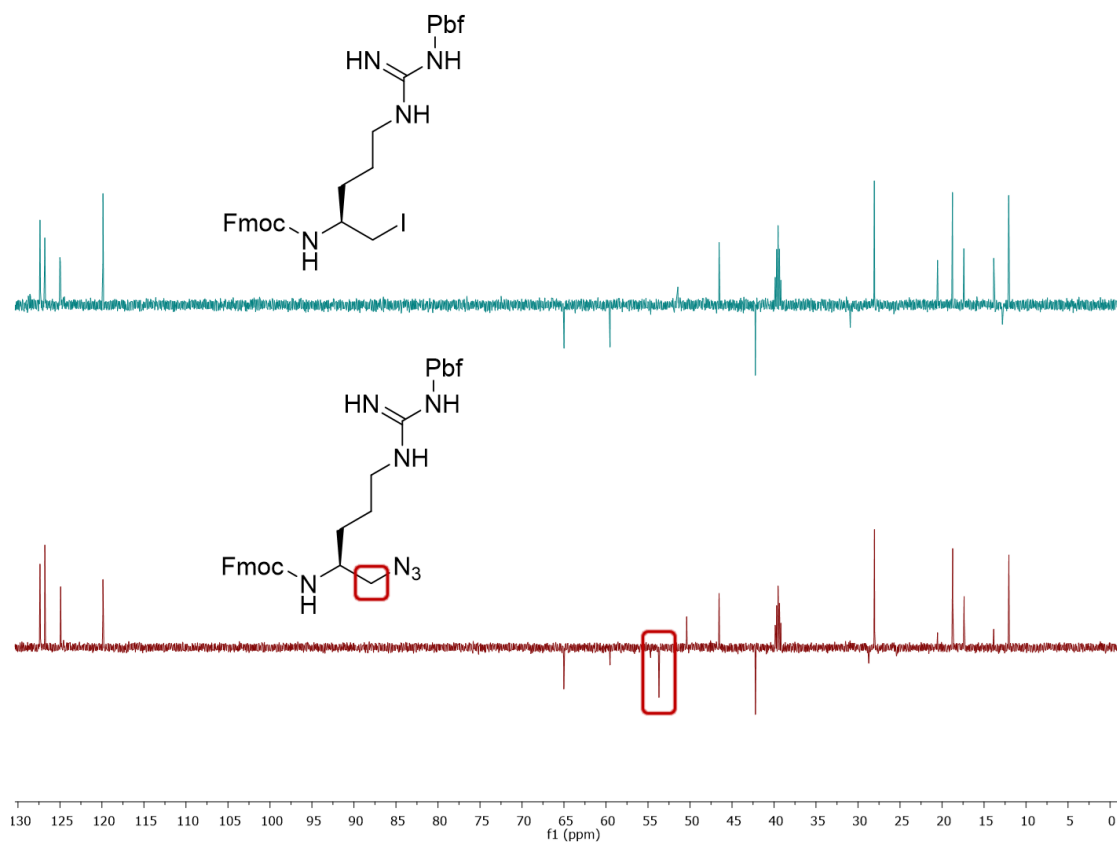
**Figure S4.108:** DEPT 135 spectra of (Top) Fmoc-Arg(Pbf)-ψ[CH₂I] starting material (**4.12c**), and (Bottom) alkyl-azide **Fmoc-Arg(Pbf)-ψ[CH₂N₃] (4.12d)** in DMSO-d_6.
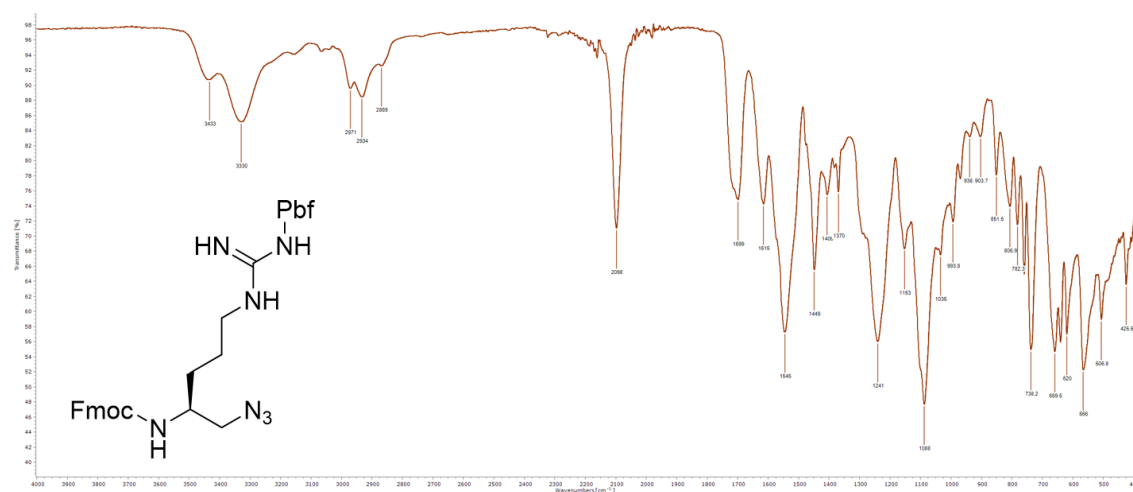
Figure S4.109: FTIR-ATR spectrum of **Fmoc-Arg(Pbf)-ψ[CH$_2$N$_3$] (4.12d)**.
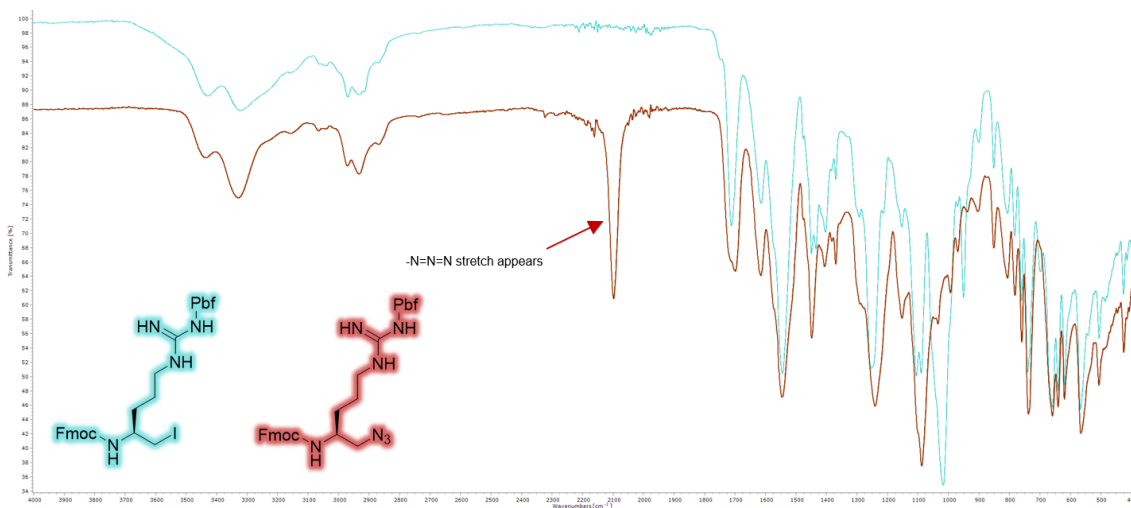
Figure S4.110: FTIR-ATR spectra of (Top) Fmoc-Arg(Pbf)-ψ[CH$_2$I] starting material (**4.12c**), and (Bottom) alkyl-azide **Fmoc-Arg(Pbf)-ψ[CH$_2$N$_3$] (4.12d)**.
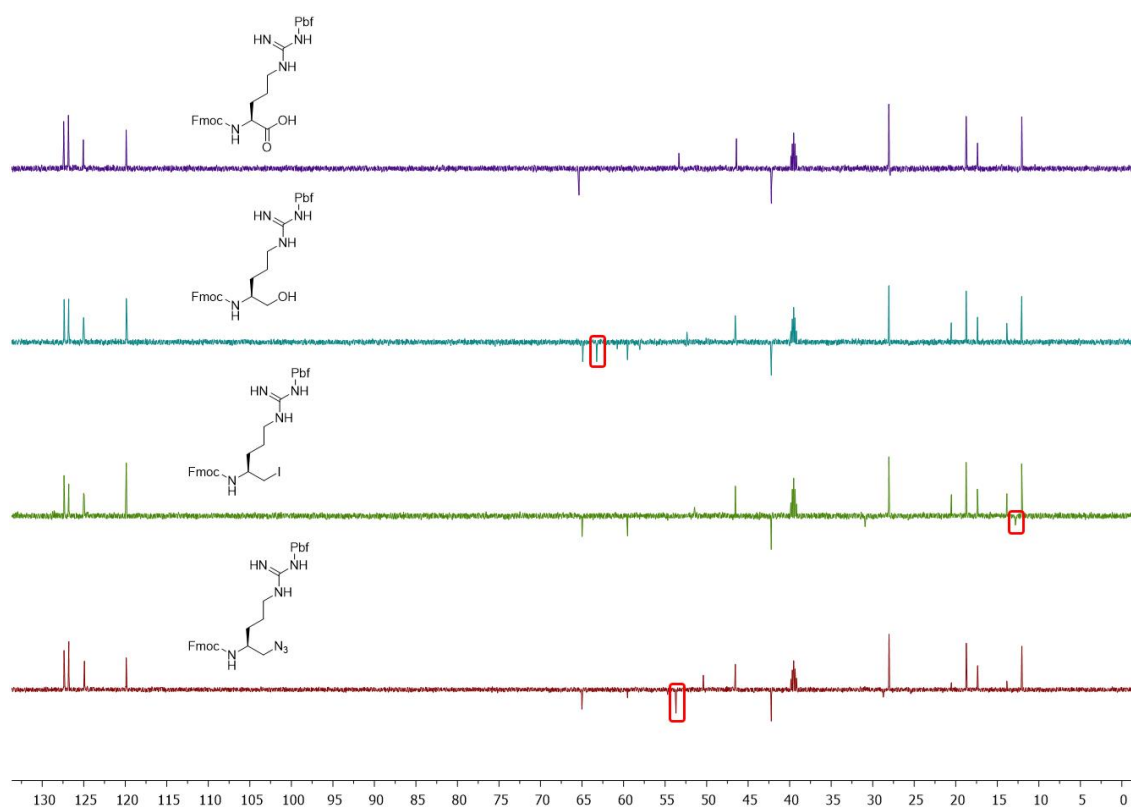
Figure S4.111: DEPT 135 comparison of the different β^*-CH$_2$ chemical shifts, from the Fmoc-Arg(Pbf)-OH starting material (purple) to the alkyl-azide (red).
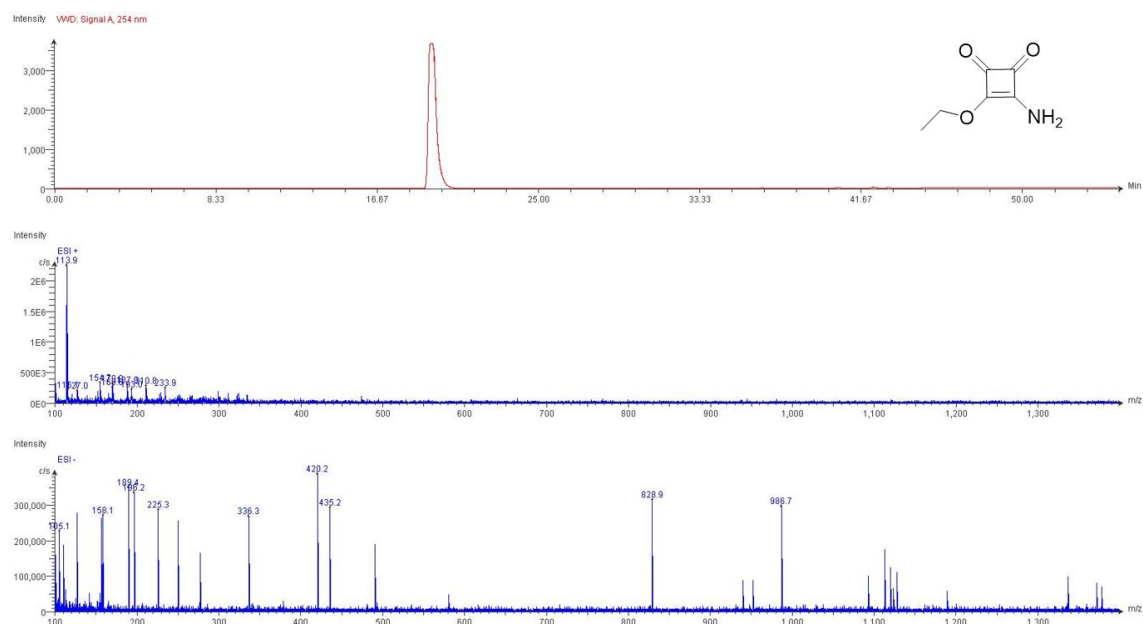
Figure S4.112: LC-MS data for **Amino squarate (ASq, 4.0a)**.
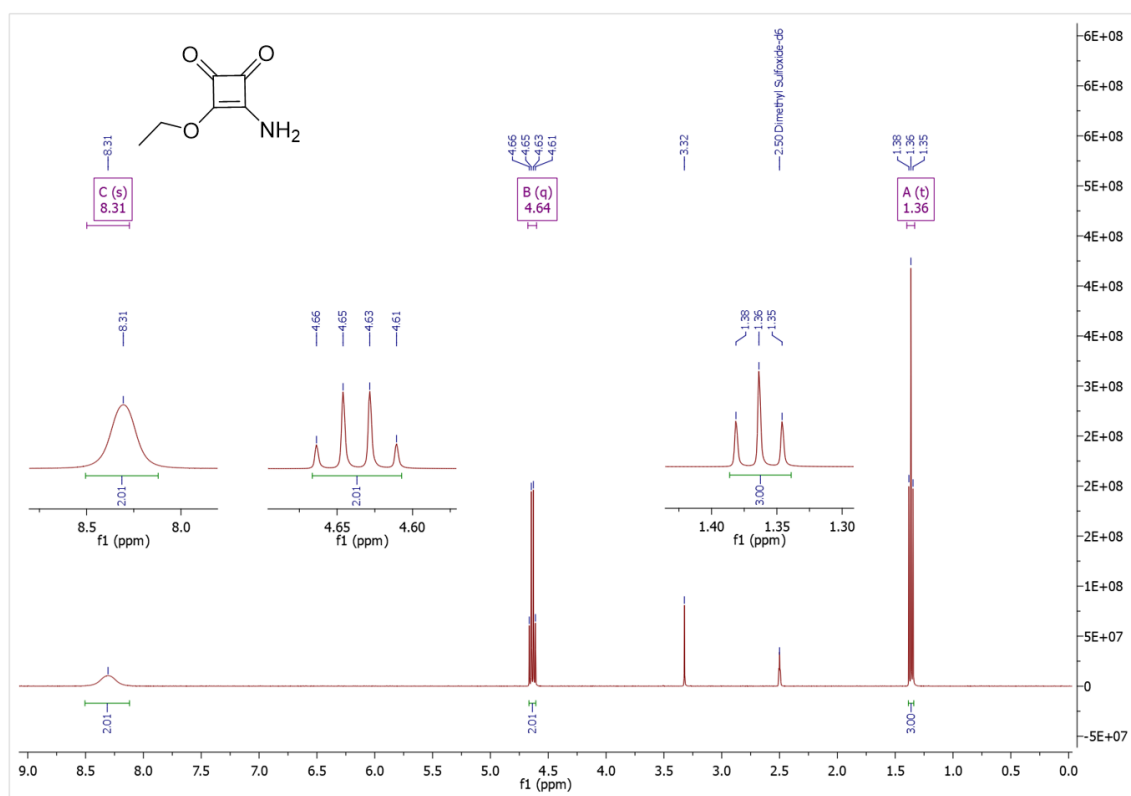
Figure S4.113: ^{1}H NMR spectrum of **Amino squarate (ASq, 4.0a)** in DMSO-d_6.
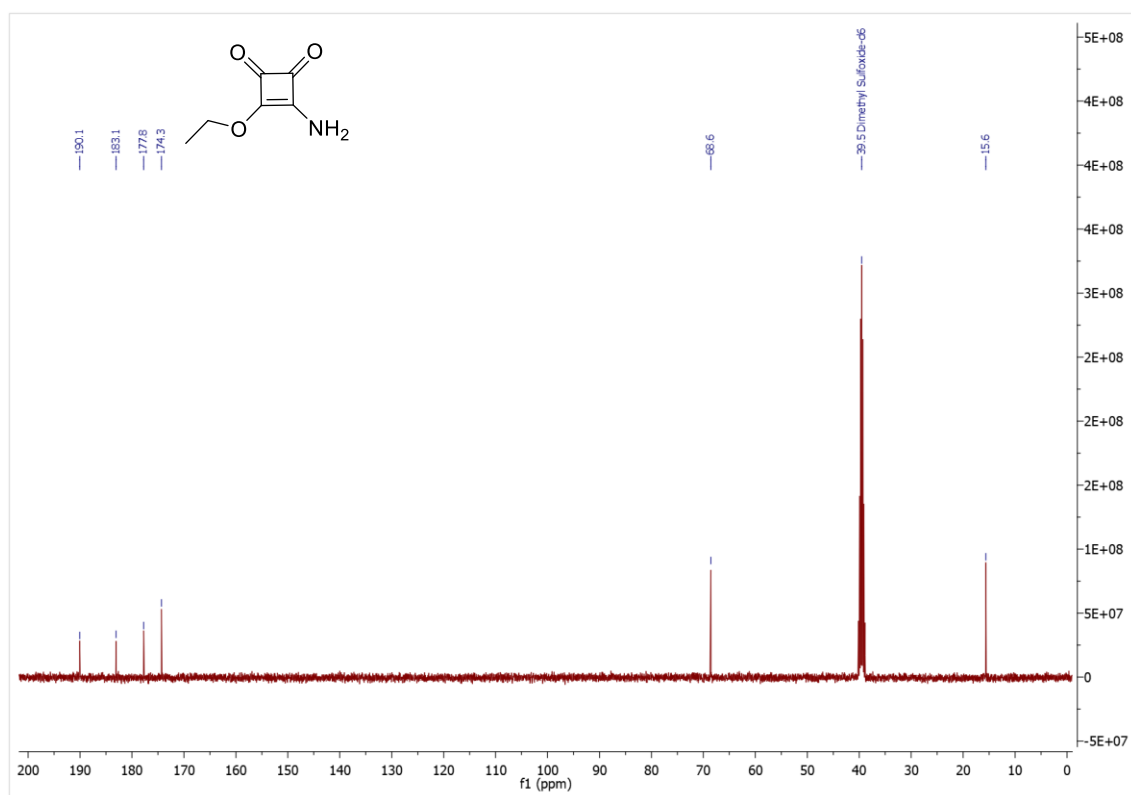
Figure S4.114: ^{13}C NMR spectrum of **Amino squarate (ASq, 4.0a)** in DMSO-d_6.
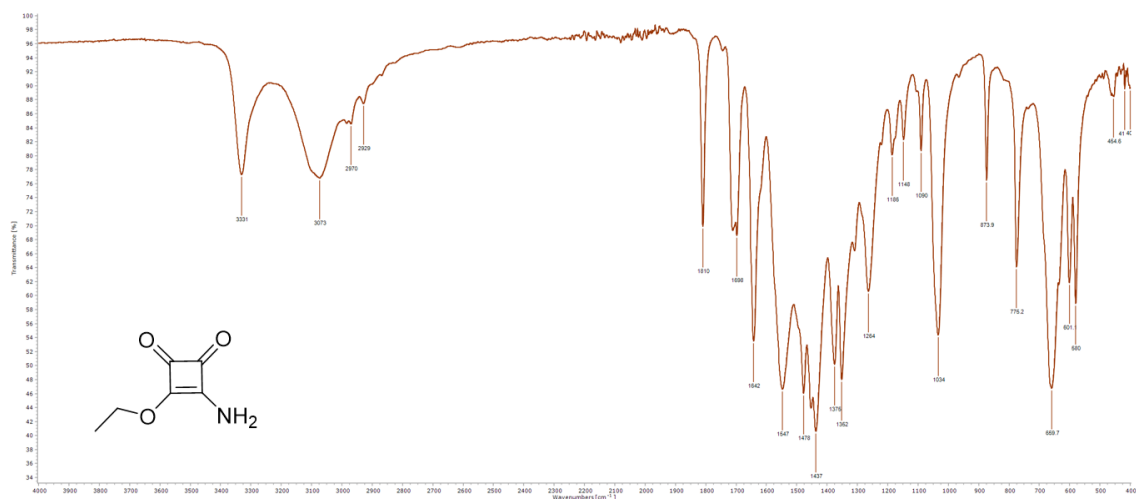
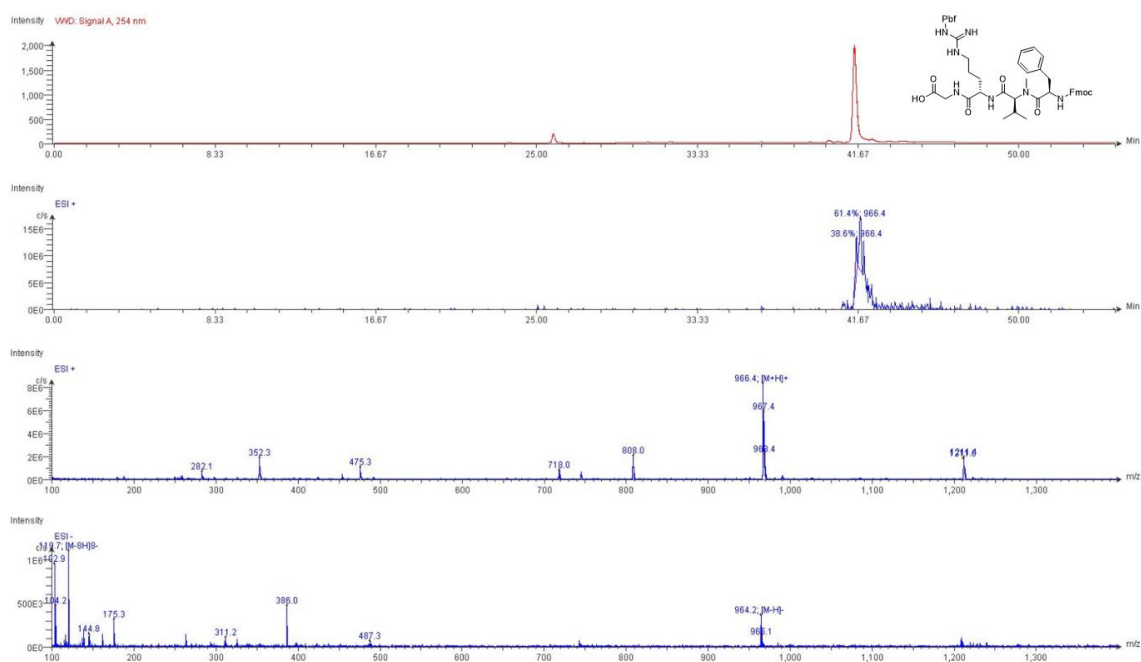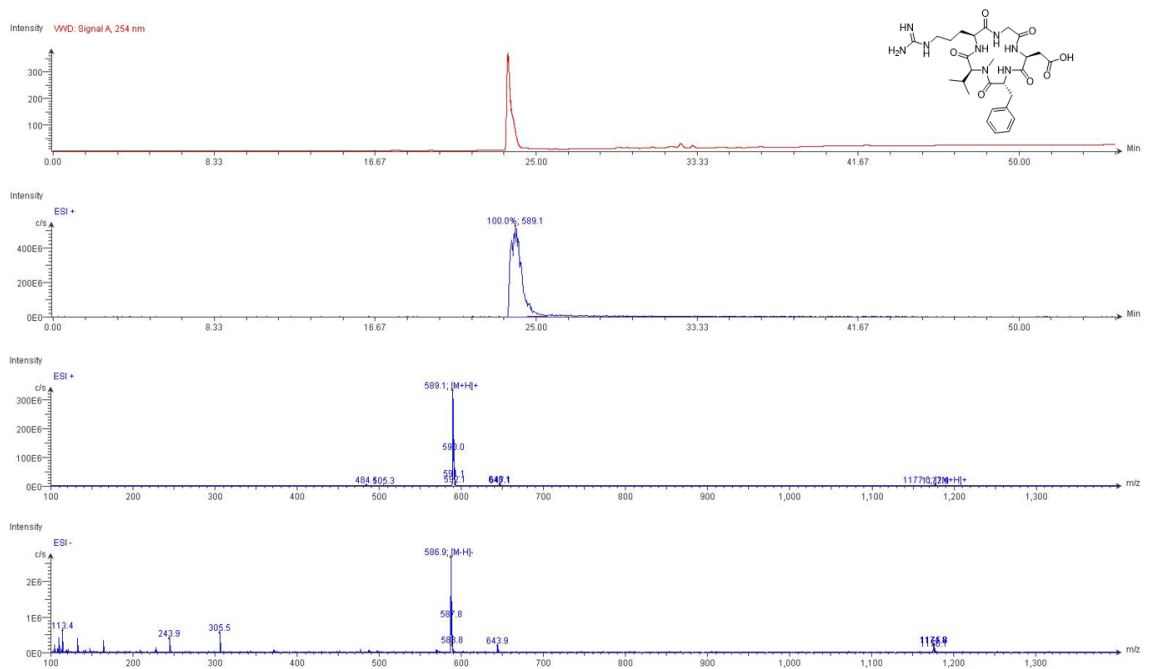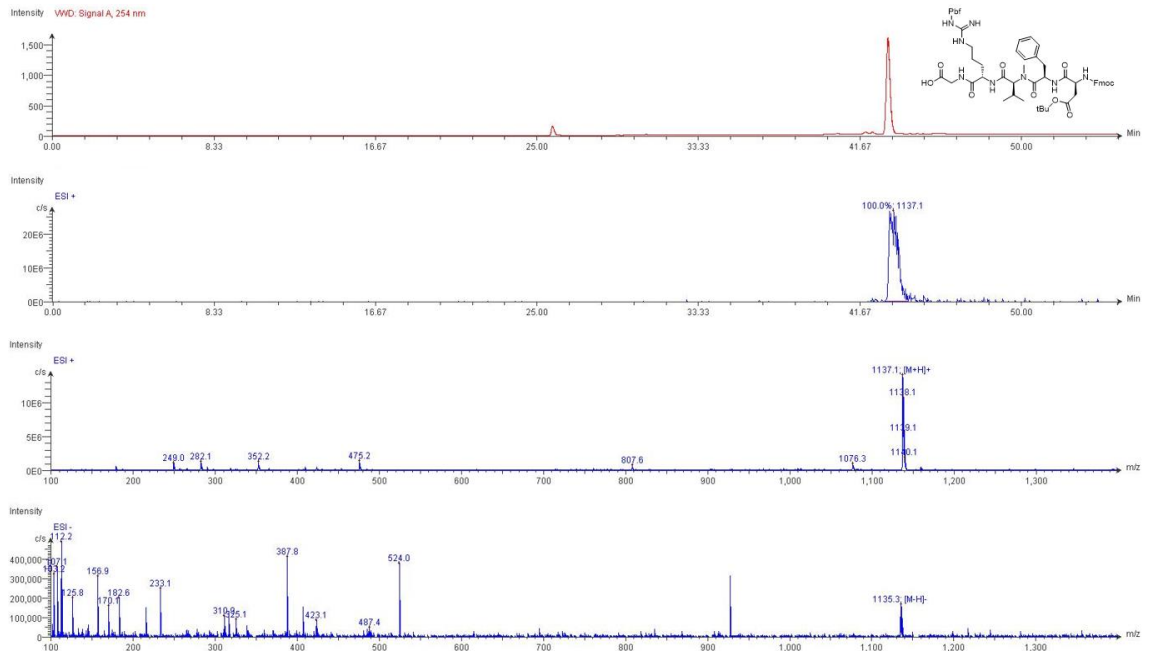**Figure S4.115:** FTIR-ATR spectrum of **Amino squarate (ASq, 4.0a)**.

Figure S4.116: LC-MS data for **Fmoc-f-*N*MeV-R(Pbf)-G-OH**.

Figure S4.117: LC-MS data for **Fmoc-D(O*t*Bu)-f-*N*MeV-R(Pbf)-G-OH**.

Figure S4.118: LC-MS data for ***c*RGDf*N*MeV – Cilengitide.**

Fin